SOLASE-H, A Laser Fusion Hybrid Study

R.W. Conn, S.I. Abdel-Khalik, G.A. Moses, G.W. Cooper,
J.E. Howard, G.L. Kulcinski, E. Larsen, C.W. Maynard,
M. Ragheb, I.N. Sviatoslavsky, W.F. Vogelsang, W.G. Wolfer,
M. Ortman, D. Smatlak, R. Watson, and M. Youssef

May 1979
(revised October 1979)

UWFDM-270

FUSION TECHNOLOGY INSTITUTE

UNIVERSITY OF WISCONSIN

MADISON WISCONSIN

SOLASE-H, A Laser Fusion Hybrid Study

R.W. Conn, S.I. Abdel-Khalik, G.A. Moses, G.W. Cooper, J.E. Howard, G.L. Kulcinski, E. Larsen, C.W. Maynard, M. Ragheb, I.N. Sviatoslavsky, W.F. Vogelsang, W.G. Wolfer, M. Ortman, D. Smatlak, R. Watson, and M. Youssef

Fusion Technology Institute
University of Wisconsin
1500 Engineering Drive
Madison, WI 53706

http://fti.neep.wisc.edu

May 1979 (revised October 1979)

UWFDM-270

SOLASE-H

A LASER FUSION HYBRID STUDY

R.W. Conn
S.I. Abdel-Khalik
G.A. Moses
G.W. Cooper*
J.E. Howard
G.L. Kulcinski
E. Larsen
C.W. Maynard
M.M.H. Ragheb
I.N. Sviatoslavsky
W.F. Vogelsang
W.G. Wolfer
M. Ortman
D.L. Smatlak
R. Watson
M.Z. Youssef

Fusion Engineering Program
Nuclear Engineering Department
University of Wisconsin
Madison WI 53706 U.S.A.

May 1979

Revised October 1979

UWFDM-270

*Presently at University of New Mexico

"LEGAL NOTICE"

"This work was prepared by the University of Wisconsin as an account of work sponsored by the Electric Power Research Institute, Inc. ("EPRI"). Neither EPRI, members of EPRI, the University of Wisconsin, nor any person acting on behalf of either:

"a. Makes any warranty or representation, express or implied, with respect to the accuracy, completeness, or usefulness of the information contained in this report, or that the use of any information, apparatus, method, or process disclosed in this report may not infringe privately owned rights; or

"b. Assumes any liabilities with respect to the use of, or for damages resulting from the use of, any information, apparatus, method or process disclosed in this report."

TABLE OF CONTENTS

I. SUMMARY, CONCLUSIONS AND OVERVIEW OF SOLASE-H

I.1. INTRODUCTION

The ultimate energy release per D-T fusion reaction can be greatly increased if the 14.1 MeV fusion neutron is used to breed fissile fuel in addition to breeding the tritium that is required for closing the fusion fuel cycle. The subsequent burning of the fissile atom releases approximately 200 MeV as compared to the 20 MeV typically produced by a single fusion reaction. This energy (or power) multiplication amplifies the impact of D-T fusion in the future energy production scenario. This impact comes from the greater power production per unit of fusion power and from the possibility of introducing these fusion hybrid reactors sooner than might be possible for pure fusion systems. In addition, the total energy per fusion reaction is so much greater in fusion-fission hybrid systems that the fusion hybrid reactor can have a cost higher than that for fusion electric power and still be economically feasible in the context of the entire energy producing system. Furthermore, the fusion performance parameters (both fusion energy gain and recirculating power fraction) can be relaxed in fusion hybrid reactors while still maintaining good economic performance. This adds to the potential for early introduction.

The technology development required for fusion-fission hybrids can draw heavily from current and future fission reactor experience, and we have used this as a guideline for this study. As an example, in the design reported here, we have used zircaloy as the structural material, employed oxide fuel, and chosen LWR fuel bundles as the fuel configuration. Clearly, any hybrid reactor scenario relies on fission reactors to produce the majority of the power. A fusion-fission hybrid reactor can support two to fifty thermal fission reactors depending upon the assumption made about hybrid blanket design, conversion ratio in the fission reactor, and the decision on whether

to reprocess the spent fission reactor fuel. This is a positive result, since fission reactors currently operate with a good performance record and produce about 13% of this nation's electric power. On the other hand, the hybrid suffers from the same criticisms that have been directed toward the fission reactor industry, particularly with regard to the fuel cycle. The question of reprocessing spent reactor fuel has raised the issue of proliferation and increased interest in the development of fuel cycles resistant to diversion.

Any study of fusion-fission hybrids, with their early introduction potential, must address these political and social issues as well as the very difficult technical ones. There has been much work on fusion-fission hybrids[1-7] and many have been related to a particular fusion system (tokamak, mirror, laser fusion, etc.). Most studies have assumed that the fissile fuel produced in the hybrid must be reprocessed before loading into the fission reactor core although there have been a few which examined the direct loading of bred fuel into the fission reactor.[4,8] If reprocessing in necessary, then the hybrid fuel cycle faces many of the same considerations that plague the fast breeder reactor program today.

In light of these concerns, it is important to address the following questions:

- CAN THE HYBRID REACTOR PLAY ANY ROLE IN A NUCLEAR FUTURE THAT DOES NOT ALLOW REPROCESSING OF THE FISSION FUEL IN THE NEAR TERM?
- CAN A HYBRID FUEL CYCLE THAT IS DIVERSION RESISTANT BE ESTABLISHED?
- WHAT PENALTY IN PERFORMANCE DOES ONE PAY FOR A HYBRID FUEL CYCLE THAT DOES NOT INCLUDE REPROCESSING?

These questions form the context into which the SOLASE-H laser fusion hybrid study has been cast. SOLASE-H is an integrated study of the important subsystems that make up a laser fusion hybrid reactor. Many of the reactor design ideas are a carryover from the SOLASE laser fusion conceptual reactor design.[9] The emphasis in SOLASE-H is on parametric analysis of five important subsystems. These include:

(1) The fission fuel cycle;

(2) Hybrid blanket design;

(3) Fusion performance;

(4) Laser design;

(5) Cavity, first wall, and mechanical design.

Some attention is given to the coupling of these subsystems to assure that the attractive parts of parameter space in each area will actually overlap one another. These analyses have been constrained by the desire to use technology assumptions that are consistent with early introduction of the hybrid.

In the following sections, a technical summary of each of the five subsystems is given. Section I.3.G is a description of the integrated SOLASE-H hybrid reactor design with a set of consistent parameters. In the following part of this introductory section, the conclusions of the SOLASE-H study are presented.

I.2 CONCLUSIONS OF THE SOLASE-H STUDY

I.2.A GENERAL

The SOLASE-H laser fusion hybrid study investigates the potential of directly enriching light water reactor (LWR) fuel assemblies in the hybrid blanket with direct transfer to the LWR without intermediate reprocessing. From these blanket design studies, several conclusions can be made regarding this fuel cycle:

1. Without reprocessing the spent LWR fuel, the direct enrichment hybrid has the potential to fuel 2 LWRs of equivalent thermal power with 4% enriched ^{233}U fuel assemblies. This low support ratio makes the system economics very sensitive to the cost of the hybrid reactor.

2. The direct enrichment of the LWR assemblies renders them highly radioactive. When transported in this radioactive state, they can be considered to meet demands for proliferation resistance.

3. When reprocessing of the LWR fuel is allowed, the SOLASE-H hybrid concept has the potential to fuel about 8 LWRs of equivalent thermal power with 4% enriched ^{233}U fuel. The increase of the support ratio reduces the sensitivity of system economics to the hybrid cost.

4. The SOLASE-H direct enrichment hybrid produces about 0.75 kg of $^{233}U/MW_t$-year. This is to be compared to 1-2 kg of $^{233}U/MW_t$-year produced in a hybrid that does not have the constraint of enriching fuel in the form of LWR assemblies. Hence, the fuel production rate is about a factor of two less in the direct enrichment approach than it would be if reprocessing of the hybrid fuel were allowed.

5. The time that is necessary to reach 4% enrichment is about two and a half years of continuous operation at a fusion power of approximately 1200 MW. It is assumed that only 70% of this power is in the form of 14.1 MeV neutrons. Thus, for characteristic values of fusion power and required fuel enrichment, the time to directly produce enriched LWR fuel in bundles is a reasonable time period (2.5-4 years).

I.2.B PARAMETRIC BLANKET DESIGN STUDIES

Blanket designs have been optimized to breed fissile fuel without subsequent fissioning subject to the constraint that the tritium breeding ratio, TBR, be larger than one. The SOLASE-H cavity and blanket is a right circular cylinder as shown in Fig. I.2-1. The end caps of the cylinder (axial blankets) are devoted to breeding only tritium, while the radial blanket is used for breeding both ^{233}U and tritium. Hence, the tritium breeding ratio in the radial blanket is actually less than one. The blanket-structural material is zircaloy, and the fuel is arranged in an LWR configuration. Choices for coolant are water, helium gas, liquid lithium, and liquid sodium. Lithium, except when properly placed, absorbs neutrons too strongly, and water overly moderates the spectrum. Helium gas must be used at high pressure. Sodium is an excellent coolant that can be used at low pressure and has been selected. Several design features have been evaluated parametrically for the radial blanket and the conclusions of these studies follow.

1. An efficient fast neutron flux trap can be created by surrounding the Na cooled fuel assemblies with pins of Li cooled by Na. Lithium poisons the thermal flux and reduces the fission rate of the bred ^{233}U. In addition, lithium breeds tritium upon capture of a neutron. The thickness of the Li zones can be tailored to maximize the fissile production rate. In this way, burnup of the fuel can be limited to 4300 MWD/MT while reaching 4% enrichment.

THE SOLASE-H LASER FUSION HYBRID

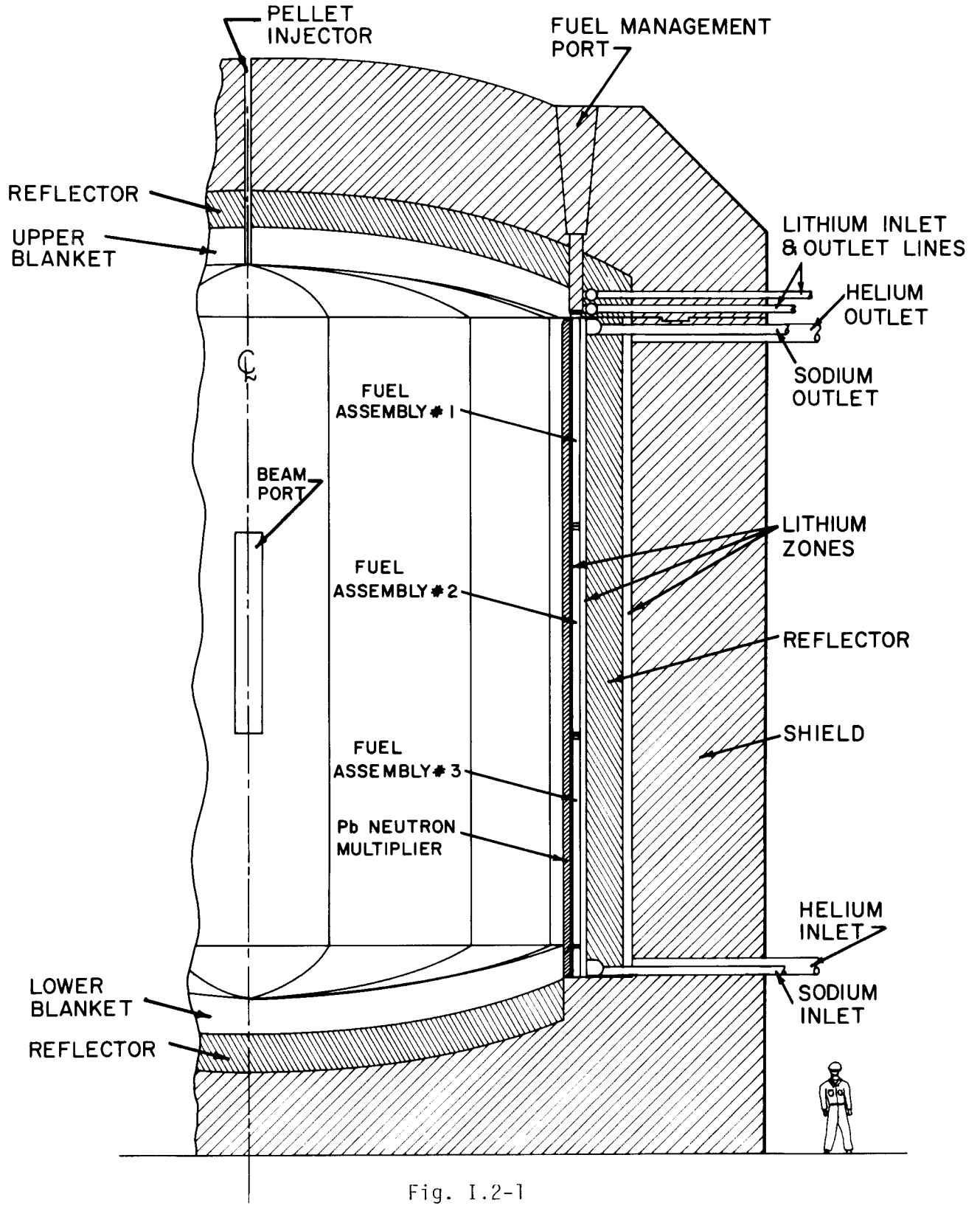

Fig. I.2-1

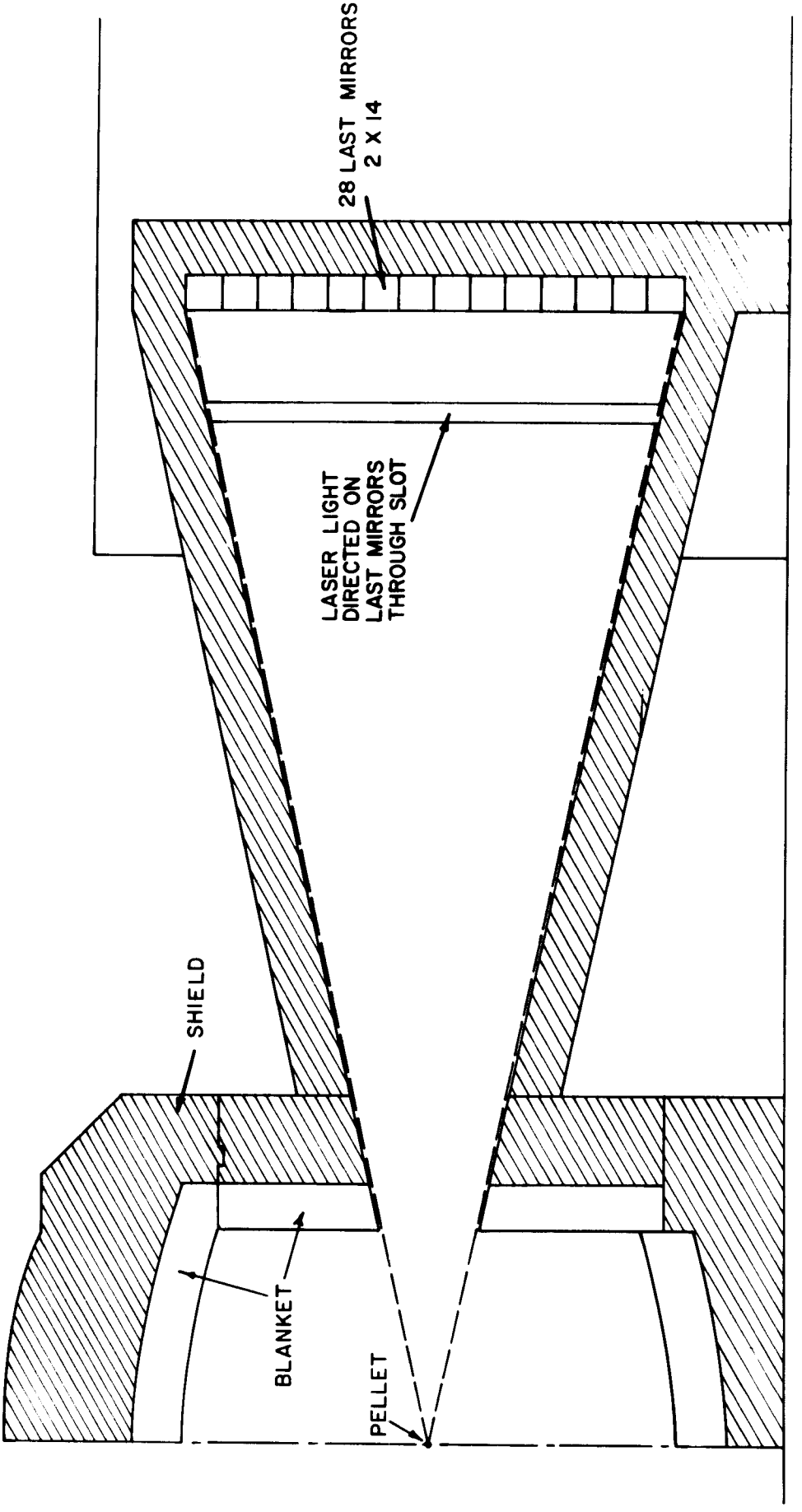
28 LAST MIRRORS
2 X 14
LASER LIGHT
DIRECTED ON
LAST MIRRORS
THROUGH SLOT
SHIELD
BLANKET
PELLET

Fig. I.2-2

2. Creating the flux trap is an important generic design feature. Filtering the thermal flux permits one to produce a flat enrichment profile across the fuel assembly. A figure of merit that minimizes the enrichment nonuniformity and maximizes the average enrichment rate can be defined. With this figure of merit, the optimim design is not the one with the flattest enrichment profile. For the optimum hybrid/LWR system, a penalty will be paid in the fission reactor for a larger hot channel factor.

3. The peak to average enrichment across the assembly for the optimum design is 1.1 with the highest enrichment at the outer edges of the assembly. Thus, the maximum peak to average value of enrichment varies by 10%.

4. LWR fuel is zircaloy clad. The radiation damage accumulated by this cladding in the hybrid is approximately 5 dpa per year per MW/m^2 of 14 MeV neutron wall loading. In the time to reach LWR enrichment, the damage level reaches about 25 dpa. This value is quite reasonable when compared to values of 100 dpa that have been accumulated in fast reactor experience. Since there should be no appreciable radiation damage to the clad in the thermal reactor spectrum, the exposure in the hybrid would seem to be tolerable. Hence, the fuel will experience cladding damage in the hybrid with low fuel burnup and high fuel burnup in the LWR without excessive cladding damage. A firmer conclusion regarding fuel and clad performance must await a complete analysis that includes these effects as an integrated study of the fuel lifetime. Such work is currently in progress.

5. Lead serves as a much better neutron multiplying material for the direct enrichment hybrid than beryllium. Lead does not soften the neutron spectrum as much which leads to a flatter enrichment profile in the fuel assembly without the loss of as many neutrons in the Li filter zones. The optimum thickness of lead multiplier is 10 cm when the volume fraction is 82% and the rest is structure and Na coolant.

6. The flux trap idea can be extended to include the replacement of some fuel assemblies with neutron scattering material such as Pb and C to scatter the neutrons into the remaining fuel assemblies. Three-dimensional Monte Carlo calculations show that this can be done with little impact on the total fissile and tritium breeding per fusion neutron. With the total breeding per fusion neutron nearly the same when half of the fuel is replaced by scattering material, the time to reach a given fuel enrichment can be drastically reduced. It is with this technique that the residence time can be limited to about 2.5 years.

I.2.C FUSION PERFORMANCE PARAMETRIC STUDIES

In the direct enrichment hybrid the blanket multiplication and the fissile breeding ratio are quite low. For these reasons the fusion power must be large in order to make the system attractive. An analysis of fusion performance in hybrids is done in SOLASE-H with particular attention to the problems of the direct enrichment approach. The following observations can be made:

1. To fuel two 700 MW_e LWRs (the same electrical output as the hybrid), about 1200 MW of fusion power is required. This high fusion power makes it difficult to simultaneously relax both the pellet yield and repetition rate in laser fusion systems. The specific choice of parameters will depend upon details of the driver.

2. Power supply costs will dominate the laser economics for hybrids just as they do for pure laser fusion systems if capacitive power supplies are used.

I.2.D HYDROGEN FLUORIDE LASER ASSESSMENT

As part of the SOLASE-H study, an assessment of the hydrogen fluoride laser was done and the following conclusions have been drawn.

1. A 2 MJ HF laser with a shaped pulse (3 ns at peak power of 300 TW) appears to be feasible. This laser can be built from 20 compact 100 kJ final amplifiers.

2. Angular multiplexing can be used to compress the natural HF pulse length of 15 ns down to 3 ns. This requires a total of 56 beams to deliver 2 MJ to the target. A pulse width of 15 ns is generally considered too long for laser fusion target performance but 3 ns should be satisfactory.

3. A total laser efficiency of about 2.5% (including an 80% beam transport efficiency) can be achieved. The electrical efficiency for this system is 25%.

4. The HF laser is likely to be repetition rate limited by chemical reprocessing and laser cavity pumping considerations. Repetition rates of 4-6 Hz are manageable.

I.2.E SUMMARY

In general, the direct enrichment hybrid approach allows the hybrid to have an impact in a nuclear future that does not have LWR fuel reprocessing in the near term. However, this option comes with a seriously degraded breeding performance compared to the application of hybrids with fuel reprocessing. Because the support ratio is low the overall system economics will more sensitively depend upon the cost of the hybrid. Hence, the near term development of the nuclear fission industry with no reprocessing coupled to hybrids has considerably more technical and economic uncertainties than the conventional approach of hybrids and reprocessed fuel.

I.3. OVERVIEW OF THE SOLASE-H STUDY

I.3.A. FISSILE FUEL CYCLE

The most important feature of the SOLASE-H study is the direct enrichment of LWR fuel assemblies in the hybrid blanket. Assemblies are manufactured using only fertile fuel. In the case of SOLASE-H, this is ThO_2. Once the average fissile enrichment reaches 4%, these assemblies are removed from the blanket and directly loaded into LWRs with no intermediate reprocessing.

We have considered two hybrid scenarios involving direct enrichment. The first assumes reprocessing of fuel is not possible. In this circumstance, can the hybrid help extend the fissile fuel supply in an economical fashion? The second scenario assumes fuel reprocessing with the hybrid functioning as a fuel factory. Enriched assemblies are exposed for a short time in the hybrid to render them radioactive and more resistant to diversion. In either case, the fuel shipped to and from the LWR is resistant to diversion by the nature of the hot fuel[10] and by the fact that the fissile material occurs only in hot fuel bundles rather than as fresh fuel pellets.

The details of the first scenario are outlined in Fig. I.3-1.

The cycle includes four steps:

1. Fertile fuel, ThO_2 or UO_2, is fabricated in a form that is directly usable in a LWR. (Other fission reactors could be included but the LWR is used here because it is the workhorse of the U.S. fission reactor industry.)
2. The cold, clean fuel assemblies, containing only fertile fuel, are placed in the hybrid blanket and carefully enriched to a nearly uniform concentration of 3-4% fissile fuel as required by the LWR.
3. The enriched, and now highly radioactive assemblies, are transferred as units directly to the LWRs for burning of the fuel.

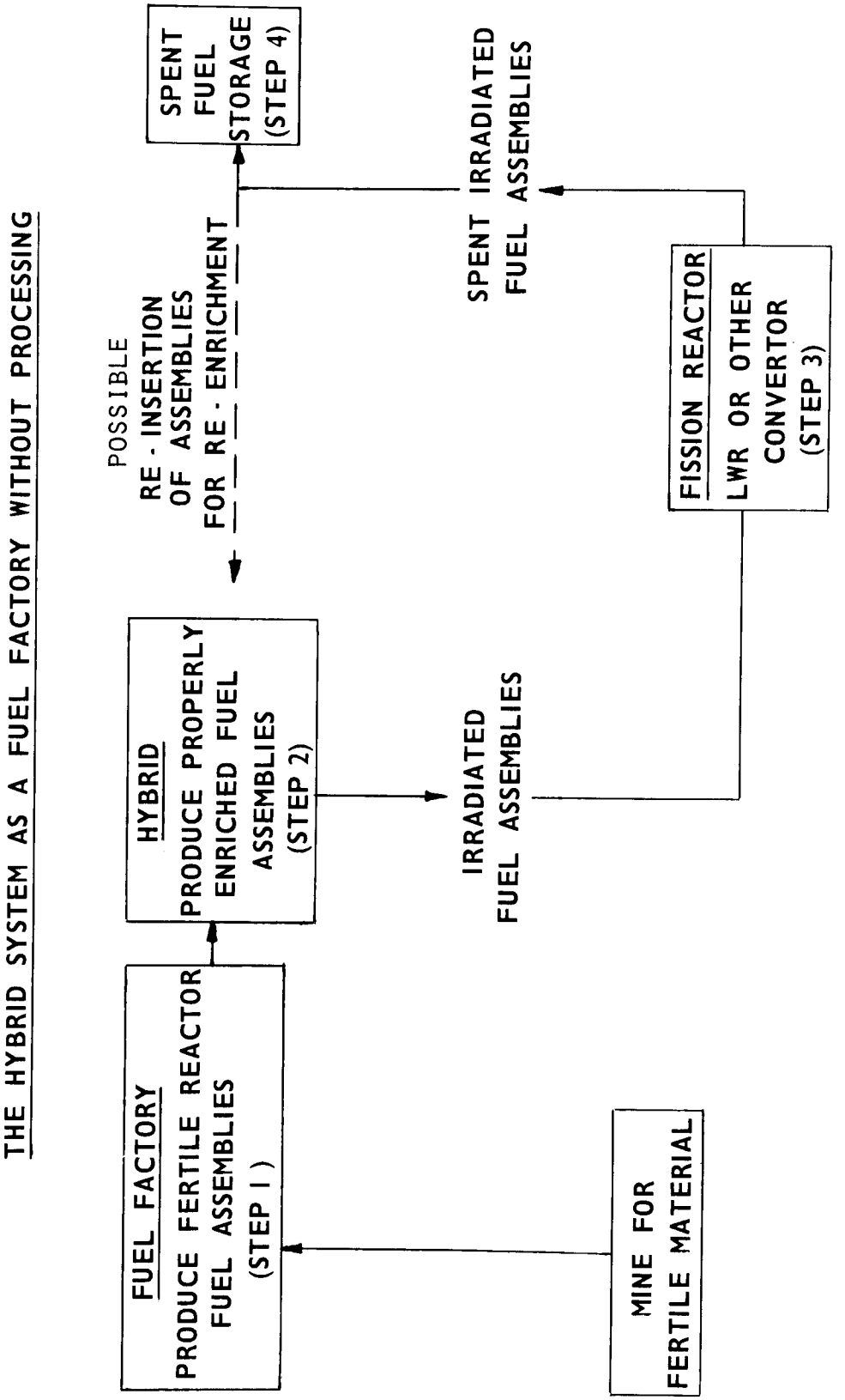
THE HYBRID SYSTEM AS A FUEL FACTORY WITHOUT PROCESSING
FUEL FACTORY
PRODUCE FERTILE REACTOR FUEL ASSEMBLIES
(STEP I)
MINE FOR FERTILE MATERIAL
HYBRID
PRODUCE PROPERLY ENRICHED FUEL ASSEMBLIES
(STEP 2)
IRRADIATED FUEL ASSEMBLIES
FISSION REACTOR
LWR OR OTHER CONVERTOR
(STEP 3)
SPENT IRRADIATED FUEL ASSEMBLIES
POSSIBLE
RE-INSERTION OF ASSEMBLIES FOR RE-ENRICHMENT
SPENT FUEL STORAGE (STEP 4)

FIG. I.3-1

4. The spent fuel from the LWR is stored until a decision is made on reprocessing or storing or both. If feasible, the spent fuel can be reinserted into the hybrid to be reenriched for further burning in the LWR. This possibility depends on both the importance of fission product buildup to LWR performance and the radiation damage to the fuel and cladding.

The attractive features of this cycle are the following:

1. The fissile fuel reserves are extended substantially. Assume the average LWR fuel enrichment is 3%. This is 4.3 times the natural abundance of ^{235}U in ^{238}U. Therefore, the fissile fuel reserves are extended by 4.3 × (Thorium Resources + Uranium Resources). Here, if we assume the thorium resources are no larger than the uranium resources, the fissile fuel supply is extended by a factor of 8 to 9 without reprocessing.
2. The system is resistant to diversion because fissile material occurs only inside highly radioactive fuel assemblies. Only fresh fertile material is fed to the hybrid, and upon removal, the fuel pellets contain fission products that are highly radioactive and the pellets themselves are contained in rod assemblies with highly activated cladding. Access to the fissile material is thus very difficult making the entire cycle diversion resistant according to the guidelines of Feiveson and Taylor.
3. The extension of the fission fuel supply using the hybrid produces additional <u>time</u> that can be used to make deliberate decisions on issues such as internationally controlled, physically secure fuel production and fuel reprocessing centers.

4. The manufacturing of fresh fertile fuel pellets can proceed without the handling problems inherent in the use of a radiation spiking material such as ^{60}Co. This avoids any legal or safety issues associated with the deliberate addition of dangerous materials.

The major disadvantage of this approach is that it does not take full advantage of the fertile fuel reserves. To achieve a fuel supply measured in thousands of years, rather than just a few hundred, fuel reprocessing is essential. With reprocessing, one hybrid reactor is only able to supply fissile fuel to about 2 LWRs of the same thermal power. This has the economic impact of increasing the effective fuel cost. Without reprocessing of the spent LWR fuel, on the order of 10 LWRs can be fueled from one hybrid of equivalent power, depending on the conversion ratio of the LWR or other convertor reactor.

The proliferation resistant fuel cycle can be extended to include reprocessing of the spent fuel if one follows a structure such as outlined by Feiveson and Taylor[10] of internationally controlled, physically secure fuel production and reprocessing sites combined with many national convertor reactors "outside the fence." This process involves the six steps outlined in Fig. I.3-2.

After mining for fertile material or utilizing the stockpile of depleted uranium (Step 1), fertile fuel is fabricated into any form suitable for use in the hybrid reactor (Step 2) and inserted into the hybrid (Step 3), where fissile material is produced. The fuel need not be in a form directly usable in a fission convertor reactor even if this were feasible. The fuel produced in the hybrid is reprocessed (Step 6) and returned to Step 2 for refabrication into properly enriched fission reactor fuel.

THE HYBRID SYSTEM AS A FUEL FACTORY WITH REPROCESSING

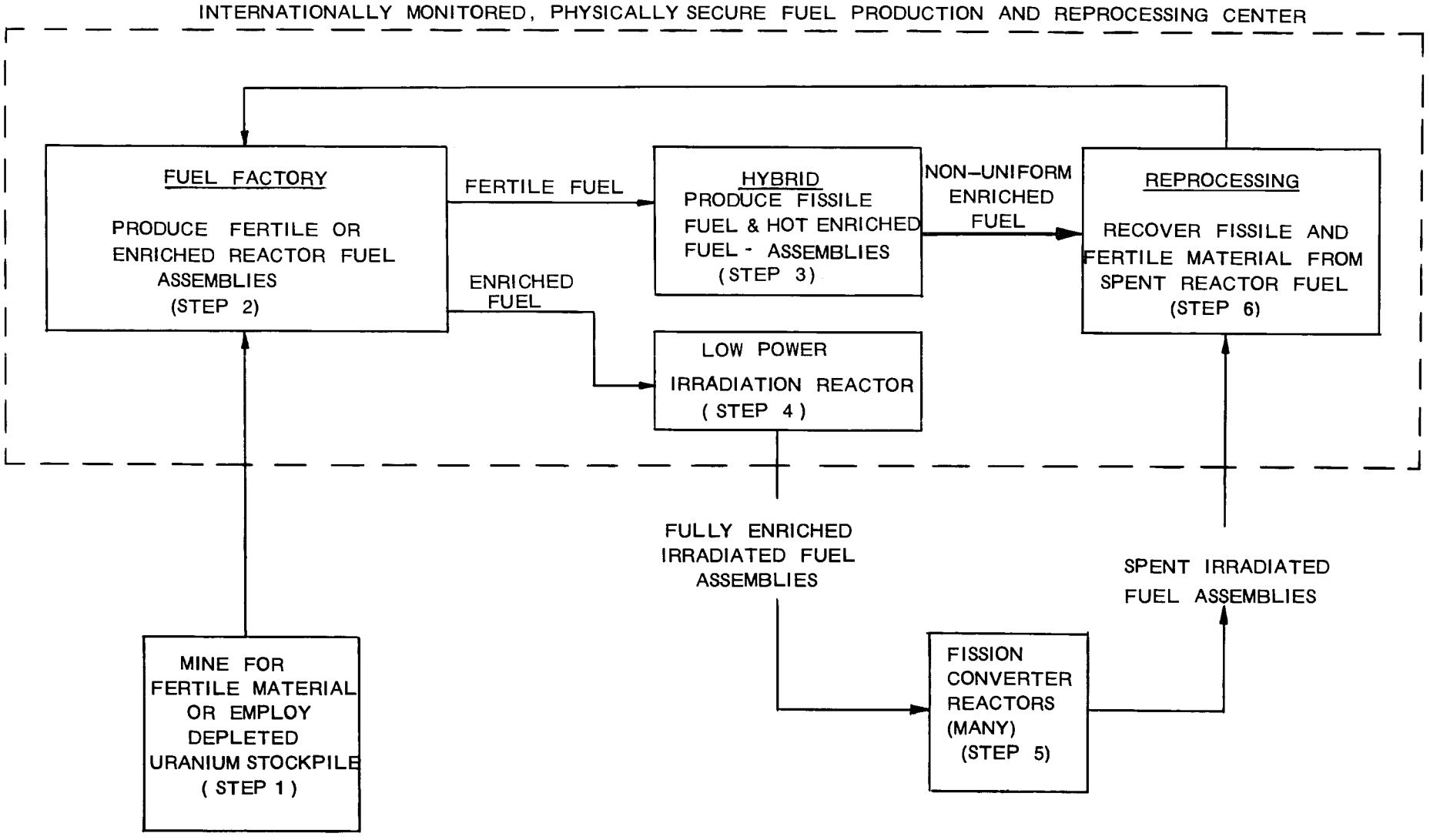

Fig. I.3-2

This fuel is now irradiated in a low power fission reactor (Step 4) to a burnup level of about 0.4 MWd/t. For LWR type fuel, this level of burnup is sufficient to render the fuel self-protecting under the guidelines of the Code of Federal Regulations. At this point, the hot fuel is shipped from the secure site to the fission convertor reactors (Step 5). Upon completion of fuel utilization in the fission reactor, the hot spent fuel is returned to the secure site for reprocessing (Step 6) and re-use of both the fertile material (in Step 3) and the fissile material (in Step 4).

The advantages of this approach are several. First, the fuel supply is measured in terms of the fertile material abundance and thus will last for thousands of years. Second, fuel shipped to and from the convertor reactors is always radioactive and would be resistant to diversion and reprocessing for the reasons described earlier. Third, the convertor reactor need not be restriced to a LWR, although using these reactors will minimize the need to develop additional fission reactor technology. Fourth, the ratio of power production outside to inside the secure site is very large. This minimizes the number of required secure sites. Finally, the use of a low power fission reactor to effectively "spike" the fresh fuel assemblies eliminates the concern about the fissile fuel distribution in an assembly that arises when the direct enrichment process is used.

I.3.B FUSION PERFORMANCE FOR HYBRIDS

In a laser fusion reactor, the relatively low laser efficiency (1-10%) must be compensated by a large target gain (100-1000) to maintain an economically acceptable recirculating power fraction (25%). Furthermore,

either very large yields (> 1000 MJ) or a large repetition rate (> 10 Hz) is necessary to produce significant amounts of power (~ 1000 MW_e). A fusion-fission hybrid reactor has the potential of reducing all of these fusion performance requirements. This is a consequence of the fusion neutron energy multiplication in the hybrid blanket resulting from fission reactions. For the direct enrichment hybrid that is the basis for the SOLASE-H study there is a desire to minimize the number of fissions in the hybrid blanket to maximize fissile fuel production. However, even with blanket designs that minimize the fission rate, the multiplication is 1.5 to 5.

This fusion neutron energy multiplication in the blanket can be related to the overall system performance by the use of three relations. The recirculating power fraction is given as

$$f_R = (\eta_{th}\ \eta_L\ G\ M)^{-1}$$

where η_{th} is the thermal efficiency of the plant, η_L is the laser efficiency, G is the target gain and M is the fusion energy multiplication due to fissions in the blanket. The gross electric power is

$$P_e = G\ E_L\ \omega\ \eta_{th}\ M$$

where E_L is the laser energy on target and ω is the pulse repetition frequency. These two simple definitions must be combined with a relationship between laser energy and target gain. This is, of course, unknown at this time, but a reasonable estimate might be

$$G = 100\ E_L(MJ)^{1.7}.$$

For laser fusion electric power reactors, it is customary to assume that the recirculating power fraction must be less than 0.25 for an economical system. In the case of a hybrid reactor, this is not necessarily true

because the hybrid reactor cost can be distributed among the costs of all of the fission reactors that it supports. Hence the net electric power produced by the hybrid can be a small fraction of the total power produced by the hybrid and fission reactor system and changes in this small fraction may make little difference to the overall cost of electricity. The average capital cost electricity for the whole system can be defined as

$$FoM = \frac{P_H C_H + NP_H C_F}{\eta_H P_H(1 - f_R) + \eta_F P_H N} \left(\frac{\$}{kW_e}\right)$$

where P_H is the thermal power of the hybrid, C_H is the cost of the hybrid in $\$/kW_t$, C_F is the cost of the fission reactor in $\$/kW_t$, N is the number of fission reactors of equal thermal power supported by the hybrid (the support ratio) and η_H and η_F are the thermal efficiencies of the hybrid and fission reactor. If we normalize the hybrid unit cost to the fission reactor unit cost

$$\delta = C_H/C_F,$$

then we can write our figure of merit as

$$\frac{FoM}{C_F} = \frac{\delta + N}{\eta_H(1 - f_R) + \eta_F N} .$$

This is plotted in Fig. I.3-3 as a function of f_R for different specific values of N and δ. If the hybrid is able to support 10 fission reactors of equivalent thermal power, then the total capital cost of electricity is insensitive to the recirculating power fraction, lines (2) and (4). However, if the hybrid is only able to support two fission reactors, as in the case of the direct enrichment scheme without fuel reprocessing, then the capital cost is quite sensitive to the recirculating power fraction. For line (1) in Fig. I.3-3,

CAPITAL COST vs. RECIRCULATING POWER FRACTION IN THE HYBRID

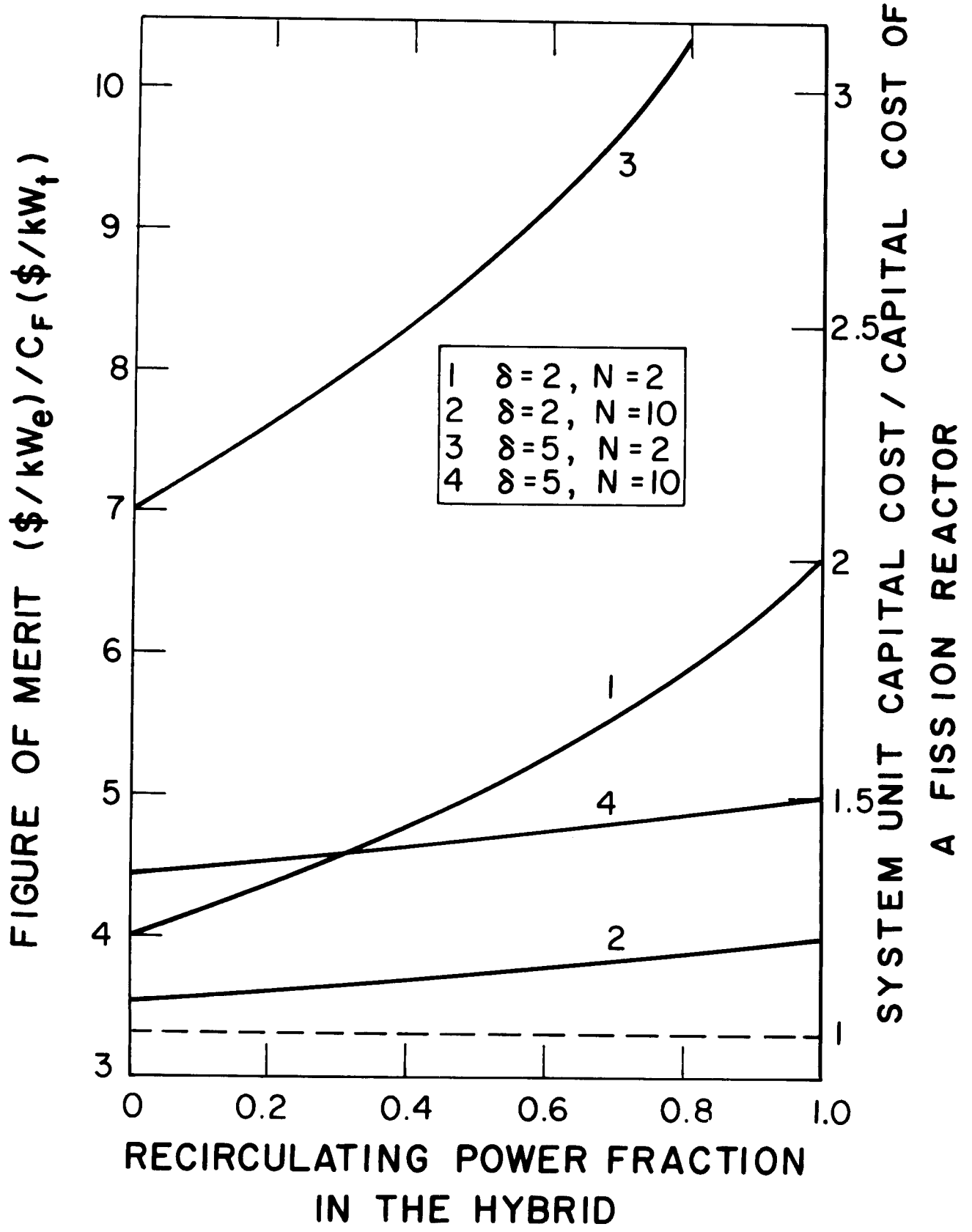

Fig. I.3-3

the total capital cost is about 1.3 times the capital cost from a fission reactor if the recirculating power fraction is taken to be 0.25, but if it is instead equal to 1.0, then the total capital cost is twice that of a fission reactor. This is the situation for the SOLASE-H study where reprocessing is not allowed. It is therefore worthwhile to look at the cost scaling of the laser fusion hybrid reactor itself as a function of the major cost items. We do this analysis assuming that the recirculating power fraction is 0.25. If the thermal efficiency is assumed to be 0.4, then the relationship between target gain, laser efficiency, and energy multiplication can be written as

$$\eta_L \; G \; M = 10.$$

This is the well known expression indicating that the product of target gain and laser efficiency must equal ten for a 25% recirculating power fraction. For pure laser fusion this expression can presumably be satisfied by a 1% efficient laser and target gain of 1000 or by a 10% efficient laser and target gain of 100. However, there are economics of scale and other engineering factors that may prohibit some ranges of η_L and G. For instance, the cavity size and hence its cost is determined by the yield from one pellet explosion. Using the above relations the yield can be expressed as a function of laser efficiency to give

$$Y(MJ) = 2.6/(M\eta_L)^{1.6} \; .$$

Thus a 1% efficient laser must give a yield of 3920 MJ to provide a 25% recirculating power fraction for M=1. If 1000 MW_e of net power is assumed, then the repetition rate will be

$$\omega(s^{-1}) = 1292(M\eta_L)^{1.6} .$$

For η_L=0.01 we find ω=0.85 Hz. Furthermore, high target gain requires a large laser energy. If the laser efficiency is low then the amount of stored energy in the capacitor banks will be very large,

$$\text{Stored Energy (MJ)} = E_L/\eta_L = 0.26/(M\eta_L)^{1.6} .$$

Hence, a 1% efficient laser requires 390 MJ of stored energy to produce 1000 MW_e of net power. Such large amounts of stored energy can make the laser system very expensive. Empirical evidence shows that the cost per joule of power supplies scales like[11]

$$C = C_o\left(\frac{\omega_o}{\omega}\right)^n$$

where C_o and ω_o are the cost per joule and the repetition rate of a reference system. The repetition rate is related to the lifetime of the system. For instance, the reference system might be one that provides 10^{10} shots over 30 years at 70% plant factor. This would give ω_o=15 Hz. The parameter, n, is determined from empirical observation to be about 1/4. Using this formula for power supply cost along with the other three formulas the cost per kilowatt installed can be expressed as

$$C\left(\frac{\$}{kW_e(net)}\right) = \frac{2000\ C_o\ \omega^{n-1}}{M\ \omega_o^{\,n}\ \eta_{th}\ G\ (1-f_r)}$$

where the normalization cost, C_o, is given in \$/J and a factor of two has been included to account for indirect costs. With this formula the power supply cost

is plotted as a function of driver efficiency for two different net electrical power outputs, 100 MW_e and 1000 MW_e, and for three different blanket energy multiplications, 1, 5, and 10, in Fig. I.3-4, assuming C_o = \$3.50/J, f_r = 0.25, and η_{th} = 0.4. Also included in Fig. I.3-4 are the specific fusion parameters associated with a power supply costs of \$200/kW_e. This value is chosen to represent the maximum allowable power supply cost assuming the total plant cost to be roughly \$2000/kW_e. (If one hybrid provides fuel for a greater number of fission reactors, it may be possible to spend a greater amount of power supplies.) For 1000 MW_e and M = 1, the minimum laser efficiency that is consistent with a power supply cost of \$200/kW_e is 4.4%. However, if M = 10, then a 1.9% laser can be used. For a power of 100 MW_e, the lasers' efficiencies for M = 1 and M = 10 are 19% and 8.1%, respectively. This clearly shows the economy of scale that is associated with power supply cost. When the power level is low, the laser must be efficient to minimize the size of the power supplies. The effect of blanket multiplication is to lower the acceptable laser efficiency, target gain, and hence laser energy. This is very important, because each individual laser type has its own efficiency. This efficiency may be too low for laser fusion electric power reactors. However, the same laser might be very attractive for hybrid applications if it has other desirable characteristics. For instance, it may be necessary to multipass the CO_2 laser to achieve efficiencies of 10% which may be needed for laser fusion, but an efficiency of 2% may be obtained without multipassing. This could greatly simplify the laser design for a hybrid reactor.

The blanket multiplication also relaxes the amount of fusion power. For 1000 MW_e and M = 10, the fusion power is only 330 MW. The laser energy and target gain are also relaxed. With a smaller yield, the cavity can be smaller and less costly. The exact scaling of cavity cost has not yet been included.

LASER PARAMETERS WHEN LIMITED TO POWER SUPPLY COST OF $200/kW_e

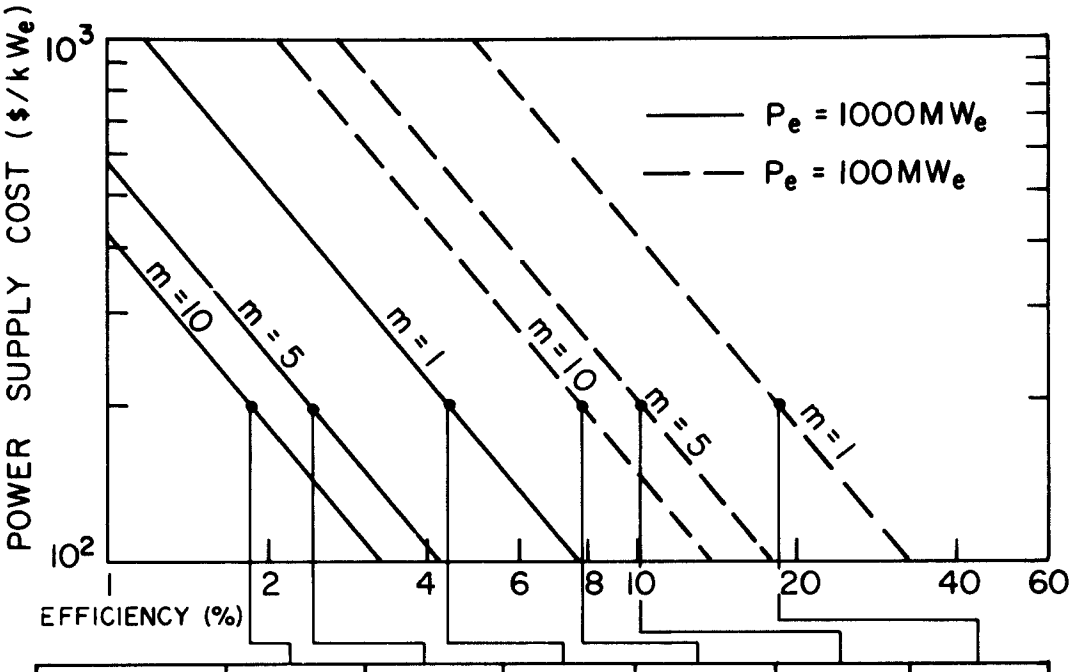

P_e (MW_e)	1000	1000	1000	100	100	100
m	10	5	1	10	5	1
η_L	.019	.0245	.044	.081	.105	.19
G	52.6	81.6	227	12.3	19	52.6
E_L(MJ)	.685	.887	1.6	.292	.377	.685
y(MJ)	36	72	363	3.6	7.2	36
$\omega(s^{-1})$	9.2	9.2	9.2	9.2	9.2	9.2

Fig. I.3-4.

These results must be treated with some caution though, because the power supply and reactor cavity cost scaling favors high repetition rate systems. Other factors such as target manufacturing, laser gas reprocessing, cavity pumping and target injection, will favor low repetition rate systems. So little is known at this time about target design and target manufacturing techniques that cost scaling estimates have not been made for this important part of the plant economics. However, laser gas reprocessing is a significant consideration in determining the SOLASE-H laser repetition rate.

Another factor important to the performance of the direct enrichment hybrid studied in SOLASE-H is the amount of fusion power. The amount of fissile fuel that is produced or conversely the length of exposure time that is needed to reach 4% fissile enrichment in the blanket will depend on the amount of fusion power. The fissile fuel production can be related to the fusion power by the formula

$$\text{kg of } {}^{233}\text{U/year} = 5.44\ P_f f_n\ (\text{UBR})\ (\text{PF})$$

where P_f is the fusion power in MW, f_n is the fraction of fusion energy in neutrons, UBR is the uranium breeding ratio, and PF is the plant factor. The coefficient for ^{239}Pu production is 5.3 rather than 5.44. The LWRs in use today operate with a fuel burnup of 33,000 MWD/MTU. Assuming 4% enrichment, 1000 MW_e, and 70% plant factor, the number of LWRs supported by one hybrid is

$$\frac{\#\ \text{of LWRs}}{\text{Hybrid}} = 5.9 \times 10^{-3}\ P_f f_n\ (\text{UBR})\ (\text{PF})$$

If the fraction of energy in neutrons and the plant factor are both 70% then the fusion power can be expressed as

$$P_f = 345\ (\#\text{-LWR})/\text{UBR}.$$

If we desire to fuel two LWRs without recycle from one hybrid with UBR=0.6, then P_f=1150 MW. This large value of fusion power that is required for the direct enrichment hybrid places more severe constraints on the fusion subsystem than might otherwise be required in other hybrid systems. Production of this high fusion power and minimization of the blanket multiplication will be dominant considerations in the design of a direct enrichment hybrid reactor.

I.3.6-1 CONCLUSIONS REGARDING FUSION PERFORMANCE FOR HYBRIDS

The fusion performance in hybrids is most strongly influenced by the fusion neutron energy multiplication in the blanket. With this multiplication a lower fusion power can be used than in a laser fusion reactor with the same electrical output. Furthermore, the requirements of target gain and laser efficiency need not be as great to restrict the recirculating power fraction to a reasonable value, 0.25. For large support ratios, the recirculating power fraction can become large without severely penalizing the overall electricity cost. Lower fusion power levels suggest that lower target gains and/or laser repetition rates can be used. However, each of these characteristics varies approximately linearly with the multiplication, and it is difficult to simultaneously relax everything by a large amount.

The particular fusion parameters to be reduced will depend on the system. In the case of lasers, the efficiency might be lowered to allow the use of an otherwise uneconomical laser candidate. The repetition rate might also be reduced to reduce the laser gas reprocessing. Lasers such as HF and KrF might be included in this category. For high efficiency drivers such as electron beams, and possibly CO_2 lasers, the target gain might be relaxed. Here there is little problem with gas reprocessing but the target performance is in question.

The cost scaling of power supplies favors high efficiency lasers, particularly at low plant power levels, ∿100-300 MW_e. In fact, drivers with efficiencies less than about 10% may be unacceptable for such low power reactors, including hybrid reactors. This is a serious problem for the low efficiency, short wavelength lasers that are expected to give very large target gain. The energy for these lasers is 2-4 MJ implying enormous amounts of stored energy. Unless alternative low cost power supplies can be developed, this approach to laser fusion may be uneconomical at the low power demonstration level of power plant development. This could severely hinder the progress toward a full scale power reactor.

For the case of the direct enrichment hybrid the blanket multiplication is low, only 1.5-5. Therefore the laser efficiency and target gain cannot be significantly relaxed over the fusion electric case. In addition, the fusion power must remain high to produce fuel for at least two LWRs per year. This fusion power level is approximately 1200 MW. Hence the yield and repetition rate cannot be significantly reduced from the fusion electric case. However, if the target gain is kept high, 200-300, then the laser efficiency can be reduced to about 2%. In this case, either a single-passed CO_2 laser or an HF laser becomes very attractive. In the SOLASE-H study, the HF laser was investigated in detail. Hence the major impact of the direct enrichment hybrid concept on the fusion performance is likely to be the allowance for a lower laser efficiency. In this case, the HF laser can become an attractive driver candidate.

I.3.C BLANKET NEUTRONICS

The basic blanket design for SOLASE-H is shown in Fig. I.3-5. The reactor cavity is cylindrical with fissile fuel only being bred in the circumferential blanket. The top and bottom blankets are devoted to breeding tritium. The radius of the cavity is taken to be 6 m and the height is 12 m. This allows 3 LWR fuel assemblies to be stacked in the blanket while the fraction of solid angle subtended by the circumferential blanket is 70%. The blanket structure is zircaloy, to be compatible with the cladding of the fuel assemblies. If stainless steel were used as the structure there is the possibility of carbon transport between it and the zircaloy cladding by the Na coolant. The first wall is 0.2 cm thick and is scalloped as shown in Fig. I.3-5 to accommodate the Na coolant pressure in the blanket. Directly behind the first wall are pins of Pb, clad in zircaloy. This Pb serves as a neutron multiplier, thus enhancing the fissile production rate.

The zone containing LWR assemblies is surrounded in the front and rear with pins containing Li. These Li zones both breed tritium and filter thermal neutrons that might otherwise diffuse into the fuel assemblies and induce fission. By poisoning the thermal flux, they enhance the uniformity of enrichment across the LWR assembly. Behind the LWR fuel zone and its Li filter is a Pb and carbon reflector. The fuel zone is therefore surrounded by fast neutron reflecting material and thermal neutron filters. The assemblies behave as a fast neutron flux trap, thus maximizing the fissile fuel breeding rate. The reflector is followed by an outer Li zone to capture any leaking neutrons.

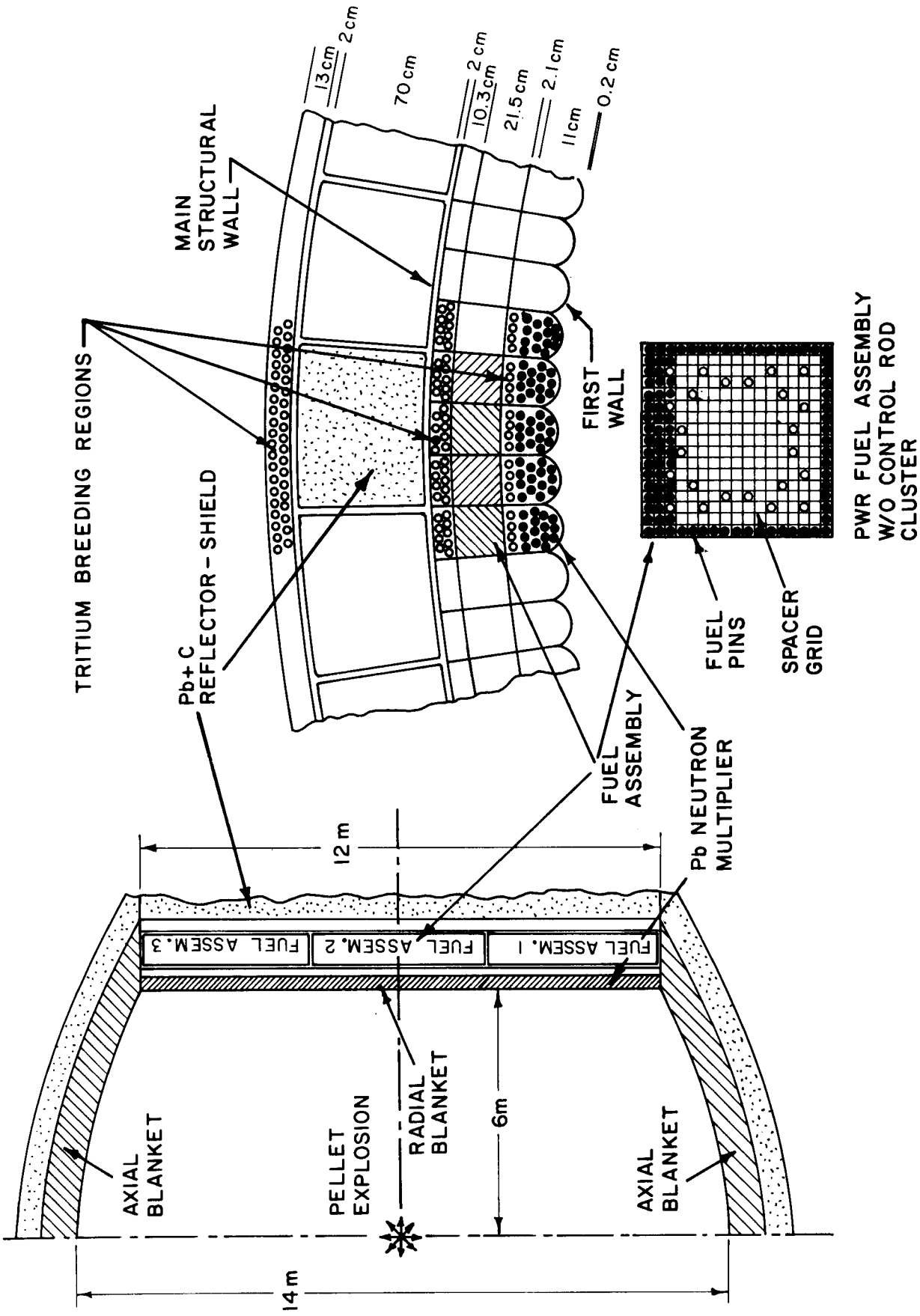
TRITIUM BREEDING REGIONS
MAIN STRUCTURAL WALL
Pb+C REFLECTOR-SHIELD
FIRST WALL
FUEL ASSEMBLY
Pb NEUTRON MULTIPLIER
FUEL PINS
SPACER GRID
PWR FUEL ASSEMBLY W/O CONTROL ROD CLUSTER
13cm
2cm
70cm
2cm
10.3cm
21.5cm
2.1cm
11cm
0.2cm
12m
FUEL ASSEM. 1
FUEL ASSEM. 2
FUEL ASSEM. 3
AXIAL BLANKET
PELLET EXPLOSION
RADIAL BLANKET
6m
AXIAL BLANKET
14m

Fig. I.3-5

This blanket is studied using both the one-dimensional ANISN neutron transport code and the three-dimensional MORSE Monte Carlo code. One-dimensional calculations are used to study the detailed spatial dependence of the neutron flux in the radial direction. The enrichment profile across the fuel assembly and the number of breeding captures per fusion neutron are studied parametrically as a function of blanket design. Once an optimum blanket design is established for the radial blanket, three-dimensional calculations are done to compute the total fissile and tritium breeding ratios and also to compute the axial enrichment profile in the fuel. In addition, these three-dimensional calculations are used to optimize the enrichment rate by reducing the fertile fuel inventory in the blanket. This is accomplished by replacing some of the fuel assemblies with neutron scattering material.

I.3.C-1. PARAMETRIC STUDIES OF RADIAL BLANKET PERFORMANCE (ONE-DIMENSIONAL)

For the purpose of parametrically studying the neutronics performance of the fissile fuel breeding zone, this radial blanket is modelled using one-dimensional spherical geometry and the ANISN neutron transport code. The calculations are done using a 25 energy group cross section set and the P_3-S_4 approximation. The most important results of these calculations are (1) the average number of fissile atoms produced per fusion neutron and (2) the enrichment profile across the fuel assembly in the radial dimension of the blanket. A flat enrichment profile is of course desired. To optimize these two performance characteristics different neutron multipliers (Be,Pb) and different coolants (Na,Li,Pb_4Li) are investigated. In addition, there is a study of the effects of the Li zones surrounding the fuel. For these calculations the blanket is modelled as shown in Fig. I.3-6. The PWR fuel assembly is chosen to have the dimensions given in Fig. I.3-7. The results of the parametric calculations are summarized in Table I.3-1.

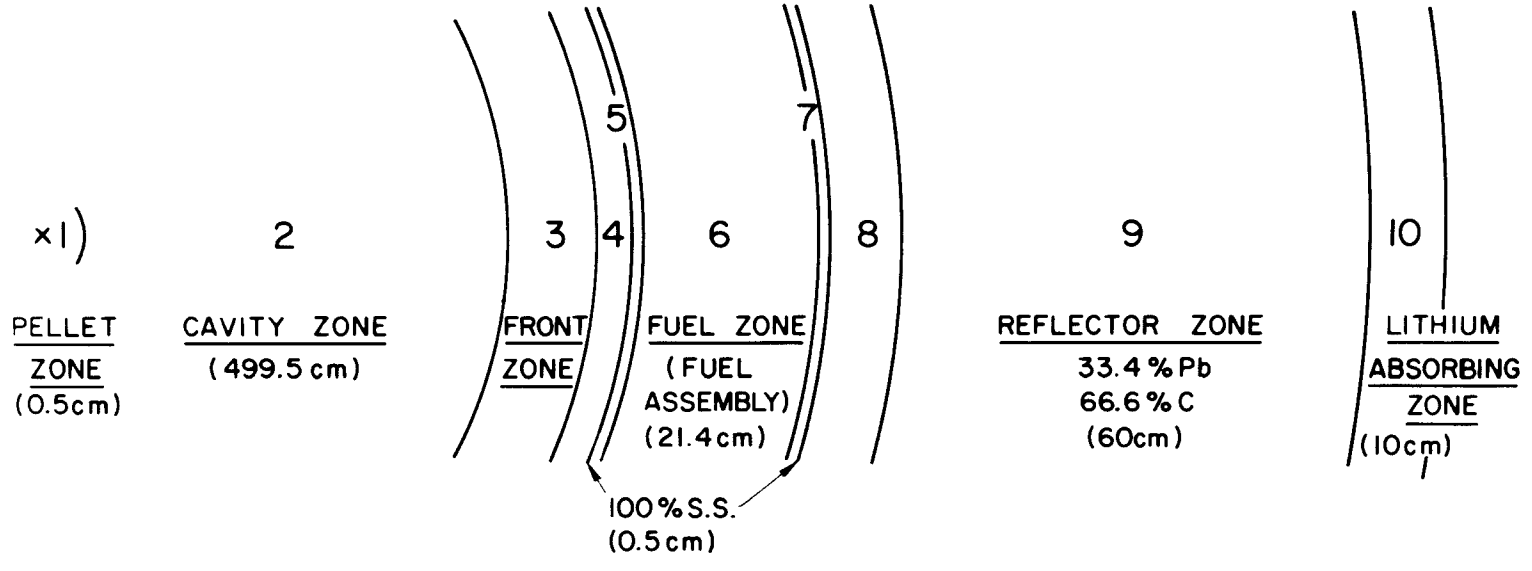

Fig. I.3-6 SCHEMATIC REPRESENTATION IN SPHERICAL GEOMETRY OF THE HYBRID BLANKET

ZONES 4 AND 8 ARE NOT INCLUDED IN THE SERIES OF BLANKETS USING Be AS FRONT ZONE MULTIPLIER

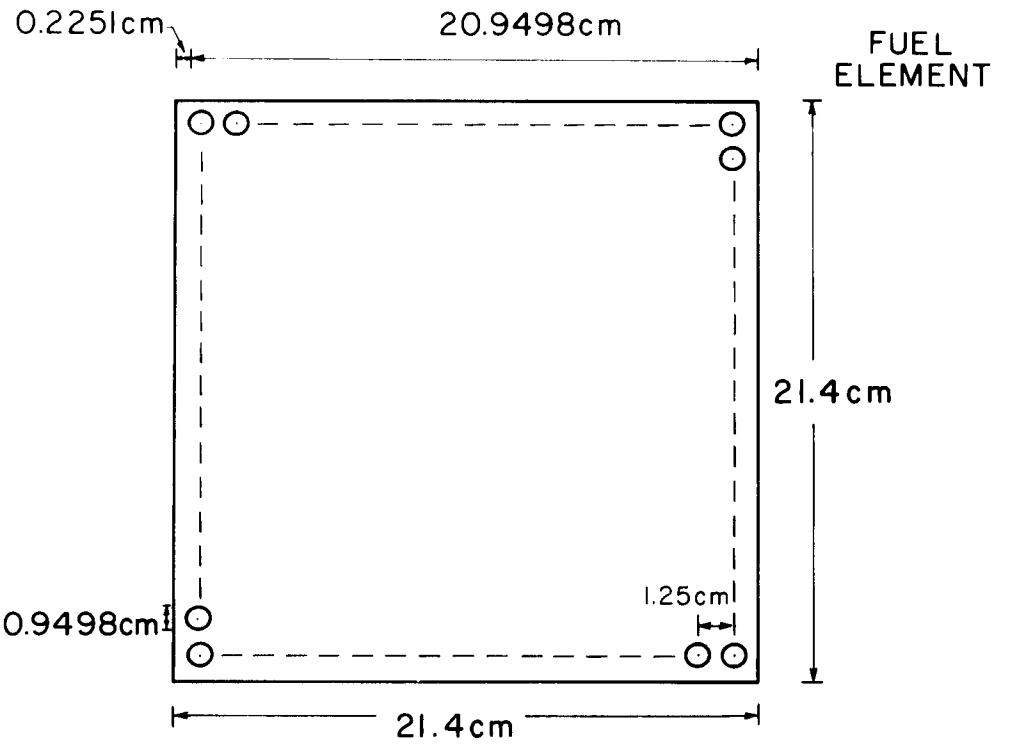

(a) THE 17X17 FUEL ASSEMBLY ;
264 FUEL ELEMENTS AND 25
LOCATIONS FOR CONTROL ROD (TOTAL 289)

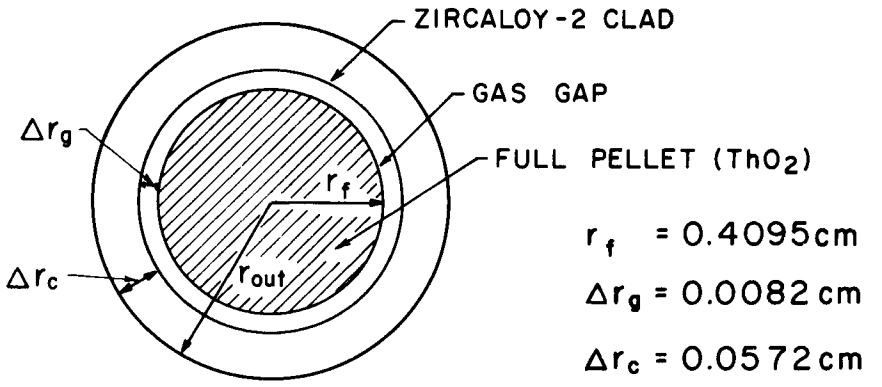

(b) FUEL ELEMENT PIN

THE FUEL ASSEMBLY AND THE FUEL PIN

Fig. I.3-7.

CASE NUMBER

Blanket	#1	#2	#3	#4	#5	#6	#7	#8	#9	#10	#11	#12	#13
Zone 1, 2	Zone 1 Point Source Within 0.5 cm Radius												
Zone 3	82.2% Be 9.3% Nat. Li Coolant 8.5% Zirc-2 (10 cm)	As #1 but with Na Coolant			As #2 (0 cm)	As #2 (5 cm)	As #2 (15 cm)	100% Pb_4-Li Nat. Li (10 cm)	As #2 Pb replaces Be (5 cm)	As #9 (10 cm)	As #9 (15 cm)	As #9 (20 cm)	As #10
Zone 4	(0 cm)								95% Nat. Li 5% SS (1.5 cm)				
Zone 5, 7	100% SS (0.5 cm)												
Zone 6	30.3% ThO_2 9.2% Zirc-2 59.2% Nat. Li Coolant 1.3% Void (21.4 cm)	As #1 but with Na Coolant	30.3% ThO_2 3.8% Nat. Li 55.4% Na Coolant 9.2% Zirc-2 7.3% Void 21.4 cm	As #3 but Li is 50% Li^6				As #1 but with Pb_4 Li Coolant. Nat. Li is Used	As #2				
Zone 8	(0 cm)								95% Nat. Li 5% SS (6 cm)				As #10 (8 cm)
Zone 9	Pb+C Mixture 66.6% C 33.4% Pb (60 cm)												
Zone 10	95% Li (50% Li^6) 5% SS (10 cm)								As #1 but Li is Natural				
Th(n,γXUBR)	0.7132	1.3357	1.1364	0.8970	0.7492	0.9040	0.8230	1.1259	0.8589	0.9567	1.0115	1.0392	0.9338
TBR	0.0998	0.0968	0.3797	0.6703	0.5226	0.5363	0.8003	0.5029	0.6152	0.5946	0.5734	0.5487	0.6254
Th($\nu\sigma_f$)	0.1158	0.1185	0.1184	0.1183	0.1909	0.1527	0.0899	0.0704	0.1218	0.0799	0.0520	0.0338	0.0799
	0.1159	1.9818											

Table I.3-1

Neutronic Results for Different Blankets

Different thicknesses of Be as the neutron multiplying material (case #'s 4, 5,6,7) yield the tritium and ^{233}U breeding ratios shown in Fig. I.3-8. As the Be thickness becomes greater there is an increase of the Be (n,2n) reactions and a decrease of the Th(n,γ) reactions. This gives a greater total breeding ratio. However, the thicker Be zone also significantly moderates the neutron spectrum resulting in the increase of the $^{6}Li(n,t)\alpha$ absorption reaction. The optimum thickness of the Be front zone is about 10 cm. In this case, the ^{233}U breeding ratio UBR=0.9 and the tritium breeding ratio TBR=0.67. This latter value meets the criterion that the tritium breeding ratio in the radial blanket be about 0.6. (It is assumed that the remainder of the tritium is produced in the top and bottom axial blankets. Three-dimensional Monte Carlo calculations are done to design the total blanket and these are summarized in the conclusions.) The second important blanket performance criterion, uniform fuel enrichment, is not met with the Be neutron multiplier blankets. The Th(n,γ) reaction rate per DT neutron is shown in Fig. I.3-9 as a function of position through the fuel assembly. The peaking of the reaction rate near the front and back of the fuel zone is due to a self-shielding effect. The effect becomes worse for thicker Be zones because the neutron spectrum is further softened. Hence, although the Be neutron multiplier increases the number of breeding captures to 1.67, it does not provide a flat enrichment profile.

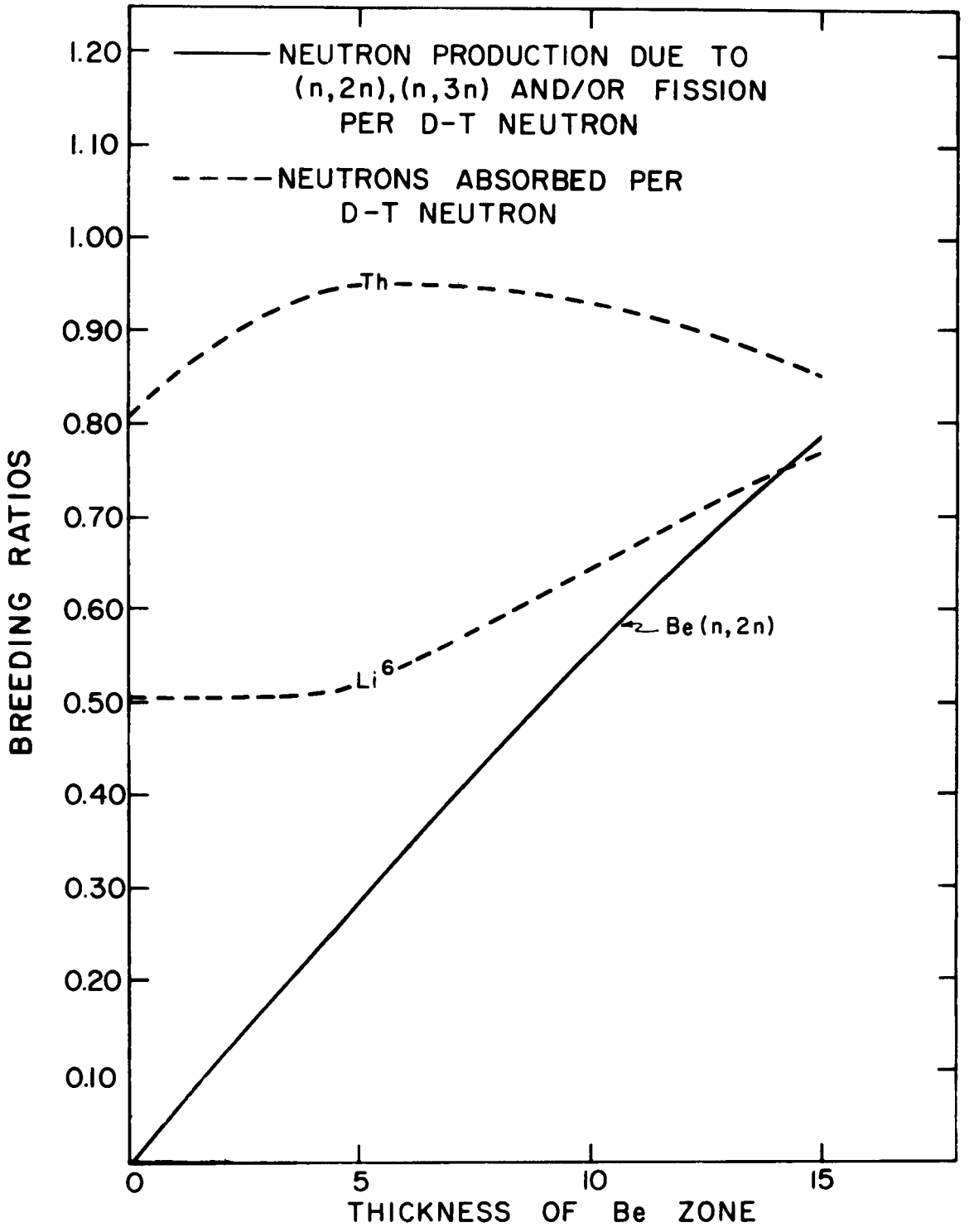

NEUTRON SOURCES AND SINKS AS FUNCTION OF Be FRONT ZONE THICKNESS

Fig. I.3-8

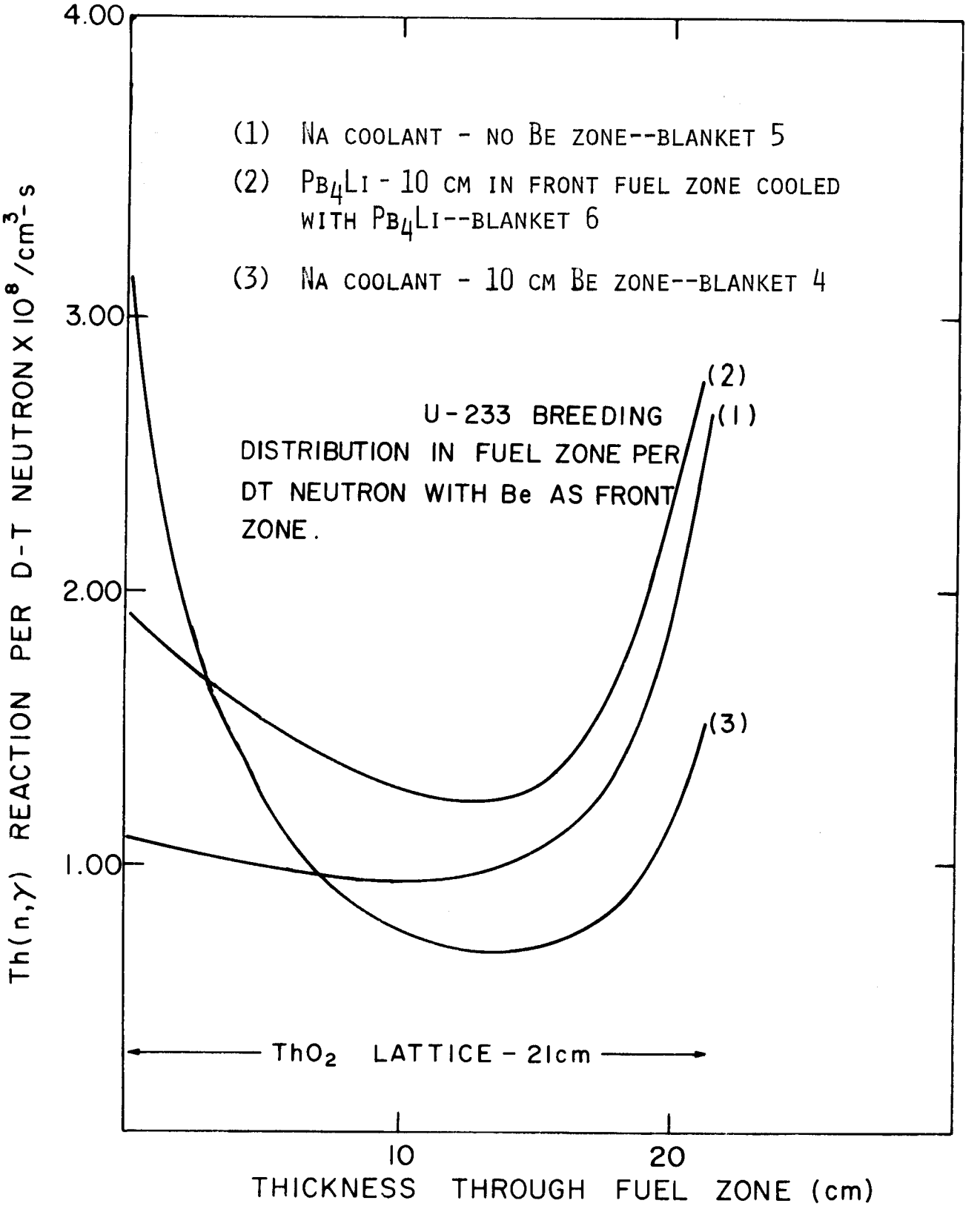
4.00
3.00
2.00
1.00
Th(n,γ) REACTION PER D-T NEUTRON X 10^8 /cm^3-s
(1) NA COOLANT - NO BE ZONE--BLANKET 5
(2) PB_4LI - 10 CM IN FRONT FUEL ZONE COOLED WITH PB_4LI--BLANKET 6
(3) NA COOLANT - 10 CM BE ZONE--BLANKET 4
U-233 BREEDING DISTRIBUTION IN FUEL ZONE PER DT NEUTRON WITH Be AS FRONT ZONE.
(2)
(1)
(3)
ThO_2 LATTICE - 21cm
10
20
THICKNESS THROUGH FUEL ZONE (cm)

Fig. I.3-9.

The use of Pb as a neutron multiplier is investigated in cases #9-13. The various blanket configurations for these cases are again shown in Table I.3-1 and Fig. I.3-6. The important neutron production and absorption reaction rates per DT source neutron are shown in Fig. I.3-10 as a function of the Pb zone thickness. In these cases the $Th(n,\gamma)$ reaction rate steadily increases with an increase of the neutron multiplier zone until a thickness of 20 cm. Furthermore, the competition between the $Th(n,\gamma)$ and $^{6}Li(n,t)\alpha$ reactions for neutron absorption does serve to flatten the $Th(n,\gamma)$ reaction rate profile in the fuel assembly. If it is assumed that the $Th(n,\gamma)$ reaction rate profile does not change when the fuel assembly is rotated 180^{o} after some exposure time, then the resultant profiles are those shown in Fig. I.3-11. As demonstrated by case #10, the profile can be made quite flat by enriching the Li zones that surround the fuel with ^{6}Li. This further shields the fuel from the thermalized neutrons that create the peaking near the edge of the assemblies. However, this increased filtering and flattening of the enrichment profile is at the expense of the average $Th(n,\gamma)$ reaction rate.

I.3.C-2 FIGURE OF MERIT FOR BLANKET PERFORMANCE

This trade-off between enrichment profile uniformity and total ^{233}U breeding ratio requires the establishment of an optimization criterion. The optimum blanket will have the smallest maximum to average $Th(n,\gamma)$ reaction rate profile, denoted by R, while having the highest value of UBR. Thus, the figure of merit, FM, can be defined as

$$FM = UBR/R \ ,$$

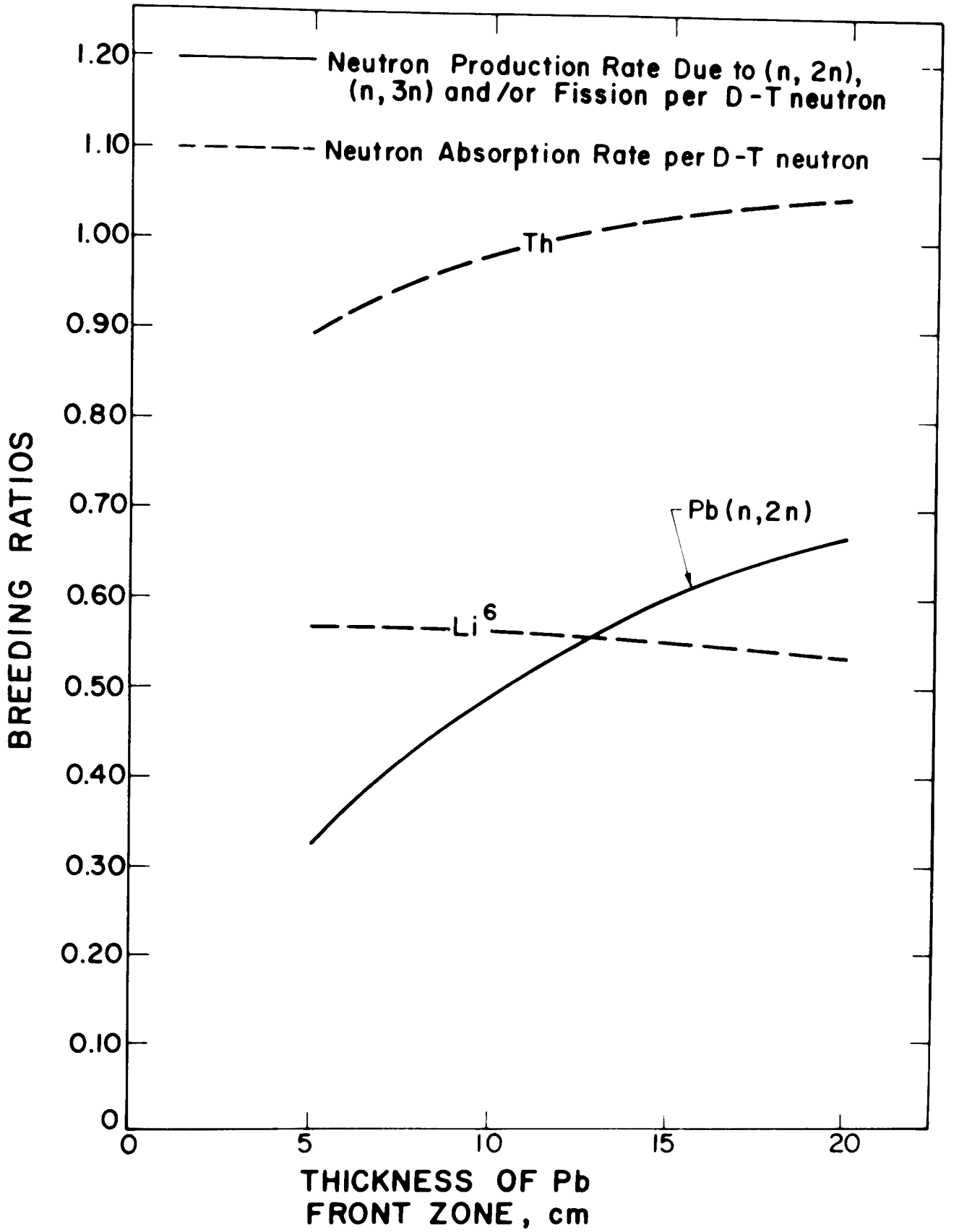
Neutron Production Rate Due to (n, 2n), (n, 3n) and/or Fission per D-T neutron
Neutron Absorption Rate per D-T neutron
Th
Pb (n,2n)
Li 6
BREEDING RATIOS
THICKNESS OF Pb FRONT ZONE, cm
1.20
1.10
1.00
0.90
0.80
0.70
0.60
0.50
0.40
0.30
0.20
0.10
0
0
5
10
15
20

Fig. I.3-10

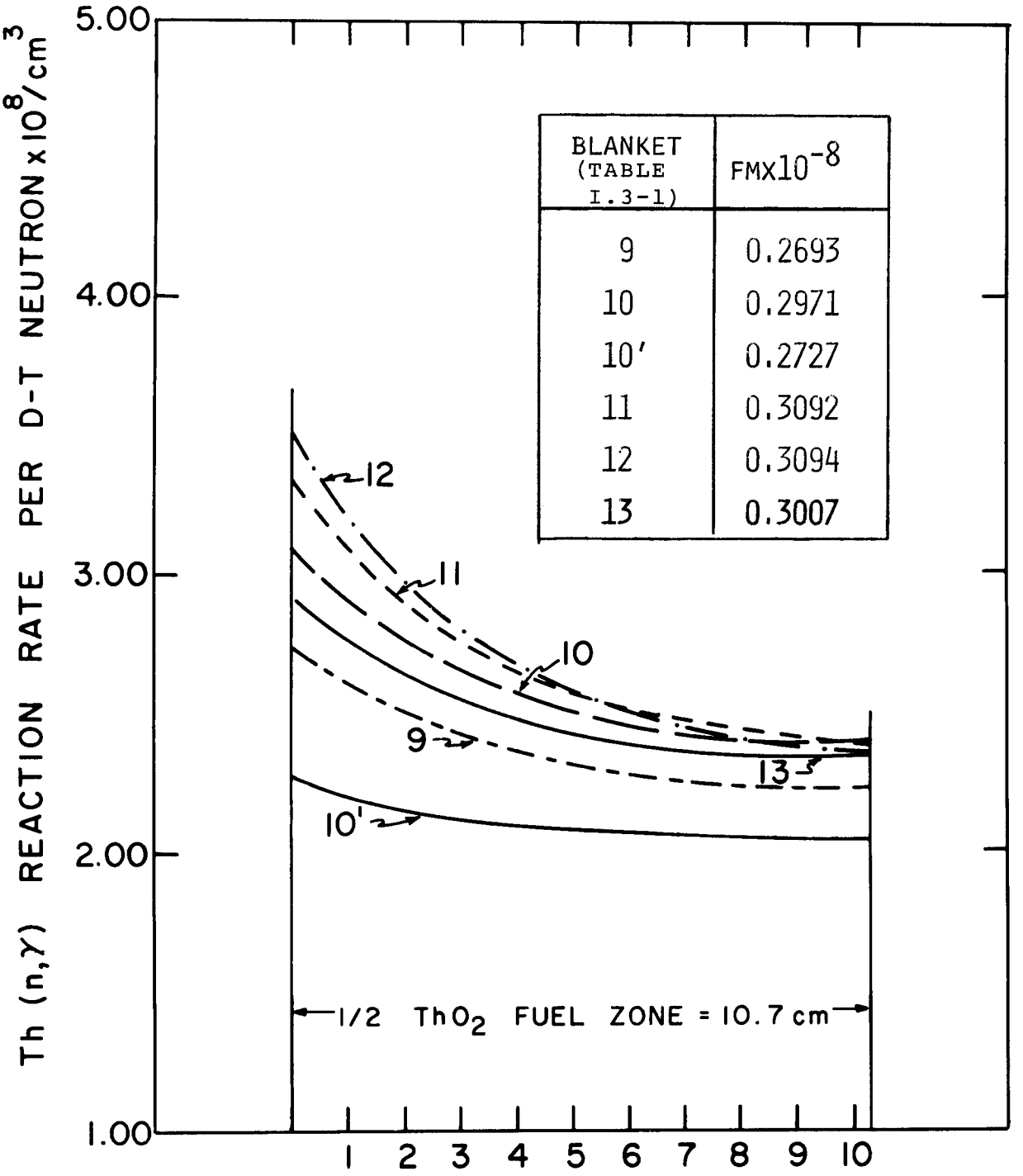

Fig. I.3-11 ^{233}U breeding rate distribution through half of the fuel zone at end of the enrichment phase. The fuel bundle has been rotated 180° at a time when the fuel is half way to the required enrichment level.

and this should be a maximum. However, FM is proportional to $(UBR)^2/Th(n,\gamma)_{max}$ since the average $Th(n,\gamma)$ reaction rate is proportional to UBR. The FM values are given in the box on Fig. I.3-10.

I.3.C-3 NEUTRONICS CONCLUSIONS

A flat enrichment profile can be achieved across the fuel assembly by filtering out thermal neutrons using surrounding Li zones. However, this flatness is achieved at the expense of the average $Th(n,\gamma)$ reaction rate. A figure of merit can be established that optimizes these two effects. The result is that the most uniform enrichment profile is not the most optimum. This means that one can afford to pay the price of a greater peaking factor in the LWR to increase the productivity of the hybrid reactor. Such a conclusion must yet be further verified by neutronics calculations in the LWR core.

To achieve the optimum combination of high breeding ratios and flat enrichment profiles, lead is a much better neutron multiplying material than beryllium. The optimized blanket according to the figure of merit is case #13. In this blanket the neutron multiplier zone is 10 cm thick and the UBR and TBR are 0.94 and 0.62, respectively. The maximum to average $Th(n,\gamma)$ reaction rate across the fuel assembly is 1.1.

These one-dimensional studies guided a three-dimensional neutronics design of the blanket where fissile and tritium breeding in the radial blanket are computed along with the tritium breeding in the axial blanket. These calculations are done by taking a pie-slice of the blanket as shown in Fig. I.3-12. In addition to the basic blanket design described earlier,

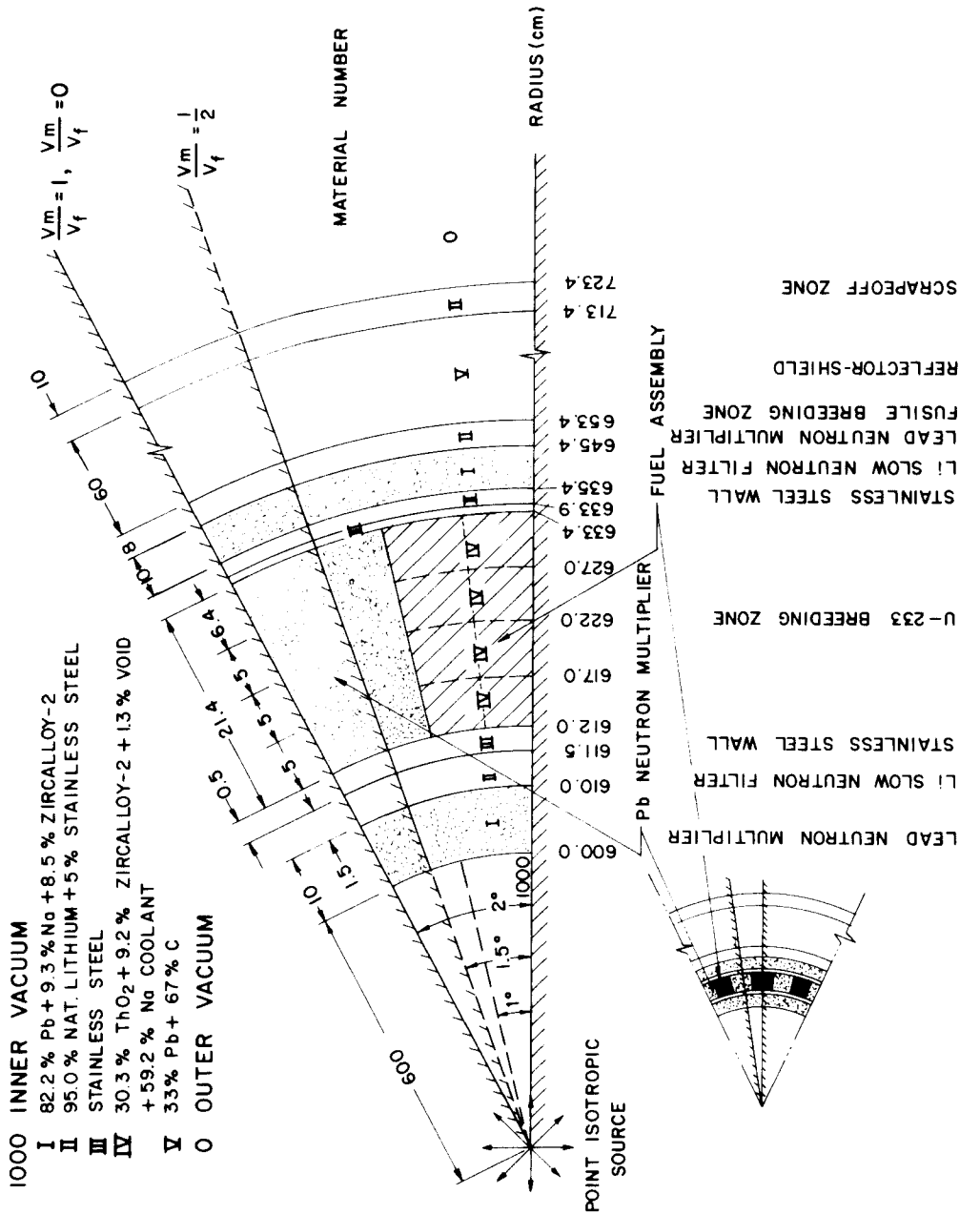
MATERIAL COMPOSITION
1000 INNER VACUUM
I 82.2 % Pb + 9.3 % Na + 8.5 % ZIRCALLOY-2
II 95.0 % NAT. LITHIUM + 5 % STAINLESS STEEL
III STAINLESS STEEL
IV 30.3 % ThO2 + 9.2 % ZIRCALLOY-2 + 1.3 % VOID + 59.2 % Na COOLANT
V 33% Pb + 67% C
0 OUTER VACUUM
Vm/Vf = 1, Vm/Vf = 0
Vm/Vf = 1/2
MATERIAL NUMBER
RADIUS (cm)
600.0
610.0
611.5
612.0
617.0
622.0
627.0
633.4
633.9
635.4
645.4
653.4
713.4
723.4
LEAD NEUTRON MULTIPLIER
Li SLOW NEUTRON FILTER
STAINLESS STEEL WALL
U-233 BREEDING ZONE
Pb NEUTRON MULTIPLIER
FUEL ASSEMBLY
STAINLESS STEEL WALL
Li SLOW NEUTRON FILTER
LEAD NEUTRON MULTIPLIER
FUSILE BREEDING ZONE
REFLECTOR-SHIELD
SCRAPEOFF ZONE
POINT ISOTROPIC SOURCE
1000
600
10
1.5
0.5
2.4
5
5
5
5
6.4
8.0
6.0
10
1°
1.5°
2°

Fig. I.3-12

these three-dimensional studies also include blanket designs where some of the fuel assemblies are replaced with neutron scattering material, to cut down the fuel inventory in the blanket.

These 3-D calculations show that an average ^{233}U breeding ratio of 0.4-0.6 can be achieved along with a tritium breeding ratio of 1.0. The breeding rate density in the fuel can be significantly increased by replacing every other fuel assembly with an equal volume of neutron scattering material such as lead. The fuel assemblies continue to be a fast neutron flux trap and this reduction of absorber material does not significantly reduce the total absorption rate in the entire blanket. But because there is only one-half as much fuel, the absorption rate density is increased and the time to reach 4% enrichment is reduced by a factor of two over the case where the blanket is fully loaded with assemblies. This lattice arrangement of the fuel assemblies and scattering material, therefore, appears to be a very attractive design feature. It, in fact, may be applied to more general hybrid reactor designs to reduce the fuel inventory if this is desirable.

There are significant enrichment nonuniformities along the axial direction. These nonuniformities can be compensated for by a fuel management program that moves fuel from the top to the bottom of the reactor as well as rotating it by 180°. This fuel management scheme has not yet been worked out.

I.3.D EFFECTS OF FUEL BURNUP

These enrichment rate calculations do not include the effect of fuel burnup. However, one-dimensional calculations that include burnup have been done to measure its effect on the time to 4% enrichment and the enrichment profile in the fuel assembly. Important changes resulting from burnup are: (1) the buildup of ^{233}U, (2) the depletion of ^{232}Th, (3) the burning of the bred ^{233}U, and (4) the buildup of fission products. Fission product buildup is not included in these studies. With such a hard spectrum this should be a reasonable approximation. The other three effects are included by solving simple rate equations for the changes in number densities between different ANISN calculations. New number densities are used in each succeeding ANISN calculation. The percentage of ^{233}U that is burned up as a function of time is shown in Fig. I.3-13 for the optimum blanket. For these one-dimensional calculations the time to 4% enrichment is about 2.6 years. Hence, approximately 11-12% of the ^{233}U is burned up before 4% enrichment is achieved. This corresponds to a heavy metal burnup of 0.44-0.48%. This also corresponds to 4300 MWD/MTU of equivalent fission reactor burnup. These calculations indicate that burnup effects will change the time to reach 4% enrichment by about 10-12%. Calculations are also done to determine the effect of burnup on the enrichment profile in the assembly after it has been rotated 180^{o} at the half-way point in its exposure time. These calculations indicate that the effect of burnup and the bred ^{233}U does not significantly affect the enrichment profile after rotation so that a simple superposition of the profiles, as shown in Fig. I.3-11, is justified.

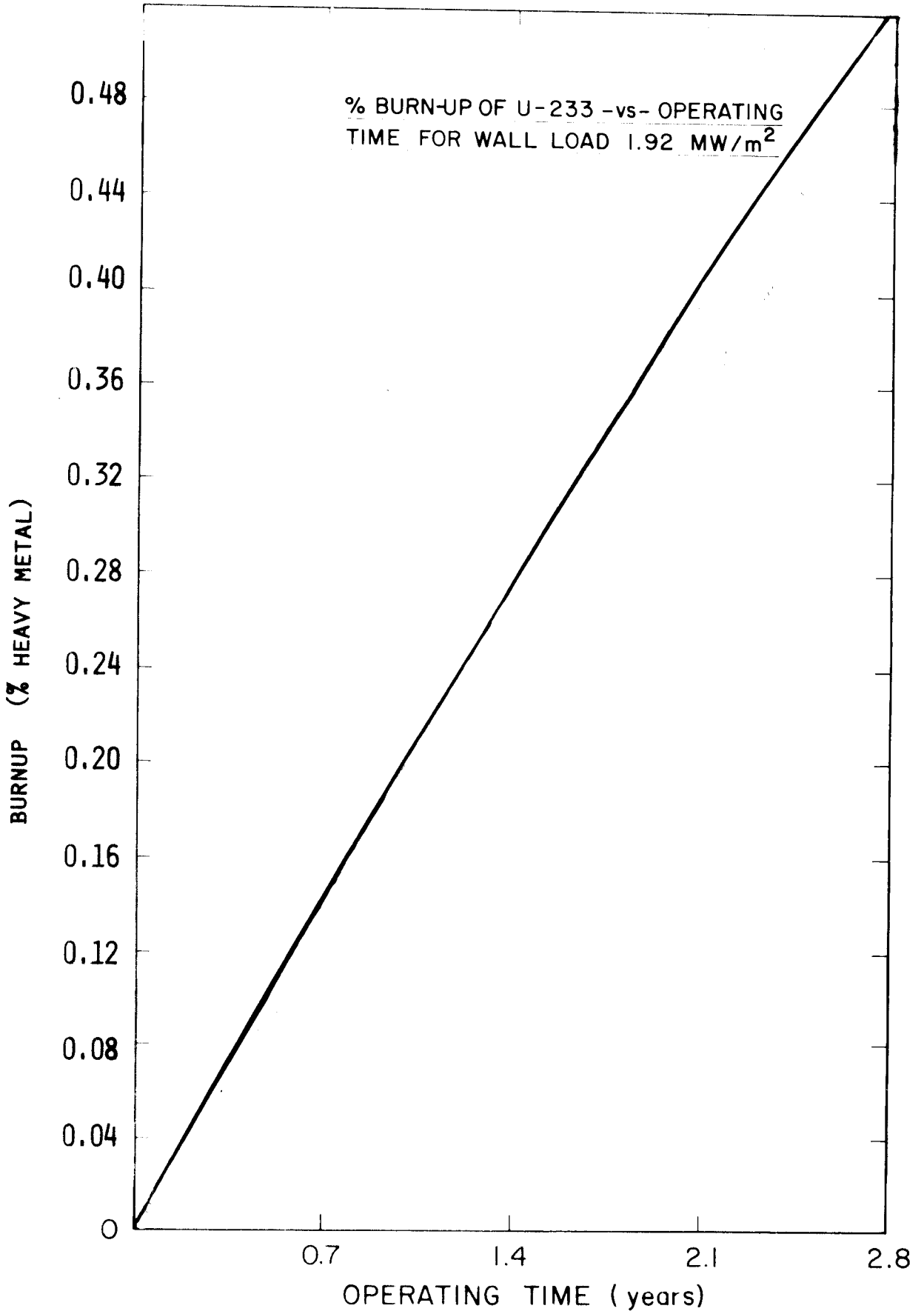
% BURN-UP OF U-233 -vs- OPERATING TIME FOR WALL LOAD 1.92 MW/m²
BURNUP (% HEAVY METAL)
0.48
0.44
0.40
0.36
0.32
0.28
0.24
0.20
0.16
0.12
0.08
0.04
0
0.7
1.4
2.1
2.8
OPERATING TIME (years)

Fig. I.3-13.

I.3.D-1 CONCLUSIONS OF BURNUP CALCULATION

The equivalent average burnup of the fuel in the hybrid blanket is only 4300 MWD/MTU. This corresponds to about 0.44-0.48% of the heavy metal being burned while in the blanket. This low burnup (i.e., fission rate) is due to the Li zones that surround the fuel assemblies and filter out the thermal flux. Hence, this fast neutron flux trap and thermal neutron filter are very effective at maximizing the fissile breeding rate while minimizing the fission rate. Such an arrangement would also be applicable to other hybrid designs where the constraints of SOLASE-H are not included.

I.3.E. HYDROGEN FLUORIDE LASER

As part of the SOLASE-H study a specific assessment of the hydrogen fluoride laser is conducted in enough detail to identify potential problems and assess the general feasibility and practicality of developing this laser as an ICF driver. Although particular parameters are used in this study to couple with the other parts of the design, discussion is given to the consequences of varying these parameters so that a more general evaluation can be made.

From the fusion performance analysis reported in section I.3.B and in Part III of the report, the HF laser appears to be a good laser candidate for hybrid reactor applications. It is capable of delivering high energy (>1 MJ) and high power (>100 TW) to the target at a modest efficiency (~2%). However, this efficiency is a combination of electrical and chemical efficiency. The electrical efficiency can be as high as 20-100%. Such a high electrical efficiency can greatly reduce the problem of the power supplies discussed in section I.3.B. The burden is then, of course, shifted to the efficiency of the chemical reprocessing. The specific design parameters that guided the investigation of the HF laser are shown in Table I.3-2, along with the parameters used in the SOLASE (laser) fusion electric power reactor study. For SOLASE-H, the laser energy on target is increased from 1 MJ to 1.6 MJ, but the power is reduced from 1000 TW to 240 TW. In SOLASE-H there is considerable attention given to pulse shaping, with the high power part of the pulse being 3 nsec long. In SOLASE the pulse length is 1 nsec. This change of parameters between SOLASE and SOLASE-H reflects the changing designs of high gain targets between 1976 and 1979. The repetition rate in SOLASE-H is considerably lower than in SOLASE to relax the requirements on laser gas reprocessing, cavity pumping, and target injection.

Table I.3-2

Design Parameters for SOLASE—An Electric Power Reactor

Energy on Target	1 MJ
Energy Generated	1.1 MJ
Peak Power on Target	1000 TW
Pulse Width (FWHM)	1 nsec
Minimum Efficiency	6.7%
Pulse Repetition Frequency	20 Hz

Design Parameters for SOLASE-H—A Laser for a Hybrid Reactor

Energy on Target	1.6 MJ
Energy Generated	2 MJ
Peak Power on Target	240 TW
Pulse Width	3 nsec
Minimum Efficiency	2.6%
Pulse Repetition Frequency	4 Hz

The HF laser considered for this study is pumped by the chemical chain reaction between H_2 and F_2 and utilizes a 3000/900/100 Torr mixture of $F_2/O_2/H_2$ (Fig. I.3-14). Once the reactions are initiated (in this case by dissociating F_2 and H_2 with an electron beam), they will proceed until all the available reactants are consumed. This has the result of increasing the electrical efficiency of the laser because additional chemical energy, and therefore light energy, is generated via the chain reaction for each initial dissociation. This increase in electrical efficiency is advantageous because it decreases the electrical energy storage requirements. The electrical and chemical efficiencies are shown in Fig. I.3-15 as a function of the hydrogen partial pressure. The most convenient configuration for the laser cavity appears to be a box in which two sides comprise the optical windows, two sides the electron beams, and two sides the gas flow channels, Fig. I.3-16. This results in a square aperture approximately 1 meter on a side. Quartz windows are available in these dimensions. In order to withstand the pressures the windows will have to be 6 to 7 cm thick. Given the aperture area of 10^4 cm^2 determined by energy density limits and a total volume of 333 ℓ, the length of the amplifier is approximately 34 cm.

Another factor that will affect the actual size of the laser cavity is the necessity to multi-pass to reduce the pulse width on target. This technique requires passing beams through the cavity sequentially in time with each beam at a slightly different angle. Thus, the size of

HYDROGEN-FLUORIDE CHEMICAL LASER

$$F + H_2 \rightarrow HF(v \leq 3) + H$$

$$H + F_2 \rightarrow HF(v \leq 6) + F$$

$$HF(v, J) \rightarrow HF(v\text{-}1, J + 1) + h\nu$$

$$2.6 < \lambda < 3.5\ \mu m$$

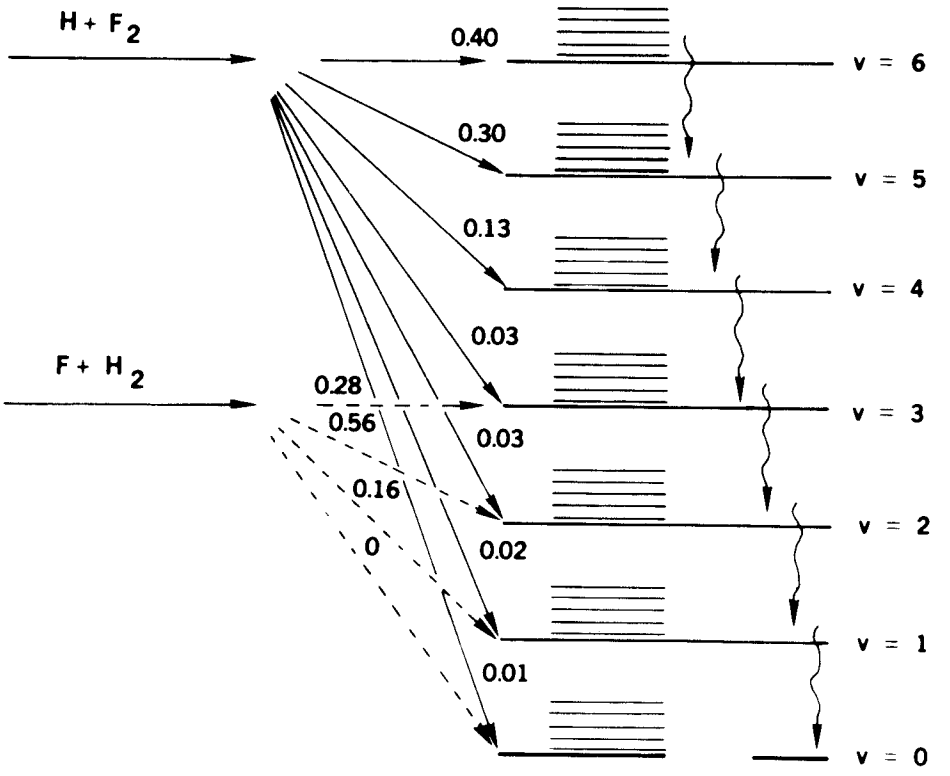

Fig. I.3-14

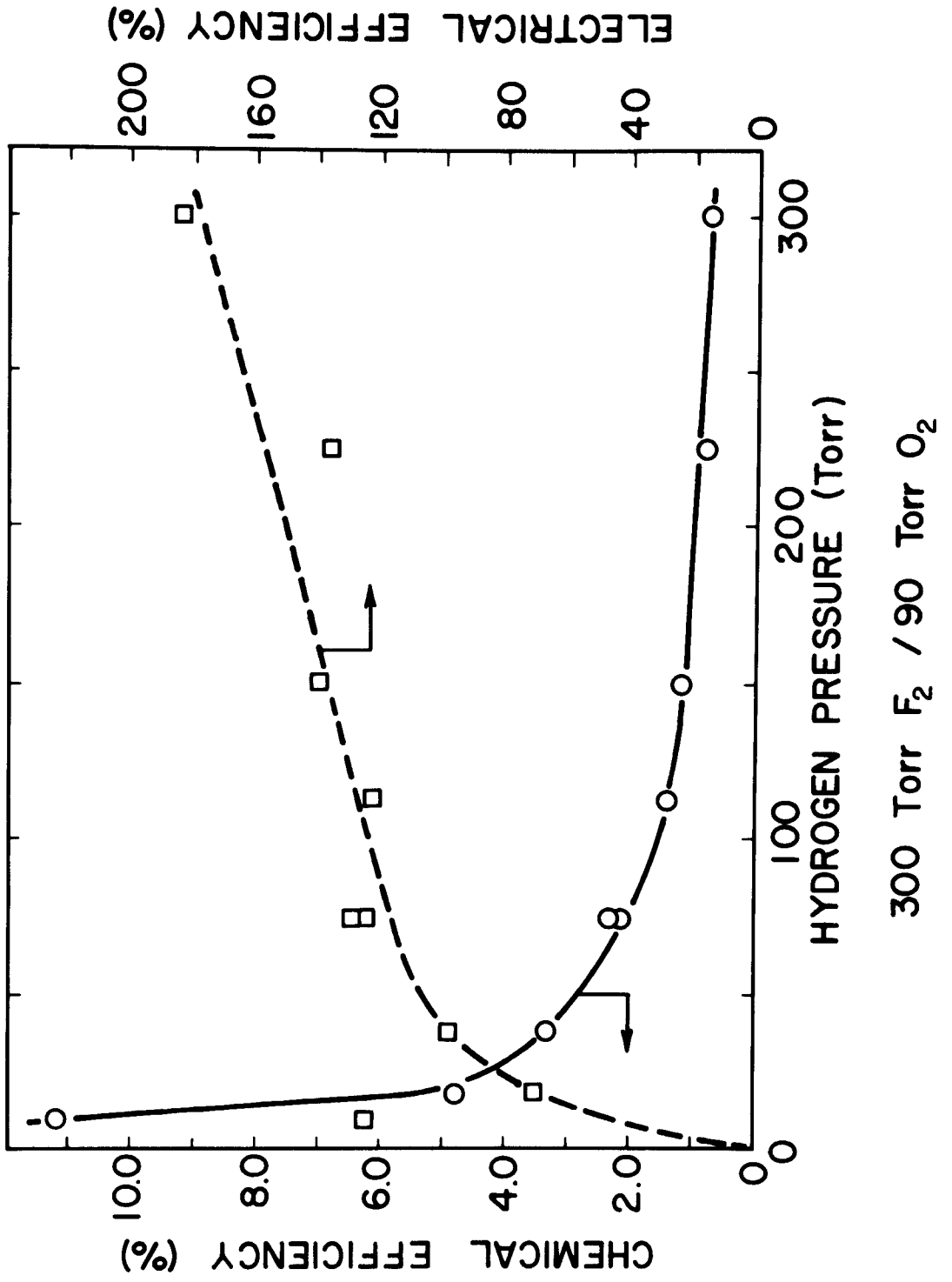
CHEMICAL EFFICIENCY (%)
ELECTRICAL EFFICIENCY (%)
HYDROGEN PRESSURE (Torr)
300 Torr F_2 / 90 Torr O_2
0
2.0
4.0
6.0
8.0
10.0
40
80
120
160
200
100
300

Fig. I.3-15.

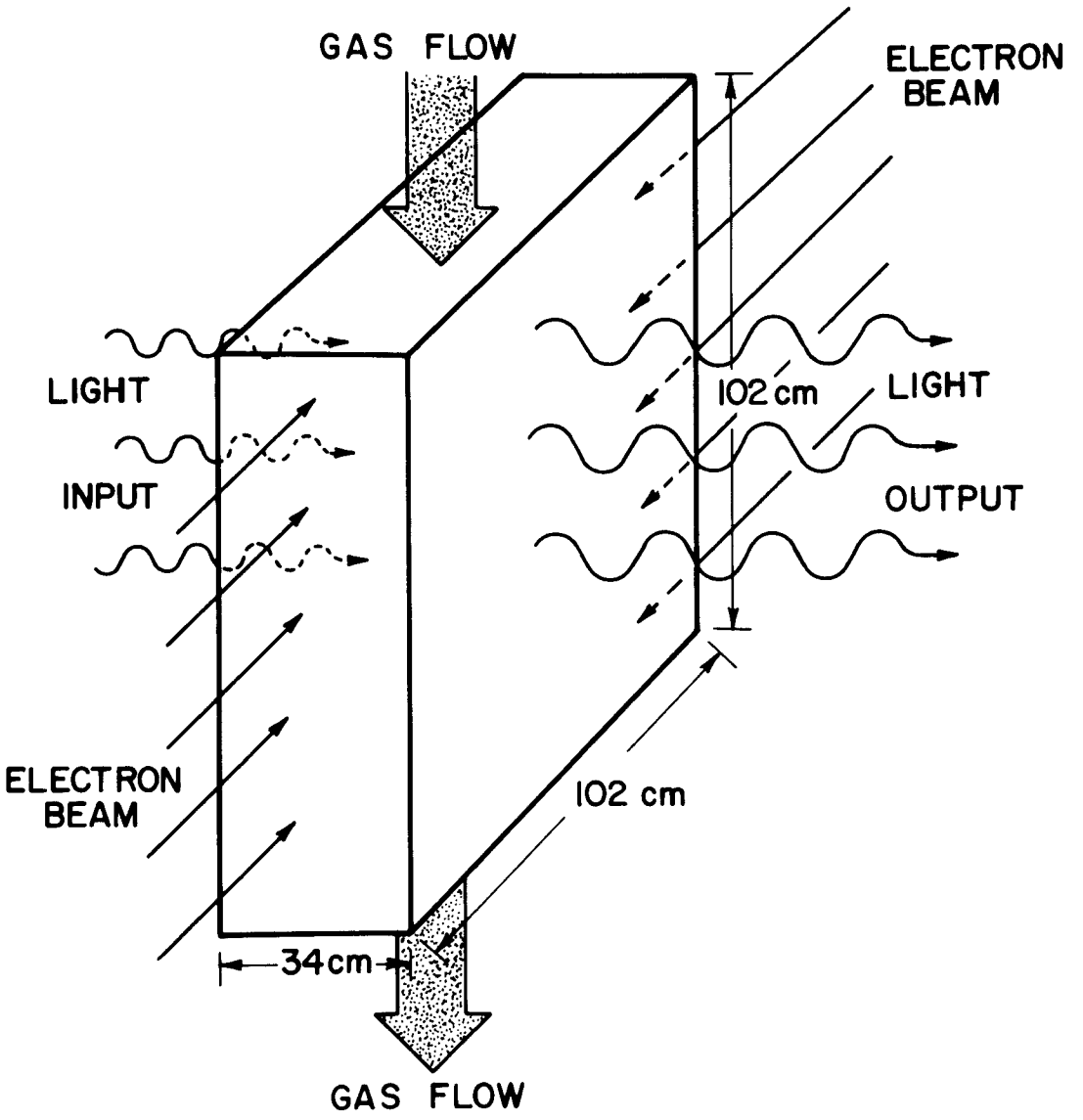

LASER CAVITY CONFIGURATION

Fig. I.3-16.

the aperture must be increased slightly such that the beam area can be 10^4 cm^2. For the base parameters, the size of the aperture must be 102 x 102 cm and have a length of 34 cm.

The natural pulse shape from the HF amplifier is unsuitable for target irradiation. For this reason the final amplifiers must be multiplexed to divide this natural pulse into a number of shorter pulses and then recombine these shorter pulses into the desired pulse shape. Beams are passed through the same amplifier at different times and at different angles (angular multiplexing). Then the beams are allowed to travel far enough that they physically separate. When physically separated each beam can be handled independently and the distance each must travel to reach the pellet can be adjusted so that they arrive at the target at the appropriate time. Such a technique appears essential because there are no known methods of electrically or mechanically switching such high energy beams on such short time scales.

One of the best schemes for extracting energy from the natural pulse appears to be to divide it into three parts, as shown in Fig. I.3-17b. Thus, three beams must be used to extract the energy: ones that extract the first 9 nsec, the next 3 nsec and the final 6 nsec as measured along the base of the pulse. Only two pulse widths, 18 nsec and 3 nsec, are required from the front-end of the laser to accomplish this. The last 9 nsec of an 18 nsec pulse from the front end is used to cover the first 9 nsec of the natural pulse from the power amplifier. This is followed by a 3 nsec pulse from the front end and this is, in turn, followed by the leading 6 nsec of another 18 nsec pulse. Since there appears to be no convenient way to combine beams, each beam must be independently transported to the target and combined at the target as illustrated in Fig. I.3-17c.

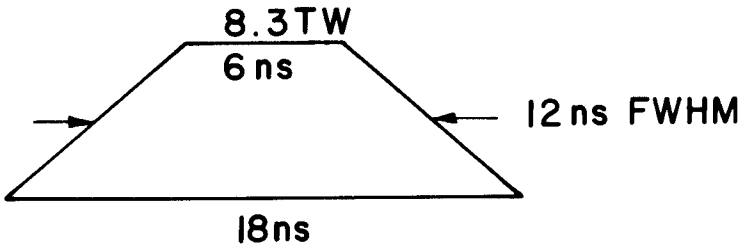

(a IDEALIZATION OF NATURAL PULSE SHAPE

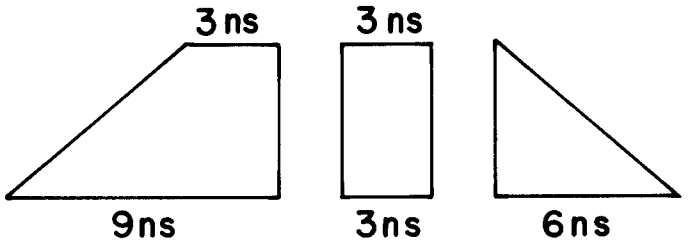

(b) DIVISION OF PULSE BY MULTIPASSING

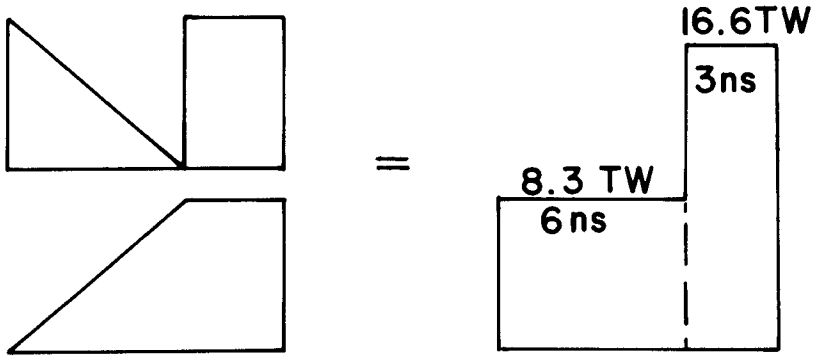

(c) PULSE SHAPING BY STACKING ON TARGET

Fig. I.3-17

Eighteen of the 20 final amplifiers can be multipassed in this manner, and the full energy from the other two can be extracted. Then a pulse, as shown in Fig. I.3-18, can be formed by using the two long pulses to form the "foot" and stacking the remaining pulses, as indicated in Fig. I.3-17c.

I.3.E-1 EFFICIENCY OF THE HF LASER SYSTEM

One of the most important parameters of the laser system is the net efficiency. This efficiency includes all of the energy costs of running the laser. It is this efficiency that largely determines the economics of the ICF reactor.

The net efficiency can be defined as

$$\eta = \frac{\text{Laser Energy } (E_L)}{E(\text{e-beam}) + E(\text{B-field}) + E(\text{chemical}) + E(\text{gas flow}) + E(\text{other})}.$$

This expression can be inverted and separated for easier evaluation. This yields:

$$\frac{1}{\eta} = \frac{E(\text{e-beam})}{E_L} + \frac{E(\text{B-field})}{E_L} + \cdots$$

or

$$\frac{1}{\eta} = \frac{1}{\eta(\text{e-beam})} + \frac{1}{\eta(\text{B-field})} + \cdots .$$

This expression separates the high grade energy (such as the e-beams) which seriously affects reliability, from low grade energy (such as gas-handling pumps) which is assumed to be reliable.

The final wall-plug efficiency of the e-beam is $\eta(\text{e-beam}) = 0.28$. The efficiency of the magnetic field required to prevent pinching of the e-beams and scattering of the e-beam to the windows is found to be $\eta(\text{B-field}) = 1.65$.

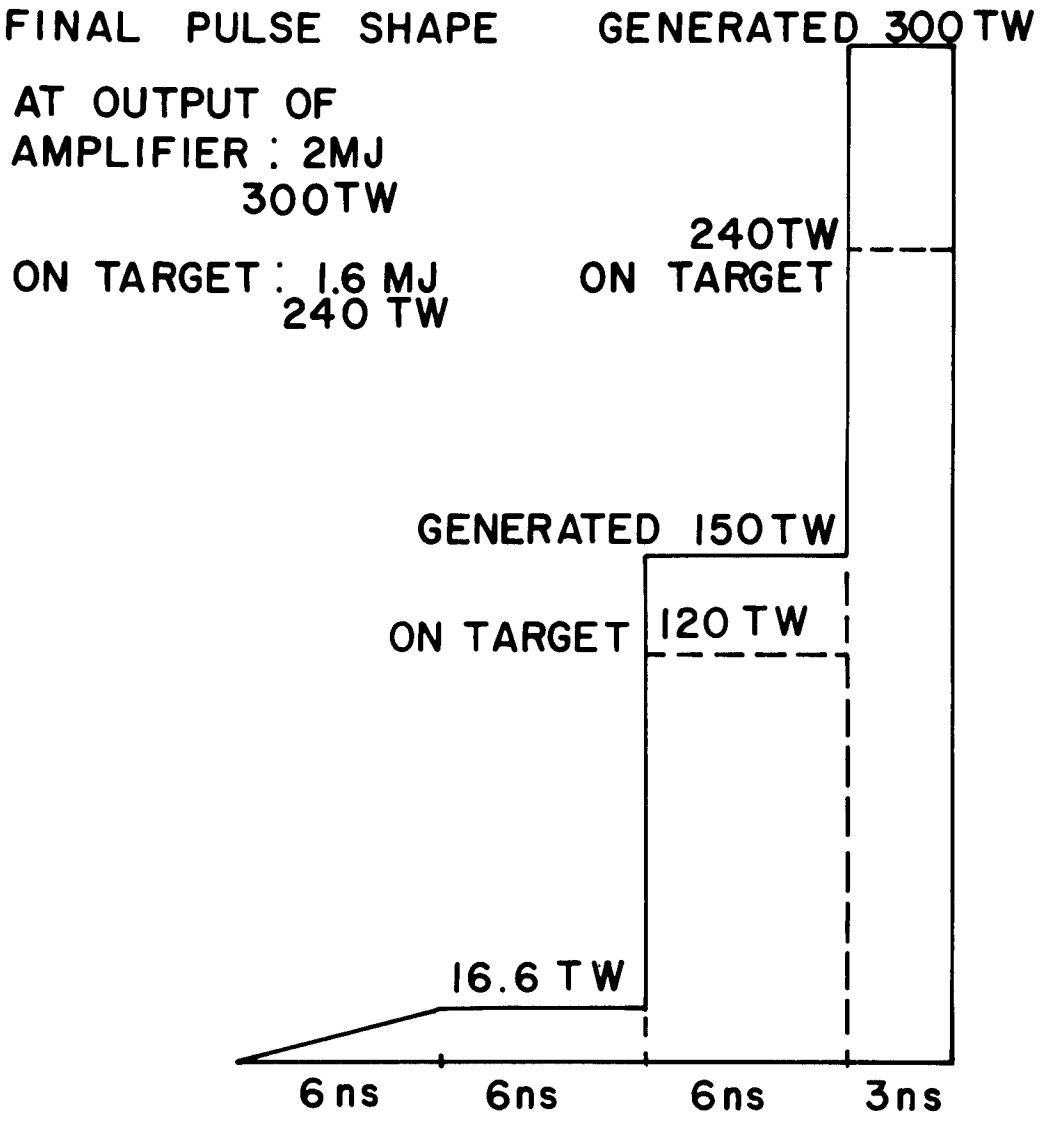
FINAL PULSE SHAPE
AT OUTPUT OF
AMPLIFIER : 2MJ
300TW
ON TARGET : 1.6 MJ
240 TW
GENERATED 300 TW
240TW
ON TARGET
GENERATED 150TW
ON TARGET 120 TW
16.6 TW
6ns
6ns
6ns
3ns

Fig. I.3-18

The factors that make up the chemical efficiency include the basic chemical efficiency (laser energy divided by the energy released by the chemical reaction), the efficiency of regeneration of the gases, and a volume efficiency, since the fuel mixture will be somewhat larger than the cavity volume. These efficiencies are summarized in Table I.3-3, and the net chemical efficiency is found to be η(chemical) = 0.04.

The net efficiency of the laser is estimated to be 3.4%. A final factor to be included is the efficiency of delivering the laser energy to the target. It is estimated that only 80% of the energy is ultimately focusable on the target. This includes effects such as imperfect beam quality, absorption by the mirrors, misalignment, and wavefront distortions. This effectively reduces the efficiency to 2.7%. Of course, increasing the fraction of focusable energy would make considerable impact on the net efficiency.

High-quality energy is represented only in the e-beam drivers and related external magnetic field supply. Thus, on a per pulse basis, the 2 MJ HF laser requires 51 MJ of low-quality energy but only 8.4 MJ of high-quality energy. Since it is the high-quality energy that seriously affects the reliability of the laser, this is a great advantage that the HF laser has over other lasers which have lower electrical efficiencies and, therefore, a greater reliance on high quality energy.

I.3.E-2 CONCLUSIONS CONCERNING THE HYDROGEN FLUORIDE LASER

The hydrogen-fluoride laser appears to be a very attractive candidate for laser fusion hybrid applications. Compact, final amplifiers can be built to provide a high energy per pulse, 100 kJ. Hence, 20 such ampli-

Table I.3-3

Efficiency of the HF Laser

$$\frac{1}{\eta(\text{total})} = \frac{1}{\eta(\text{e-beam})} + \frac{1}{\eta(\text{B-field})} + \frac{1}{\eta(\text{chemical})}$$

$$+ \frac{1}{\eta(\text{gas flow})} + \frac{1}{\eta(\text{other})}$$

$$\eta(\text{e-beam}) = \frac{E_L}{E(\text{deposited})} \times \frac{E(\text{deposited})}{E(\text{e-beam})} \times \frac{E(\text{e-beam})}{E(\text{Marx})} \times \frac{E(\text{Marx})}{E(\text{wall plug})}$$

$$= 0.53 \times 0.7 \times 0.8 \times 0.95 = 0.28$$

$$\eta(\text{B-field}) = \frac{E_L}{E(\text{B-field})} = \frac{100}{60} = 1.66$$

$$\eta(\text{chemical}) = \frac{E_L}{E(\text{exothermic})} \times \frac{E(\text{exothermic})}{E(\text{regenerated chemicals})}$$

$$\times \frac{\text{volume laser cell}}{\text{volume of } H_2\text{-}F_2\text{-}O_2} = 0.11 \times 0.40 \times 0.90 = 0.04$$

$$\eta(\text{gas flow}) = \frac{E_L}{E(\text{gas flow})} = \frac{100}{59} = 1.7$$

$$\eta(\text{other}) >> 1 (\text{assumed negligible})$$

$$\eta(\text{total}) = 0.027$$

fiers will provide 2 MJ of laser energy. The laser can operate at a net efficiency of 2-3% with a very high electrical efficiency, 25%. This minimizes the reliability problems of handling large amounts of "high quality" energy. This, of course, shifts the burden to the chemical processing of the laser gas. However, these processes are well established, hence, the most important question is the economics rather than the technical feasibility of them. The gas handling limits the repetition rate to about 4-6 Hz. For this reason, the HF laser may not be as attractive for fusion electric power reactors as some other candidates.

Short pulses must be obtained through multiplexing the amplifiers. This complicates the optics system. In the SOLASE-H study, 56 separate beams must be used to compress the pulse to 3 nsec. If shorter pulse lengths are required, then the HF laser becomes questionable due to further complications of the optics system. However, if longer pulses can be tolerated, then this laser appears even more attractive.

Another significant question is the HF laser wavelength of 2.6-3.5 μm. This is not likely to be the optimum wavelength for laser-target interaction, but depending on the target design, this may be adequate. This problem awaits more experimental evidence before a final decision can be made.

I.3.F CAVITY FIRST WALL ANALYSIS

The first wall in SOLASE-H is 2 mm of zircaloy and is 6 m from the target microexplosion. It is scalloped to sustain the pressure of the Na coolant behind it, Fig. I.3-5. It is protected from the pellet debris and X-rays by 0.25-1.0 torr of Xe gas. It is assumed that the Xe gas will attenuate all target X-rays and pellet debris so that this energy is reradiated to the wall. At such low densities and high temperatures (> 50 eV) the gas must be modelled using the Coronal rather than the Saha model of ionization. This affects the computed charge state by about 20-30%. It is assumed that the target X-rays and debris deposit their energy in the gas so that the temperature distribution looks like that in Fig. I.3-19. When the gas motion and reradiation are modelled using a hydrodynamics model the results are those shown in Fig. I.3-20. From this figure it can be seen that there is a synergistic effect between the gas motion and reradiation. When the gas is modelled with the reradiation mechanism "turned on" the resulting pressure wave at the first wall is very weak giving an overpressure of only 30 torr. When the reradiation is "turned off", so that all of the target debris and X-ray energy is trapped in the gas, the pressure wave is much stronger and the overpressure is 90 torr.

The reradiation process is described using three different models. Two of the models assume the gas is thin to the radiation so that it freely escapes. These models differ in the initial temperature profile in the gas. One assumes that the gas starts at a uniform temperature while the other assumes that there is a temperature profile, Fig. I.3-20. The third model assumes a temperature profile, but also assumes that the gas is thick to the radiation so that it must diffuse to the first wall. The effective

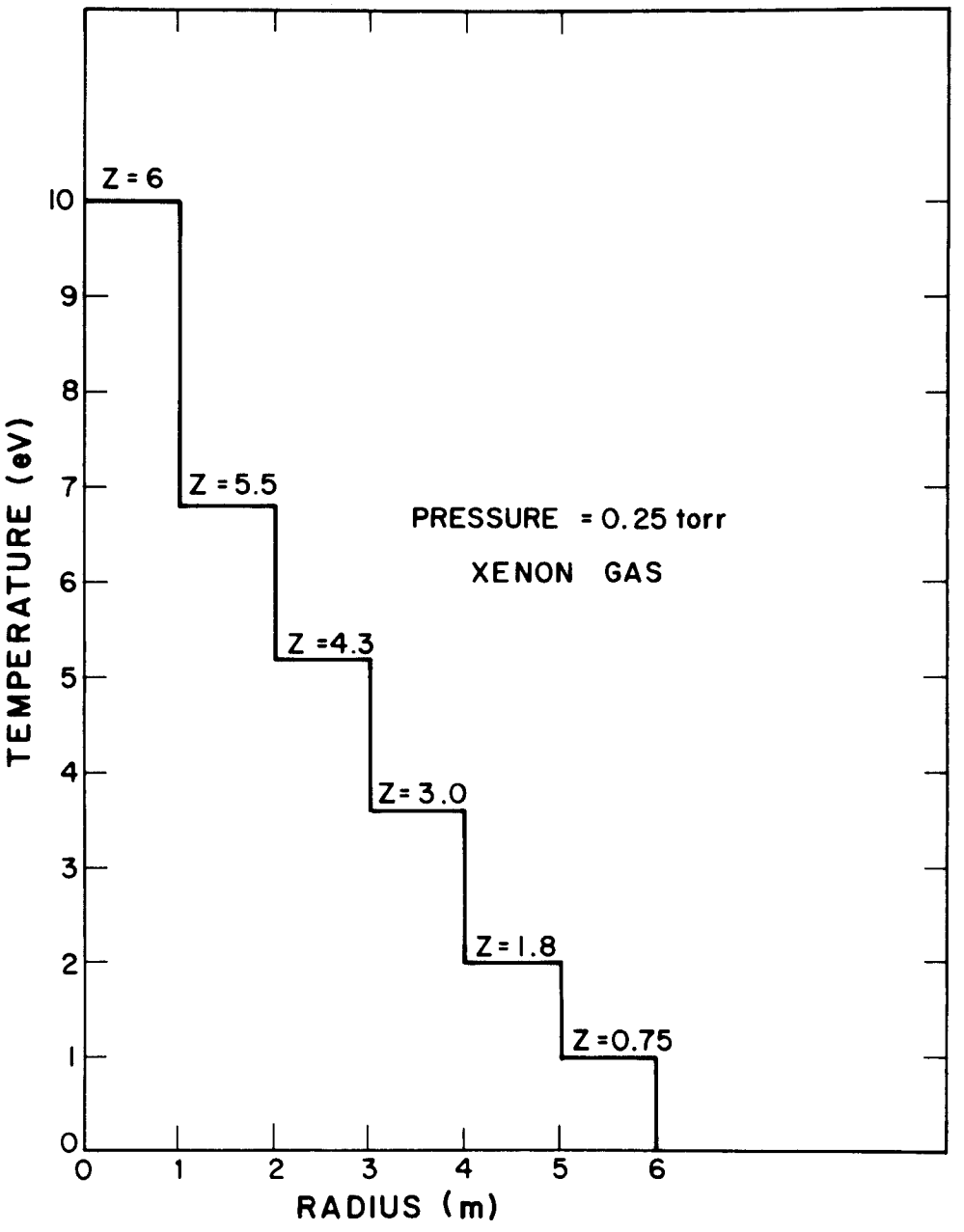
Z = 6
Z = 5.5
Z =4.3
Z= 3.0
Z= 1.8
Z =0.75
PRESSURE = 0.25 torr
XENON GAS
TEMPERATURE (eV)
RADIUS (m)
0
1
2
3
4
5
6
7
8
9
10

Fig. I.3-19

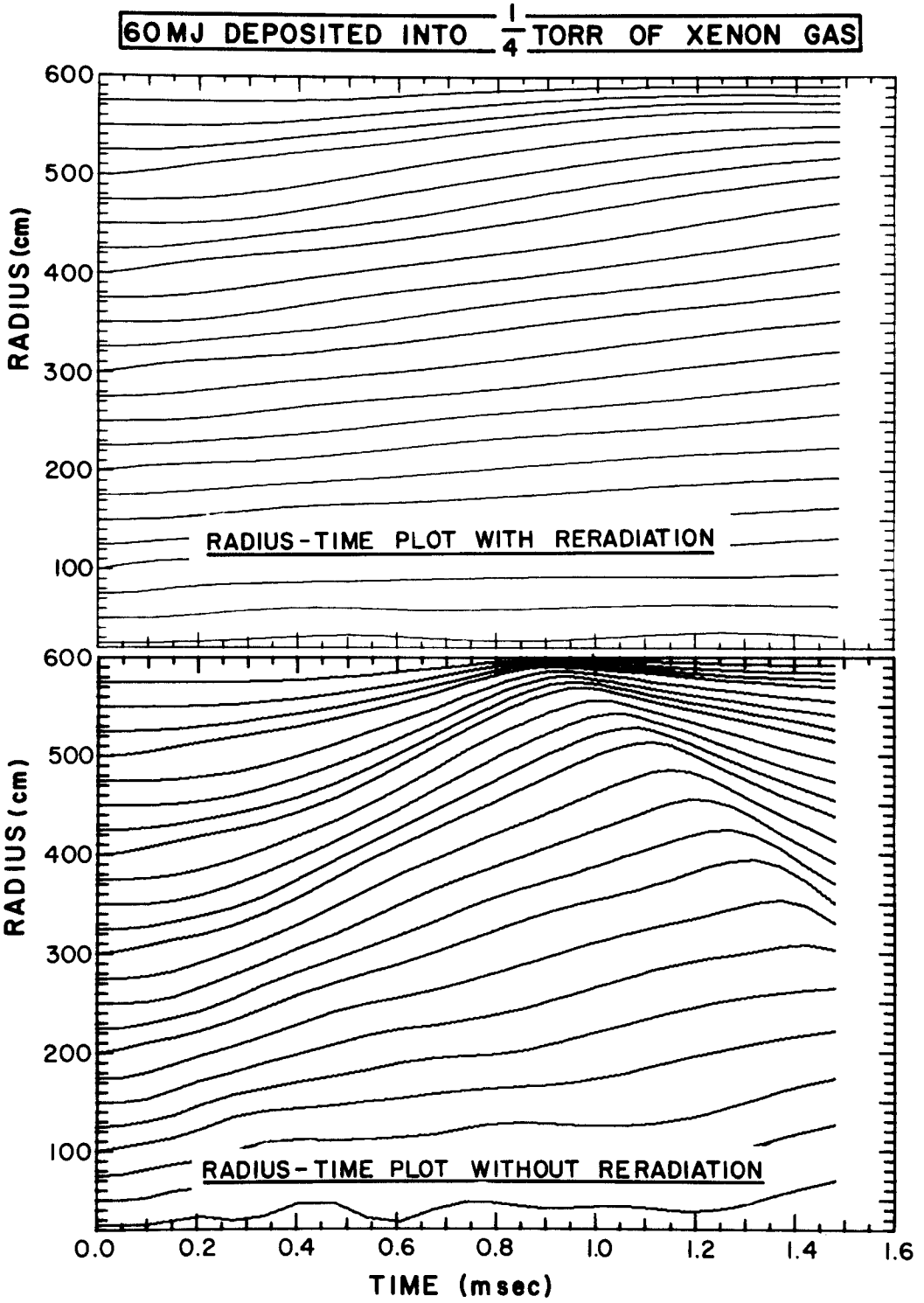
60 MJ DEPOSITED INTO 1/4 TORR OF XENON GAS
RADIUS (cm)
600
500
400
300
200
100
RADIUS-TIME PLOT WITH RERADIATION
RADIUS-TIME PLOT WITHOUT RERADIATION
0.0
0.2
0.4
0.6
0.8
1.0
1.2
1.4
1.6
TIME (msec)

Fig. I.3-20

power radiated by the gas using these three models is shown in Fig. I.3-21. It is seen that although the radiation diffusion model slows the reradiation rate slightly, it does not have an overwhelming effect. This means that the basic atomic processes responsible for the emission of the radiation will dominate the reradiation rate at the wall.

The temeperature rise in the first wall is shown for 0.5 and 1 torr of Xe cavity gas and zircaloy and stainless steel wall material in Fig. I.3-22. Although the temperature rise is greater for the zircaloy wall, the resulting stresses are actually greater for the stainless steel (see Table I.3-4).

Stainless steel is a poor first wall choice because of its large modulus E and thermal expansion coefficient α. Other materials rate even better than zircaloy when compared on the basis of a figure of merit for thermal shock stresses (Table I.3-5). It has been proposed that a figure of merit be defined as:

$$f = \frac{\sigma_y K(1-\nu)}{E\alpha\sqrt{\beta}} = \text{figure of merit}$$

where: E = Young's modulus

α = thermal expansion coeff.

β = thermal diffusivity = $\frac{K}{\rho c_p}$

σ_y = yield strength

K = thermal conductivity

ν = Poisson's ratio

This figure of merit represents the ratio of yield strength to the thermal stress in a semi-infinite solid subjected to a suddenly applied heat flux, q''_o. In this case, the compressive thermal stress is given by:

$$\sigma_{th} = \frac{2}{\sqrt{\pi}} \frac{q''_o}{K} \frac{E\alpha}{(1-\nu)} \frac{\sqrt{kt}}{\rho c_p}$$

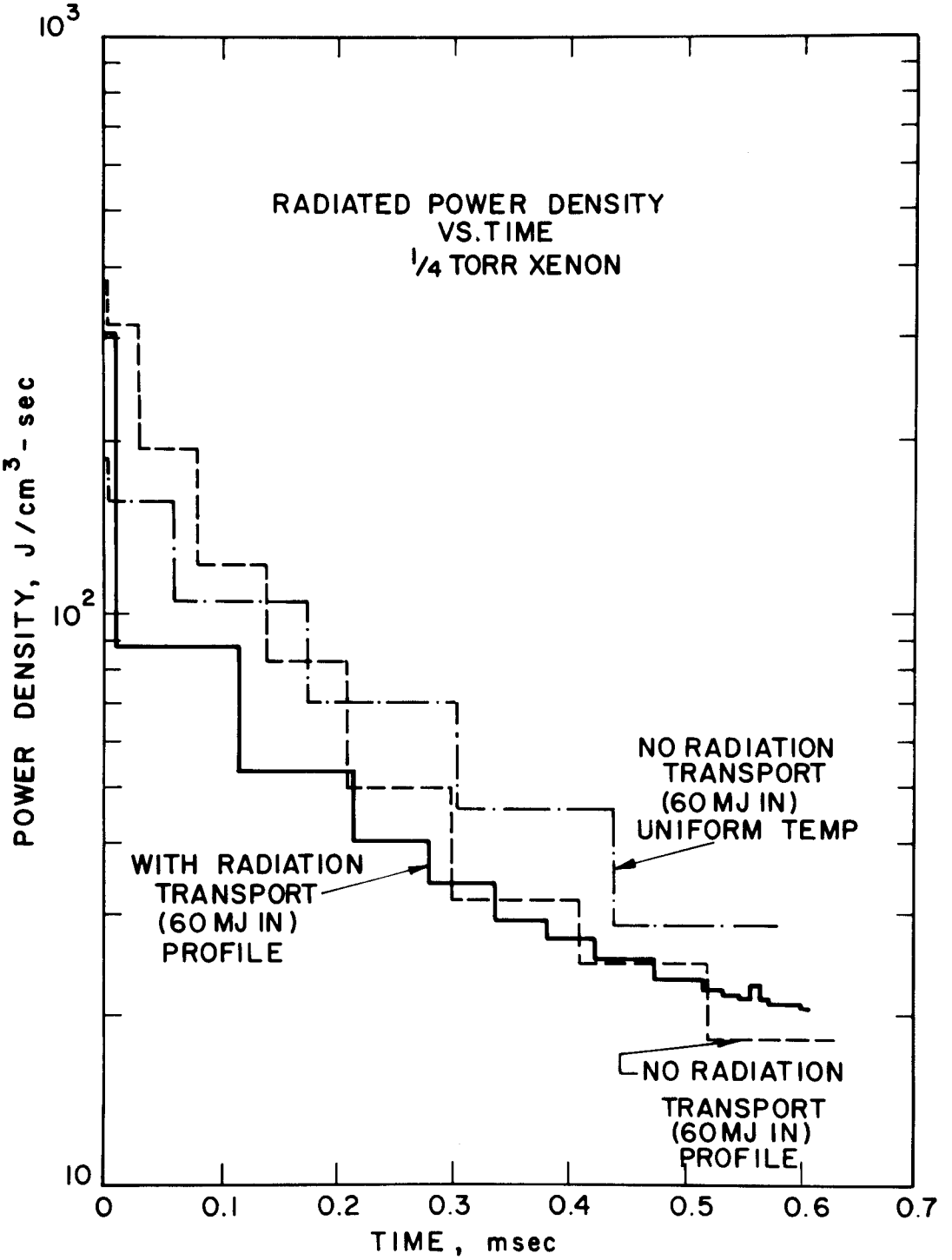
RADIATED POWER DENSITY
VS. TIME
1/4 TORR XENON
POWER DENSITY, J/cm³-sec
TIME, msec
10³
10²
10
0
0.1
0.2
0.3
0.4
0.5
0.6
0.7
NO RADIATION TRANSPORT (60 MJ IN) UNIFORM TEMP
WITH RADIATION TRANSPORT (60 MJ IN) PROFILE
NO RADIATION TRANSPORT (60 MJ IN) PROFILE

Fig. I.3-21

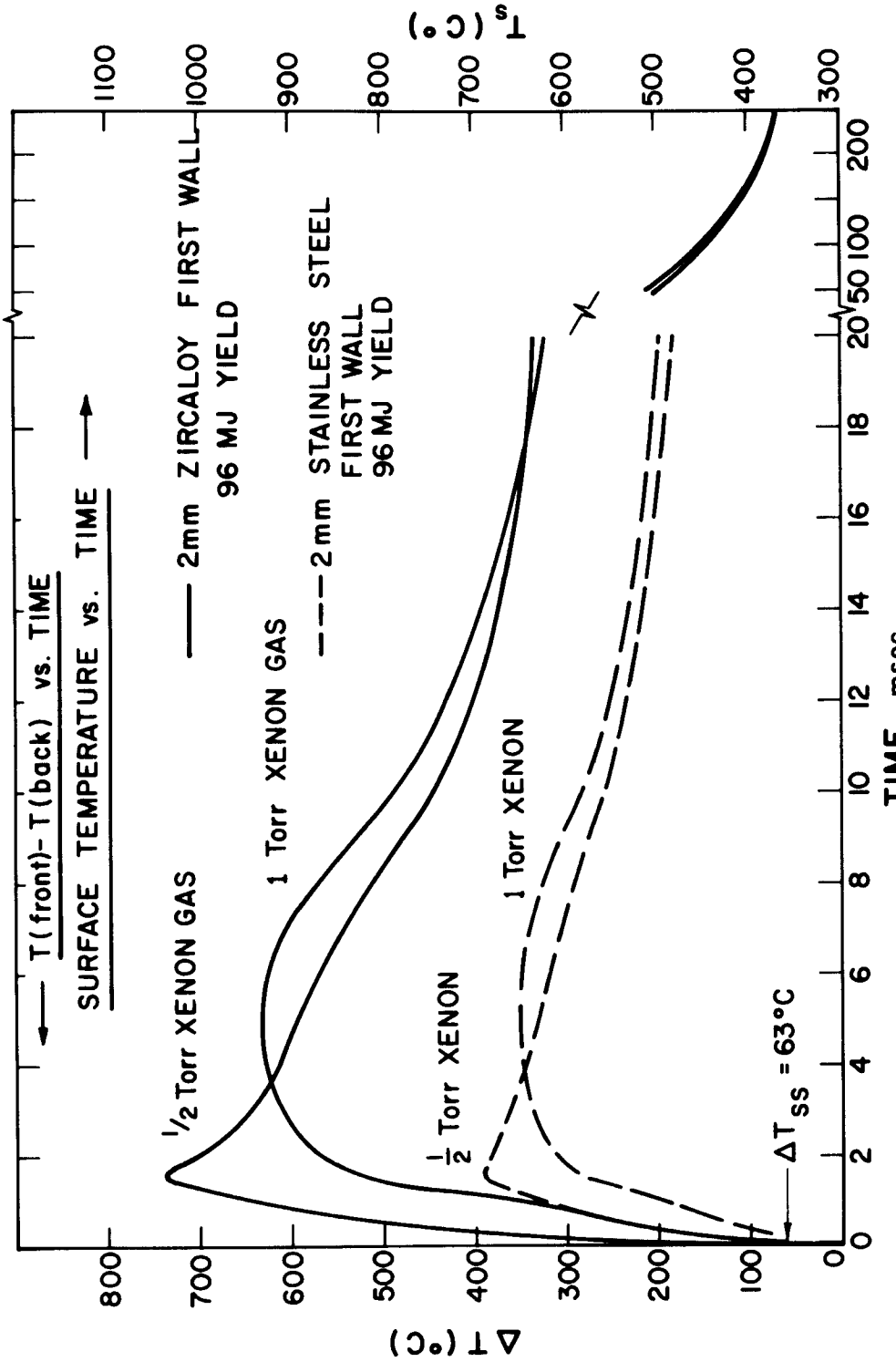
T(front)-T(back) vs. TIME
SURFACE TEMPERATURE vs. TIME
2mm ZIRCALOY FIRST WALL
96 MJ YIELD
2mm STAINLESS STEEL
FIRST WALL
96 MJ YIELD
1/2 Torr XENON GAS
1 Torr XENON GAS
1/2 Torr XENON
1 Torr XENON
ΔT_ss = 63°C
ΔT (°C)
T_s (°C)
TIME, msec

Fig. I.3-22

Table I.3-4

Material Properties

Metal	E (psi)	α ($^\circ C^{-1}$)	k (W/cm°C)	ν	σ_y(@400°C) (psi)	$\frac{E\alpha}{1-\nu}$ (psi/°C)
S.S.	28×10^6	18×10^{-6}	0.173	0.33	50,000	756
Zr-2	11×10^6	6.5×10^{-6}	0.125	0.33	30,000	107

Stress Summary

Metal	Xe Pressure	ΔT_{max} at surface	Maximum Net Compressive Stress	Maximum Net Tensile Stress	Yield Strength σ_y(@400°C)
S.S.	1/2 torr	390°C	-262 ksi	36 ksi	50 ksi
S.S.	1	350	-235	33	50
Zr-2	1/2	740	- 65	14	30
Zr-2	1	630	- 55	13	30

When compared with the traditional thermal stress parameter, $\frac{\sigma_y K(1 - \nu)}{E\alpha}$, the figure of merit, "f," contains an extra factor $\frac{K}{\rho c_p}$. Physically, this accounts for the rate of change of surface temperature due to thermal diffusion for a given applied heat flux. The larger value of "f" is preferred. Clearly, SiC and graphite appear to be better choices with respect to minimizing thermal stresses.

Table I.3-5

Thermal Shock Stress Figure of Merit

Material	Figure of Merit	Preference
SiC	18.7	1
Graphite	18.2	2
Zircaloy	14.2	3
Stainless Steel	0.6	4

I.3.F-1 CONCLUSIONS OF THE CAVITY AND FIRST WALL ANALYSIS

The reradiated energy from the cavity gas will have a spectrum such that the gas is neither totally thick nor thin to the radiation. However, by modelling the energy escaping to the wall in the two limits it is found that the heat flux at the wall and the resultant temperature rise is not significantly different. The heat flux is determined by the gas reradiation rate, a quantity that is not well known.

Temperature rises in the wall for 96 MJ of energy reradiated are very high, resulting in unacceptable thermal stresses. The mechanical stresses from the blast overpressure are negligible in comparison. However, the large ΔT's occur over a very thin layer in the wall and over a short time. This complicates the structural analysis of the wall. The quasi-steady state stresses are manageable. These transient stresses could be reduced by lowering

the target yield, increasing the repetition rate, and increasing the cavity size. Increasing the cavity gas pressure from 0.5 torr to 1.0 torr only reduces the stresses by 15%. Stainless steel is a particularly unsuitable choice for first wall material according to these criteria.

I.3.G SYSTEM INTEGRATION INTO SOLASE-H REPRESENTATIVE DESIGN

The SOLASE-H laser fusion hybrid reactor study includes the parametric analysis of five separate areas: (1) fission fuel cycle, (2) hybrid blanket design, (3) fusion performance requirements, (4) HF laser, and (5) cavity, first wall, and mechanical design. These topics are discussed in sections I.3.A-F of this introductory part of the SOLASE-H report. In this section, a set of self-consistent parameters that represent SOLASE-H as an integrated reactor design will be discussed.

The self-consistent set of parameters for SOLASE-H are listed on Tables I.3-6 to I.3-8. The cavity and blanket design are shown in Figs. I.3-23 and 24. The cavity geometry in SOLASE-H is a right circular cylinder with a radius of 6 m and a height of 12 m. This shape is necessary to accommodate the LWR fuel assemblies in the hybrid blanket. The radial blanket subtends 70% of the solid angle at the target. The axial blankets are used exclusively for tritium breeding.

The fusion power in SOLASE-H is 1240 MW. It is assumed that 70% of this (or 868 MW) is in the form of 14 MeV neutrons and that the other 30% (372 MW) is in X-rays and charged particle debris. This rather high level of fusion power is required to produce a ^{233}U breeding rate that will fuel 2-3 LWRs of equivalent thermal power. This high fusion power level is one of the characteristics of the direct enrichment hybrid. To achieve such fusion power in a laser driven reactor requires either a large yield or a

Table I.3-6

SOLASE-H PARAMETERS

Cavity Shape	Cylindrical
Cavity Radius	6 m
Cavity Height	12 m
Structure - Blanket	Zircaloy
- First Wall	2 mm Zircaloy
First Wall Protection	1.0 torr Xenon Gas
Fusion Power	1240 MW
Pellet Yield	310 MJ
Neutrons	217 MJ
X-rays and Ions	93 MJ
Pellet Gain	194
Pulse Repetition Freq.	4 s^{-1}
Laser Energy (on target)	1.6 MJ

Table I.3-7

SOLASE-H PARAMETERS

Fusion Power	1240 MW
Average Thermal Power	2655 MWt
Thermal Power Range	2390-2920 MWt
Per Cent Variation	(19%)
Gross Elect. Output	946 MWe
Net Elect. Output	700 MWe
Recirc. Power Fraction	26%
Radial Blanket Power Mult.	1.5 - 5
Neutron Wall Loading (Max)	1.9 MW/m^2
Coolant	Na
Coolant Temperatures	300-350°C
Tritium Breeding Ratio	1.08
Tritium Breeding Material	Li
Fertile Material	ThO_2
U^{233} Production Rate	0.43/Fusion Neutron
	2.03 Tonnes/yr
	0.77 kg/MW_t-year
Fuel Form	(17x17) PWR Assemblies
Number of Assemblies	270
Time to 4% Enrichment	2.6 yr
Max/Ave. Enrichment (Radial)	1.1
Neutron Multiplier	Pb
Number of LWRs supported without reprocessing (700 MWe)	2

Table I.3-8

SOLASE-H PARAMETERS

Laser Type	Hydrogen-Fluoride
Laser Energy	2 MJ
Net Efficiency	2.6%
Electrical Eff.	24%
Wavelength	2.7 - 3.5 μm
Maximum Power	300 TW
Pulse Length (Multiplexed)	3 ns
Number of Final Amplifiers	20
Last Mirror Position	22 m
Number of Last Mirrors	56
Illumination	Two-sided

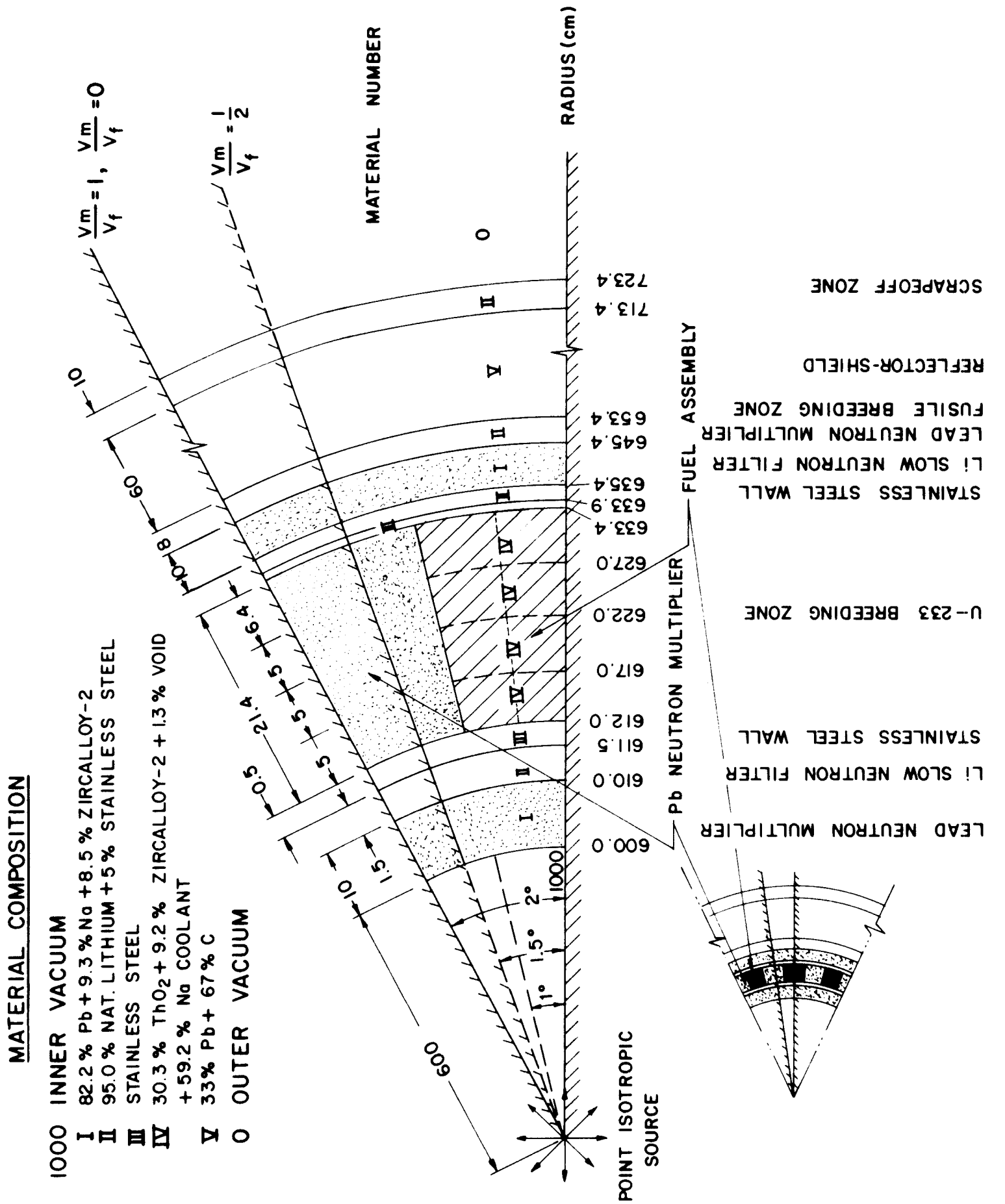
MATERIAL COMPOSITION
1000 INNER VACUUM
I 82.2% Pb + 9.3% Na + 8.5% ZIRCALLOY-2
II 95.0% NAT. LITHIUM + 5% STAINLESS STEEL
III STAINLESS STEEL
IV 30.3% ThO2 + 9.2% ZIRCALLOY-2 + 1.3% VOID + 59.2% Na COOLANT
V 33% Pb + 67% C
0 OUTER VACUUM
Vm/Vf = 1, Vm/Vf = 0
Vm/Vf = 1/2
MATERIAL NUMBER
RADIUS (cm)
SCRAPEOFF ZONE
REFLECTOR-SHIELD
FUSILE BREEDING ZONE
LEAD NEUTRON MULTIPLIER
LI SLOW NEUTRON FILTER
STAINLESS STEEL WALL
FUEL ASSEMBLY
U-233 BREEDING ZONE
STAINLESS STEEL WALL
LI SLOW NEUTRON FILTER
LEAD NEUTRON MULTIPLIER
Pb NEUTRON MULTIPLIER
POINT ISOTROPIC SOURCE
600.0
610.0
611.5
612.0
617.0
622.0
627.0
633.4
633.9
635.4
645.4
653.4
713.4
723.4
1000
600
10
60
10
0.5
21.4
6.4
5
5
5
10
1.5
2°
1.5°
1°

Fig. I.3-23

THE SOLASE-H LASER FUSION HYBRID

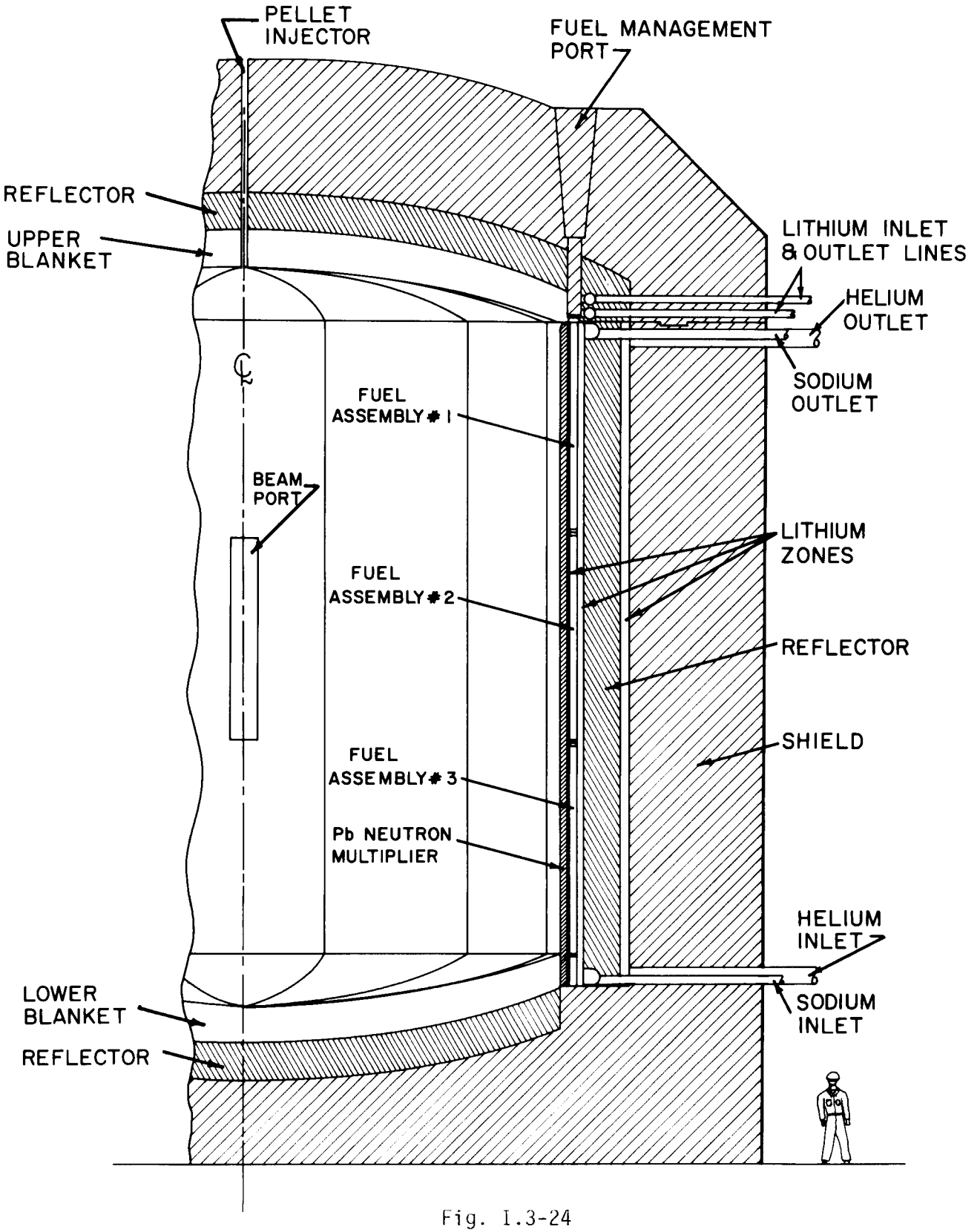

Fig. I.3-24

large repetition rate. For SOLASE-H we chose to consider a yield of 310 MJ and a repetition rate of 4 Hz. This matches nicely to the hydrogen fluoride laser because this laser is capable of delivering high energy per pulse but is repetition rate limited by gas reprocessing problems. The laser energy on target is 1.6 MJ. This gives a target gain of 194. This large target gain is likely to be the most uncertain aspect of the fusion parameters in SOLASE-H. The large laser energy on target should help to increase the probability of this gain. However, the relatively long wavelength of the HF laser, 2.7-3.5 μm, leaves considerable question about this postulated target performance. It is assumed that 30% (or 93 MJ) of the thermonuclear microexplosion energy is in the form of X-rays and charged particle debris. No specific partitioning of the energy between these two forms has been assumed. No target design calculations are done to verify either the gain or the output spectra of the X-rays and debris. The output spectra are assumed to be soft enough that they are stopped in 1 torr of Xe gas that fills the reactor cavity.

A hydrogen fluoride laser is used in the SOLASE-H reactor study. The HF laser represents an established laser technology that meets the requirements of near term technology development. A 2 MJ laser is designed to deliver pulses to the targets at a rate of 4 Hz. Only 1.6 MJ or 80% of the laser output is assumed to reach the target. The remaining 20% is lost in the beam transport system. No detailed design of the beam transport system is done. As mentioned earlier, the wavelength of the HF laser is in a range between 2.7-3.5 μm. The maximum power of the laser pulse is 300 TW, but only 240 TW (80%) reaches the target. The pulse width at this high power is 3 nsec. The pulse is shaped in time and this should increase the chances of reaching the assumed target gain of 194. There are 20 final amplifiers; 18 of these are multiplexed to increase the laser efficiency. The net efficiency is 2.6% but the electrical efficiency

is 24%. This high electrical efficiency reduces the power supply requirements. The remainder of the efficiency is contributed by the chemical reprocessing of the HF laser gas. This chemical reprocessing and the gas flow through the amplifiers limit the repetition rate to about 4-6 Hz. For higher repetition rates the gas handling problems become significantly greater.

There are 56 beams incident on the target from two sides. The last mirrors on each side are arranged in a 2 x 14 array so that the beam port penetrations through the blanket most closely match the geometry of the stacked fuel assemblies. In this way, the minimum number of assembly locations, 12, are lost to the beam ports. The final mirrors are located 22 m from the target explosion.

The first wall of SOLASE-H is 2 mm of zircaloy. It is protected from the pellet blast by 1 torr of Xe gas in the cavity. This gas absorbs the 93 MJ of X-rays and ionic debris and reradiates the energy to the first wall in a long (~ msec) pulse. The temperature rise in the first wall surface is computed to be about 600°C and the maximum overpressure from the blast wave is 250 torr. This overpressure should be acceptable but the surface temperature rise is quite large. This could be reduced by enlarging the cavity or by increasing the repetition rate and reducing the yield per shot. The calculations of the heat flux incident on the wall are also rather uncertain (although improvements were made over the SOLASE calculations). The intent in SOLASE-H is to investigate the possibility of protecting a bare metal wall with the Xe buffer gas. The results show that this is likely to be possible but further analysis is required to substantiate the exact range of parameters.

The fusion power in SOLASE-H is 1240 MW but the thermal power varies between 2390-2920 MW. The average thermal power is 2655 MW. This 19% variation is due to the changing blanket energy multiplication as the LWR assemblies are enriched. To compute this energy variation it is assumed that the blanket is in an equilibrium cycle with four batches of assemblies. The first batch is being enriched from 0% to 1.0%. The second batch is enriched from 1% to 2 %, etc. The blanket multiplication then varies from 2.86 to 3.72. If the total blanket inventory is enriched from 0% to 4% then the multiplication varies between 1.5-5. The average power of 2655 MW is converted at an efficiency of 35% to 946 MW of gross electric power. The recirculating power fraction is 26% of this or 246 MW. Hence the net electric power is 700 MW.

The radial blanket consists of a 2 mm zircaloy first wall followed by a Pb neutron multiplier zone. The Pb is contained in tubes and is cooled by Na. The Na has an inlet temperature of 300°C and an exit temperature of 350°C. The first wall is operated at 300°C except for the transients during the pulse of reradiated energy from the Xe buffer gas. This neutron multiplier zone is followed by a Li zone and then the LWR fuel assemblies. Another Li zone is directly behind the assemblies. The Li in these zones is contained in tubes that are cooled by Na. The Li zones serve as a thermal neutron filter to minimize the fission rate in the fuel assemblies. The fuel assemblies are also cooled by Na. A Pb plus C reflector is behind the back Li zone to reflect fast neutrons back into the fuel assemblies. With this configuration the assemblies are a fast neutron flux trap. Behind the reflector is another Li zone followed by a shield. The total blanket thickness without the shield is 1.11 m.

The blanket contains 270 (17x17) PWR fuel assemblies that are initially loaded with ThO_2. Every other assembly position around the circumference is replaced by a neutron scattering zone to reduce the fuel inventory. These assemblies are enriched to an average ^{233}U concentration of 4% in 2.6 years. This is the equivalent of 0.77 kg of $^{233}U/MW_t$-year or 0.43 ^{233}U nuclei/fusion neutron. These numbers do not include a plant factor or burnup. The maximum to average fuel enrichment across the assembly is 1.1 and is acheived by rotating the assembly during its exposure time. Uniform enrichment along the axial direction must be achieved by moving the assembly to different axial positions in the blanket. This fuel management scheme has not been assessed in detail. Assuming a fuel burnup of 30,000 MWD/MTU in the fission reactors and no reprocessing of the spent fuel, the SOLASE-H hybrid can fuel ~ 2 LWRs of equivalent thermal power.

References for Section I

1. L.M. Lidsky, "Fission-Fusion Systems: Hybrid, Symbiotic and Augean ", Nucl. Fusion 15, 151 (1975).

2. R.P. Rose et al., "Fusion-Driven Breeder Reactor Design Study", Final Report, WFPS-TME-043, May 1977.

3. R.G. Mills, "Systems Analyses of Fusion-Driven Fission", Proc. of 3rd ANS Topical Meeting on the Technology of Controlled Nuclear Fusion, CONF-780508, 9-11 May 1978, p.1143.

4. K.R. Schultz, D.J. Bender, J.D. Lee, "Preliminary Evaluation of the ^{233}U Refresh Cycle Hybrid Power System Concept", Proc. 3rd ANS Topical Meeting on the Technology of Controlled Nuclear Fusion, CONF-780508, 9-11 May 1978, p. 149.

5. J.D. Lee, "Nuclear Design of the LLL-GA U_3Si Blanket", Proc. 3rd ANS Topical Meeting on the Technology of Controlled Nuclear Fusion, CONF-780508, 9-11 May 1978, p. 219.

6. J.A. Maniscalco, "A Conceptual Design Study for a Laser Fusion Hybrid", 2nd ANS Conf. on the Technology of Controlled Nuclear Fusion, CONF-760935-P2, 21-23 Sept. 1976, p. 657.

7. W.O. Allen and S.L. Thomson, "Electron Beam Fusion-Fission Reactor Studies", 3rd ANS Topical Meeting on the Technology of Controlled Nuclear Fusion, 9-11 May 1978, Santa Fe NM.

8. A.I. Kaznoff, R.W. Lambert, and T.M. Snyder, "Reconstitution of a Laser Fusion Breeding Blanket as BWR Fuel", General Electric Company, Nuclear Energy Group, San Jose, CA, Feb. 1978.

9. R.W. Conn, et al., "SOLASE, A Laser Fusion Reactor Study", Univ. of Wisconsin Fusion Design Memo, UWFDM-220, Nuclear Engineering Dept., Univ. of Wisconsin, 1977. Also, R.W. Conn, "Reactor Aspects of Laser Fusion", International Scientific Forum on an Acceptable Future of Nuclear Energy for the World, Univ. of Miami, Center for Theoretical Studies, Coral Cables, Florida, Nov. 1977.

10. H.A. Feiveson and T.B. Taylor, "Alternative Strategies for International Control of Nuclear Power", Report Prepared for the 1980's Project of the Council on Foreign Relations (Oct. 1976).

11. G.A. Moses, S.I. Abdel-Khalik, R.W. Conn, "Power Supply Costs for Inertial Confinement Reactors", UWFDM-243, University of Wisconsin, March 1978.

II.1. The Direct Enrichment Hybrid/LWR Fuel Cycle

A fusion-fission hybrid reactor utilizes the 14.1 MeV DT fusion neutrons for breeding fissile material in the hybrid reactor blanket. This bred fuel can be removed periodically from the blanket and burned in conventional fission reactors or it can be burned "in situ" in the hybrid blanket itself. During the last five years there have been many studies of hybrids for a variety of fusion systems (i.e. tokamak, mirror, laser fusion, electron beam fusion).[1-7] Such fusion-fission hybrid reactors appear to be attractive because they produce two revenue sources, electric power and fuel for conventional fission reactors, at a fusion performance level that is less than that required for pure fusion reactors. The additional revenue source, fissile fuel, strengthens the economic perspective of the fusion system. The reduced fusion performance is allowable because the 14.1 MeV DT neutron energy is multiplied in the hybrid blanket by the fission process. For the hybrid operating as a fuel factory where fissions are minimized, the blanket energy multiplication is still typically 2-10. In the second option where the fuel is allowed to burn in the hybrid itself, the multiplication may be as high as 40-50 depending on how close the blanket approaches criticality. It is argued that this relaxation of the fusion energy requirement may allow hybrid reactors to make an impact on the world's energy production problem at an earlier date than pure fusion reactors. However, the hybrid reactor may also appear unattractive if it is considered to have both the disadvantages of complex fusion systems and the radioactive waste, criticality, and proliferation problems of fission reactors.

The SOLASE-H laser fusion hybrid reactor study investigates the possibility of minimizing the perceived disadvantages of the hybrid by operating with low k_{eff} in the blanket, utilizing a proliferation resistant fuel cycle that allows direct enrichment of PWR fuel assemblies in the hybrid and transfer of the irradiated assemblies to the fission reactor, without intermediate reprocessing. This fuel cycle part of the study establishes the potential role of the hybrid for a nuclear future that includes no immediate reprocessing or development of the LMFBR. This study is, in fact, a continuation of the SOLASE[8] conceptual laser fusion reactor design.

Only 0.7% of natural uranium is the fissile ^{235}U isotope. The remaining 99.3% is ^{238}U. Other fissile isotopes can be manufactured by the absorption of a neutron in ^{232}Th and ^{238}U to produce ^{233}U and ^{239}Pu respectively. Once these artificial fissile materials have been produced they can be mixed with their corresponding fertile material at a 3-4% concentration and fabricated into fuel assemblies for use in fission reactors. The production of these artificial fissile isotopes is, of course, the purpose of the fusion hybrid reactor. However, the reprocessing of the material produced in the hybrid to remove fission products and the fabrication into cold, clean fuel assemblies exposes the hybrid fuel to the same proliferation considerations as the fast breeder fuel cycle. Because this fuel is easily handled and the fissile material can be removed by chemical rather than physical processes, the fuel is most vulnerable to diversion for the purposes of nuclear weapons development. Feiveson and Taylor[9,10] have argued that spent or highly radioactive fuel is self-protecting. Such assemblies weigh nearly half a ton. They argue that stealing such irradiated assemblies would require heavy cranes, tons of shielding containers, and a

large vehicle for transporting the stolen, shielded assemblies. Further, the fissile ^{233}U or ^{239}Pu must still be separated from the dangerously radioactive fuel.

The fusion-fission hybrid fuel cycle proposed here directly enriches the fertile fuel to 3-4% fissile concentration in the hybrid blanket. This process also makes the fuel highly radioactive so that it is rendered diversion resistant. The details of this fuel cycle are outlined in Fig. II.1-1.

The cycle includes four steps:

1. Fertile fuel, ThO_2 or UO_2, is fabricated in a form that is directly usable in a LWR. (Other fission reactors could be included but the LWR is used here because it is the workhorse of the U.S. fission reactor industry.)
2. The cold, clean fuel assemblies, containing only fertile fuel, are placed in the hybrid blanket and carefully enriched to a nearly uniform concentration of 3-4% fissile fuel as required by the LWR.
3. The enriched, and now highly radioactive assemblies, are transferred as units directly to the LWRs for burning of the fuel.
4. The spent fuel from the LWR is stored until a decision is made on reprocessing or storing or both. If feasible, the spent fuel can be re-inserted into the hybrid to be re-enriched for further burning in the LWR. This possibility depends on both the importance of fission product buildup to LWR performance and the radiation damage to the fuel and cladding.

THE HYBRID SYSTEM AS A FUEL FACTORY WITHOUT PROCESSING

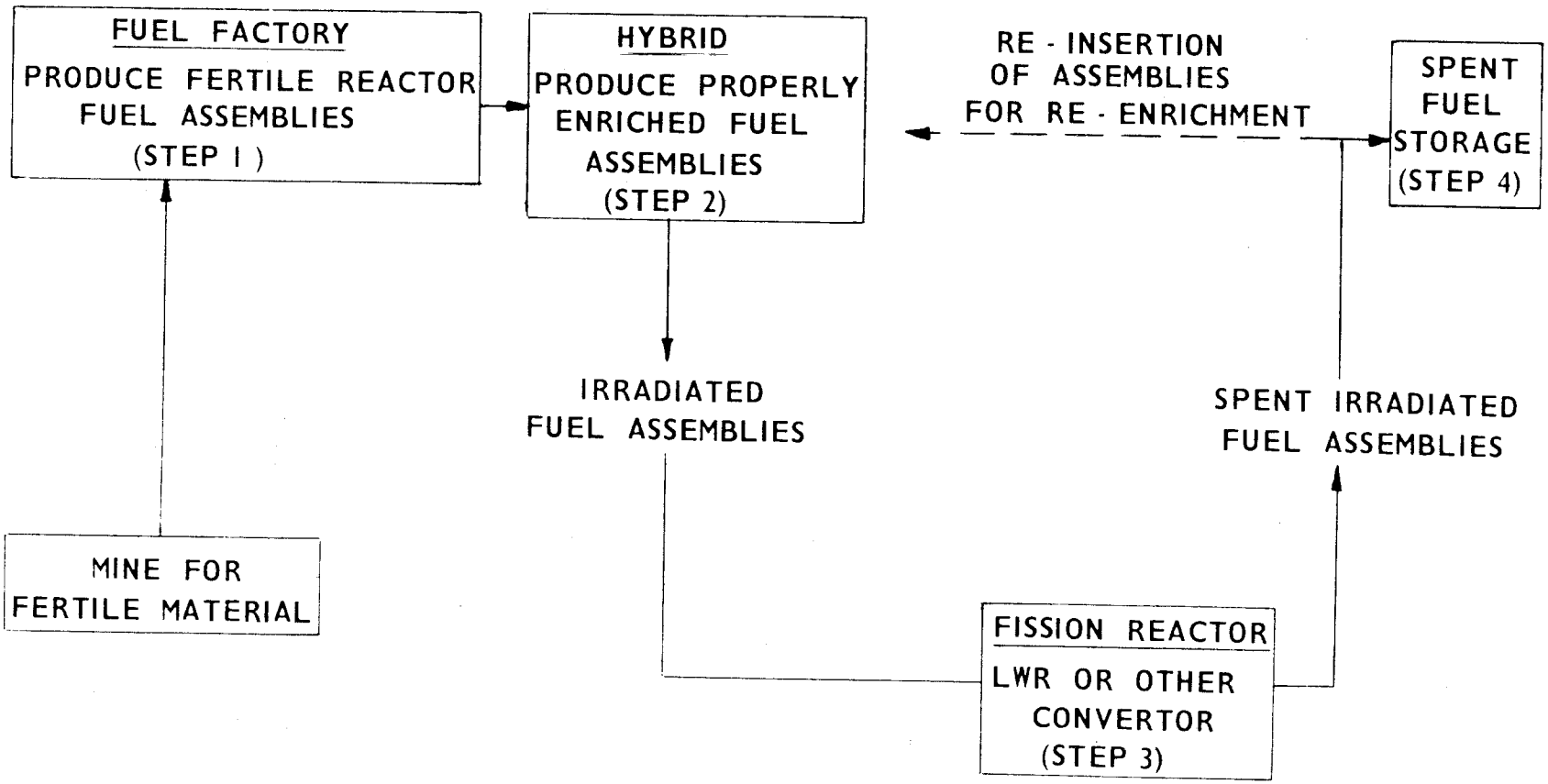

Fig. II-1

The attractive features of this cycle are the following:

1. The system is resistant to diversion because fissile material occurs only inside highly radioactive fuel assemblies. Only fresh fertile material is fed to the hybrid, and upon removal, the fuel pellets contain fission products that are highly radioactive and the pellets themselves are contained in rod assemblies with highly activated cladding. Access to the fissile material is thus very difficult, making the entire cycle proliferation resistant according to the guidelines of Feiveson and Taylor.
2. The fissile fuel reserves are extended substantially. If the average LWR fuel enrichment is assumed to be 3%, the fissile fuel reserves are extended by 4.3 x (Thorium Resources + Uranium Resources). According to Staatz and Olsen,[11] the occurrence of thorium is widespread but the resources are not well known because present demand is low. The demand in 1968 was for only about 125 tons of ThO_2. Estimates of the thorium content of the earth's crust range from 6 to 13 appm. Identified world thorium resources recoverable primarily as a by-product or co-product are about 1.4 million tons, one-third of which occurs in a deposit near Elliot Lake, Canada. The general understanding is that large additional resources would be found with additional exploration. If we assume the thorium resources are no larger than the uranium resources, the fissile fuel supply is extended by a factor of 4 to 5 without reprocessing.

3. The extension of the fission fuel supply using the hybrid produces additional time that can be used to make deliberate decisions on issues such as internationally controlled, physically secure fuel production and fuel reprocessing centers.[9,10]
4. The manufacturing of fresh fertile fuel pellets can proceed without the handling problems inherent in the use of a radiation spiking material such as ^{60}Co. This avoids any legal or safety issues associated with the deliberate addition of dangerous materials.

The major disadvantage of this system is that it does not take full advantage of the fertile fuel reserves. To achieve a fuel supply measured in thousands of years, rather than just a few hundred, fuel reprocessing is essential. Without reprocessing, one hybrid reactor is only able to supply fissile fuel to about 2.5 LWRs of the same thermal power. This has the economic impact of increasing the effective fuel cost. With reprocessing of the spent LWR fuel, on the order of 10 LWRs can be fueled from one hybrid of equivalent power, depending on the conversion ratio of the LWR or other convertor reactor.

The proliferation resistant fuel cycle can be extended to include reprocessing of the spent LWR fuel if one follows the structure outlined by Feiveson and Taylor of internationally controlled, physically secure fuel production and reprocessing sites combined with many national convertor reactors "outside the fence". This process involves the four steps outlined in Fig. II.1-2.

THE HYBRID SYSTEM AS A FUEL FACTORY WITH REPROCESSING

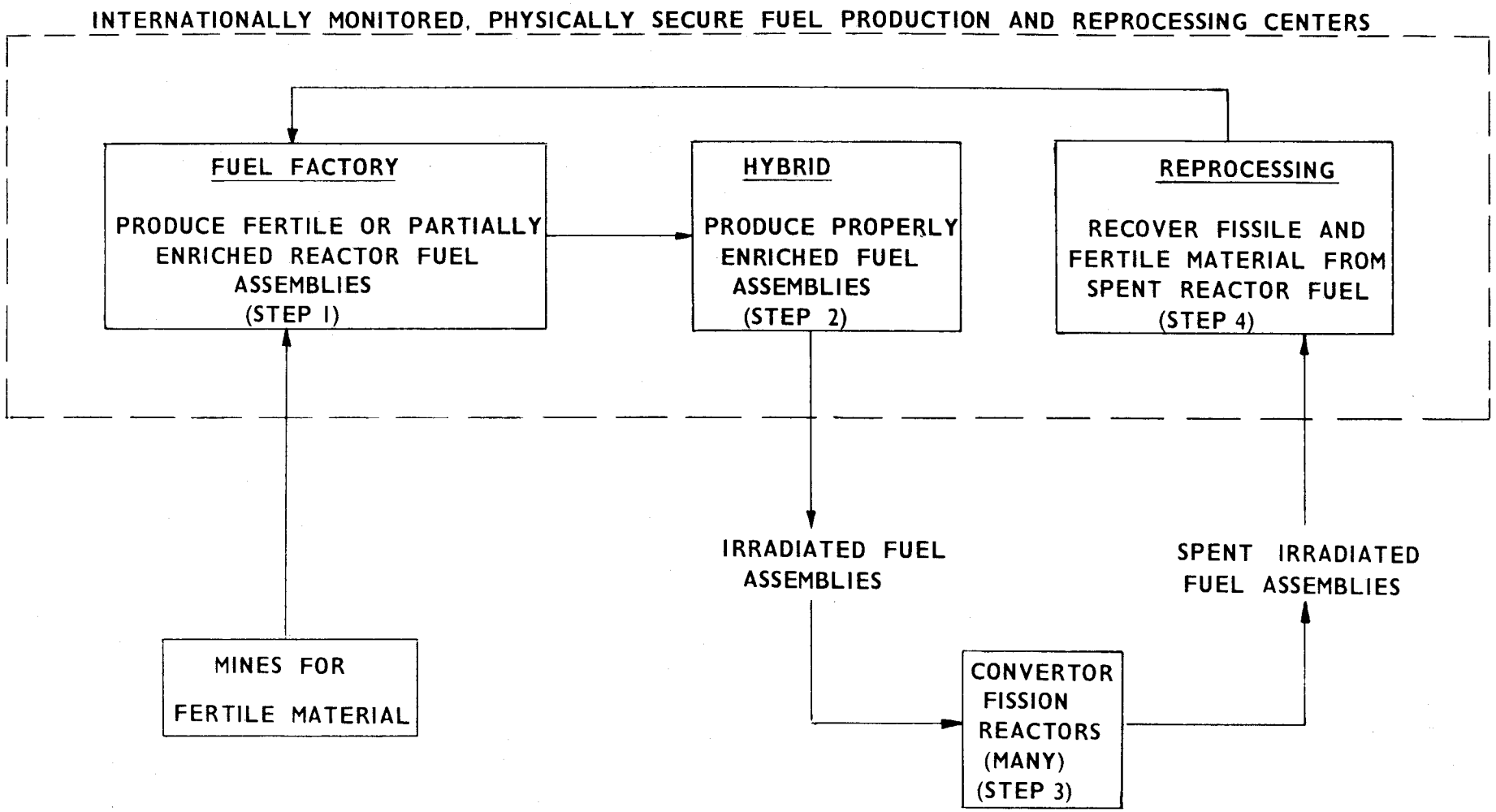

Fig. II.1-2

1. Fresh ThO_2 or UO_2 fuel is fabricated in assemblies that are directly usable in a LWR or other convertor reactor. This step will also involve the fabrication of enriched fuel assemblies at the secure site using fissile fuel from the reprocessing step. We propose that such fuel be only partially enriched (for example, to just 2% even though about 3-4% is required) and that the hybrid be used to produce the required additional enrichment.
2. The fuel assemblies are irradiated in the hybrid blanket to produce the required fissile enrichment.
3. The fuel is transferred directly to the fission reactor and burned.
4. The spent fuel assemblies are shipped back to the physically secure site for reprocessing. The reprocessing plant removes fission products and sends the fissile material to the fuel factory for fabrication into new fuel assemblies.

The advantages of this approach are the following:

1. The fuel supply is measured in terms of the fertile material abundance. All estimates show that such fuel supplies will last for thousands of years.
2. Fuel shipped to and from the convertor reactors is always highly radioactive and would be resistant to diversion and reprocessing for the reasons described earlier.
3. The convertor reactor need not be restricted to a LWR although using these reactors will minimize the need to develop additional fission reactor technologies.

The potential success of these fuel cycles depends upon two key technical questions: (1) Can the hybrid reactor produce uniformly enriched fuel at an acceptable fusion performance level when the blanket design is constrained to accommodate LWR fuel assemblies? (2) Can a standard LWR burn the irradiated fuel? The first of these questions was the major emphasis of the SOLASE-H laser fusion hybrid study.

The remaining sections in Part II of this report include neutronics calculations that provide numerical estimates of the hybrid blanket performance when it is constrained to directly enrich LWR fuel assemblies. These are detailed one dimensional S_n calculations that determine fissile breeding rates and spectral shaping of the neutron flux in the fuel assembly region of the blanket, and three dimensional Monte Carlo calculations that determine the combined fissile and tritium breeding rates as well as axial enrichment nonuniformity in the fuel assemblies. This provides input to an "in-blanket" fuel management scheme to smooth out the nonuniformities. The question of radiation damage to the fuel in the SOLASE-H blanket is being investigated in a follow-on study.

References for Section II.1

1. L. M. Lidsky, "Fission-Fusion Systems: Hybrid, Symbiotic and Augean", Nucl. Fusion 15, 151 (1975).

2. R. P. Rose, et al., "Fusion-Driven Breeder Reactor Design Study", Final Report, WFPS-TME-043, May 1977.

3. R. G. Mills, "System Analysis of Fusion-Driven Fission", Third ANS Topical Meeting on the Technology of Controlled Nuclear Fusion, May 9-11, 1978, Santa Fe, NM.

4. D. J. Bender (LLL); K. R. Schultz, R. H. Brogli and G. R. Hopkins (GA), "Performance Parameters for a ^{233}U Refresh Cycle Hybrid Power System", Third ANS Topical Meeting on the Technology of Controlled Nuclear Fusion, May 9-11, 1978, Santa Fe, NM.

5. J. D. Lee, "Nuclear Design of the LLL-GA U_3Si Blanket", Third ANS Topical Meeting on the Technology of Controlled Nuclear Fusion, May 9-11, 1978, Santa Fe, NM.

6. J. A. Maniscalco, "A Conceptual Design Study for a Laser Fusion Hybrid", Technology of Controlled Nuclear Fusion, September 21-23, 1976, Richland, WA, CONF-760935-P2, 657 (1976).

7. W. O. Allen and S. L. Thomson, "Electron Beam Fusion-Fission Reactor Studies", Third ANS Topical Meeting on the Technology of Controlled Nuclear Fusion, May 9-11, 1978, Santa Fe, NM.

8. R. W. Conn, et al., "SOLASE, A Laser Fusion Reactor Study," Univ. of Wisconsin Fusion Design Memo, UWFDM-220, Nuclear Engineering Dept., Univ. of Wisconsin, 1977. Also, R. W. Conn, "Reactor Aspects of Laser Fusion", International Scientific Forum on an Acceptable Future of Nuclear Energy for the World, Univ. of Miami, Center for Theoretical Studies, Coral Cables, Florida, Nov. 1977.

9. H. A. Feiveson and T. B. Taylor, "Alternative Strategies for International Control of Nuclear Power", Report Prepared for the 1980's Project of the Council on Foreign Relations (Oct. 1976).

10. H. A. Feiveson and T. B. Taylor, Bull. of the Atomic Sci. 32, 14 (1976).

11. M. H. Staatz and J. C. Olsen, in "United States Mineral Resources", U. S. Geological Survey Prof. Paper 820 (1973), p. 468.

II.2. Blanket Performance Analysis of Laser Fusion Hybrids

II.2.A. Objective of the Neutronics Study

The primary objective of the neutronics study reported here has been to maximize the fissile fuel production rate in a hybrid reactor subject to the constraints that the fissile fuel distribution in the fuel zone be as uniform as possible and that the tritium breeding ratio (TBR) be at least 1. We have primarily considered hybrids which produce uranium-233 from thorium because U-233 is a better performing fuel in LWRs, particularly PWRs. However, similar studies can be done on the production of plutonium-239. The constraint of a uniform U-233 distribution throughout the fuel assembly used in the fuel zone is aimed primarily at minimizing the hot spot factor one would calculate for the enriched fuel assembly loaded into a LWR.

II.2.B. The Blanket Configuration and Calculational Model

Spherical geometry, one-dimensional calculations have been performed to assess the effects of parameter and design variations and to search for optimum blanket performance. In this regard, two main blanket configurations shown in Fig. II.2-1 have been studied. The first blanket series utilizes beryllium as a neutron multiplier front zone while lead is used in the second series. Lead and beryllium enhance the neutron generation throughout the blanket and replace a U-238 fast fission plate utilized in other studies.[1-5] In addition to introducing plutonium into a U-233 fuel cycle, the fission plate would also increase the thermal power generated in the blanket. This would yield excess electricity which could be sold to reduce the overall plant running cost. However, the power increase with time

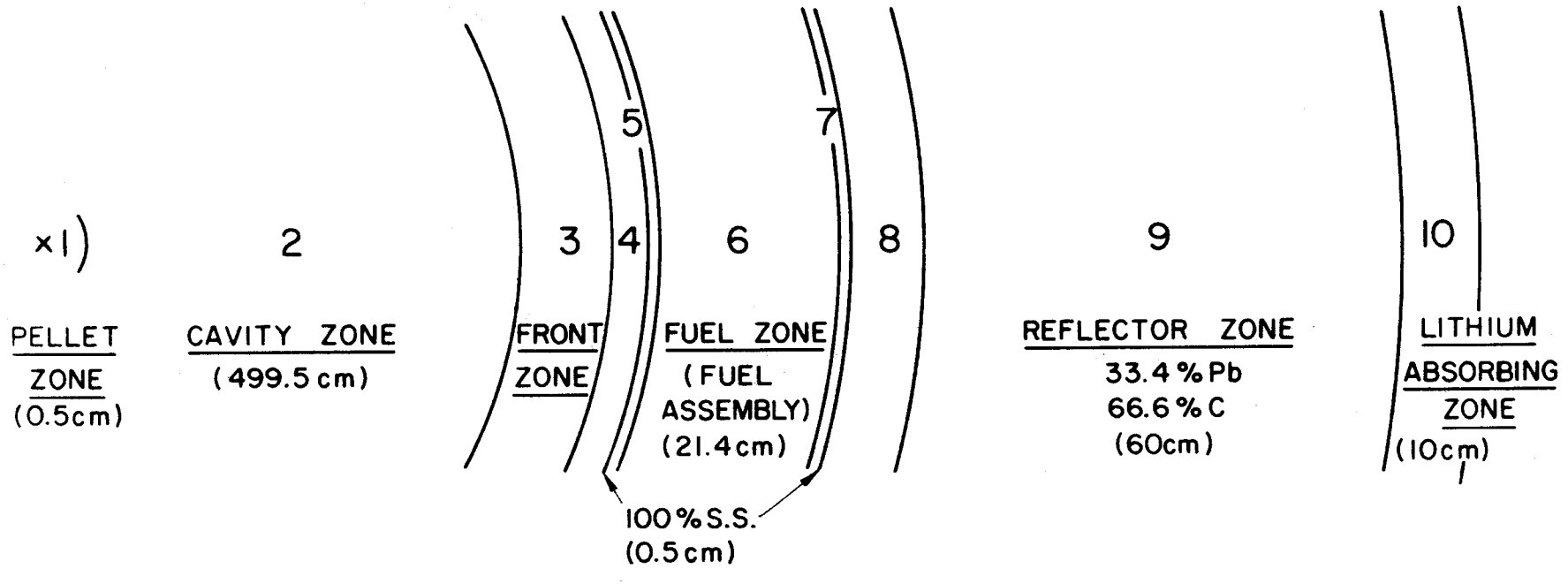

Fig. II.2-1 SCHEMATIC REPRESENTATION IN SPHERICAL GEOMETRY OF THE HYBRID BLANKET

ZONES 4 AND 8 ARE NOT INCLUDED IN THE SERIES OF BLANKETS USING Be AS FRONT ZONE MULTIPLIER

makes the design of the cooling system more difficult. In our design, the main concern has been to maximize U-233 production subject to the constraints on fuel production and tritium breeding already mentioned and to ensure sufficient power to make the plant at least self-sufficient in power.

For both classes of reactor blankets (beryllium or lead as a neutron multiplier), the U-233 breeding zone (fuel zone) consists of just one fuel assembly row located behind the neutron multiplier zone. A reflector is positioned behind the fuel zone and consists of 1/3 Pb and 2/3 graphite by volume. The thickness of this reflector is held at 60 cm in all cases. A final liquid lithium neutron absorbing region is located at the outer portion of the blanket.

The fuel zone is thus located in a flux trap between the reflector and the neutron multiplying zone. For this reason, two relatively thin neutron absorbing lithium zones are located immediately in front of and behind the fuel assembly zone in the series of blankets utilizing lead as front zone neutron multiplier. This achieves two ends: 1. Thermal neutrons which would be absorbed at the edge of the fuel assembly are filtered out. Thus, only harder neutrons penetrate and this produces a more uniform U-233 production rate. 2. The neutrons absorbed in the lithium help to meet the constraint that the tritium breeding ratio be 1.

A square single PWR assembly has 264 fuel elements arranged in a 17 x 17 array and is 21.4 cm on a side. The fuel pins have an outer diameter of 0.9498 cm and a square pitch of 1.25 cm. Zircaloy-2 is utilized as the cladding material with a thickness of 0.0572 cm. The ThO_2 fuel pellet diameter is 0.819 cm. Each fuel assembly contains 25 empty locations of outer diameter 0.9498 cm and are reserved for the control rods when the

fuel assembly is extracted from the blanket and used in LWRs. The dimensions of the fuel assembly and the fuel pins are shown in Fig. II.2-2. The fuel assembly used in this study is typical of those used in a PWR.[9] The volume percentages corresponding to the dimensions shown in Fig. II.2-2 are: 30.3% ThO_2, 9.2% Zircaloy-2, 1.3% void and 59.2% coolant. When the fuel assembly is placed in the blanket, the fuel zone will occupy a region 21.4 cm thick. This is held constant for the blankets studied.

To simulate a laser fusion hybrid, the neutron source is localized in a zone 0.5 cm radius at the center of the reactor. The first wall is at a radius of 5 m in the survey calculations. However, in the final design, the optimized blanket is reconfigured to closely approximate the engineering features and the cylindrical geometry of the actual hybrid concept. That design is shown in Fig. II.2-3. The pellet in that design is centered at 6m from the firstwall and the cylindrical radial blanket section is 12 m high. The top and bottom axial caps are designed to produce tritium. Since the caps are devoted solely to tritium production, one requires less tritium breeding in the radial section. As such, we have used a value of 0.6 as the constraint on the TBR in these parametric calculations.

The neutronic calculations were performed using the one-dimensional discrete ordinate neutron transport code ANISN. A 25 neutron energy group cross section library has been used based on the DLC-2D[7] library which was generated from ENDF/B III with the SUPERTOG[8] code using a 1/E weighting spectrum for the GAM-II 100-group structure. The energy boundaries for the 25 groups are given in Table II.2-1.

Figure II.2-1 shows the different zones of the blanket for both series mentioned earlier. Zones 4 and 8 are not included in the Be front zone series.

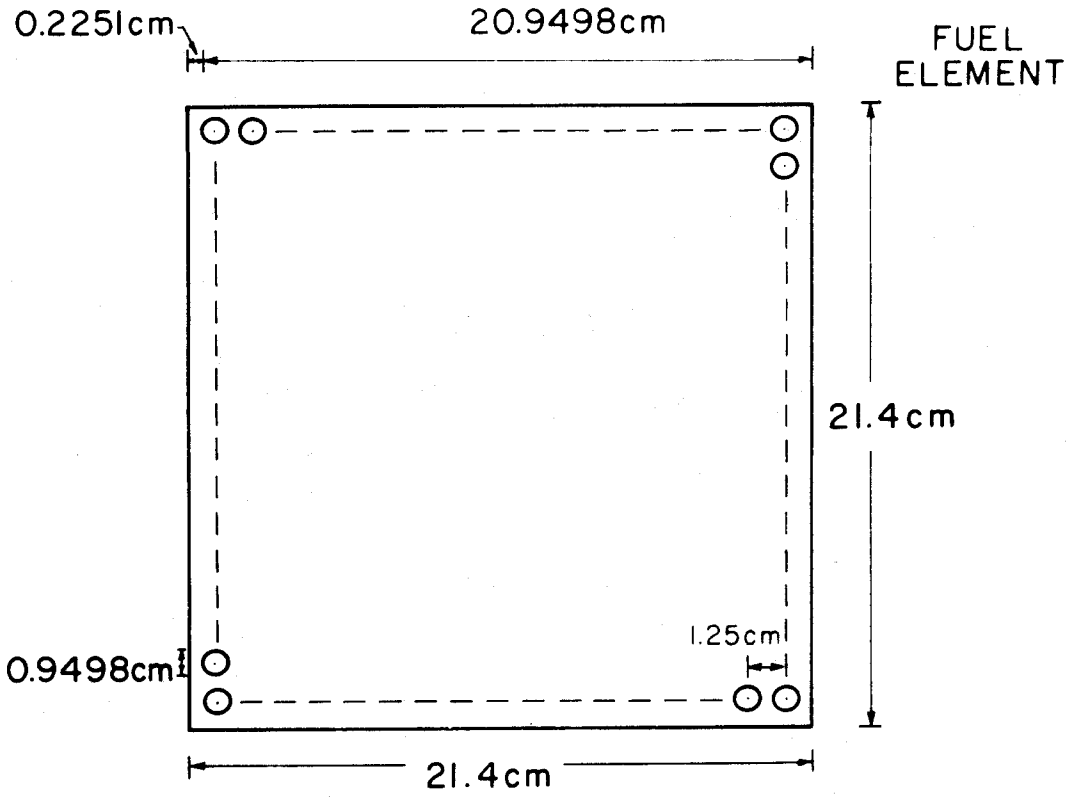

(a) THE 17X17 FUEL ASSEMBLY ;
264 FUEL ELEMENTS AND 25
LOCATIONS FOR CONTROL ROD (TOTAL 289)

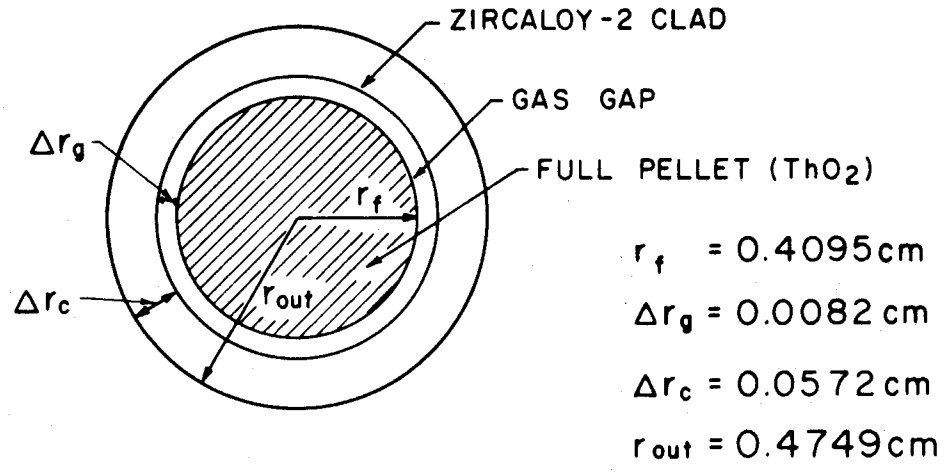

(b) FUEL ELEMENT PIN

Fig. II.2-2 THE FUEL ASSEMBLY AND THE FUEL PIN

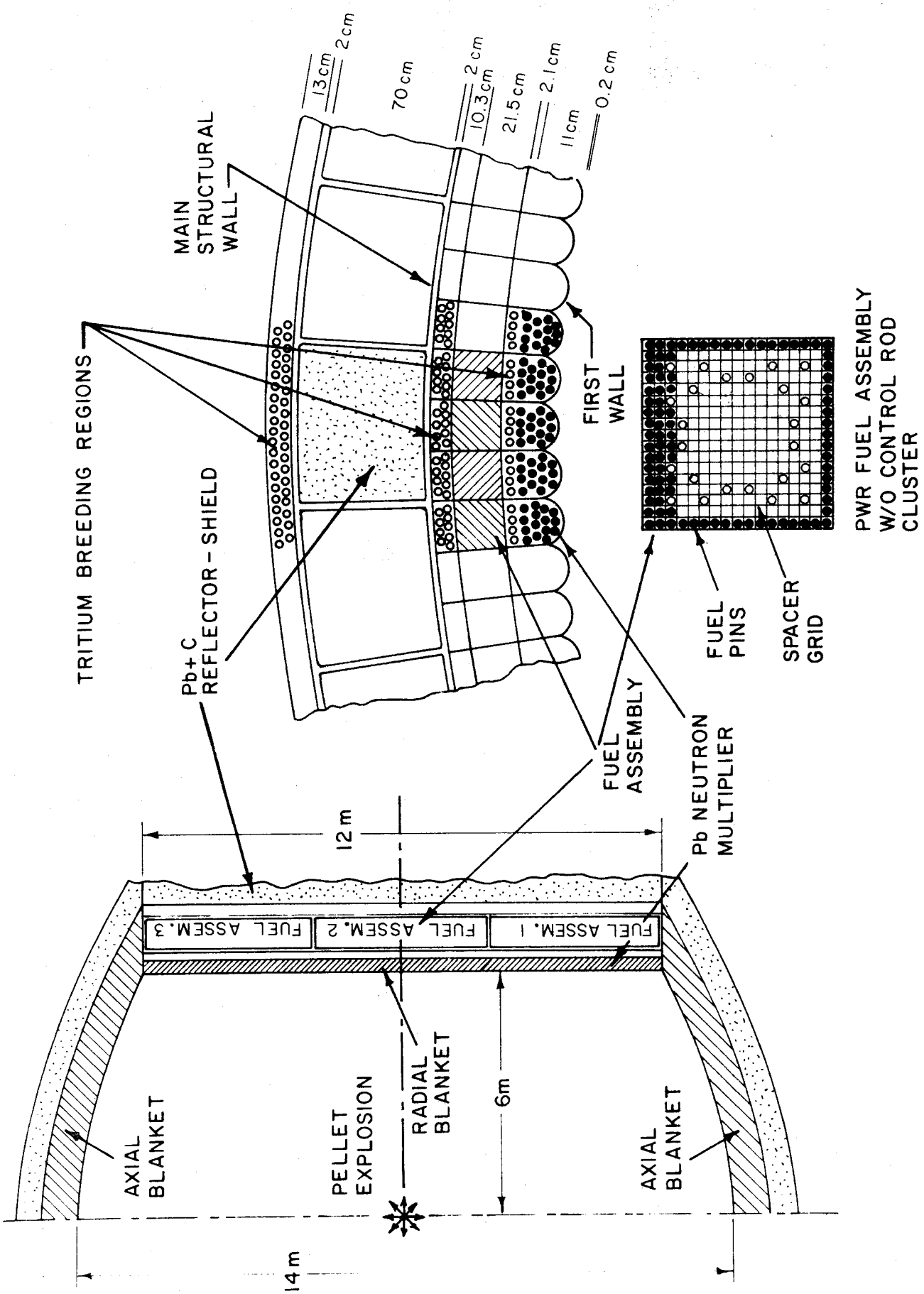
TRITIUM BREEDING REGIONS
MAIN STRUCTURAL WALL
Pb+C REFLECTOR-SHIELD
FIRST WALL
FUEL ASSEMBLY
Pb NEUTRON MULTIPLIER
FUEL PINS
SPACER GRID
PWR FUEL ASSEMBLY W/O CONTROL ROD CLUSTER
13cm
2cm
70 cm
2 cm
10.3cm
21.5 cm
2.1cm
11cm
0.2 cm
12 m
FUEL ASSEM. 1
FUEL ASSEM. 2
FUEL ASSEM. 3
AXIAL BLANKET
PELLET EXPLOSION
RADIAL BLANKET
6m
AXIAL BLANKET
14 m

Fig. 2-3

Table II.2-1 Energy Boundaries for the 25 Neutron Energy Groups

Group	Energy End Boundaries (eV)	Group	Energy End Boundaries (eV)
1	1.4918 + 07→1.3499 + 07	14	2.4660 + 06
2	1.2214 + 07	15	1.3534 + 06
3	1.1052 + 07	16	7.4274 + 05
4	1.0000 + 07	17	4.0762 + 05
5	9.0494 + 06	18	1.6573 + 05
6	8.1873 + 06	19	3.1878 + 04
7	7.4082 + 06	20	3.3546 + 03
8	6.7032 + 06	21	3.5358 + 02
9	6.0653 + 06	22	3.7267 + 01
10	5.4881 + 06	23	3.9279 + 00
11	4.4933 + 06	24	4.1399 - 01
12	3.6788 + 06	25	2.2200 - 02
13	3.0119 + 06		

The constituents and the volume percentages in the different zones of the large number of cases studied are summarized on Table II.2-2. We also give the results for the U-233 breeding ratio UBR (U-233 atoms produced per D-T neutron) and the tritium breeding ratio TBR. Note that cases with Li cooling and Na cooling have been also considered in this parametric study.

II.2.C. Beryllium as the Neutron Multiplier

Several different blankets utilizing Be as front zone material were studied. Zircaloy-2 is chosen as the structural material for this zone. The volume percentages are: 82.2%-Be, 9.3% coolant and 8.5% Zircaloy-2. The type of coolant in this study is either natural Li or Na.

In blanket #1, natural Li is used as coolant in the front zone (10 cm) and in the fuel zone. Enriched lithium (50% Li-6) is used in the lithium absorbing zone (zone 10). The UBR and TBR are 0.71 and 1.1, respectively; when using Na as the coolant in the front and fuel zones (blanket #2), the UBR increases to 1.34 and the TBR dropped to 0.097. Although the utilization of the D-T neutron in fuel and tritium production is higher in blanket #1 (0.71 + 1.1 = 1.81) than in blanket #2 (1.43), the UBR is noticeably higher in blanket #2.

The 25 locations reserved for control rods were filled with natural lithium in blanket case #3, then 50% enriched lithium and Na as the coolant (blanket #4). The competition between Li and Th to absorb neutrons in the fuel zone tends to decrease the UBR (to 1.14) and to increase the TBR (to 0.38) in blanket #3. The corresponding values in blanket #4 are UBR = 0.9 and TBR = 0.67. One should notice that TBR + UBR is almost the same for blanket #3 and 4. This shows that increasing TBR is at the expense of decreasing UBR.

CASE NUMBER													
Blanket	#1	#2	#3	#4	#5	#6	#7	#8	#9	#10	#11	#12	#13
Zone 1, 2	Zone 1 Point Source Within 0.5 cm Radius Zone 2 Void 499.5 cm Thickness												
Zone 3	82.2% Be 9.3% Nat. Li Coolant 8.5% Zirc-2 (10 cm)	As #1 but with Na Coolant			As #2 (0 cm)	As #2 (5 cm)	As #2 (15 cm)	100% Pb_4-Li Nat. Li (10 cm)	As #2 Pb Replaces Be (5 cm)	As #9 (10 cm)	As #9 (15 cm)	As #9 (20 cm)	As #10
Zone 4	(0 cm)								95% Nat. Li 5% SS (1.5 cm)				
Zone 5, 7	100 % SS (0.5 cm)												
Zone 6	30.3% ThO_2 9.2% Zirc-2 59.2% Nat. Li Coolant 1.3% Void (21.4 cm)	As #1 but with Na Coolant	30.3% ThO_2 3.8% Nat. ^6Li 55.4% Na Coolant 9.2% Zirc-2 7.3% Void 21.4 cm	As #3 but Li is 50% Li^6				As #1 but with Pb_4Li Coolant. Nat. Li is Used	As #2				
Zone 8	(0 cm)								95% Nat. Li 5% SS (6 cm)				As #10 (8 cm)
Zone 9	Pb+C Mixture 66.6% C 33.4% Pb (60 cm)												
Zone 10	95% Li (50% Li^6) 5% SS (10 cm)								As #1 but Li is Natural				
Th(n,γ)X(UBR)	0.7132	1.3357	1.1364	0.8970	0.7492	0.9040	0.8230	1.1259	0.8589	0.9567	1.0116	1.0392	0.9338
TBR	0.0998	0.0968	0.3797	0.6703	0.5226	0.5353	0.8003	0.5029	0.6152	0.5946	0.5734	0.5487	0.6254
Th($\nu\sigma_f$)	0.1158	0.1185	0.1184	0.1183	0.1909	0.1527	0.0899	0.0704	0.1218	0.0799	0.0520	0.0338	0.0799
	0.1159	1.9818											

Table II.2-2

Neutronic Results for Different Blankets

The effect of the Be front zone thickness was studied via the cases, blanket #5 (0 cm front zone), blanket #6 (5 cm), blanket #4 (10 cm) and blanket #7 (15 cm). In these blankets the coolant in the front zone and fuel zone is Na and the 25 locations reserved for control rods were filled with 50% Li-6 enriched lithium. The back lithium zone waskept at 10 cm with 50% Li-6 enriched lithium. Table II.2-3 gives the reaction rates for blanket cases #4, #6 and #7, respectively. The first 7 rows of this table show the reaction rates which lead to neutron multiplication, in particular the (n,2n) reaction for the structural materials and (n,2n),(n,3n)x2 and $(n,\nu\sigma_f)$ reactions for Th. Rows 8 to 17 give the absorption rate in the entire blanket while rows 18 to 21 give the reaction rates for breeding U-233 and tritium. The neutron multiplication and absorption rates in the fuel and structural materials as a function of the Be zone thickness are shown in Fig. II.2-4. The tritium production rate and the U-233 breeding rate are shown in Fig. II.2-5. For a 5 cm Be front zone, the main source of neutron multiplication comes from the (n,2n), (n,3n) and fast fission reactions in Th. However, there is noticeable neutron multiplication from (n,2n) reactions in Be. As the thickness of the Be zone increases, the (n,2n) reaction rate in Be increases and overrides the neutron multiplication due to Th at about a 6 cm Be zone thickness. Further increase of this thickness results in larger neutron multiplication in Be. However, an increase in the Be zone thickness leads to a softer neutron spectrum throughout the blanket. This leads to a decreased rate of fission, (n,2n), and (n,3n) reactions in Th.

The main source of neutron absorption is due to Th (n,abs) and Li^6(n,abs) as shown in Fig. II.2-4, Fig. II.2-5, and Table II.2-3. The

Table II.2-3

Reaction Rates of Blanket #6, #4 and #7 per D-T Neutron

Type	Reaction	Blanket #6 (5 cm)	Blanket #4 (10 cm)	Blanket #7 (15 cm)
Source	Th (n,2n) + (n,3n) + (n,$\nu\sigma_f$)	0.3645	0.2775	0.2077
	Be (n,2n)	0.2848	0.5585	0.7876
	Structure (n,2n)	0.0957	0.0958	0.0961
	Na (n,2n)	0.0035	0.0027	0.0022
	Pb (n,2n)	0.0643	0.0471	0.0344
	D-T neutron	1.0	1.0	1.0
	SUM	1.8129	1.9815	2.1279
Sink	Th (n,abs)	0.9481	0.9319	0.8501
	Be (n,abs)	0.0347	0.0732	0.1175
	Structure (n,abs)	0.0918	0.1399	0.2032
	Na (n,abs)	0.0519	0.0612	0.0928
	^{6}Li (n,abs)	0.5202	0.6477	0.7677
	^{7}Li (n,abs)	0.0001	0.0001	0.0001
	Pb + C (n,abs)	0.1251	0.0957	0.0723
	O	0.0337	0.0262	0.0199
	Leakage	0.0084	0.0064	0.0049
	SUM	1.8138	1.9825	2.1284
Breeding	Th (n,γ)	0.9040	0.8970	0.8230
	^{6}Li (n,t)α	0.5308	0.6667	0.7974
	^{7}Li (n,t)nα	0.0045	0.0036	0.0078
	Li (n,t)	0.5353	0.6703	0.8003

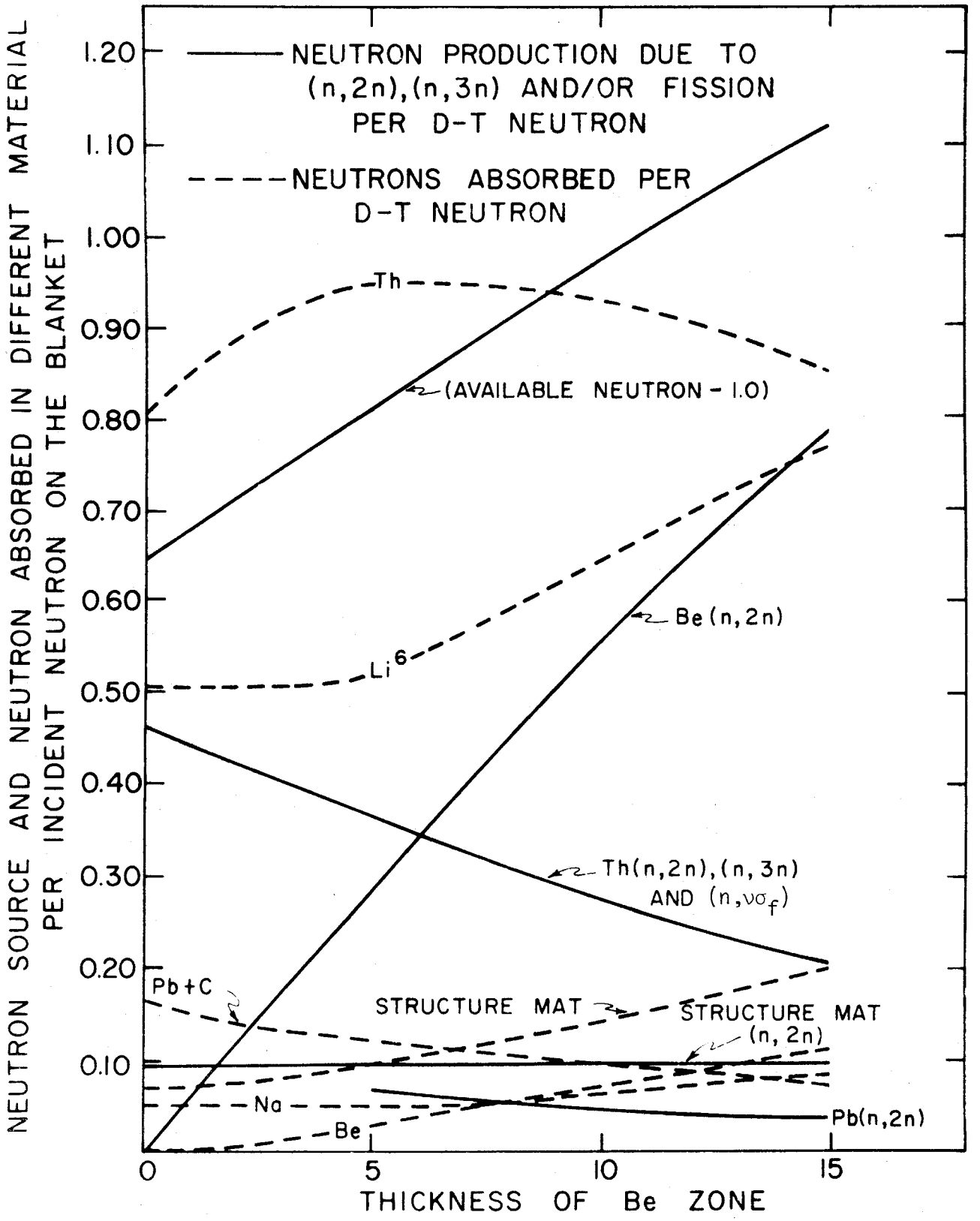

Fig. II.2-4 NEUTRON SOURCES AND SINKS AS FUNCTION OF Be FRONT ZONE THICKNESS

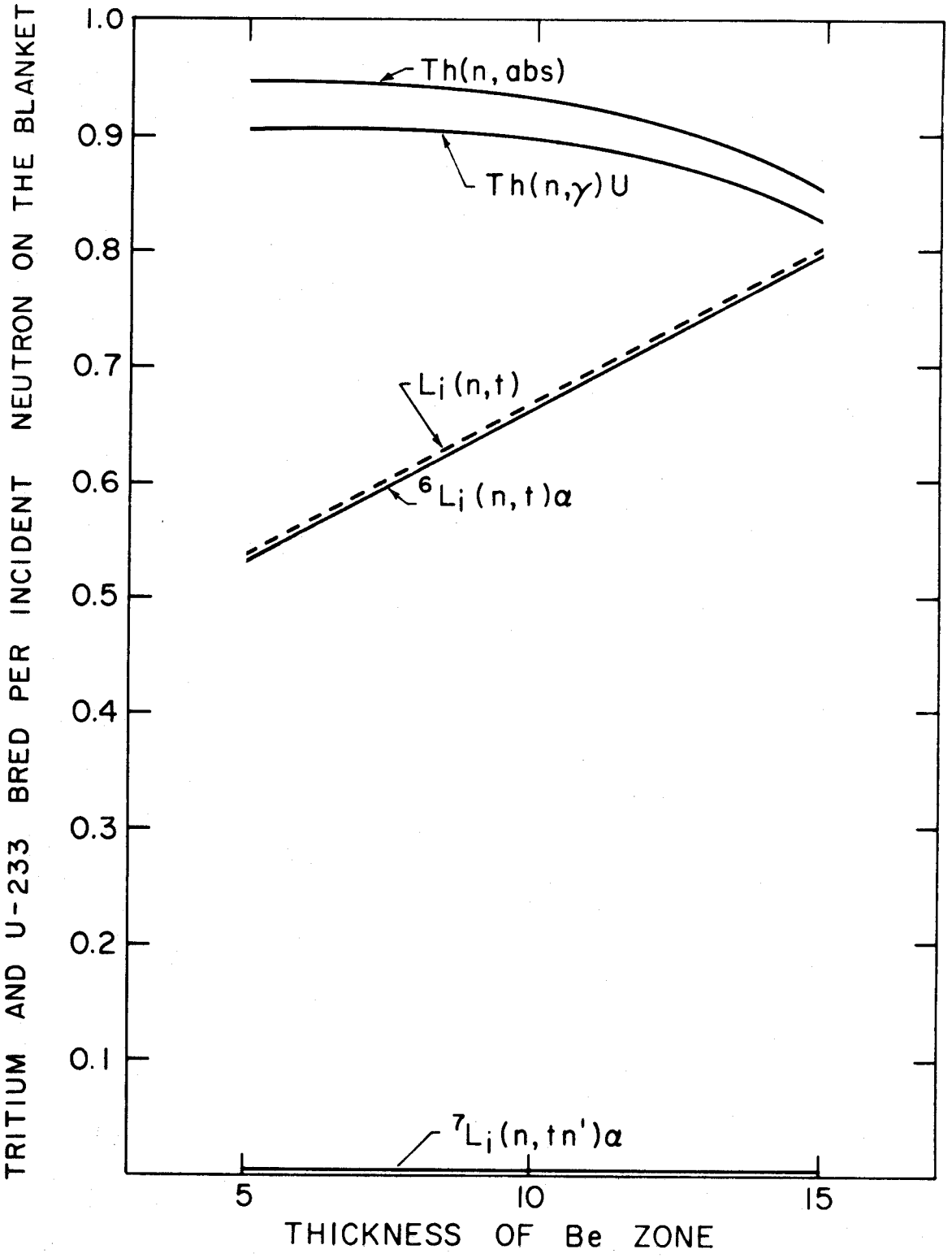

Fig. II.2-5 TRITIUM AND U-233 BREEDING RATES AS FUNCTION OF Be FRONT ZONE THICKNESS PER D-T NEUTRON

percentage of neutrons absorbed in Th compared to the total number of neutrons available is 52.3%, 47%, and 40% for the 5 cm, 10 cm and 15 cm Be zone thickness cases, respectively. For Li^6, the corresponding values are 28.6%, 32.7% and 36%, respectively. The main sources of neutron production are the Th(n,2n), Th(n,3n), Th(n,$\nu\sigma_f$) and Be(n,2n) reactions. The percentage of neutrons from Th compared to the total neutrons available in the blanket are 20%, 14% and 9.8% for 5, 10 and 15 cm Be front zone cases, respectively. The corresponding values for the Be(n,2n) reaction are 15.7%, 28.2% and 37%, respectively. This shows the effectiveness of Be as a front zone neutron multiplying material. In going from 0 cm to 5 cm Be front zone thickness, the UBR increases from 0.75 to 0.9. It then slightly decreases as the Be zone thickness increases further. In contrast, TBR increases monotonically as the front zone thickness increases. This again is due to the increasingly softer spectrum produced by neutron moderation in Be which permits the $Li^6(n,t)\alpha$ reaction to dominate capture in thorium. The optimum thickness for the Be front zone is about 10 cm. In this case, the UBR is 0.9 and the TBR is 0.67. The latter value meets the requirement that the TBR in the spherical mock-up calculations be ~0.6. The end caps in the final design make up the remainder.

The constraint of uniform U-233 distribution throughout the fuel assembly is not met in this series of blankets. The Th(n,γ) reaction rate per D-T neutron throughout the fuel zone is shown in Fig. II.2-6 for blankets #4, #5, #6 and #7, respectively. The reaction rate first decreases and then increases again due to the neutrons from the reflector zone. As the thickness of the Be zone increases, the curves tend to increase in front and decrease in the back. The minimum occurs even closer to the back edge. In general, the fuel zone in this series is self-shielded to fissile fuel production.

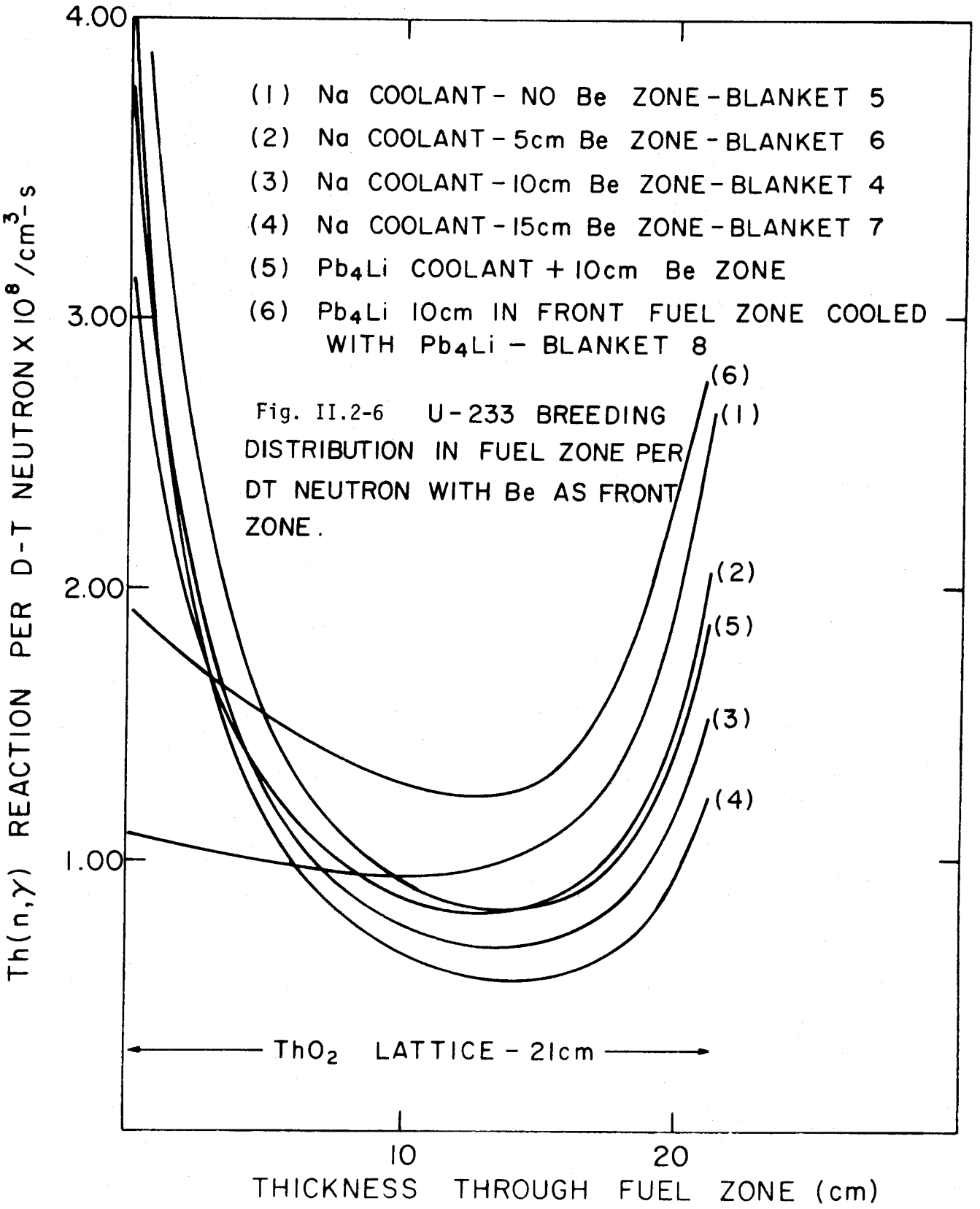

Fig. II.2-6 U-233 BREEDING DISTRIBUTION IN FUEL ZONE PER DT NEUTRON WITH Be AS FRONT ZONE.

When Pb_4Li eutectic replaced the Na coolant of blanket #1, the UBR and TBR become 1.1 and 0.68, respectively. However, the Th(n,γ) curve is still steep both in the front and the back edges of the fuel zone (see Fig. 6,II.2-6,curve 5). When 100% Pb_4Li is used as a front zone neutron multiplier (blanket #8) and Pb_4Li is the coolant in the fuel zone, the steepness of the U-233 production rate near the front edge of the fuel zone decreases noticeably (again see Fig. II.2-6, curve 6).

The adequate performance of blankets using Pb and Li in front of the fuel zone leads us to the second series of blankets that utilizes the Pb as a base for the front zone.

II.2.D Lead as the Neutron Multiplier

Cases 9 through 13 are blanket models with varying thicknesses of the Pb containing neutron multiplier zone (zone #3). Further, the multiplier zone is followed by 1.5 cm of natural liquid lithium (with volume percentage of 95% Li and 5% S.S.) and the fuel zone is followed by a 6 cm zone of 95% natural Li and 5% S.S. The purpose of these zones as thermal neutron filters and tritium breeders was discussed earlier. For blanket #10, with a 10 cm Pb multiplier zone, the UBR and TBR are 0.96 and 0.6, respectively. The competition between the Th(n,γ) and the Li^6(n,t)α reactions for neutron absorption does serve to flatten the Th (n,γ) reaction rate profile in the fuel assembly.

Various reaction rates per D-T neutron for cases of 5 cm, 10 cm, 15 cm and 20 cm Pb front zone thickness are give in Table II.2-4 and are shown on Fig. II.2-7. These cases are blankets #9, #10, #11 and #12, respectively. Blanket #10' is the same as blanket #10 with 50% Li-6 enriched Li in zone 4.

Table II.2-4

Reaction Rates of Blanket #9, #10, #10', #11, #12, and #13 per D-T Neutron

Blanket / Parameter	#10' (10 cm)	#9 (5 cm)	#10 (10 cm)	#11 (15 cm)	#12 (20 cm)	#13 (10 cm)
Th(n,γ)	0.7886	0.8589	0.9567	1.0116	1.0392	0.9339
max/min after rotation	1.0739	1.2114	1.2694	1.3412	1.4318	1.2185
TBR(Li-6)	0.7722	0.5774	0.5707	0.5585	0.5395	0.5983
TBR(Li-7)	0.0189	0.0378	0.0239	0.0149	0.0092	0.0271
TBR (total)	0.7910	0.6152	0.5946	0.5734	0.5487	0.6254
Fraction of TBR from Zone 4	0.1434	0.1664	0.1979	0.2294	0.2674	0.1874
Fraction of TBR from Zone 8	0.7812	0.6779	0.6609	0.6392	0.6116	0.6876
Fraction of TBR from Zone 10	0.0754	0.1557	0.1412	0.1313	0.1211	0.1250
Th ($n,\nu\sigma_f$)	0.0798	0.1218	0.0799	0.0520	0.0338	0.0799
Th (n,2n)	0.0633	0.1020	0.0634	0.0390	0.0239	0.0634
Th (n,3n)x2	0.0379	0.0619	0.0379	0.0230	0.0138	0.0379
Sum Th	0.1810	0.2857	0.1812	0.1140	0.0715	0.1812
Pb(n,2n)	0.4937	0.3239	0.4938	0.6008	0.6668	0.4919
Fraction Pb(n,2n) from Zone 3	0.9514	0.8776	0.9513	0.9757	0.9868	0.9551
Fraction Pb(n,2n) from Zone 9	0.0486	0.1224	0.0487	0.0243	0.0132	0.0449
Pb(n,abs)	0.0692	0.0967	0.0976	0.1024	0.1095	0.0918
$\frac{Pb(n,abs)}{Pb(n,2n)}$	0.1401	0.2987	0.1977	0.1705	0.1642	0.1867

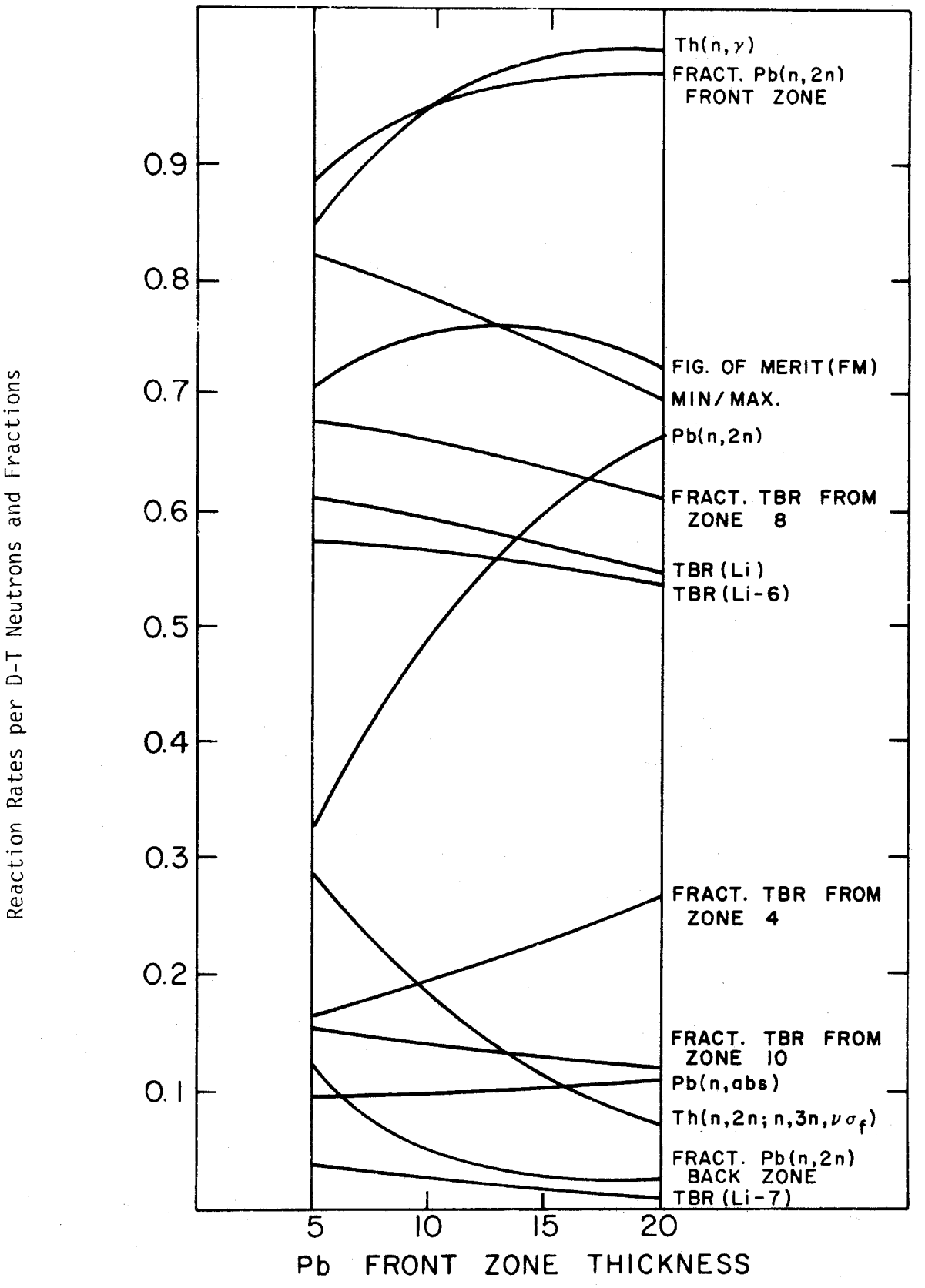

Fig. II.2-7 THE REACTION RATES PER D-T NEUTRON V S. Pb FRONT ZONE THICKNESS

Increasing the Pb zone thickness increases the Th(n,γ) reaction rate but the increase is slowed when the zone thickness exceeds about 15 cm. The $Li^6(n,t)\alpha$ reaction rate steadily decreases as the front zone thickness increases. Almost all of the tritium is produced by the $Li^6(n,t)\alpha$ reaction. The fraction of tritium produced in zone 4 increases from 17% to 27% as the front zone thickness increases from 5 cm to 20 cm because the spectrum becomes softer. The highest fraction of tritium produced is in zone 8 (~65% for blanket #10). This fraction decreases as the front zone thickness increases. The Li back zone contributes ~14% to the total tritium produced. This fraction decreases steadily as the front zone thickness increases.

The main source of neutron multiplication is the Pb(n,2n) reaction. It increases from ~0.32 to ~0.67 per D-T neutron as the front zone thickness increases from 5 cm to 20 cm. This shows the effectiveness of Pb as a front zone neutron multiplier. As expected, the fraction of Pb(n,2n) reactions from the front zone is much higher than the corresponding value in the reflector zone (~95% for blanket #10) and increases as the front zone thickness increases. The absorption rate in Pb is small (0.098 for blanket #10). The value of Pb(n,abs)/Pb(n,2n) decreases as the front Pb zone thickness increases.

The radial profiles for the Th(n,γ) reaction rate through the fuel zone are shown on Fig. II.2-8. These curves are much less steep than the corresponding ones shown in Fig. II.2-6 where Be is the neutron multiplier. To flatten the Th(n,γ) reaction rate profile at the back edge of the fuel zone and to gain a higher value of TBR, blanket #10 is modified by increasing the Li zone thickness behind the fuel zone from 6 cm to 8 cm.

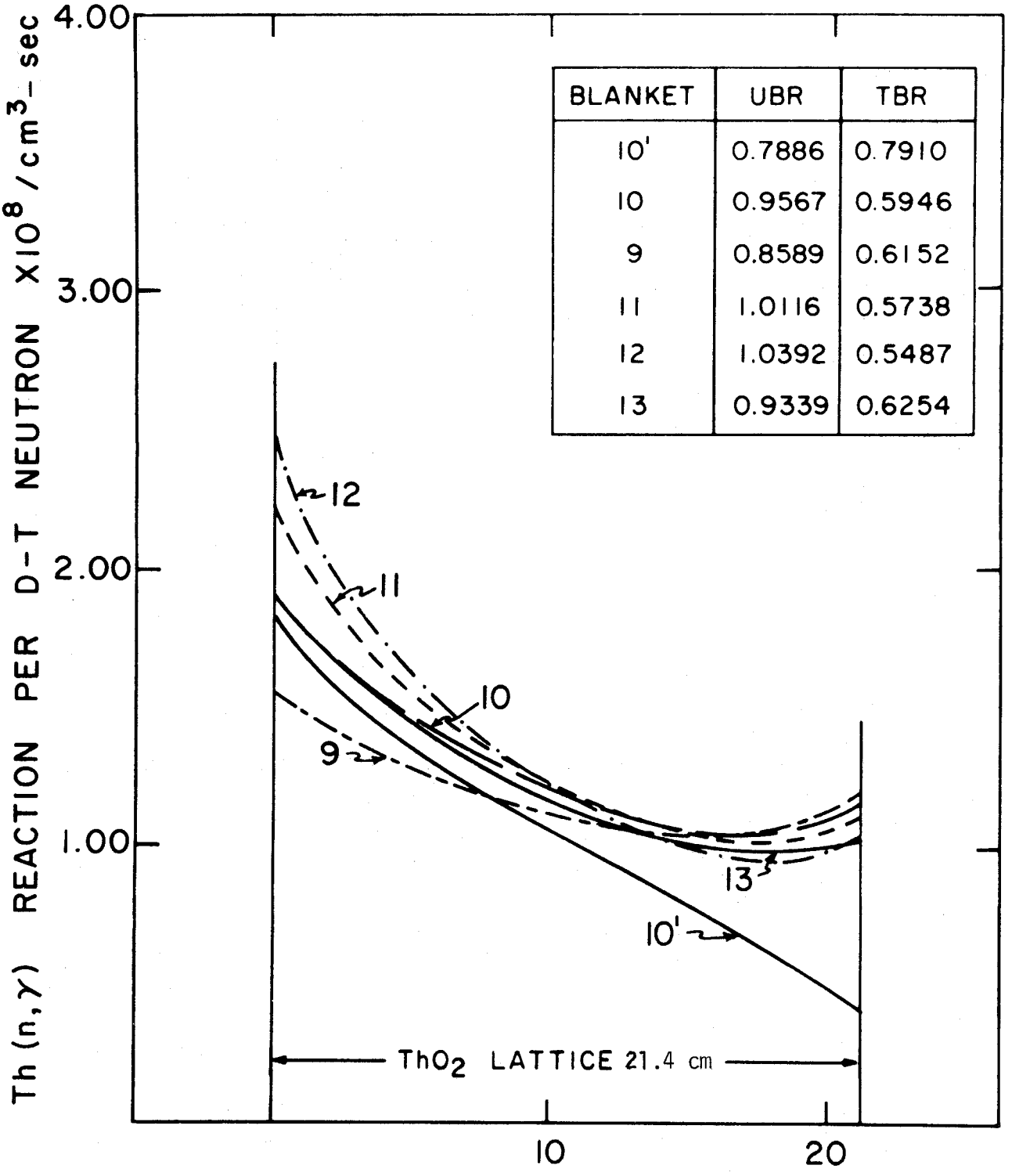

BLANKET	UBR	TBR
10'	0.7886	0.7910
10	0.9567	0.5946
9	0.8589	0.6152
11	1.0116	0.5738
12	1.0392	0.5487
13	0.9339	0.6254

Fig. II.2-8 U-233 BREEDING RATE DISTRIBUTION IN FUEL ZONE PER D-T NEUTRON WITH Pb AS THE FRONT ZONE NEUTRON MULTIPLIER

The UBR and TBR for this modified blanket (blanket #13) are 0.94 and 0.63, respectively. The reaction rates for this blanket aregiven in Table II.2-4 and the Th(n,γ) reaction rate across the fuel zone is shown in Fig. II.2-8.

II.2.E. Optimization Criteria

From the analysis just discussed, one is motivated to use lead as the neutron multiplier in the blanket front zone since the Th(n,γ) reaction rate profile in the fuel zone is more uniform. The spectrum in the fuel zone is harder. In addition, lead, unlike beryllium,does not pose a resource availability problem. Further, for the lead based blankets, the optimized one should meet the following requirements:

. Maximum U-233 production rate with as flat a U-233 distribution across the fuel assembly as possible.

. TBR ~0.6. Overall TBR $\gtrsim$ 1.0.

The first requirement shortens the residence time of the fuel to reach a specified enrichment. The constraint of a flat U-233 profile minimizes hot spot problems when the fuel assembly is placed directly in an LWR without an intermediate reprocessing step.

To begin the optimization search, it is assumed that the Th(n,γ) reaction rate profile across the fuel zone does not change when the fuel assembly is rotated 180° after some exposure time. The resultant curve, obtained by the addition of the Th(n,γ) profile to its spacially reversed value to account for the 180° rotation, is symmetric. This assumption has been verified and is discussed in the next section devoted to the burnup calculations. The resultant curve based on the blanket clean condition composition (i.e., at the beginning of life of the blanket) is taken as the base for choosing the optimized blanket in our design.

The resultant curves obtained for blankets #9, #10, #10', #11, #12 and #13 are shown in Fig. II.2-9. The maximum-to-minimum value of these curves is given in Table II.2-4.

According to our criteria and constraints, the optimized blanket will be the one having the smallest maximum-to-average $Th(n,\gamma)$ reaction rate, denoted by R, for its resultant curve while having a high value of UBR. Thus, the figure of merit, FM, is UBR/R and this should be a maximum. However, FM is proportional to $(UBR)^2/Th(n,\gamma)_{max}$ since the average $Th(n,\gamma)$ reaction rate value is proportional to UBR. The FM values $x10^{-8}$ are given in Fig. II.2-9.

Although blanket #12 has the highest value of FM, blanket #13 is chosen as the optimized one to gain the economic benefit of a 10 cm front zone rather than 20 cm (this is a thinner and cheaper blanket). The FM values are nearly equal in both cases. The optimized blanket #13 has TBR = 0.625 which meets the second constraint cited earlier.

II.2.F. Conclusions

An optimized blanket utilizing lead as a front zone neutron multiplier has been chosen. It has a UBR and TBR of 0.94 and 0.625, respectively. This blanket has a high figure of merit value and a nearly flat U-233 production rate across the fuel zone. Carrying out a 180° fuel assembly rotation after half the residence time to reach a specified enrichment will give a symmetric U-233 distribution in the fuel assembly.

The final SOLASE-H fission-fusion laser driven hybrid reactor is based on the optimized blanket obtained from this study. This final design is given in Fig. II.2-3. We turn now to the influence of burnup on the fuel assembly performance in the hybrid.

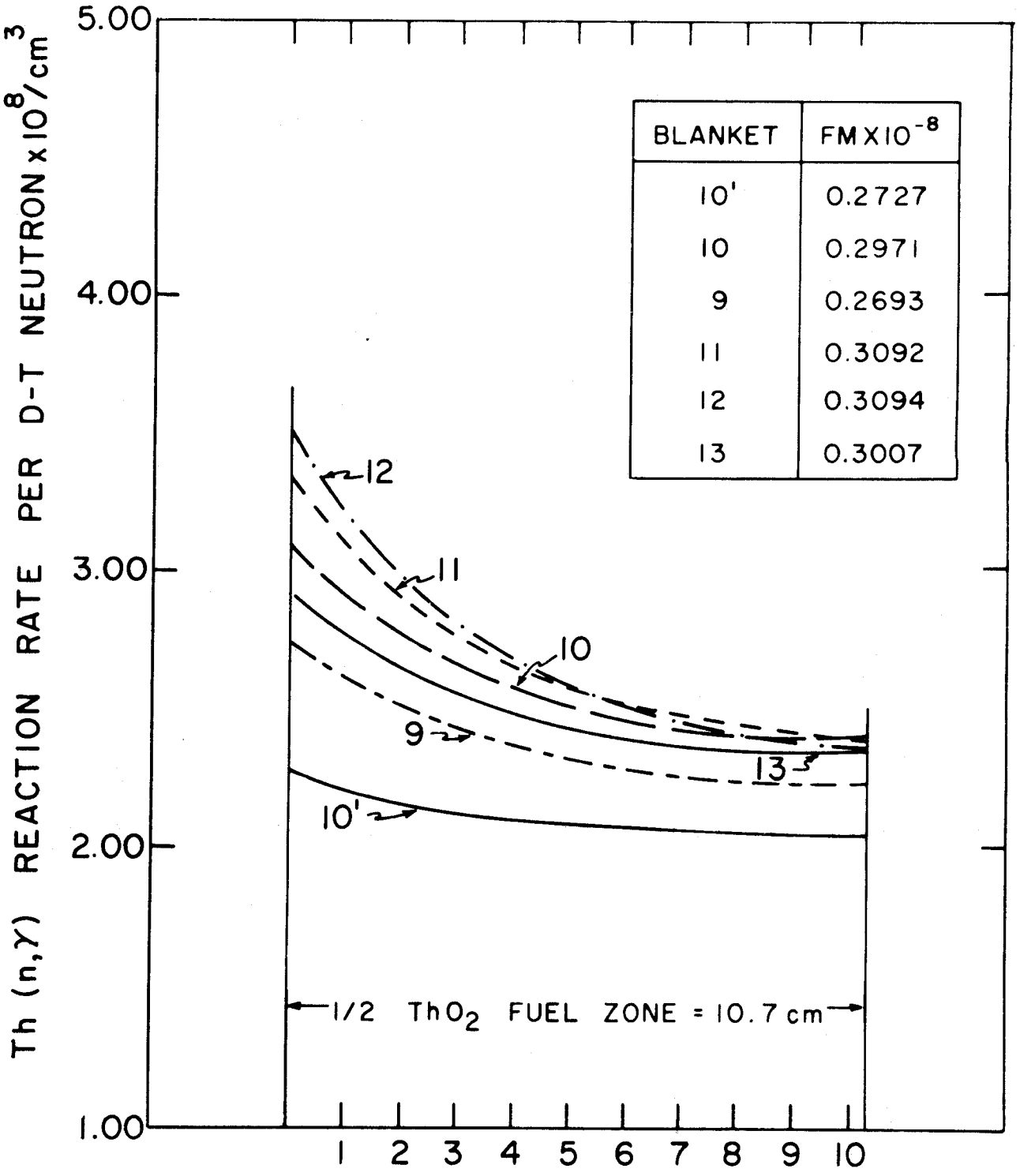

Fig. II.2-9 U-233 BREEDING RATE DISTRIBUTION THROUGH 1/2 OF THE FUEL ZONE AFTER ROTATION

References for Section II.2

1. K.R. Schultz, R.H. Brogli, G.R. Hopkins, M. Jonzen, and G.W. Shirley, "A U-233 Fusion-Fission Power System Without Reprocessing", A preliminary report, General Atomic GA-A14635, UC-code, Sept. (1977).

2. S.F. Su, G.L. Woodruff, N.J. McCormick, "A High-Gain Fusion-Fission Reactor for Producing U-233", University of Washington, Nuc. Technology, Vol. 29, p. 392, June (1976).

3. A.C. Cook and J.A. Maniscalco, "U-233 Breeding and Neutron Multiplying Blankets for Fusion Reactors", Lawrence Livermore Laboratories (LLL), Reprint UCRL-77284, Sept. (1975).

4. J.A. Maniscalco, "A Conceptual Design Study for Laser Fusion Hybrid", Reprint UCRL-78682, Sept. (1976).

5. J.A. Maniscalco, L.F. Hansen, and W.O. Allen, "Scoping Studies of U-233 Breeding Fusion Fission Hybrid", (LLL) Reprint UCRL-80585, May (1978).

6. W.W. Engle, Jr., "A User's Manual for ANISN", RISC-CCC-82, Oak Ridge National Lab. (1967).

7. R.Q. Wright and R.W. Rossin, "DLC-2D/100G Neutron Transport Cross Section Data Generated by SUPERTOG from ENDF/B3", RISC data package DLC-2, July (1973).

8. R.Q. Wright, et al., "SUPERTOG: A Program to Calculate Fine Group Constants and Pn Scattering Matrices from ENDF/B", ORNL-TM-2679 (1969).

9. Duderstadt, J.J., "Nuclear Reactor Analysis", John Wiley & Sons, Inc., pg. 635 (1976).

II.2. Burnup Calculations for the Optimization Studies

II.3.A. Introduction

The performance of the blankets studied in Section II.2 will undergo noticeable changes during operation. The fissile nuclide U-233 bred throughout the fuel zone, the depletion of Th-232 and the tritium production rates will vary with time. Detailed time-dependent calculations are necessary to follow changes in both the blanket's composition and performance. Such analysis is also required to accurately assess the fuel production rate and its spacial distribution across the fuel assembly (fuel zone).

The important parameters are: the depletion of Th-232 atoms; the build-up of U-233 atoms, and its effect on the neutron population and energy multiplication, M (defined as the total energy deposited throughout the blanket per 14.1 MeV D-T neutron); and the buildup of actinides and fission products.

There are several burnup codes[1-2] which evaluate the nuclide densities and the build up of fissionable nuclides as a function of the operating time. These codes have the following characteristics:

- One point depletion codes, i.e., ones which evaluate the depletion of atoms at one spatial point only.
- The number of neutron energy groups used are few (4 energy groups in the CINDER[1] code and 3 energy groups in ORIGIN[2]).
- The neutron cross sections used in these codes are based essentially on the spectra encountered in fast reactors.

First, based on unit-source neutron intensity, the ANISN[3] code can be used to calculate a 25-group neutron flux throughout the blanket. This flux, when combined with the actual D-T neutron source intensity, determines the neutron absolute flux level in the blanket. The flux, along with the nuclide

densities at the beginning of a particular time step is then used with the burnup code to evaluate new nuclide densities at the end of this time step. These are used in a new ANISN calculation for the next time step and the process is repeated.

For preliminary survey calculations, more simplified burnup procedures have been used in this study to evaluate the net fissile fuel production (U-233) and its spatial distribution across the fuel zone. The effect of fission product poisoning is not taken into consideration nor is the production of other daughter nuclides such as Pa-233 ($Th^{232}(n,2n)Pa^{233}$). This simplifying assumption is reasonable here since the blankets studied were optimized for maximum fuel production without the use of a fission plate of fissile isotopes intended to enhance neutron production.[4-9] Accordingly, the number of fissions per D-T neutron is small and the effect of fission product poisoning should be less harmful neutronically. In our study, the neutron population is enhanced by the (n,2n) reaction in lead (or Be) as mentioned in section II.2.

In the burnup model adopted, the time variation in atomic density at each point throughout the fuel zone is calculated using the neutron flux (25-group) at that point. We do not use an average value through a certain subregion with a fewer number of energy groups (3-4) as in the case when using burnup codes like CINDER and ORIGIN.

The neutron source is obviously localized outside the fuel zone. As such, fissile fuel production across the fuel zone decreases far from the source. A scheme to rotate the fuel assembly after a given operating time is necessary to obtain a flatter fissile fuel distribution.The criteria adopted for

optimizing the lead front zone neutron multiplier to meet this requirement is discussed in section II.2.E.

In the burnup model adopted in this study, the important parameters to be evaluated are:

(1) Th-232 and U-233 atomic densities as a function of time.

(2) The percent burnup of the bred U-233 as a function of time.

(3) U-233 and tritium production rate before and just after fuel assembly rotation at any particular time.

Based on these parameters, the time at which rotation of the fuel assembly takes place and the extra time needed to reach a specified U-233 enrichment are evaluated subject to the constraint of as even a fissile fuel distribution as possible. The parameters in (1) and (2) above are evaluated for the different blankets utilizing lead as front zone neutron multiplier (see section II.2), while parameters in (3) and the rotation scheme are evaluated for the optimized blanket. The configuration of these blankets are given in Fig. II.3-1 and Table II.3-1a,b.

In the following, the burnup model and the results in (1), (2) and (3) above are given.

II.3.B. Th-232 and U-233 Atomic Densities as Function of the Operating Time

Only the densities of Th-232 and U-233 were considered to vary with time. In this case, the rate of change of these nuclide densities is given by

$$\frac{dN^{(2)}(x,t)}{dt} = \sum_i N^{(1)}(x,t)\phi_i(x,t)\sigma_\gamma^{(i,1)} - \sum_i N^{(2)}(x,t)\phi_i(x,t)\sigma_a^{(i,2)} \quad (1)$$

$$\frac{dN^{(1)}(x,t)}{dt} = -\sum_i N^{(1)}(x,t)\sigma_a^{(i,1)}\phi_i \quad (2)$$

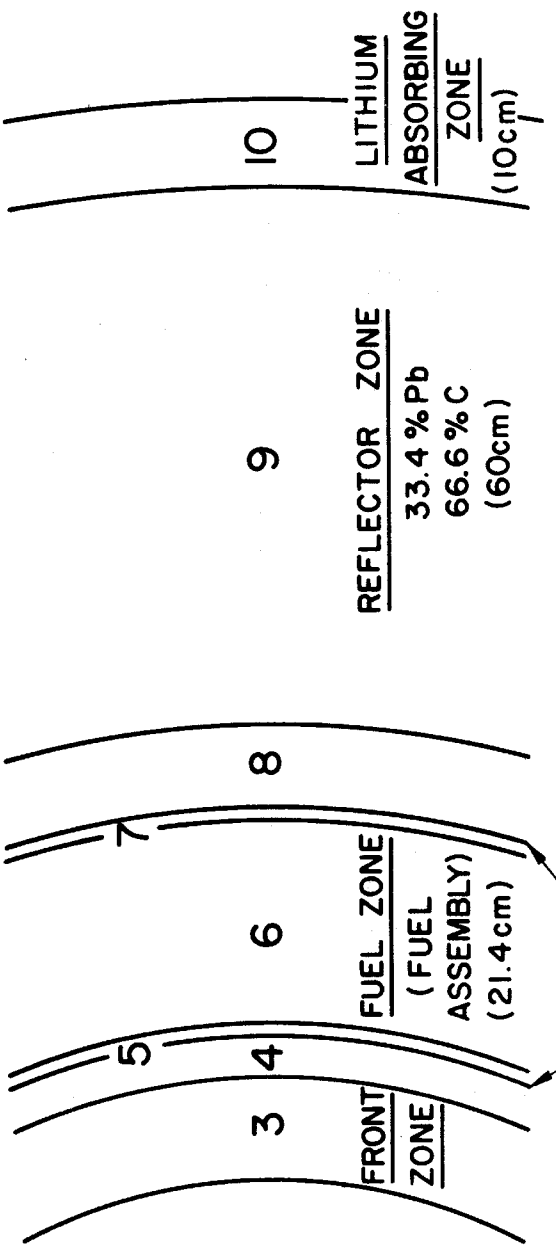

Fig. II.3-1 Configuration of the different blankets utilizing Pb as the front zone neutron multiplier (See Table II.3-1).

Table II.3-1a

Zone Composition and Thickness

Zone	Thickness	Composition
1	0.5 cm	Laser Pellet
2	499.5 cm	Vacuum
3	X cm (see table II.3-1b)	82.2% Pb 9.3% Na 8.5% Zirc-2
4	1.5 cm	95% Li 5% S.S.
5	0.5 cm	100% S.S.
6	21.4 cm	30.3% ThO_2 9.2% Zirc-2 1.3% Void 59.2% Na
7	0.5 cm	100% S.S.
8	Y cm (see table II.3-1b)	95% Li 5% S.S.
9	60 cm	33% Pb 67% C
10	10 cm	95% Li 5% S.S.

Table II.3-1b

Different Blankets Studied for Burnup Calculations

Zones / (a) Blanket #	Zone 3 (X) cm	Zone 4	Zone 8 (Y) cm	U-233 Breeding Ratio UBR(b)	Tritium Breeding Ratio TBR(c)
10'	10 cm	1.5cm-nat Li	6cm-50% Li^6	0.7886	0.791036
9	5 cm	"	6cm-nat Li	0.8589	0.6152
10	10 cm	"	"	0.9567	0.5946
11	15 cm	"	"	0.0116	0.5734
12	20 cm	"	"	1.0392	0.5487
13(d)	10 cm	"	8cm	0.9339	0.6254

(a) See Section II.2
(b) U-233 atoms produced in the fuel zone/D-T neutron
(c) Tritium atoms produced in the blanket/D-T neutron
(d) The optimized blanket

where $N^{(2)}(x,t)$ = U-233 atomic density at position x at time t

$N^{(1)}(x,t)$ = Th-232 atomic density at position x at time t

$\phi_i(x,t)$ = Neutron flux of energy group i at position x and time t

$\sigma_\gamma^{(i,1)}$, $\sigma_a^{(i,1)}$ = Microscopic capture and absorption cross section of Th-232 of energy group i, respectively.

$\sigma_a^{(i,2)}$ = Microscopic absorption cross section of U-233 of energy group i.

The fission yield of Th-232 and U-233 and their radioactive decay were ignored in eq. (1) and (2) [$t_{1/2}$ (Th-232) = 1.41 x 10^{10}yr and $t_{1/2}$ (U-233) = 1.65 x 10^5yr].

Upon solving eq. (1) and (2) we get

$$N^{(1)}(x,t) = N^{(1)}(x,t_o)e^{-b(t-t_o)} \tag{3}$$

$$N^{(2)}(x,t) = \frac{c}{a-b} N^{(1)}(x,t_o)[e^{-b(t-t_o)} - e^{-a(t-t_o)}] + N^{(2)}(x,t_o)e^{-a(t-t_o)} , \tag{4}$$

where

$$a \equiv a(x) = \sum_i \phi_i \sigma_a^{(i,2)}$$

$$b \equiv b(x) = \sum_i \phi_i \sigma_a^{(i,1)}$$

$$c \equiv c(x) = \sum_i \phi_i \sigma_\gamma^{(i,1)} ,$$

with the assumption that the neutron flux does not change with time. $N^{(2)}(x,t_o)$ and $N^{(1)}(x,t_o)$ are the atomic densities of U-233 and Th-232, respectively, at position x and initial time $t = t_o$. The amount of U-233 generated $G(x,t_1 \to t_2)$ in a time interval $t_1 \to t_2$ at position x is

$$G(x,t_1\rightarrow t_2) = -\frac{c}{b}N^{(1)}(x,t_o)[\bar{e}^{b(t_2-t_o)} - \bar{e}^{b(t_1-t_o)}]$$

$$= -\frac{c}{b}N^{(1)}(x,t_1)[\bar{e}^{b(t_2-t_1)} - 1] \qquad (5)$$

The amount of U-233 consumed between t_1 and t_2 is

$$C(x,t_1\rightarrow t_2) = \int_{t_1}^{t_2} a\, N^{(2)}(x,t)dt. \qquad (6)$$

With $N^{(2)}(x,t)$ given by eq. (4) and expressed in terms of t, we find

$$N^{(2)}(x,t) = \frac{c}{a-b}N^{(1)}(x,t_1)[\bar{e}^{b(t-t_1)} - \bar{e}^{a(t-t_1)}] + N^{(2)}(x,t_1)\bar{e}^{a(t-t_1)}.$$

From eq. (6), we find also

$$C(x,t_1\rightarrow t_2) = \frac{ac}{a-b}N^{(1)}(x,t_1)[\frac{\bar{e}^{b(t_2-t_1)} - 1}{(-b)} - \frac{\bar{e}^{a(t_2-t_1)} - 1}{(-a)}]$$

$$- N^{(2)}(x,t_1)[\bar{e}^{a(t_2-t_1)} - 1] \qquad (7)$$

where,

$$N^{(1)}(x,t_1) = N^{(1)}(x,t_o)\bar{e}^{b(t_1-t_o)} \qquad (8)$$

$$N^{(2)}(x,t_1) = \frac{c}{a-b}N^{(1)}(x,t_o)[\bar{e}^{b(t_1-t_o)} - \bar{e}^{a(t_1-t_o)}]$$

$$+ N^{(2)}(x,t_o)\bar{e}^{a(t_1-t_o)} \qquad (9)$$

In terms of $N^{(1)}(x,t_o)$ and $N^{(2)}(x,t_o)$, eq. (7) can be expressed as:

$$C(x,t_1\rightarrow t_2) = \frac{ac}{a-b}N^{(1)}(x,t_o)[\frac{\bar{e}^{b(t_2-t_o)} - \bar{e}^{b(t_1-t_o)}}{(-b)} - \frac{\bar{e}^{a(t_2-t_o)} - \bar{e}^{a(t_1-t_o)}}{(-a)}]$$

$$- N^{(2)}(x,t_o)[\bar{e}^{a(t_2-t_o)} - \bar{e}^{a(t_1-t_o)}] \qquad (10)$$

The enrichment at a certain position x and time t is defined as

$$E(x,t) = \frac{N^{(2)}(x,t)}{N^{(1)}(x,t)} = \frac{\text{Net U-233 atoms/cm}^3}{\text{Th-232 atoms/cm}^3} \qquad (11)$$

The fraction of fissile nuclide burned, $Bu(x,t_o\rightarrow t)$ is defined as

$$Bu(x,t_o\rightarrow t) = \frac{C(x,t_o\rightarrow t)}{G(x,t_o\rightarrow t)}$$

$$= \frac{\text{U-233 atoms consumed/cm}^3 \text{ in the interval } t_o \to t}{\text{U-233 atoms generated/cm}^3 \text{ in the interval } t_o \to t}$$

and the initial conditions are

$$\left.\begin{aligned} t &= t_o = 0 \\ N^{(2)}(x,t_o) &= 0 \\ N^{(1)}(x,t_o) &= N^{(1)} = \text{initial Th-232 atomic density} \\ &\qquad \text{throughout the fuel zone.} \end{aligned}\right\} \qquad (12)$$

If the variation of Th-232 atomic density with time is slight, as it turns out to be the case in the blankets studied, we can consider

$$N^{(1)}(x,t) \cong N^{(1)}$$

This is equivalent to considering $b \to 0$ in eq. (3). In this case, we have from eq. (5)

$$G(x,t_1 \to t_2) \cong -\frac{c}{b} N^{(1)}[e^{-bt_2} - e^{-bt_1}] \qquad (13)$$

and

$$G(x,0 \to t) \cong -\frac{c}{b} N^{(1)}[e^{-bt} - 1] \qquad (14a)$$

$$\simeq c N^1 t \ , \quad c \equiv c(x), \qquad (14b)$$

i.e., the U-233 generation is linear with time. Also from eq. (10)

$$C(x,t_1 \to t_2) \cong \frac{ac}{a-b} N^{(1)}[-\frac{e^{-bt_2} - e^{-bt_1}}{b} + \frac{e^{-at_2} - e^{-at_1}}{a}] \ , \qquad (15)$$

and

$$C(x,0 \to t) \cong \frac{ac}{a-b} N^{(1)}[-\frac{e^{-bt} - 1}{b} + \frac{e^{-at} - 1}{a}] \ . \qquad (16)$$

For $b \to 0$, this reduces to

$$C(x,0 \to t) = cN^{(1)}[t - \frac{1-e^{-at}}{a}] \ , \qquad (17)$$

and for small values of a, we finally find,

$$C(x,0\to t) \simeq \frac{ac\, N^{(1)}{}_t{}^2}{2} \tag{18}$$

Thus the consumption of U-233 up to time t is quadratic in time for small a and b→0. In this case, the fraction of U-233 burned is

$$Bu(x,0\to t) = \frac{C(x,0\to t)}{G(x,0\to t)} \simeq \frac{at}{2} \ . \tag{19}$$

which is linear in time. The net U-233 generated at point x and time t under these assumptions is

$$\begin{aligned} N^{(2)}(x,0\to t) &= G(x,0\to t) - C(x,0\to t) \\ &= c\, N^{(1)}{}_t - acN^{(1)}{}_t{}^2 \\ &= c\, N^{(1)}{}_t \quad \text{for small } at^2 \end{aligned} \tag{20}$$

One should notice that a, b and c are functions of position.

II.3.C. Effect of Varying the Pb Neutron Multiplier Front Zone Thickness on the U-233 Bred After Operating Time t

The amount of U-233 produced, consumed and the fraction burned throughout the fuel zone as a function of the operating time has been calculated for the blankets utilizing Pb as a front zone multiplier and shown in Fig. II.3-1 and Table II.3-1. The total U-233 generated in the fuel zone, $G_t(t)$, is

$$G_t(t) = \int G(\vec{x},0\to t)d\vec{x} \tag{21}$$

The amount of U-233 consumed up to time t in the fuel zone, $C_t(t)$, is

$$C_t(t) = \int C(\vec{x},0\to t)d\vec{x} \ . \tag{22}$$

The fraction burned, $BU_t(t)$, is

$$BU_t(t) = \frac{C_t(t)}{G_t(t)} \quad , \tag{23}$$

the net U-233 produced in the fuel zone, $U_t(t)$, is

$$U_t(t) = G_t(t) - C_t(t), \tag{24}$$

and the enrichment at that time, $E_t(t)$, is

$$E_t(t) = \frac{U_t(t)}{TH(t)} \simeq \frac{U_t(t)}{TH_o} \tag{25}$$

where $$TH(t) = \int N^{(1)}(\vec{x},0\rightarrow t)d\vec{x} \quad ,$$

the total Th-232 atoms in the blanket at time t and TH_o is its atom inventory at t=0.

The values of $G_t(t)$ and $C_t(t)$, expressed in kg of U-233 and the percentage of burnup are shown in Fig. II.3-2 and Fig. II.3-3 for a wall loading of 1.92 MW/m^2. The 25-group fluxes at each spatial point within the fuel zone determined at t=0 (clean condition)were used to evaluate the space dependent coefficients a, b and c. More accurate results necessitate the use of the neutron flux after each time step with the new atomic densities, as mentioned in the introduction. This, however, has been done for the optimized blanket (blanket #13) as will be discussed later.

As shown in Fig. II.3-2, the U-233 generated, $G_t(t)$, varies linearly in time for each blanket and the U-233 consumed up to time t, $C_t(t)$, is quadratic in t. The percentage of U-233 burned, $BU_t(t)$, is almost linear as shown on Fig. II.3-2 and deviates from linearity only after ~2.1 year. This can be shown by considering the fraction of U-233 burned at point x after time

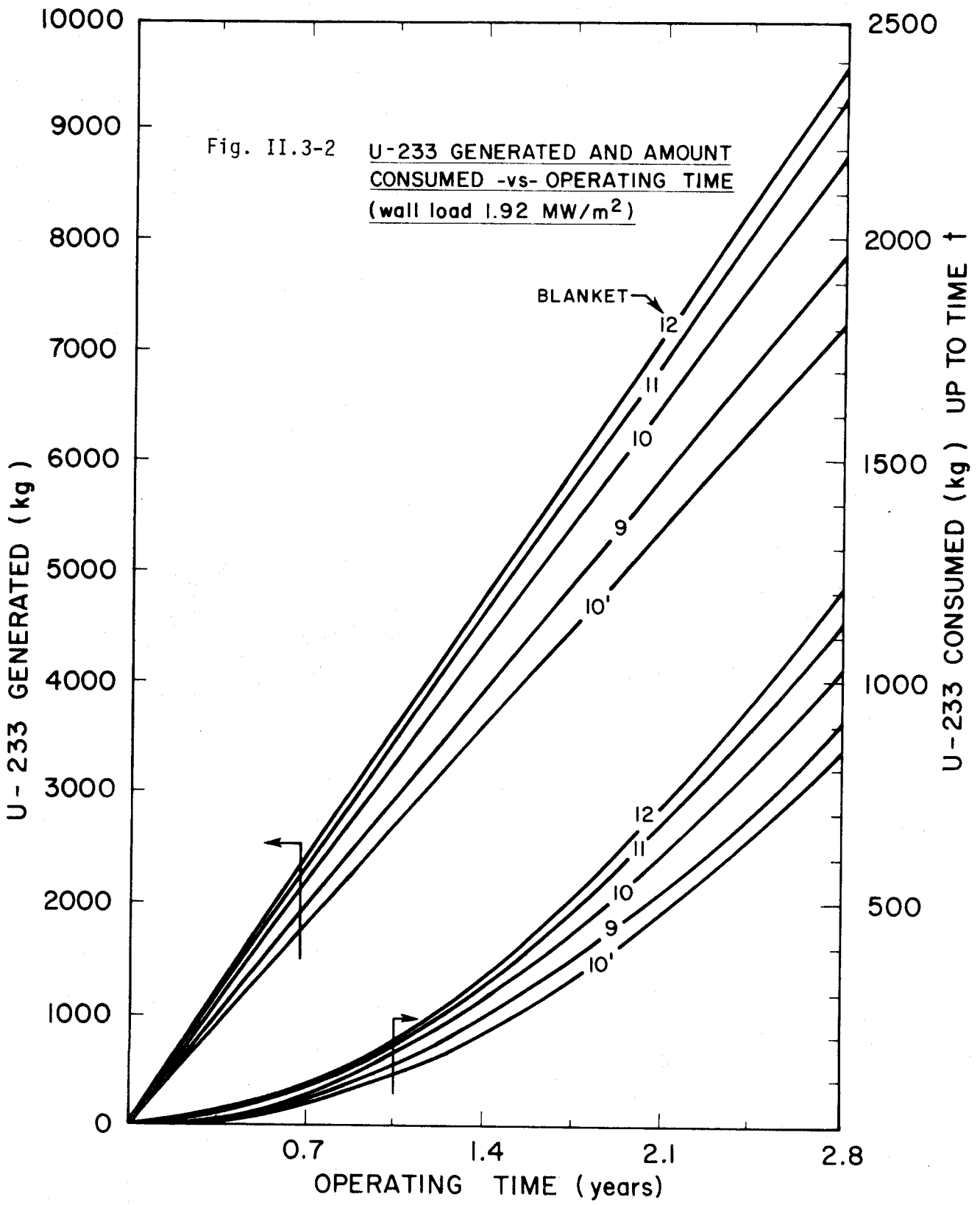

Fig. II.3-2 U-233 GENERATED AND AMOUNT CONSUMED -vs- OPERATING TIME (wall load 1.92 MW/m^2)

Fig. II.3-3 % BURN-UP OF U-233 -vs- OPERATING TIME FOR WALL LOAD 1.92 MW/m^2

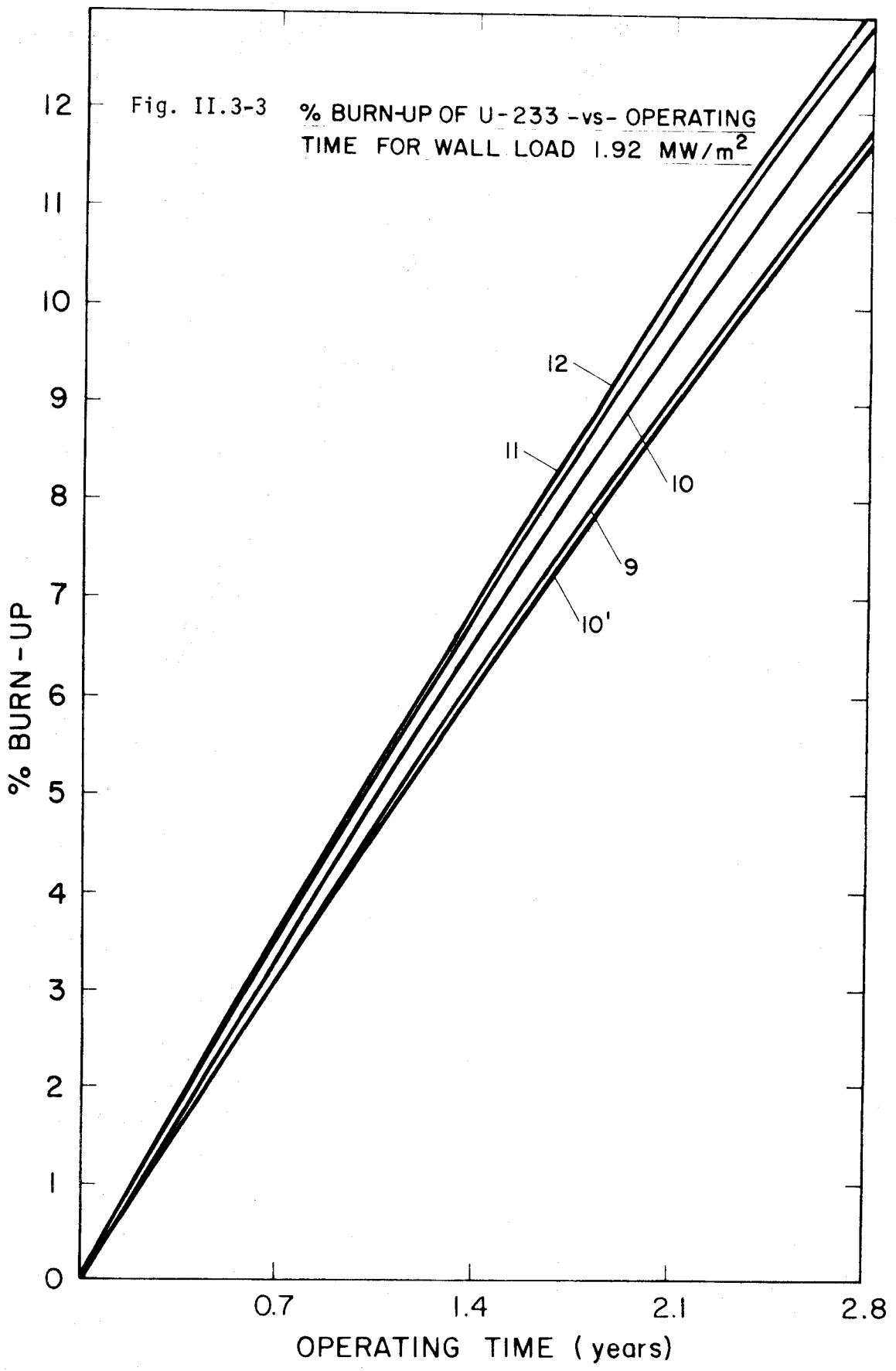

t [see eq. (14-a) and eq. (16)]:

$$BU(x,0\to t) \cong \frac{C(x,0\to t)}{G(x,0\to t)}$$

$$= \frac{\frac{ac}{a-b}\, N^{(1)}\left[-\frac{e^{-bt}-1}{b} + \frac{e^{-at}-1}{a}\right]}{\frac{c}{b} N^{(1)}\left[e^{-bt}-1\right]}, \qquad (26)$$

where $N^{(1)}(x,t)$ is considered constant at $t_o = 0$. With $b\to 0$, it reduces to

$$BU(x,0\to t) \simeq 1 + \frac{e^{-at}-1}{at}, \qquad (27)$$

which has an exponential term. For a non-negligible value of the exponent (large t), the integrated value $BU_t(t)$ is non-linear in time.

Blanket #12 has the highest fuel production rate (see Table II.3-1) while blanket #9 has the lowest value among blankets #9, #10, #11 and #12. As mentioned before, increasing the Pb front zone thickness increases the fuel production rate and decreases the tritium production rate. However, the change in these rates is less pronounced when the Pb front zone thickness exceeds 10 cm (see Section II.2).

The differences in the values of $G_t(t)$, $C_t(t)$ and $BU_t(t)$ for blankets #9, #10, #11 and #12 are less pronounced for shorter operating times. This is shown in Fig. II.3-4 where these values are plotted after 1.05 yr and 2.1 yr for these different blankets. The slope in the curves of $G_t(t)$, $C_t(t)$ and $BU_t(t)$ shown in Fig. II.3-4 is larger when the front zone thickness is small. One should notice that at any operating time, although the amount of U-233 produced increases as the front zone increases, the amount of U-233 consumed also increases and curves for $C_t(t)$ do not cross one another.

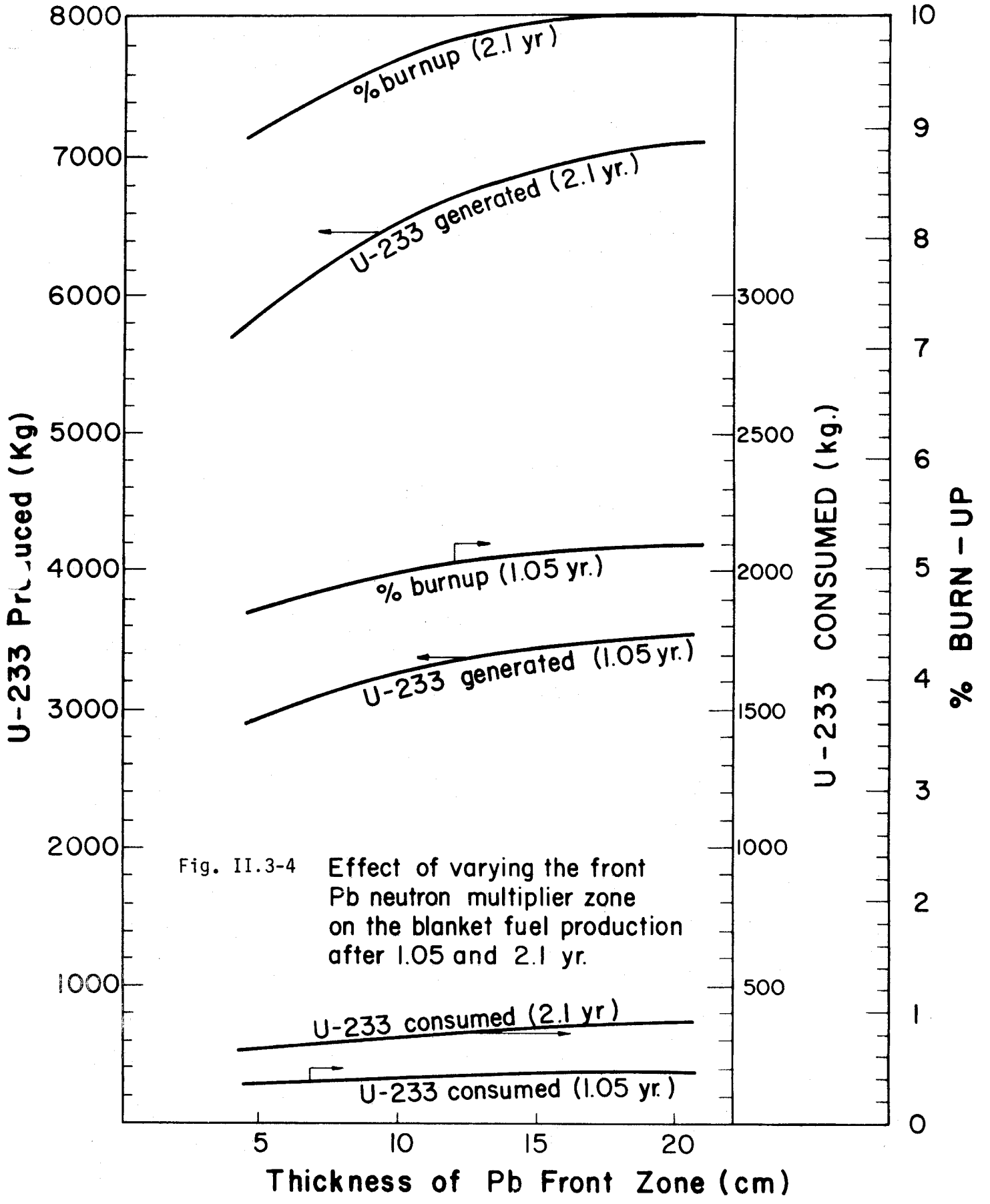

Fig. II.3-4 Effect of varying the front Pb neutron multiplier zone on the blanket fuel production after 1.05 and 2.1 yr.

To study the effect of non-uniform fissile fuel production rates across the fuel, the time needed to reach a specific enrichment (~4%) at each point and for each blanket is calculated. This is shown in Fig. II.3-5 for a wall loading of 1.92 MW/m^2. This time is higher for regions further from the D-T neutron source. For blanket #10', (see Table II.3-1), the time to enrichment increases as we reach the outer edge since the fissile fuel production rate decreases across the fuel zone. The results in Fig. II.3-5 are inversely proportional to the fuel production rate discussed previously in section II.2. The points near the inner edge of the fuel zone (close to the source) reach 4% enrichment faster than the points near the outer edge. The curves for blanket #12 and the optimized blanket #13 are shown separately in Fig. II.3-6 and Fig. II.3-7, respectively. Also shown are curves for the time needed to reach 4% enrichment without considering the burning of bred U-233. From these figures, one observes the following:

- The time to enrichment is inversely proportional to $Th(n,\gamma)$ reaction rate per D-T neutron.
- Including U-233 burning implies each point requires a longer time to reach the specified enrichment.
- About 12% of U-233 generated is consumed during the enrichment process.

The results shown in Figs. II.3-5, II.3-6 and II.3-7 are useful if there is a shifting scheme to move one fuel element in the fuel assembly from one position to another or to retrieve certain fuel elements after reaching a

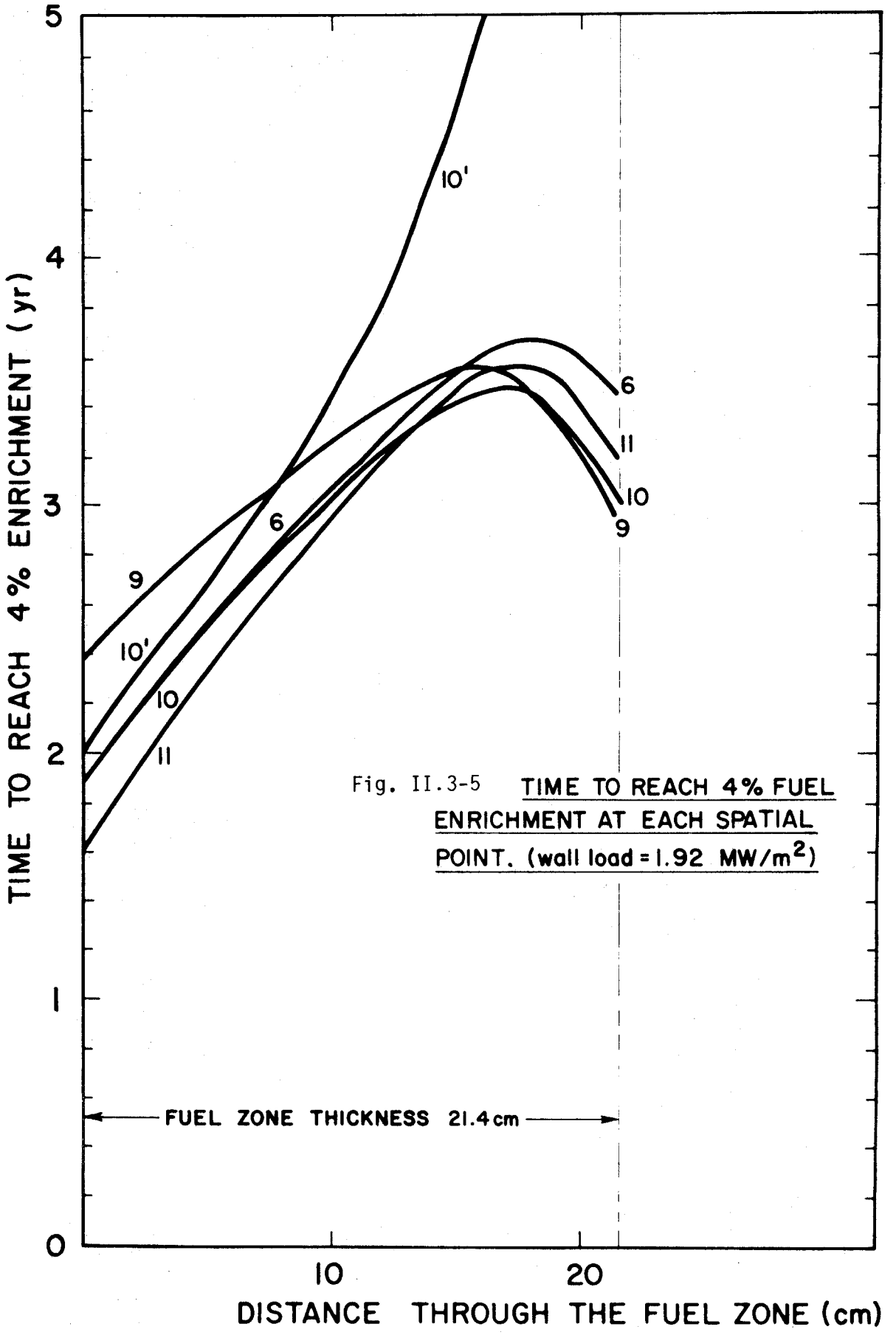

Fig. II.3-5 TIME TO REACH 4% FUEL ENRICHMENT AT EACH SPATIAL POINT. (wall load = 1.92 MW/m^2)

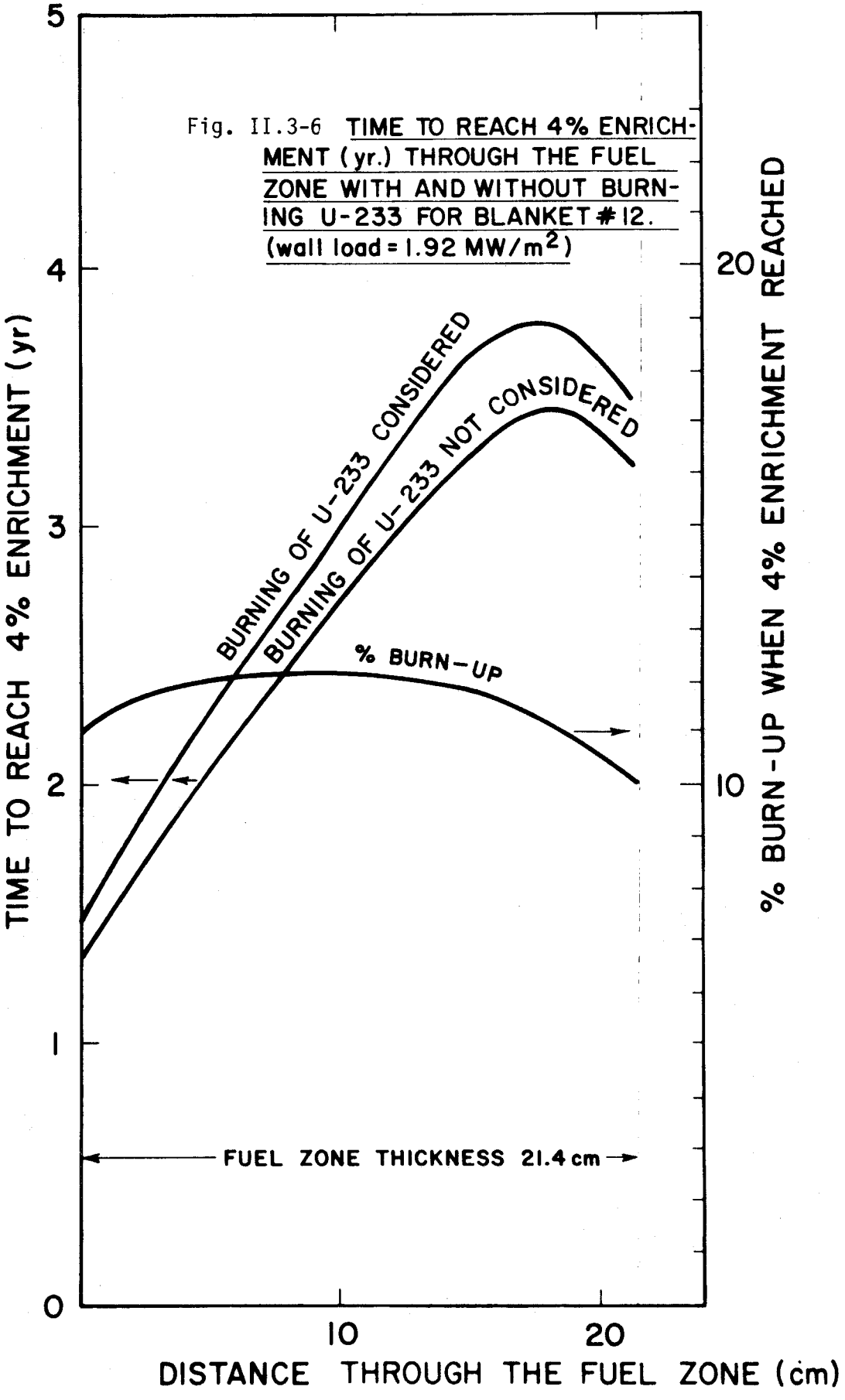

Fig. II.3-6 TIME TO REACH 4% ENRICHMENT (yr.) THROUGH THE FUEL ZONE WITH AND WITHOUT BURNING U-233 FOR BLANKET #12. (wall load = 1.92 MW/m^2)

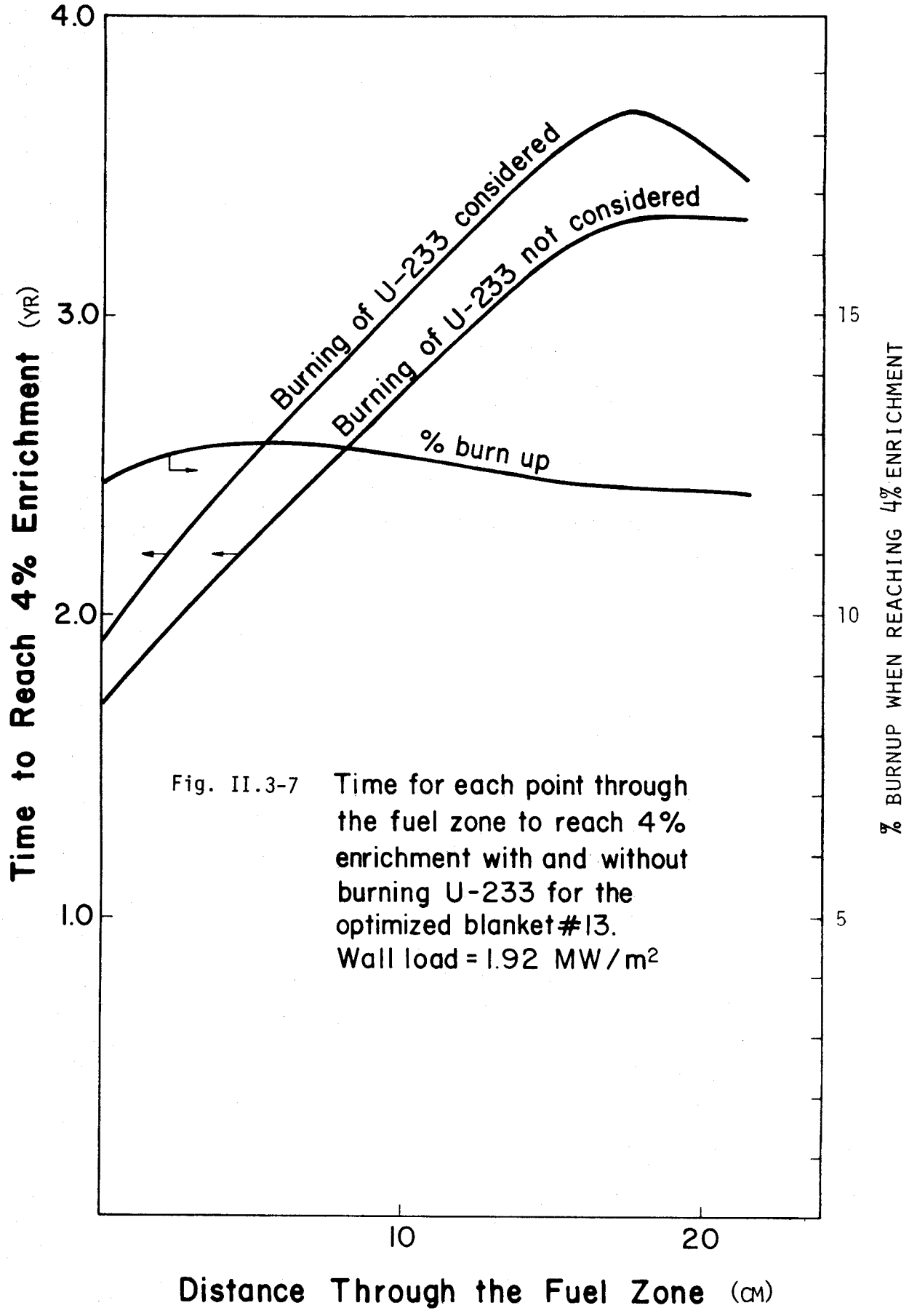

Fig. II.3-7 Time for each point through the fuel zone to reach 4% enrichment with and without burning U-233 for the optimized blanket#13. Wall load = 1.92 MW/m^2

specified enrichment. In our design, however, the fuel assembly is extracted from the blanket after reaching a specific overall enrichment. It is rotated 180° after approximately half of the residence time in the blanket to assure a flatter fissile fuel distribution across the assembly. This rotation scheme is discussed later for the optimized blanket #13.

The time needed to reach a specific overall enrichment, $E_t(t)$, defined as the ratio of the total U-233 atoms produced in the fuel zone to the total Th-232 atoms present at time t, is shown in Table II.3-2. In this table, we summarize the results of fuel production and consumption in blankets #10', #9, #10, #11,#12 and the optimized blanket #13 after reaching 4% enrichment. The corresponding values without allowing for the depletion of Th-232 and U-233, denoted by fresh condition, are also given for comparison. One should notice that the parameter RT = $(UBR)_0$ T(4%)/Th(Kg) is almost identical for all the blankets. $(UBR)_0$ is the uranium breeding ratio at the beginning of life of the blanket and T(4%) is the time to reach an overall enrichment of 4%. The value of RT is nearly constant because as $(UBR)_0$ increases, T(4%) decreases. Thus, lesser amounts of Th-232 (although small) are depleted.

The results tabulated in Table II.3-2 are evaluated using the 25-neutron group flux at clean condition, ϕ_o. More accurate results are obtained if the variation of the flux due to U-233 build up and Th-232 depletion are taken into consideration. This has been done for the optimized blanket #13 and is described below.

Table II.3-2

The Blanket Parameters After Reaching 4% Fuel Enrichment Using ϕ_o and Wall Loading of 1.92 MW/m^2

Parameter \ Blanket		#10' (10 cm)[a]	#9 (5 cm)	#10 (10 cm)	#11 (15 cm)	#12 (20 cm)	#13[b] (10 cm)
Time to Reach 4% Enrichment T(4%)yrs	Actual	3.514	3.108	2.840	2.737	2.719	2.914
	Fresh Cond.	3.070	2.765	2.531	2.440	2.420	2.593
U-233 Generated (kg) x 10^{-3}		8.793	8.493	8.643	8.805	8.981	8.654
U-233 Consumed (kg) x 10^{-3}		1.267	1.108	1.109	1.123	1.152	1.121
Net U-233 (kg) x 10^{-3}		7.526	7.385	7.534	7.682	7.829	7.533
Th-232 (kg) x 10^{-4}	Actual	18.733	18.381	18.753	19.122	19.489	18.751
	Fresh Cond.	19.635	19.261	19.635	20.013	20.394	19.635
% Burn Up		14.413	13.053	12.837	12.756	12.824	12.957
RT[c] x 10^5	Actual	1.479	1.450	1.450	1.450	1.450	1.450
	Fresh Cond.	1.233	1.233	1.233	1.233	1.233	1.233

(a) Pb front zone thickness
(b) The optimized blanket
(c) RT = $(UBR)_o$ T(4%)/Th(kg)

II.3.D. The Burnup Calculation for the Optimized Blanket

The atomic density of Th-232 and U-233 after 0.7 yr are evaluated at each spatial point in the fuel zone of blanket #13 with a wall load of 1.92 MW/m^2. The fuel zone is divided into 3 subzones and the average density of Th-232 and U-233 in these subzones is evaluated. Using these densities, the flux ϕ_1 after 0.7 years of operation is evaluated using the ANISN code. The flux ϕ_1 is then used to evaluate the Th-232 and U-233 densities at the end of the next time step Δt of 0.7 years. These densities, along with the ANISN code, are then used to evaluate a new flux, ϕ_2, after 1.4 years of operation.

The parameters of interest at the beginning of life, after 0.7 years and 1.4 years of operation are tabulated in Table II.3-3. The values of the UBR and TBR increase with time due to the enhanced number of neutrons in the blanket from U-233 fissioning. The number of neutrons produced by U-233 fission is larger by a factor of 1.8 than those from Th-232 fission after 0.7 yr. This factor is 3.6 after 1.4 years of operation. The UBR increases by 3.5% after 0.7 yr and nearly twice as much (7.4%) after 1.4 years. The TBR increases by 6.4% after 0.7 yr and by 13.2% after 1.4 years. The variation of UBR and TBR is nearly linear with time. The U-233 production rate across the fuel zone is shown in Fig. II.3-8 at fresh condition, after 0.7 yr and after 1.4 yr along with their percentage increase. The percentage increase in Th(n,γ) reaction rate is nearly linear with time. This is shown in Fig. II.3-8 where the percentage increase of U-233 production rate after 1.4 years compared to the corresponding value after 0.7 yr is slightly larger than the percentage increase after 0.7 yr compared to

Table II.3-3

Parameters v.s. Operating Time for Blanket #13 per D-T Neutron

Parameter	Fresh Cond.	After 0.7 Year	After 1.4 Years
UBR $\equiv Th(n,\gamma)$	0.9338	0.9673	1.0026
$Li^6(n,T)\alpha$	0.5983	0.6379	0.6805
$Li^7(n,tn')\alpha$	0.0271	0.0274	0.0277
TBR (total)	0.6254	0.6652	0.7082
$Th(n,\nu\sigma_f)$	0.0799	0.0822	0.0848
Th(n,2n)	0.0634	0.0628	0.0622
Th(n,3n)x2	0.0379	0.0374	0.0370
Pb(n,2n)	0.4919	0.4920	0.4921
$U^{233}(n,\nu\sigma_f)$	0	0.1474	0.3048

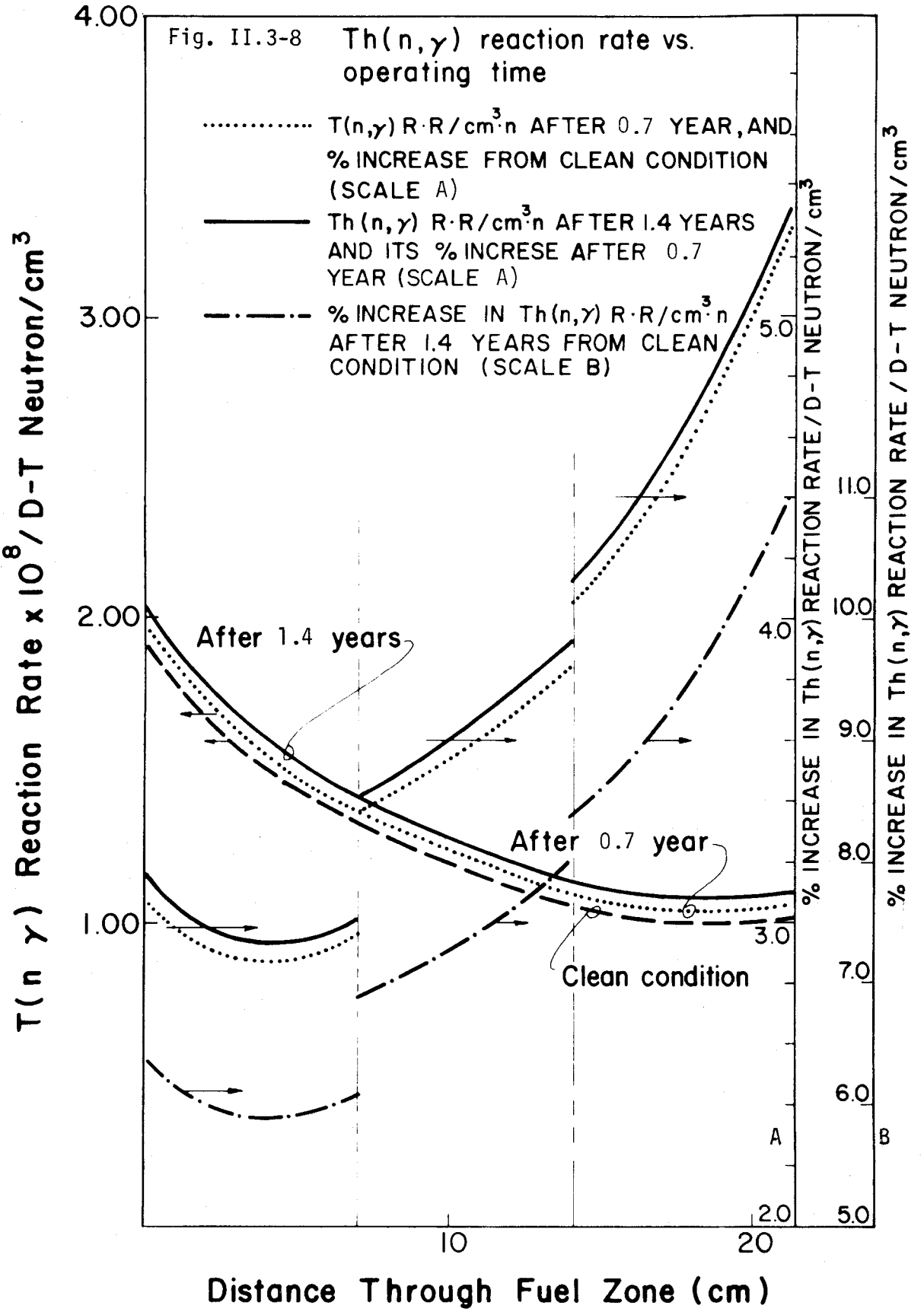
Fig. II.3-8 Th(n,γ) reaction rate vs. operating time
T(n,γ) R·R/cm³·n AFTER 0.7 YEAR, AND % INCREASE FROM CLEAN CONDITION (SCALE A)
Th(n,γ) R·R/cm³·n AFTER 1.4 YEARS AND ITS % INCRESE AFTER 0.7 YEAR (SCALE A)
% INCREASE IN Th(n,γ) R·R/cm³·n AFTER 1.4 YEARS FROM CLEAN CONDITION (SCALE B)
After 1.4 years
After 0.7 year
Clean condition
T(n γ) Reaction Rate x 10⁸/D-T Neutron/cm³
% INCREASE IN Th(n,γ) REACTION RATE/D-T NEUTRON/cm³
% INCREASE IN Th(n,γ) REACTION RATE/D-T NEUTRON/cm³
Distance Through Fuel Zone (cm)
4.00
3.00
2.00
1.00
10
20
5.0
4.0
3.0
2.0
11.0
10.0
9.0
8.0
7.0
6.0
5.0
A
B

the corresponding value at the beginning of life (clean condition). The largest percentage increase in U-233 production rate occurs at the outer edge of the fuel zone (~ 5.3% after 0.7 yr and ~ 11% after 1.4 yr). The corresponding lowest value occurs at ~ 4 cm through the fuel zone (~ 2.9% after 0.7 yr and 5.8% after 1.4 yr). The net U-233 atoms/cm^3 and the fuel enrichment across the fuel zone after 1.4 yr are shown on Fig. II.3-9 and Fig. II.3-10, respectively. These curves are evaluated with ϕ_0 only and with ϕ_0 and ϕ_1.

An estimate of the errors in the important integrated design parameters after 1.4 years of operation evaluated by using the fresh condition flux, ϕ_0, is given in Table II.3-4 where these parameters are evaluated with ϕ_0 only, then with ϕ_0 and ϕ_1 (the flux after 0.7 yr). From this table one can see that the error obtained, when we use only ϕ_0, is small (~ 2%).

Since the production of tritium increases with time, procedures for retrieving the non-constant production rate of tritium should be taken. Also, a reliable cooling system to remove the increasing heat that is deposited in the blanket, particularly in the fuel zone, should be designed.

II.3.E. Effect of Fuel Assembly Rotation on the Fissile Fuel and Tritium Production

The effect of a mid-life 180^0 fuel assembly rotation on the blanket performance (UBR, TBR, etc.) has been studied for the optimized blanket #13.

First, the fuel zone is divided into 3 subzones and the average value of Th-232 and U-233 atomic densities after 1.4 years was evaluated in these subzones using ϕ_0 and ϕ_1. The flux, ϕ_2, in the blanket (before rotation) is then evaluated using the ANISN code along with the other blanket parameters. These parameters are then re-evaluated but with the fuel assembly being rotated. In the input

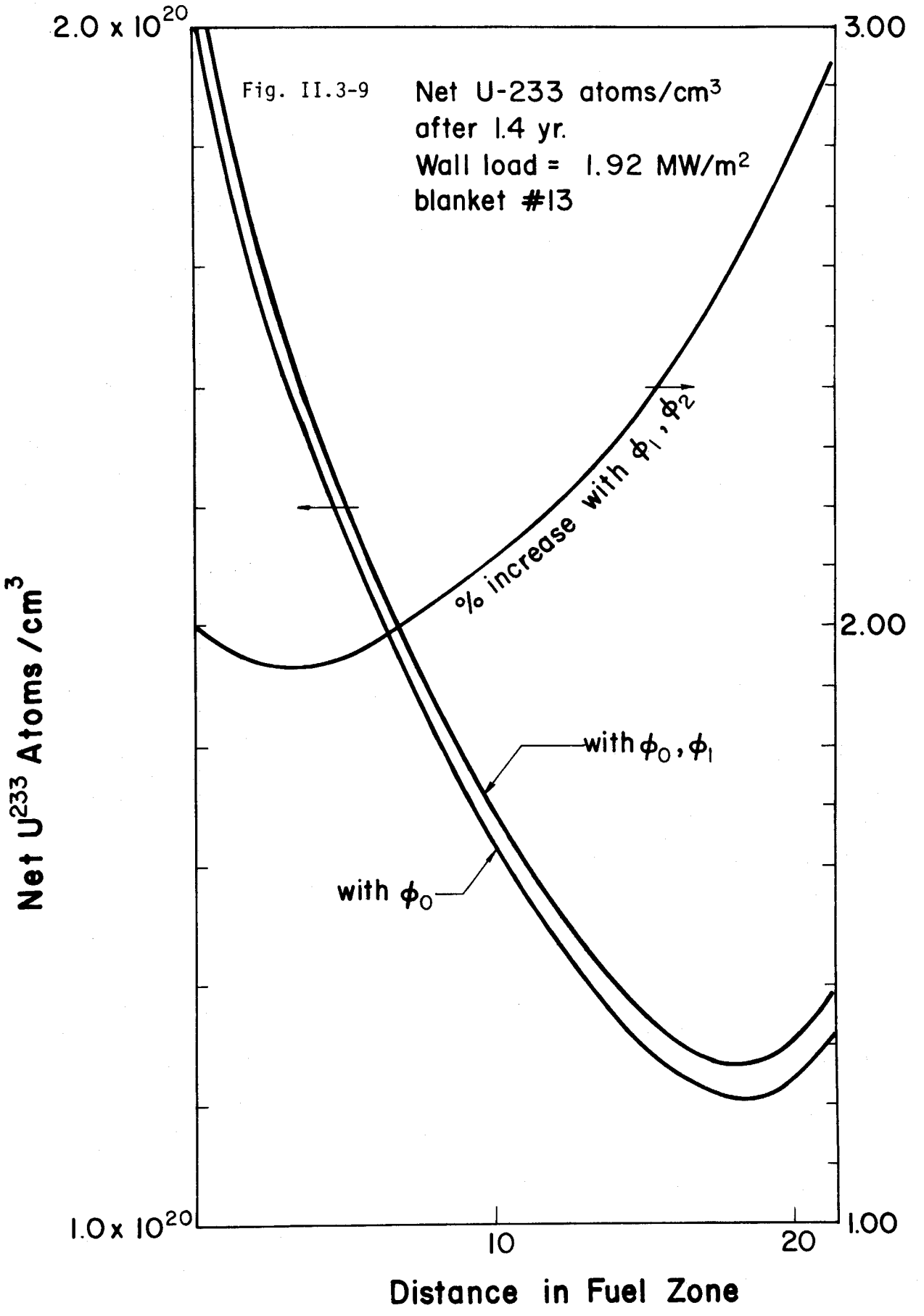
Fig. II.3-9
Net U-233 atoms/cm3
after 1.4 yr.
Wall load = 1.92 MW/m2
blanket #13
2.0 x 10^20
1.0 x 10^20
3.00
2.00
1.00
% increase with φ1, φ2
with φ0, φ1
with φ0
Net U233 Atoms /cm3
% Increase
10
20
Distance in Fuel Zone

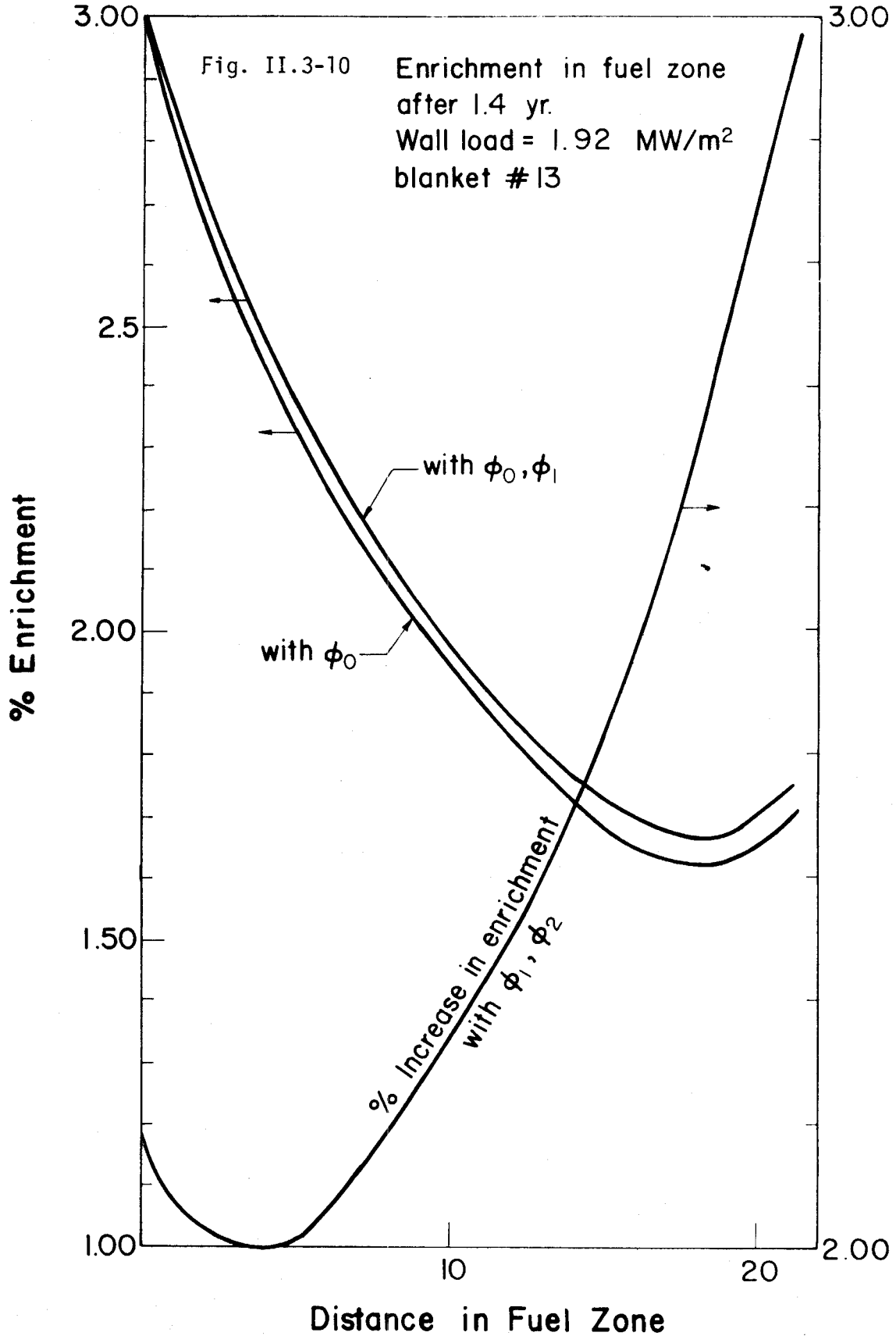
Fig. II.3-10
Enrichment in fuel zone
after 1.4 yr.
Wall load = 1.92 MW/m²
blanket #13
3.00
2.5
2.00
1.50
1.00
% Enrichment
with ϕ_0, ϕ_1
with ϕ_0
% Increase in enrichment
with ϕ_1, ϕ_2
3.00
2.00
% Increase in Enrichment
10
20
Distance in Fuel Zone

Table II.3-4

The Integrated Parameters for Blanket #13 After 1.4 yrs

Parameter	With ϕ_o	With ϕ_o & ϕ_1
Th (kg) x 10^{-5}	1.921	1.920
U-233 Net (kg) x 10^{-3}	3.936	4.022
Enrichment (%)	2.049	2.086
% Change in Th(kg)		-0.05%
% Change in U-233		+2.18%
% Change in Enrichment		+2.2%

to ANISN that is equivalent to replacing the back subzone by the front subzone keeping the middle subzone unchanged. The results are given in Table II.3-5 and the fissile fuel production rates are plotted in Fig. II.3-11 after 1.4 yrs of operation with and without rotation.

As tabulated in Table II.3-5, there is a slight decrease in the fissile fuel and tritium production rates when the fuel assembly is rotated (~0.5% for UBR and ~0.8% for TBR). The conclusion is that these rates will not significantly change upon rotation. Since this is true for operating times of 1.4 yr, it should be true for shorter operating times.

This test analysis enables us to rotate the fuel assembly half-way to the time required to reach a specific overall fuel enrichment (~4%). The fuel assembly is then left in the blanket to reach this enrichment. The resulting fissile fuel distribution will be symmetric.

II.3.F. The Time Needed to Reach 4% Enrichment for the Optimized Blanket

An accurate estimate of the time needed for blanket #13 to reach 4% fuel enrichment, T(4%), is obtained by using the flux in the fresh condition, ϕ_0, the flux after 0.7 yr, ϕ_1, and the flux after 1.4 yr, ϕ_2. The 0.7 yr time-step used is large but sufficient since the fission rate and the buildup of U-233 in the blanket is comparatively low. It should be mentioned that although the neutron flux is recalculated only at the end of each time step (0.7 yr), the Th-232 and U-233 densities are evaluated sequentially at the end of smaller sub-timesteps (1 month).

Two types of approximation were used to evaluate T(4%), the forward difference, F.D. and central difference, C.D., approximation. These approximations are shown schematically on Fig. II.3-12 along with the timestep at which each

Table II.3-5

The Parameters of Blanket #13 After 1.4 Yr of Operation With and Without Rotating the Fuel Assembly.*

Parameter	Fuel Assembly Not Rotated	Fuel Assembly Rotated
UBR $\equiv Th(n,\gamma)$	1.0026	0.9980
$Li^6(n,t)\alpha$	0.6805	0.6750
$Li^7(n,Tn')\alpha$	0.0277	0.0277
TBR (total)	0.7087	0.7027
$Th(n,\nu\sigma_f)$	0.0848	0.0845
Th(n,2n)	0.0622	0.0624
Th(n,3n)x2	0.0370	0.0371
Pb(n,2n)	0.4971	0.4921
$U^{233}(n,\nu\sigma_f)$	0.3048	0.2845

* Values given are per D-T neutron

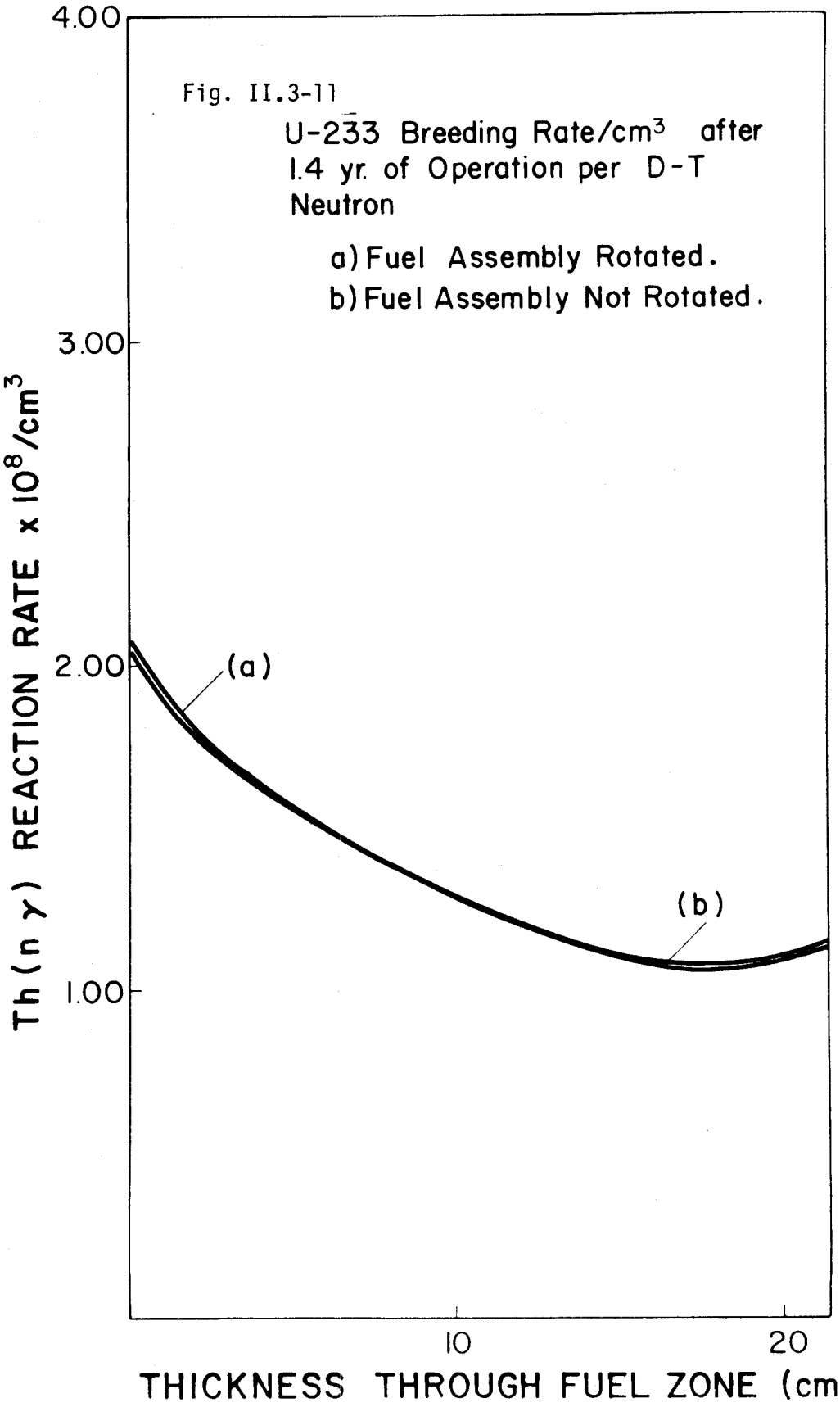

Fig. II.3-11

U-233 Breeding Rate/cm^3 after 1.4 yr. of Operation per D-T Neutron

a) Fuel Assembly Rotated.

b) Fuel Assembly Not Rotated.

Fig. II.3-12 A SCHEMATIC DIAGRAM FOR THE F.D. AND C.D. APPROXIMATION AND THE TIME INTERVAL

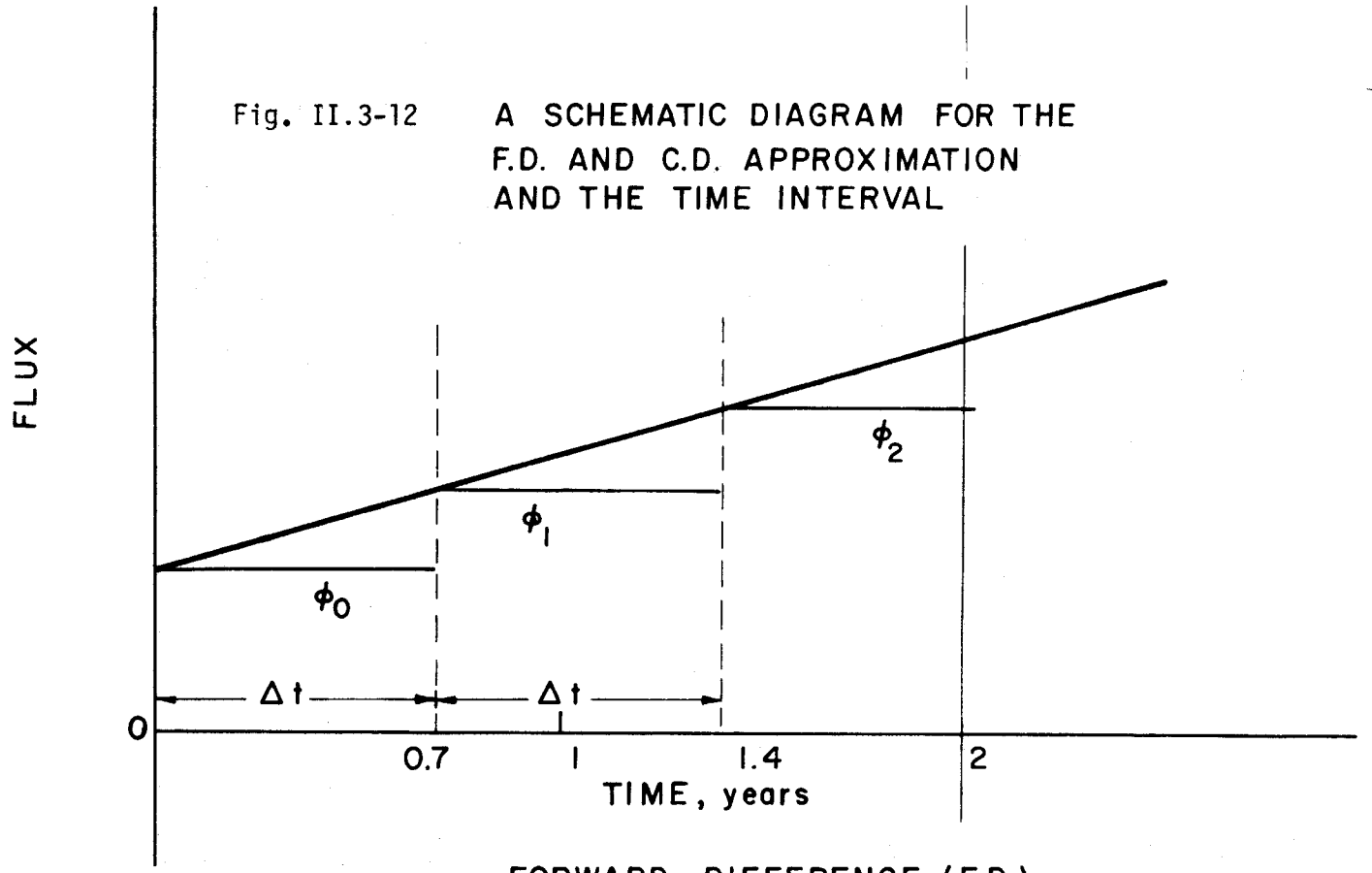

FORWARD DIFFERENCE (F.D.)

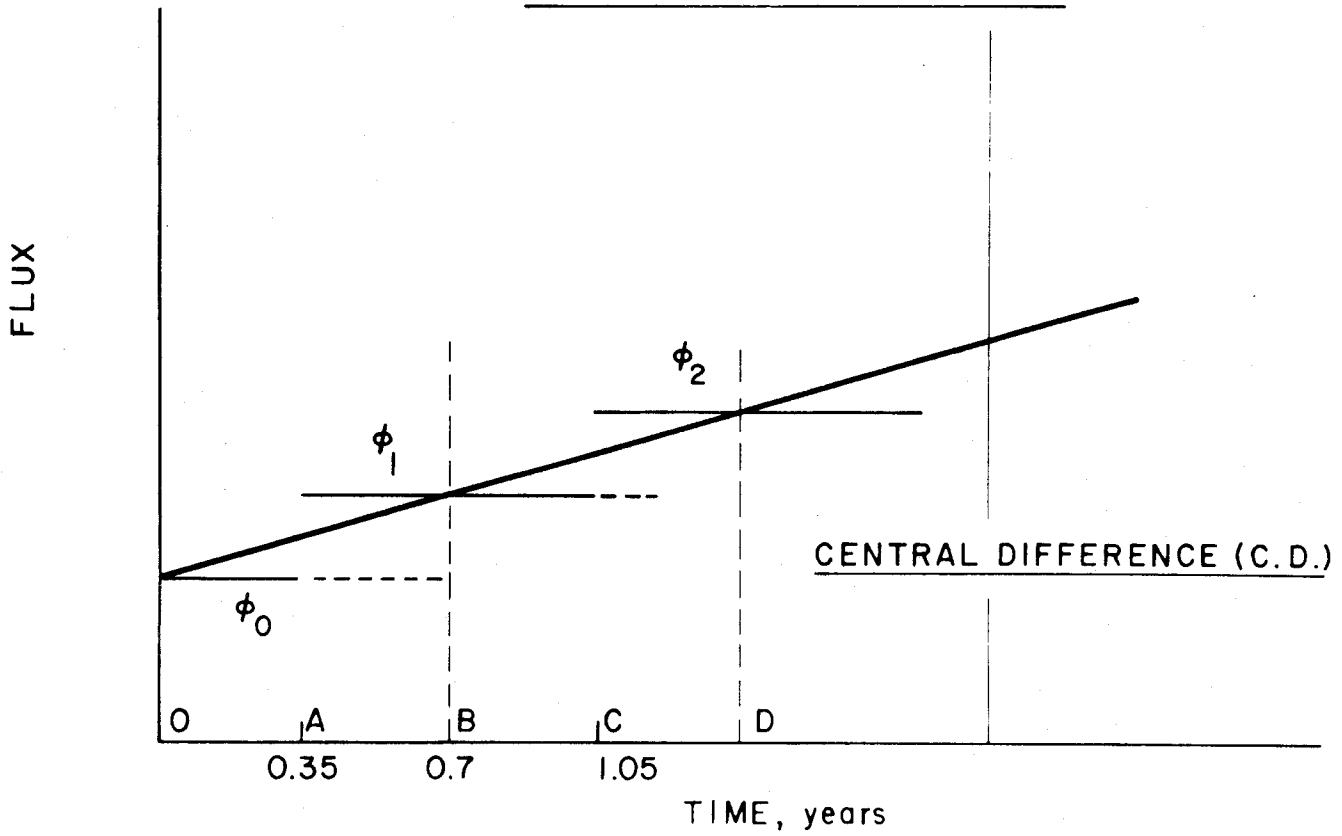

ϕ_o, ϕ_1, and ϕ_2 are assumed to be used in the calculation. The parameters of interest, T(4%), $G_t(T)$, $C_t(T)$, Th(T) and $BU_t(T)$ when blanket #13 reaches 4% enrichment are given in Table II.3-6. Determination of T(4%) used in our rotation scheme was based on using ϕ_o, ϕ_1, and ϕ_2 in the C.D. scheme. This is denoted "approximation #4" in Table II.3-6. The values of the parameters of interest using other approximations are introduced in Table II.3-6 for comparison. These approximations are:

Approximation 1: ϕ_o is used only; Th-232 and U-233 depletion is not considered.

Approximation 2: ϕ_o is used only; Th-232 and U-233 depletion is considered.

Approximation 3: ϕ_o and ϕ_1 are used; Th-232 and U-233 depletion is considered.

Approximation 4: ϕ_o, ϕ_1, and ϕ_2 are used; Th-232 and U-233 depletion is considered.

The values in Table II.3-6 are given for both F.D. and C.D. approximations. From this table we note that allowing for U-233 and Th-232 depeletion increases the value of T(4%). Also, the F.D. approximation overestimates this time.

From Table II.3-6, the time needed to reach 4% enrichment for the optimized blanket is 2.72 yr. The U-233 generated is ~8.66×10^3 kg, the U-233 consumed is ~1.11×10^3 kg, the net U-233 is ~7.56×10^3 kg and the Th-232 left in the blanket is ~1.87×10^5 kg.

The time needed to reach other values of enrichment (using different approximations in the C.D. case) can be obtained from Fig. II.3-13 which illustrates the variation of the enrichment with time. Once notices that this variation is nearly linear.

Table II.3-6

Parameters of Blanket #13 When Reaching 4% Enrichment (Using Different Approximations)
Wall Load 1.92 MW/m^2

Approx. # / Parameter	Th & U Depletion is not Considered	Th & U Depletion is Considered			Type of Approx.
	Appr. 1	Appr. 2	Appr. 3	Appr. 4	
T(4%) (yr)	2.593	2.9136	2.7977	2.7175	C.D.
		2.9136	2.8137	2.7490	F.D.
U-233 Generated (kg) x 10^{-3} $G_t(T)$	7.887	8.654	8.6579	8.6629	C.D.
		"	"	8.6626	F.D.
U-233 Consumed (kg) x 10^{-3} $C_t(T)$	0	1.121	1.1251	1.1052	C.D.
		"	1.1252	1.1302	F.D.
Net U-233 (kg) x 10^{-3}	7.887	7.5331	7.5327	7.5578	C.D.
		7.5331	7.5327	7.5323	F.D.
Th-232 (kg) x 10^{-5} Th(kg)	1.964	1.8751	1.8751	1.8749	C.D.
		"	"	1.8750	F.D.
% Burnup $BU_t(T)$	0	12.96	12.99	12.76	C.D.
		"	"	13.05	F.D.
Enrichment %	4	4	4	4	Both

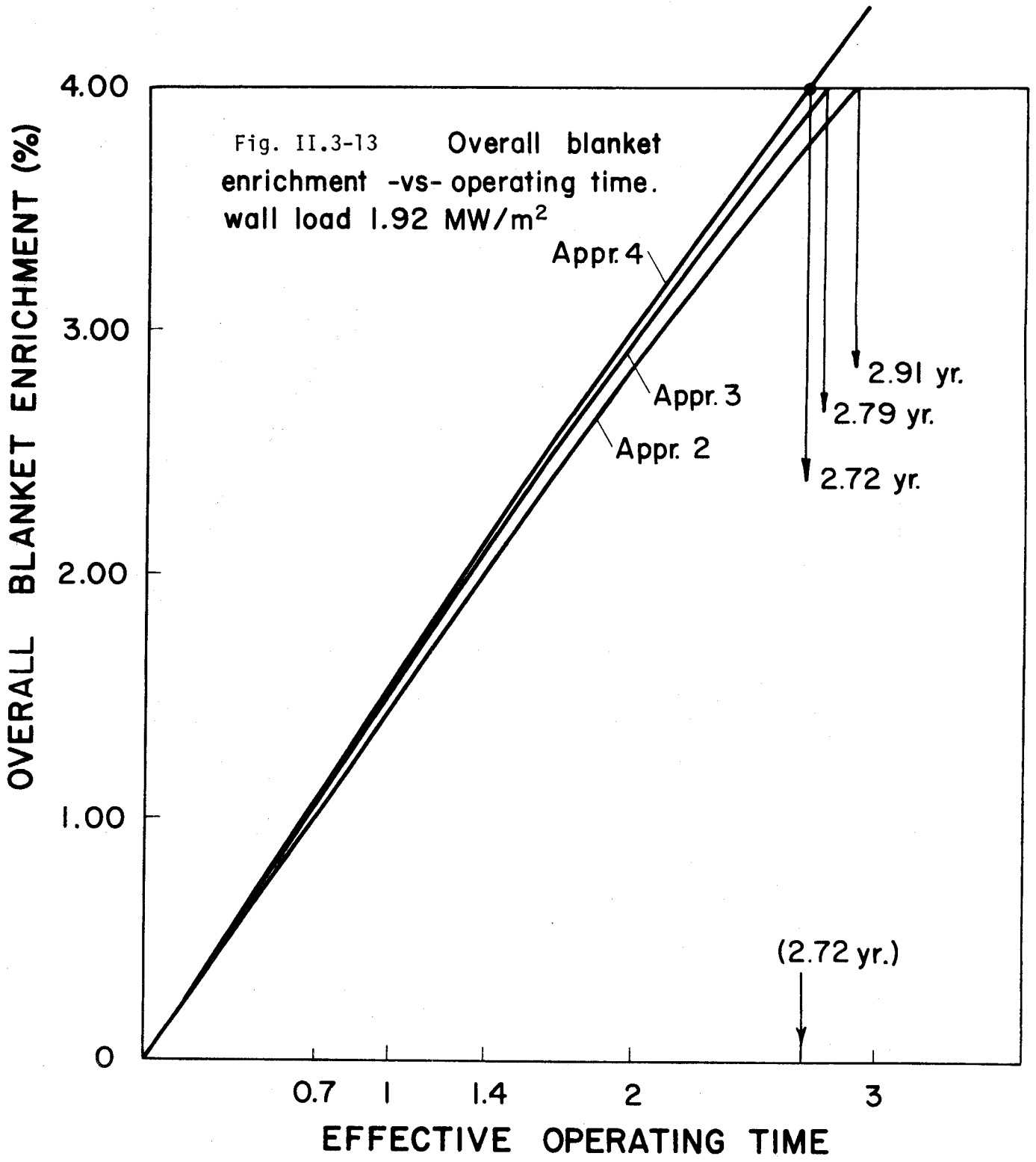

Fig. II.3-13 Overall blanket enrichment -vs- operating time. wall load 1.92 MW/m^2

As expected, approximation 4 gives shorter time to reach a given enrichment compared to other approximations.

II.3.G. Conclusions

The time for the optimized blanket to reach 4% enrichment is calculated to be ~2.72 yr. Accordingly, the 180° rotation is done after ~ 1.4 yr. When the fuel assembly is left in the blanket to complete the 2.72 yr, the distribution of the net U-233 atoms across the fuel assembly will be symmetric. This distribution is shown in Fig. II.3-14 where the net U-233 atom distribution after 2.72 yr without rotation is also shown for comparison. The total Th-232 used in the spherical model of this blanket is ~1.96 x 10^5kg at fresh condition. After 2.72 yr of continuous operation, the Th-232 present is 1.87 x 10^5kg. The net U-233 produced is 7.56 x 10^3 kg. Just 12.7% of the fuel produced is burned up in the hybrid and the overall enrichment is then ~4%. The maximum value of U-233 atomic density across the fuel assembly is 3.1 x 10^{20} atoms/cm^3 (see Fig. II.3-14) and occurs at the fuel assembly's edges. The minimum value, which is at the assembly's center, is 2.47 x 10^{20} atoms/cm^3. The corresponding values of the enrichment are 4.69% and 3.75%, respectively. The maximum to minimum value is 1.26 for both. Further study of the performance of this fuel assembly in a LWR is needed to provide information regarding the heat transfer and the radiation damage level with such an enrichment distribution across the fuel assembly.

We turn now to the final section on neutronics in which multidimensional effects were studied using the Monte Carlo method.

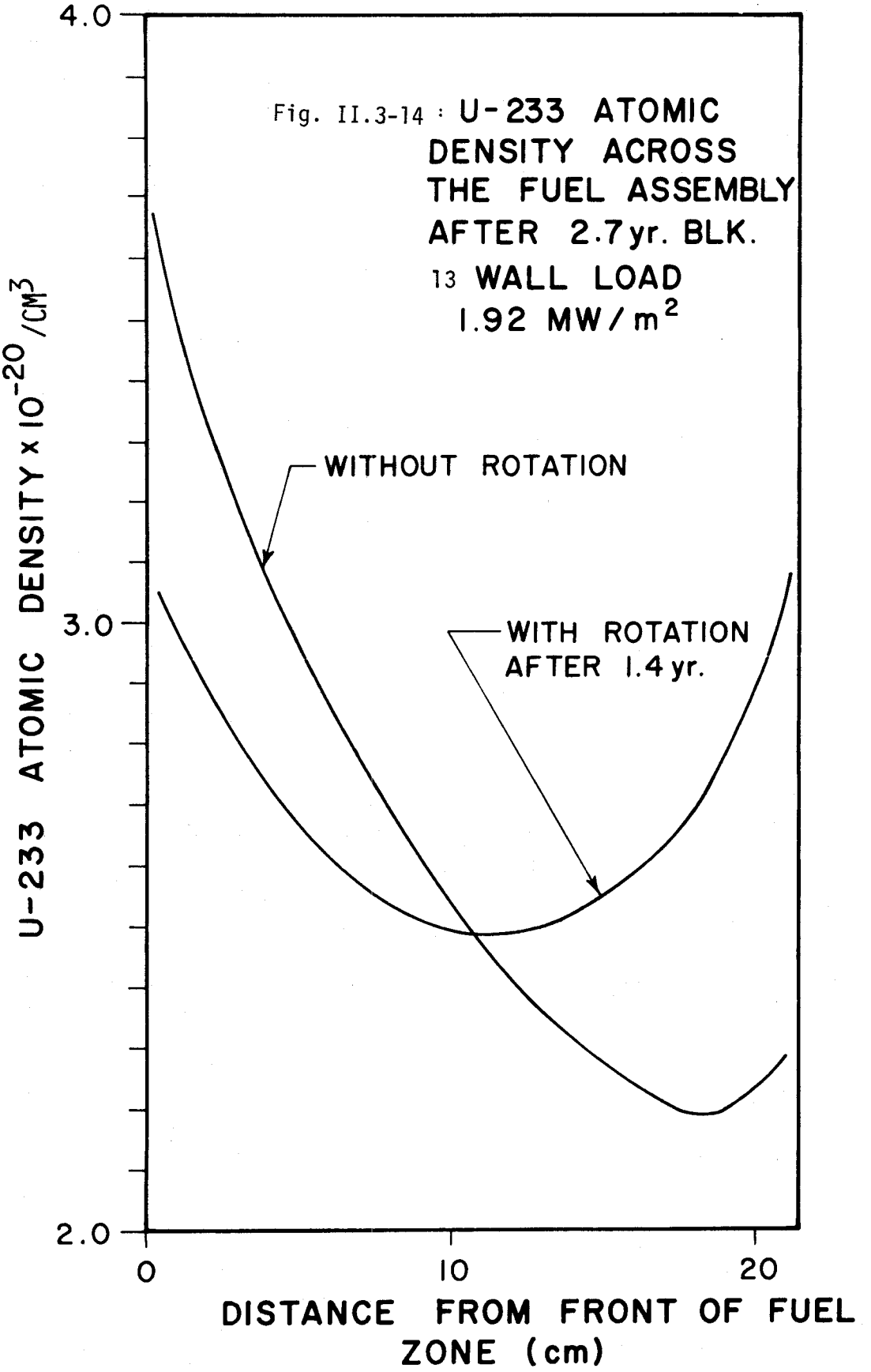

Fig. II.3-14 : U-233 ATOMIC DENSITY ACROSS THE FUEL ASSEMBLY AFTER 2.7 yr. BLK. 13 WALL LOAD 1.92 MW/m^2

References for Section II.3

1. T. R. England, "CINDER - A One Point Depletion and Fission Product Program", WAPH-TM-344, Westinghouse Electric Corp., Pittsburgh, Penn. (1964).

2. M.J. Bell, "ORIGIN - Isotope Generation and Depletion Code", ORNL-4628, Oak Ridge National Laboratory, May (1973).

3. W. W. Engle, Jr., "A User's Manual for ANISN"- RISC-CC-82, Oak Ridge National Lab. (1967).

4. K. R. Schultz, R. H. Brogli, G. R. Hopkins, M. Jonzen, and G. W. Shirley, "A U-233 Fusion-Fission Power System Without Reprocessing", A Preliminary Report, General Atomic GA-A-14635 - UC-Code, Sept. (1977).

5. S. F. Su, G. L. Woodruff, N. J. McCormick, "A High-Gain Fusion-Fission Reactor for Producing U-233", University of Washington, Nucl Tech., Vol. 29, pg. 392, June (1976).

6. A. C. Cook and J. A. Maniscalco, "U-233 Breeding and Neutron Multiplying Blankets for Fusion Reactors", Lawrence Livermore Lab. (LLL), Reprint UCRL-77284, Sept. (1975).

7. J. A. Maniscalco, "A Conceptual Design Study for Laser Fusion Hybrid", LLL Reprint UCRL-78682, Sept. (1976).

8. See the Proceedings US-USSR Symposium on Fusion-Fission Reactors, July (1976).

9. See the Third ANS Topical Meeting on the Technology of Controlled Nuclear Fusion, May 9-11, (1978).

II.4. Three-Dimensional Neutronics Analysis

II.4.A. Scope and Findings

As a complement to the Discrete Ordinates one-dimensional neutronics studies of the last section, a three-dimensional Monte Carlo study of the SOLASE-H Fusion-Fission hybrid reactor was undertaken. A blanket design recommended by the one-dimensional studies was considered for further analysis. This analysis aimed at:

1. The investigation of the asymmetry effects resulting from the actual reactor geometry as a right circular cylinder with a point fusion source at its center. (The one-dimensional studies considered a one-dimensional spherical geometry.)
2. Studying the feasibility of the concept of using a lattice configuration in the radial blanket in view of increasing the breeding densities in the fuel assemblies. This would lead to shorter times to attain specified enrichments and the use of smaller fuel inventories.
3. Increasing the fissile breeding by suitable three-dimensional configurations.

Complete details of the study can be found in Ref. 1. The findings of the study can be summarized as follows:

1. Severe nonuniformities and asymmetries in the spatial distribution of the fissile enrichment axially and radially are detected. Suppression of these nonuniformities is thought to require elaborate blanket spectra shaping and on-power fuel irradiation and management programs.

2. The use of a lattice configuration in the radial blanket with the Light Water Reactor (LWR) ThO_2 fuel assemblies embedded in a Pb matrix, acting as neutron multiplier and moderator, does in fact lead to higher breeding densities in the fuel assemblies. This results in shorter residence times in the fusion reactor to attain average projected enrichments. Fuel inventories in this case are also substantially smaller.
3. Preceding the axial tritium breeding blanket by a Pb neutron multiplier enhances fissile breeding in the radial blanket at the expense of the tritium breeding in the axial blanket. This offers the possibility of controlling the desired ratio of fissile to fusile breeding.

Three basic designs were considered, and the neutron multiplier to fuel volume ratio for the suggested lattice configuration was varied. The time in years to attain an average 4 percent enrichment in the fertile fuel, the estimated fissile production in metric tons, the fissile nuclei production per source neutron, and the tritium yield per source neutron are for a suggested design: 2.27, 2.18 , 0.464, and 1.11, respectively. If a lattice configuration is not used, and the neutron multiplier does not cover the whole inner surface area of the reactor cavity, for a configuration suggested by one-dimensional studies, these numbers are: 4.45, 2.24, 0.479, and 1.12. The former suggested design is also associated with a 50% reduction in the fuel inventory compared to the latter.

In the following sections some details of the calculations are outlined.

II.4.B. Three-Dimensional Parametric Cell Calculations

II.4.B-1. Introduction

The reactor geometry considered is shown in Fig. II.4-1. Three LWR fuel assemblies of 4 m length each are placed on top of each other. They surround as a radial cylindrical blanket the point 14 MeV neutron source resulting from the laser-induced fusion reactions at the center of a cavity of 6 m radius and 12 m height. An axial blanket is placed at the top and bottom of the radial blanket, and is used solely for tritium breeding. A stainless steel structure is used. A 67 v/o C-33 v/o Pb mixture is used as a reflector-shield for both the radial and axial blankets. Pb canned in Zircaloy-2 and cooled by Na is used as the neutron multiplier. Pb was preferred to Be since it does not pose toxicity and availability problems, and leads to a harder spectrum in the blanket. This will reduce the fissioning of the ^{233}U produced by thermal neutrons. In the radial blanket, a Pb zone faces the 14 MeV neutron flux to take advantage of the threshold Pb(n,2n) reaction for the three considered designs I, II and III. In design III, a Pb zone also faces the neutron source in the axial blanket. In the radial blanket, the first Pb layer

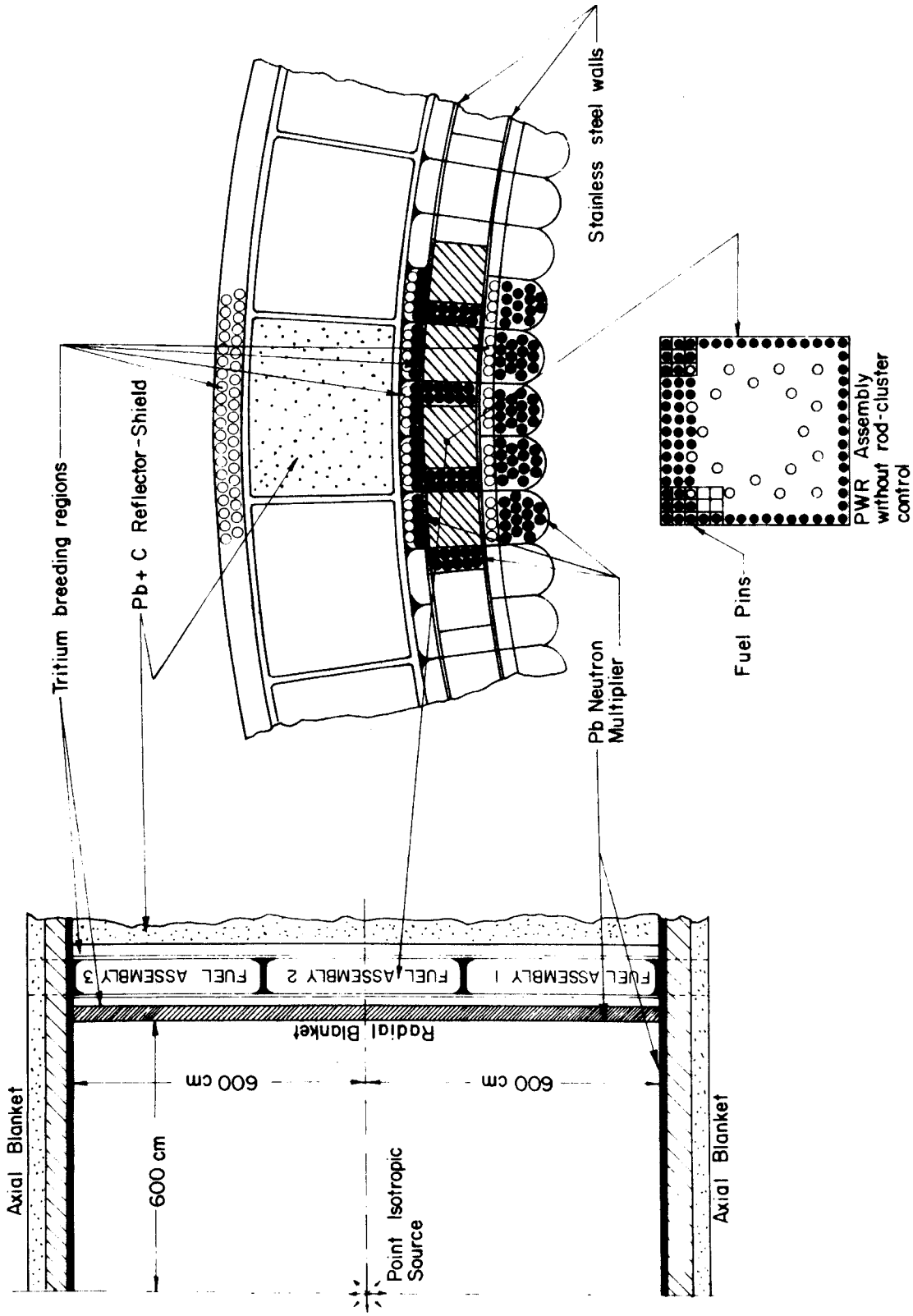
Stainless steel walls
Tritium breeding regions
Pb + C Reflector-Shield
Pb Neutron Multiplier
Fuel Pins
PWR Assembly without rod-cluster control
FUEL ASSEMBLY 3
FUEL ASSEMBLY 2
FUEL ASSEMBLY 1
Radial Blanket
Axial Blanket
600 cm
600 cm
600 cm
Point Isotropic Source
Axial Blanket

Fig. II.4-1

is followed by a thin layer of natural lithium canned in stainless steel, which filters slow neutrons and prevents them from reaching the next zone containing the Zircaloy-2 clad and Na-cooled ThO_2 fuel assemblies. Filtering of the slow neutrons is beneficial for tritium breeding and for avoidance of the fissioning of the bred ^{233}U. Another thin region of Li follows the fissile breeding region to filter the slow neutron flux component returning from the reflector. This filtering has another beneficial effect in that it reduces the formation of the U-233 in the outer layers of the fuel assemblies since the Th-232 (n,γ) U-233 reaction behaves in a 1/v manner. This will otherwise lead to a nonuniform enrichment of the fuel, resulting in turn in nonuniform power generation when the fuel assemblies are later used in a LWR. A third fusile breeding zone follows the reflector in the radial blanket to intercept leaking neutrons, and is followed by the biological shield. In preliminary studies, the fuel assemblies were placed next to each other. This resulted in a rather large fuel inventory, and a long time to attain a specified average enrichment of the irradiated fuel. It was reasoned that since the neutron source in the system is constant, reducing the fertile fuel inventory would lead to higher fissile breeding densities and subsequent shorter times to attain a required fissile enrichment. This could obviously have been achieved by reducing the system size, but this approach was precluded by transient heating of the first wall by the microexplosion. To obtain the necessary fusion power consistent with the understanding of laser fusion physics it was decided that the first wall radius must

be at least 6 m. Because the reactor dimensions were constrained by the fusion parameters, the fuel inventory reduction had to be accomplished by replacing part of the fuel with a material which would scatter the neutrons azimuthally into the fuel assemblies, with minimal absorption, so that the neutron economy would not be affected significantly. Pb was chosen for this purpose, due to its added advantage as a neutron multiplier. It will also not excessively thermalize the spectrum, which is required to avoid excessive fissioning of the bred U-233. A lattice configuration was chosen with the Pb neutron multiplier/moderator surrounding the fuel assemblies as shown in Fig. II.4-1. In Design I the fuel zone is followed by a Li zone preceding the reflector in the radial blanket, whereas in Designs II and III this Li zone is preceded by a Pb zone. A three-dimensional study was needed to investigate the suggested concept of a lattice configuration, which is not conveniently described by either one or two-dimensional models. Moreover, in a related study of a magnetically-protected first wall laser driven reactor, Ragheb, Cheng, and Conn[2] reported severe asymmetry effects in the axial direction caused by the source-reactor geometry, and the magnitude of this effect needed to be studied. Inhomogenities in fissile production are detected in the axial and radial directions. The suggested lattice configuration achieves its intended purpose of increased breeding densities and results in shorter

enrichment times. A parametric study is carried out with respect to v_m/v_f, the multiplier-moderator to fuel volume ratio in the breeding region. The calculational models used in the investigation are described in the next subsections.

II.4.B-2. The Monte Carlo Calculational and Geometric Models

The total 14 MeV neutron power of 868 MW corresponds to an isotropic neutron source at the center of the reactor cavity of 3.85×10^{20} source neutrons/second.

Due to symmetry, only the upper part of the reactor is considered. This upper part is now divided into three regions of 200 cm each in the axial direction denoted as: central part of radial blanket, middle part of radial blanket, and upper part of radial blanket. Each part is then divided into several radial regions. For the cell calculations, "pie-slice" configurations were considered corresponding to different multiplier-moderator to fuel volume ratios, as shown in Figs. II.4-2 and II.4-3. Radially, each axial region is divided into several regions: a Pb multiplier zone (10 cm) followed by a tritium breeding zone (1.5 cm), then by a fissile breeding zone (21.4 cm). The fissile breeding zone is enclosed within two 0.5 cm thick stainless steel walls. Adjacent to the fuel zone is the neutron multiplier/moderator zone. Different v_m/v_f ratios correspond to different azimuthal angles for the "pie-slice". Values of v_m/v_f = 0, 0.5, and 1 correspond to azimuthal angles for the unit cell of 1.0^o, 1.5^o, and 2^o, respectively.

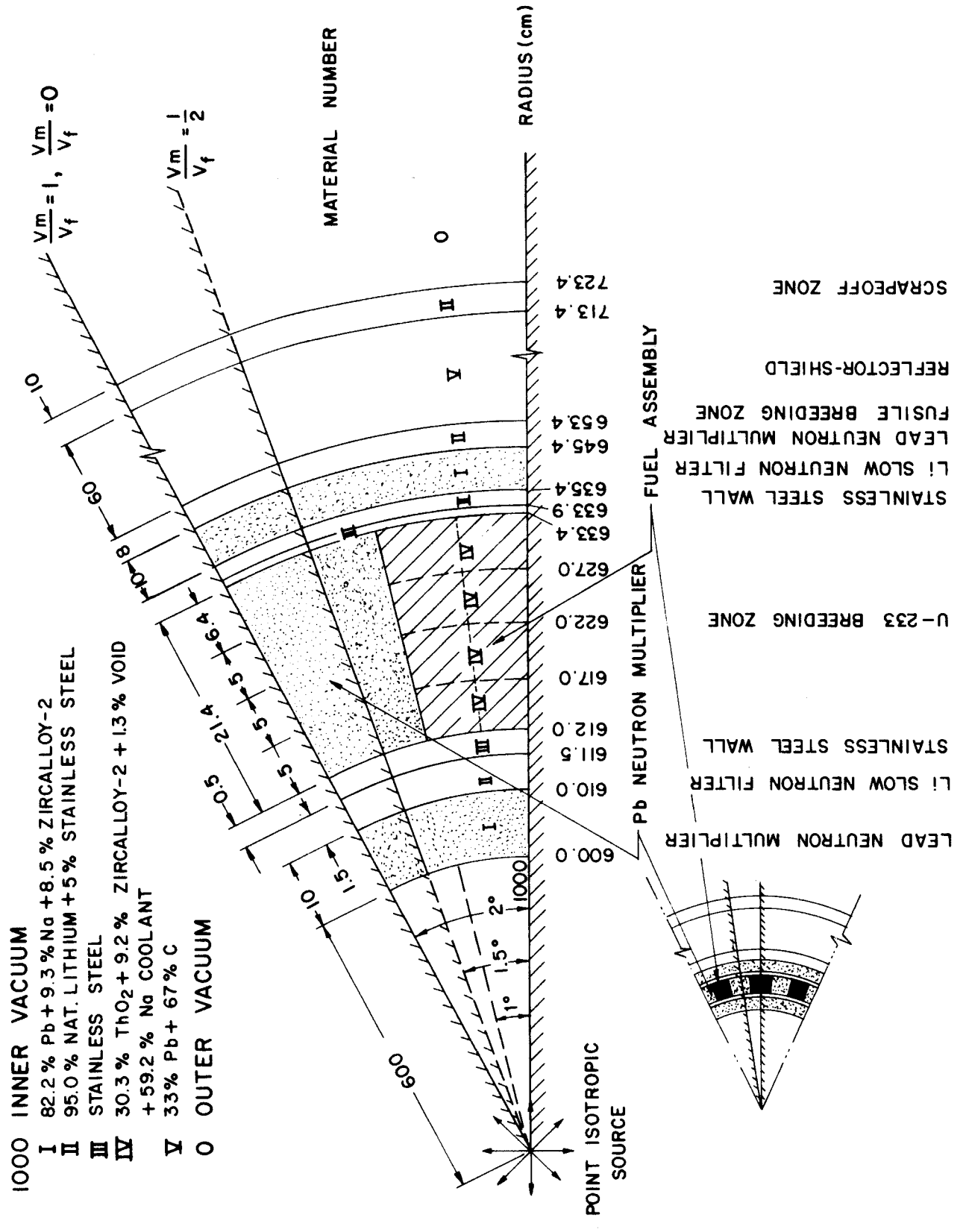
MATERIAL COMPOSITION
1000 INNER VACUUM
I 82.2 % Pb + 9.3 % Na + 8.5 % ZIRCALLOY-2
II 95.0 % NAT. LITHIUM + 5 % STAINLESS STEEL
III STAINLESS STEEL
IV 30.3 % ThO2 + 9.2 % ZIRCALLOY-2 + 1.3 % VOID + 59.2 % Na COOLANT
V 33% Pb + 67% C
0 OUTER VACUUM
MATERIAL NUMBER
RADIUS (cm)
Vm/Vf = 1, Vm/Vf = 0
Vm/Vf = 1/2
SCRAPEOFF ZONE
REFLECTOR-SHIELD
FUSILE BREEDING ZONE
LEAD NEUTRON MULTIPLIER
Li SLOW NEUTRON FILTER
STAINLESS STEEL WALL
FUEL ASSEMBLY
U-233 BREEDING ZONE
Pb NEUTRON MULTIPLIER
Li SLOW NEUTRON FILTER
STAINLESS STEEL WALL
LEAD NEUTRON MULTIPLIER
POINT ISOTROPIC SOURCE
723.4
713.4
653.4
645.4
635.4
633.9
633.4
627.0
622.0
617.0
612.0
611.5
610.0
600.0
1000
2°
1.5°
1°
10
60
8
0.4
21.4
5
5
5
0.5
1.5
10
600

Fig. II.4-2

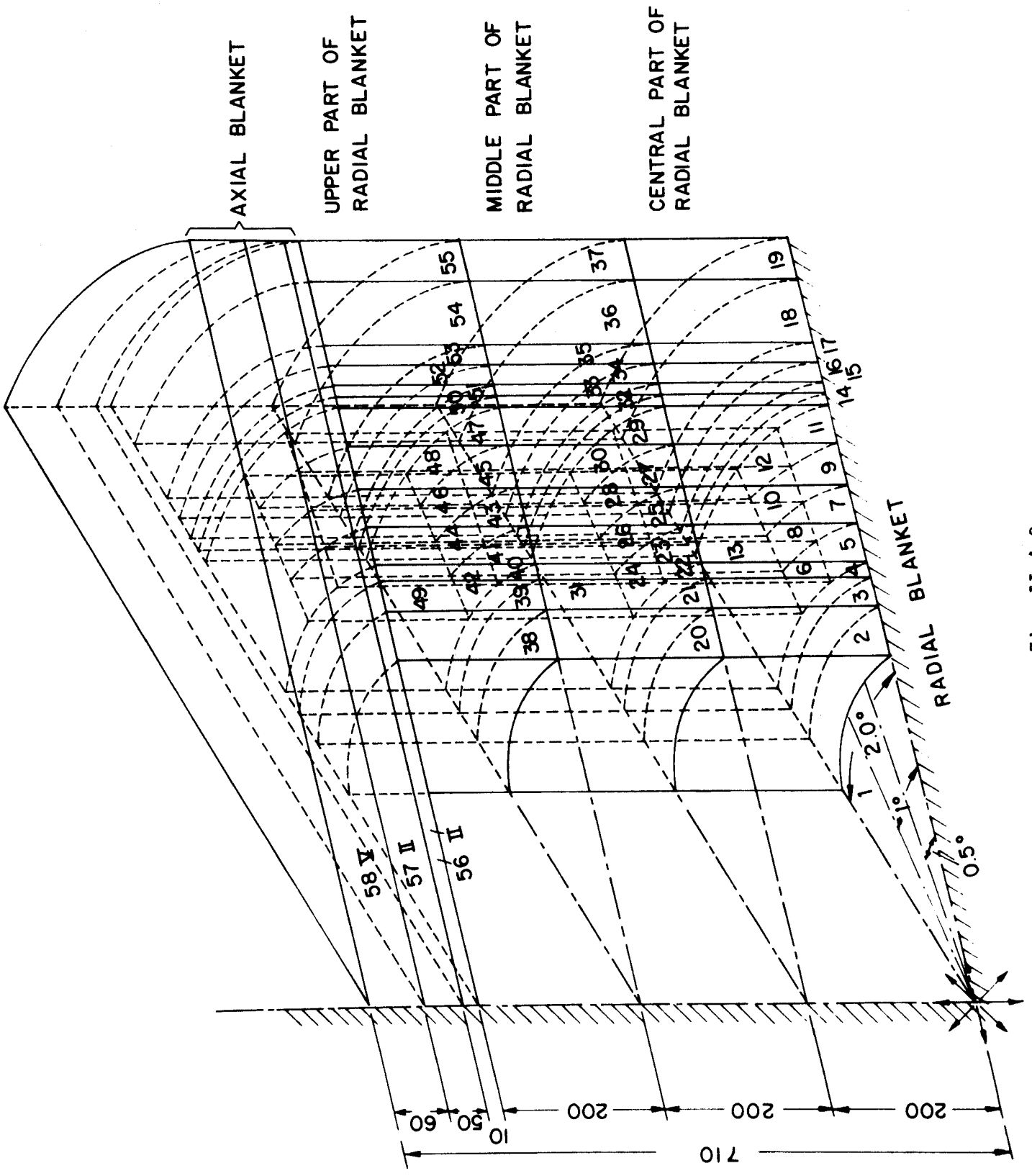
AXIAL BLANKET
UPPER PART OF RADIAL BLANKET
MIDDLE PART OF RADIAL BLANKET
CENTRAL PART OF RADIAL BLANKET
RADIAL BLANKET
2.0°
1°
0.5°
58 VI
57 II
56 II
60
50
10
200
200
200
710

Fig. II.4-3

Notice that the views in Figs. II.4-2 and II.4-3 represent half a unit cell because of the azimuthal symmetry of the unit cells. In Design I the fissile breeding zone is followed by an 8 cm thick tritium breeding zone, then by the reflector and a final Li zone. Designs II and III differ from Design I in the inclusion of a 1.5 cm Li filtering zone followed by a 10 cm thick Pb neutron multiplying zone before an 8 cm tritium breeding zone directly preceding the reflector. To investigate the radial distribution of the quantities of interest, the fissile breeding zone was subdivided into 4 radial regions of 5,5,5 and 6.4 cm, respectively. In Design III the axial blanket is composed of a 10 cm Pb neutron multiplying zone, followed by a 50 cm natural Li blanket and a 60 cm reflector. In Designs I and II, no axial Pb multiplier zone was used. Instead, a 60 cm thick blanket followed by a 60 cm reflector were used.

The MORSE Monte Carlo code[4,5] was used in the calculations. However, the RSIC-communicated version does not treat external source-driven multiplying media. Modifications for treating the slowing down of the 14 MeV fusion neutrons in multiplying media with statistical weighting were implemented. Details of the methodology adopted is reported elsewhere.[3]

II.4.B-3. Material Compositions and Cross Section Data

The material compositions considered and the corresponding nuclei densities are shown in Table II.4-1. For the fuel assemblies, these

Table II.4-1 Elemental Compositions of Material Mixes

Material Composition	Elements	Nuclei Densities Nuclei/(barn.cm)
Neutron Multiplication Zones 82.2 v/o Pb + 9.3 v/o Na + 8.5 v/o Zircaloy-2	Ni Cr Fe Pb Na Zr Sn	.18314-5 .32965-5 .43953-5 .25345-1 .23657-2 .35983-2 .54941-4
Fusile Breeding Zones 95 v/o Natural Lithium + 5 v/o Stainless Steel	Ni Cr Fe Li-6 Li-7	.46900-3 .72500-3 .30705-2 .31514-2 .39321-1
Stainless Steel Structure	Ni Cr Fe	.93800-2 .14500-1 .61400-1
Fissile Breeding Zones 30.3 v/o ThO_2 + 9.2 v/o Zircaloy-2 +1.3 v/o Void + 59.2 v/o Na Coolant	Ni Cr Fe O Na Zr Sn Th	.19929-5 .35872-5 .47829-5 .13871-1 .15032-1 .39156-2 .59786-4 .69353-2
Reflector-Shield 33 v/o Pb + 67 v/o C	C Pb	.53487-1 .11161-1

correspond to a standard PWR assembly with an array of 17 x 17 fuel pins, and 21.4 cm side-length. Each assembly contains 264 fuel elements of 0.9498 cm outer diameter and a 1.25 cm square pitch. The cladding is Zircaloy-2 of 0.0572 cm thickness. Fuel pellet diameters are thus 0.819 cm. Twenty-five locations for the control rod clusters used in a LWR are present, but are not used. The fuel breeding zone consists of a single row of fuel assemblies interspersed with regions of Pb neutron multiplier/moderator. To provide efficient cooling, both the neutron multiplying and the fissile breeding zones are cooled with Na, but will be water-cooled when used in a LWR. In the tritium breeding zone natural lithium was used and leads to an acceptable breeding ratio. Higher breeding values can be obtained by using a higher Li-density material such as Li_2O, or by slightly enriching the Li in the ^6Li isotope. The reflector is a mixture of Pb and C to act as a primary gamma shield on the one hand, and to slow down the leaking fast neutrons by inelastic scattering reactions on the other.

The transport cross-sections were taken from the coupled 100 n-21 γ group cross section library prepared for EPR calculations by Plaster, Santoro, Roussin, and Ford III[6,7] and designated as DLC-37B by the Radiation Shielding Information Center.[8] These were computed from the ENDF/B-IV data file.

Reaction cross sections were used as group collapsed data from the work of Abdou and Roussin.[10] A 25-group neutron structure was used.

Results of computations are discussed in the next section.

II.4.C. Discussion of Results

II.4.C-1. Fissile and Tritium Breeding

Tables II.4-2, II.4-3, and II.4-4 show a summary for the tritium and ^{233}U breeding in Designs I, II and III, respectively. It should be remembered that Designs II and III have a Pb zone between the fissile breeding zone and the reflector, so that the fertile fuel is surrounded by Pb in a flux trap, whereas Design I has only a tritium breeding zone at this location. A Pb multiplier zone also precedes the axial blanket in Design III. For the cases where the suggested lattice configuration is not used ($v_m/v_f = 0$) one obtains a Th(n,γ) reaction per source neutron of 0.479, 0.504 and 0.613 for Designs I, II and III, respectively. The corresponding tritium productions per source neutron are 1.12, 1.09 and 0.945. Lattice configurations for $v_m/v_f = 0$, 0.5, 1 were investigated for the three designs. The tritium breeding increases for higher values of v_m/v_f, whereas the fissile breeding goes down. The decrease in Design III is slower than in Design I. In the last column of Tables II.4-2, II.4-3, and II.4-4, the sum of the tritium and ^{233}U breeding seems to remain almost constant for each design. In all cases the axial blanket contributes more to the tritium production than the radial blanket, mostly from reactions with Li-6. The addition of the 10 cm Pb zone before the reflector in Design III improved the fissile breeding in the radial blanket substantially and is recommended as a design feature.

Table II.4-2 Breeding in Hybrid Reactor Blanket as a Function of v_m/v_f (Nuclei/Source Neutron) Design I

v_m/v_f	Th(n,γ)	T6+		T7		T6 + T7 Axial and Radial Blankets	T6 + T7 + Th(n,γ)
		Radial Blanket	Axial Blanket	Radial Blanket	Axial Blanket		
0	4.79-1±1.15-2	3.20-1±1.13-2	5.82-1±1.06-2	2.44-2±2.62-3	1.94-1±8.05-3	1.12+0±1.77-2	1.60+0±2.11-2
1/2	3.93-1±7.99-3	3.80-1±1.39-2	6.26-1±1.29-2	1.79-2±1.89-3	1.96-1±7.50-3	1.22+0±2.05-2	1.61+0±2.20-2
1	3.40-1±7.85-3	4.22-1±1.58-2	6.29-1±1.62-2	2.04-2±2.49-3	2.06-1±6.22-3	1.28+0±2.36-2	1.62+0±2.49-2

+T6 and T7 are tritium yields from reactions with ^6Li and ^7Li, respectively

Table II.4-3 Breeding in Hybrid Reactor Blanket as a Function of v_m/v_f (Nuclei/Source Neutron) Design II

v_m/v_f	Th(n,γ)	T6+		T7		T6 + T7 Axial and Radial Blanket	T6 + T7 + Th(n,γ)
		Radial Blanket	Axial Blanket	Radial Blanket	Axial Blanket		
0	5.04-1±1.24-2	3.18-1±1.23-2	5.74-1±1.19-2	1.96-2±2.15-3	1.80-1±7.48-3	1.09+0±1.88-2	1.59+0±2.25-2
1/2	4.23-1±8.32-3	3.45-1±1.18-2	6.45-1±1.10-2	1.11-2±1.34-3	1.90-1±9.76-3	1.19+0±1.89-2	1.61+0±2.07-2
1	3.56-1±7.29-3	3.90-1±1.35-2	6.35-1±1.08-2	1.60-2±1.70-3	1.94-1±7.14-3	1.24+0±1.88-2	1.60+0±2.02-2

+ T6 and T7 are tritium yields from reactions with ^6Li and ^7Li, respectively

Table II.4-4 Breeding in Hybrid Blanket as a Function of v_m/v_f (Nuclei/Source Neutron) Design III

v_m/v_f	Th(n,γ)	T6+		T7		T6 + T7 Axial and Radial Blanket	T6 + T7 + Th(n,γ)
		Radial Blanket	Axial Blanket	Radial Blanket	Axial Blanket		
0	6.13-1±1.53-2	3.29-1±1.26-2	5.37-1±2.00-2	1.17-2±1.51-3	6.73-2±6.26-3	9.45-1±2.45-2	1.56+0±2.89-2
1/2	5.31-1±9.31-3	4.10-1±1.33-2	5.63-1±1.16-2	1.59-2±2.07-3	7.15-2±6.48-3	1.06+0±1.89-2	1.59+0±2.11-2
1	4.64-1±8.58-3	4.81-1±1.55-2	5.45-1±1.53-2	1.34-2±1.77-3	7.02-2±5.31-3	1.11+0±2.25-2	1.57+0±2.41-2

+ T6 and T7 are tritium yields from reactions with ^{6}Li and ^{7}Li, respectively

However, the addition of the neutron multiplying zone in Design III in front of the axial blanket did not help in increasing the tritium breeding in the axial blanket. As a matter of fact, it decreases the breeding from the ^{7}Li isotope.

The results show that the tritium breeding in the axial blanket is a function of the v_m/v_f ratio in the radial blanket. Thus, the two blankets are closely coupled neutronically. One-dimensional models using simple solid angle weightings must therefore be used with caution when drawing final conclusions about such 3-dimensional problems.

Tables II.4-5, II.4-6, and II.4-7 display the breeding densities of tritium and ^{233}U fuel production, defined as:

$$\text{Breeding Density} = \frac{\text{Number of fusile or fissile nuclei produced per 14.0 MeV source particle}}{\text{Total volume of breeding zone in cm}^3} .$$

These values have a one-to-one correspondence to those in Tables II.4-2, II.4-3, and II.4-4. The fissile breeding densities increase with increasing values of v_m/v_f. The increase is much more pronounced in Design III than in Designs I and II. Note that increased values of the breeding densities mean shorter times to attain a required average fuel enrichment, using a smaller fertile inventory. This is the major merit of using a Pb multiplier in front of the axial blanket and a lattice configuration in which Pb surrounds the fertile fuel. In the next section we investigate the spatial distribution of fissile production.

Table II.4-5 Average Breeding Densities in Hybrid Reactor Blanket as a Function of v_m/v_f (Nuclei/Source Neutron-cm^3 of Breeding Zone) Design I

v_m/v_f	Th(n,γ)	$^6Li(n,\alpha)T$		$^7Li(n,n'\alpha)T$		Total Tritium Production Density
		Radial Blanket	Axial Blanket	Radial Blanket	Axial Blanket	
0	4.77-9	3.19-9	2.95-9	2.44-10	9.83-10	3.76-9
1/2	5.87-9	3.89-9	3.17-9	1.79-10	9.93-10	4.10-9
1	6.77-9	4.21-9	3.19-9	2.04-10	1.04-09	4.30-9

Table II.4-6 Average Breeding Densities in Hybrid Reactor Blanket as a Function of v_m/v_f (Nuclei/Source Neutron-cm^3 of Breeding Zone) Design II

v_m/v_f	Th(n,γ)	$^6Li(n,\alpha)T$		$^7Li(n,n'\alpha)T$		Total Tritium Production Density
		Radial Blanket	Axial Blanket	Radial Blanket	Axial Blanket	
0	5.01-9	2.96-9	3.49-9	1.82-10	1.09-9	4.01-9
1/2	6.32-9	3.21-9	3.92-9	1.03-10	1.16-9	4.83-9
1	7.08-9	3.63-9	3.86-9	1.49-10	1.18-9	4.56-9

Table II.4-7 Average Breeding Densities in Hybrid Reactor Blanket as a Function of v_m/v_f (Nuclei/Source Neutron - cm^3 of Breeding Zone) Design III

v_m/v_f	Th(n,γ)	$^6Li(n,\alpha)T$		$^7Li(n,n'\alpha)T$		Total Tritium Production Density
		Radial Blanket	Axial Blanket	Radial Blanket	Axial Blanket	
0	6.10-9	3.06-9	3.27-9	1.09-10	4.09-10	3.48-9
1/2	7.93-9	3.82-9	3.42-9	1.48-10	4.35-10	3.90-9
1	9.23-9	4.48-9	3.32-9	1.25-10	4.27-10	4.08-9

II.4.C-2. Spatial Distribution of Fissile Fuel Production

Spatial nonuniformities in the fissile fuel production are detected in all cases. Figs. II.4-4, II.4-5, and II.4-6 show the distribution of fuel production per source neutron in the fuel assemblies both radially and axially for Designs I, II and III. These figures reveal that the $Th(n,\gamma)$ reaction rate per source neutron is largest near the front edge of the fuel assemblies facing the plasma, especially around the center of the reactor cavity. For the three designs considered, increased values of v_m/v_f lead to higher breeding densities. This will result in metallurgical and heat transfer problems when operated in the LWRs, resulting in uneven burnup of the fuel. However, the bred ^{233}U in the outer layers of the assemblies will also be burned in situ faster than the inner layers. Thus, these two balancing effects will tend to cancel each other, and no general conclusions can be drawn without further three-dimensional burnup studies both in the hybrid reactor and the LWRs. In the axial direction, the peaking at the edges of the fuel assemblies is still present. This effect is caused by the geometry of the reactor as a cylinder with a point source at its center leading to different effective optical thicknesses to be seen by the neutrons moving axially away from the center. It seems that an elaborate spectral tailoring by changing the effective optical thicknesses of the blanket regions moving axially is needed, coupled to an irradiation and fuel management program. This will depend on the degree of uniformity required by the LWR.

DESIGN I

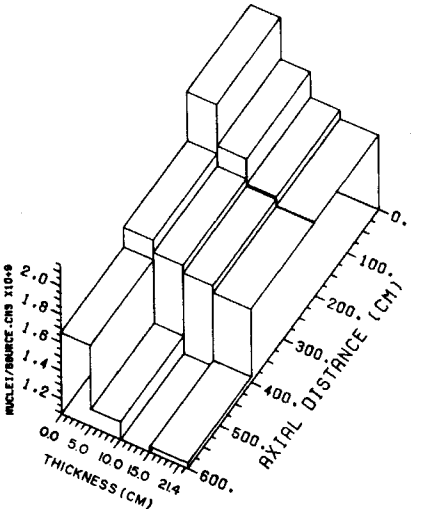

FISSILE PRODUCTION DENSITY IN FUEL ASSEMBLIES VM/VF=0.0

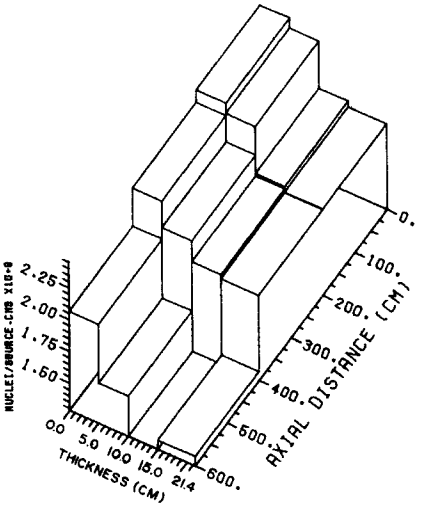

FISSILE PRODUCTION DENSITY IN FUEL ASSEMBLIES VM/VF=0.5

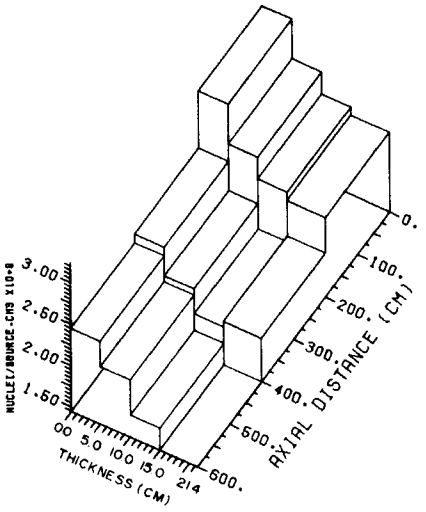

FISSILE PRODUCTION DENSITY IN FUEL ASSEMBLIES VM/VF=1.0

Fig. II.4-4

DESIGN II

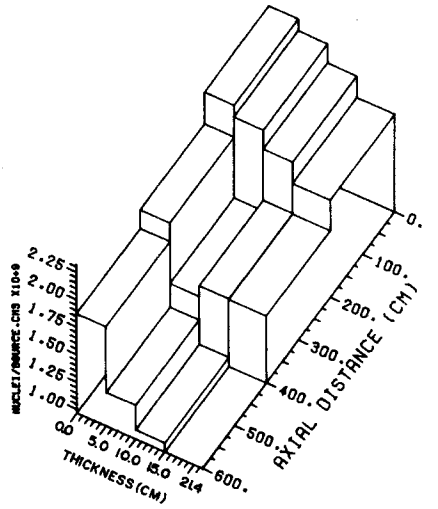

FISSILE PRODUCTION DENSITY IN FUEL ASSEMBLIES VM/VF=0.0

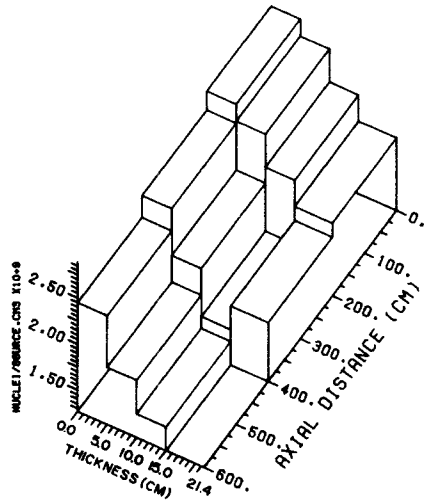

FISSILE PRODUCTION DENSITY IN FUEL ASSEMBLIES VM/VF=0.5

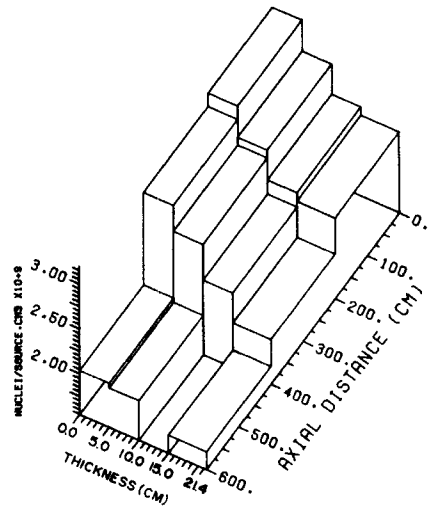

FISSILE PRODUCTION DENSITY IN FUEL ASSEMBLIES VM/VF=1.0

Fig. II.4-5

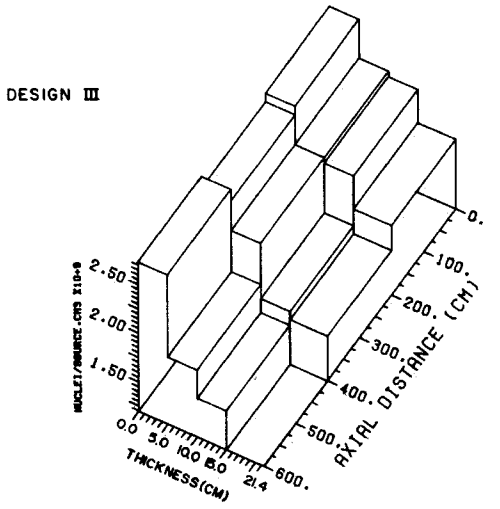

FISSILE PRODUCTION DENSITY IN FUEL ASSEMBLIES VM/VF=0.0

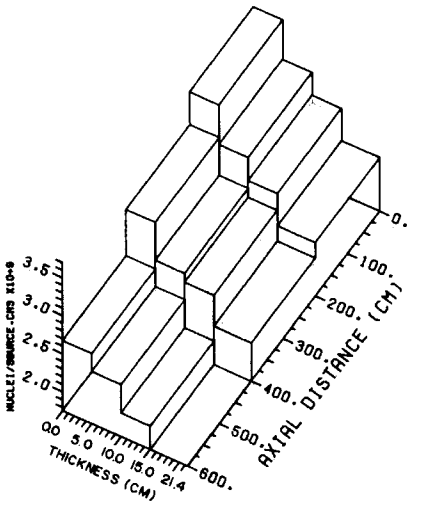

FISSILE PRODUCTION DENSITY IN FUEL ASSEMBLIES VM/VF=0.5

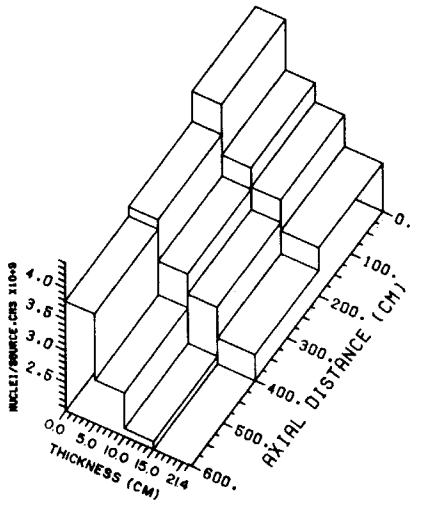

FISSILE PRODUCTION DENSITY IN FUEL ASSEMBLIES VM/VF=1.0

Fig. II.4-6

In some cases peaking occurs both at the reflector and plasma sides of the fuel assemblies. In the one-dimensional studies, reduction in the nonuniformity is achieved by use of Li zones around the fissile breeding zone. This does not help the axial distribution and the azimuthal and axial tailoring of the flux trap has not been carried out here.

Fig. II.4-7 shows that whereas the fissile breeding decreased as v_m/v_f increased, the tritium breeding increased, so that the two reactions are competing and one is increased or decreased at the expense of the other. Fig. II.4-8 shows the effect of the lattice configuration in increasing the breeding densities and, consequently, the time to attain a given enrichment, as shown in the next section.

II.4.C-3. Effect of Lattice Configuration on Fissile Production Rate

In Table II.4-8 we show the yearly ^{233}U production for Designs I, II and III for different values of v_m/v_f.

The fissile fuel production per year has been calculated from the relationship:

$$K\left(\frac{v_m}{v_f}\right) = U\left(\frac{v_m}{v_f}\right) \cdot S_n \cdot \frac{M_f}{A_v} \cdot Y\left(\frac{g}{year}\right) \qquad (1)$$

where: $U(\frac{v_m}{v_f})$ is the fissile nuclei yield per source neutron,

S_n is the 14 MeV neutron source $\left(4.005 \times 10^{20} \frac{neutrons}{sec}\right)$,

A_v is Avogadro's number,

M_f is the atomic weight of the fissionable nuclide, M_f (^{233}U) = 233.0396,

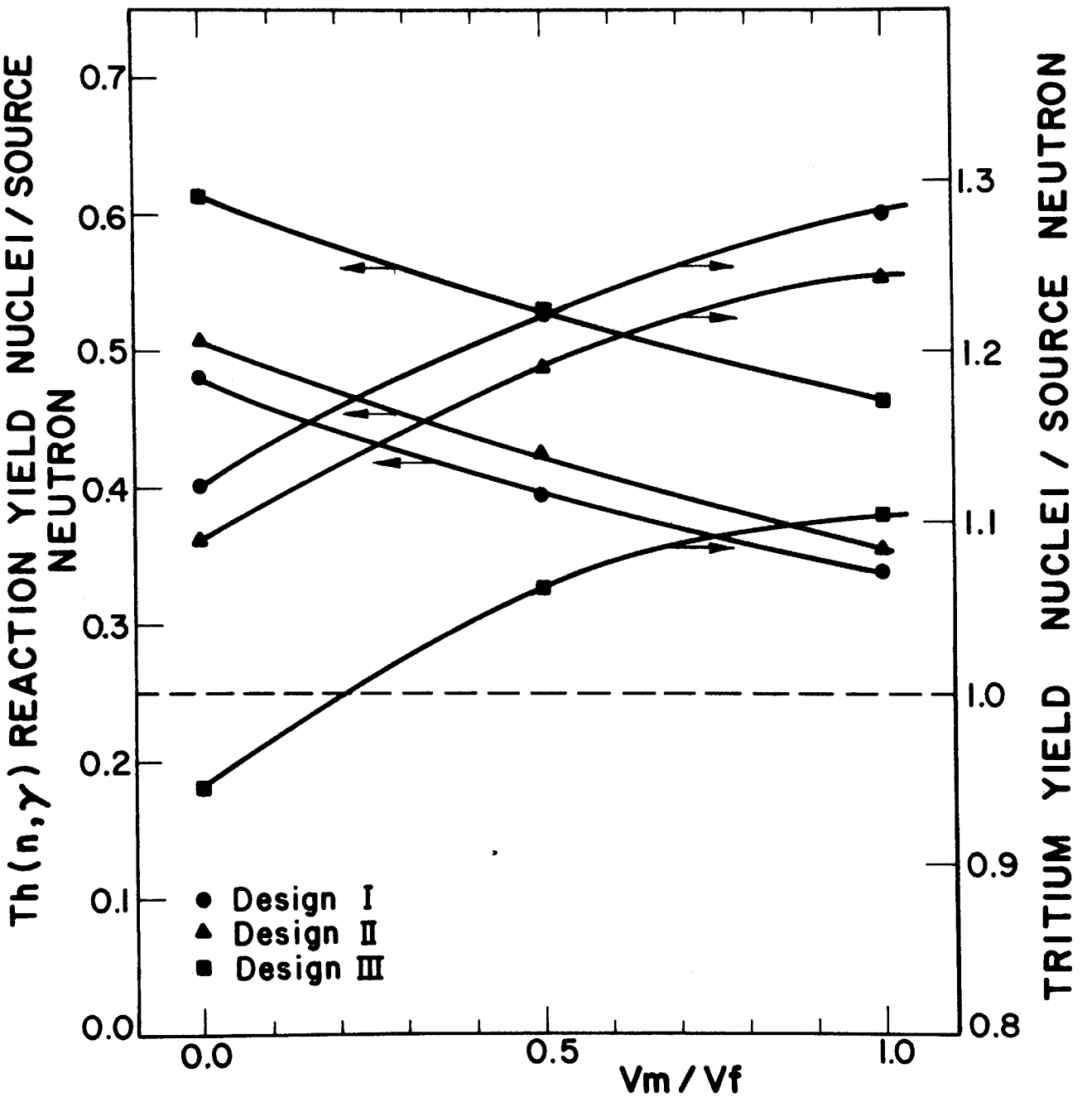
Th(n,γ) REACTION YIELD NUCLEI / SOURCE NEUTRON
TRITIUM YIELD NUCLEI / SOURCE NEUTRON
Vm / Vf
0.0
0.5
1.0
0.1
0.2
0.3
0.4
0.6
0.7
0.8
0.9
1.1
1.2
1.3
Design I
Design II
Design III

Fig. II.4-7

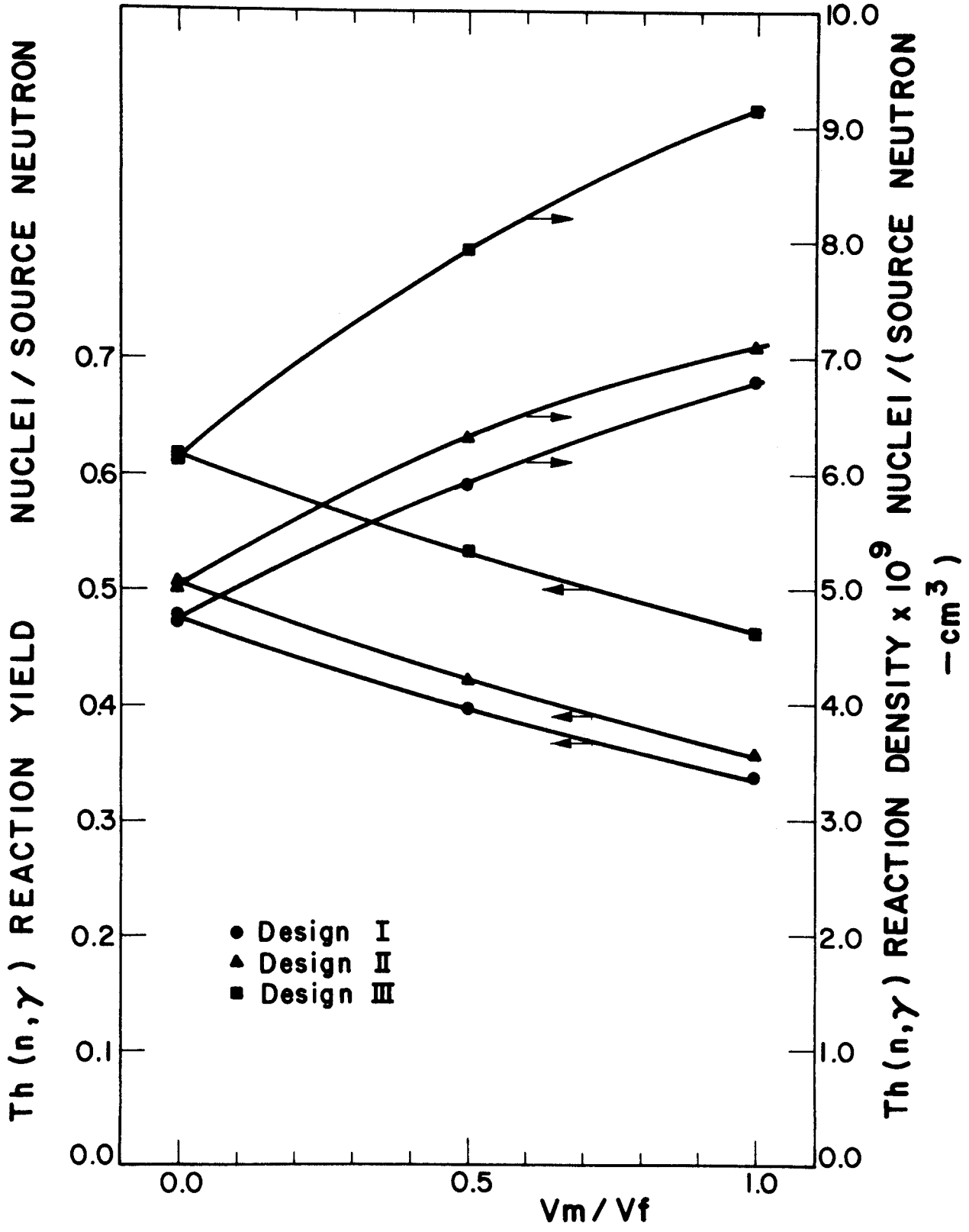
Th (n,γ) REACTION YIELD NUCLEI / SOURCE NEUTRON
Th (n,γ) REACTION DENSITY x 10^9 NUCLEI / (SOURCE NEUTRON - cm^3)
Vm / Vf
0.0
0.5
1.0
0.1
0.2
0.3
0.4
0.6
0.7
2.0
3.0
4.0
5.0
6.0
7.0
8.0
9.0
10.0
● Design I
▲ Design II
■ Design III

Fig. II.4-8

Table II.4-8 Economic Parameters for Hybrid Reactor Blanket as a Function of v_m/v_f for Designs I, II, III

Design	v_m/v_f	Yearly Production of Fissile Fuel (^{233}U) (MT /year)	Time to attain an Average 4% Enrichment in Fresh Fuel Batch (years)	Reduction in Fuel Inventory (Percentage)
I	0.0	2.24	4.45	0
	0.5	1.85	3.59	33
	1.0	1.6	3.12	50
II	0.0	2.36	4.22	0
	0.5	1.99	3.32	33
	1.0	1.67	2.96	50
III	0.0	2.87	3.47	0
	0.5	2.50	2.65	33
	1.0	2.18	2.27	50

Th(n,γ) reaction is considered as the ^{233}U producing reaction.
No burnup was considered.

$\frac{V_m}{V_f}$ is the neutron multiplier-moderator to fuel volume ratio,

$Y = 3.154 \times 10^7$ is a conversion ratio from years to seconds.

It can be noticed from the results of Table II.4-8 that a reduction in the fuel inventory by going from $V_m/V_f = 0$ to 0.5 and 1.0 corresponds to slower reduction in the yearly fissile fuel production. This is caused by the higher breeding densities achieved by the suggested lattice configuration. This will also lead to a reduction in the time required to attain a certain fuel enrichment, as shown below.

Let us first define the "enrichment potential" **r as:**

$$r = \frac{\text{Total weight of fissile material}}{\text{Initial inventory of fertile material}} \quad . \qquad (2)$$

Notice that the "enrichment" is usually defined as:

$$r' = \frac{\text{Weight of fissile material}}{\text{Total fuel weight (fertile \& fissile)}} \quad .$$

Now, the time in years to attain a given enrichment potential r can be expressed as:

$$\tau_r \left(\frac{V_m}{V_f}\right) = \frac{r}{\frac{V_m}{K(\frac{V_m}{V_f})}} \left\{ V_{fr} \left(\frac{V_m}{V_f}\right) \alpha_{fm} \rho(fm) \cdot \left(\frac{\rho(f)}{\rho(fm)}\right)\right\} \text{(years)} \qquad (3)$$

where r is the enrichment potential,

$\frac{V_m}{V_f}$ is the neutron multiplier-moderator to fuel volume ratio,

V_{fr} is the volume of the fuel region (cm^3),

K is the yearly production of fissile fuel $(\frac{g}{year})$,

α_{fm} is the volume fraction of fuel material (ThO_2) in the fuel plus coolant region (30.3695% in our design),

$\rho(fm)$ is the density of fuel material, $\rho(ThO_2) = 10.01 \frac{g}{cm^3}$,

$\frac{\rho(f)}{\rho(fm)}$ is the weight fraction of fuel in fuel material; for ThO_2:

$$\frac{\rho(Th)}{\rho(ThO_2)} = 0.8788.$$

As shown in Table II.4-8, τ_r can be substantially reduced, particularly for Design III, by using the suggested lattice configuration and a neutron multiplier zone in front of the axial blanket, at the expense of a reduction in the overall fissile fuel production, and a substantial reduction in the fuel inventory.

It should be noticed that Design III is superior to Design I both in overall yearly fissile production and the time required to attain a given enrichment. If Design I for $v_m/v_f = 0.0$ is considered as a base case arrived at from one-dimensional scoping studies, then Design III for $v_m/v_f = 1.0$ from three-dimensional studies leads to almost the same fissile fuel production with about half the time to attain a given enrichment, together with a 50% reduction in the fuel inventory.

II.4.D. Conclusions and Recommendations

Our study suggests that the adoption of a lattice configuration achieves its intended purpose of increasing the breeding densities in the fertile fuel, leading in turn to shorter times in the hybrid to attain a given average enrichment. This is also associated with

a reduction in the fuel inventory with corresponding economic and safety implications. While this is accomplished at the expense of a reduction in the overall fissile fuel production, further refinements in the design details may overcome this problem in view of the constancy of the sum of fusile and fissile breeding. Materials other than Pb with low parasitic absorption should be investigated as lattice scatterer materials. Preceding the tritium-breeding axial blanket by a Pb multiplying zone is found to increase the fissile breeding in the radial blanket at the expense of a reduction of tritium breeding in the axial blanket, and is recommended as a design feature. The neutronic coupling between the axial and radial blankets questions the validity of simple solid angle weighting of one-dimensional calculations used in some previous studies. Severe non-uniformities in the spatial distribution of the fissile enrichment are detected radially and axially. The design of detailed spectral shaping and on-power fuel irradiation and management programs is necessary for the eventual application of such a concept. Detailed burnup and economic calculations for both the hybrid and the LWRs are needed to assess the hybrid's commercial feasibility. Further neutronics cell calculations considering the fuel pins in the fuel assemblies and self-shielded cross-section data are needed for more reliable estimates of breeding. Some form of reprocessing or at least refabrication could be used profitably to produce suitable LWR fuel without penalties from non-uniform enrichment or elaborate fuel management in the hybrid. This might be accomplished by irradiation of single fuel pins rather than whole fuel assemblies. Enrichment of single fuel pellets embedded in graphite spheres, in a pebble bed concept, then assembling them into fuel pins and assemblies, would provide uniform enrichment, and is an interesting concept which bears further investigation.

References for Section II.4

1. M.M.H. Ragheb, M.Z. Youssef, S.I. Abdel-Khalik, and C.W. Maynard, "Three-Dimensional Neutronics Analysis of the SOLASE-H Laser Fissile-Enrichment-Fuel-Factory", UWFDM-266, Fusion Research Program, The University of Wisconsin (1978).

2. M.M.H. Ragheb, E. Cheng, and R.W. Conn, "Monte Carlo Study of Asymmetric Effects in a Magnetically-Protected-First-Wall Gas Driven Reactor", Atomkernenergie (ATKE), 31, Lfg. 4 (1978), p. 217.

3. M.M.H. Ragheb and C.W. Maynard, "Monte Carlo Statistical Weighting Methods for External-Source-Driven Multiplying Systems", UWFDM-265, Fusion Research Program, Univ. of Wisconsin (October 1978).

4. M.B. Emmett, "The MORSE Monte Carlo Radiation Transport Code System", ORNL-4972, Oak Ridge National Laboratory (1975).

5. RSIC Code Package CCC-203 "MORSE-CG", Radiation Shielding Information Center, ORNL (1976).

6. D.M. Plaster, R.T. Santoro, and W.E. Ford III, "Coupled 100-Group Neutron and 21-Group Gamma-Ray Cross Sections for EPR Calculations", ORNL-TM-4875, Oak Ridge National Laboratory (1975).

7. W.E. Ford III, R.T. Santoro, R.W. Roussin, and D.M. Plaster, "Modification Number One to the Coupled 100 n-21 γ Cross Section Library for EPR Calculations", ORNL-TM-4259, Oak Ridge National Laboratory (1976).

8. DLC-37B Data Library, Radiation Shielding Information Center, Oak Ridge National Laboratory (1975).

9. G.D. Joanou and J.S. Dudek, "GAM II, A B3 Code for the Calculation of Fast Neutron Spectra and Associated Multigroup Constants", GA-4265, General Atomic (1973).

10. M.A. Abdou and R.W. Roussin, "MACKLIB, 100 Group Neutron Fluence-to-Kerma Factors and Reaction Cross Sections Generated by the MACK Computer Program From Data in ENDF Format", ORNL-TM-3995 (1974).

III. Laser Fusion Requirements and First Wall Protection

III.1. Laser and Target Performance Requirements for Hybrids

III.1.A. General Analysis

In a pure laser fusion reactor the relatively low efficiency laser driver must be compensated by a large target gain to maintain an economically acceptable recirculating power fraction. A fusion-fission hybrid reactor has the potential of reducing the target performance requirements necessary for an economic system. It may also allow a lower laser efficiency and repetition rate. This relaxation of the fusion performance is a consequence of two considerations: (1) The fusion neutron energy is multiplied in the blanket by the fissioning of fertile and bred fissile fuel. The large fission yield (~200 MeV) compared to the fusion yield (~17.6 MeV) will substantially multiply the fusion neutron energy if only a small fraction of the fusion neutrons induce fission. This additional power will help to compensate for the lower efficiency laser driver. (2) The bred fissile fuel can be periodically removed from the hybrid and burned in conventional fission reactors. It therefore serves as an additional revenue source that enhances the hybrid system economics.

The first of these factors, the fusion neutron energy multiplication in the blanket, can be related to the overall system performance by the use of four simple relations. The recirculating power fraction in a hybrid can be written as

$$f_R = [\eta_{th}\eta_L G(f_n M_n + (1-f_n))]^{-1} \qquad (1)$$

where f_R is the recirculating power fraction, η_{th} is the gross thermal efficiency of the power cycle, η_L is the net laser efficiency, G is the thermonuclear gain of the target, M_n is the blanket multiplication of the

fusion neutron energy, and f_n is the fraction of fusion energy in neutrons. For notational convenience we define

$$M = f_n M_n + (1-f_n) \tag{2}$$

as the net energy multiplication of the hybrid system. Then the expression for recirculating power becomes

$$f_R = [\eta_{th}\eta_L\ G\ M]^{-1} \tag{3}$$

The value of f_n is typically 0.60-0.80 depending on the target design. If we choose $f_R = 0.25$, $\eta_{th} = 0.4$, and $M = 1$, then we find

$$\eta_L G = 10. \tag{4}$$

This is the well known result for pure fusion reactors. The product, $\eta_L G$, is called the fusion gain and is a measure of the recirculating power fraction. For a recirculating power fraction of 25%, a pellet gain of 100 will be sufficient for a 10% efficient laser while a gain of 1000 is necessary if the laser efficiency is only 1%. Most lasers considered as fusion drivers have efficiencies within this range. The economically allowable recirculating power fraction therefore places constraints on the performance of the fusion pellets and their driver.

Another parameter that is important to system performance is the amount of electrical power that is produced. This is given by

$$P_e = G\ E_L\ \omega\ \eta_{th}\ M \tag{5}$$

where P_e is the electrical power, E_L is the laser energy, and ω is the pulse repetition frequency. The electrical power produced by the reactor will be important to the cost of components that are sensitive to an economy of scale.

This is certainly the experience with fission reactors being built today.

To analyze hybrid system performance, an expression that relates the target gain to the incident laser energy is also required. Whereas the first two expressions are simple definitions, this third expression will depend in a complex way on the target design, laser pulse shape, laser wavelength, etc. No such expression is available today. The determination of this relationship is of course the goal of the laser fusion experimental program in this country. However, for the purposes of this analysis a simple formula that roughly reproduces the available information about anticipated target performance can be given as

$$G = 100\ E_L^{1.7} \tag{6}$$

where E_L is measured in MJ. This formula predicts that a 1 MJ laser gives a gain of 100, a 3.9 MJ laser gives a gain of 1000, and a 300 kJ laser gives a gain of 13. This is most certainly a very crude estimate but very likely does not under-rate the current understanding of target performance within this range of laser energies.

The final formula that is required for this analysis relates the cost of the major driver/pellet system components to the other fusion physics parameters. Here we assume that the capacitive power supplies that are needed to drive the laser are the dominant cost driver. The power supplies have been previously identified as a major problem in the driver economics.[1] When more understanding of the pellet manufacturing, cavity pumping, laser gas handling, and other costs is developed, then this can be included in the system performance evaluation as well. The analysis done here must presume that the power supply costs, and not the pellet manufacturing or gas handling

facility or the cavity pumping equipment are the major cost driver. Although the calculations are self-consistent, the conclusions are not immune to change from considerations that are not included in the model. These additional constraints are likely to be important because they all tend to favor a low repetition rate while the power supply costs favor a high repetition rate.

Empirical evidence indicates that high voltage power supply lifetime can be increased by de-rating the actual voltage used in the operation of the power supply. If the voltage is derated then the power supply capacity is decreased and thus more volume is required to provide an equal amount of energy. With these considerations taken into account, the power supply cost can be expressed as

$$C = C_o\left(\frac{\omega_o}{\omega}\right)^n \tag{7}$$

where C_o and ω_o are the cost per unit of stored energy and the repetition rate associated with a reference power supply. The reference repetition rate is related to the lifetime of the supply. For instance, the reference system might be one that provides 10^{10} shots over 30 years of power plant life at a 70% plant factor. This would give a reference repetition rate of 15 Hz. The parameter, n, is determined from empirical observation to be about 1/4. Using these four formulae the power supply cost can be expressed

$$C\left(\frac{(\$)}{kW_e(net)}\right) = \frac{2000\, C_o\, \omega^{n-1}}{M\, \omega_o^n\, \eta_{th} G(1-f_R)} . \tag{8}$$

where the normalization cost, C_o, is given in \$/J and a factor of 2 has been included to account for indirect costs. With these formulas, the cost of

power supplies as a function of the laser (or more generally) driver efficiency can be obtained. The procedure for accomplishing this is:

(1) Choose a value of η_L

(2) Evaluate the target gain needed to satisfy the recirculating power fraction constraint

$$G = (f_R \, \eta_{th} \, \eta_L \, M)^{-1} \tag{9}$$

(3) Evaluate the laser energy necessary to achieve this target gain

$$E_L = (G/100)^{0.588} \tag{10}$$

(4) Evaluate the repetition frequency needed to produce the desired amount of electrical power

$$\omega = P_e/(G \, E_L \, \eta_{th} \, M) \tag{11}$$

(5) Compute the power supply cost using the formula in Eqn. 8.

The results of parametric calculations are shown in Fig. III.1-1. The total power supply cost (direct and indirect) is plotted as a function of the driver efficiency for two different net electrical power outputs, 1000 MW_e and 100 MW_e, and for three different net blanket energy multiplications, 1, 5, and 10. The recirculating power fraction was held fixed at 0.25 and the thermal efficiency was set at 0.40. The reference cost of the power supplies was taken to be \$2.50/joule for a reference repetition frequency of 15 Hz. This was determined by using cost data for the ANTARES power supplies. These supplies have a cost of \$0.50/J and an expected lifetime of 10^6 shots. If these supplies were de-rated to obtain a lifetime of 10^{10} shots, then the total cost would be \$5.00/J. We then cut this cost by a factor of two to take account of technical and manufacturing improvements associated with larger scale production of such power supplies. This reference cost must

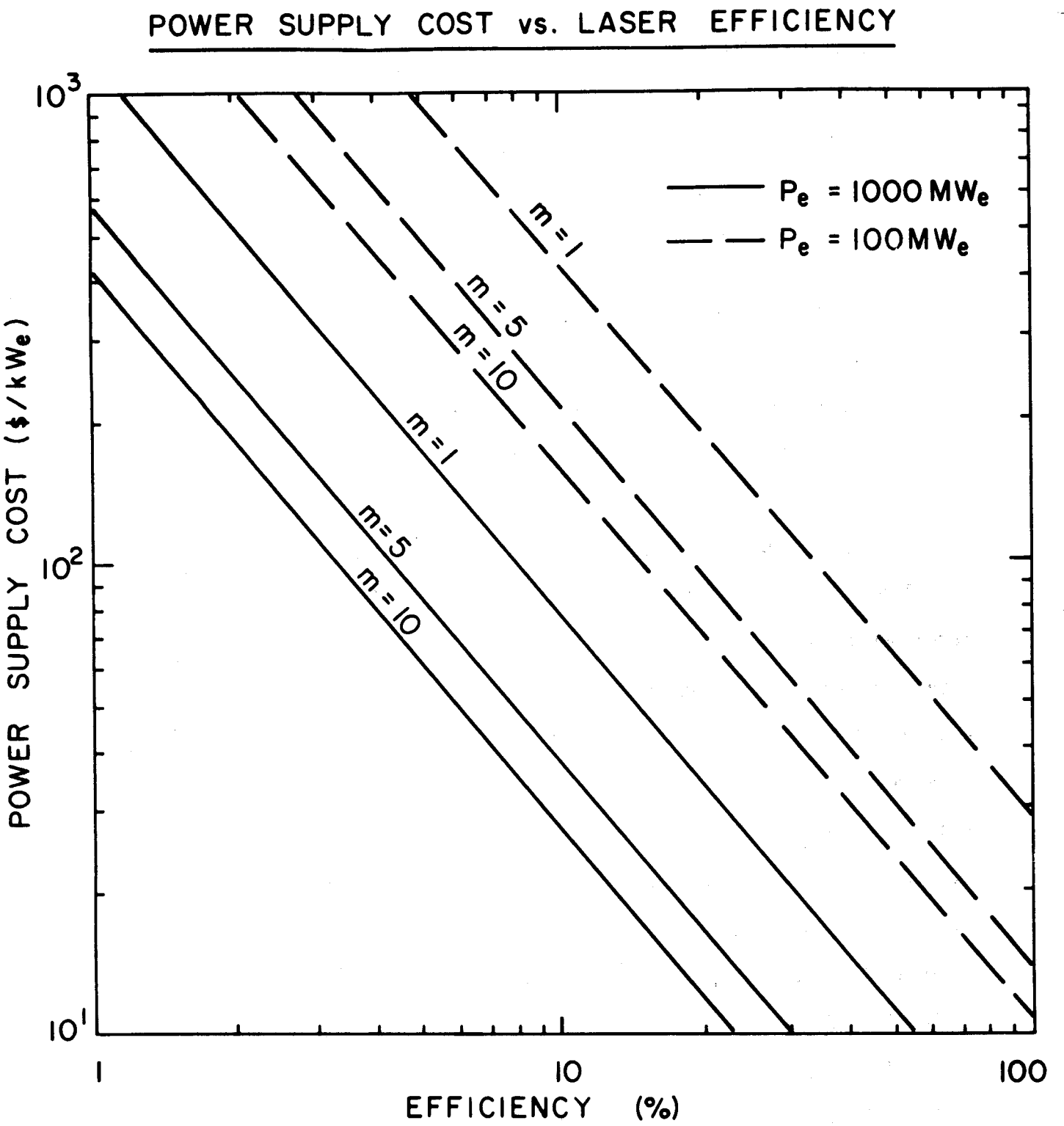
POWER SUPPLY COST vs. LASER EFFICIENCY
10^3
10^2
10^1
POWER SUPPLY COST ($/kWe)
P_e = 1000 MWe
P_e = 100 MWe
m=1
m=5
m=10
m=1
m=5
m=10
1
10
100
EFFICIENCY (%)

Fig. III.1-1

therefore be considered an optimistic choice relative to the state-of-the-art in power supplies. All costs in this analysis are simply proportional to this reference cost. It is instructive to look at the relative costs for these different systems. The 100 MW_e power plant has significantly higher power supply costs than 1000 MW_e plants. This clearly demonstrates the economy of scale associated with the power supply cost dependence. The higher cost results from the fact that the pellet gain (at any given laser efficiency) must be chosen to be consistent with the recirculating power fraction. This high gain then requires a large laser energy. Hence the only control of the power output (at a given laser efficiency) is the repetition rate. A low repetition rate is not desirable from a power supply cost standpoint and therefore the cost per kW_e is higher for low power output. The curves in Fig. III.1-1 clearly extend beyond the maximum upper cost value that could be afforded in an economical system. As a point of reference, suppose that the total power plant cost is \$2000/kW_e(net) and suppose that the power supplies cannot cost more than 10% of the total. This limits their cost to \$200/kW_e. The result of this limitation is shown in Fig. III.1-2. This figure indicates that a 1000 MW_e pure fusion reactor must have a laser efficiency of at least 4.4% to limit the power supply costs to \$200/kW_e. If a 1000 MW_e hybrid reactor with a net energy multiplication of 5 is used then the laser efficiency must be at least 2.45%. If the energy multiplication is 10, then a 1.9% efficient laser will suffice. Because all laser efficiencies are not available, that is each different laser has its own specific efficiency, this reduction in acceptable laser efficiency that results from the blanket multiplication could have a significant impact on the introduction of laser

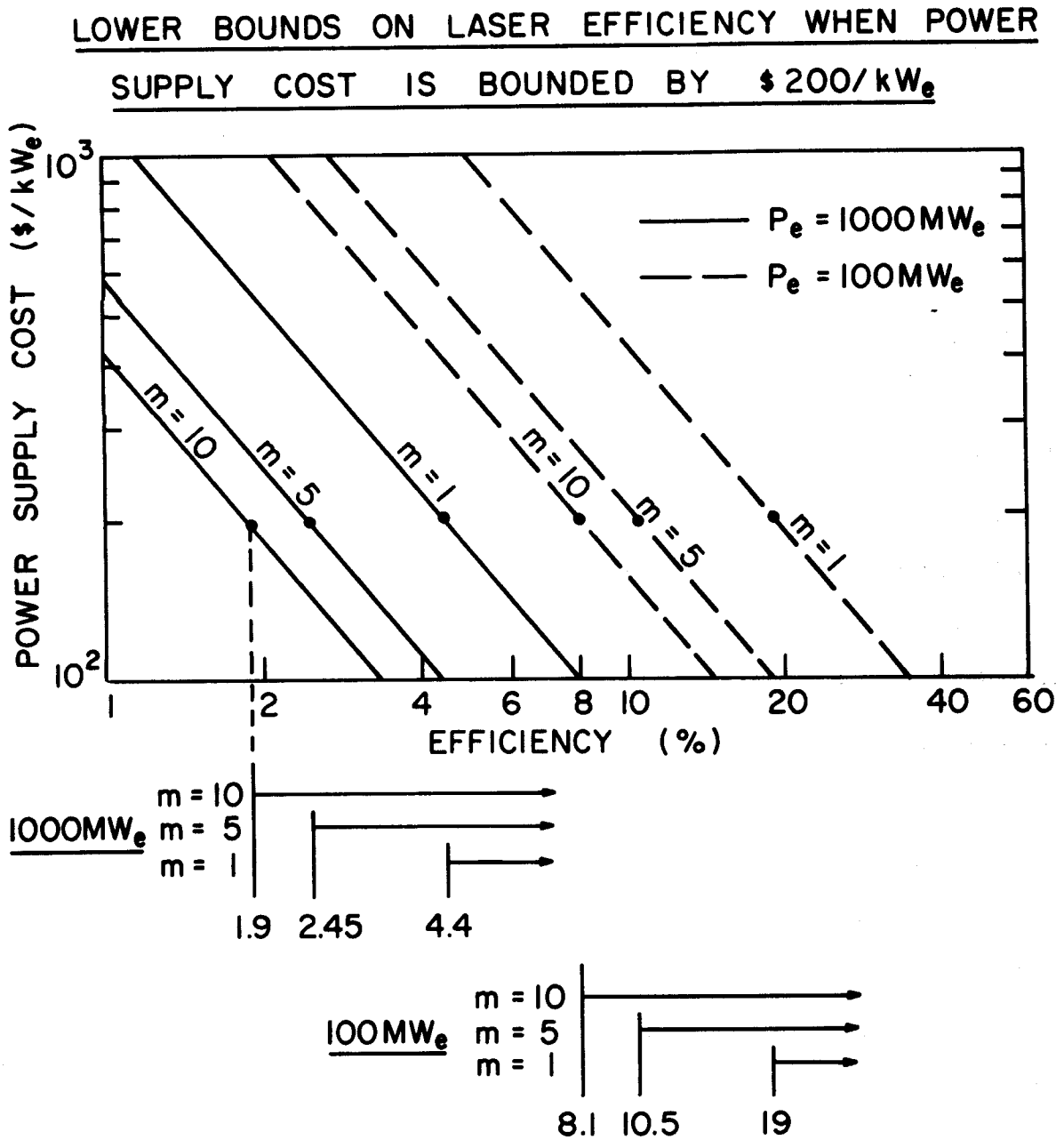
LOWER BOUNDS ON LASER EFFICIENCY WHEN POWER SUPPLY COST IS BOUNDED BY $200/kWe
POWER SUPPLY COST ($/kWe)
10^3
10^2
Pe = 1000MWe
Pe = 100MWe
m = 10
m = 5
m = 1
1
2
4
6
8
10
20
40
60
EFFICIENCY (%)
1000MWe
m = 10
m = 5
m = 1
1.9
2.45
4.4
100MWe
m = 10
m = 5
m = 1
8.1
10.5
19

Fig. III.1-2

fusion. It may place into the potential fusion driver category some low efficiency lasers (with other possible desirable characteristics such as short wavelength) that might otherwise be excluded. For the 100 MW_e plant the situation is substantially different. Here the acceptable driver efficiencies are so high, 19%, 10.5% and 8.1%, for blanket multiplications of 1, 5 and 10, that the issue becomes a matter of particle beam drivers vs. lasers. It is unlikely that any laser will have an efficiency of 19%. However, drivers such as relativistic electron beams or ion beams have the potential of operating at efficiencies even higher than this. An efficiency of 8 or 10% is within the range of the CO_2 laser (in a multipass mode of operation). Therefore, it is possible to consider a 100 MW_e hybrid using a laser driver but this driver technology would not scale to a 100 MW_e pure fusion reactor. A complete list of the relevant fusion parameters associated with each of these limiting laser efficiencies is shown in Fig. III.1-3.

Since this analysis is based, in part, upon parameters and constraining relations that are not well established it is most appropriate to vary these parameters and view the effect on the power supply costs. One such parameter is the reference power supply cost of \$2.50/joule. However, because the computed cost in $/$kW_e$ is simply linearly proportional to this quantity we choose not to bother with this trivial case. The dependence on the value of "n" that appears in Eqn. 7 is more subtle and should be investigated. Note that the economic preference for high efficiency drivers and higher repetition rates rather than more stored energy and lower repetition rates, associated with lower efficiency lasers, is the result of the parameter "n" in Eqn. 7 being less than one. If n=1, then the power supply cost would be constant for all laser efficiencies. The analysis shown in Fig. III.1-1 was redone using

LASER PARAMETERS WHEN LIMITED TO POWER SUPPLY COST OF $200/kW$_e$

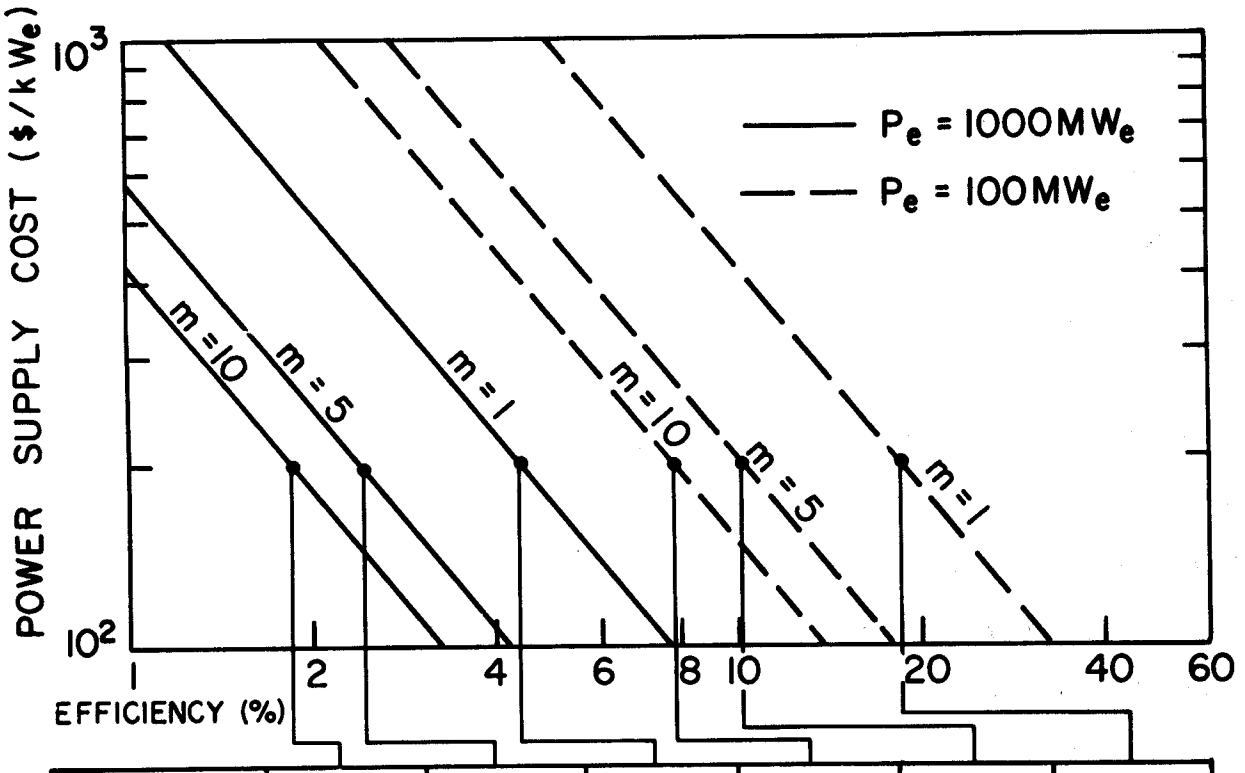

P_e (MW_e)	1000	1000	1000	100	100	100
m	10	5	1	10	5	1
η_L	.019	.0245	.044	.081	.105	.19
G	52.6	81.6	227	12.3	19	52.6
E_L (MJ)	.685	.887	1.6	.292	.377	.685
y (MJ)	36	72	363	3.6	7.2	36
ω (s^{-1})	9.2	9.2	9.2	9.2	9.2	9.2

Fig. III.1-3

n=1/2. These results are given in Fig. III.1-4 and III.1-5. In Fig. III.1-4 it is seen that the power supply cost for a 1000 MW_e reactor with M=1 is less for the n=1/2 scaling if the laser efficiency is less than 7.4%. For laser efficiencies above 7.4%, the n=1/4 scaling provides the lowest cost. This demonstrates that as "n" approaches a value of one, the relative cost benefits of high efficiency drivers over low efficiency drivers disappears. The fusion parameters associated with the minimum acceptable laser efficiency are shown in Fig. III.1-5. For a 1000 MW_e reactor with M=1, the minimum laser efficiency is now 3.5% rather than 4.4%. All of the conclusions remain the same as for the calculations with n=1/4 scaling but the minimum efficiencies are consistently lower in this case.

Another assumption that should be tested is the relation between target gain and laser energy. The relation used in the preceding calculations, Eqn. 6, is likely to be optimistic. By this we do not mean to imply that it is unachievable but only that it represents the predictions of highly optimized targets. A more complete technical discussion of these issues is presented in Section III.1.B. We might therefore look at the consequences of a relation such as

$$G = 50\, E_L^{1.7} \quad . \tag{12}$$

This relation predicts that a laser energy 1.5 times greater than that used in Eqn. 6 is required to produce the same gain. However, the scaling of the gain with the laser energy, the exponent 1.7, is the same. Therefore, the expression in Eqn. 12 assumes that the implosion dynamics are the same as those represented by Eqn. 6 but that only 2/3 of the laser energy is available to drive the implosion. This could result from less than optimum illumination

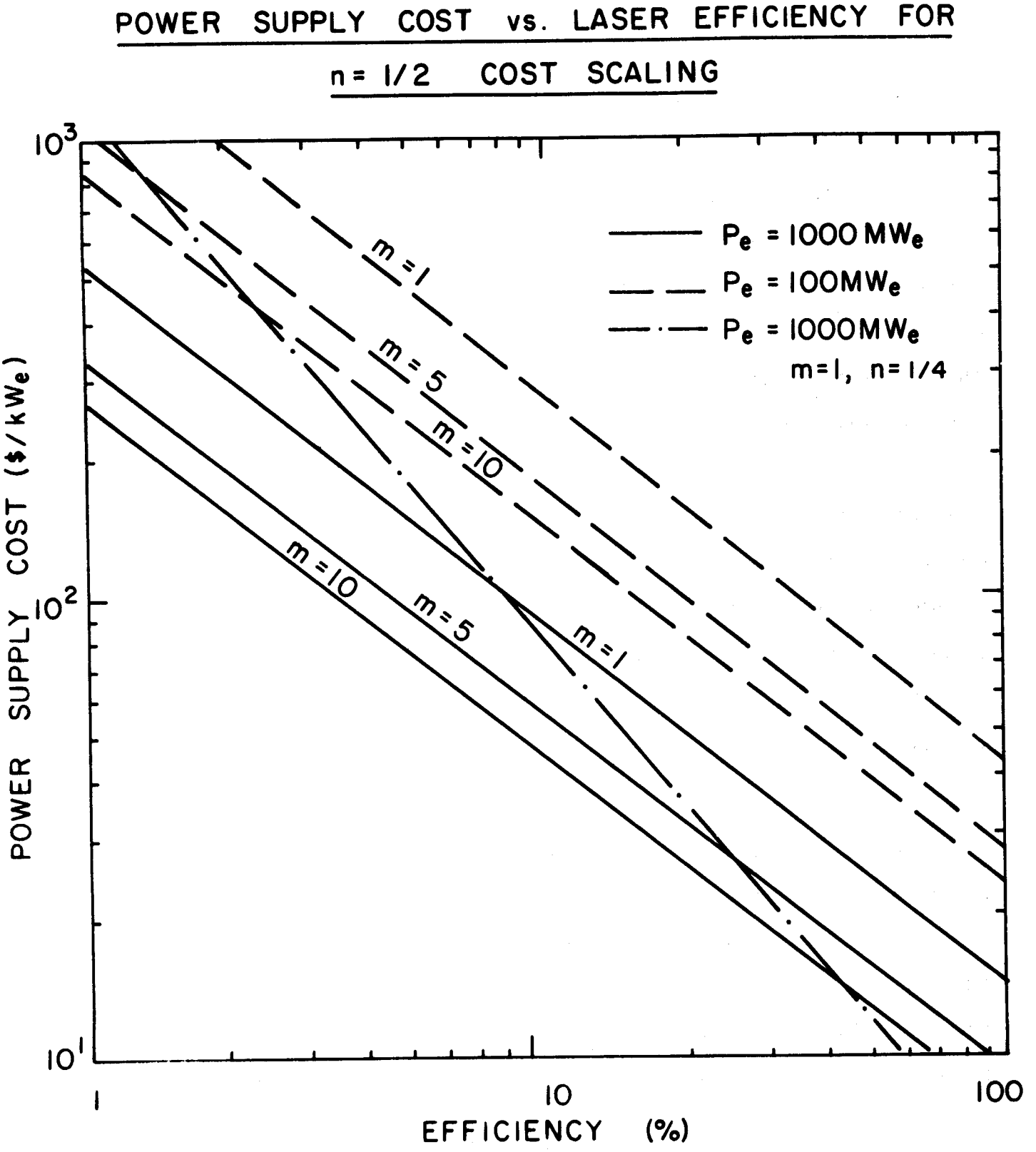
POWER SUPPLY COST vs. LASER EFFICIENCY FOR
n = 1/2 COST SCALING
10^3
10^2
10^1
POWER SUPPLY COST ($/kW$_e$)
1
10
100
EFFICIENCY (%)
P_e = 1000 MW$_e$
P_e = 100MW$_e$
P_e = 1000MW$_e$
m=1, n=1/4
m=1
m=5
m=10
m=10
m=5
m=1

Fig. III.1-4

LASER PARAMETERS WHEN LIMITED TO POWER SUPPLY COST OF $200/kW$_e$ FOR n = 1/2 COST SCALING

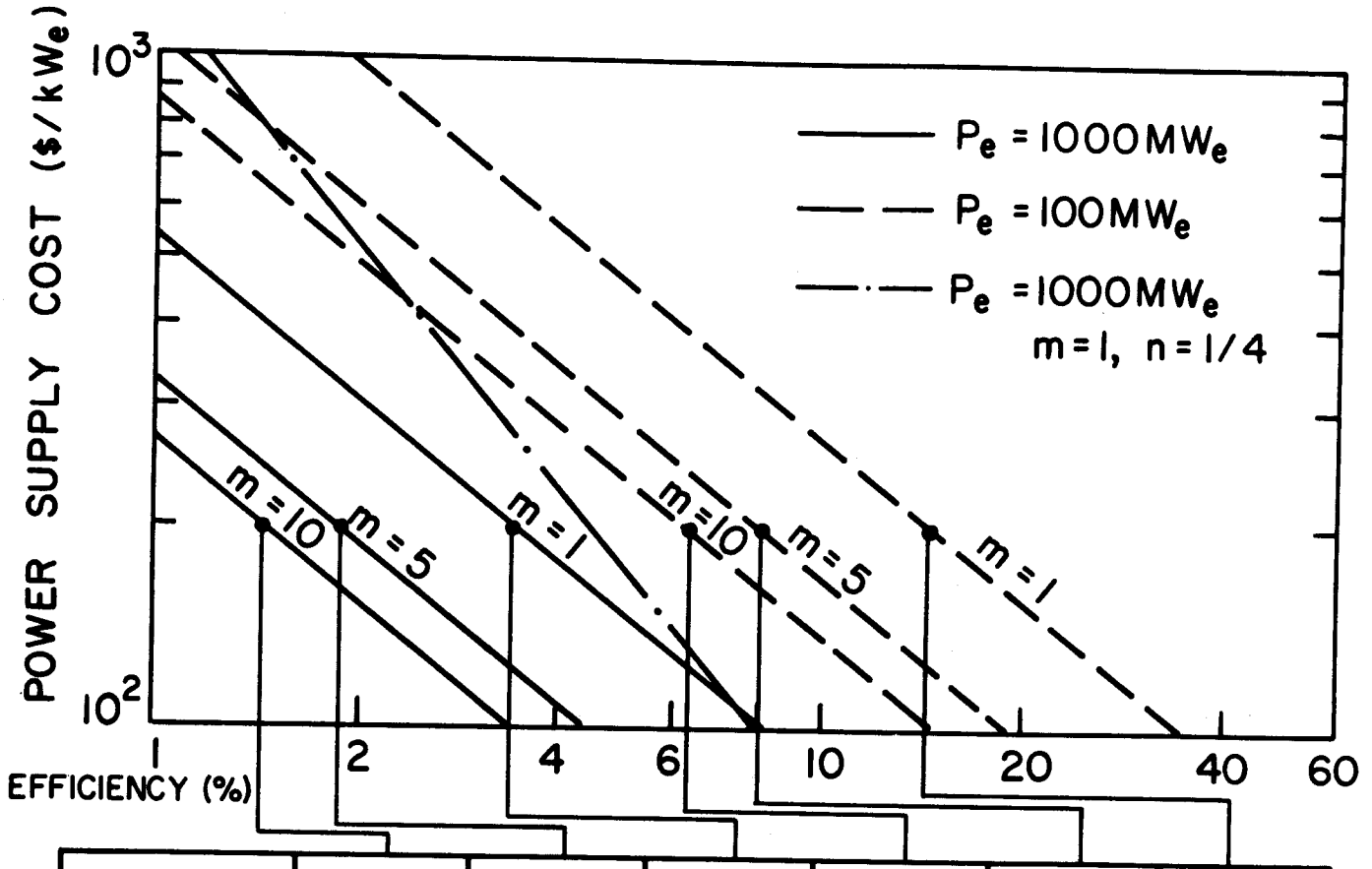

P_e(MW$_e$)	1000	1000	1000	100	100	100
m	10	5	1	10	5	1
η_L	.0145	.019	.035	.063	.079	.145
G	69	105	286	16	25	69
E_L(MJ)	.804	1.03	1.85	.340	.442	.804
y(MJ)	55	108	529	5.4	11	55
$\omega(s^{-1})$	6	6	6	6	6	6

Fig. III.1-5

efficiency, for instance. A similar cost analysis was done using Eqn. 12 rather than Eqn. 6 and it is shown in Fig. III.1-6. This change places more severe constraints on the minimum allowable laser efficiency. A comparison with Fig. III.1-2 shows that for the 1000 MW_e reactor with M=1, the minimum laser efficiency is now 5.8% rather than 4.4%. Also the slope of the lines in Fig. III.1-6 is steeper than the lines in Fig. III.1-2. This steepening of the curves tends to further increase the attractiveness of high efficiency drivers over low efficiency drivers.

The preceding analysis indicates that the introduction of a hybrid blanket with a net energy multiplication of 5-10 can significantly decrease the required laser/target performance. This could have important effects on the introduction of laser fusion as an energy source because each particular laser (or particle beam) driver has its own inherent efficiency. If, for instance, one assumes less than optimistic pellet scaling (Fig. III.1-6), then the introduction of a blanket with a multiplication of 10 reduces the necessary laser efficiency from 5.8% to 2.4% and the pellet gain from 172 to 42. At 2.4% efficiency, both the CO_2 and HF lasers are good driver candidates. However, at 5.8% the HF laser is probably ruled out and the CO_2 laser must be multipassed. This added complication might prove to be too complex for reliable operation. An almost endless number of interpretations of these results could be presented. This will not be done because, as stated in the beginning of this section, there are likely to be important constraints that are not included in this analysis. These would all tend to limit the maximum allowable repetition rate. However, for the calculations done here, the repetition rates vary between 5-10 sec^{-1} for the cases with maximum

LASER PARAMETERS WHEN LIMITED TO POWER SUPPLY COST OF $200/kW_e$ FOR GAIN SCALING OF $G = 50E_L^{1.7}$

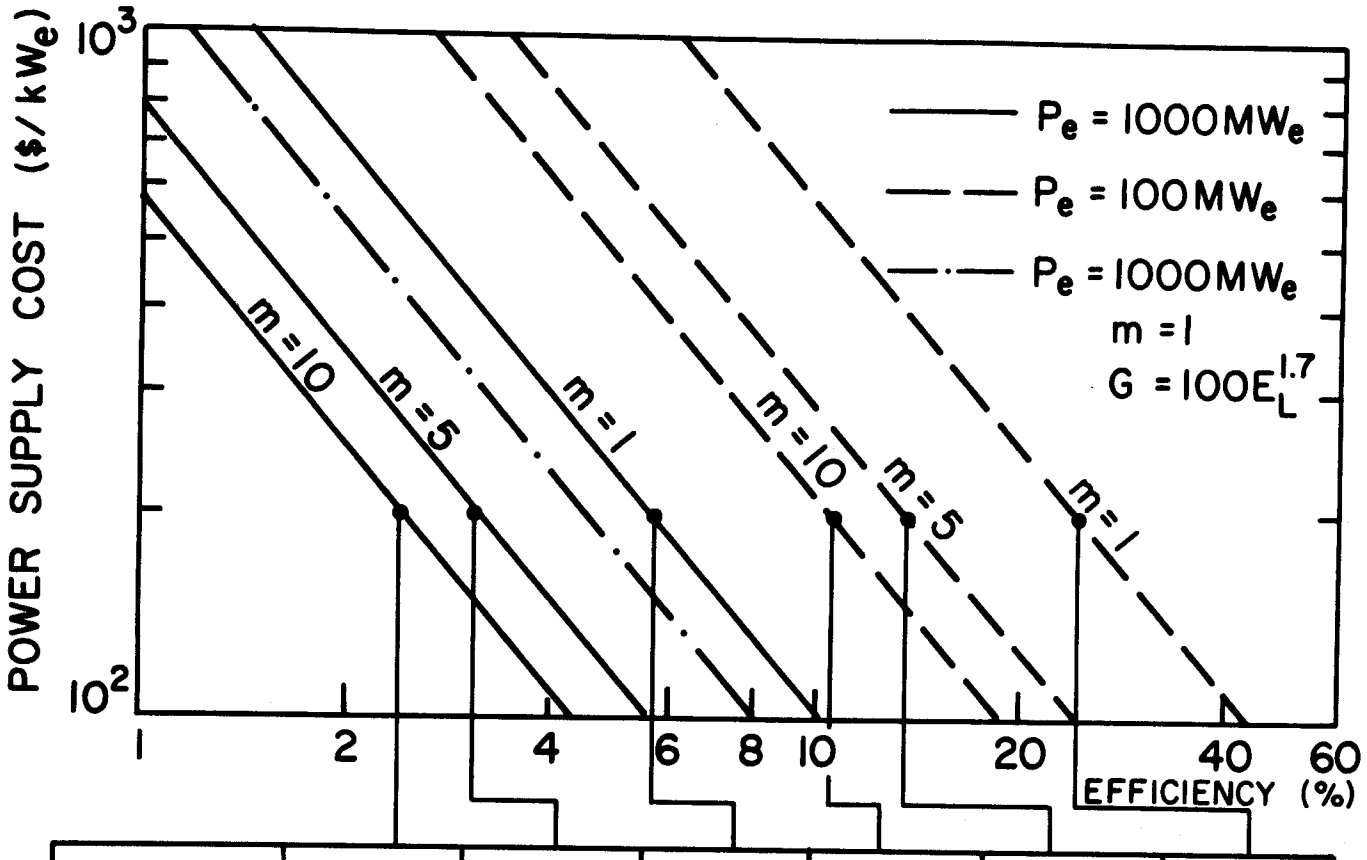

$P_e(MW_e)$	1000	1000	1000	100	100	100
m	10	5	1	10	5	1
η_L	.024	.031	.058	.105	.135	.245
G	42	64	172	9.5	15	41
$E_L(MJ)$	.902	1.16	2.07	.377	.493	.890
y(MJ)	38	74	356	3.6	7.4	36.5
$\omega(s^{-1})$	8.8	8.9	9.3	9.3	9.1	9.1

Fig. III.1-6

allowable power supply cost. These frequencies seem to be reasonable and hence there is a good chance that the frequency limit imposed by other constraints will be greater than these, producing a "window" in parameter space where laser fusion hybrids can meet all of the economic and technical constraints.

An equally important issue in the assessment of hybrid reactor systems is the production of fissile fuel. There are two general types of hybrid blanket designs that fulfill this purpose. (1) The neutron spectrum is kept as hard as possible to maximize the production of fuel and minimize the burnup of the bred fissile fuel in the blanket. The energy multiplication associated with such blanket designs is about 2-5. (2) The neutron spectrum is allowed to thermalize so that much of the bred fuel is burned in the blanket. This type of blanket design generally has a much larger energy multiplication of 10-50. Clearly, the energy multiplication in the blanket is related to the blanket criticality by

$$M_n = (1-k)^{-1}. \qquad (13)$$

Hence, a high multiplication is the result of a blanket configuration that is nearly critical. One must then question whether there is any advantage of a hybrid operating in a nearly critical configuration over a LMFBR, for instance. This is a very complex issue that will not be addressed here in detail.

In the type (1) blanket design, the bred fissile fuel can be periodically removed from the hybrid and used in conventional LWRs. It is this type of blanket that has been investigated in the SOLASE-H study, thus the emphasis in this discussion will be the impact of this blanket design on the pellet/driver requirements. Our neutronics studies have shown that the amount of fissile

material produced and unburned is essentially proportional to the number of 14 MeV neutrons generated from the fusion reaction. If the hybrid reactor is designed to be a fuel factory, as it is in our study, then it is desirable to have a relatively large fusion power. This of course is in contradiction to the prospect of hybrids reducing the necessary fusion performance. It is also desirable to limit the blanket energy multiplication. Clearly, a large fusion power, further multiplied in the blanket, results in a very large thermal power.

The fissile fuel production can be related to the fusion power by the following formula:

$$\frac{\text{kg of U-233}}{\text{year}} = 5.44\ P_f\ f_n\ (\text{UBR})\ (\text{PF}) \qquad (14)$$

where P_f is the fusion power in MW, f_n is the fraction of fusion energy in 14 MeV neutrons, UBR is the uranium breeding ratio and PF is the plant factor of the hybrid reactor. This formula has been evaluated for U-233 production. The coefficient for ^{239}Pu production is 5.3 rather than 5.44. The LWRs in use today operate with a fuel burnup of 33,000 MWD/MTU. If the fuel enrichment is taken to be 4%, then the burnup can be expressed as 0.825 GWD/kg U-233. If the typical fission reactor has a plant factor of 70% so that a 1000 MW_e reactor, generating 3000 MW_t, operates for 758 GWD/year, then it consumes 919 kg of U-233 per year. Thus, the number of 1000 MW_e fission reactors that the hybrid can support, without fuel recycle, is

$$\frac{\text{\#-LWR}}{\text{hybrid}} = 5.9 \times 10^{-3}\ P_f\ f_n\ (\text{UBR})\ (\text{PF}). \qquad (15)$$

Therefore the fusion power is given by

$$P_f = 169\ (\#\text{-LWR})/[f_n(\text{UBR})\ (\text{PF})]. \qquad (16)$$

If the fraction of energy in 14 MeV neutrons and the plant factor are both taken to be 0.7 we find

$$\boxed{P_f = 345\ (\#\text{-LWR})/\text{UBR}.} \qquad (17)$$

This simple formula is the result of many assumptions, LWR fuel burnup, fuel enrichment, etc. It must therefore be treated with caution. However, it can serve as a quick guide to the required fusion performance for a hybrid. Suppose that we desire to fuel 2 LWRs <u>without recycle</u> using hybrids with a ^{233}U breeding ratio of 0.6. This then requires 1150 MW of fusion power. The constraints placed on the fusion target and driver by this large power requirement are likely to dominate the constraints imposed by the recirculating power fraction requirements discussed in the first part of this section. This is the case in the SOLASE-H study.

Finally, the thermal energy equivalent of the fissile fuel produced by the hybrid can be compared to the thermal energy produced in the hybrid itself by the formula

$$\frac{\text{MWD (LWR)}}{\text{MWD (hybrid)}} = 6 \times 10^3\ \text{UBR}(M_n)f_n/M \qquad (18)$$

where we have again assumed no recycle and 33,000 MWD/MTU in the LWR. In Eqn. 18 we show the uranium breeding ratio to be a function of the blanket multiplication. If UBR increases more than linearly with increasing M_n then Eqn. 18 shows that a large blanket multiplication is desirable. Neutronics studies show that UBR increases only slightly with increasing M_n, hence the best energy ratio of LWR

to hybrid is likely to be insensitive to M. However, large values of M are desirable from a pellet/driver performance point of view. These two opposing constraints indicate the presence of an optimum blanket multiplication. Such an optimum value will depend on the economics of the hybrid/LWR system. The necessary cost information is not available at this time but the identification of these opposing constraints is of course important.

Using the arguments presented in this section, a set of consistent pellet/laser parameters were chosen for the SOLASE-H study. This set of performance parameters allows a coupling between the laser, pellet and the cavity volume. This in turn determines the first wall neutron and heat loading which are important to the analysis of radiation damage and mechanical design of the blanket. These parameters are discussed in the following section.

III.1.B. Fusion Parameters for the SOLASE-H Reactor Study

The fusion parameters for the SOLASE-H reactor study are given in Table III.1-1. The choice of parameters is designed to mitigate the problems uncovered in the SOLASE laser fusion conceptual reactor study. A 2 MJ hydrogen fluoride laser is used. It is assumed that 80% of this energy is focusable on the target. This is a more conservative estimate than the 10% losses assumed in SOLASE. Therefore, the target is irradiated with 1.6 MJ of 2.7-3.5 μm light. In the SOLASE study it was found that high gains were difficult to achieve with only 1 MJ of laser energy. Therefore, the hybrid laser energy has been boosted by 60%. The irradiation is nonuniform, from two opposite sides, and is in the form of a shaped pulse, Fig. IV.1-10. The target gain is 194 giving a yield of 310 MJ. The target gain is increased by 30% over the value of 150 used in SOLASE. This is not a desirable result. However, it is necessary to achieve acceptable hybrid performance. It is assumed that 70% of the fusion energy is in the form of neutrons and 30% is in X-rays and charged particles. In the SOLASE study, 80% of the fusion energy was in neutrons and this was too high. The laser efficiency, including chemical reprocessing of the HF and the 20% loss of energy in the beam transport, is 2.63%. The pulse repetition frequency is 4 Hz. This relaxes the requirements on the pulsed power supplies. Power supply lifetime was found to be a problem generic to all laser fusion reactor designs. The blanket multiplication varies, due to the buildup of fissile fuel. In a "clean condition" where only fertile fuel

Table III.1-1 Fusion Parameters for the Hybrid Study

Total Laser Energy	2 MJ
Laser Energy on Target	1.6 MJ
Laser Efficiency	2.6%
Laser Wavelength	2.7-3.5 μm
Target Gain	194
Target Energy Yield	310 MJ
Neutrons (70%)	217 MJ
Ions + X-rays (30%)	93 MJ
Pulse Repetition Frequency	4 Hz
Fusion Power	1241 MW
Blanket Multiplication	1.58-5
Thermal Power	2400-2900 MW
Recirculating Power Fraction	0.26-0.21

is present the multiplication is 1.58. At the end of 2.7 years when the fuel assemblies are fully enriched to 4% the blanket multiplication is 5. This leads to variations in the thermal power and recirculating power fraction of 2400-2900 MW and 0.26-0.21, respectively.

No detailed target design for the hybrid study has been done to verify this performance. However, these parameters fall within the range of those quoted in the literature and it should be noted that particular attention is given to pulse shaping. The pulse shape that was chosen is closely coupled to the design of the multipassed HF laser but is meant to serve as only an example. Other similar pulse shapes, determined by detailed target design calculations, can be easily accommodated by this type of laser design. It should also be pointed out that the pulse shaping is accomplished by pulse stacking on the target. In other words, the target is not irradiated by all laser beams at all times. This appears to be a very attractive technique for pulse shaping with nonuniform illumination but the target response must again be verified and this was not done in this study.

Many design constraints must be met when choosing a set of fusion parameters. The cavity volume is determined by the magnitude of a single target explosion rather than the time averaged fusion power. This is a very important distinction between inertial and magnetic confinement reactor designs. To minimize the cavity volume, a low yield, high repetition rate system would be desirable. To meet recirculating power fraction requirements this would also imply a low energy laser. Such a set of parameters

is not consistent with the current understanding of laser-target dynamics. Laser energies in the megajoule energy range are necessary and target gains between 100-1000 give yields of 100-1000 MJ. Clever methods of protecting the first wall from the target explosion are necessary. In addition, a high laser pulse repetition rate places a greater burden on the laser gas handling system. For the HF laser design this may in fact determine the most economic choice of target gain rather than the recirculating power fraction. The problem of cavity volume, and therefore blanket volume, is particularly important in this hybrid design. The LWR fuel must reside in the blanket until it reaches 4% enrichment. For a fixed fusion power the exposure time needed to reach this enrichment decreases with decreasing blanket volume. A smaller blanket volume results in a smaller inventory of fertile fuel, hence it will enrich faster. It would be desirable to have a cavity radius of less than six meters, but this would require fusion parameters that are not consistent with current predictions of laser-target performance.

III.1.B-1. Target Output Spectra

As discussed earlier, the target yield will determine the volume of the cavity. In this hybrid design, gas protection of the stainless steel first wall is used. It is assumed that the target X-rays and debris will be stopped in the 0.5 torr of xenon buffer gas in the cavity. There appears to be little difficulty in stopping the debris ions in six

meters of gas. The X-ray spectrum must be soft enough (or hard enough) that the first wall temperature rise is small. Many parametric studies of X-ray spectra for differing target designs have been done and are reported elsewhere. For the hybrid study it is assumed that 30% of the fusion yield is in the form of X-rays and ions. This is 93 MJ of energy. The exact partitioning of energy is not specified. However, the parametric studies indicate that target designs producing soft X-ray spectra also result in a small fraction of the total energy in X-rays. This fraction might be as low as 1-2%. Because the gas is assumed to stop all of this energy before it reaches the first wall and because the exact energy deposition profile in the gas is not important, as will be explained later, the hybrid cavity design is insensitive to the target debris characteristics. Therefore, a combination of the gas response to the energy deposition and the first wall response to the gas reradiation and overpressure will determine the minimum cavity size. These issues will be discussed in detail in Section III.2.

III.1.C. Studies of Target Gain

Parametric studies have been done to determine the dependence of target gain on the inertial confinement parameter, ρR, the ignition temperature, and the efficiency of the implosion process. These studies form a basis for predicting the likelihood of achieving the target gains requisite for power plant applications. This is an extension of previously reported work.[2]

The target gain can be factored into the product of two terms,

$$G = G_c \, \eta_H \tag{19}$$

where $G_c = Y/E_c$ is the ratio of thermonuclear yield and the energy invested in the target core, that part of the target that either burns or acts as a tamper for the burning fuel. The factor $\eta_H = E_c/E_L$ is the fraction of laser energy input that ultimately ends up in the target core at the instant of ignition. Clearly we have $0 \leq \eta_H \leq 1$ and $G_c >> 1$. We shall call G_c the gain on core and η_H the hydrodynamic implosion efficiency. This study will not deal with the implosion efficiency. This factor is a complex function of the laser light absorption process and implosion dynamics, and is very sensitive to the specific target design. The value of η_H varies between 5% and 20% depending on the target design. The study will instead investigate the gain on core. The compressed DT target core at the instant of ignition is modelled as shown in Fig. III.1-7. It has a constant density, ρ, and is compressed to some value of ρR. It is centrally ignited by a hot "microcore" that is characterized by a value, ρR_μ, and this microcore has an ignition temperature, T_μ. The temperature of the remainder of the core is $T = T_0 \, (\rho/\rho_0)^{2/3}$ where $T_0 = 1$ eV and $\rho_0 = 0.213$ g/cm^3. This is the temperature for a plasma adiabatically compressed from solid density if the initial temperature was 1 eV. It is very important to compute this temperature in a consistent way if comparisons of gain are to be made because much of the energy invested in the target core is contained in this cold compressed plasma.

COMPRESSED PELLET CORE

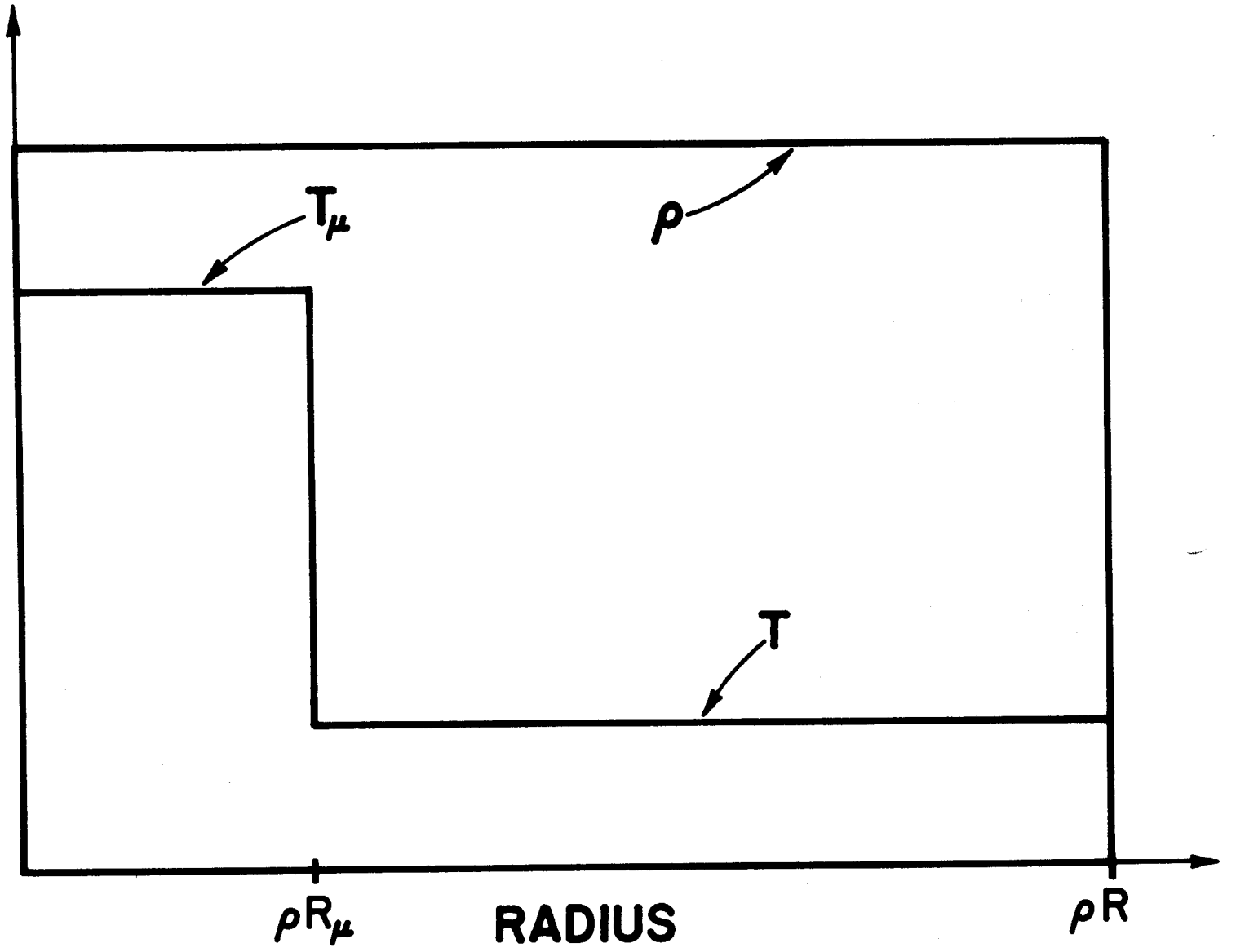

Fig. III.1-7

The energy invested in the core at the instant of ignition can be written as

$$E_c = 3\ nkT_\mu\ (\tfrac{4\pi}{3} R_\mu^3) + 3\ nkT\ (\tfrac{4\pi}{3} (R^3 - R_\mu^3)) + 1/2\ (m - m_\mu)\ u_c^2 \qquad (20)$$

where the first term is the internal energy of electrons and ions in the microcore, the second term is the internal energy of the electrons and ions in the cool compressed surrounding core, and the third term is the energy associated with the inward fluid motion of the surrounding core at the instant of ignition. It is assumed that prior to ignition the entire core is moving inward at some collapse velocity, u_c, and at the instant of ignition this kinetic energy is converted to internal energy in the microcore to reach the ignition temperature. However, the remainder of the core may still have this inward velocity at ignition. This is essentially wasted energy. The ideal situation would be for the compressed core to reach stagnation with all of the inward fluid motion converted to the internal energy of the microcore. The collapse velocity, u_c, needed for ignition may be roughly estimated as

$$u_c^2 \simeq v_{th\mu}^2 = 3\ kT_\mu/m_{DT} \qquad (21)$$

where $v_{th\mu}$ is the thermal velocity of the DT plasma at the ignition temperature. To allow a variation of this parameter we insert a factor, b, into Eq. 21 to get

$$u_c^2 = 3\ bkT_\mu/m_{DT}\ . \qquad (22)$$

If b = 0 then the ideal stagnation condition is met. Then Eq.20 becomes

$$E_c = 3\ nkT_\mu\ (\frac{4\pi}{3} R_\mu^3) + 3\ nkT\ (\frac{4\pi}{3} (R^3 - R_\mu^3)) + 3/2\ \frac{(m-m_\mu)}{m_{DT}}\ bkT_\mu\ . \quad (23)$$

We can write

$$R^3 = \frac{3m}{4\pi\rho}\ ,\ R_\mu^3 = \frac{3m_\mu}{4\pi\rho}\ ,\ C_v = \frac{3k}{m_{DT}}\ ,\ a = (\frac{\rho R_\mu}{\rho R})^3 \quad (24)$$

and Eq. 23 reduces to

$$E_c = mC_v\ [T_\mu\ (a + \frac{b}{2} - \frac{ab}{2}) + T\ (1 - a)] \quad (25)$$

or

$$E_c = mC_v\ [T_\mu\ (a + \frac{b}{2} - \frac{ab}{2}) + \frac{T_o^*\ \rho R}{m^{1/3}}\ (1 - a)] \quad (26)$$

where $T_o^* = T_o\ (\frac{3\rho_o^2}{4\pi})^{-1/3}$.

The yield can be written as

$$Y = Y_o m\ f_B(\rho R, \rho R_\mu, T_\mu) \quad (27)$$

where Y_o is the specific yield (330 MJ/mg for DT) and f_B is the fractional burnup of the fuel. The fractional burnup is a function of the core conditions at ignition. The gain on core can now be written as

$$G_c = \frac{Y_o}{C_v}\ f_B(\rho R, \rho R_\mu, T_\mu)\ [T_\mu(a + \frac{b}{2} - \frac{ab}{2}) + T_o^*\ \rho R\ (1 - a)/m^{1/3}]^{-1}\ . \quad (28)$$

The only "unknown" in this expression is the fractional burnup. This is found using the PHD-IV plasma hydrodynamic-thermonuclear burn simulation code for

combinations of ρR, ρR_μ, and T_μ. Many calculations are done to determine the ignition temperature as a function of ρR_μ. This is a threshold phenomenon where below the ignition temperature the yield is very low and any temperature above the ignition temperature results in the same yield. The temperature profiles during the burn of a DT core are shown in Fig. III.1-8. Each of these simulations gives one "data point" in this analysis. A summary of the most important calculational results is given in Table III.1-2 for different values of b. This data can be plotted in a variety of ways. Figure III.1-9 is a plot of the gain-on-core vs. ρR for different values of b. Each point on these curves uses the optimum combination of T_μ and ρR_μ to achieve the highest gain. Note that for b = 0, the maximum gain is at $\rho R = 3$ g/cm^2. However, for b > 0 the gain is maximized at higher values of ρR. This parameter study was limited to the range $2 \leq \rho R \leq 5$ because the compressions needed for $\rho R > 5$ g/cm^2 are enormous. Figure III.1-10is a plot of the combinations ofρR_μ and T_μ that result in ignition for different values of ρR. As the central ignitor becomes larger the ignition temperature is reduced. This is important because a lower ignition temperature implies that a smaller collapse velocity is needed. This result is only apparent when b > 0. Figure III.1-11 is a plot of the gain on core as a function of b for different values of ρR_μ. When b = 0 the smallest value of ρR_μ gives the highest gain on core. However, the gain on core drops off very rapidly for this case. As the value of ρR_μ increases the magnitude of G_c decreases but it is less sensitive to the parameter, b. This shows that for large values of ρR_μ the target

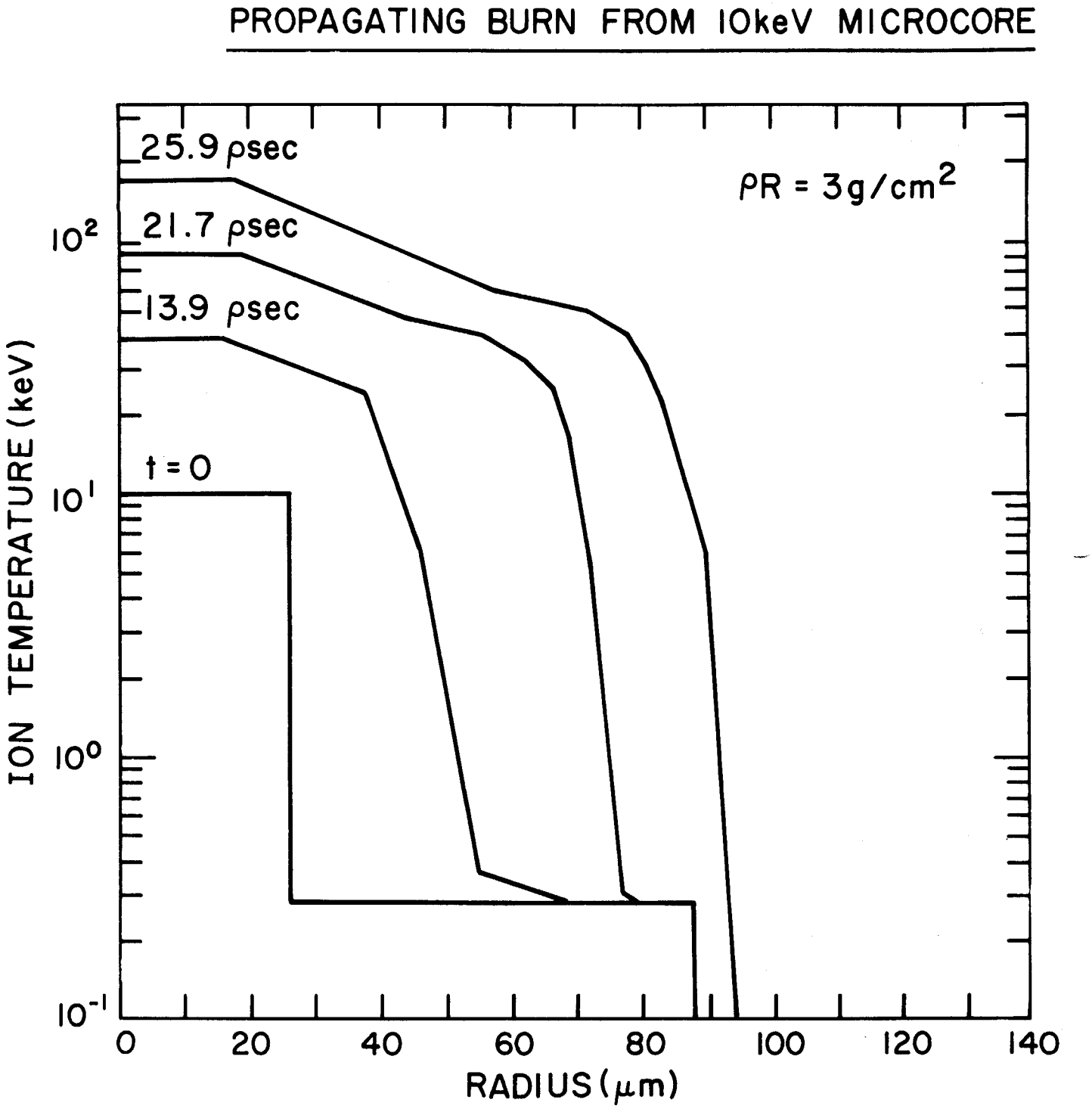
PROPAGATING BURN FROM 10keV MICROCORE
25.9 ρsec
21.7 ρsec
13.9 ρsec
t = 0
ρR = 3g/cm²
ION TEMPERATURE (keV)
10²
10¹
10⁰
10⁻¹
0
20
40
60
80
100
120
140
RADIUS (μm)

Fig. III.1-8

Table III.1-2 Results of PHD-IV Thermonuclear Burn Parameter Study

ρR	ρR_μ	T_μ	Gc b=0	0.2	0.5	0.8	1.0
2	0.4	17	2690	318	137	87.2	70.2
2	0.5	11	2342	507	206	136	108
2	0.7	6	1785	669	345	232	191
2	1.0	5	900	555	353	258	219
3	0.4	10	5286	727	317	202	163
3	0.5	7	4969	962	436	281	228
3	0.7	5	4316	1233	595	392	320
3	1.0	4	3066	1287	688	470	387
3	3.0	3	226	226	226	226	226
5							
5	0.5	6	3811	1063	510	336	273
5	0.7	5	4294	1392	691	460	376
5	1.0	4	4019	1577	825	559	460
5	1.5	3	3374	1713	985	691	577

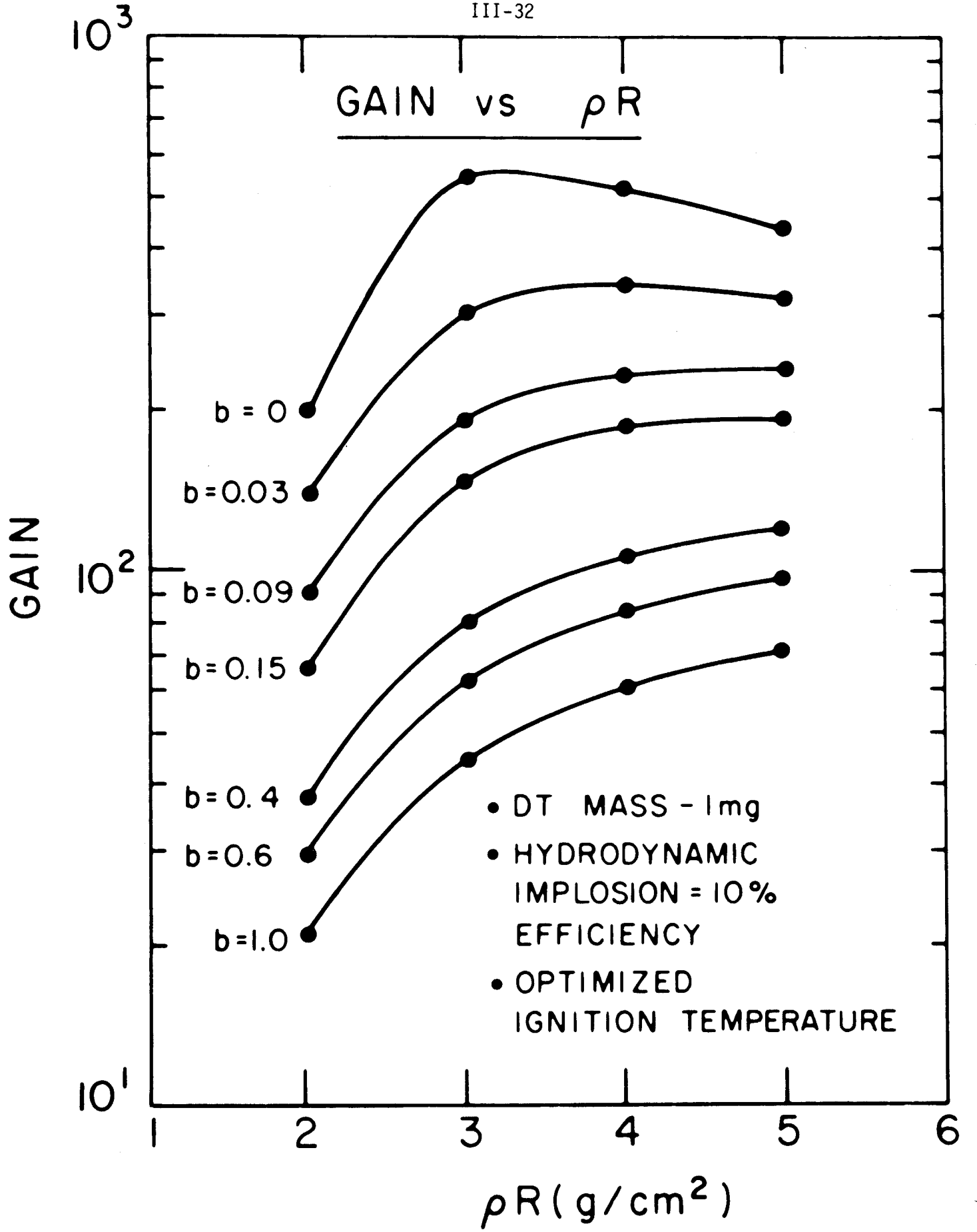
GAIN vs ρR
GAIN
10^3
10^2
10^1
b = 0
b = 0.03
b = 0.09
b = 0.15
b = 0.4
b = 0.6
b = 1.0
• DT MASS - 1mg
• HYDRODYNAMIC IMPLOSION = 10% EFFICIENCY
• OPTIMIZED IGNITION TEMPERATURE
1
2
3
4
5
6
ρR (g/cm²)

Fig. III.1-9

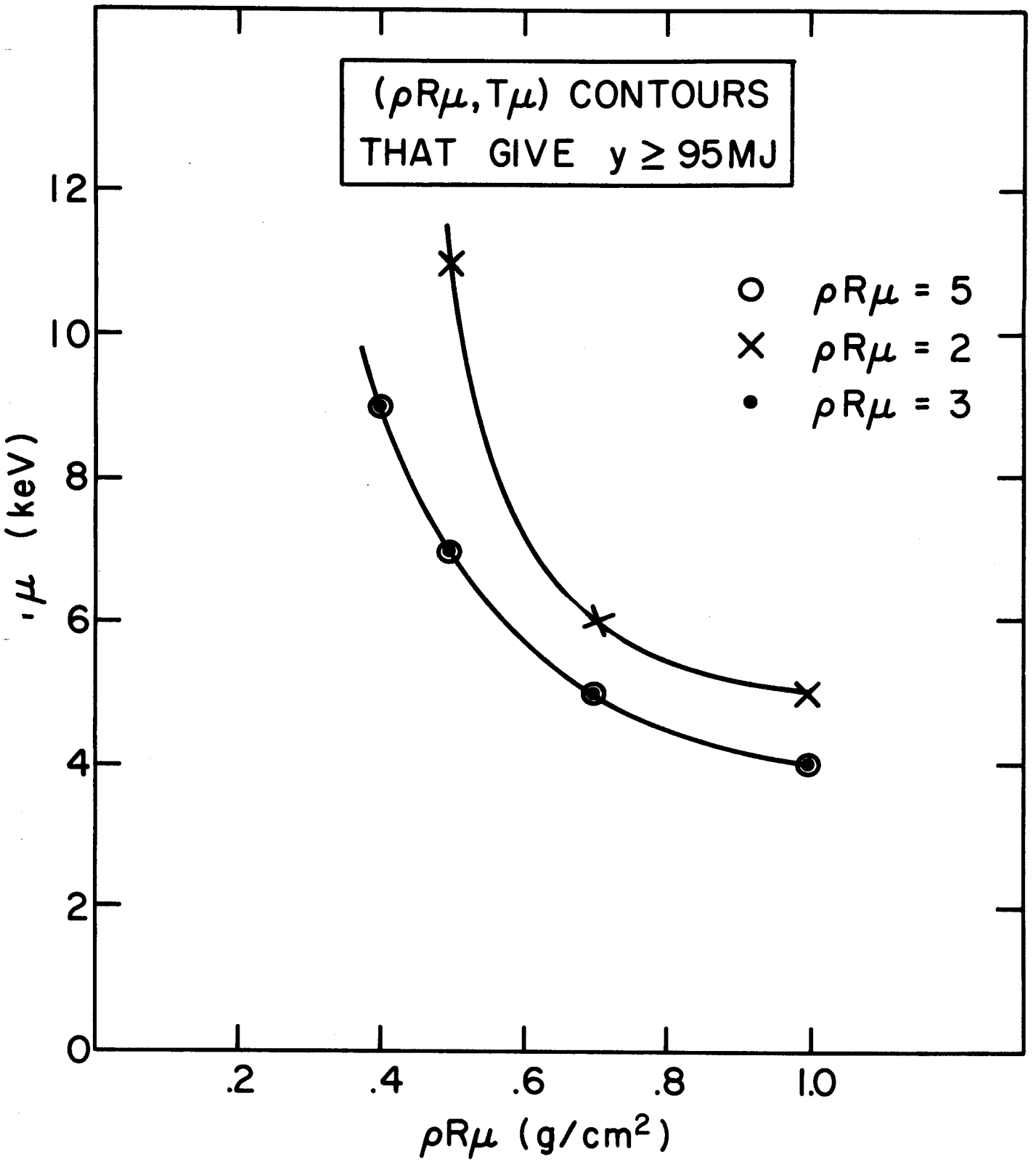
(ρRμ, Tμ) CONTOURS
THAT GIVE y ≥ 95MJ
ρRμ = 5
ρRμ = 2
ρRμ = 3
Tμ (keV)
ρRμ (g/cm²)
0
2
4
6
8
10
12
.2
.4
.6
.8
1.0

Fig. III.1-10

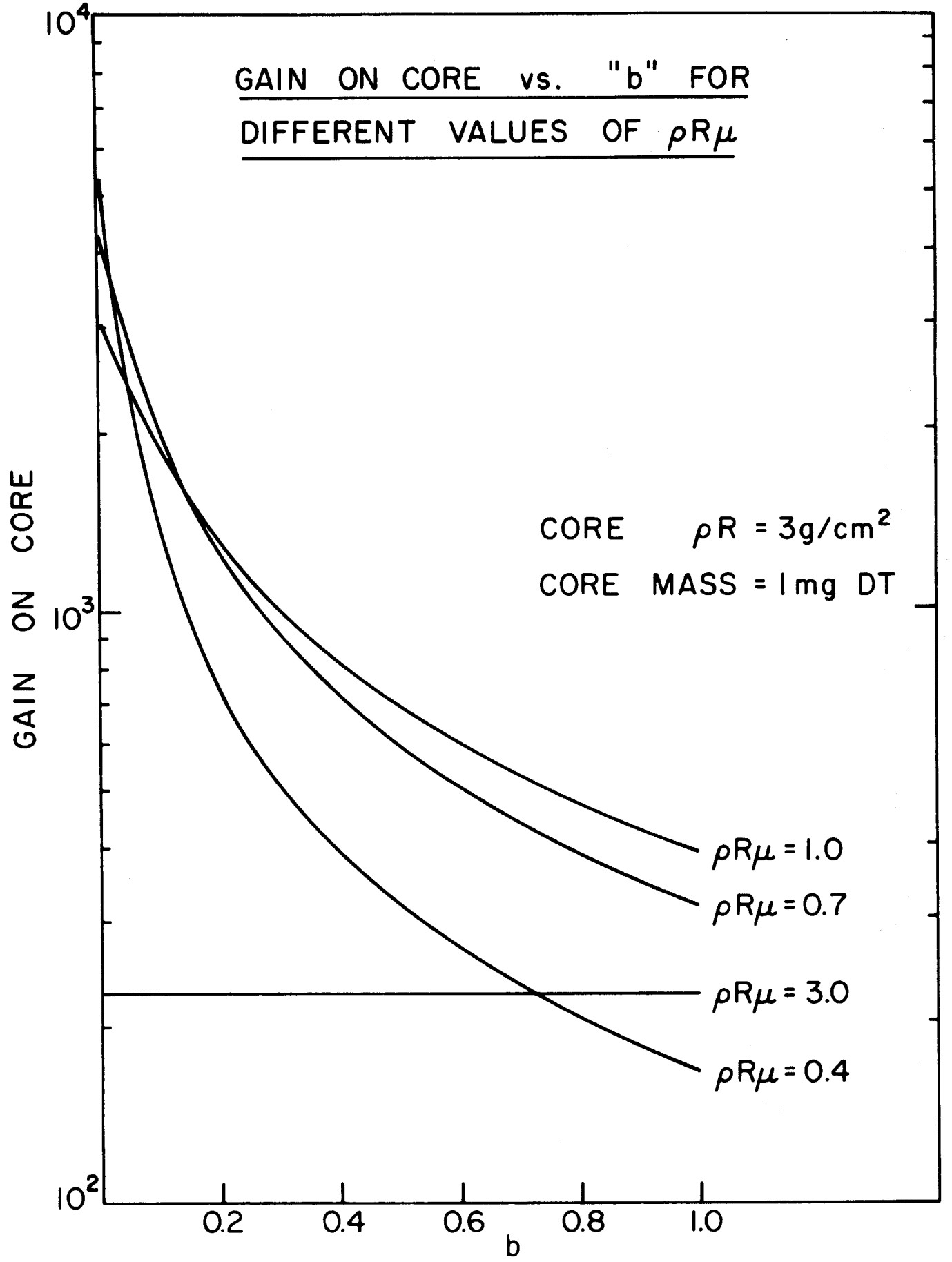
GAIN ON CORE vs. "b" FOR
DIFFERENT VALUES OF ρRμ
GAIN ON CORE
10^4
10^3
10^2
CORE ρR = 3g/cm^2
CORE MASS = 1 mg DT
ρRμ = 1.0
ρRμ = 0.7
ρRμ = 3.0
ρRμ = 0.4
0.2
0.4
0.6
0.8
1.0
b

Fig. III.1-11

response will be less sensitive to small differences in the implosion dynamics. If a gain on core of 2000 is desired (to combine with an implosion efficiency of 10% to give a pellet gain of 200) then Fig. III.1-11 shows that the ρR_μ = 1.0 g/cm^2 and ρR_μ = 0.7 g/cm^2 cases will allow this result using larger values of b than the ρR_μ = 0.4 g/cm^2 case. However, it also shows that there is very little room for error, b $\simeq$ 0.1, in the target fabrication and the laser pulse shape if gains of 200 are necessary. If the target gain could be relaxed to 50 by the use of a high efficiency driver, such as an ion beam, then a gain on core of 500 (η_H = 10%) would allow b to be greater than 0.6. Such target designs would have a much higher chance of success than the high gain targets. However, for laser drivers, the lower gain means that a higher pulse repetition frequency and/or laser energy are necessary to achieve the same fusion power. This is in conflict with the technological problems associated with power supplies and their lifetimes.

In conclusion, target gains greater than 50 appear difficult to achieve without very optimum conditions. This leads one to look for high energy, high efficiency drivers such as ion beams to maximize the likelihood of success.

References for Section III.1

1. G. Moses, R. Conn, S. Abdel-Khalik, "Power Supply Costs for Inertial Confinement Fusion Reactors", UWFDM-243, March 1978.

2. G. Moses, "Thermonuclear Burn Characteristics of Compressed DT Pellets", UWFDM-198, Feb. 1977.

III.2. First Wall Protection by a Buffer Gas

III.2.A. Introduction

The first wall in a laser fusion reactor is exposed to neutrons, X-rays and charged particle debris from the target explosion. The long mean free path of 14 MeV neutrons results in a volumetric heating of the first wall and blanket. Their major influence on first wall design is the result of radiation damage effects and this is discussed in Part V. The ion debris and soft X-rays have short mean free paths (~ μm's) in most structural materials and thus represent a surface heat source to the first wall. Typically, about 70% of the fusion power is in the form of neutrons and the remaining 30% of the energy is partitioned between the X-rays and ions. Therefore, the surface heat flux on the first wall will be as much as 43% of the neutron wall loading. For neutron wall loadings of 1-2 MW/m^2, considered to be necessary for economically sized reactors, the average surface heat flux is 0.4-0.9 MW/m^2. However, this average value is not indicative of the problem because the target explosion releases this energy in 100 ps - 10 ns pulses. Therefore, the instantaneous heat flux can be as high as 2.5×10^8 MW/m^2! Parametric studies of first wall response to X-rays and ions with varying energy spectra show that a bare unprotected first wall will not survive the surface temperature rise resulting from this very high instantaneous heat flux.

The first wall must therefore be protected from the ions and soft X-rays. A variety of schemes have been proposed to do this. The concept used in the SOLASE design was to fill the cavity with a low pressure

(0.1-1.0 torr) noble gas. This scheme was also chosen for the hybrid study and a more complete analysis of the idea is included in this report. Xenon gas is chosen for this study because it has better X-ray attenuation and ion stopping properties than either helium, neon or argon. Since the spectra of X-rays and ions from the target explosion are not well characterized at this time we also choose xenon because it attenuates the widest range of possible spectra. The gas pressure is chosen so that the instantaneous heat load on the first wall is reduced to an acceptable value by attenuation of the X-rays and ions in the gas. This heats the gas to 1-10 eV temperatures and it then reradiates this energy to the first wall in a pulse of about 1-2 msec duration. This reduces the instantaneous heat flux by about 10^5 and the first wall can then conduct energy to the coolant behind it without experiencing an excessive temperature rise.

There are many questions that must be answered in regard to the feasibility of this concept. These include:

a) What are the X-ray and ion spectra resulting from the target explosion?

b) What is the attenuation of the X-ray and ion energy in the gas?

c) How does the gas behave once it has absorbed the X-ray and ion energy?

   i) Gas reradiation mechanisms and radiation transport

   ii) Gas hydrodynamic motion and overpressure on the first wall

d) How does the first wall respond to the reradiated energy and overpressure?

i) Evaporation

ii) Mechanical and thermal stresses

e. Can the laser beams be propagated to the target without interference from laser induced gas breakdown?

i) Where does breakdown occur

ii) Will breakdown affect target performance

All of these questions have been addressed in varying degrees. The following sections will concentrate on questions (c) and (d). The analysis will be presented in a parametric fashion along with the parameters used for the hybrid design.

III.2.B. X-ray and Ion Attenuation in the Xenon Buffer Gas

A great number of parametric calculations have been done to determine the first wall temperature rise as a function of the X-ray and ion spectra and the density of buffer gas. These results are reported elsewhere and will not be repeated here. In the SOLASE-H study it was decided to investigate the possibility of using a metallic first wall protected by xenon gas. In the SOLASE conceptual reactor design the first wall was made of graphite. A metallic first wall will attenuate the transmitted X-rays in a shorter distance than the graphite and hence will suffer a greater surface temperature rise. However, a metallic right circular cylinder is an attractive reactor cavity configuration so that it is important to determine whether this wall and the gas protection offer a viable design. The first wall temperature rise for stainless steel is plotted as a function of the blackbody temperature of the X-ray spectrum for different gas densities in Fig. III-2-1. These calculations have been done for a 10 MJ X-ray yield.

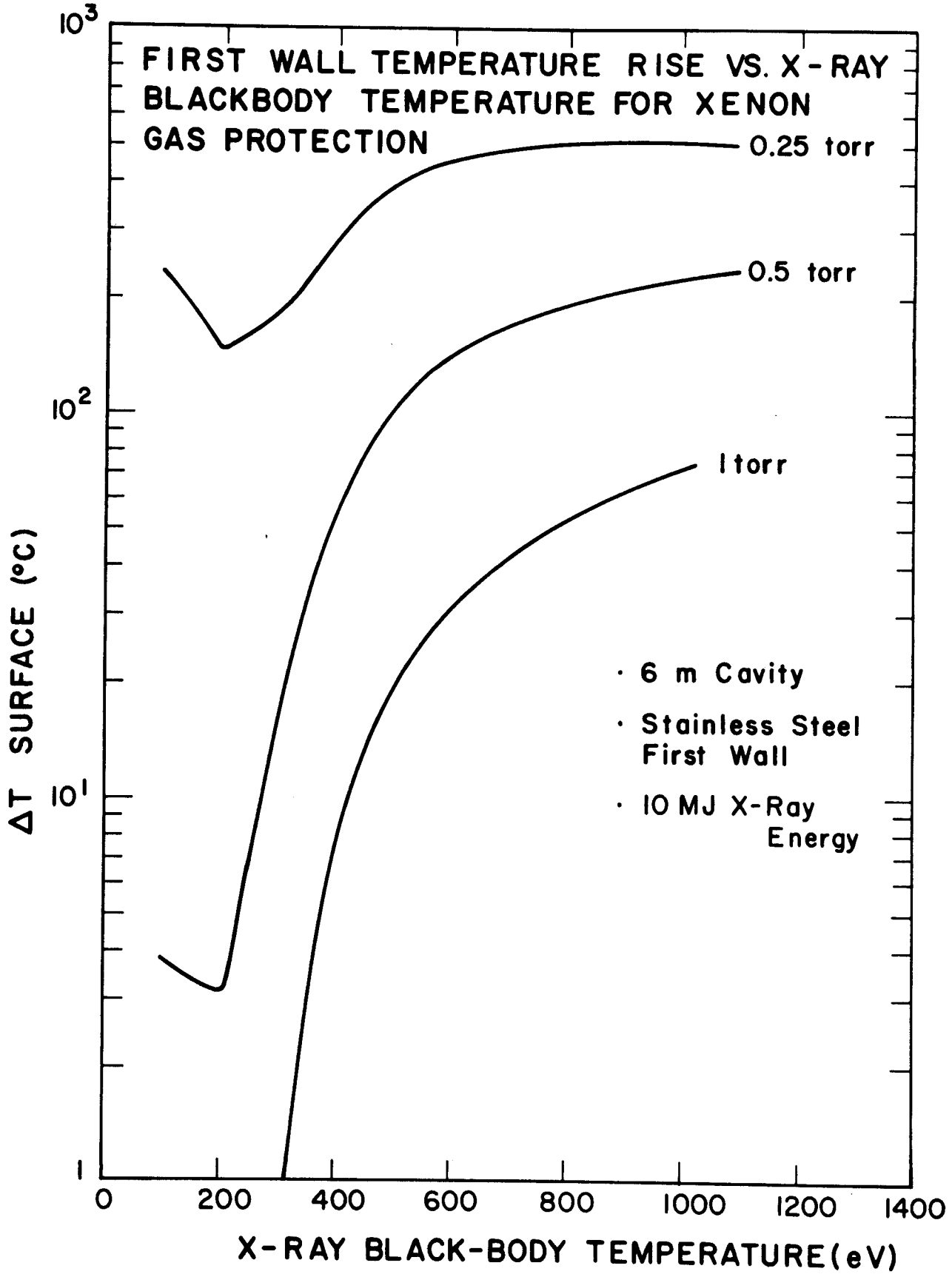
FIRST WALL TEMPERATURE RISE VS. X-RAY BLACKBODY TEMPERATURE FOR XENON GAS PROTECTION
0.25 torr
0.5 torr
1 torr
· 6 m Cavity
· Stainless Steel First Wall
· 10 MJ X-Ray Energy
ΔT SURFACE (°C)
10³
10²
10¹
1
0
200
400
600
800
1000
1200
1400
X-RAY BLACK-BODY TEMPERATURE(eV)

Fig. III.2-1

However the temperature rise scales linearly with the energy so that these curves can be used to determine the response for an arbitrary amount of X-rays. We see that the temperature rise in the wall is very large for the entire range of spectra if only 0.25 torr of Xe gas is included in the cavity. This must be added to the temperature rise resulting from the gas reradiation as well. For 0.5 torr the situation is much better. Here the temperature rise can be limited to less than 10°C if the blackbody temperature of the X-rays is less than 275 eV. The 1 torr case would limit the temperature rise to 10°C for blackbody spectra less than 425 eV. Because no pellet spectra are available, it is impossible to assess, at this time, whether the calculations prove or disprove the viability of protecting metal first walls with xenon gas. However we can proceed by computing the first wall response to the reradiated energy from the gas. This will be an equally important factor in proving the viability of this design. These next calculations will in no way depend on the X-ray and ion spectra from the target. We will simply assume that all of the X-ray and ion energy is absorbed by the gas.

III.2.C. Buffer Gas Reradiation

The X-ray and charged particle debris from the target explosion deposit their energy in the xenon buffer gas in about 1-10 μsec. This heats the gas to temperatures of 1-10 eV and the gas subsequently reradiates the energy to the first wall.

There are three processes by which the gas may reradiate this energy: bremsstrahlung (free-free transitions), line radiation (bound-bound) and recombination (bound-free). Not all of these mechanisms will occur to the same degree for a given plasma density and temperature range. It will be shown that recombination is the dominant radiation process for the xenon buffer gas.

The mean ionization level of a plasma is determined by the balance between collisional and radiative atomic processes. Ionization occurs by a collisional mechanism:

$$A + e^- \rightarrow A^+ + e^- + e^- \ ,$$

while recombination may be either collisional, via three-body recombination, or radiative:

$$A^+ + e^- + e^- \rightarrow A + e^-$$

$$A^+ + e^- \rightarrow A + h\nu \ .$$

The distribution of charge states will be described by the following expression:

$$\frac{n_{z-1}}{n_z} = \frac{n_e(\alpha_z + n_e Q)}{n_e S_{z-1}} \qquad (1)$$

where n_z = number density of ions in ionization state z

α = radiative recombination coefficient

Q = coefficient for three-body collisional recombination into the ground state

S = collisional ionization coefficient

Usually a plasma can be described by one of two limiting cases. Where collisional recombination is the dominant mechanism (i.e. $\alpha << Qn_e$), the energy is distributed according to the Boltzmann distribution law and the Saha equations will apply:

$$\frac{n_{z-1}}{n_z} = \frac{n_e Q}{S_{z-1}} \qquad (2)$$

or

$$\frac{n_{z-1}}{n_e n_z} = \frac{Q}{S_{z-1}} = 2 \frac{u_m}{u_{m-1}} \left(\frac{2\pi m_e kT}{h^2}\right)^{3/2} e^{-I_m/kT} \qquad (3)$$

where the u_m are the electronic partition functions. This is known as the Local Thermodynamic Equilibrium, or LTE, model.

When the electron density is low, radiative recombination is more important than three-body recombination. Then $\alpha >> n_e Q$ and

$$\frac{n_{z-1}}{n_z} = \frac{\alpha_z}{S_{z-1}} \quad . \qquad (4)$$

This is called the Coronal Limit. The plasma is described by the Corona model, wherein collisional ionization is balanced by radiative recombination. In this model electrons are assumed to have a Maxwellian distribution and most ions are to be found in their ground state with only a negligible fraction in the excited states. Since the ionization and recombination processes are both two-body, the distribution of ionization levels will not be dependent on density.

LTE or Saha equilibrium describes high density plasmas such as those found in electromagnetic discharge tubes while the Corona model is suitable for low density plasmas such as stellar atmospheres or exploding wire plasmas. Figure III.2-2 shows the mean ionization of xenon as a function of temperature as calculated by both the Saha equations and the Corona model.

A quantitative criterion for the application of the Corona model is the following:

$$n_e < 10^{16} \, (kT_e)^{7/2} \, cm^{-3} \qquad (5)$$

for kT_e in eV. For the densities and temperatures ($n \sim 10^{15} - 10^{16}$, $T_e < 10$ eV) of interest for the xenon buffer gas, this condition is met.

The equations of state for xenon are readily generated using the Steady State Corona model. The fraction n_z of z-times ionized atoms is determined from the following set of equations:

$$\alpha_z \, n_z = S_{z-1} \, n_{z-1} \, , \; 1 \leq z < z_m \qquad (6)$$

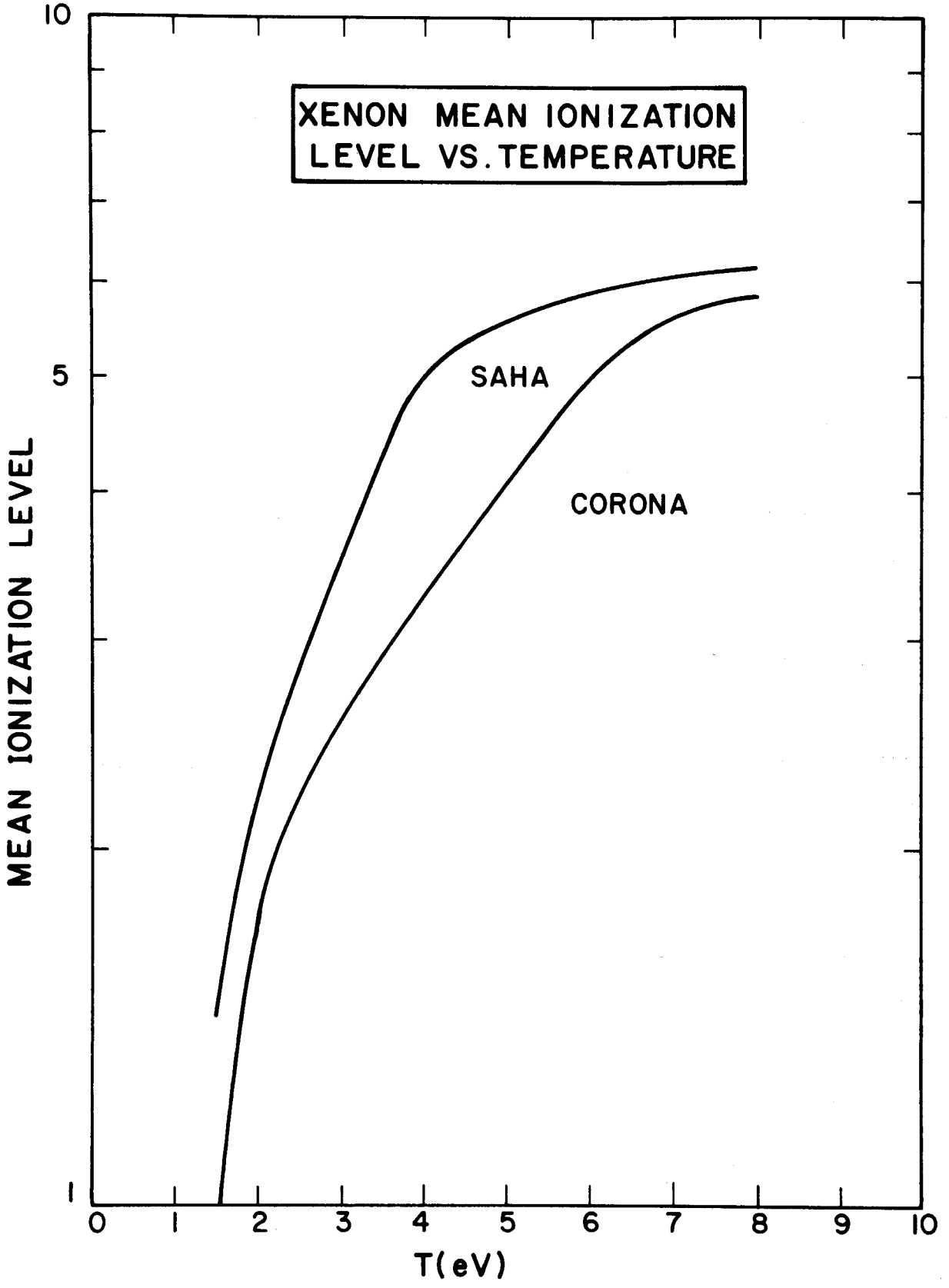
XENON MEAN IONIZATION LEVEL VS. TEMPERATURE
SAHA
CORONA
MEAN IONIZATION LEVEL
T(eV)
10
5
1
0
1
2
3
4
5
6
7
8
9
10

Fig. III.2-2

where z_m is the atomic number of the atom. These relations are solved to yield

$$n_z = \left(\frac{S_0}{\alpha_1}\right)\left(\frac{S_1}{\alpha_2}\right).....\left(\frac{S_{z-1}}{\alpha_z}\right) n_o \qquad (7)$$

$$n_o = \left[1 + \sum_{z=1}^{z_m} \left(\frac{S_0}{\alpha_1}\right)\left(\frac{S_1}{\alpha_2}\right).....\left(\frac{S_{z-1}}{\alpha_z}\right)\right]^{-1} \qquad (8)$$

where

$$\frac{\alpha_{z+1}}{S_z} = 7.87 \times 10^{-9} \frac{I_z}{n_z} \left(\frac{I_z}{kT}\right)^{3/2} \exp\left(\frac{I_z}{kT}\right) . \qquad (9)$$

Here I_z is the ionization potential in eV for ions in charge state z going to z+1, kT is the plasma temperature in eV, and n_z is the number of outer shell electrons in state z. The ionization potentials for the elements up to Lawrencium (z=103) have been calculated by Carlson, et al.

The fraction of atoms in charge state z, n_z, is calculated with a computer using the above equations. This quantity is shown for xenon in Fig. III.2-3 as a function of z for selected temperatures.

The mean ionization level of the gas will depend on temperature and is given by

$$\bar{z} = \sum_{z=1}^{z_m} z n_z . \qquad (10)$$

Figure III.2-4 shows $\bar{z}$ for xenon.

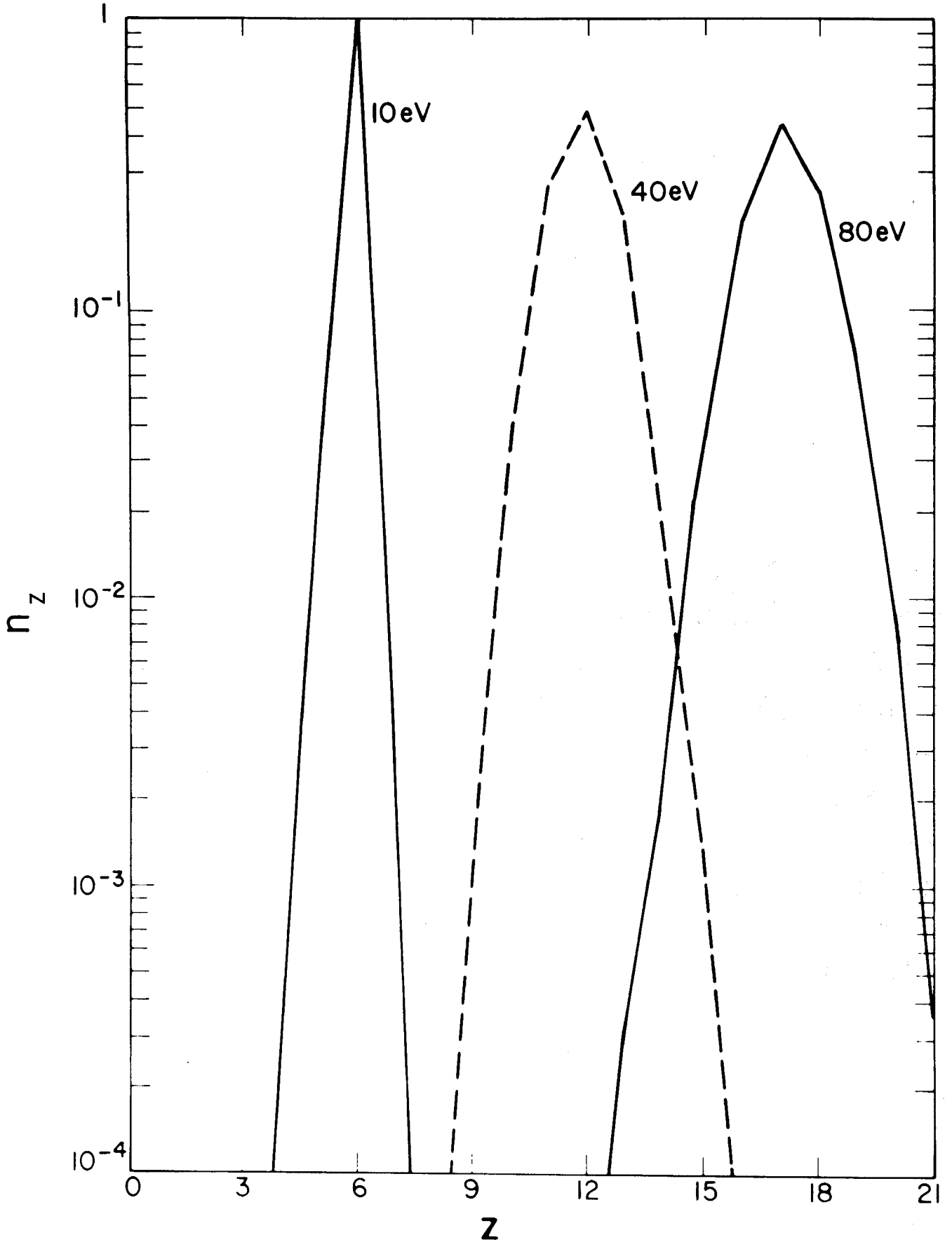

Fig. III.2-3

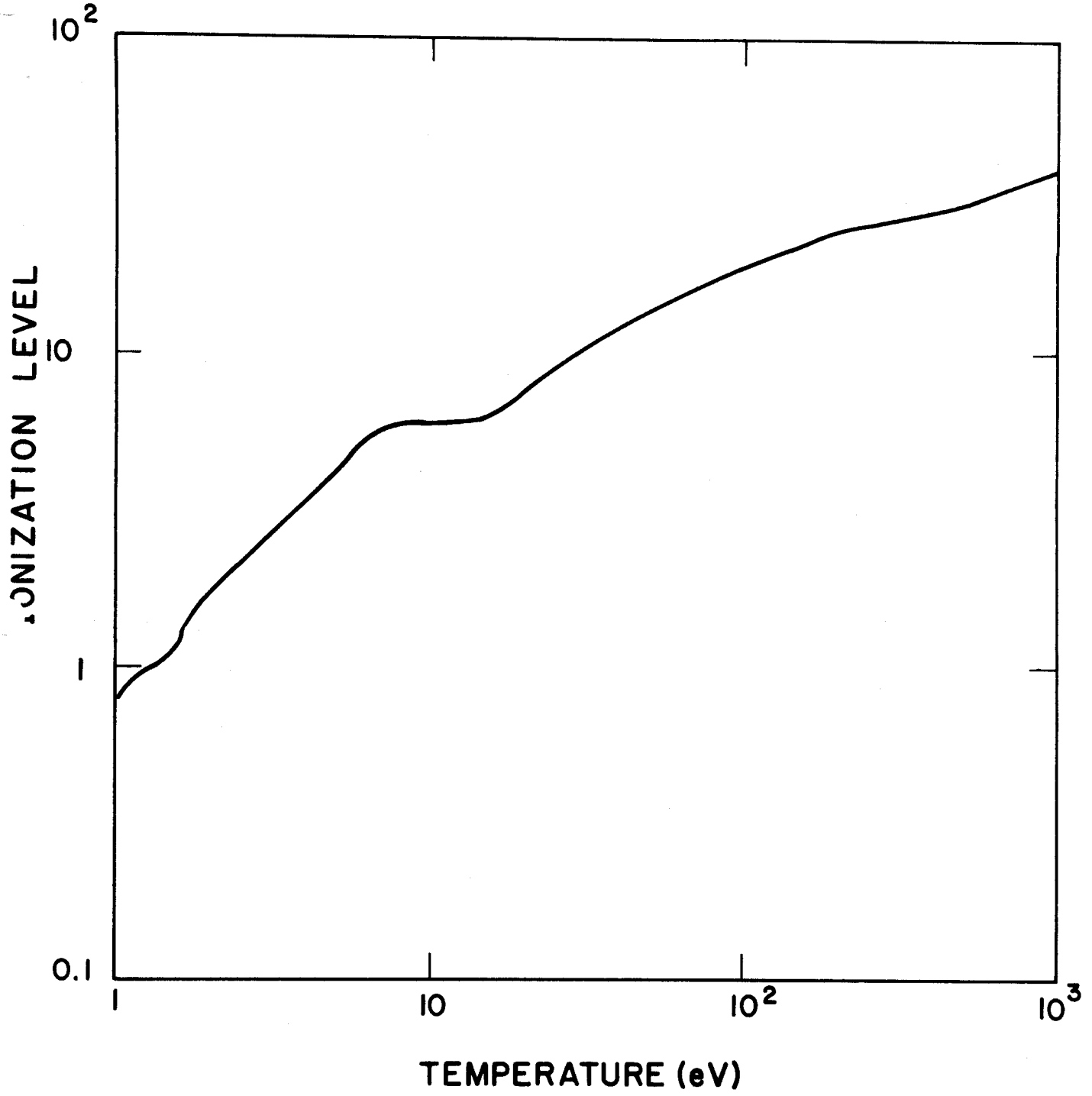

Fig. III.2-4

For an atom in charge state z, the total internal energy will be the sum of the ionization energy and the kinetic energy. If [z] ≡ the greatest integer less than z, the total internal energy per atom will be

$$E \doteq \frac{3}{2}(1 + \bar{z})\ kT + \sum_{j=1}^{[z]} I_j + (\bar{z} - [z])\ I_{[z]+1} \ . \qquad (11)$$

Armed with this knowledge, the radiated power density due to recombination may be determined from

$$P_r = 1.69 \times 10^{-32}\ n_e\ T_e^{1/2} \sum_z \left[z^2\ n(z)\ \frac{I_{z-1}}{T_e}\right] \text{ J/cm}^3\text{-s} \qquad (12)$$

where I_{z-1} and T_e are in eV.

The power density of bremsstrahlung radiation is given by:

$$P_{Br} = 1.57 \times 10^{-34}\ n_e\ T_e^{1/2} \sum [z^2 n(z)] \text{ J/cm}^3\text{-s} \qquad (13)$$

for T_e in eV and the summation is carried out over all ionization states z.

The ratio of bremsstrahlung to recombination radiation will be

$$\frac{P_{Br}}{P_r} = 9 \times 10^{-3}\ \frac{\Sigma[z^2 n(z)]}{\Sigma[z^2 n(z)(\frac{I_{z-1}}{T_e})]} \ . \qquad (14)$$

For the conditions of interest here this ratio is on the order of 10^{-3} so that bremsstrahlung carries a negligible fraction of the energy and thus can be safety omitted from the calculations.

For an optically thin plasma the power density of line radiation may be found via

$$P_L = 7 \times 10^{-25}\, T_e^{1/2}\, n_e \sum_{n,z} \frac{\sigma^z}{g^z_{Ni}}\, n(z)\, \exp\left(\frac{-E^z_{Ni}}{T}\right) \text{ W/cm}^3 \qquad (15)$$

where g^z_{Ni} is the oscillator strength for the electronic transition N→i which is characterized by an energy difference E^z_{Ni} for the atom in charge state z.

Since most energy radiated will be in the resonance line, i.e. the transition N→N+1 for N the principal quantum number of the outer shell electron in state z, one can simplify Eqn. 15 by assuming that this is the only important transition. The oscillator strength for this transition is assigned the value one-half; E^z_{Ni} may be estimated from

$$E^z_{Ni} = (\alpha z)^2 \frac{m_o c^2}{2} \left[\frac{1}{N^2} - \frac{1}{(N+1)^2}\right] \qquad (16)$$

where α is the fine structure constant and $m_o c^2$ is the electron rest mass (0.511 MeV). With these simplifications Eq. 15 becomes

$$P_L \simeq 3.5 \times 10^{-25}\, T^{-1/2}\, n_i^2\, \bar{z} \left\langle \exp\left[-\frac{E^2_{Ni}}{T}\right]\right\rangle \text{ W/cm}^3 \,. \qquad (17)$$

For the temperatures and densities of interest the ratio of this quantity to the recombination radiation is on the order of 10^{-4}. So we see that bremsstrahlung and line radiation play a negligible part in the reradiation process and that recombination is the important mechanism.

In Fig. III.2-5 is plotted the instantaneous value of the recombination power density in xenon as a function of the xenon pressure for differing amounts of deposited energy. [The xenon pressure is computed at room temperature so that it is actually a measure of the density (1 torr = 3×10^{16} cm^{-3}). The volume of xenon that is uniformly heated by the specified energy

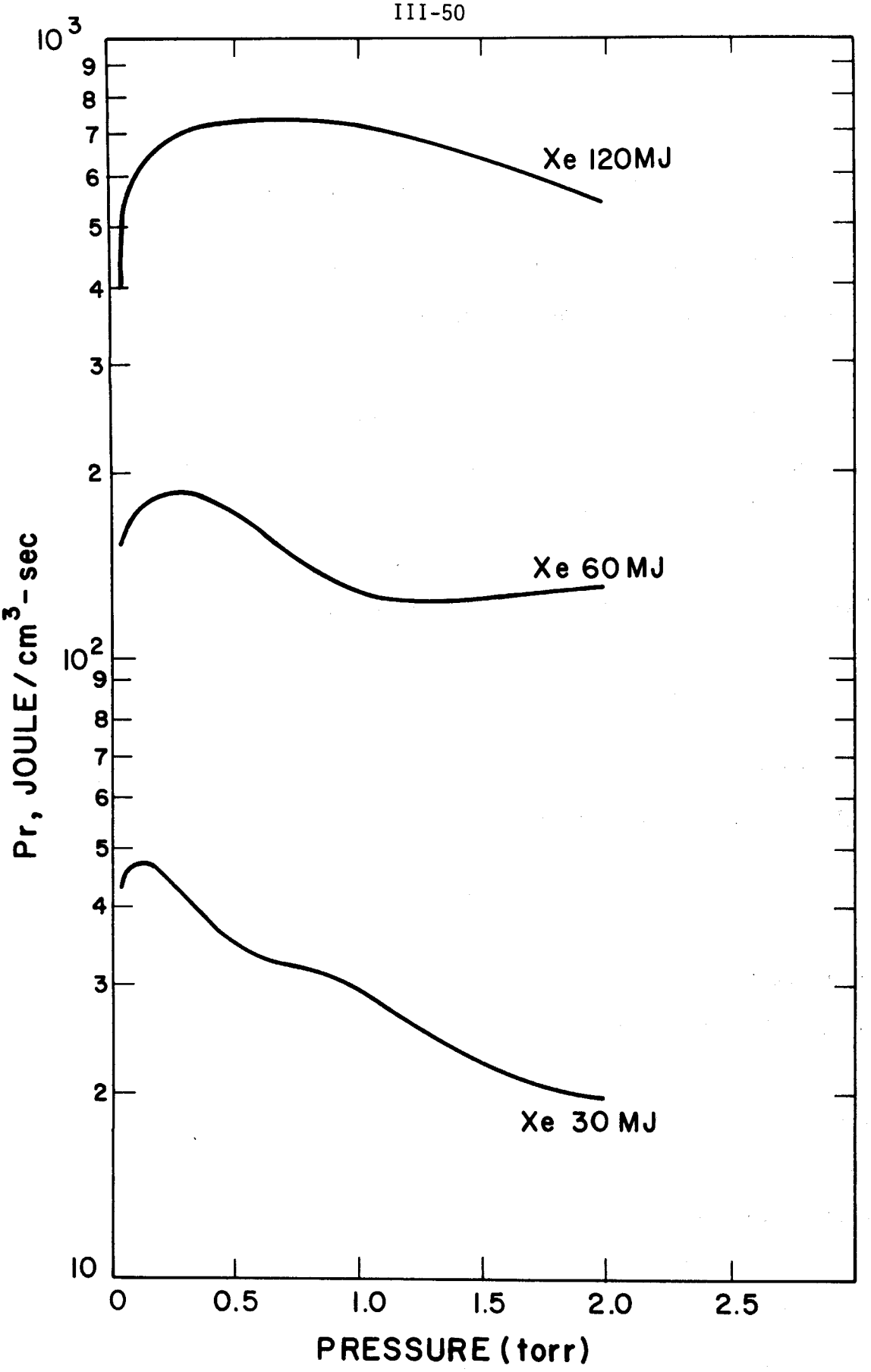
Xe 120MJ
Xe 60 MJ
Xe 30 MJ
Pr, JOULE/cm³-sec
PRESSURE (torr)
10³
9
8
7
6
5
4
3
2
10²
9
8
7
6
5
4
3
2
10
0
0.5
1.0
1.5
2.0
2.5

Fig. III.2-5

inputs is 452.39 m^3 (a 6 m radius sphere). This corresponds to the volume of the hybrid cavity]. The structure in these curves results from the effects of reaching different ionization levels. The instantaneous power density does not tell the complete story though because the power density changes as the plasma radiates away its energy. The total radiated power in a 6 m cavity as a function of time for different xenon pressures is plotted in Fig. III.2-6. This was for an energy input of 60 MJ. The initial decay is nearly exponential with a decay time of about 2 msec. This is valid for the first millisecond of the reradiation. This time scale is sufficiently long that the first wall can accommodate the surface heat flux without excessive temperature rise. This is, of course, the key to the success of the gas protection concept. The gas must "hold up" the energy from the explosion for a time sufficient to allow the first wall to conduct the energy to its back surface.

III.2.D. Radiation Transport in the Buffer Gas

If the partially ionized xenon gas is optically thin then the heat flux at the first wall can be computed using the expression for the recombination radiation power density given by Eqn. 12. However, if the plasma is optically thick (i.e. the photon mean free paths are significantly shorter than the radius of the cavity) then a treatment of the radiation diffusion must be done to compute the heat flux at the first wall.

The mean free path may be calculated from the photoelectric cross-sections for the various ionization states of xenon, if they are known. Or it may be found using k_ν, the absorption coefficient,

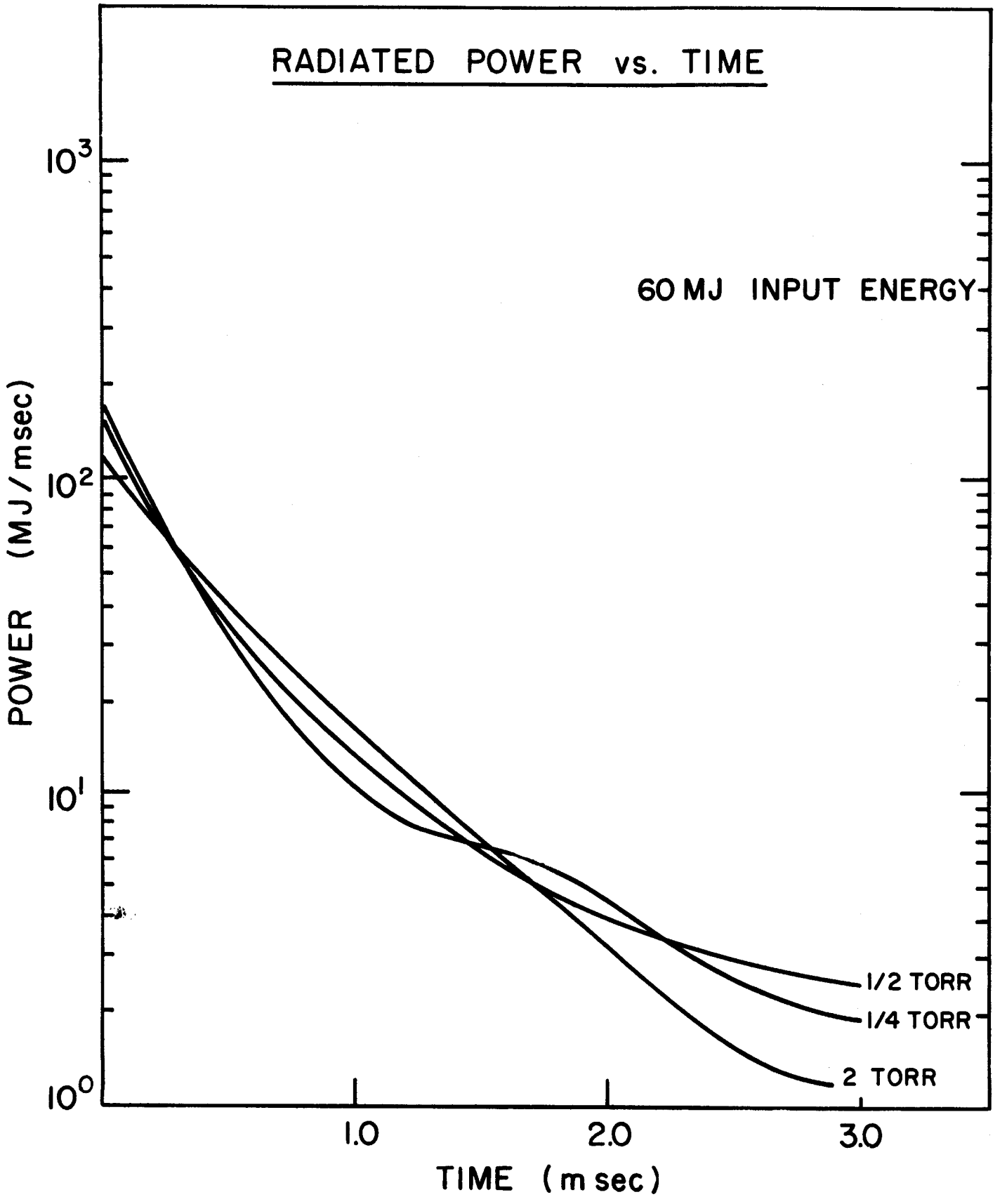
RADIATED POWER vs. TIME
60 MJ INPUT ENERGY
POWER (MJ/msec)
10^3
10^2
10^1
10^0
1.0
2.0
3.0
TIME (m sec)
1/2 TORR
1/4 TORR
2 TORR

Fig. III.2-6

$$k_\nu = \frac{32\pi^2}{3\sqrt{3}} \frac{e^6 z^2 N}{h^4 c \nu^3} I$$

$$= 0.96 \times 10^{-7} \frac{N z^2}{T_{o_K}^2} \frac{2x_L}{x^3} \text{ cm}^{-1} \qquad (18)$$

where $x_1 = I/kT$, $x = h\nu/kT$, N is the density (cm^{-3}), and z is the charge state. The mean free path is the reciprocal of this quantity. This formula is valid for high energy photons ($h\nu > I$) which are absorbed by atoms and ions in the ground or a low excitation state.

In either case the mean free paths are found to be from 10-50 cm. Since this is less than 1/10 of the chamber radius, the assumption of optical thinness is a poor one and absorption and re-emission should be taken into account. This can be done if the photoelectric cross-sections for neutral and ionized states of xenon are known so that the full radiation transport calculation may be carried out. These cross sections can be approximated using a semi-classical model of the atom. These calculations are currently being carried out.

However, it is instructive to use a heuristic approach to the problem where we calculate the photon diffusion time and compare it with the time over which the energy is radiated away. If λ is the mean free path of the photon and c its speed, then

$$t_d \simeq \frac{R^2}{\lambda c} = 2.4 \times 10^{-7} \text{ sec} \qquad (19)$$

using typical parameters (R = 6 m, $\lambda \simeq 50$ cm). This diffusion time is very short compared to the source time, i.e. the rate at which recombination photons are created. This implies that the photon diffusion will cause any initial temperature gradient in space to flatten out almost instantaneously; that is, become isothermal. In addition, this means that the radiation diffusion process does not significantly affect the rate at which the heat flux is delivered to the first wall. The diffusion time is an order of magnitude less than the free streaming transit time to the wall, but remains three orders of magnitude less than the characteristic time of the reradiation process. This is a very important result for it shows that although the radiation is diffusion limited, the reradiation process itself is the most important factor governing the rate at which the gas loses energy.

III.2.E. Buffer Gas Motion

Nonuniform energy deposition profiles resulting from the attenuation of X-rays and pellet debris in the buffer gas creates pressure gradients. These in turn lead to hydrodynamic motion of the gas. This hydrodynamic motion, in the form of a pressure wave, results in an overpressure on the first wall. In the next section it will be shown that the gas response is indeed in the form of a pressure wave and not a shock wave. In this section we present the model used to describe the response of the buffer gas to the energy deposition from the target debris and X-rays.

The buffer gas response is modelled by the hydrodynamics computer code, FIRE. This code solves the one fluid-one temperature plasma hydrodynamics equations in one spatial dimension. It uses lagrangian coordinates and tabulated equation of state data for the pressure and internal energy that were generated using the Corona model (see Section III.2.C). Radiation can be treated using either a pure radiative power loss term in the temperature equation or by using an effective radiation temperature approximation for radiation transport. The thermal conductivity of xenon at low temperatures is fitted to experimental results and this is matched at high temperatures to the formula of Spitzer. The first wall is modelled as a zero velocity boundary condition on the outside of the spherical plasma and the overpressure is determined by the pressure in the outermost spatial zone in the plasma. A standard explicit finite difference solution to the equation of motion is employed. This requires a Courant condition to maintain numerical stability. The coupled temperature equations are solved using an implicit Crank-Nicholson finite difference method with the nonlinear coefficients evaluated explicitly.

III.2.F. Results of Gas Response to Deposited Energy

III.2.F-1. Nonuniform Temperature Profile

For the purposes of calculating the buffer gas response in the laser fusion hybrid cavity it was assumed that the pellet X-ray and ion debris

energy were deposited in the gas in the profile shown in Fig. III.2-7. This energy deposition profile was obtained from X-ray and ion attenuation calculations in the SOLASE study. In the hybrid study it simply serves as a convenient model because no specific X-ray and ion spectra are used. This energy/atom profile corresponds to profiles of temperature and charge states as shown in Fig. III.2-8. Here the 6 m radius spherical cavity is divided into 6 concentric shells of 1 m thickness for the model calculation. (It should be noted that each of these six regions is further divided into finite difference zones.) This particular temperature and charge state distribution is for 60 MJ of deposited energy and 0.25 torr of xenon. They are computed using the Corona model. The 60 MJ of deposited energy might correspond to a total pellet yield of 200 MJ, assuming 30% of the energy is in X-rays and ions. The radiated power density in MJ/ms is plotted as a function of time following the energy deposition in Fig. III.2-9. In this calculation the pure radiation loss approximation was used. It is seen that the initial exponential decay time is about 1 msec. The total energy radiated as a function of time is shown in Fig. III.2-10. Here it is seen that 90% of the 60 MJ is radiated in 3 msec. Figure III.2-11 is a radius-time plot of the gas motion during the reradiation time. Each line on the plot follows the trajectory of mass shells that originated at equally spaced radii at time t=0. The very smooth and gentle trajectories indicate that no shock wave is present and that the overpressure on the first wall

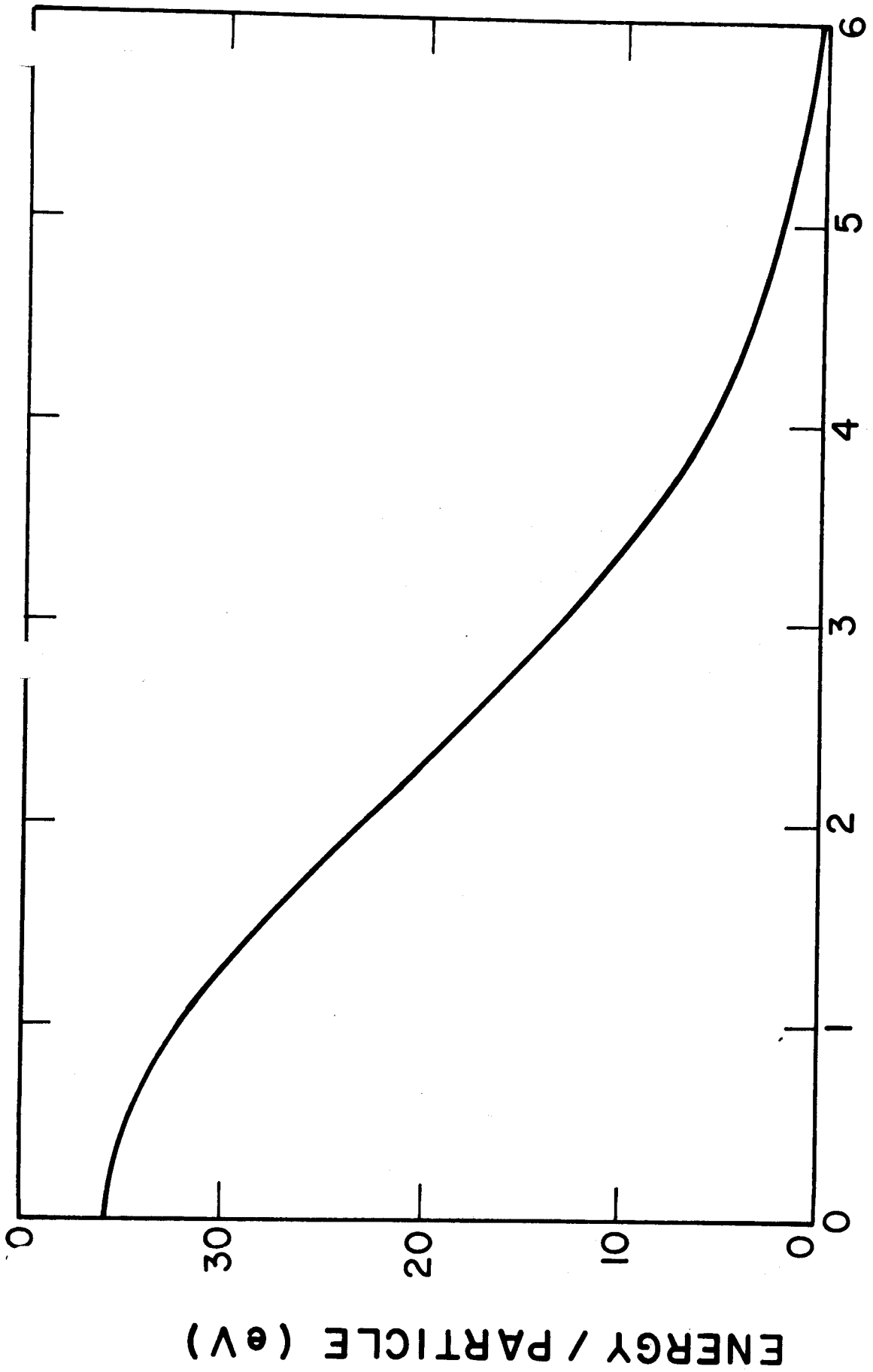

Fig. III.2-7

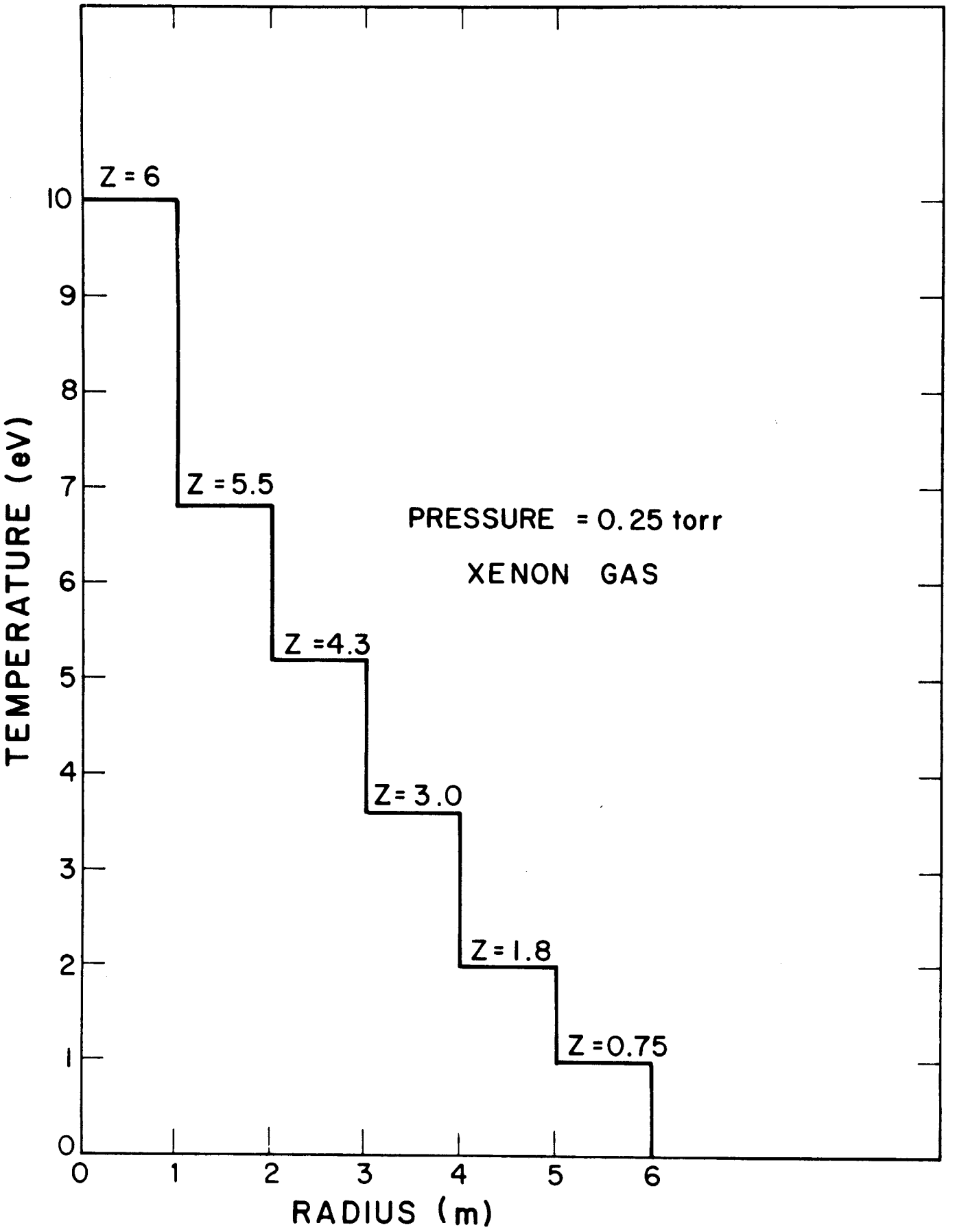
Z = 6
Z = 5.5
Z = 4.3
Z = 3.0
Z = 1.8
Z = 0.75
PRESSURE = 0.25 torr
XENON GAS
TEMPERATURE (eV)
RADIUS (m)
0
1
2
3
4
5
6
7
8
9
10

Fig. III.2-8

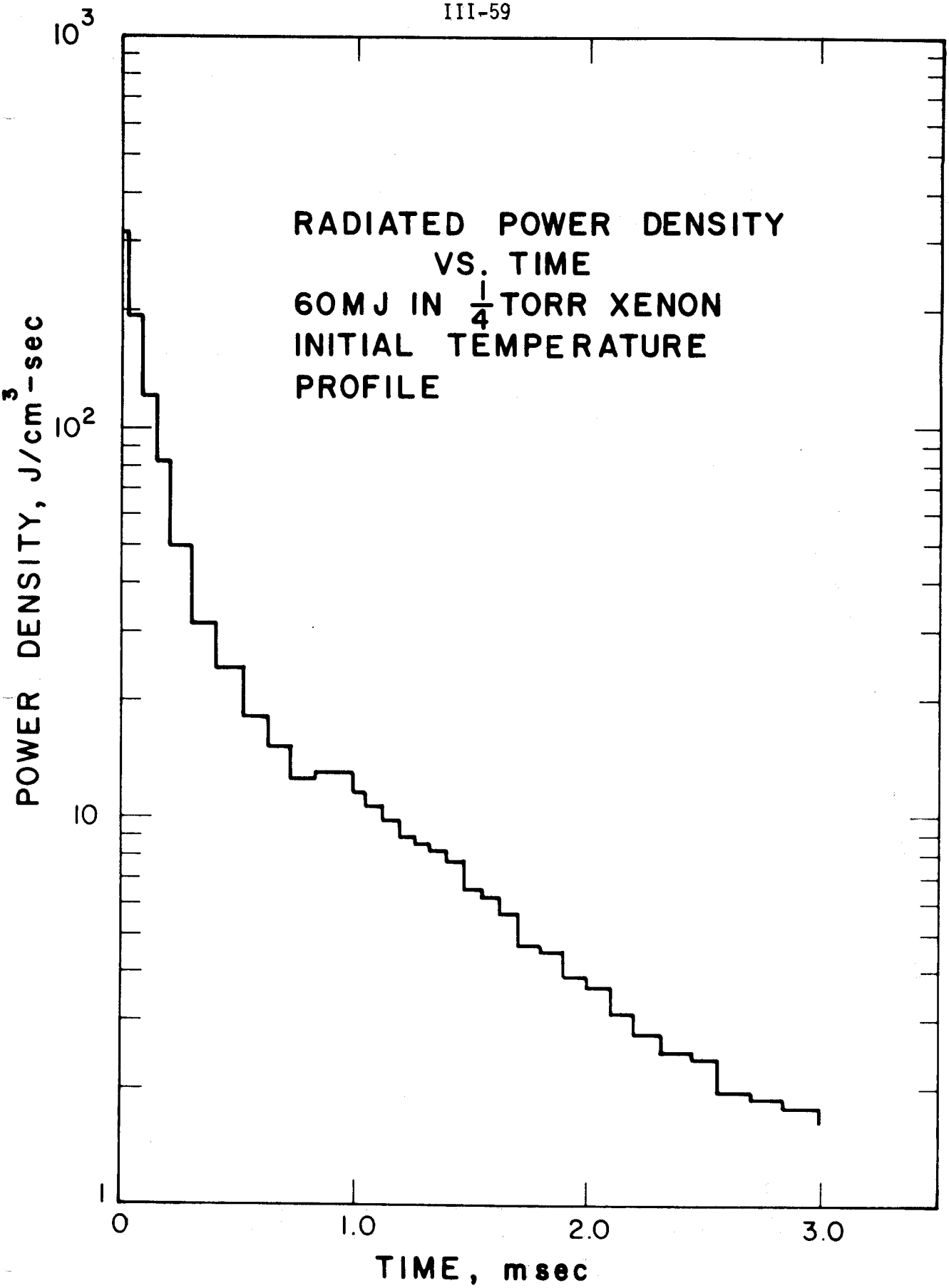
RADIATED POWER DENSITY
VS. TIME
60MJ IN 1/4 TORR XENON
INITIAL TEMPERATURE
PROFILE
POWER DENSITY, J/cm³-sec
10³
10²
10
1
0
1.0
2.0
3.0
TIME, msec

Fig. III.2-9

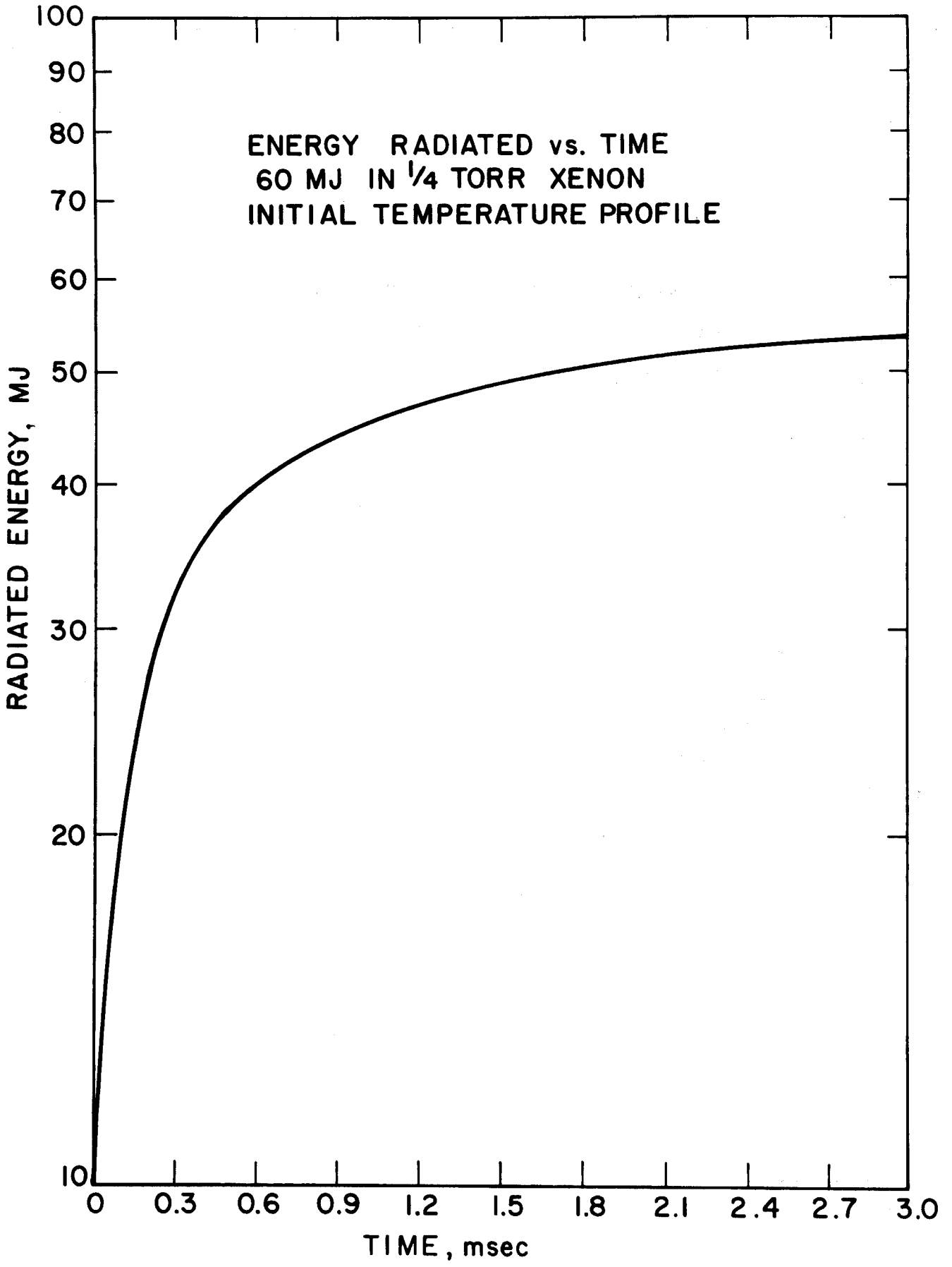
ENERGY RADIATED vs. TIME
60 MJ IN 1/4 TORR XENON
INITIAL TEMPERATURE PROFILE
RADIATED ENERGY, MJ
100
90
80
70
60
50
40
30
20
10
0
0.3
0.6
0.9
1.2
1.5
1.8
2.1
2.4
2.7
3.0
TIME, msec

Fig. III.2-10

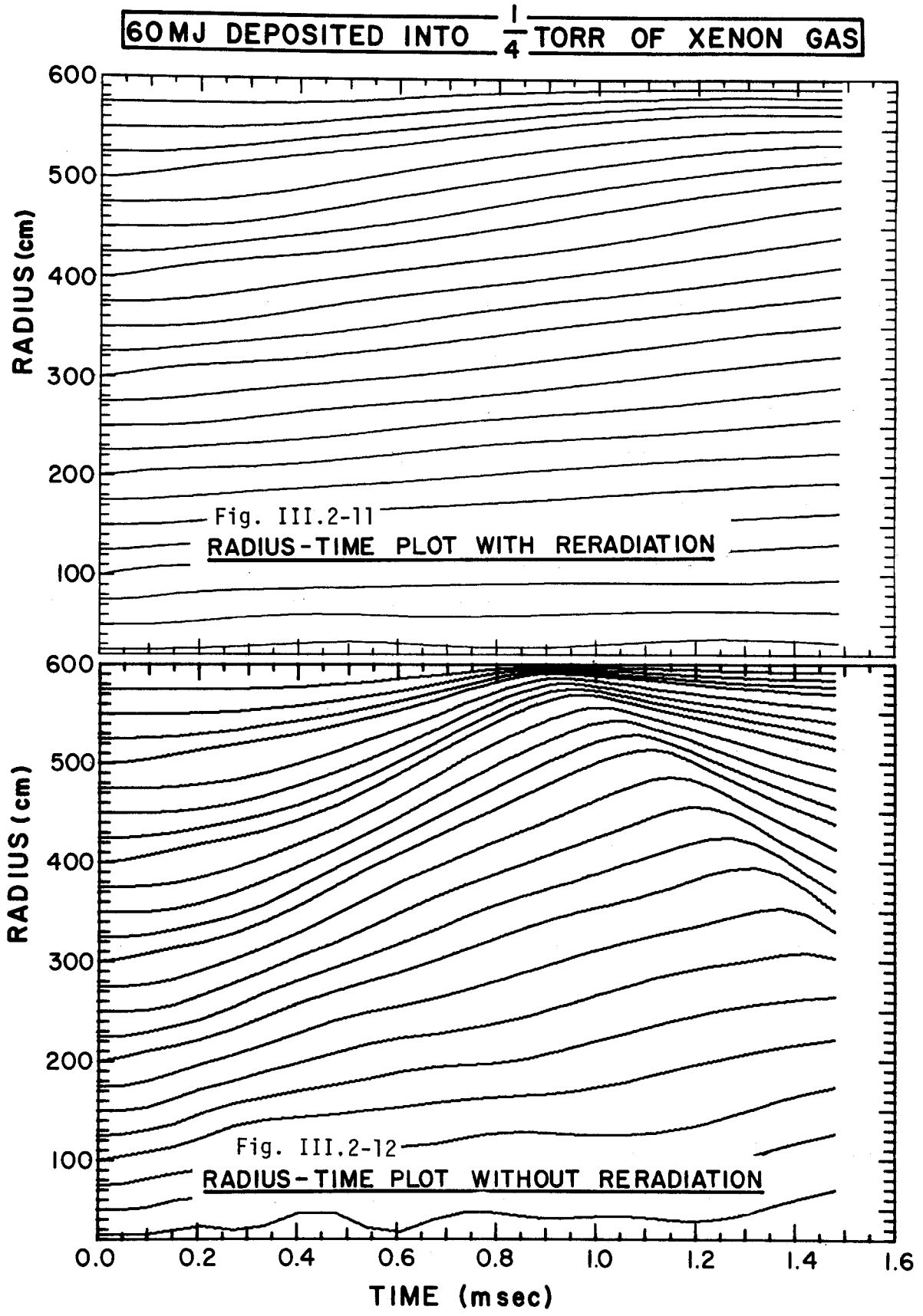
60 MJ DEPOSITED INTO 1/4 TORR OF XENON GAS
RADIUS (cm)
600
500
400
300
200
100
Fig. III.2-11
RADIUS-TIME PLOT WITH RERADIATION
RADIUS (cm)
600
500
400
300
200
100
Fig. III.2-12
RADIUS-TIME PLOT WITHOUT RERADIATION
0.0
0.2
0.4
0.6
0.8
1.0
1.2
1.4
1.6
TIME (msec)

is due to a very weak pressure wave. The maximum overpressure comes at 1.2 msec and is only 30 torr. Figure III.2-12 is a radius-time plot of the same problem only in this case the radiation loss was "turned off" in the code. The gas was not allowed to reradiate the deposited energy and there was a movement outward due to the pressure gradient established by the initial temperature profile. The behavior shown in this figure is still a pressure wave, and not a shock wave, but it is much stronger. The maximum overpressure is 90 torr and it occurs at 0.9 msec. It should be noted that the thermal conduction in the xenon is not strong enough to relax the initial temperature profile. These two figures very graphically demonstrate the coupling between the gas reradiation and the gas dynamics. The pressure wave is significantly weakened by the loss of energy to radiation. Consequently, the overpressure at the first wall is very low. Similar calculations have been done at different gas densities. The results of 60 MJ of energy deposited into a 6 m cavity filled with 0.5 torr of xenon are shown in Fig. III.2-13. In Fig. III.2-14 the total radiated energy vs. time is shown for both the Saha and Coronal model of the equation of state. There is very little difference between the two results even though the gas is well within the temperature and density range for the Coronal model.

III.2.F-2. Uniform Temperature Profile

Although the pellet X-ray and debris energy is deposited in the gas so that a nonuniform temperature profile is created, the results of section III.2.D indicate that this temperature profile might relax to

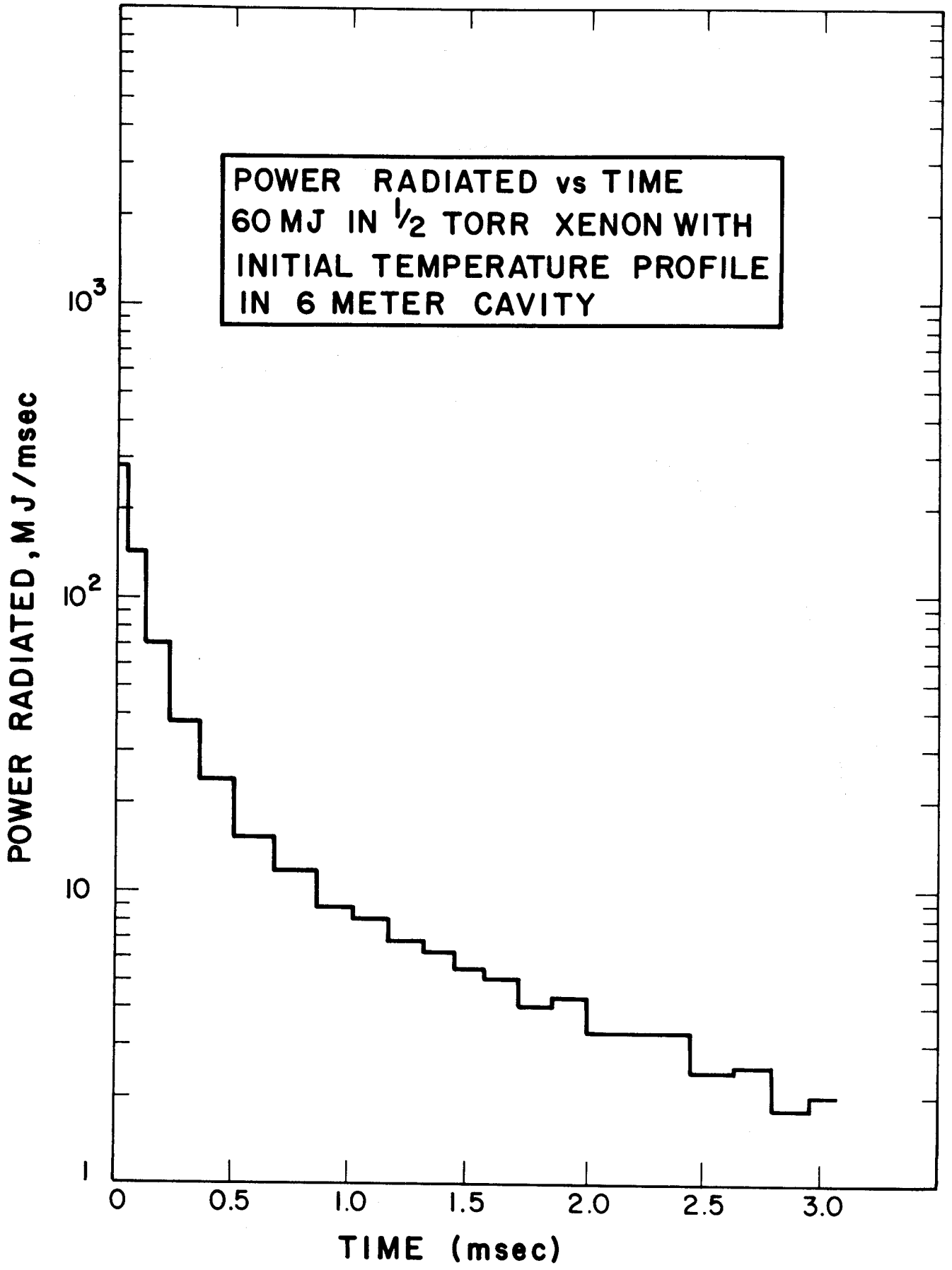
POWER RADIATED vs TIME
60 MJ IN 1/2 TORR XENON WITH
INITIAL TEMPERATURE PROFILE
IN 6 METER CAVITY
POWER RADIATED, MJ/msec
10³
10²
10
1
0
0.5
1.0
1.5
2.0
2.5
3.0
TIME (msec)

Fig. III.2-13

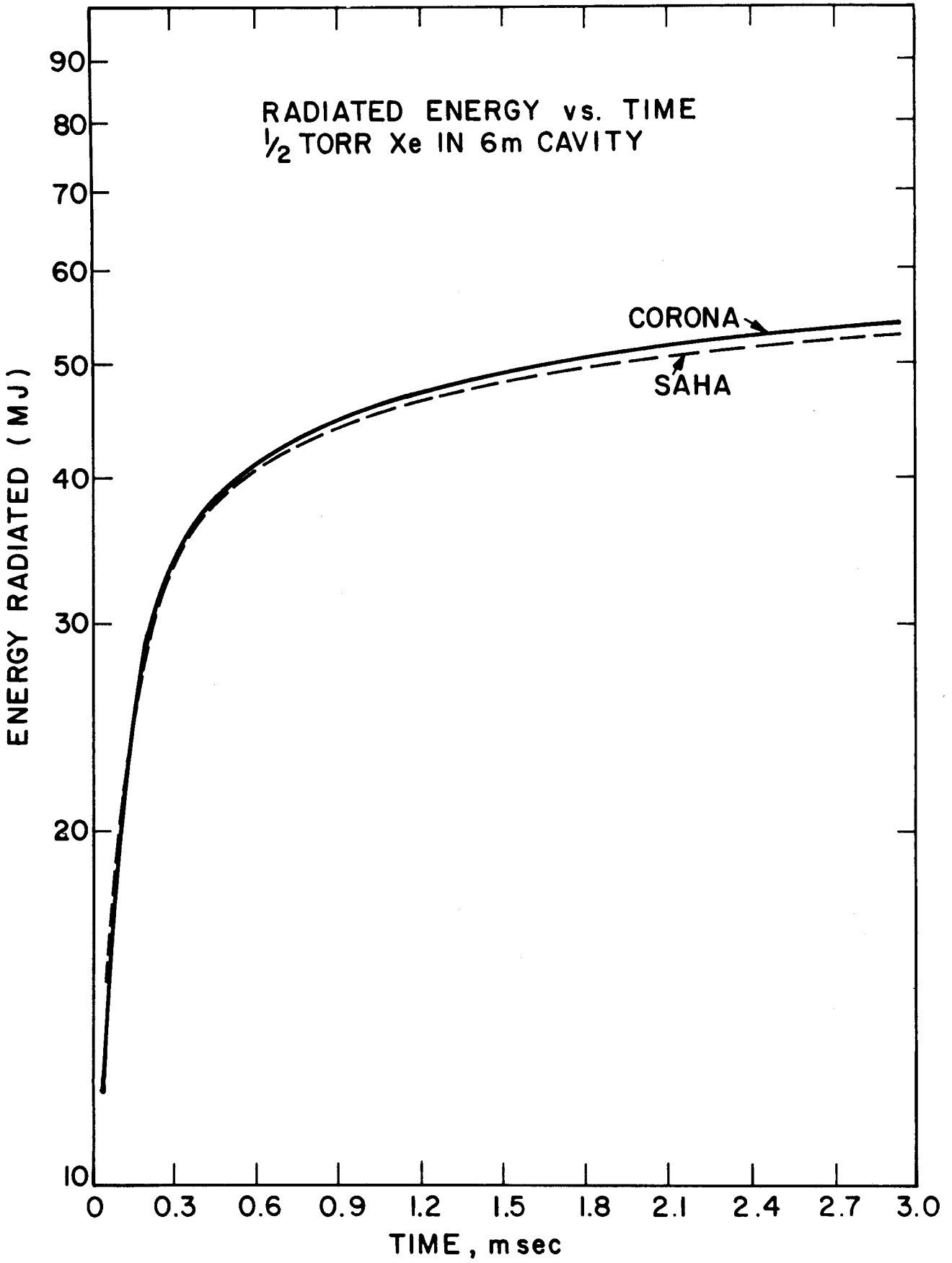
RADIATED ENERGY vs. TIME
½ TORR Xe IN 6m CAVITY
CORONA
SAHA
ENERGY RADIATED (MJ)
90
80
70
60
50
40
30
20
10
0
0.3
0.6
0.9
1.2
1.5
1.8
2.1
2.4
2.7
3.0
TIME, msec

Fig. III.2-14

a uniform temperature by the process of radiation diffusion. This should occur on microsecond time scales. Hence, a better approximation to the gas dynamics might be to assume that the energy is uniformly deposited in the gas and allow the isothermal gas to radiate using the pure radiation loss term again. This is done for the cases of 60 MJ deposited into 0.25, 0.5, and 2. torr of xenon and the results are shown in Fig. III.2-15. Because the gas is initially at a lower temperature in these cases, the exponential time constant is longer than for the nonuniform temperature profiles where the gas in the center zone was quite hot. Here it is about 2 msec rather than 1 msec. This, of course, is a desirable result because the purpose of the gas is to spread the time over which the heat flux is incident on the first wall. The rate at which the gas reradiates is nearly the same for the 0.25, 0.5, and 2. torr cases.

III.2.F-3 Comparison of Nonuniform and Uniform Temperature Profile Calculations with Pure Radiation Loss to Radiation-Hydrodynamics Calculations with Radiation Diffusion

To most accurately model this problem we require a coupled hydrodynamics-radiation diffusion calculation. This was done for the case of 0.25 torr of xenon with 60 MJ deposited into it. Because good opacity data was not available, the Rosseland mean free path was taken to be 1 cm when estimating the "radiation conductivity" in the radiation temperature diffusion equation. The same initial temperature profile that was used in the previous calculations was used as the initial condition in this calculation. Figure III.2-16 shows the plasma temperature profile in the 6 m cavity for different times during the simulation. We see that the temperature does in fact relax from its

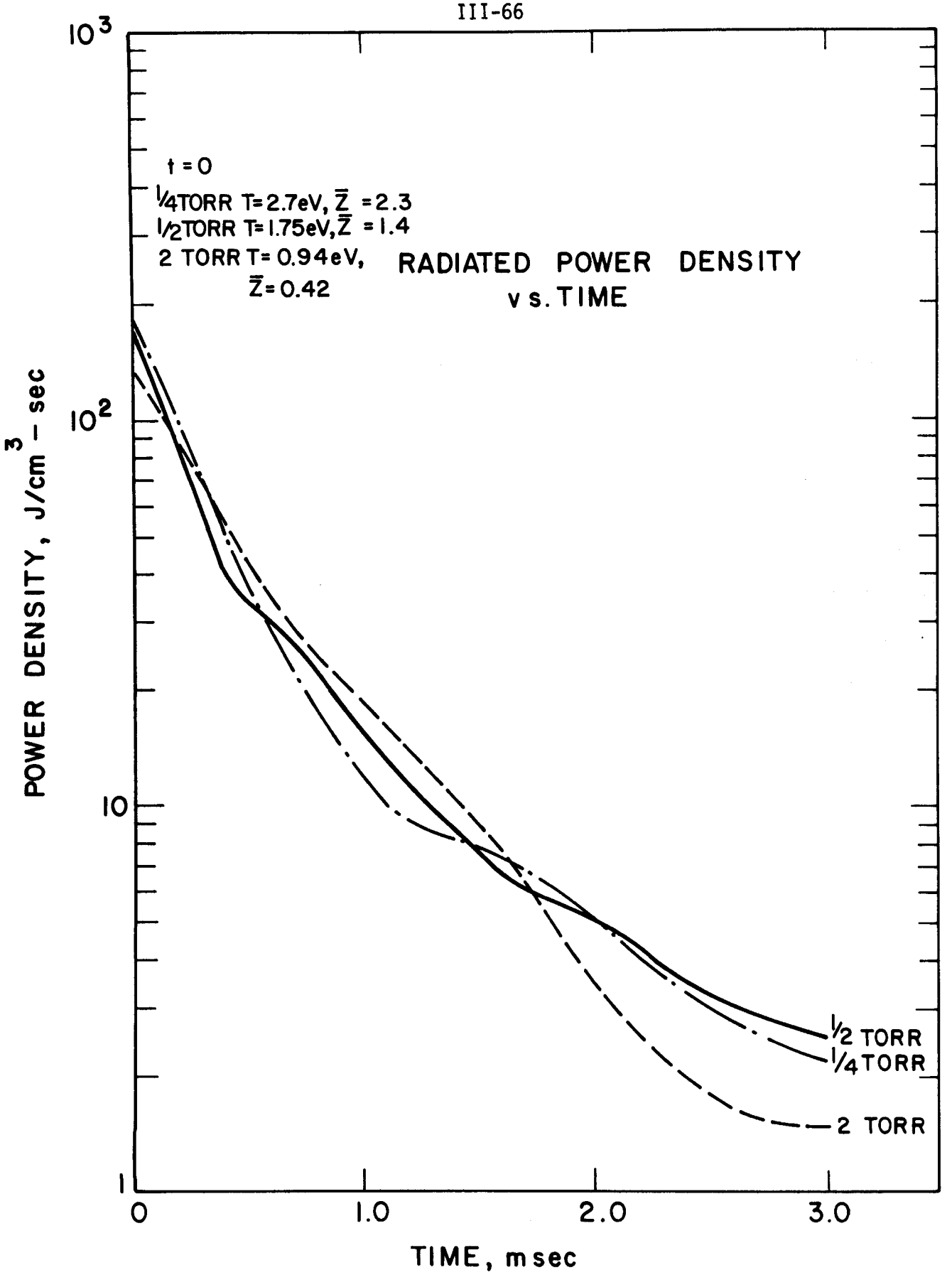
t = 0
¼TORR T=2.7eV, $\bar{Z}$ =2.3
½TORR T=1.75eV, $\bar{Z}$ =1.4
2 TORR T=0.94eV, $\bar{Z}$=0.42
RADIATED POWER DENSITY
vs. TIME
POWER DENSITY, J/cm³ - sec
TIME, msec
10³
10²
10
1
0
1.0
2.0
3.0
½ TORR
¼TORR
2 TORR

Fig. III.2-15

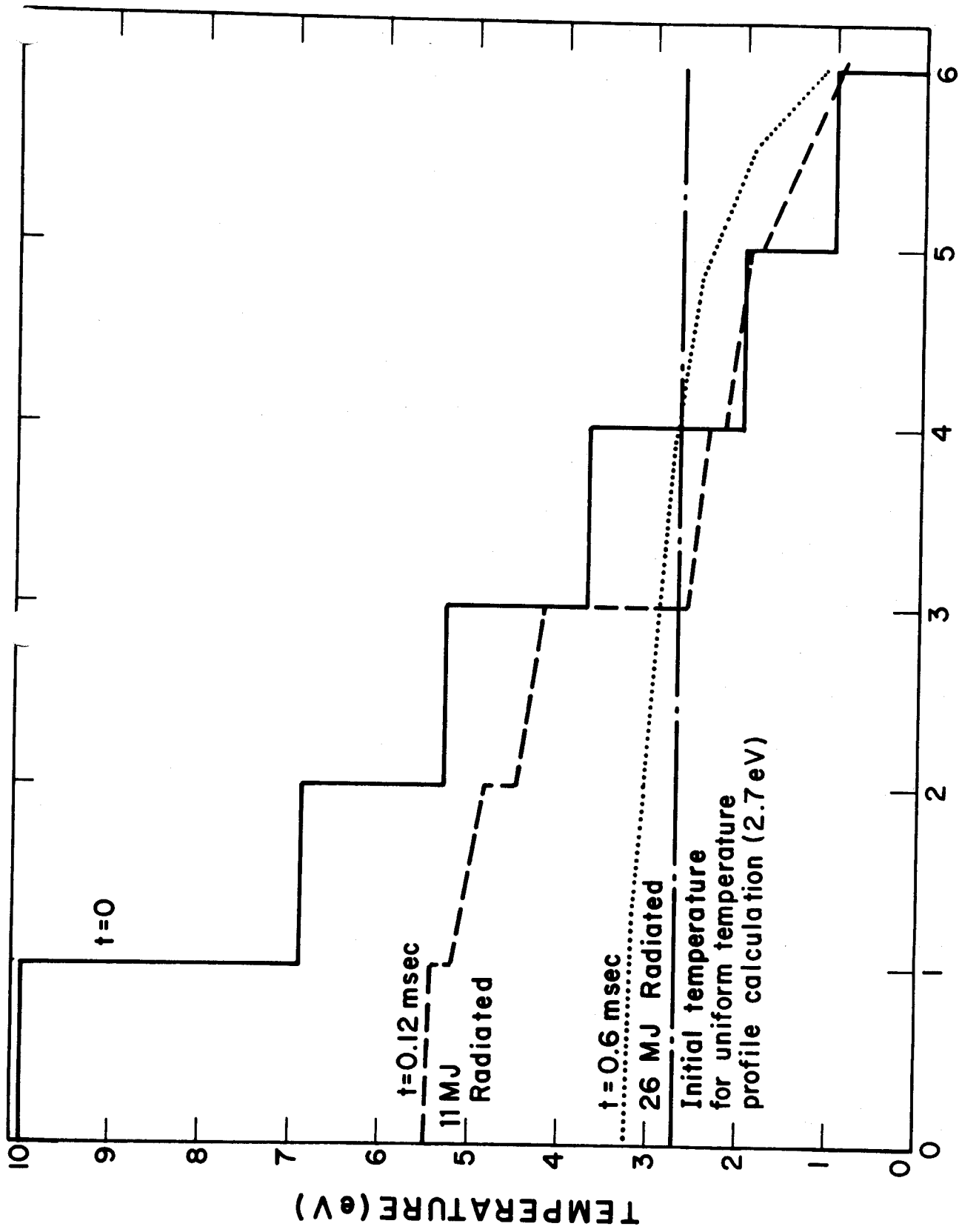
TEMPERATURE (eV)
RADIUS (m)
t=0
t=0.12 msec
11 MJ
Radiated
t=0.6 msec
26 MJ Radiated
Initial temperature
for uniform temperature
profile calculation (2.7 eV)

Fig. III.2-16

initial profile to a rather flat profile in about 0.6 msec. However, during this time the gas also radiates away about one half of its energy. Hence the uniform temperature profile discussed in the previous section is an inadequate approximation to the actual reradiation process. The three different models are compared in Fig. III.2-17. In this figure the energy radiated across the outer boundary of the plasma in the radiation diffusion calculation is converted to an effective radiated power density to compare with the other two models. The model with no radiation diffusion and an initial temperature profile radiates most strongly at early times because the plasma in the cavity center is hot, 10 eV. At later times (> 0.2 msec) the uniform temperature model radiates more strongly than the temperature profile model. This is because by this time the hot plasma in the center has cooled down and the plasma near the outer boundary of the cavity is hotter in the uniform temperature case than in the temperature profile case. Recall the temperature was 2.7 eV everywhere in the uniform temperature case while the outer 2 m of the cavity in the profile case were at a lower temperature (see Fig. III.2-16). The radiation diffusion model is different than both of the other two because the energy lost in this case is dependent on the temperature and its gradient at the first wall.

III.2.F-4 Radiation Diffusion Calculations for 96 MJ of Energy in the Buffer Gas

Many of the calculations discussed in the previous sections were also done for 96 MJ of energy deposited in the gas. In this case it was assumed that the pellet yield was 320 MJ and 30% of this was in the form of X-rays and ions. This, in fact, is the choice used for the SOLASE-H design. The

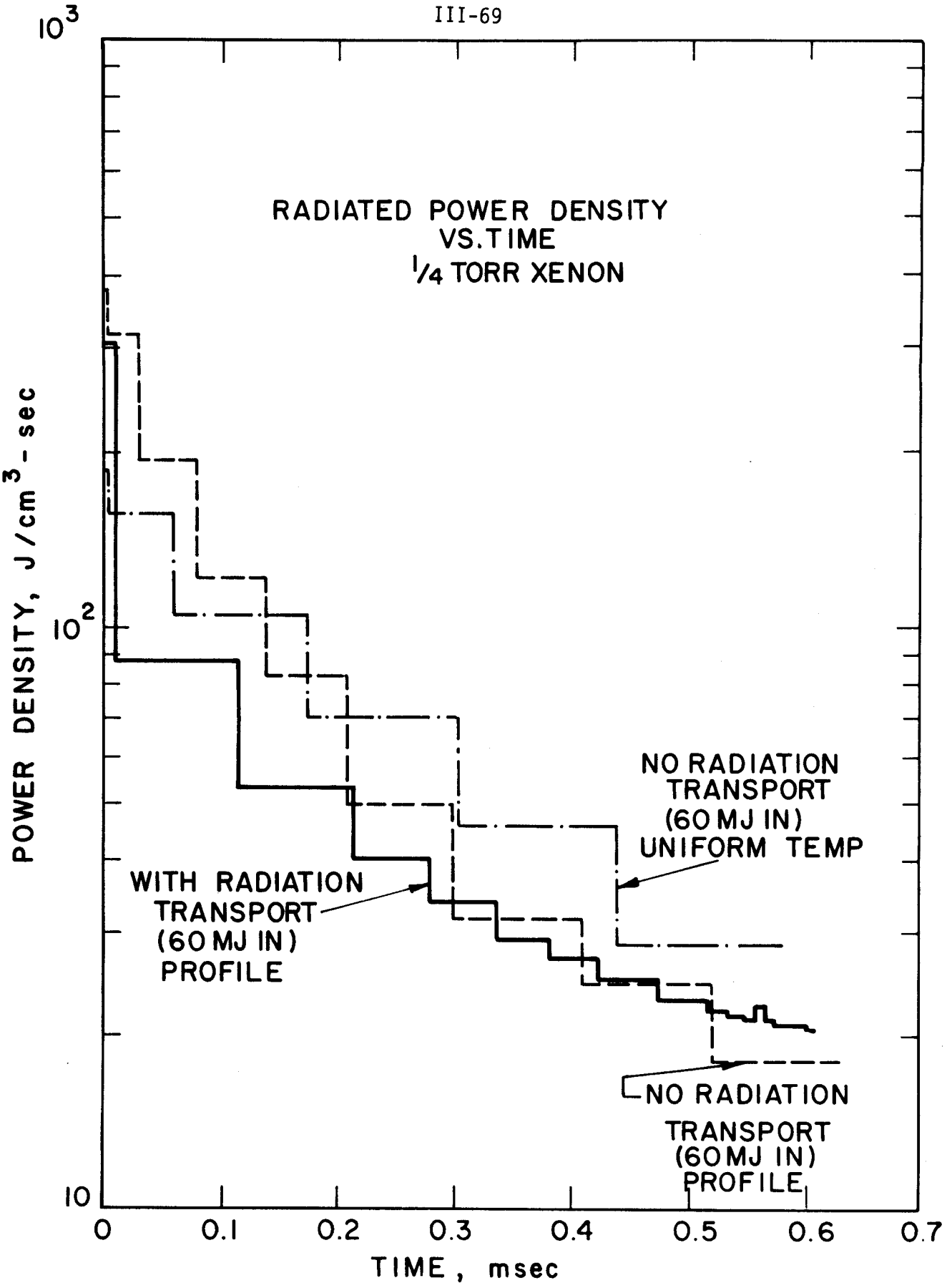
RADIATED POWER DENSITY
VS. TIME
1/4 TORR XENON
POWER DENSITY, J/cm³-sec
10³
10²
10
0
0.1
0.2
0.3
0.4
0.5
0.6
0.7
TIME, msec
NO RADIATION TRANSPORT (60 MJ IN) UNIFORM TEMP
WITH RADIATION TRANSPORT (60 MJ IN) PROFILE
NO RADIATION TRANSPORT (60 MJ IN) PROFILE

Fig. III.2-17

goal of this analysis is to determine the maximum amount of energy that can be satisfactorily handled by the gas protection scheme. More deposited energy results in higher gas temperatures and shorter reradiation times. This of course defeats the purpose of the gas protection, to spread the energy in time. The calculations at 96 MJ were done for 0.5 and 1.0 torr of gas. Figures III.2-18 and III.2-19 show the radiated power as a function of time for the temperature profile and uniform temperature models with the pure radiation loss approximation. For the temperature profile model the exponential decay time is about 0.1 msec and for the uniform temperature model the decay time is about 0.25 msec. Figure III.2-20 is a plot of the pressure at the first wall as a function of time for the temperature profile model. The maximum pressure occurs at 0.9 msec and is equal to 45 torr. This calculation was then run with the radiation diffusion model. The results are shown in Fig. III.2-21 where the heat flux at the first wall is plotted as a function of time. In this case the decay time is about 0.7 msec and the peak heat flux occurs 0.12 msec after the reradiation starts. This time displacement is due to the diffusion time of the radiation starting from the center of the cavity. The heat flux actually increases for a period of about 0.3 msec at 0.9 msec after the start of the problem. This increase is due to the arrival of the pressure wave at the first wall. This compresses the gas near the wall and raises its temperature. The maximum overpressure is 179 torr. Although the temperature profile model without radiation diffusion predicts the correct arrival time of the pressure pulse, it underestimates its strength. From these calculations and those discussed in the preceding sections we conclude that the complete radiation-hydrodynamics

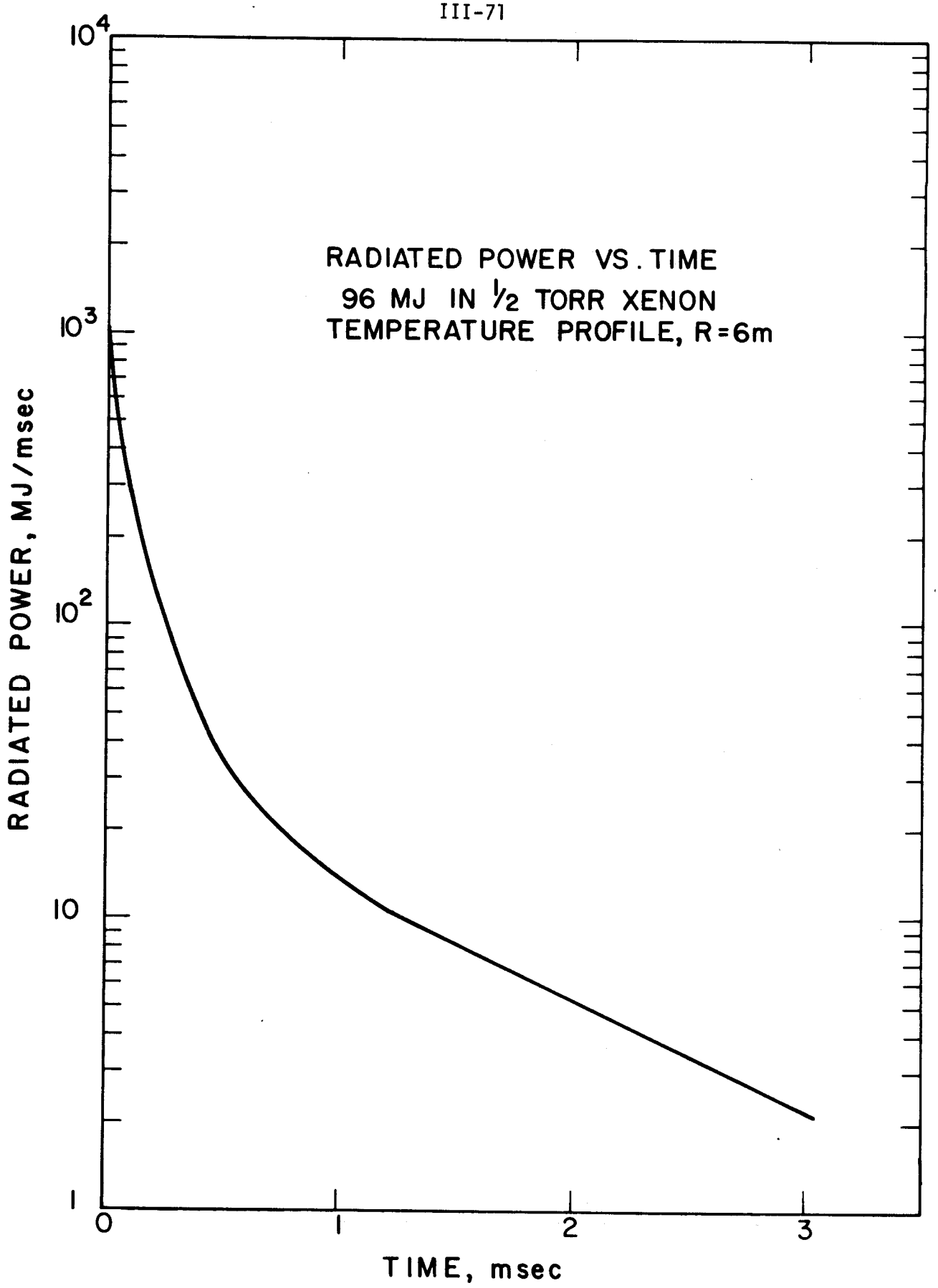
RADIATED POWER VS. TIME
96 MJ IN ½ TORR XENON
TEMPERATURE PROFILE, R=6m
RADIATED POWER, MJ/msec
TIME, msec
10⁴
10³
10²
10
1
0
1
2
3

Fig. III.2-18

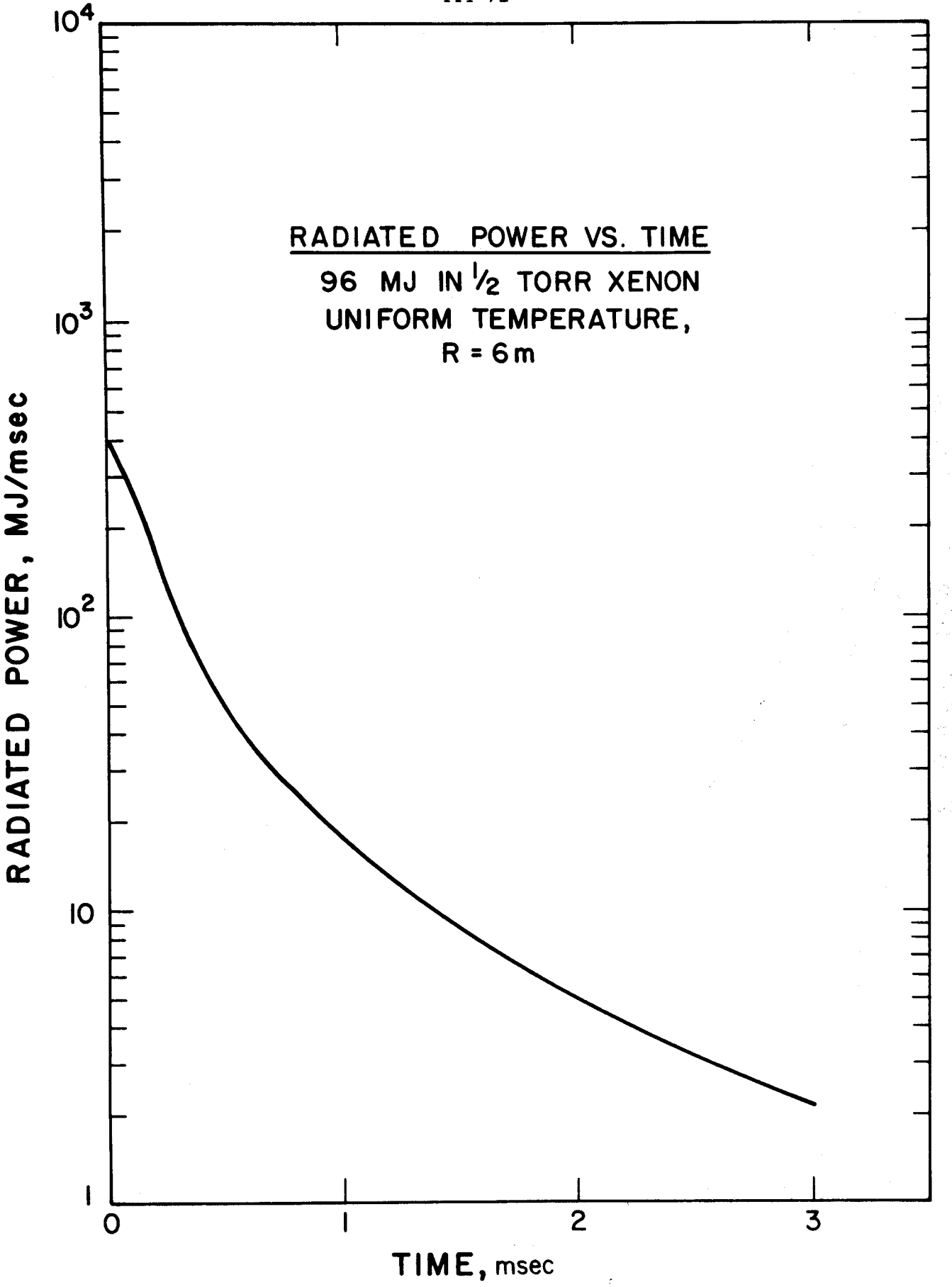
RADIATED POWER VS. TIME
96 MJ IN 1/2 TORR XENON
UNIFORM TEMPERATURE,
R = 6m
RADIATED POWER, MJ/msec
TIME, msec
10^4
10^3
10^2
10
1
0
1
2
3

Fig. III,2-19

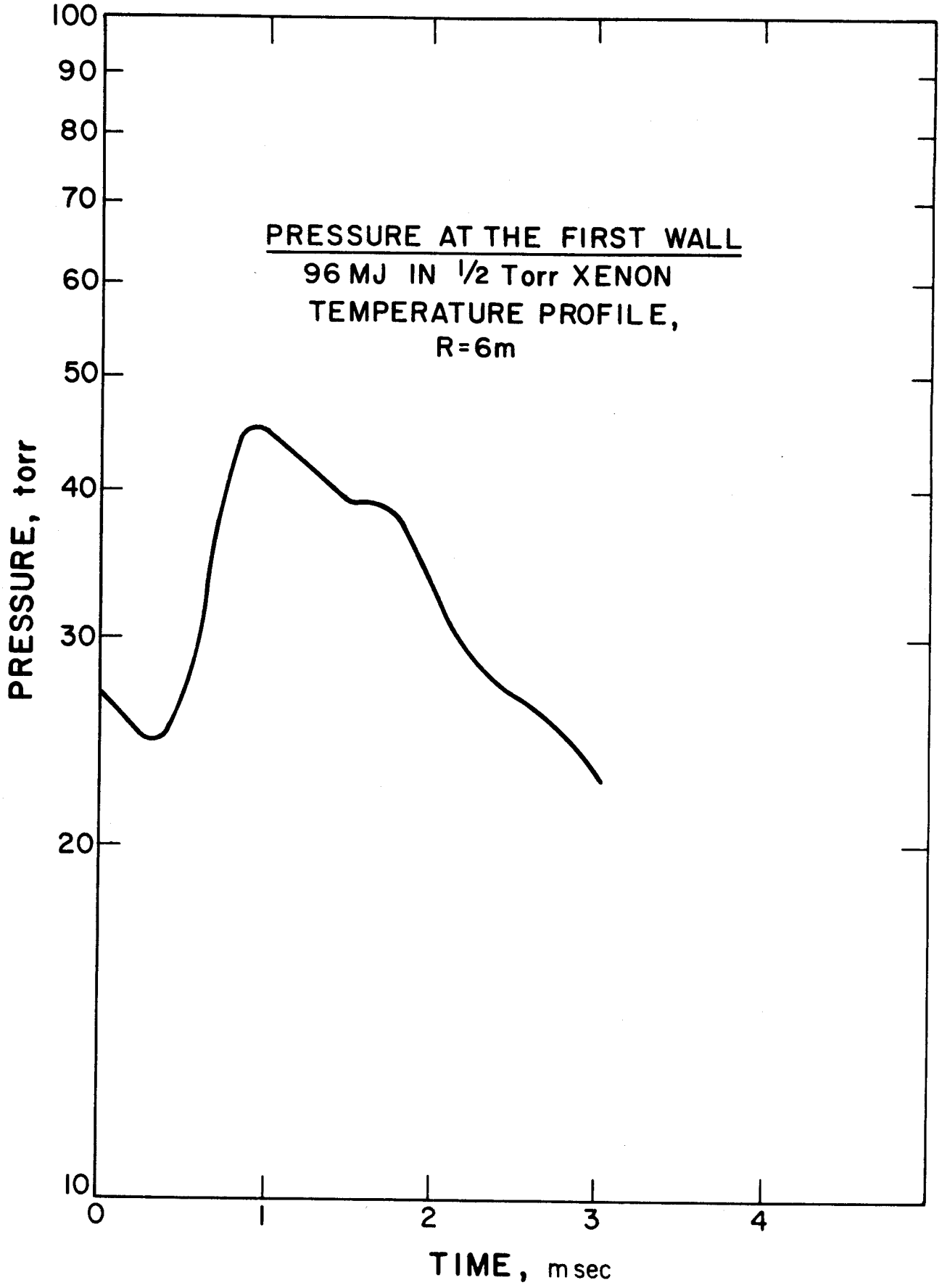
PRESSURE AT THE FIRST WALL
96 MJ IN 1/2 Torr XENON
TEMPERATURE PROFILE,
R=6m
PRESSURE, torr
100
90
80
70
60
50
40
30
20
10
0
1
2
3
4
TIME, msec

Fig. III.2-20

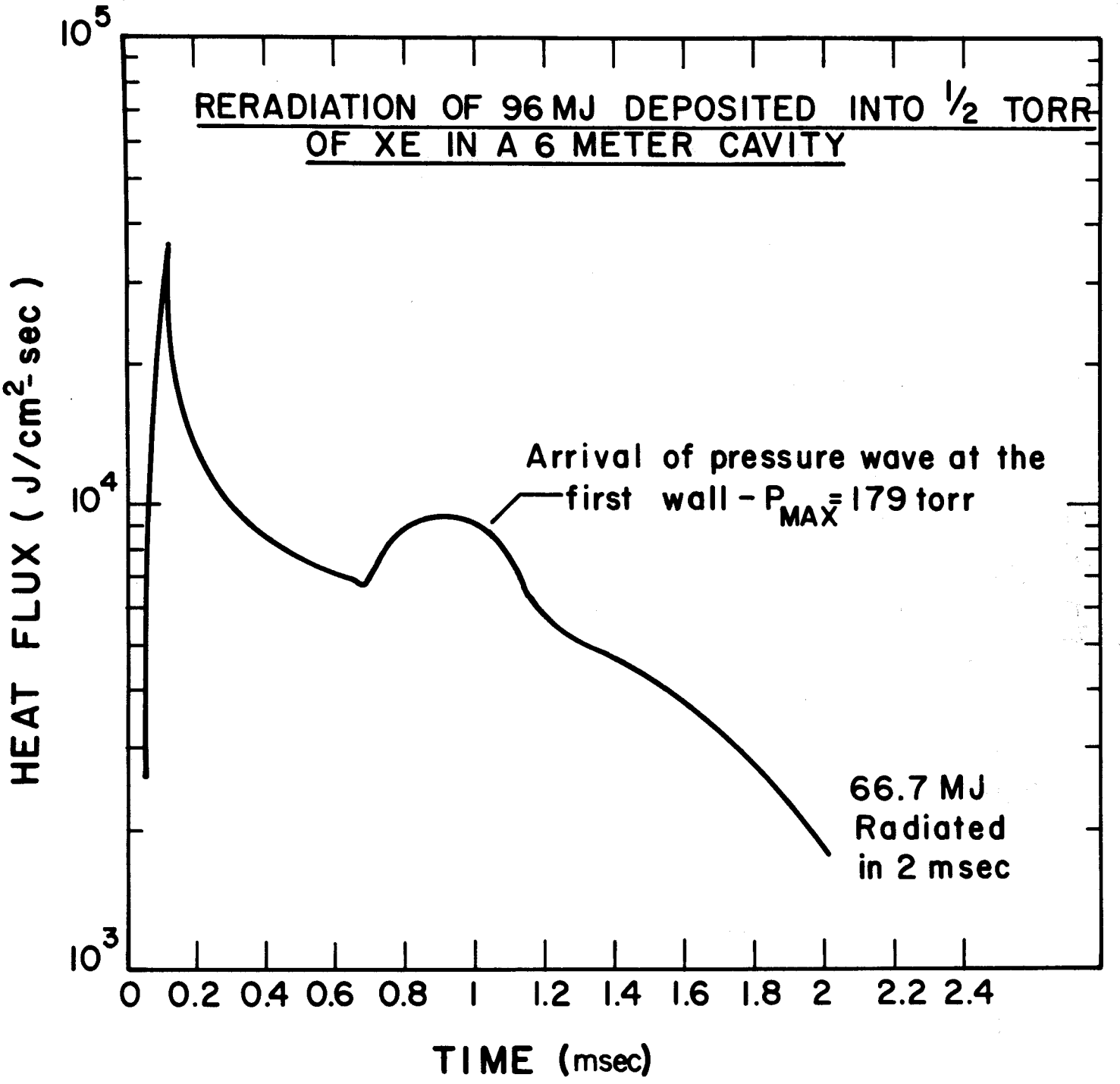
RERADIATION OF 96 MJ DEPOSITED INTO ½ TORR OF XE IN A 6 METER CAVITY
Arrival of pressure wave at the first wall - P_{MAX} = 179 torr
66.7 MJ Radiated in 2 msec
HEAT FLUX (J/cm²-sec)
TIME (msec)
10⁵
10⁴
10³
0 0.2 0.4 0.6 0.8 1 1.2 1.4 1.6 1.8 2 2.2 2.4

Fig. III.2-21

reatment of the buffer gas response is necessary to adequately model this problem.

Figure III.2-22 is a plot of the heat flux at the first wall as a function of time for 96 MJ of energy deposited into 1 torr of xenon in a 6 m cavity. In this case the maximum heat flux is much lower but the pressure wave has a significant heating effect on the gas near the wall. The maximum overpressure in this case is 257 torr.

Before the feasibility of the gas protection concept can be assessed the first wall response to the incident heat fluxes that were presented in section III.2.F must be analyzed. This is done in the following section.

III.2.G. First Wall Response to Reradiated Energy

The reradiation calculations presented in the previous sections represent a surface heat flux to the first wall. The first wall response will depend on the time dependent behavior of the heat flux as well as the thickness and material properties of the wall itself. The thermal response problem was modelled as shown in Fig. III.2-23. The time dependent temperature diffusion equation

$$\rho c \frac{\partial T}{\partial t} = \frac{d}{dx} K \frac{d}{dx} T(x,t)$$

was solved numerically using a standard Crank-Nicholson implicit finite differencing technique. The boundary condition at the back of the wall was taken to be a fixed temperature, T_o, and the boundary condition at the front of the wall was specified by q(t), the surface heat flux. The surface heat flux was repetitively applied to the wall with a specified frequency. The finite difference code therefore computed the transient response of the wall as well as the cyclic steady state. In the cases studied here the cyclic steady state was reached in 1.25 sec or 5 cycles.

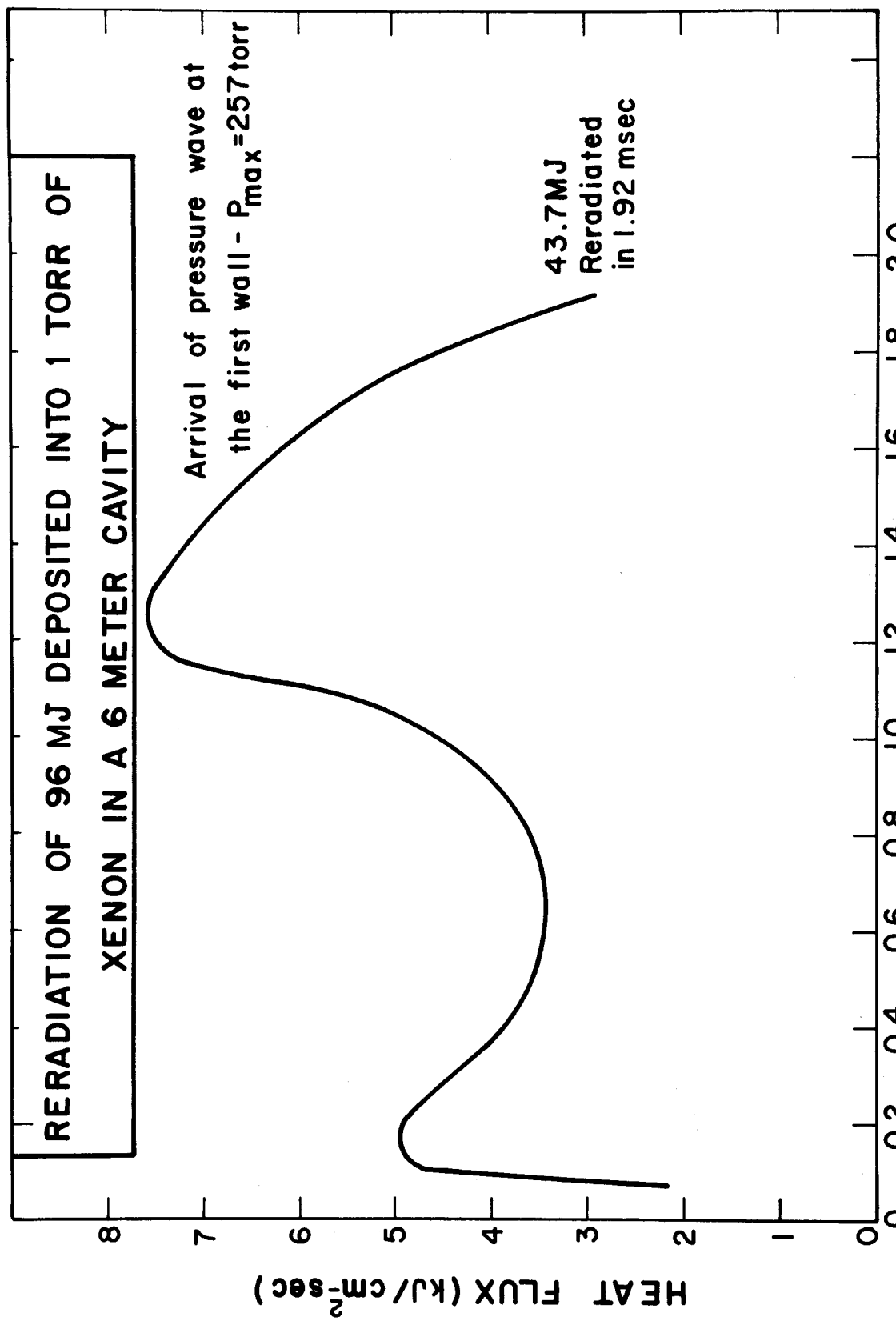
REIRADIATION OF 96 MJ DEPOSITED INTO 1 TORR OF XENON IN A 6 METER CAVITY
Arrival of pressure wave at the first wall - P_{max}=257torr
43.7MJ Reradiated in 1.92 msec
HEAT FLUX (kJ/cm^{2}sec)
TIME (msec)
0
1
2
3
4
5
6
7
8
0
0.2
0.4
0.6
0.8
1.0
1.2
1.4
1.6
1.8
2.0

Fig. III.2-22

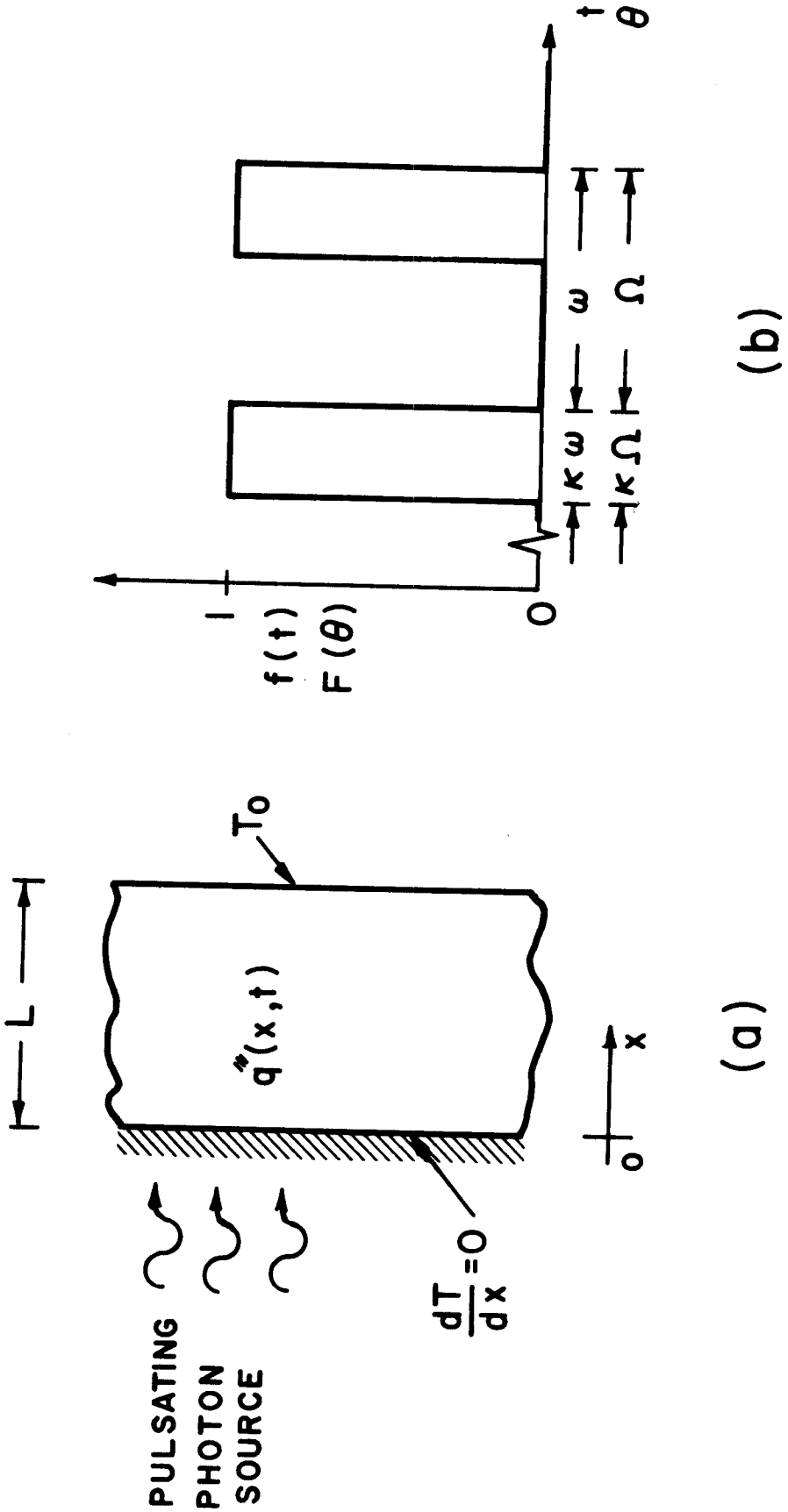
PULSATING
PHOTON
SOURCE
L
T_o
$q''(x,t)$
$\frac{dT}{dx}=0$
x
o
(a)
f(t)
F(θ)
1
0
κω
κΩ
ω
Ω
t
θ
(b)

Fig. III.2-23

It should be noted that a dimensionless analytic solution to this problem has been previously developed by S.I. Abdel-Khalik and reported in UWFDM-220, the "SOLASE Report". This analytic solution may give more insight into the relative importance of the varying factors that affect the thermal response of the wall. However, it was also felt that a numerical solution to the general heat transfer problem would be useful for integration into a system of codes to model the cavity and first wall response to the target explosion. Recall that the input for this analysis is given by the heat fluxes plotted in Fig. III.2-21 and 22. Figure III.2-24 is a plot of the maximum temperature difference, between the front and back surfaces of the wall, as a function of time for the heat fluxes resulting from 96 MJ deposited into 0.5 and 1.0 torr of xenon gas. In both cases the minimum temperature difference is about 65°C. The pulse rate is 4 Hz. As one would expect, the 0.5 torr case has the largest temperature difference, about 740°C, while the 1.0 torr case has a maximum ΔT of 620°C. However the maximum ΔT in the 0.5 torr case has a rather narrow peak in time as compared to the 1.0 torr case. This could have a significant influence on the structural load carrying properties of the wall. This will be discussed further in Part V. The temperature profile in the wall as a function of position for different times during the transient response within a cycle shows that only the front half of the wall is subjected to large temperature rises.

These calculations demonstrate that although melting of the wall does not occur, the temperature on the front surface is raised to values above ½ the melting point. The structural integrity of the wall will therefore depend on the results of a more detailed structural analysis. This work is in progress. Should these calculations verify that the load carrying performance of the wall is satisfactory then it is likely that a metal right circular

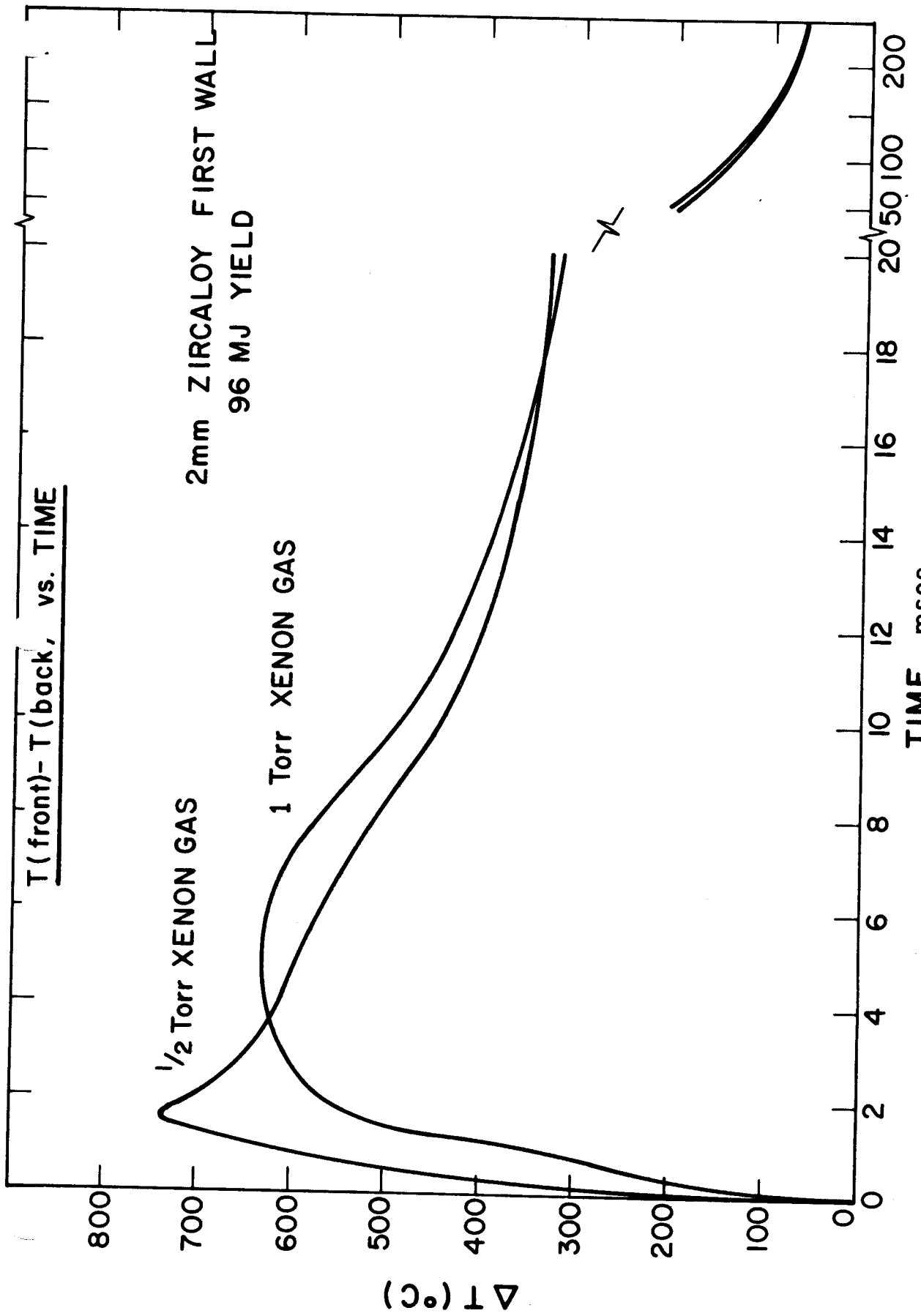
T(front)- T(back, vs. TIME
2mm ZIRCALOY FIRST WALL
96 MJ YIELD
1/2 Torr XENON GAS
1 Torr XENON GAS
ΔT (°C)
TIME, msec
0
100
200
300
400
500
600
700
800
2
4
6
8
10
12
14
16
18
20
50
100
200

Fig. III.2-24

cylinder, protected by xenon gas, is a viable laser fusion reactor cavity. Such a simple design would most certainly be very attractive from an engineering standpoint.

III.2.H Further Analysis

The goal of this analysis was to determine the upper limits of the fusion and buffer gas parameters that are still consistent with adequate protection of a metallic first wall, by xenon gas. The analysis presented here is far more advanced than that reported in UWFDM-220. However, there remain several unanswered problems that are important to the analysis and hence the final conclusions. The most important of these is the opacity data for xenon gas in the range of 1-10 eV. Such data do not exist at this time. It is of course very important to the reradiation properties of the gas. Further work is in progress on this problem. A second problem is the modelling of the initial conditions of the fireball. It is assumed that the target X-rays and ions instantaneously deposit their energy in the gas. A more accurate treatment must include the dynamic interaction between the pellet debris and the buffer gas. The initial X-rays from the pellet will ionize the gas and the subsequent pellet debris will therefore be interacting with a partially ionized plasma, rather than an unionized gas. In addition the fluid effects of the expanding target pushing against the buffer gas, and the possible shock generation, must be investigated. A coupled calculation of the gas dynamics and reradiation and the first wall response is necessary to determine the transient conditions. It would also be interesting to investigate the response of various other noble gases such as neon and argon. The viability of these other gases would of course depend upon the spectra of the target debris.

The conclusion of this reported work is that the protection of metallic walls by a buffer gas appears to be feasible. This positive result encourages us to proceed with a more detailed study of the problem.

IV.1. An Assessment of the Hydrogen-Fluoride Chemical Laser as a Driver for an ICF-Hybrid Reactor

IV.1.A. Introduction

In this report we evaluate the hydrogen-fluoride (HF) chemical laser as a driver for an ICF-hybrid reactor. The approach taken was to design in sufficient detail an HF laser system in order to identify potential problems and assess the general feasibility and practicality of developing this laser as an ICF driver. The particular performance characteristics chosen for this design evolved from the hybrid blanket and pellet physics studies reported in parts II and III of this report. Although particular parameters are used in this study to couple with the other parts of the design, discussion is given to the consequences of varying these parameters so that a more general evaluation can be made.

This section begins with a discussion of the laser performance requirements and the reasons we chose the HF laser for this design study. This discussion is followed by the detailed design of the laser obtained from scaled-up experimental results. Even though the system was not optimized, we conclude that the HF laser is an attractive candidate for an ICF driver. There are still problems to be overcome in the development of a large HF laser but these are no more severe (and frequently less severe) than for other laser candidates. The principal question will likely be the compatibility of the HF laser with the ultimate requirements imposed by the pellet physics, particularly with respect to wavelength, pulse width, and efficiency.

IV.1.A-1. Performance Requirements of the Laser

Because we are considering a laser fusion hybrid reactor design certain of the stringent requirements placed on a pure ICF laser can be relaxed

because of both the energy multiplication present in the fertile blanket and the fissile fuel production. In choosing those characteristics which could be relaxed one must be consistent with present understanding of both the laser and pellet physics; therefore, the selection is not an arbitrary one. As an additional guide, we used the results of the SOLASE study[1] to relax those parameters that would have the greatest impact on increasing the feasibility of an ICF laser design.

Table IV.1-1 lists the range of performance characteristics and other practical considerations thought necessary of a pure ICF laser[2] and Table IV.1-2a lists some of the specific characteristics chosen for the SOLASE laser.[1] The properties of the hybrid system would apparently allow the relaxation of three basic laser parameters: namely, the total energy on target, the pulse repetition frequency, and the efficiency. However, the pellet physics suggests that the total energy on target cannot be relaxed below ~ 1 MJ and may actually have to be increased. Fortunately, the total energy requirement does not appear to be an insurmountable obstacle to the design of an ICF laser and an increase in the total energy by a factor of 2 or 3 beyond 1 MJ will probably not dramatically increase the difficulties that have already been encountered. (This depends somewhat on the particular laser involved.) For further increases in laser energy, questions concerning overall system reliability and the absolute physical size and cost become increasingly serious.

Table IV.1-1

Requirements for a Pure ICF Laser

Performance Requirements	
Energy	1-5 MJ
Peak Power	100-1000 TW
Pulse Width (FWHM)	$\leq$ 3 nsec
Wavelength	0.3-10.6 μm
Practical Considerations	
Efficiency	$\geq$ 2-10%
Pulse Repetition Frequency	1-30 Hz
A Saturation Flux Near Optical Damage Thresholds	
High Reliability	
Minimal Maintenance	
Low Capital Costs	

Table IV.1-2a

Design Parameters for SOLASE

Energy on Target	1 MJ
Energy Generated	1.1 MJ
Peak Power on Target	1000 TW
Pulse Width (FWHM)	1 nsec
Minimum Efficiency	6.7%
Pulse Repetition Frequency	20 Hz

Table IV.1-2b

Design Parameters of a Laser for a Hybrid Reactor

Energy on Target	1.6 MJ
Energy Generated	2 MJ
Peak Power on Target	240 TW
Pulse Width	3 nsec
Minimum Efficiency	2.6%
Pulse Repetition Frequency	4 Hz

Relaxation of the pulse rate and efficiency requirements, on the other hand, appears both feasible and desirable. Slowing the pulse rate will reduce problems in almost all aspects of the laser system. It will have a major effect on the gas handling system for example, but the greatest impact will be on the energy storage system. In the SOLASE study[1] we found the energy storage system to be perhaps the weakest aspect of the laser design because state-of-the-art lifetimes and reliabilities of components such as capacitors and switches are totally inadequate for high repetition-rate, long-lived ICF lasers. By lowering the pulse rate, the effective operating time can be increased; that is, if a system is rated for 10^9 shots, it will take longer to reach that value (for a constant energy delivered) as one lowers the pulse rate. Thus, lowering the repetition rate, while not really solving any of the problems of the energy storage system, will relax the requirements imposed on the components.

Reducing the minimum efficiency required is advantageous because this allows a greater number of potential laser candidates to be considered which in turn increases the probability of finding a suitable ICF laser. We found in SOLASE,[1] however, that another consideration is the absolute cost of the laser system and as the electrical efficiency is lowered the cost of the energy storage system may become prohibitively expensive. Thus, there may be a lower bound on the efficiency dictated by cost even if energy balance considerations indicate lower efficiencies would be permissible.

Taking the hybrid blanket performance and the above factors into consideration, we developed a set of performance characteristics that our

hybrid laser system must meet. These are listed in Table IV.1-2b. Comparing the hybrid and SOLASE requirements, the total energy on target was increased from 1 to 1.6 MJ, while the pulse rate and minimum efficiency were relaxed from 20 Hz and 6.7% to 4 Hz and 2.6%, respectively. Note that the pulse width was also increased from 1 nsec (FWHM) to 3 nsec (FWHM). This was possible because of new concepts in target designs (see part III) and not because the reactor is now a hybrid.

IV.1.A-2. Choice of the Laser System

In the hybrid study we decided to approach the laser system differently than was done in SOLASE. In SOLASE[1] an attempt was made to design as generic a laser as possible in order to examine the problems that are common to the design and construction of almost any ICF laser. In the hybrid study we decided to examine a specific laser system in detail. In keeping with the philosophy of the hybrid blanket design, we also wished the laser to represent "near-term" technology. Thus, the laser chosen must be a well established laser and require no major breakthroughs to be implemented beyond those required for almost any laser system (for example, all require vastly improved energy storage systems). Finally, if the above criteria were met, we wished to select a laser that had not previously been examined in detail.

By examining only the established lasers the field of ICF laser candidates can be reduced to four: CO_2, Nd:glass, iodine, and HF. We tentatively eliminated the CO_2 laser because the SOLASE laser[1] was closely modelled after CO_2. The Nd:glass laser, although well established in a single-shot basis, needs considerable development to demonstrate that it can be a viable, high-pulse-rate laser of reasonable efficiency. The iodine laser is an excellent laser from nearly all aspects but one: the efficiency. State-of-the-art iodine

systems are limited to an efficiency $\lesssim$ 0.75% which is probably too low even for a hybrid reactor. It is possible that improved pump sources will be found that will result in the necessary improvement in the efficiency but we feel that this constitutes a major breakthrough that we are attempting to avoid. The HF chemical laser, on the other hand, appears to meet all our criteria.

In the past the HF laser has been eliminated from serious consideration because of its high gain, unproven beam quality, and long pulse widths. However, during the past year experiments conducted at Sandia Laboratories[3,4] have shown that the high-gain HF amplifiers can be controlled and that good beam quality can be obtained from an HF oscillator-amplifier system. The remaining objection of long pulse widths can be circumvented by extracting the energy in a series of short pulses as opposed to one long pulse[5]. In addition, new concepts in target designs continue to (apparently) increase the permissible laser-pulse width which makes the HF laser's natural-pulse width increasingly compatible with ICF requirements. Thus, the most serious objections have been or can be eliminated. The HF laser has two other important advantages. One is that it has a very high energy density which results in a very compact system. The second is that it has a high <u>electrical</u> efficiency which to a degree ameliorates the energy storage problems. (This advantage is offset somewhat by the short time scales in which the laser must be pumped and by the need for continuous chemical reprocessing.) Thus, the HF laser appears to be the best choice for our hybrid laser system study.

<u>IV.1.A-3. Overview of the Laser System</u>

The HF laser considered for this study is pumped by the chemical chain reaction between H_2 and F_2 and utilizes a 3000/900/100 Torr mixture of

$F_2/O_2/H_2$. The chain reaction is initiated by an electron beam which has a pulse width of 20 nsec (FWHM). The natural pulse width of the laser is 12 nsec (FWHM). The laser lases on a number of P-branch transitions whose wavelengths vary from 2.6 to 3.5 μm.

The total energy generated by the laser is ~ 2 MJ. The energy is delivered in a 240 TW, 3-nsec (FWHM) pulse at a repetition rate of 4 Hz. It was assumed that ~ 80% of the initial 2 MJ is focusable so that about 1.6 MJ is actually incident on the target.

The system includes 20 final amplifiers each of which generates 100 kJ of laser energy. The amplifiers have square optical apertures that are 102 x 102 cm and have a length of 34 cm. Two electron beams irradiate each cavity from opposite sides and deposit a total energy of 193 kJ in the gas. Each Marx generator must store ~ 170 kJ. Energy is extracted from eighteen of the amplifiers in a series of three short pulses that are combined on target in a manner that gives the desired pulse shape. From the remaining two amplifiers a single long pulse is extracted.

Because the laser is chemically pumped the gas is continuously reprocessed. The HF is removed by a KF chemical trap to a concentration of $\tilde{<}$ 1 Torr. Then H_2 and F_2 are regenerated by the electrolysis of the resulting HF-KF eutectic mixture.

The net electrical and chemical efficiencies of the laser are 24% and 4%, respectively. The net efficiency of the entire laser system including an estimate of all recirculating power costs is 2.7%.

IV.1.B. Characteristics of the HF Laser

The HF chemical laser, as the name implies, is pumped by a chemical reaction that yields HF in vibrationally excited states. A large number of reactions

involving a variety of fluorine and hydrogen donor molecules can be utilized to pump the laser. In particular our laser will use H_2 and F_2 as the reactants to take advantage of the chemical chain reaction. In nearly all systems an external energy source such as a discharge, electron beam or flashlamp is used to initiate the reaction by dissociating the fluorine-donor molecule. The resulting free-fluorine atom then attacks the hydrogen donor producing HF in a vibrationally-rotationally excited state. Vibrational levels up to $\sim$ v = 6 can be populated but the majority of the laser energy originates from the v = 3, 2, and 1 vibrational levels. If the reaction proceeds rapidly enough, population inversions will occur on a number of vibrational-rotational transitions whose wavelengths vary from 2.6 to 3.5 μm. The pertinent reactions and a schematic of HF energy levels is shown in Fig. IV.1-1.

Once the reactions are initiated (in our case by dissociating F_2 and H_2 with an electron beam), it will proceed until all the available reactants are consumed. This has the result of increasing the electrical efficiency of the laser because additional chemical energy, and therefore light energy, is generated via the chain reaction for each initial dissociation. This increase in electrical efficiency is advantageous because it decreases the electrical energy storage requirements.

Because the HF laser is a chemical laser one must consider not only the electrical efficiency but also the chemical efficiency. The basic

HYDROGEN-FLUORIDE CHEMICAL LASER

$$F + H_2 \rightarrow HF(v \leq 3) + H$$

$$H + F_2 \rightarrow HF(v \leq 6) + F$$

$$HF(v, J) \rightarrow HF(v-1, J + 1) + h\nu$$

$$2.6 < \lambda < 3.5\ \mu m$$

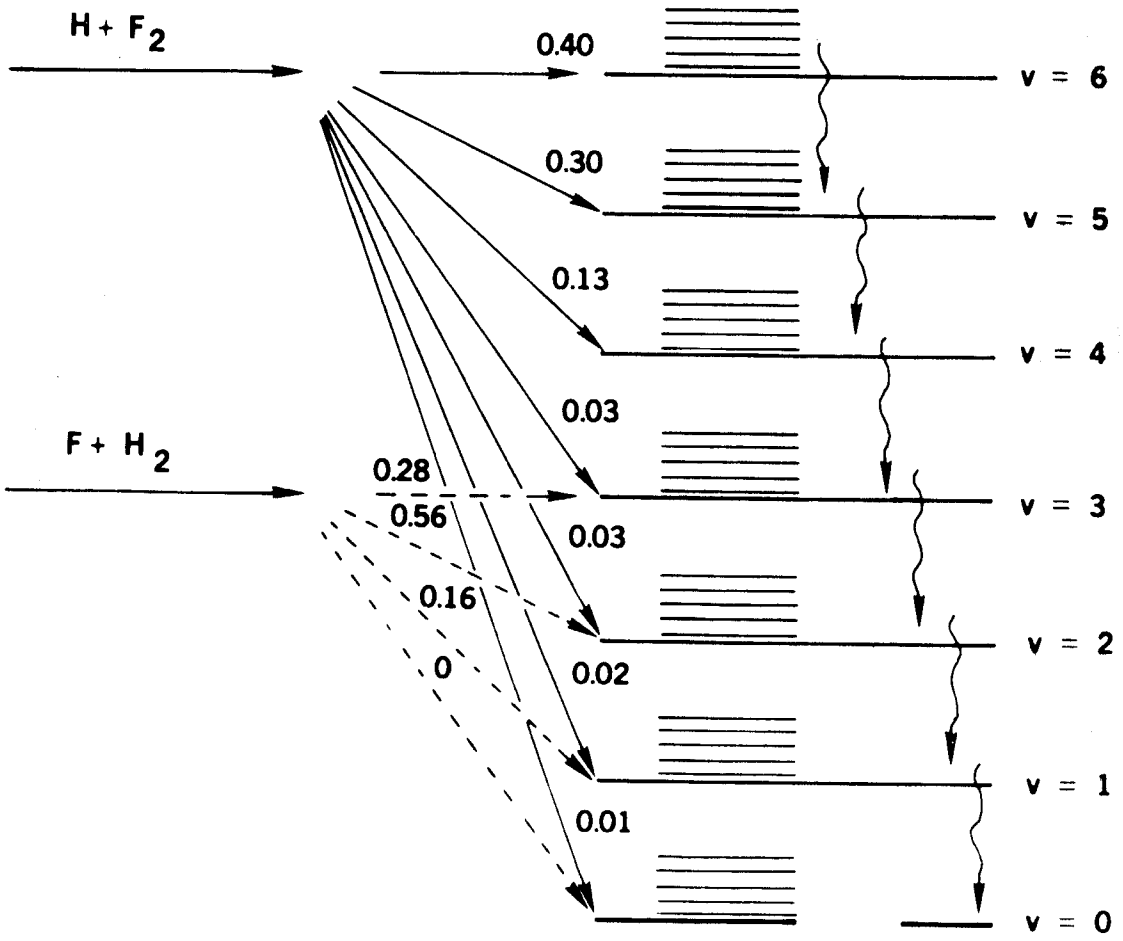

Fig. IV.1-1

electrical and chemical efficiencies can be defined as the laser energy out divided by the total electrical energy deposited in the gas and the total chemical energy released by the reaction, respectively. However, to get the total electrical and chemical efficiencies one must include the efficiency of depositing energy into the gas and the efficiency of reprocessing the gas. The overall efficiency of the laser is then determined from the total electrical and chemical efficiencies plus all additional recirculating power costs. The fact that HF is a chemical laser also means that the laser medium must be continuously reprocessed. That is, the newly formed HF must be removed from the residual gases and regenerated into H_2 and F_2 before it can be used again.

One significant advantage of many lasers is that energy can be deposited and stored in the upper laser level over a relatively long period of time and then extracted in a short pulse. Thus, the laser serves as an energy compressing medium. This is not true of HF because energy deposited in its upper laser levels is rapidly removed by both collisional deactivation by other molecules and by amplified spontaneous emission. As a result, laser energy must be extracted as the chemical energy is deposited or it is lost. This makes it difficult to efficiently obtain very short pulses because it requires that the chemical burn time be approximately the same length as the desired optical pulse. The natural-pulse width can be decreased by increasing both the total pressure and rate at which the free fluorine atoms are initially created. Unfortunately, it is probably not feasible to reduce the natural pulse width to the requisite 1 to 3 nsec (FWHM) because

of the e-beam requirements; however, a laser pulse width of ~ 12 nsec (FWHM) is plausible. A shorter pulse could be cut from an oscillator and then amplified but because only the energy that is generated while the pulse is passing through the amplifier will be extracted, the system would be very inefficient. An alternative is to cover the entire natural pulse with a series of short pulses and combine these on target to give the desired pulse shape. This can be accomplished by using a scheme called angular multiplexing[5] which is similar to the multi-passing technique used in SOLASE.[1] This is discussed further in Sec. IV.1.C and in the appendix to IV.1.

Figures IV.1-2 to 4 present data that are particularly relevant to the design of our HF laser. Figure IV.1-2 gives the basic chemical and electrical efficiencies measured as a function of hydrogen partial pressure obtained from Sandia experiments.[6] Note that electrical efficiencies in excess of 100% can be obtained but only by sacrificing the chemical efficiency. It appears from the data that the maximum net efficiency occurs for an $F_2/O_2/H_2$ mixture of 300/90/10 for which the electrical efficiency is approximately 60%. It should also be pointed out that the values of the chemical efficiency shown in the figure are based on conservative estimates and that the actual chemical efficiency may be as much as 50% greater.[4]

Figure IV.1-3 shows the variation of laser output as a function of hydrogen partial pressure, again from the experiments described in Ref. 6. The active volume in these experiments was 32.3 liters from which the energy density can be calculated. Since the energy density should scale directly with the total pressure, one can calculate from this data the energy density available for any pressure-mixture combination.

ELECTRICAL EFFICIENCY (%)
200
160
120
80
40
0
CHEMICAL EFFICIENCY (%)
10.0
8.0
6.0
4.0
2.0
0.0
0
100
200
300
HYDROGEN PRESSURE (Torr)
300 Torr F_2 / 90 Torr O_2

Fig. IV.1-2

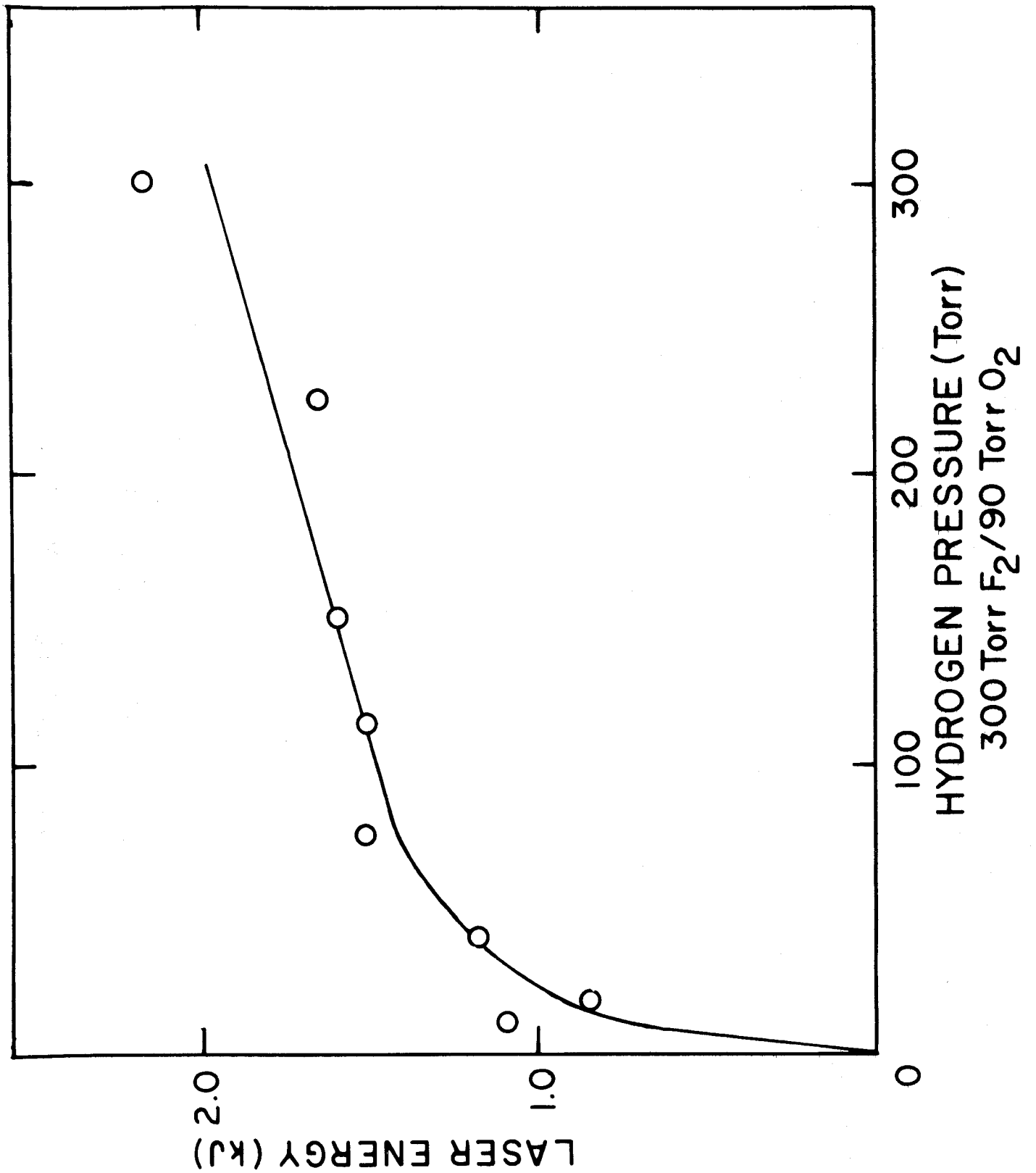
LASER ENERGY (kJ)
2.0
1.0
0
100
200
300
HYDROGEN PRESSURE (Torr)
300 Torr F_2/90 Torr O_2

Fig. IV.1-3

Figure IV.1-4 indicates the fraction of the total available energy that can be extracted from an amplifier as a function of input beam intensity.[3] This data was obtained at a total pressure of 1240 Torr with an $F_2/O_2/H_2$ ratio of 1/0.3/0.25. This data indicates that in order to extract ~ 90% of the available energy the input intensity must be $\geq 10^7$ W/cm^2. However, any input $\gtrsim 10^4$ W/cm^2 will adequately control amplified stimulated emission (ASE) providing that the entire amplifier volume is covered by the extracting beam during the entire pumping process.

IV.1.C. The Final Amplifier Design

As discussed in Sec. IV.1.A, the principal performance requirements that our specific laser design must meet are a total output of 2 MJ, a pulse width of ~ 3 nsec (FWHM), and a minimum efficiency of 2.6%. In addition to meeting these goals, we also wished the design to represent "near-term" technology, if possible. Thus, the design should incorporate only modest extrapolations of state-of-the-art technology and laser parameters. In order to make a realistic design we have not tried to optimize the HF laser, but have merely extrapolated from presently available experimental results to higher pressures and larger volumes.

The HF laser has a good data base upon which to make the necessary extrapolations. To date, the HF laser has one of the largest recorded energy outputs[6] for a short pulse laser: 4.2 kJ in a 25-nsec pulse (FWHM). In addition, experimental data exists on efficiency, energy extraction and beam quality of high energy (100-200 J) amplifiers.

HF AMPLIFIER ENERGY

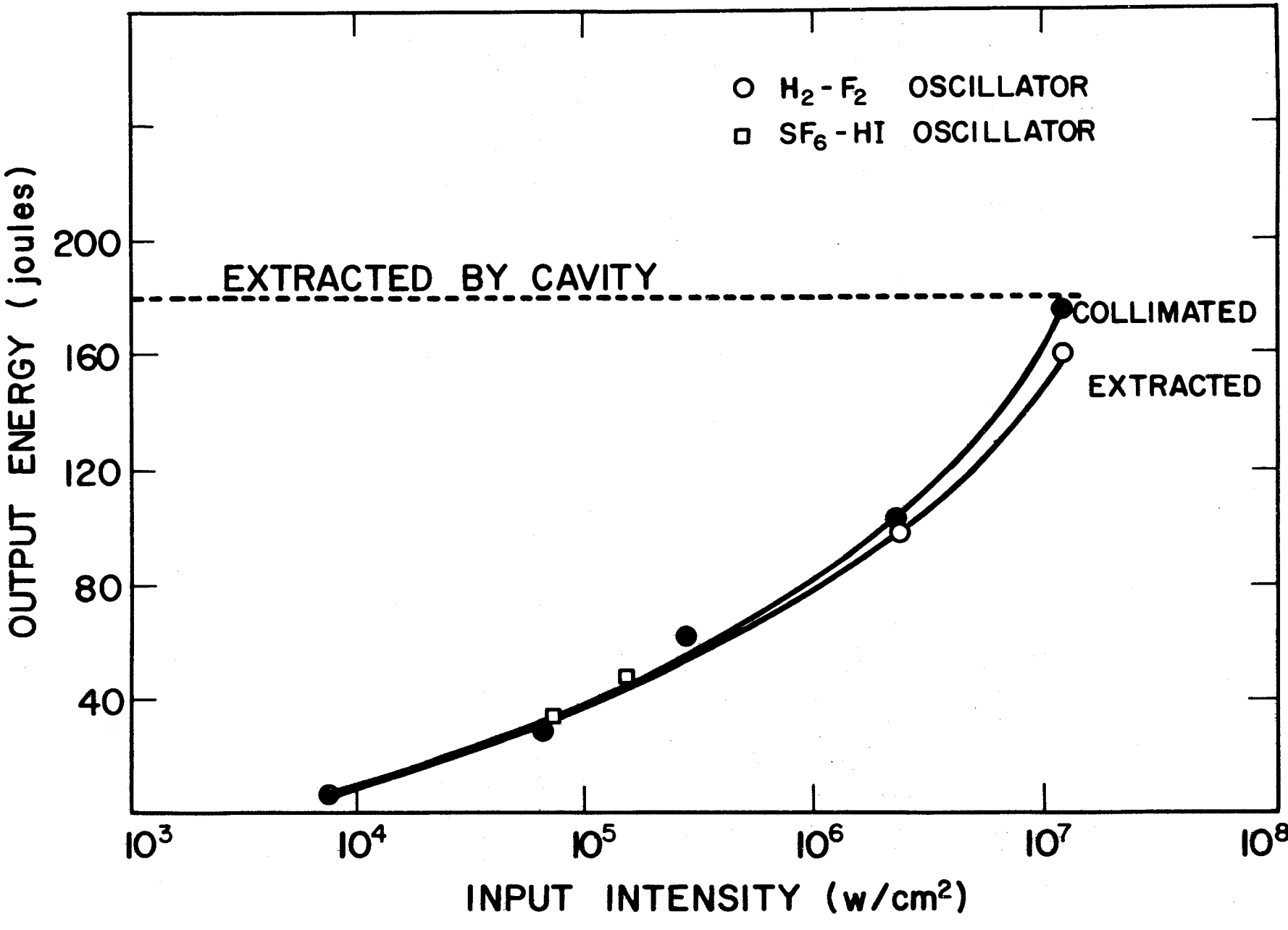

IV-16

Fig. IV.1-4

Before going into the design details it will be beneficial to describe the general design and point out those parameters that once chosen define the rest of the design. As in SOLASE,[1] the laser will consist of several final power amplifiers and a front end that drives them. Through the amplifiers will flow an F_2, H_2 and O_2 laser mixture. Electron beams will initiate the chain reaction to produce HF lasing. The laser radiation will be extracted in a series of short pulses. Finally, HF molecules will be removed from the spent laser gas and reprocessed into H_2 and F_2.

In designing a laser one must make appropriate but realistic choices for the efficiency, the natural-pulse width, the optical energy output per final amplifier, and the optical damage threshold of the amplifier windows. In making these choices, other parameters such as gas pressure, mixture, and physical dimensions become essentially fixed. Also, the combination of the natural-pulse width and desired pulse shape largely determines the particulars of the multi-passing (i.e. angular multiplexing) scheme. A final factor that can affect the design is the possibility of laser-induced gas breakdown within the laser cavity.

Turning to the details of our design, we will first examine the question of the laser energy output per final amplifier. The principle constraint is that the total energy from all amplifiers must equal 2 MJ. Within the constraint one must choose a combination of energy per amplifier and total number of amplifiers that is both practical and realistic. From a practical and capital cost standpoint one would like to minimize the number of final amplifiers. Reducing the number of amplifiers makes the system more compact,

less expensive, and more manageable because of the fewer components required. This also makes the optics more manageable because it reduces the number of optical beams that must be handled. Reducing the number of amplifiers, however, requires an increase in the energy per amplifier. In increasing the energy, one also increases the probability that the extrapolations used will not be valid, resulting in a more questionable design. Also, it will be more difficult to manage and control the greater electrical, chemical, and optical energies present.

After considering the above factors, we chose 100 kJ to be the laser energy per final amplifier. Thus, twenty final amplifiers are required to generate 2 MJ. We feel that a 100 kJ module is realistically obtainable and that the electrical and chemical energies present are quite manageable. The principal question appears to be not whether 100 kJ is feasible but rather the quantitative validity of our extrapolations. On the other side we feel that the number of amplifiers (20) and the number of optical beams (56) are within practical limits.

A second parameter to choose is the operating efficiency. The efficiency as a function of H_2 partial pressure for a particular HF experiment[6] is shown in Fig. IV.1-2. There are arguments for operating at high electrical efficiencies but we chose to operate at the maximum net efficiency for which the basic electrical efficiency is approximately 60%. The particular mixture that gives the maximum net efficiency is $F_2/O_2/H_2$ = 300/90/10. This hydrogen-lean mixture also has the advantage

of greatly reducing the gas handling problems over those for more hydrogen-rich mixtures which are required if higher electrical efficiencies are desired. From the data[6] in Fig. IV.1-3 one can calculate that for this mixture at 400 Torr, 33.3 J/ℓ of optical energy can be extracted. This energy density should scale directly with the total pressure for a constant mixture ratio.

The third parameter to choose is the natural-pulse width. One of the performance requirements imposed on our laser is that the laser pulse on target have a width $\lesssim$ 3 nsec (FWHM). Unfortunately, because of e-beam limitations the natural-pulse width of the HF laser cannot be made this short. Instead one must rely on multi-passing techniques to generate the desired short pulse as will be discussed. However, to minimize the complexity of the system it is desirable to make the natural-pulse width as short as possible. Realistically this width is about 10 to 15 nsec (FWHM).

Experimentally it has been found that the pulse width is roughly inversely proportional to the pressure. The experimentally determined pulse width (FWHM) at 400 Torr of our particular mixture is approximately 100 nsec.[6] Extrapolation from this data indicates that increasing the total pressure to 4000 Torr will decrease the pulse width to about 10 nsec. At this pressure the extractable energy density is ~ 333 J/ℓ so that a 300 liter cavity should yield a 100 kJ output. However, a computer simulation[7] of an amplifier with these parameters, but configured as an oscillator, gave an output of 92.2 kJ and a pulse width of 14 nsec (FWHM) (see Fig. IV.1-5). A somewhat longer pulse is expected for an oscillator

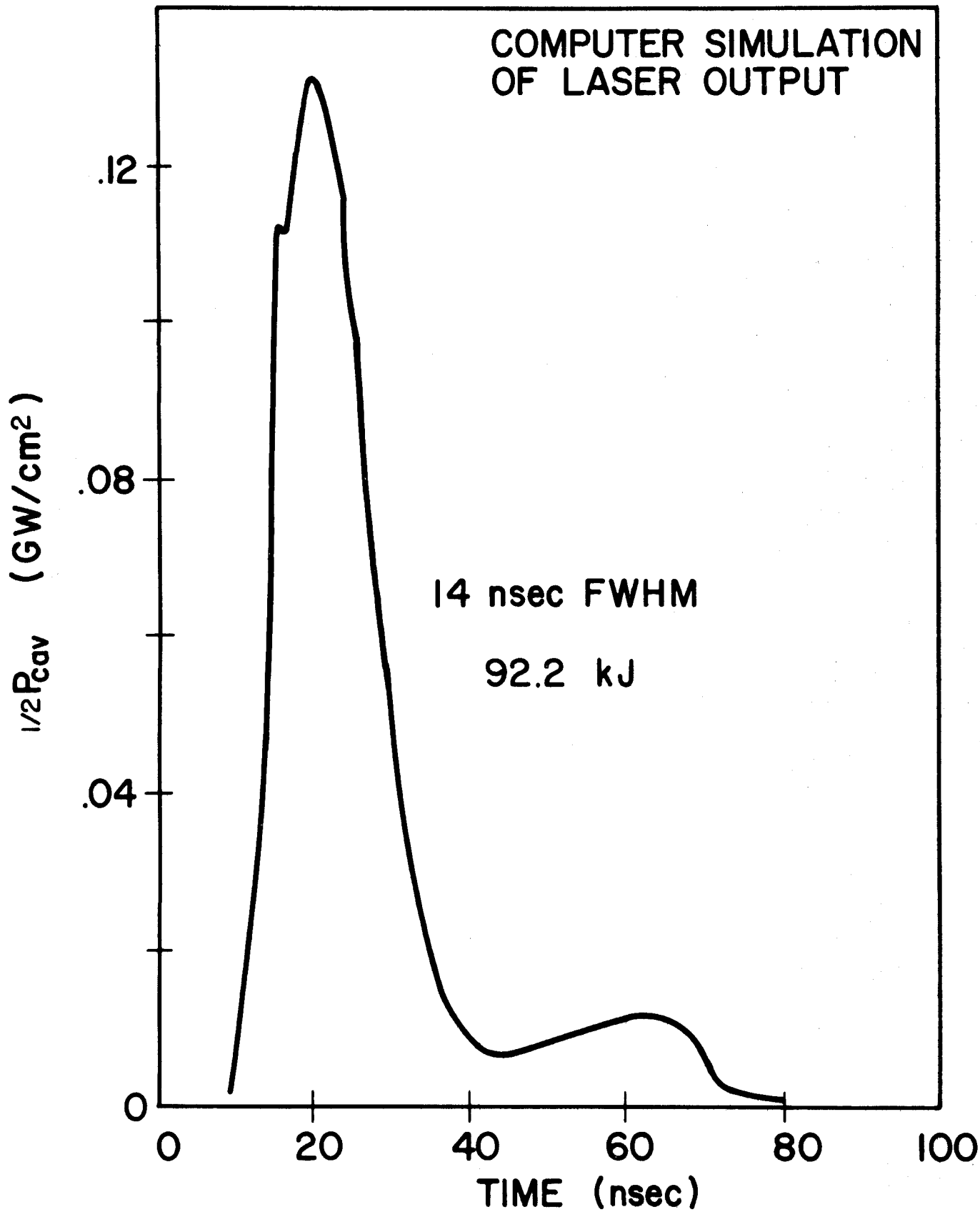
COMPUTER SIMULATION
OF LASER OUTPUT
14 nsec FWHM
92.2 kJ
1/2Pcav (GW/cm2)
.12
.08
.04
0
0
20
40
60
80
100
TIME (nsec)

Fig. IV.1-5

as opposed to an amplifier because of the many transit times in the oscillator. This may account in part for the discrepancy. It is difficult to evaluate which extrapolation is more accurate. As a compromise, we have taken the pulse width to be an average of the two or 12 nsec (FWHM), and to be conservative, we have taken the available energy density to be 307 J/ℓ as given by the kinetics code. This energy density requires a volume of ~ 325 liters to yield a 100 kJ output.

The above calculations assume a fresh mixture of pure F_2, O_2 and H_2; however, a realistic mixture will probably have some residual HF present from previous shots. This residual HF can be very detrimental to the laser performance because of absorption and deactivation of the excited HF molecules. A plot[7] of the laser output as a function of HF (v = 0) pressure is shown in Fig. IV.1-6. For our design we will assume a residual concentration of ~ 1 torr of HF. This reduces the original calculated laser output from 92.2 kJ to 90 kJ. To account for the reduced output, the volume was further increased to 333 liters.

The optical aperture that is required can be calculated from the optical damage threshold of the windows and the total energy in each beam. Because of the great technological difficulty of fabricating large sapphire windows, we are assuming that quartz windows will be satisfactory. Unfortunately, commercial quartz, even the best "IR" grade, has an absorption band at 2.7 μm. However, this absorption is not inherent to the quartz itself but to the manufacturing process which introduces OH radicals into the quartz. It is believed this problem can be eliminated by substituting D_2 for H_2 in the manufacture of quartz. Until this is verified, however, the availability

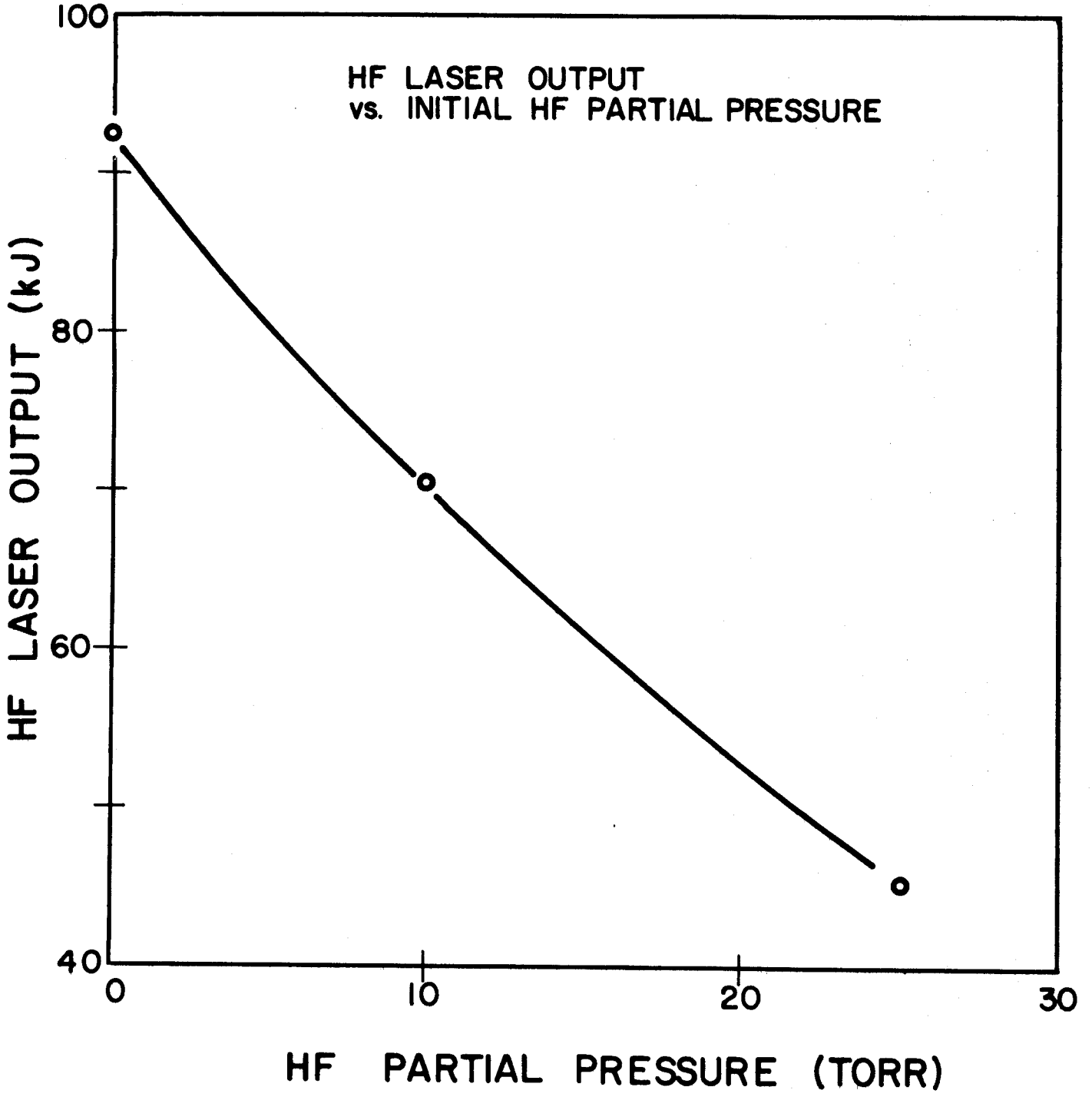
HF LASER OUTPUT
vs. INITIAL HF PARTIAL PRESSURE
HF LASER OUTPUT (kJ)
100
80
60
40
0
10
20
30
HF PARTIAL PRESSURE (TORR)

Fig. IV.1-6

of sufficiently large windows will remain one of the primary question marks of this HF laser design. Assuming quartz is available, a reasonably conservative operating intensity for a 12-nsec (FWHM) pulse is ~ 10 J/cm^2. Because of the high gain, the beam can be taken to be relatively uniform over its cross section. Thus, for 100-kJ output an aperture area of ~ 10^4 cm^2 is required to keep the intensity $\lesssim$ 10 J/cm^2. The most convenient configuration for the cavity appears to be a box in which two sides comprise the optical windows, two sides the electron beams, and two sides the gas flow channels. This results in a square aperture approximately 1 meter on a side. Quartz windows are available in these dimensions. In order to withstand the pressures the windows will have to be 6 to 7 cm thick. Given the aperture area of 10^4 cm^2 and a total volume of 333 ℓ, the length of the amplifier is determined to be approximately 34 cm.

One other factor will affect the actual size of the laser cavity and that is the necessity to multi-pass in order to reduce the pulse width on target. This technique requires passing beams through the cavity sequentially in time with each beam at a slightly different angle. This will be discussed in more detail, but the net effect is that one can no longer extract energy from the entire aperture area. Thus, the size of the aperture must be increased slightly such that the beam area can be 10^4 cm^2. For our parameters, the size of the aperture must be 102 x 102 cm. Thus, the cavity in our design will have a square aperture of 102 x 102 cm and a length of 34 cm. A schematic of the cavity is shown in Fig. IV.1-7.

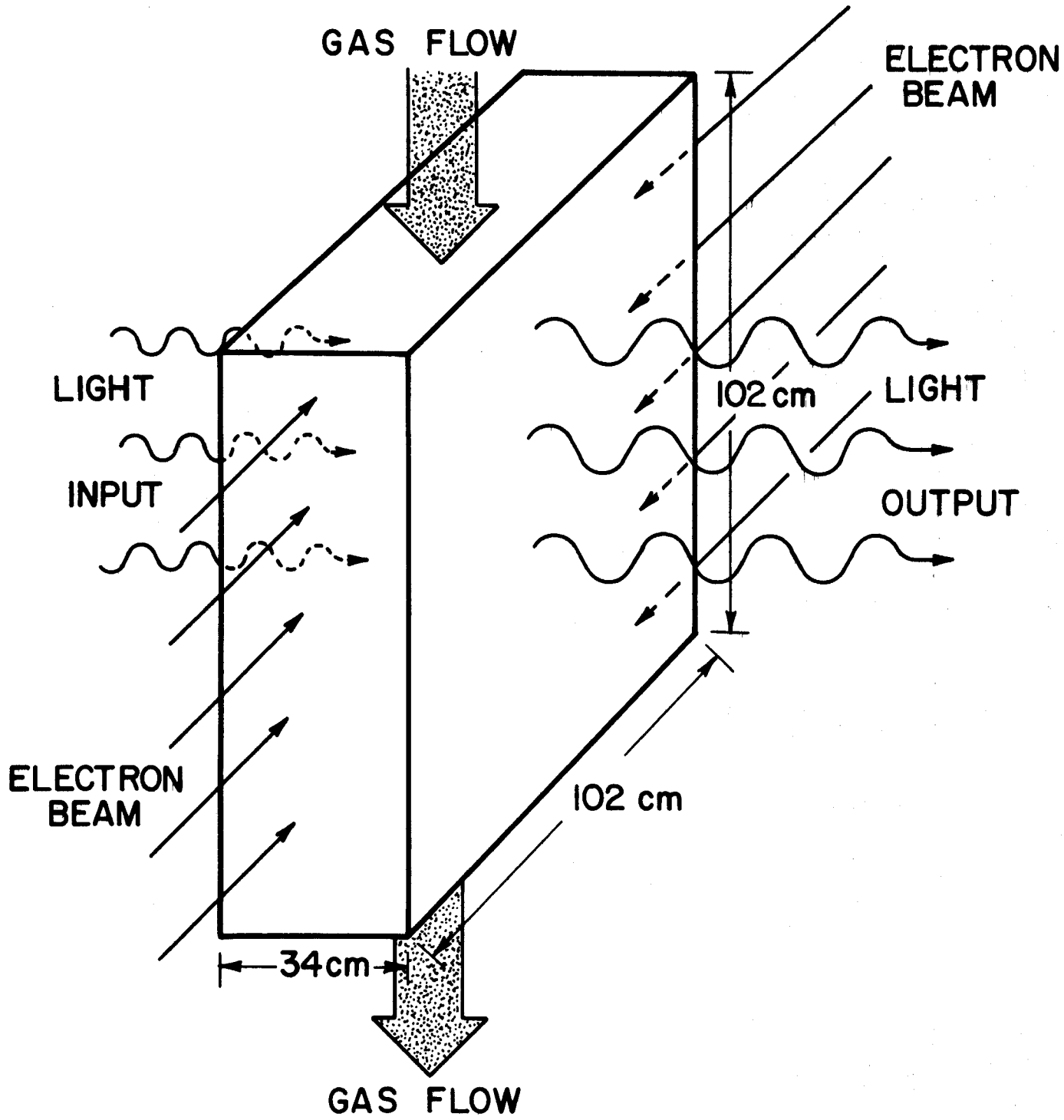

LASER CAVITY CONFIGURATION

Fig. IV.1-7

Having now defined the basic parameters of the laser one must investigate the possibility of laser-induced gas breakdown within the laser cavity. Should the light intensity be sufficient to break down the gas the result at best would be degradation of the beam quality and at worst the total absorption and reflection of the light which will result if the electron density reaches the plasma cutoff frequency for our particular wavelength ($n_e \simeq 1.2 \times 10^{20}/cm^3$ for HF wavelengths). All such effects are to be avoided.

Since there are no data on laser-induced breakdown for typical HF laser gas mixtures or their major constituents, we must extrapolate from other data. Rockwood, et al.[8] developed a basic breakdown scaling relationship, $ft_p \sim \frac{\omega^2}{N}$, where f is the light intensity, t_p is the pulse width, ω the laser frequency, and N is the number density of the medium. Technically this equation is only applicable for $t_p << 10^{-9}$ sec and our pulse width is 12 nsec, but this expression should give a rough estimate of the breakdown threshold. Using data for CO_2 wavelength radiation in an $He/N_2/CO_2$ mixture[8] yields a threshold of 3×10^9 W/cm^2. Using data for ruby light[9] in H_2 gives a value of 1.7×10^9 W/cm^2. The peak flux in our design is 8.3×10^8 W/cm^2. These calculations indicate that our laser would operate near the breakdown threshold and because of the qualitative nature of the estimates may actually exceed the threshold. A potentially favorable factor is the high electron affinity exhibited by both F_2 and O_2 that could significantly raise the threshold. It should also be noted that the laser intensity only reaches its peak value near the exit of the laser cavity. We decided not to change our parameters based on possible gas breakdown, but we do emphasize that this could be a potential problem for our particular design parameters. Note that this problem if it arises can be avoided by selecting an appropriate set of operating parameters. We

strongly suggest that breakdown in HF laser mixtures be investigated experimentally to give a good data base so that this problem can be more accurately evaluated.

The preceding discussion has basically defined the laser parameters of the final amplifier, but what has not been examined is the pulse shaping that is required. The type of pulse shape that will ultimately be required is of course not known at this time. After examining the question, however, we felt that a pulse that approximates the one shown in Fig. IV.1-8 would be reasonable. Since our natural-pulse width is 12 nsec (FWHM) (see Fig. IV.1-9a), it clearly must be altered in some way to meet our criteria. One could simply extract a 3-nsec portion of the pulse, but this would be a very inefficient use of the available energy. A better approach is to extract the entire energy available by having not just one but a series of short pulses that cover the entire pulse. Since the beams are extracted from the same amplifier but at different times, one must be capable of handling the beams independently so that they can be forced to arrive at the target at the appropriate time. This problem is identical to that faced in extracting multiple beams from the SOLASE laser[1] and indeed can be solved by applying the same multi-passing technique. (It should be noted that the fundamental physics that dictate the use of the multi-passing technique are quite different in the two systems.)

To briefly explain, in the multi-passing technique one successively passes each beam through the amplifier at a slightly different angle. Then one allows the beams to travel far enough that they physically separate. When separated,

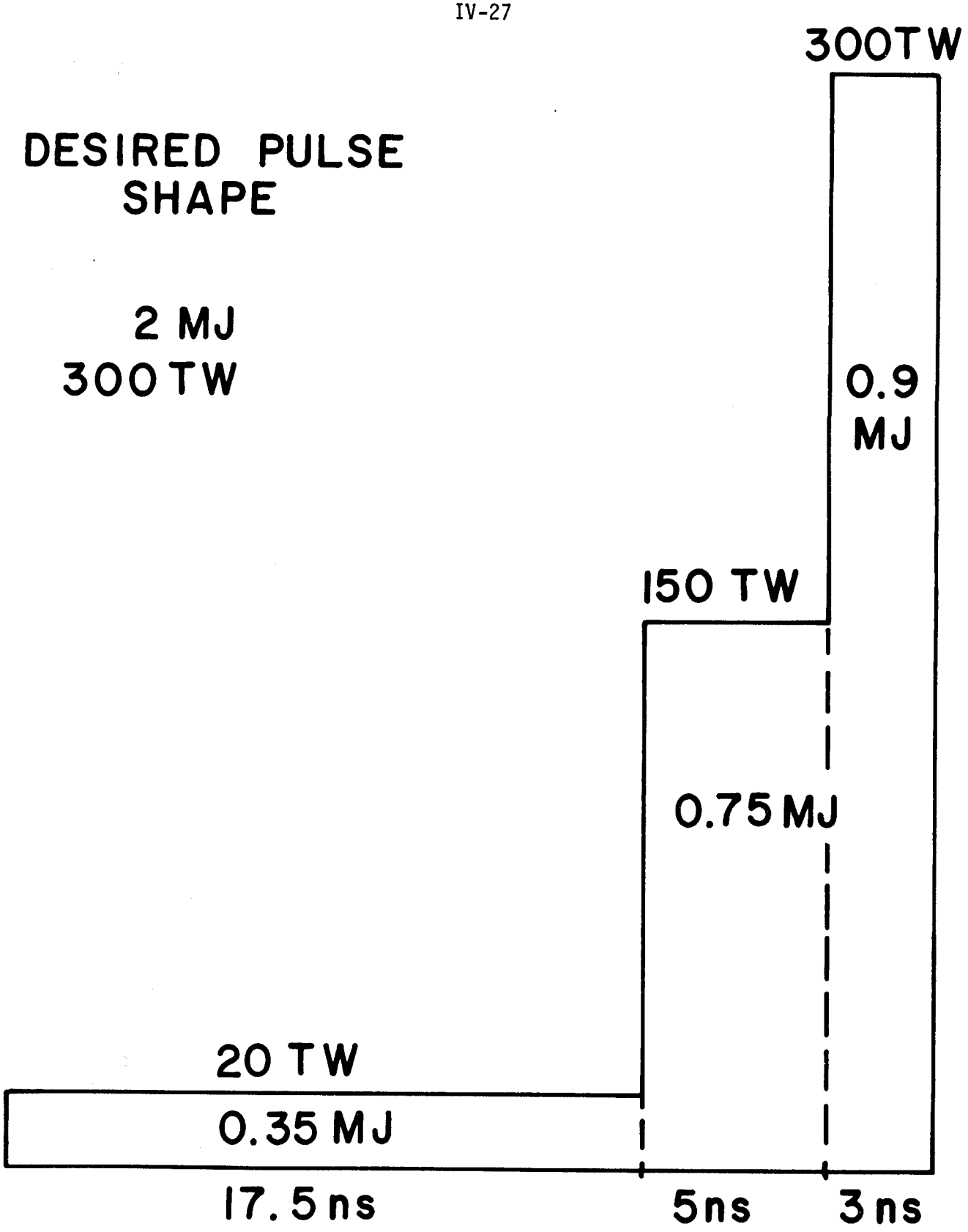
DESIRED PULSE SHAPE
2 MJ
300 TW
300TW
0.9 MJ
150 TW
0.75 MJ
20 TW
0.35 MJ
17.5 ns
5ns
3 ns

Fig. IV.1-8

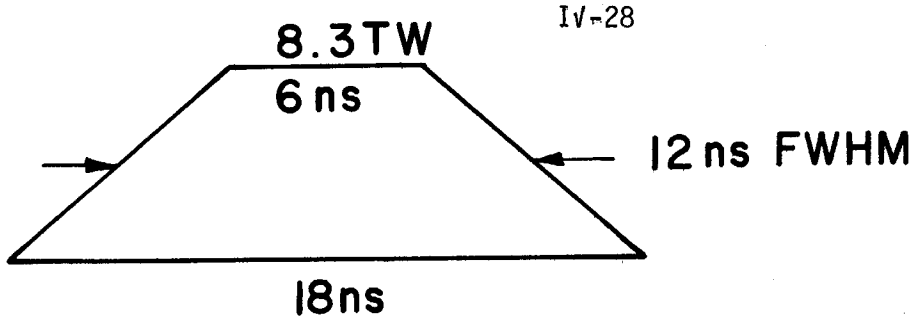

(a IDEALIZATION OF NATURAL PULSE SHAPE

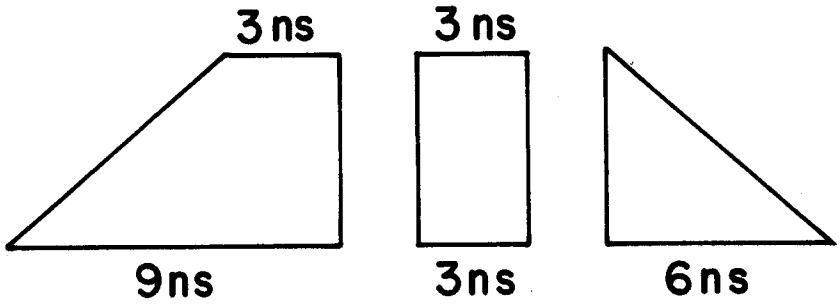

(b) DIVISION OF PULSE BY MULTIPASSING

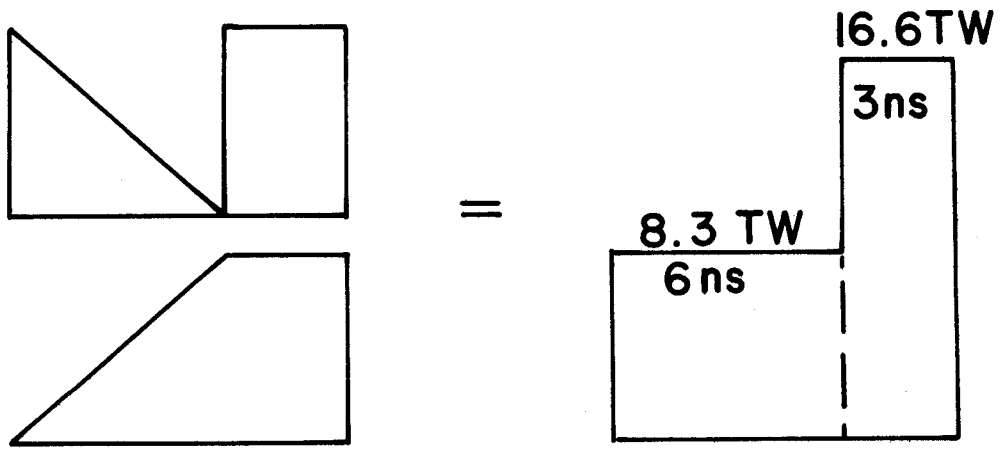

(c) PULSE SHAPING BY STACKING ON TARGET

Fig. IV.1-9

each beam can be handled independently and the distance each must travel to reach the pellet can be adjusted so that they arrive at the target at the appropriate time. This technique has been discussed with respect to an HF laser by Sandia Laboratories and they have called it angular multiplexing.[5] Note that laser radiation must cover the high-gain HF amplifier at all times to suppress ASE. Such a technique appears essential because there are no known methods of electrically or mechanically switching such high energy beams on such short time scales.

The natural pulse of our system is 12 nsec wide and has a peak power of ~ 8.3 TW. The shape is approximately trapezoidal and is assumed to be as illustrated in Fig. IV.1-9a for computational purposes. One of the best schemes for extracting the energy appears to be to divide it into three parts as shown in Fig. IV.1-9b. Thus, three beams must be used to extract the energy: ones that extract the first 9 nsec, the next 3 nsec, and the final 6 nsec as measured along the base of the pulse. Only two pulse widths, 18 nsec and 3 nsec, are required to accomplish this as discussed in the next section. Since there appears to be no convenient way to combine beams, each beam must be independently transported to the target and combined at the target as illustrated in Fig. IV.1-9c.

We will multi-pass eighteen of the twenty amplifiers in this manner and extract the full energy in one pulse from the other two. Then a pulse as shown in Fig. IV.1-10 can be formed by using the two long pulses to form the "foot" and stacking the remaining pulses as indicated in Fig. IV.1-9c. Two

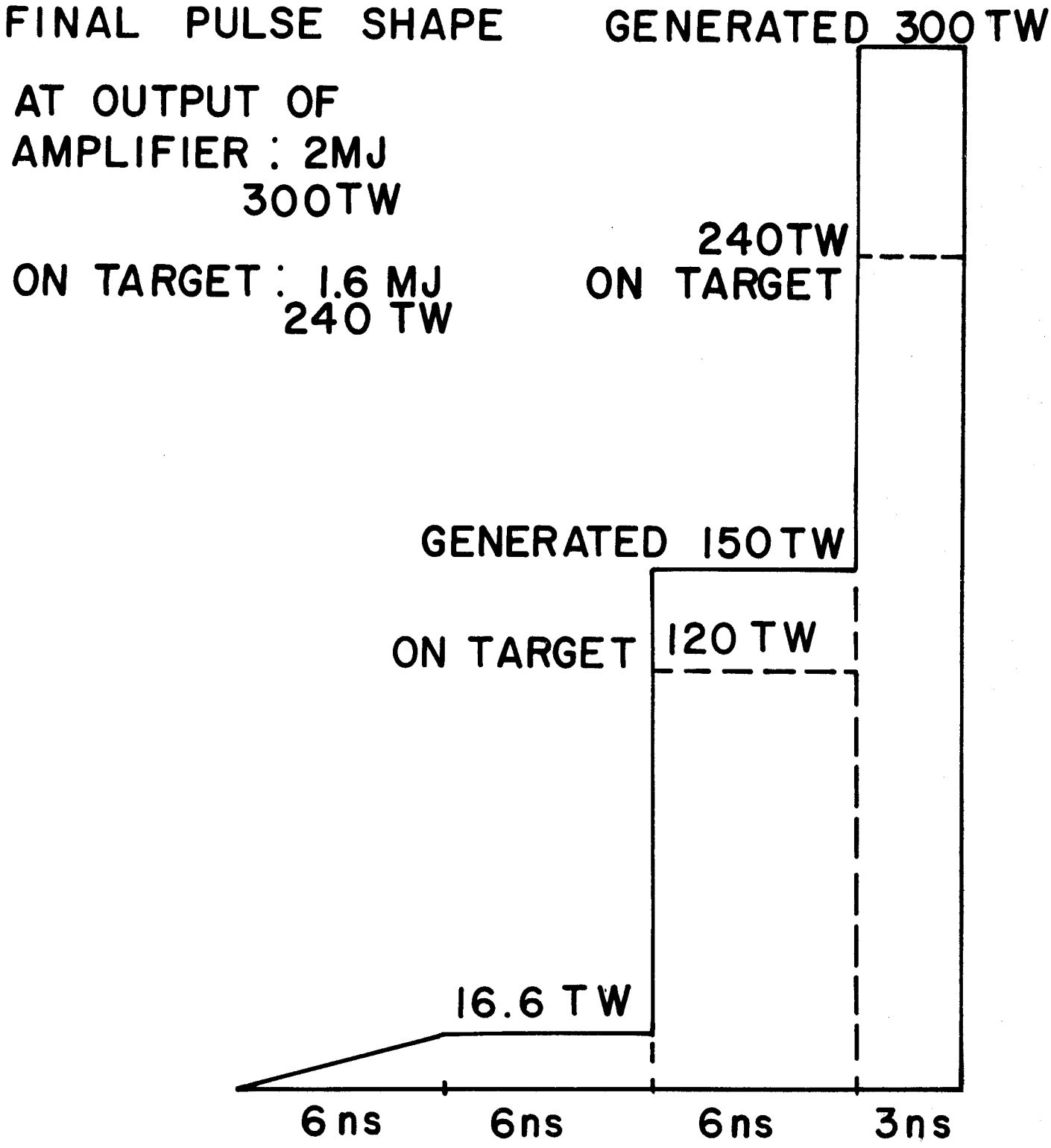
FINAL PULSE SHAPE
AT OUTPUT OF
AMPLIFIER : 2MJ
300TW
ON TARGET : 1.6 MJ
240 TW
GENERATED 300 TW
240TW
ON TARGET
GENERATED 150TW
ON TARGET
120 TW
16.6 TW
6ns
6ns
6ns
3ns

Fig. IV.1-10

values for the power and energy have been indicated in Fig. IV.1-10. The higher of the two represent the laser output of the amplfiers and the lower values represent the energy and power on target. The energy on target was estimated to be about 80% of the energy generated by the laser. The estimate included such factors as window and mirror losses, beam quality, alignment errors, and phase-front distortions.

In multi-passing the final amplifiers several factors must be considered. The principal consideration is the trade-off between the distance between input and output optics that is required for the beams to separate and the fraction of the total volume that is extracted per beam. The details of the geometry are given in the appendix to this chapter. We chose 24 meters to be the distance between input and output optics. This means that ~ 96% of the volume can be extracted. To account for this slight decrease in volume extracted the aperture had to be increased by ~ 2% on each side: from 100 to 102 cm.

IV.1.D. The Front End of the HF Laser System

The purpose of the front end of the laser system is to generate laser beams with the appropriate characteristics to effectively extract energy from the final power amplifiers. Parameters of particular importance include the beam quality, the intensity, the pulse width, and the spectral overlap. The beam quality, which determines the focusability of the beam, must be maintained as high as possible throughout the preamplifier system because

the beam quality at the exit of an amplifier can be no better than that of the input beam. The input intensity is important because the extractable energy is a function of intensity. The front end must also generate pulses of the appropriate widths. This is particularly important because multi-passing is used in our system. Finally, good spectral overlap between the oscillator and the amplifiers is essential since only when there is overlap will the optical energy be amplified and ultimately extracted.

In our particular design, the front end must generate pulses capable of driving final amplifiers from which a single, 12-nsec (FWHM) pulse is extracted and amplifiers from which a series of short pulses are extracted. Thus, one must be able to cut pulses of the appropriate widths from the original pulse generated by the master oscillator. For the single-passed amplifier the required covering pulse must be $\geq$ 18 nsec in duration. As discussed in the previous section the multi-passed amplifiers must have three successive covering pulses having widths of 9 nsec, 3 nsec, and 6 nsec, respectively.

The simplest method of obtaining this goal is illustrated in Fig. IV.1-11. This requires the generation of just two basic pulse widths, 18 nsec and 3 nsec. The three pulses required can be obtained by simply splitting the original 18 nsec pulse twice. It must be remembered that in the HF laser, energy can only be extracted as it is generated and that it is only generated during the natural 12-nsec (FWHM) pulse width. Therefore, the leading edge of the 18-nsec pulse that covers the first 9 nsec of the natural pulse

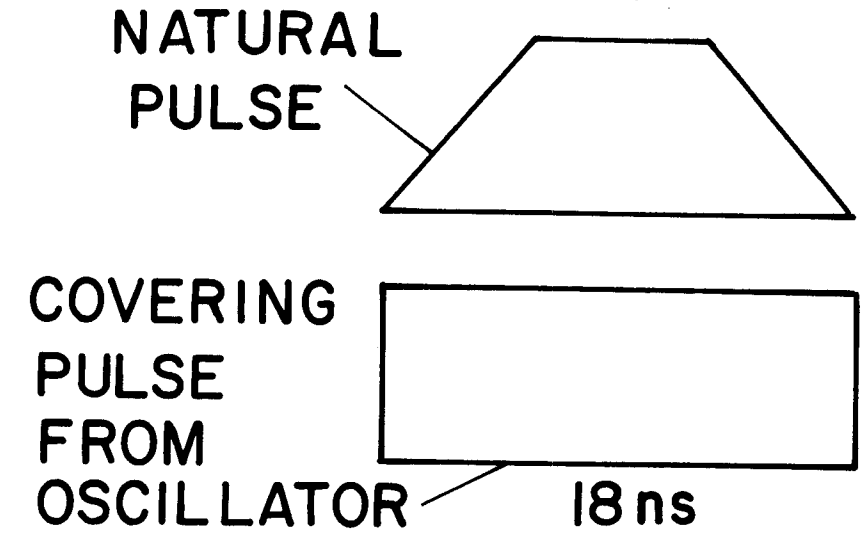

(a) SINGLE PULSE EXTRACTION

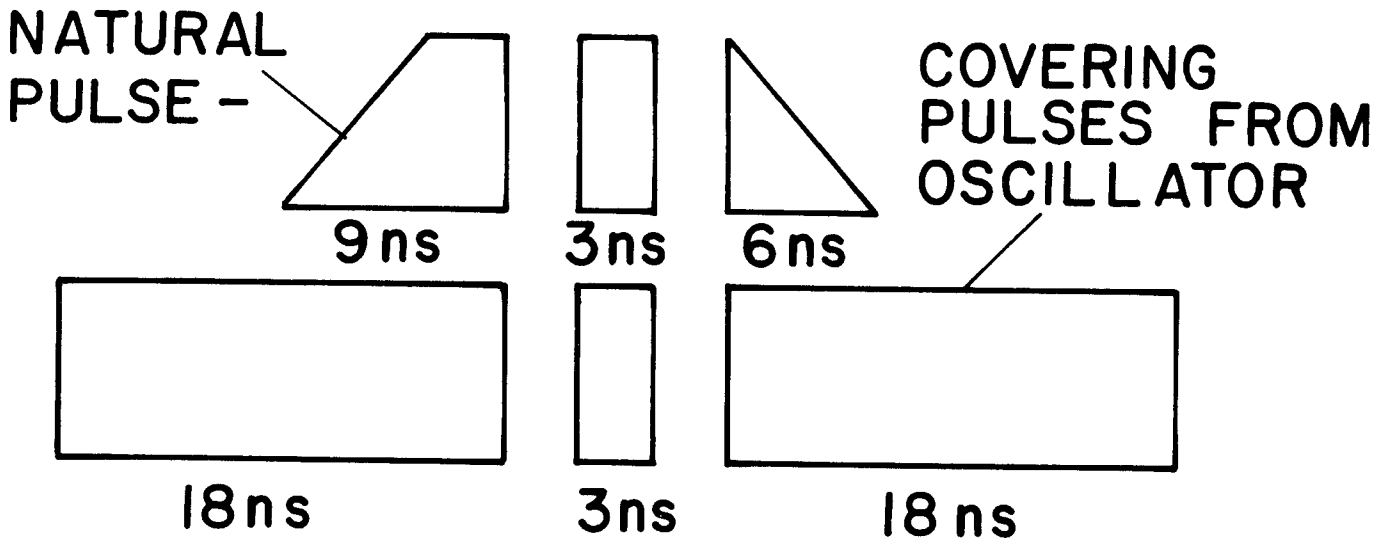

(b) MULTIPASSED EXTRACTION

Fig. IV.1-11

should not be amplified nor should the trailing edge of the second 18 nsec pulse. Realistically, however, one would expect some gain in these regions so that the leading and trailing edges should experience some amplification. This could result in a small prepulse from the leading edge but this should be of little consequence in our design because we actually specified a relatively high-energy "foot" in the ideal pulse shape (see Fig. IV.1-8) and a prepulse should just increase this slightly. Also, due to the method we chose to stack pulses, much of the energy in the trailing edge will actually appear on target in the peak of the pulse which is beneficial.

If a prepulse does occur and should it ultimately be deemed undesirable, it can be eliminated by covering the initial 9 nsec of the natural pulse with one of equal duration as shown in Fig. IV.1-12. This will require the generation of a third pulse with a 9-nsec duration. If this does not fully eliminate the prepulse an off-target bias beam could be used to control the ASE. At this time we feel the first approach is satisfactory and will utilize it in our design.

A successful method for the generation of these short pulses has been developed[10] and is illustrated in Fig. IV.1-13. A master oscillator, preamplifier system generates an initial pulse that is typically 1 J and 100 nsec in duration.[10] To extract short pulses, a polarization technique is utilized which incorporates an electro-optic switch and Brewster-angle beamsplitter. The electro-optic switch rotates the linearly-polarized laser beam 90^{0} for a time period equal to the desired pulse width. After amplification the total pulse strikes the Brewster-angle beamsplitter and

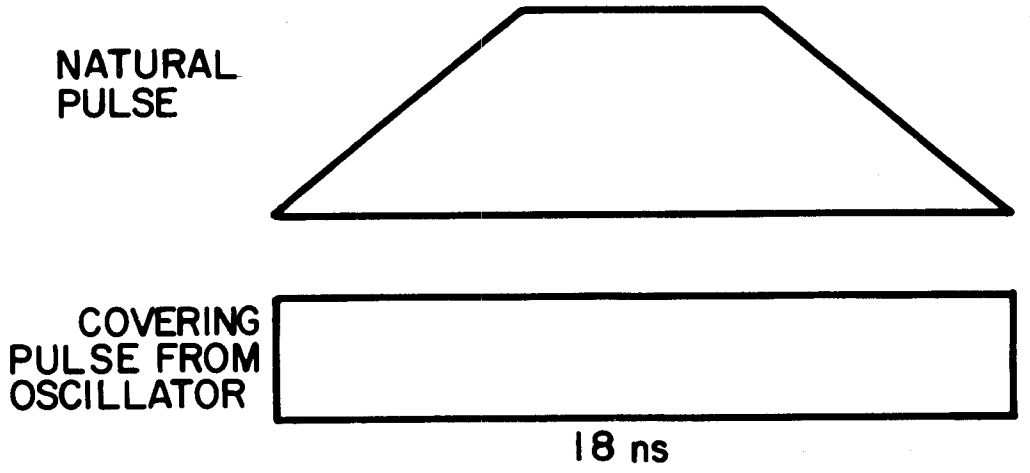

(a) SINGLE PULSE EXTRACTION

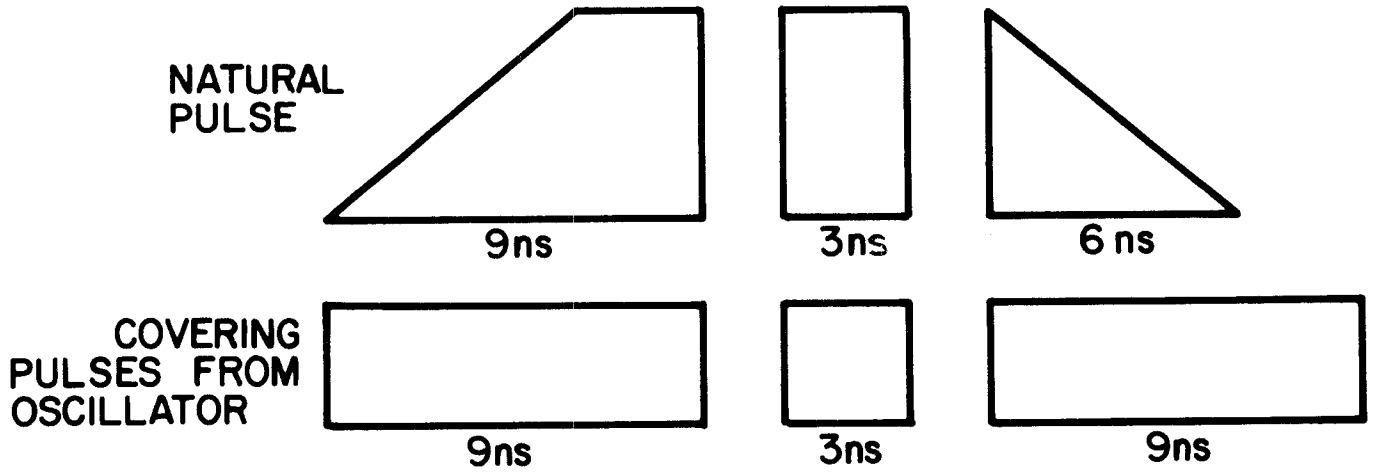

(b) MULTIPASSED EXTRACTION

Fig. IV.1-12

MASTER OSCILLATOR – SHORT PULSE GENERATION

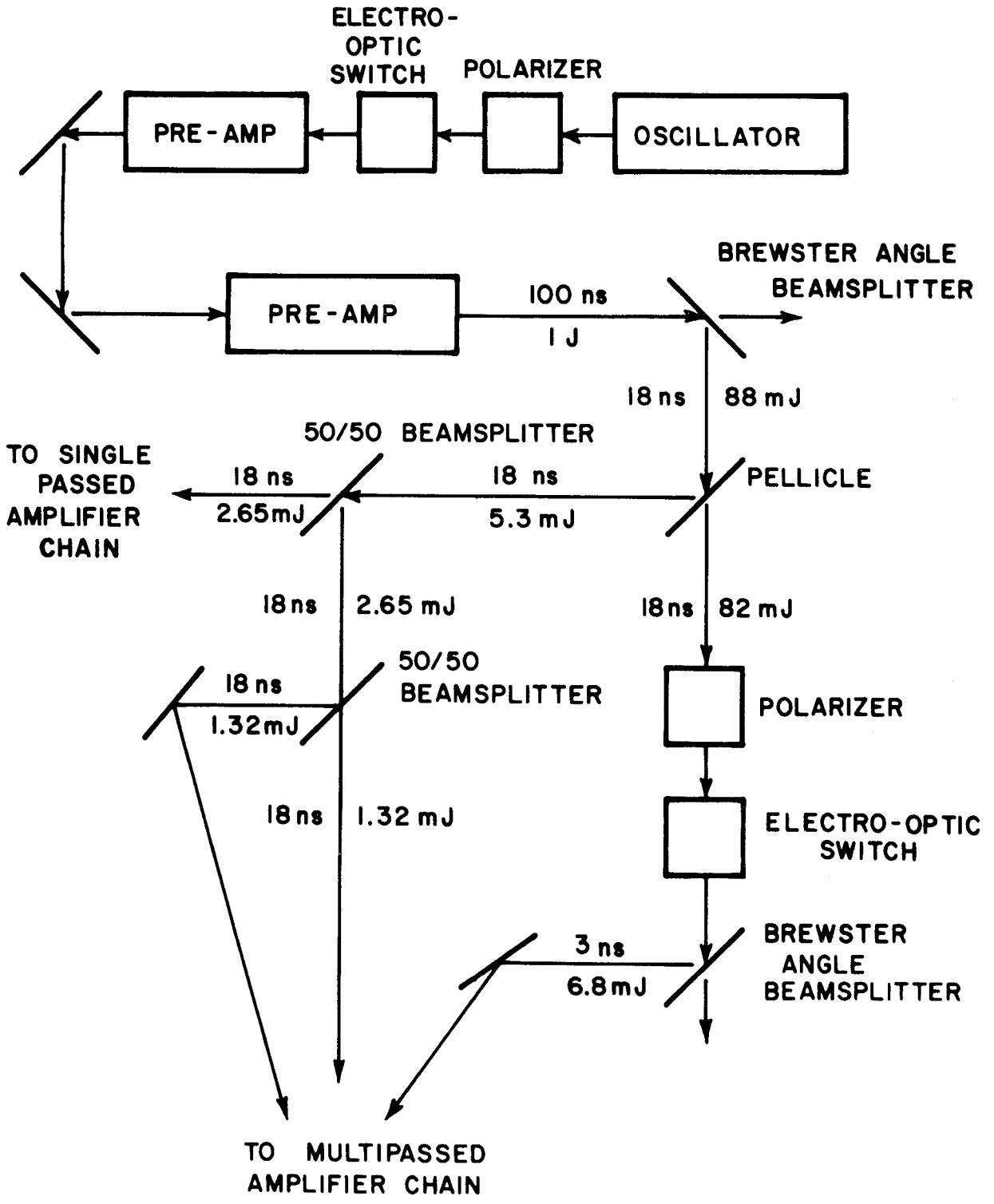

Fig. IV.1-13

because of the difference in polarization the rotated portion is reflected while the remaining portion is transmitted. In this manner the desired short pulse is cut from the long pulse. Short pulses with good contrast ratios have been obtained in this manner.

In our particular design we must generate two short pulses of 18-nsec and 3-nsec duration each. This can be accomplished by basically using the above technique twice. As illustrated in Fig. IV.1-13, we will first cut an 18-nsec pulse from the beam. This 18 nsec pulse is then split by a pellicle, which minimizes dispersion of the beam. The reflected part is split twice more to form the three 18-nsec pulses required to cover both the single and multi-passed amplifiers. The transmitted beam passes through another electro-optic switch which rotates a portion of the beam for 3 nsec. As before, the rotated, 3-nsec pulse is reflected by a Brewster-angle beam-splitter while the remaining portion is not.

The pulse that the master oscillator generates must have good spectral overlap with that of the F_2-H_2 amplifiers in order to obtain a good extraction efficiency. One approach is to develop an oscillator that operates on F_2-H_2 mixtures. However, recent experiments at Sandia[4] have demonstrated that the spectrum produced by an SF_6-HI fueled oscillator yields the same extraction efficiency as an F_2-H_2 oscillator. Either one would appear to be a suitable candidate for the master oscillator.

Having generated the proper short pulses it is necessary to amplify them to sufficient size and intensity to drive the final amplifiers. Specifically, the beam must cover the entire amplifier aperture ($\sim 10^4$ cm^2)

with an intensity of $\geq 10^7$ W/cm^2. The total energy required for either the single pass or the sum total of the three multi-passed beams is ~ 1800 J. In our design there are 20 final amplifiers, two that are single-passed and 18 that are multi-passed.

One approach to amplifying these pulses is to have a chain of pre-amplifiers for each of the 20 final amplifiers. However, because of the relatively small amount of total energy present in the front end, an attractive alternative is to have only a few chains of preamplifiers and split these beams into the appropriate number of beams after amplification. In particular, one can consider two chains, one for the single-passed amplifiers and one for the multi-passed amplifiers. The reason for this division is that each of the preamplifiers in the multi-passed chain must be multi-passed as well to suppress ASE. This configuration greatly simplifies the front end design but requires the development of non-dispersive, 50/50 beamsplitters for the multi-line HF laser. Such beamsplitters have not been demonstrated but are plausible and their development is being pursued.[11]

A preliminary examination of the requirements for the preamplifier chain revealed no special problems that had not been addressed in the final amplifier design. Also it was noted that there is comparatively little energy in the front end so that efficiency is not of major concern. For these reasons we did not attempt a detailed front end design but merely calculated some typical preamplifier parameters in order to get an indication

of what such a system might look like. For simplicity, we decided to use the same gas mixture and pressure in each of the preamplifiers as in the final amplifiers. We then designed a system to amplify the pulses to the desired total energy. Note that this may not result in a strictly valid set of pulses to drive the final amplifiers because the energy will not be distributed such that the intensity is $\geq 10^7$ W/cm^2 at all times. However, our parameters closely approximate those that are ideally required so that our design should not be dramatically different from an optimum one. In designing an actual front end one would vary the gas mixture and pressure to optimize pulse amplification and facilitate amplifier design.

The front end parameters that we calculated are summarized in Fig. IV.1-14 and 15 and in Tables IV.1-3 and 4. The input pulses to the first preamplifiers are from the short pulse generation system shown in Fig. IV.1-13. In the single-pass chain the pulse is amplified to 6850 J and then split in half to drive the two single-pass, final amplifiers. In the other chain the energy in each preamplifier is extracted by three successive beams. The total energy in the three beams is ~ 33 kJ. Each of the three beams will then be split into 18 equal beams to drive the 18 multi-passed, final amplifiers.

SINGLE PASS AMPLIFIER CHAIN

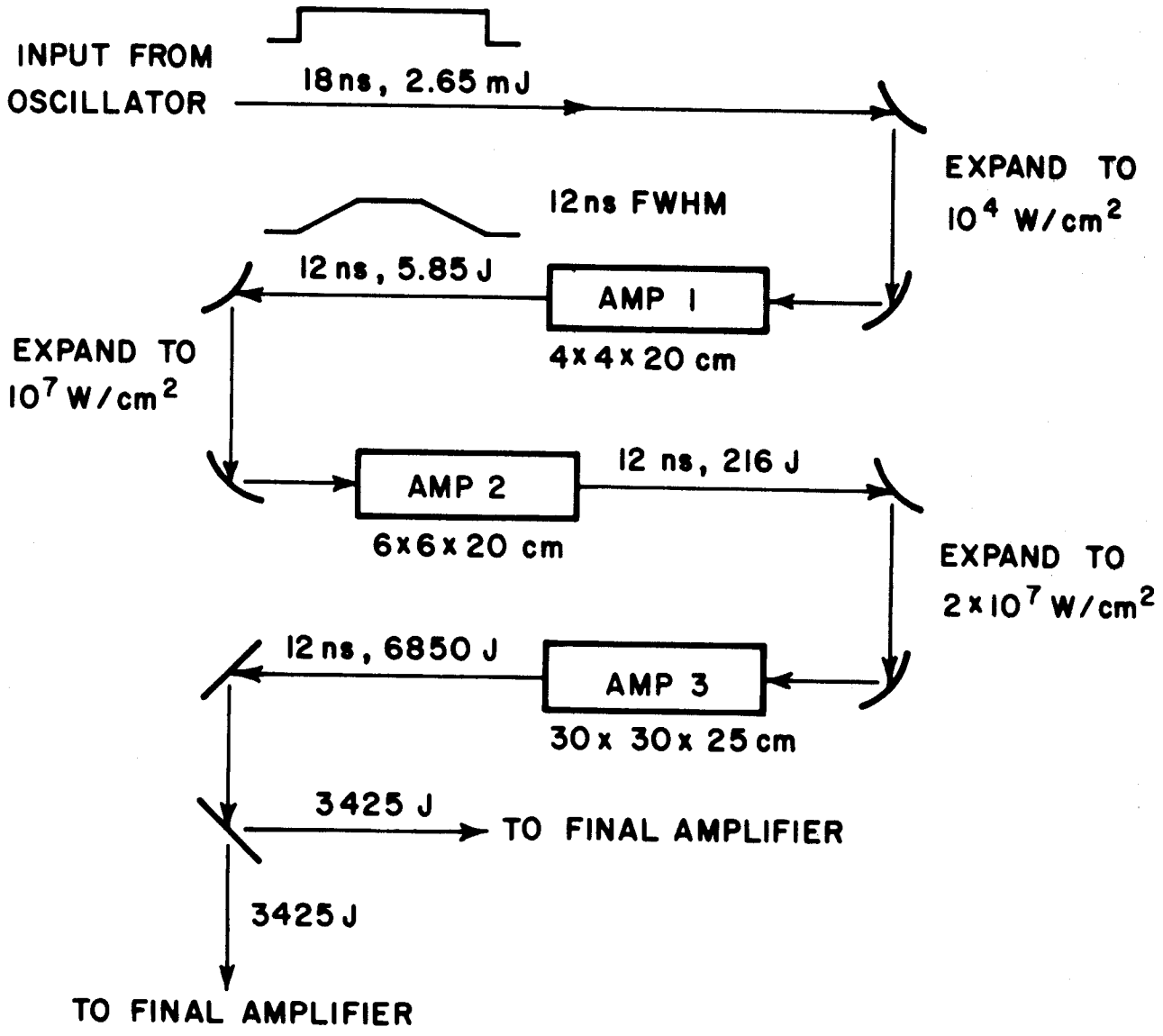

Fig. IV.1-14

MULTIPASSED AMPLIFIER CHAIN

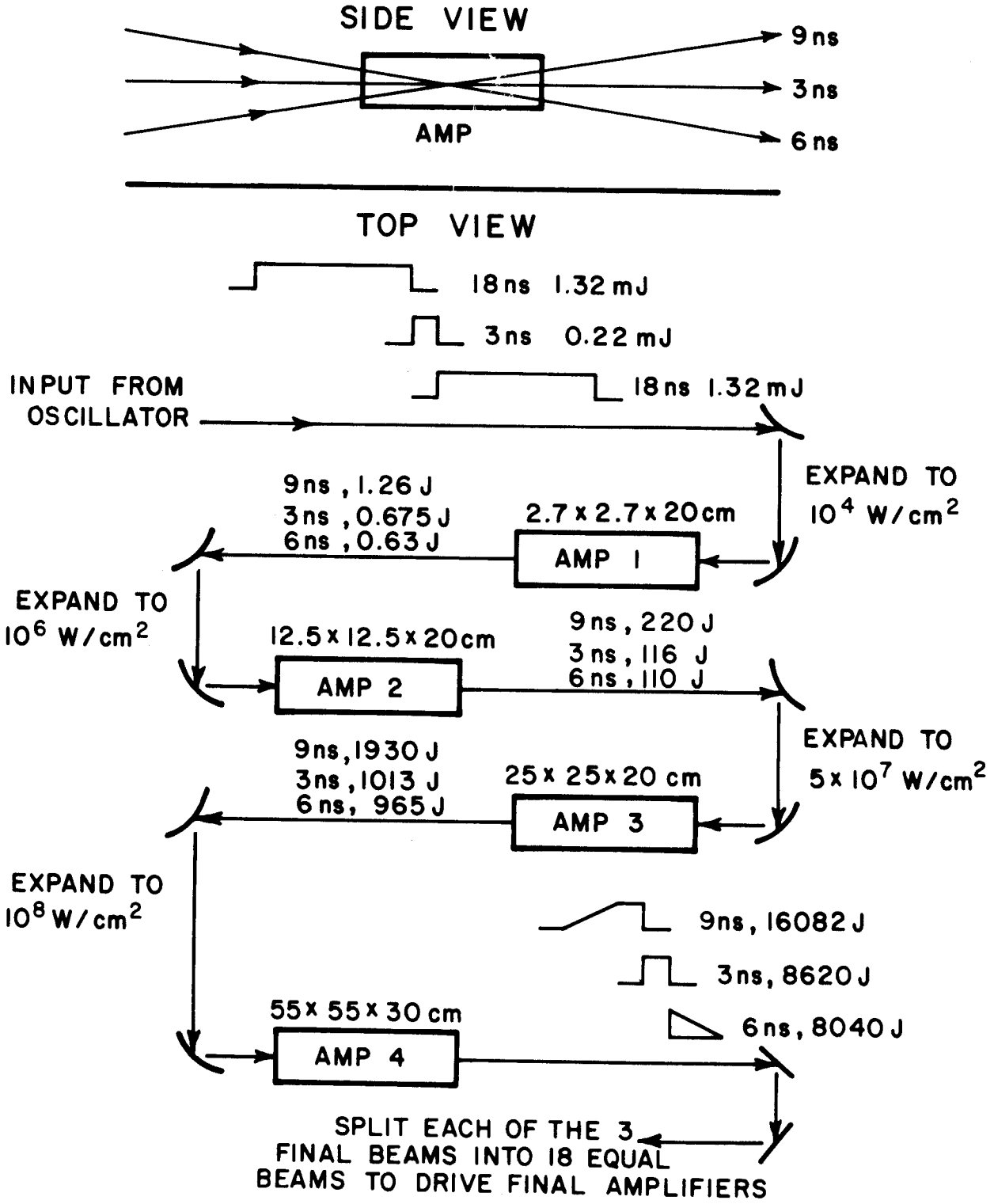

Fig. IV.1-15

Table IV.1-3

18 nsec Preamplifier Chain Parameters

Amplifier	1	2	3
Aperture (cm^2)	16 (4x4)	36 (6x6)	900 (30x30)
Length (cm)	20	20	25
Input Energy (J)	0.002	4.3	216
Output Energy (J)	5.85	216	6850
Input Intensity (W/cm^2)	10^4	10^7	$2x10^7$
Output Intensity (W/cm^2)	$3x10^7$	$5x10^8$	$6x10^8$

Table IV.1-4

Multi-passed Preamplifier Chain Parameters
(Pass Sequentially 9 ns, 3 ns, and 6 ns Pulses)

Amplifier		1	2	3	4
Aperture (cm^2)		7.3 (2.7x2.7)	156 (12.5x12.5)	625 (25x25)	3025 (55x55)
Length (cm)		20	20	20	30
Input Energy (J)	9 ns	0.0013	0.89	183	1650
	3 ns	0.0002	0.47	93.8	907
	6 ns	0.0013	0.45	91.5	825
Output Energy (J)	9 ns	1.26	220	1930	16080
	3 ns	0.68	116	1013	8620
	6 ns	0.63	110	965	8040
Input Intensity (W/cm^2)		10^4	10^6	$5x10^7$	10^8
Output Intensity (W/cm^2)		$3x10^7$	$2.5x10^8$	$5x10^8$	$8.5x10^8$

IV.1.E. The Gas Handling System

IV.1.E-1. Introduction

The gas handling and reprocessing system for an HF laser presents special, but not unique, problems of managing highly corrosive gas mixtures, large over-pressures, and continuous reprocessing. While the difficulties associated with these are considerable, they are not exceptional except when compared with particularly benign lasers such as CO_2. The problems appear much less formidable when compared with iodine, rare-gas halogen, group VI, or mercury halide lasers. The latter two systems in particular will probably present gas handling problems of an equal if not more insidious nature. Given the experiences of the chemical industries which handle fluorine and hydrogen-fluoride, the problems of gas handling in the HF laser system appear quite manageable.

In order to identify the questions that must be addressed, we will begin by describing the basic requirements that the gas-handling system must meet. As discussed in Sections IV.1.B and C the laser is based on the chemical reactions of H_2 and F_2 to form HF. Mixtures of H_2 and F_2 tend to be explosively unstable so that the first requirement is to obtain stable mixtures (on a molecular scale) that do not ignite until triggered externally. Once triggered, the rapid release of energy into the gas causes large over-pressures and high temperature gradients. The resulting density gradients must be eliminated prior to the next laser pulse if high beam quality is to be maintained. After the completion of the chain reaction the HF must be separated from the remaining F_2 and O_2 in the gas mixture and then reprocessed into H_2 and

F_2 for reuse. (The oxygen is added to the F_2-H_2 mixture to eliminate spontaneous detonations.) The final requirement is that all materials be compatible with F_2 and HF. Thus, the gas handling can be divided into three stages: mixing, burning and reprocessing.

IV.1.E-2. The Mixing and Flow of the Laser Mixture

The most important consideration is whether or not our particular mixture of 3000/900/100 Torr of $F_2/O_2/H_2$ is stable. Any mixture that spontaneously detonates cannot be associated with a viable system. A graph[12] of pressures at which spontaneous detonation occurs for various static mixtures is shown in Fig. IV.1-16. Detonation occurs for points on the curves and at all higher pressures. This data indicates that our mixture should be stable. An additional safety margin is provided by the fact that our system is flowing, and flowing mixtures are more stable than static mixtures since most detonations are wall related.

The basic flow pattern will be to have "slugs" of fuel separated by a non-combustible buffer zone. Ideally this fuel slug should be just the size of the laser cavity. If it were smaller, insufficient optical energy would be generated; if larger, inefficient use of the chemical energy would result. The buffer zone serves to prevent flame propagation upstream and to help reestablish uniform flow conditions prior to the next pulse.

There are several possible approaches to generating the required flow pattern. One is to separate fuel slugs with an inert gas such as He or Ar. A second approach is to have a continuous flow of an F_2-O_2 mixture to which H_2 and an inert gas are alternately added to form the fuel and buffer zones, respectively. A third possibility is to simply have a fuel region separated

STABILITY REGIONS

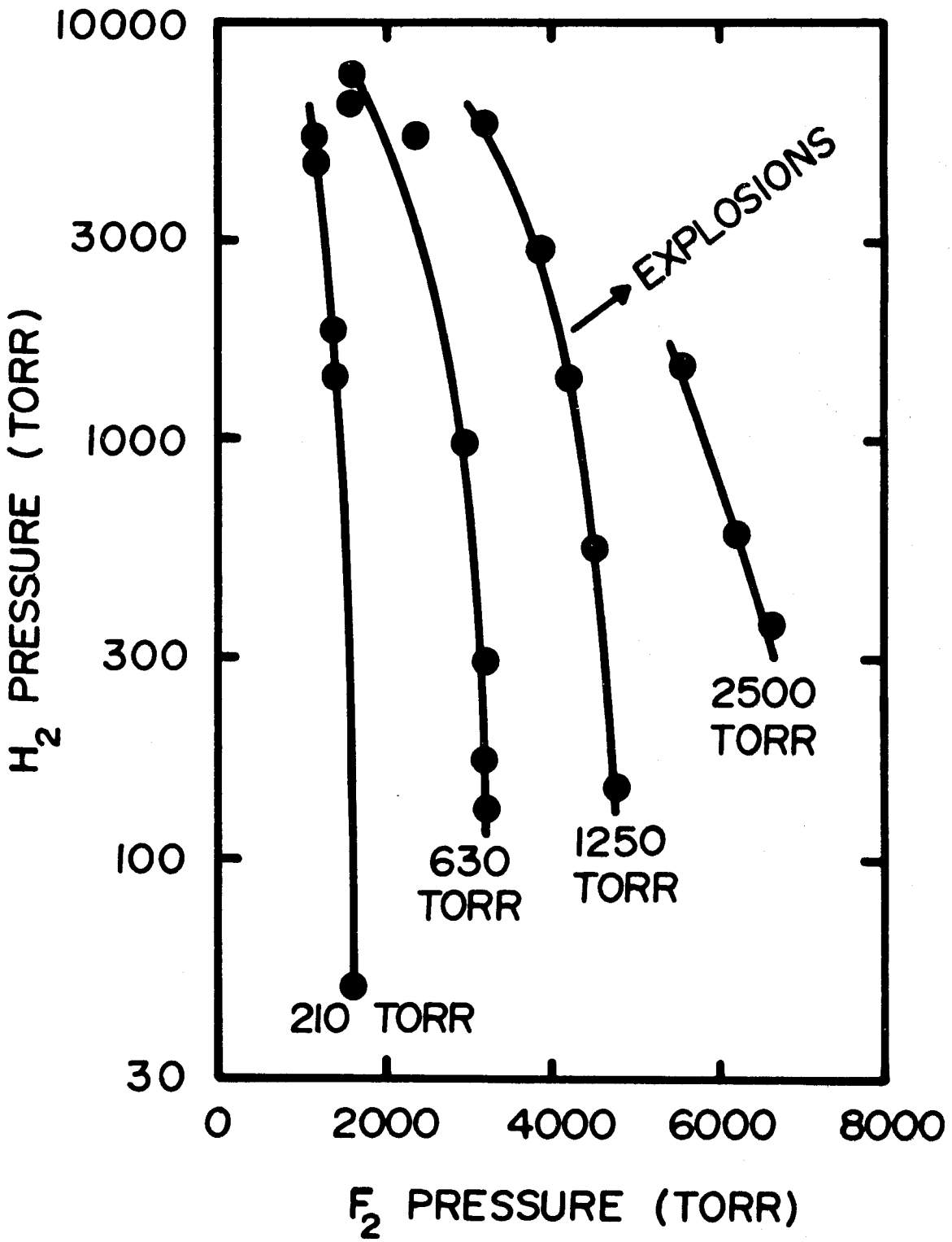

Fig. IV.1-16

by a pure F_2-O_2 zone without adding any inert gas. The first two approaches greatly increase the reprocessing requirements because the inert gas must be removed from the residual fuel mixture. There also will be difficulties with index of refraction matching near the interface regions. Finally the valving system required will be more complex than in the third scheme. This third scheme also has problems, however, resulting from the fact that there will be a pressure differential between the fuel and buffer zones. This results in index of refraction gradients and enhanced H_2 diffusion out of the fuel zone. After consideration of the various approaches we chose the third for our design for two basic reasons: first, its simplicity and secondly, the fact that the pressure differential is small for our parameters (1 part in 40) so that the detrimental effects should be small. It should be pointed out that one of the alternative schemes could be used if our choice proves unworkable.

Thus, our system will have a continuous flow of F_2 and O_2 into which H_2 will be injected. A principle requirement is that the H_2 must mix thoroughly on a molecular scale before the reaction is initiated. Thus, sufficient time must be allowed after injection for mixing to occur. However, one also wishes to minimize the necessary mixing time to reduce H_2 diffusion out of the desired fuel zone. This problem can be adequately resolved by turbulently injecting the H_2 into the F_2-O_2 mixture. This requires only a few centimeters for complete mixing (equivalent to a few milliseconds in time at our flow rates).

Thus, the H_2 will be injected from a mixing head that can be placed a few centimeters from the cavity. The H_2 will be turbulently injected through a large number of orifices spaced across the mixing head. A constant pressure F_2-O_2 mixture will continuously flow through the mixing head. An important consideration in determining the chemical efficiency of the laser is the speed at which the H_2 valves can be opened and closed. For maximum efficiency one would ideally like a square fuel slug as shown in Fig. IV.1-17a that is exactly the length of the laser cavity. In reality, however, the slug will look like that in Fig. IV.1-17b in which the rise and fall times are determined largely by the valving speed but also by diffusion. The valving speed for state-of-the-art valves[13] is < 5 msec and since our slugs are 125-msec long (1 meter at 8 m/sec) this component of the chemical efficiency is > 90%. In this study we will assume an efficiency of 90%.

Another consideration in establishing a flow is possible boundary layer effects. One such effect can result from the velocity differential between the flow at the center of the channel and at the walls. This can greatly deform the slug and is, of course, undesirable. This can be countered by having turbulent flow and minimizing the flow distance so that effects have less time to establish. Because of the turbulent injection of H_2 into the F_2-O_2 flow stream and the short flow distance, deformation of the slug should not be a serious problem in our system. A second approach should be mentioned, however, and it is to establish the flow of a non-reacting gas mixture at the wall. To minimize problems of

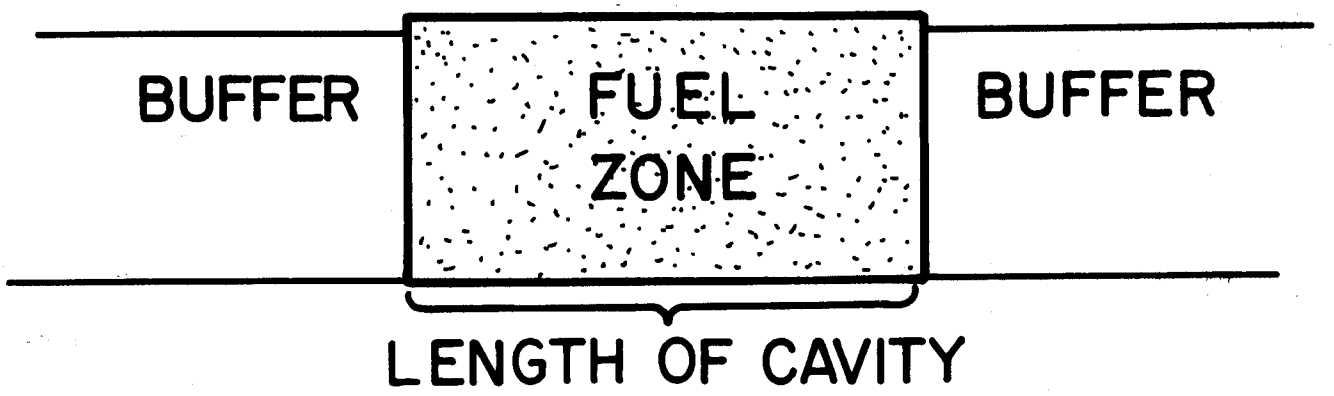

(a) IDEAL FUEL ZONE

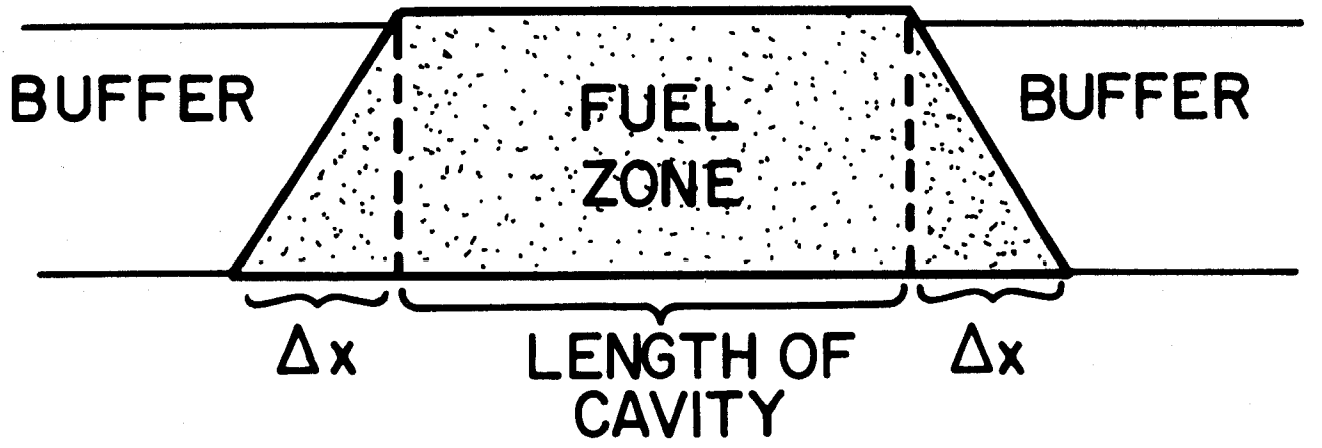

(b) REALISTIC FUEL ZONE

Fig. IV.1-17

reprocessing and index matching this should probably be the pure F_2-O_2 mixture. This would greatly reduce the drag on the fuel slug itself reducing any deformation. This technique has the additional advantage of isolating the fuel from the wall. This could reduce spontaneous detonations if they become a problem, because many detonations are triggered by wall effects. However, the application of this technique does not appear necessary for our parameters.

IV.1.E-3. Post-Detonation Effects

During the chemical burn a tremendous amount of energy is released almost instantaneously into a small volume of gas. The result is the formation of strong shock waves and temperature gradients in the flow channel. One problem that can arise from these phenomena is the triggering of premature detonations by hot reaction products that have propagated upstream. Another problem is that these density gradients create index-of-refraction gradients, which if not suppressed prior to the next pulse will result in very poor optical beam quality. The small scale density variations $(\frac{\Delta\rho}{\rho})$ must be kept to less than about 10^{-3} for acceptable beam quality.[14] The exact requirement depends on the laser cavity dimensions, the optical aperture, the focal length of the last mirror, the wavelength, and the required spot size on the target. In addition, large scale gradients (i.e., the size of the chamber) must also be kept below minimum values to prevent unacceptable phase front distortions. Unfortunately, the shock waves cannot be merely swept away by the incoming gas but instead continuously reflect back and forth through the

flow channel until gradually dissipated by loss of energy. Specially designed muffler systems must be incorporated into the flow channel to greatly decrease the time required to dissipate the shock waves.

To examine the post-detonation effects in more detail, a simple schematic of the situation is shown in Fig. IV.1-18. The gas is at an initial pressure and temperature P_o and T_o which in our design equal 4000 Torr and 300°K, respectively. During the burn the pressure and temperature rise to values P_1 and T_1. This sets up a shock wave of pressure P_{s1} which in reflecting off the mixing head exerts a pressure, P_{s2}.

The over-pressure and temperature rise can be estimated by calculating the energy released and assuming that the gas comes to thermal equilibrium with only HF, F_2, and O_2 present. This ignores possible dissociation and O_2 reactions. The reaction yields about 65 kcal per mole of HF formed. The change in temperature is related to the change in energy by

$$\Delta T = \frac{\Delta E}{C_v}$$

where C_v is the constant volume heat capacity. Assuming that $C_v \simeq 5$ cal/mole-K and that the volume does not change during the energy release we find

$$\frac{\Delta P}{P_o} = \frac{\Delta T}{T_o} = \frac{26{,}000}{T_o} \; C_{H_2} \; ,$$

where C_{H_2} is the H_2 mole fraction. For our parameters, $T_o = 300^oK$ and $C_{H_2} = 1/40$ so that

$$\frac{\Delta P}{P_o} = \frac{\Delta T}{T_o} = 2.2 \; .$$

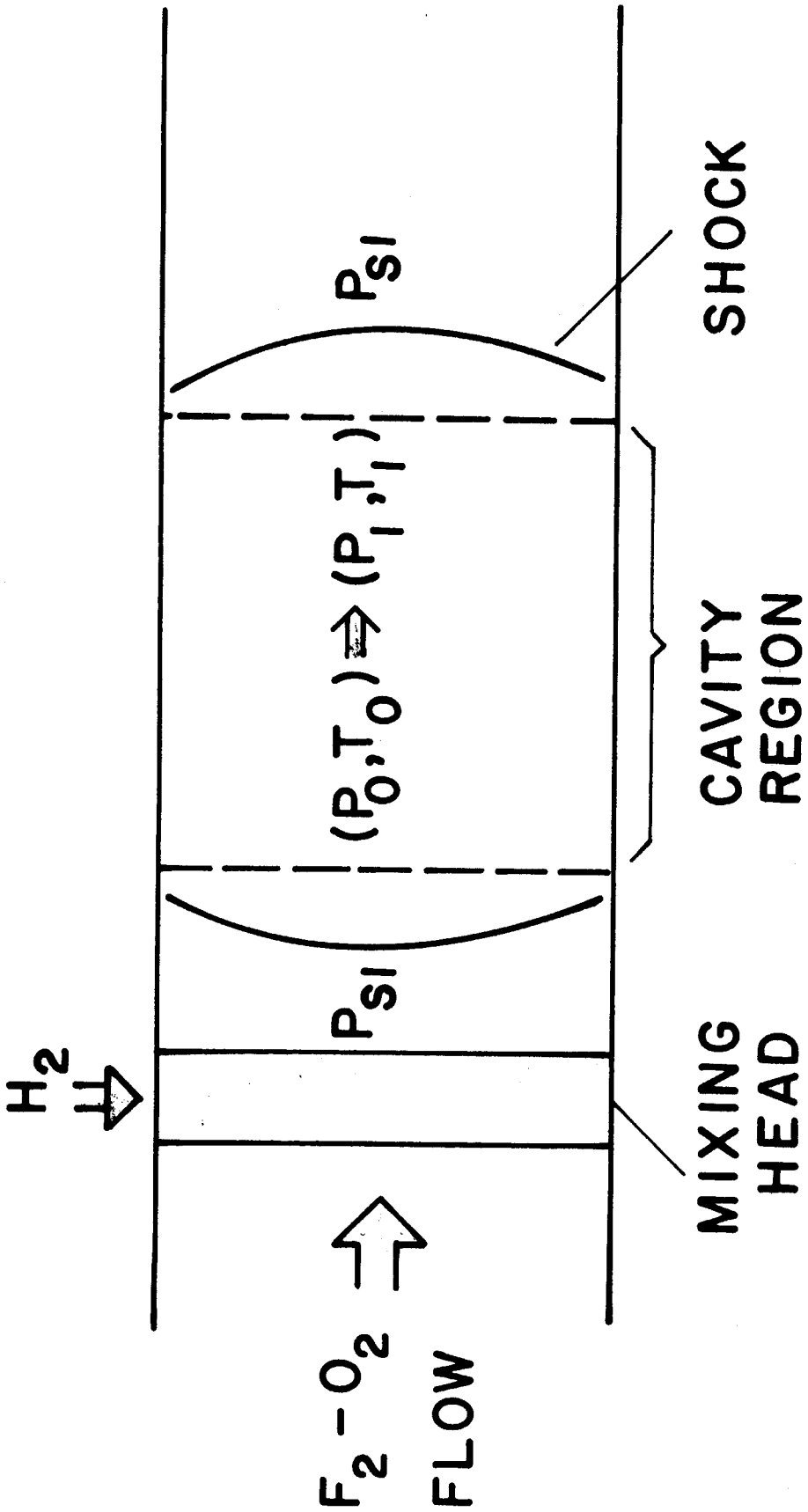
H_2
$F_2 - O_2$ FLOW
MIXING HEAD
P_{SI}
$(P_O, T_O) \Rightarrow (P_1, T_1)$
P_{SI}
CAVITY REGION
SHOCK

Fig. IV.1-18

From this relation one can calculate that the gas in the cavity will instantaneously rise to a temperature T_1 of 950°K and a pressure P_1 of 12,000 Torr.

A detailed shock tube analysis[15] was performed for a system with these parameters. The analysis assumed ideal gas behavior and that the mixing head perfectly reflected the shock. These calculations yielded a shock wave pressure P_{s1} of 8000 Torr, a reflected shock wave pressure P_{s2} of 14,400 Torr on the mixing head and a gas temperature adjacent to the mixing head of only 450°K.

To adequately handle these pressure and temperature effects the gas handling system must be able to reestablish a uniform, room-temperature gas flow in about one-half the time between laser pulses (~ 125 msec in our design) and prevent any flame propagation upstream. TRW has examined these problems for several ICF laser candidates[14] including an HF laser. The particular HF laser system that they studied had a considerably higher H_2 concentration than our design and therefore a much higher over-pressure ($\Delta P/p = 7$ as opposed to $\Delta P/p = 2$). They concluded that a suppression system could be designed for their choice of HF laser parameters that would perform adequately with respect to beam quality at repetition rates of up to 10 Hz. Since their requirements were more stringent than ours with respect to both over-pressure and repetition rate, we conclude that an appropriate muffler system such as a vented duct device can be designed to give satisfactory performance in our system, although no detailed design will be proposed.

A more complicated problem is the propagation of hot reaction products upstream which can result in several detrimental effects. One is flame propagation upstream. Another related problem is the premature detonation of a fuel slug by residual reaction products anywhere in the flow channel. The third is the need to remove all temperature and pressure gradients prior to the succeeding pulse. This latter was discussed above and it was concluded that such gradients can be eliminated in a sufficiently short time. However, if the reaction products travel far enough upstream the process of removing gradients will be greatly hindered. The net result of these potential problems is that one wants to minimize the propagation of products upstream.

There are two methods that will totally prevent the propagation past the mixing head. One is to use mechanical valves to isolate the upstream channel until all major over-pressures are eliminated and the other is to have fully choked flow in the mixing head. Neither technique is particularly desirable. Stopping the flow with a valve will cause small shock waves in the upstream channel - exactly what we want to prevent - and will put stress on the pumps. To operate at choked flow requires that the ΔP in the mixing be at least equal to the maximum over-pressure at the mixing head (14,400 Torr in our design). This would require intolerably high pumping powers.

After some consideration, it was decided that some flow upstream could be tolerated in the F_2-O_2 channel. It was noted that the shock wave

was rather weak (it more closely approximates the CO_2 case studied by TRW in which the $\Delta P/p = 1.5$).[14] Most of this shock wave can probably be reflected by either the mixing head or a special plate designed to reflect the shock wave but not inhibit the steady flow. Thus, one would not expect any extensive propagation further upstream and any products can probably be swept out by the natural flow of the gas. However, some shock wave damping will probably be required in the upstream channel. In addition, there is no H_2 present so that there is no threat of spontaneous detonations. We assumed, somewhat arbitrarily, that the ΔP required to reestablish the flow is only 350 Torr. We feel, however, that the problem will have great impact on the laser performance and should be examined in greater detail.

The situation is quite different for the H_2 stream. If hot reaction products which are primarily composed of F_2 and O_2 were to propagate up the H_2 channel, the result would almost certainly be a spontaneous detonation. This must be prevented. It should be noted that under <u>normal</u> operating conditions the H_2 valves will be closed at times of major over-pressures. By the time the valves must open to produce a new fuel slug ($\sim$ 125 msec after the previous pulse) all pressure variations should have been suppressed so that only a modest ΔP in the H_2 orifices should be required to prevent any back flow into the H_2 channel. However, for safety reasons (a valve fails to close, for example) the H_2 orifices should be operated with a ΔP at least equal to the maximum over-pressure or 14,400 Torr in our design. This should prevent any flame propagation up the H_2 flow channel. Fortunately, the H_2 mass flow in our design is

a small fraction of the total so that this large ΔP does not significantly increase the pumping power requirements (see Section IV.1.G).

A final aspect of post-detonation effects that must be considered is whether the cyclic temperatures and pressures will present any special materials problems. A number of materials have been found capable of handling F_2 and HF including nickel, copper, aluminum, monel and stainless steel, many of which perform well at elevated temperatures. However, these all resist corrosion by the formation of a protective layer of various fluorine compounds. It is possible that the cyclic stresses could cause flaking or cracking of this layer which could promote corrosion. This is also an area that requires further investigations.

To summarize, it appears that post-detonation effects can be adequately and economically controlled. The potential problems are greatly ameliorated by our choice of a hydrogen-lean mixture and low repetition rate. Increasing either the H_2 concentration or the repetition rate will increase the difficulties of coping with these effects. These post-detonation effects will probably be the limiting factors on the maximum H_2 concentration that can be used and the maximum repetition rate that can be obtained in a practical HF laser system.

IV.1.E-4. Chemical Reprocessing

An essential requirement of the gas-handling system is the capability of reprocessing the spent-fuel mixture. This is necessary because the pumping process relies on the reactions of H_2 and F_2 to form HF and, in order to reuse the gas, HF must be regenerated into H_2 and F_2. Another reason for removing the HF is that small residual amounts of HF in the

initial laser mixture can be very detrimental to the optical output; the addition of as little as 25 Torr of HF to the 4000 Torr mixture reduces the optical output by a factor of two[7] (see Fig. IV.1-6). Thus, although most of the spent fuel consists of F_2 and O_2 which can be reused without reprocessing, HF must be removed from this spent fuel to levels on the order of 1 Torr for an efficient system.

The intial $F_2/O_2/H_2$ fuel mixture in our system is at a pressure of 3000/900/100 Torr. After the burn the gas is essentially a mixture of F_2, O_2 and HF. This assumes virtually no formation of H_2O or other species. From computer simulations of other mixtures these assumptions appear quite valid.[7,15] Thus, the problem is to efficiently remove a small amount of HF from a large amount of F_2-O_2. Ideally one would like to remove the HF without perturbing the F_2-O_2 flow which could be a closed loop. This goal is not realistic, however, and one must chose a method that minimizes the perturbation. It should also be pointed out that although we expect negligible water formation, the system must be kept free of H_2O because it tends to trigger spontaneous detonations and increase the corrosiveness of the gases. In addition, it is likely that methods for removing corrosion products will be necessary. However, in this design we will address only the removal of HF.

There appear to be at least two viable techniques for separating HF from the remaining gases. One is to simply cool the gas. Because HF has the highest boiling point of any of the constituents, it will condense out first. (This would also remove any water vapor present.) The second method is to chemically trap the HF molecules. One of the most attractive chemical traps is the absorption of HF by KF.

The cooling approach, although viable, could prove very costly in terms of the energy requirements. In order to reduce the HF partial pressure[16] to ~ 1 Torr the mixture must be cooled to ~ -100°C. Since the HF constitutes only a small fraction of the mixture most of the energy is wasted in cooling the rest of the gas. In addition, the F_2-O_2 must be reheated to room temperature before being reused in the laser so that the chemical reaction rate will be sufficiently rapid.

Chemical trapping appears more attractive, particularly if KF is used for the trap. In this system the gas mixture would flow over the KF and HF would be absorbed into the KF to form a eutectic mixture. Figure IV.1-19 shows the vapor pressure of HF versus temperature for the reactions,[17]

$$KHF_{2(s)} \rightleftharpoons KF_{(s)} + HF_{(g)} \cdot$$

This data indicates that by lowering the gas from its initial temperature of ~ 650°C to 125-175°C, one should lower the partial pressure of HF to < 1 Torr. Thus, one reason for the attractiveness of this method is the relative ease by which HF can be separated from the system. The other principal reason is its compatibility with the prevalent method of F_2 production.

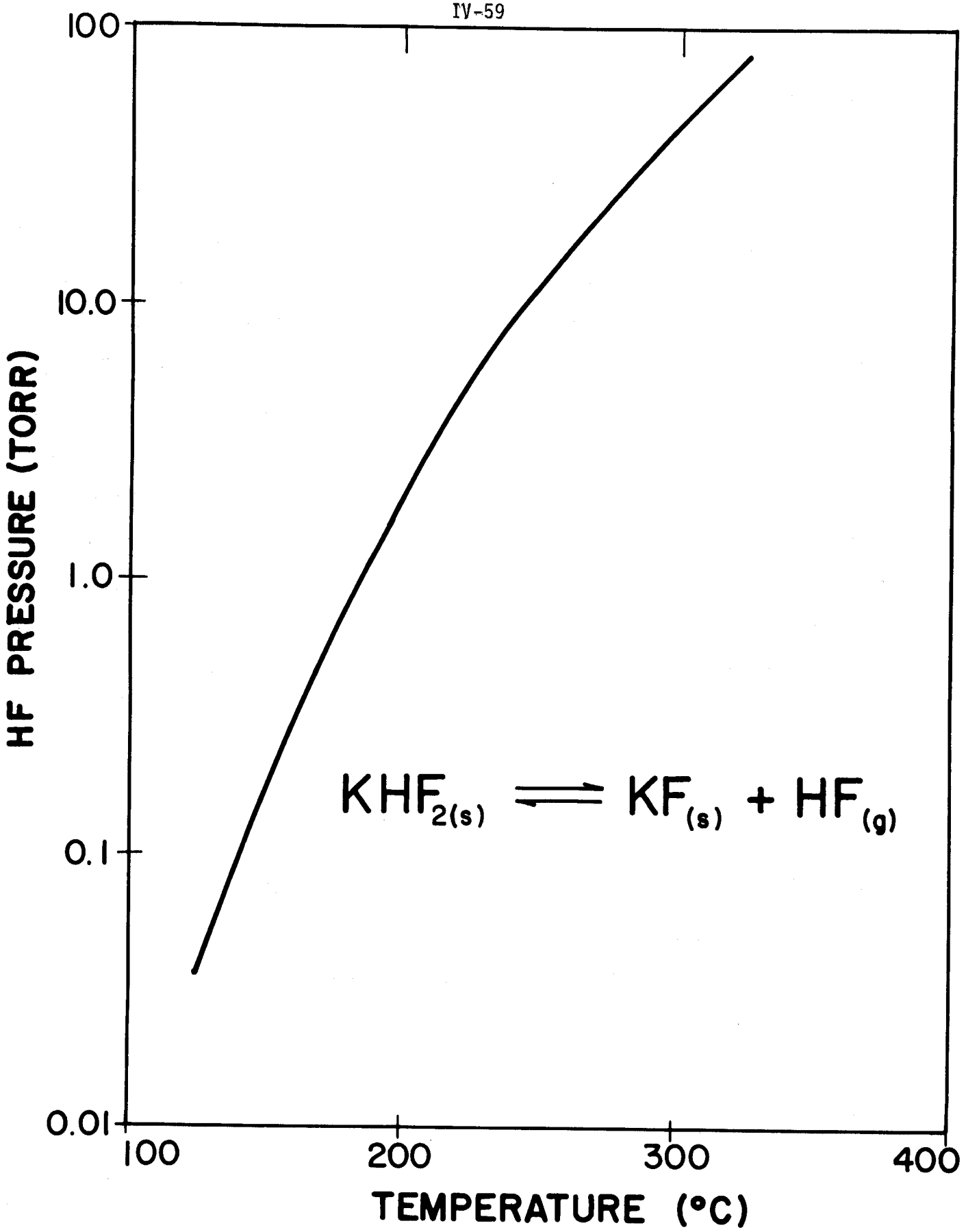
100
10.0
1.0
0.1
0.01
HF PRESSURE (TORR)
100
200
300
400
TEMPERATURE (°C)
KHF2(s) ⇌ KF(s) + HF(g)

Fig. IV.1-19

Fluorine is usually produced by the electrolysis of HF.[18] However, because the electrical conductivity of pure HF is too poor to perform electrolysis, a eutectic mixture of KF-HF is used instead.[18] Of course, this eutectic mixture is exactly what is formed in our chemical trap. Thus, one can regenerate H_2 and F_2 by the electrolysis of the trap mixture itself.

This chemical trapping and reprocessing technique has the great advantage of being based on a long established technology. Thus, developmental work required for its implementation should be minimal since it is known to be a successful system. However, the technique is not necessarily the optimum technique for the reprocessing of HF. A typical value for the efficiency[11] of this process is about 0.4 where the efficiency is defined as the energy released in the chemical reaction divided by the energy required to regenerate the reactants.

It should be strongly emphasized that this is a large chemical plant. For our parameters $\sim 5.7 \times 10^5$ kg of HF are generated per day which means $\sim 5.4 \times 10^5$ kg of F_2 must be regenerated per day. As a comparison, the largest fluorine plants in existence[14] generate $\sim 5 \times 10^3$ kg per day of F_2. Thus, a small increase in reprocessing efficiency or basic laser chemical efficiency would have a large effect on the system as a whole.

The fact that vast quantities of HF must be recycled also strengthens the arguments for our particular choice of parameters. Our decision to operate at the maximum net efficiency happens to coincide with operating at the maximum chemical efficiency. This, of course, minimizes the HF production per joule of optical energy out. We also wanted to reduce the repetition rate to as low a value as possible, primarily to relax the requirements on the energy storage systems. However, since the HF production rate is directly proportional to the pulse rate for a fixed laser output energy, reducing the pulse rate also reduces the amount of HF to be reprocessed. As pointed out above a low repetition rate also ameliorates the problems of post-detonation effects by allowing more time for their suppression.

Thus, we can conclude that, although large quantities of gas must be handled, there appear to be no technological limitations particularly in light of the vast experience of the fluorine industry. Our choices of maximum chemical efficiency, hydrogen-lean mixtures, and low repetition rates help minimize potential gas handling problems. One question that has not been addressed but which could seriously affect the economics of the system is the absolute cost of the chemical reprocessing system.

IV.1.F. The Electron Beam Driver

IV.1.F-1. Introduction

Although the HF chemical laser is pumped by a chemical reaction, the reaction itself must be triggered by an external energy source. Several types of sources can be used to initiate the reaction, but the most appropriate and efficient source for our purposes is the electron beam. The purpose of the e-beam is to dissociate the F_2 and/or H_2 into atoms, thereby initiating the $F + H_2 \rightarrow HF + H$ and $H + F_2 \rightarrow HF + F$ reactions. Electron beam initiation is advantageous because it is possible to deposit a large amount of energy in the gas in a very short time. This means that the atomic production rate and therefore the chemical reaction rate will be as high as possible for a given pressure. This in turn results in the shortest laser pulse width allowable. In addition the e-beam energy can be deposited relatively uniformly, resulting in a uniform burn which is essential for high beam quality.

The most practical configuration for our design is to have two electron beams irradiate the cell from opposite sides (see Fig. IV.1-7). Although there are probably more optimum configurations for the e-beam itself (such as using a radial diode), the two-sided scheme allows ample room for both optics and gas flow (which a radial diode does not). In addition, with this configuration the self-induced magnetic fields of the opposing beams cancel, minimizing any pinching of the beams. A final advantage is that the variation of energy deposition across the cavity is such that the sum of the two beams results in relatively uniform energy deposition.

IV.1.F-2. Electron Beam Design

For our particular mixture, the basic electrical efficiency (laser

energy out divided by the energy deposited in the gas) is 0.6. Using the data of Fig. IV.1-2 and 3 indicates that depositing a total of 167 kJ in the gas should give an optical output of 100 kJ. This assumes each diode had an area of 3000 cm^2 (30 x 100), but for reasons discussed in Sec. IV.1.C the final diode area is 3468 cm^2 (34 x 102). Assuming that the e-beam energy density must remain the same, the total energy deposition required for the final parameters is 193 kJ. Thus, the electrical efficiency drops from 0.6 to 0.53.

Figure IV.1-20 gives the energy that must be handled by each of the various stages in the e-beam and the approximate conversion efficiency between stages. The energy that must be stored in each Marx generator is about 170 kJ. This is quite large for a single Marx generator but is still within state-of-the-art.[19]

The operating voltage of the diode can be determined by examining the electron range in the gas. For our gas mixture, the majority of the electron beam energy is deposited in the first seven-tenths of its range. Therefore, the voltage should be chosen so that seven-tenths of the range equals the cavity width (~ 102 cm). Since the range of the electrons has not been measured for our specific mixture, we estimated the range from data in Ar. This should be similar because of the high concentration of F_2 in our system which has a mass and atomic number comparable to that of Ar. For Ar the range of a 2.0 MeV electron is ~ 101 cm. Thus, the desired diode voltage is approximately 2.0 MV. It follows that the pulse-forming line (PFL) must be charged to 4 MV by the Marx generator.

Electron Beam Energy Flow
(Two E-Beams Per Amplifier)

Component	Transfer Efficiency	Energy (kJ) Per Amplifier	Per E-Beam
Charging Supply		350	175
↓	0.95		
Marx Generator		335	170
↓	0.9		
Pulse Forming Lines		300	150
↓	0.9		
Diode		270	135
↓	0.5-0.7		
Gas		190	95
↓	0.53		
Laser Energy		100	

Figure IV.1-20

The pulse width must be short enough to meet laser requirements but still be compatible with our "near-term" technology criteria. A 20-nsec (FWHM) trapezoidal pulse (10 nsec at peak, 30 nsec at base) is within state-of-the-art technology[20] and appears adequate with respect to the laser criteria.[7]

Knowing the energy, voltage and pulse width of the e-beam, one can approximate the current from the relation

$$I = \frac{E}{Vt} \quad ,$$

which yields 3.4 MA for our parameters. This corresponds to a current density of $\sim$ 1 kA/cm^2.

Ideally the deposition of the e-beam energy should be as uniform as possible. Although sufficient uniformity may prove difficult to obtain, our particular choice of e-beam parameters and configuration will help to maximize the uniformity of deposition. For example, our choice of electron range results in a deposition profile such that two opposing beams combine to give relatively uniform energy deposition across the cavity.[21] In addition, the self-induced magnetic fields of the two beams will cancel which will minimize any pinching of the beams in the cavity itself.

There are two additional effects related to the e-beam propagation that must be considered. One is the scattering of the electrons by the

gas into the quartz windows which will result in their optical degradation. The other problem is the pinching of the e-beams due to the self-induced magnetic field in the diode. The scattering problem can be eliminated by applying a magnetic field to confine the electrons to the cavity and thereby keeping them from striking the windows. The pinching problem can be solved by applying an external magnetic field, increasing the number of diodes, or a combination of the two.

To examine the scattering problem in greater detail, the magnetic field required to protect the windows has been estimated[11] to be about 6 kG. This value was obtained by rough extrapolation from the results from another case (a 0.5 kG field was found sufficient to control a 70 cm diameter e-beam operating at a voltage of 0.3 MeV over a distance of 40 cm in a 1 atm mixture of 70% He and 30% F_2).[22] The exact scaling laws that should be applied are not precisely known so that the final answer was increased by 50% as a safety factor.

To establish this field will require the expenditure of considerable energy. To help estimate this, the energy contained in the entire field which results in a 6 kG field in the cavity and diodes has been calculated[7] to be 115 kJ. The problem becomes one of designing a system that minimizes the cost of establishing this field. One cannot economically run a normal magnet continuously because of the I^2R losses, but it may be possible to use pulsed magnetic fields and recover as much as 50% of the energy by

alternately charging the bank in opposite directions. A better approach may be to use a continuously-running, superconducting magnet. Once operating, the only energy cost is the removal of heat - a cost that can be made as low as desirable by adding sufficient insulation. However, until a detailed estimate of the energy cost of the superconducting magnet can be made, we will assume about one-half of the total energy in the field is lost per laser pulse or about 60 kJ.

Turning to the problem of pinching in the diode, the e-beam will pinch if the current in the beam exceeds the critical current which is defined as the current which induces a self-magnetic field with a strength such that the electron's Larmor radius equals the diode anode-cathode gap spacing. The critical current can be calculated using the relation[23]

$$I_c = \frac{8.5(\beta\gamma)}{\pi} \left(\frac{\ell}{d}\right)$$

where $\beta\gamma$ is the relativistic factor, ℓ is the length of the diode, and d is the diode gap spacing. For our parameters the critical current is 510 kA. Since our total current (3.4 MA) exceeds this value, we would expect pinching to occur. This pinching can be prevented by either increasing the number of diodes or by applying an external magnetic field to cancel the effects of the self-induced field. Increasing the number of diodes can prevent pinching because it magnetically isolates sections of the current and thereby reduces the self-induced magnetic field. For

our parameters a minimum of seven diodes would be required to eliminate pinching in the diodes by this method. In order to prevent pinching by applying an external magnetic field, the applied field must equal the self-induced field in order for the effects to cancel. Therefore, the fields must be of equal strength. If only a single diode were used a field of ~ 23 kG would be required to cancel the self-induced field effects.[11]

For our design we decided to use a combination of these two methods. To prevent the scattering of electrons into the windows we have already applied a field of 6 kG which must also be present in the diodes. To take advantage of this we chose to increase the number of diodes such that the self-induced field effects are just cancelled by the 6 kG field. By using 4 diodes the self-induced field decreases to about 5.7 kG and is approximately equal to the 6 kG applied field. Thus, the use of 4 diodes should prevent pinching in our design. With these two modifications, the e-beam energy should be deposited relatively uniformly across the cavity, although detailed electron transport calculations should be performed to verify this.

Each of the four diodes will be 8.5 x 102 cm, carry a current of 850 kA, and have an impedance of 2.4 Ω. We have initially chosen to use water-insulated-strip lines for the pulse forming lines (PFL). A schematic[21] of these are shown in Fig. IV.1-21. In order to accommodate the geometry, we have incorporated both a section of the PFL which acts as an intermediate storage capacitor and a vacuum transmission line.

THE ELECTRON BEAM PULSE FORMING LINES

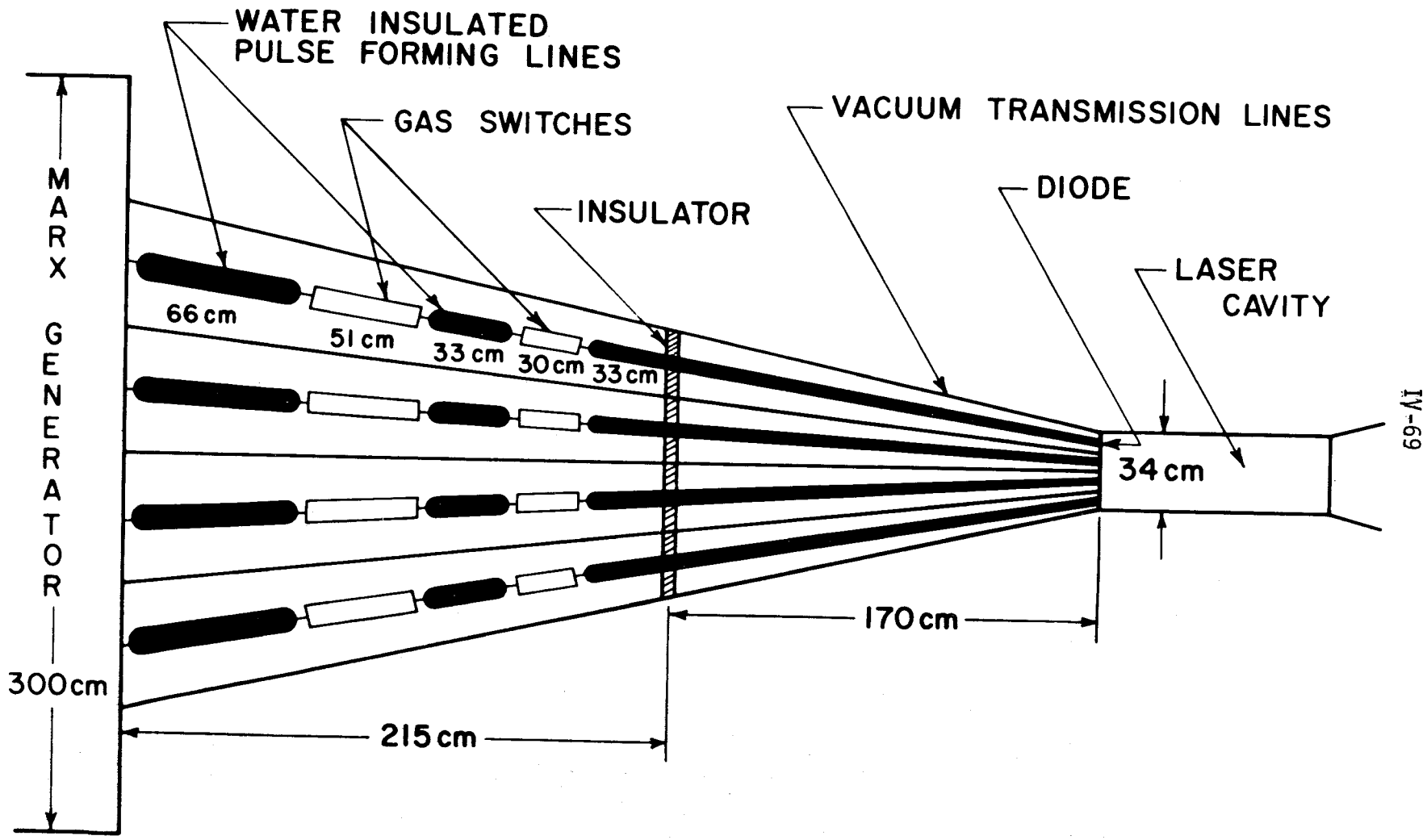

Fig. IV.1-21

The intermediate store if actually present would introduce an additional energy transfer inefficiency of about 0.95 that must be included in the overall e-beam efficiency. However, it is felt that an alternative configuration could be designed which would eliminate the need for an intermediate store.[21]

The number of switch channels required in our system could vary from about 40 to 80. At present, the most suitable switches appear to be high-pressure, gas spark gaps. Liquid-dielectric spark gaps would be more compact and have lower inductances but the mechanical stresses induced by the shock waves generated in the gap will probably be intolerable in a high-repetition-rate device.[24] Unfortunately, state-of-the-art spark gaps do not meet our requirements but it is not unreasonable to assume that such gaps can be developed. Ideally one would like to use pressurized air as the dielectric medium but use of the more expensive SF_6 with a reprocessing system may prove essential.

Each Marx generator must store 170 kJ at 4 MV. The volume[21] required for such a capacitor bank is roughly a box 2.3 x 2.3 x 6.6 meters. The oil insulated tank to house these capacitors will be about 3 x 3 x 9 meters. A schematic of the e-beam system[21] with these dimensions (sans the external magnetic field coils) is shown in Fig. IV.1-22. The exact shape of the Marx generator can be varied providing that the volume is kept constant.

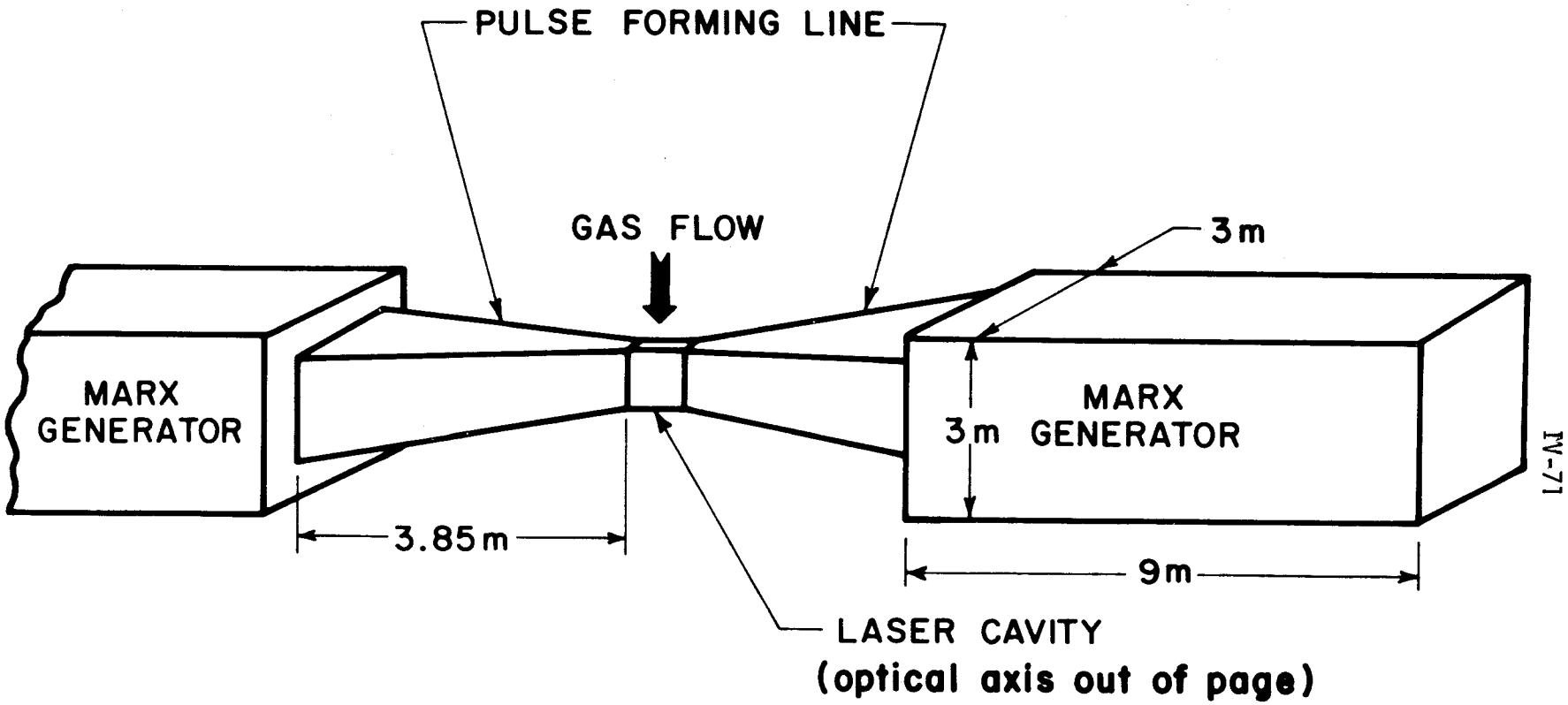

ELECTRON BEAM CONFIGURATION FOR THE HF LASER

Fig. IV.1-22

IV.1.F-3. Electron Beam Foils

The e-beam foils constitute a very critical component of the e-beam device. The foil is necessary to isolate the high pressure of the laser gas (in our case 4000 Torr ambient plus 14,400 Torr shock) from the hard vacuum ($\sim 10^{-6}$ Torr) required in the diode. Thus, the foil must stand off this pressure differential without leakage or significantly deforming. To meet this criterion the foil should be as thick as possible. A second requirement, however, is that the e-beam energy deposited in the foil should be minimized. This implies that the foil should be as thin as possible. Thus, one must compromise between strength and energy loss in the foil. As a result, foils are typically 25 to 50 μm thick. The HF laser system imposes a third criterion in that the foil must be corrosion resistant to F_2 and HF. This, for example, eliminates titanium from consideration although it is otherwise one of the best choices.

In choosing a foil material, one would like, in general, to have as low an atomic number, Z, as possible. This is because the energy deposition increases with Z, the bremsstrahlung losses increase with Z, and the backscattered electrons increase with Z and all of these effects are detrimental to foil performance. One harmful effect that decreases with increasing Z is radiation damage of the foil by the e-beam. The extent of damage depends on the atomic recoil energy and for a given electron energy, the recoil energy will drop below the damage threshold if the Z is sufficiently high.[25] These radiation damage effects can be minimized, however, by operating at a temperature $\lesssim 0.3$ of the melting point.[26] Preliminary examination indicates that effects that drive one to low Z materials will dominate.

Materials that appear to best meet our requirements are nickel and stainless steel. Nickel is probably preferable with respect to corrosion, but stainless steel is stronger. One problem that has not been addressed is the immunity of these materials to corrosion under cyclic stress conditions. The possible difficulties lie in the fact that the corrosion resistance is attained by the formation of a hard, impermeable fluorine compound on the outer surface of the material. It is possible that the constant temperature fluctuations will result in the cracking or flaking of this protective coating which would allow further corrosion to take place.

The fraction of energy that will be deposited in the foil can be calculated from the range of the electron in a given foil material. Assuming the foil is iron (Fe) the range of 2 MV electrons is ~ 0.17 cm. For a typical foil that is 50-μm thick, this corresponds to about 3% of an electron range. Thus, the energy deposited[21] is about 6 or 7% of the total energy or ~ 2.5 J/cm^2. From this, the instantaneous temperature rise was estimated to be about 100^{o}C. This will induce stresses in the foil that will seriously limit the foil lifetime, although the heat itself can probably be readily removed.

Because of the large surface area the foil must be supported by a habachi structure. The structures can be composed of tubes through which water could flow to provide cooling. It may also be possible to control the e-beam trajectories such that they pass primarily between the support structure to minimize e-beam absorption in the supports. One

relies then on scattering in the gas to distribute the energy uniformly across the cavity.

IV.1.F-4. Lifetimes and Reliabilities of the Electron Beams

In the SOLASE study[1] we found that the projected lifetimes and reliabilities of energy storage systems were severely inadequate for reactor applications. Unfortunately, these problems also exist for the e-beam accelerators discussed here. Except for the examination of e-beam foils, we have not significantly extended the SOLASE studies in this particular area.

However, it is beneficial to point out specific differences between the e-beam accelerators to be used to drive the HF laser and electrical energy storage systems to be used by other lasers. These differences were mentioned previously and include lower energy storage requirements per joule of laser output and shorter delivery time in the HF laser system. The first results in smaller storage systems for a given laser output resulting in lower costs and higher reliability. Shorter pulse durations are technologically more difficult to obtain but this design is still within the state-of-the-art.[20] Also in comparing specifically the SOLASE and hybrid design the pulse repetition rate was reduced from 20 Hz to 4 Hz. This has the effect of extending the "lifetime" of components such as capacitors and switches, which are rated for a specific number of shots, by a factor of five and reducing vacuum system and cooling requirements.

Because of the problems associated with electrostatic storage systems, we briefly examined alternative energy storage devices. Homo-polar generators are inexpensive and have high energy densities but the transfer times are limited to $\gtrsim$ 1 msec.[27] This is much too long to be of practical use for laser

systems considered today. If a suitable laser could be found that can be pumped in a millisecond at low voltage, this would be an ideal energy storage device. Another type of system is inductive storage. These devices apparently would cost more than homo-polar generators but not as much as electrostatic systems.[27] Their operating parameters are more appropriate, however, to ICF lasers than homo-polar devices. The main problem with them is the lack of a non-destructive opening switch which currently limits their usefulness in high-repetition-rate systems.

Thus, we conclude that whatever form of energy storage one chooses, considerable research and development will be required to develop a practical, economic system for an ICF reactor.

IV.1.G. Efficiency of the HF Laser System

One of the most important parameters of the laser system is the net efficiency of the laser. This efficiency includes all of the energy costs of running the laser. It is this efficiency that largely determines the economics of the ICF reactor.

The net efficiency can be defined as

$$\eta = \frac{\text{Laser Energy } (E_L)}{E(\text{e-beam})+E(\text{B-field})+E(\text{chemical})+E(\text{gas flow})+E(\text{other})} .$$

This expression can be inverted and separated for easier evaluation. This yields:

$$\frac{1}{\eta} = \frac{E(\text{e-beam})}{E_L} + \frac{E(\text{B-field})}{E_L} + \ldots$$

or

$$\frac{1}{\eta} = \frac{1}{\eta(\text{e-beam})} + \frac{1}{\eta(\text{B-field})} + \cdots \quad .$$

We will calculate each independently. This also has the advantage of separating the high grade energy (such as the e-beams) which seriously affects reliability from low grade energy (such as gas-handling pumps) which is assumed to be reliable.

The e-beam efficiency was discussed in Section IV.1.F-2 and is summarized in Table IV.1-5. The final wall-plug efficiency of the e-beam is η(e-beam) = 0.28.

The efficiency of the magnetic field required to prevent pinching of the e-beams and scattering of the e-beam to the windows was discussed in Section IV.1.F-2 and is also summarized in Table IV.1-5. The final efficiency of this was found to be η(B-field) = 1.66.

The factors that make up the chemical efficiency have been discussed individually but not combined until now. These include the basic chemical efficiency (laser energy divided by the energy released by the chemical reaction), the efficiency of regeneration of the gases, and a volume efficiency since the fuel mixture will be somewhat larger than the cavity volume. These efficiencies are summarized in Table IV.1-5 and the net chemical efficiency is found to be η(chemical) = 0.04.

The energy required to flow the gas has not been calculated previously. We will make three assumptions: that the buffer zone is equal to the fuel zone in volume, that the H_2 must be introduced at a pressure of 14,400 Torr to prevent propagation of reaction products upstream, and that the ΔP of the F_2-O_2 mixture is 350 Torr. Using a technique described by TRW,[14] the power requirement can be related to the mass flow ($\dot{m}$), the pressure ratio (P_2/P_1), the compression efficiency (η) and the type of gas. The relation[14] is

Table IV.1-5

Efficiency of the HF Laser

$$\frac{1}{\eta(\text{total})} = \frac{1}{\eta(\text{e-beam})} + \frac{1}{\eta(\text{B-field})} + \frac{1}{\eta(\text{chemical})} + \frac{1}{\eta(\text{gas flow})} + \frac{1}{\eta(\text{other})}$$

$$\eta(\text{e-beam}) = \frac{E_L}{E(\text{deposited})} \times \frac{E(\text{deposited})}{E(\text{e-beam})} \times \frac{E(\text{e-beam})}{E(\text{Marx})} \times \frac{E(\text{Marx})}{E(\text{wall plug})}$$

$$= 0.53 \times 0.7 \times 0.8 \times 0.95 = 0.28$$

$$\eta(\text{B-field}) = \frac{E_L}{E(\text{B-field})} = \frac{100}{60} = 1.66$$

$$\eta(\text{chemical}) = \frac{E_L}{E(\text{exothermic})} \times \frac{E(\text{exothermic})}{E(\text{regenerated chemicals})} \times \frac{\text{volume laser cell}}{\text{volume of } H_2\text{-}F_2\text{-}O_2}$$

$$= 0.11 \times 0.40 \times 0.90 = 0.04$$

$$\eta(\text{gas flow}) = \frac{E_L}{E(\text{gas flow})} = \frac{100}{59} = 1.7$$

$\eta(\text{other}) \gg 1$ (assumed negligible)

$\eta(\text{total}) = 0.027$

$$\frac{P}{\frac{\dot{m}RT_1}{(\frac{\gamma}{\eta})}} = (\frac{\gamma}{\gamma-1}) \left[(\frac{P_2}{P_1})^{\gamma-1/\gamma} - 1\right] = f(\gamma, P_2/P_1) \ ,$$

where P is the power and RT_1 is the product of the gas constant and pump inlet temperature. This function has been calculated by TRW and a graph of it appears in Ref. 12. Assuming a temperature of 300°K and a compressor efficiency of 83% yields

$$\frac{P}{\dot{m}} = 3000 \ f(\gamma, P_2/P_1) \ \frac{\text{joules/sec}}{\text{moles/sec}} \ .$$

In our system the pressure ratios are 3.5 and 1.1 for H_2 and F_2-O_2, respectively. The corresponding f values are 1.5 and 0.1. For each pulse one must pump 2.1 moles of H_2 and 166 moles of F_2-O_2. Substituting into the above relations one finds that it takes 9.3 and 49.7 kJ/pulse to flow the H_2 and F_2-O_2, respectively. Note that even though the H_2 has a much higher ΔP, the F_2-O_2 mixture is the major contributor to the pumping power requirements. The total energy required is 59 kJ/pulse so that the efficiency is 1.7.

There are a number of other recirculating power costs that must be accounted for in a realistic system. These include the cooling of the optics, the cooling of the e-beam components, and the pressurizing and flowing of the dielectrics in the spark gaps. These and other costs should be negligible compared to any of the above so that we have not attempted to assign specific values to these.

The net efficiency of the laser can now be estimated. Summing the reciprocals of the individual efficiencies yields an overall efficiency of 3.37%. A final factor to be included is the efficiency of delivering the

laser energy to the target. We estimated that only 80% of the energy is ultimately focusable on the target. This includes effects such as imperfect beam quality, absorption by the mirrors, misalignment, and wavefront distortions. This effectively reduces the efficiency to 2.7%. Of course, increasing the fraction of focusable energy would make considerable impact on the net efficiency.

The major contributor to the overall efficiency of the HF laser is the chemical efficiency. Thus, the only way to make a major impact on the net efficiency is to substantially improve the chemical processes. The basic chemical efficiency [E_L/E (exothermic)] can probably be improved by a further decrease in the hydrogen partial pressure providing the trend of Fig. IV.1-2 continues. (It should also be noted that the chemical efficiency in Fig. IV.1-2 is a conservative estimate and may be as much as 50% higher.)[11] The electrical efficiency is dropping rapidly in this region, however, and this could offset any gain in chemical efficiency. The other factor is the regeneration efficiency. It may be possible to improve the state-of-the-art regeneration process by discovery of a catalyst, for example. Of course, one cannot assume such a process until it is actually developed.

Finally, we will examine the requirements of the HF laser with respect to high-and low-quality energy. We feel that high-quality energy is represented only in the e-beam drivers and related external magnetic field supply. Thus, on a per pulse basis, our 2 MJ HF laser requires 51 MJ of low-quality energy but only 8.4 MJ of high-quality energy. Since it is the high-quality energy that seriously affects the reliability of the laser, this is a great advantage that the HF laser has over other lasers which have lower electrical efficiencies and, therefore, a greater reliance on high-quality energy.

IV.1.H. Summary and Conclusions

In order to assess the potential of the HF chemical laser as an ICF driver, we completed a detailed conceptual design of an HF laser. In particular, we designed a laser whose performance characteristics are compatible with the hybrid reactor discussed in Part II. Table IV.1-6 lists many of the specific laser parameters. In addition, we examined the impact on overall laser performance if certain parameters were varied from the specific values chosen. This helps give a more complete picture of the HF laser.

In general, we found the HF laser to be a very attractive ICF laser candidate. The principal questions appear not to concern the feasibility of building such an HF laser, but whether the laser-performance characteristics will be compatible with requirements ultimately dictated by the laser-pellet physics - in particular, pulse width, wavelength and efficiency requirements. Of course, there still remain questions to be answered concerning the physics and technology required for the development of an HF laser for ICF applications. Below we discuss briefly the principal advantages and disadvantages of the HF laser, the more critical extrapolations we made in our design, and the technological advances we postulated.

Probably the two most important characteristics of HF that could affect its viability as an ICF laser are its wavelength and pulse width. The laser actually lases on a number of transitions whose wavelengths vary from $\sim$ 2.6 to 3.5 μm. Because of the multiple wavelength nature, it is very difficult to conceive of an efficient process for wavelength doubling. Thus, 3.0 μm light must be suitable for imploding a pellet if HF is to be a viable ICF laser.

Table IV.1-6

The HF Laser Parameters

TOTAL LASER ENERGY	2 MJ
ENERGY ON TARGET	1.6 MJ
PEAK POWER ON TARGET	240 TW
PULSE WIDTH	~ 3 nsec
NET LASER EFFICIENCY	2.7%
ELECTRICAL EFFICIENCY	24%
CHEMICAL EFFICIENCY	4%
PULSE REPETITION FREQUENCY	4 Hz
NUMBER OF FINAL AMPLIFIERS	20
LASER ENERGY PER AMPLIFIER	100 kJ
OPTICAL APERTURE	102 x 102 cm
CAVITY LENGTH	34 cm
TOTAL PRESSURE	4000 Torr
$F_2/O_2/H_2$ RATIO	3000/900/100
CHEMICAL REACTION INITIATED BY ELECTRON BEAM	$F + H_2 \rightarrow HF + H$, $H + F_2 \rightarrow HF + F$
ELECTRON BEAM VOLTAGE	2 MV
ELECTRON BEAM PULSE WIDTH	20-nsec (FWHM)
LASER ENERGY EXTRACTION	18 Multi-Passed Amplifiers 2 Single-Passed Amplifiers
NUMBER OF BEAMS EXTRACTED PER MULTI-PASSED AMPLIFIER	3
TOTAL NUMBER OF LASER BEAMS	56

Pulse width compatibility is a more involved question. Original thinking was that the laser energy must be delivered in a pulse $\lesssim$ 1 nsec (FWHM) but new concepts appear to allow pulses of 1 to 3 nsec (FWHM). Unfortunately, the natural-pulse width of HF is limited to ~ 10 to 15 nsec (FWHM). This forces one to either extract a single pulse of desired length or a series of these pulses. The first is very inefficient as much of the available energy is not utilized. The latter is more efficient but can become complicated optically. In our particular design we chose to generate a 3 nsec pulse by extracting three beams from each amplifier during each pumping cycle. This required a total of 56 individual beams each of which must be transported to the target. This we feel is a manageable number. However, if the pulse width must be reduced to 1 nsec or less the number of beams will triple if one still covers the entire pulse. The practicality of handling 150 beams in a reactor environment must be seriously examined. Thus, the shorter the pulse width that is required, the less suitable HF becomes. Conversely, if pulse widths of 10 to 20 nsec prove suitable for ICF, the HF laser becomes very attractive. Laser pulse widths of 10 nsec have been seriously discussed recently for megajoule-type lasers.[28] It should be pointed out that the number of beams required is directly related to the total laser energy. The number of beams increases with the laser energy (unless one assumes that the beams are incredibly large in both size and energy). Thus, the number of beams required will be large for any laser system although the need for multi-passing increases the problem.

Another important parameter is the net efficiency of the laser which largely determines the economics of the reactor. For a pure laser-fusion reactor the exact efficiency required is determined by an energy balance

between the pellet gain, the recirculating power fraction, the laser efficiency, and the net plant efficiency. The situation is complicated in the hybrid because of the energy gain in the blanket and the fissile fuel produced. In addition, there may be a minimum efficiency required which is dictated by the absolute cost of the laser system.

For our particular parameters the efficiency of the HF laser is ~ 2.7%. This includes all significant recirculating power costs and the efficiency of the beam transport to the target. This is respectable in that very few lasers will have net efficiencies exceeding this, but it is still questionable whether it is sufficiently high. The projected efficiency required for our hybrid is 2.6%, so that our HF laser appears to just satisfy this requirement. (The 2.6% requirement is obtained from a relationship between the net plant efficiency, the recirculating power fraction, the pellet gain, the average blanket energy multiplication, and the laser efficiency. This is discussed in detail in Part III.)

In addition to having a reasonable net efficiency, the HF laser is of special interest because its wall-plug electrical efficiency is 24%. This means that the energy storage system is considerably smaller per joule of optical output than for any other laser currently being considered for ICF applications. This should considerably reduce the capital and maintenance costs which we found to be a serious problem in the SOLASE study.[1] Also, the reliability of lower energy systems should be greater.

The penalty for having such a high electrical efficiency is that the burden is shifted to the chemical-regeneration system. The HF laser has such a high electrical efficiency because the laser is actually pumped by a chemical reaction. This necessitates the reprocessing of the laser mixture. On the positive side the chemical regeneration of H_2 and F_2 from HF is a well established, reliable process that should be readily adapted to our system. On the negative side the chemical processes are relatively inefficient

and contribute most to the low net efficiency. The basic chemical efficiency (laser energy out divided by chemical energy released) is 11% for our design parameters and the gas regeneration efficiency is 40%. The former can probably be increased by further reduction in the H_2 partial pressure but only at the cost of decreasing the electrical efficiency. The latter might be increased by improving the chemical process - possibly by the discovery of a suitable catalyst - but such a discovery cannot be relied upon. Even so, the chemical efficiency is not intolerably low unless the absolute capital cost of the chemical plant is too high ($\sim 5 \times 10^5$ kg of HF must be reprocessed per day).

A final area related to the efficiency which we have not examined in detail is the efficiency of delivering the energy generated to the target. We estimated 80% of the energy is ultimately focusable on target. Losses result from poor beam quality, absorption by mirrors and windows, misalignment, and wavefront distortions. One would like this efficiency to be higher than 80% but it may be even lower. This is a critical area that must be examined thoroughly.

Another important issue with respect to HF lasers is gas handling. Large volumes of explosive, corrosive gases must be handled. This could be a distinct disadvantage. However, for our particular choice of parameters the problems appear manageable. The principal advantage of our design

parameters results from the choice of a hydrogen-lean mixture which yields only modest temperature and pressure rises compared to more hydrogen-rich mixtures. Thus, density gradients can be readily eliminated between pulses. Also, materials problems should be minimal as there is vast experience in handling these gases at moderate temperatures, although a special problem area could be the e-beam foil which is subjected to considerable temperature cycling that could promote corrosion. The modest over-pressures also reduce pumping power requirements and the low repetition rate of 4 Hz allows ample time to eliminate all shock waves and temperature gradients between pulses. The low repetition rate also helps to minimize the volume of gas that must be handled. Thus, the gas-handling problems for our parameters are manageable. If one chose a hydrogen-rich mixture one must contend with large over-pressures and very high temperatures which greatly increase the gas-handling problems. Similarly, a significant increase in the repetition rate increases problems by increasing the volume of gas that must be recycled (for a constant laser output per pulse) and reducing the time available for shock suppression.

The very high chemical energy densities available from an HF laser mixture, although resulting in gas-handling problems, are also advantageous in that they create high optical energy densities which allow very compact systems. This is not only an advantage because of the smaller size, but also because it is ideal for multi-pass extraction which is essential for our design. (The "pancake" configuration of the cavity allows a very high fraction of the volume to be extracted compared to the CO_2 laser in SOLASE,[1] for example.)

However, the high-pressure and high-optical energies also mean that one is operating near laser-induced gas-breakdown thresholds. If such breakdown occurs in the cavity the propagation of the beam could be terminated.

The principal extrapolation in our design is simply our assumption that the power amplifier behaves as predicted from data taken at laser energies of only 0.1 to 4 kJ. We feel reasonably confident that 100 kJ modules can be built, the only question being the specific parameters. The other critical assumption is that one can effectively extract energy by multi-passing. This has not been verified experimentally, but such experiments are already being planned.[11] A final assumption we made was that we do not get laser-induced-gas breakdown for our parameters, although calculations indicate that we are operating near threshold. Experiments must be performed to investigate this problem before serious development can begin.

We postulate that the most critical advance in technology is long-lived, reliable, low-cost, repetitively pulsed, e-beam machines. We feel that this area requires considerable research and development before a practical e-beam will exist. It should be emphasized that this problem is not limited to HF lasers but is common to all potential ICF drivers.

Another postulated advance is the development of large, high-quality optical windows for the power amplifiers. This will be a problem for most lasers, but is particularly difficult for HF. This is because commercial quartz has an absorption band at HF wavelengths and other

more suitable materials, such as sapphire, are very difficult to manufacture in sufficiently large sizes. Fortunately, the absorption in quartz is not inherent to the quartz, but is introduced by the formation of OH radicals in the manufacturing process. It has been postulated that if D_2 is used in place of H_2 in the manufacturing process, then this absorption band can be eliminated. This has not been demonstrated, but it does seem highly probable because special manufacturing processes have already greatly reduced the amount of absorption. Thus, we assumed that quartz can be used in our design, but this requires development before it can be implemented. It should be pointed out that quartz can be manufactured in sufficiently large sizes.

We also postulated a non-dispersive, large, 50/50 beamsplitter. These do not exist today, but attempts are now being made to develop one.[11] This is not an essential component of our design, but was introduced because it results in a simpler design. Since an HF laser can be designed without such beamsplitters, the development of them is not critical to the implementation of our HF laser design.

To conclude, we found the HF laser to be a very attractive ICF laser candidate. We found that, at least for our parameter range, the advantages far outweigh the disadvantages. There is also a strong data base on relatively high energy HF oscillators and amplifiers which gives us some confidence in our extrapolations. The majority of the gas handling technology required is well established. Optical problems appear solvable. The critical technological problem appears to be in electrical energy storage which is common to all ICF laser candidates. Thus, the principal question appears to be whether the HF laser wavelength, pulse width, and efficiency will ultimately prove compatible with the laser-pellet physics.

Acknowledgement: It is with great pleasure that the author thanks R.A. Gerber, K.R. Prestwich, F.K. Truby, J.B. Moreno, J. Cummings, and J.B. Gerardo, all of Sandia Laboratories, for their valuable contributions to this study.

References for Part IV.1

1. R. W. Conn et al., "SOLASE, A Laser Fusion Reactor Study", Fusion Research Program Report UWFDM-220, University of Wisconsin (1977) (To be published by EPRI); and G. A. Moses, S. I. Abdel-Khalik, and R. W. Conn, "Power Supply Costs for Inertial Confinement Fusion Reactors", Fusion Research Program Report UWFDM-243, University of Wisconsin (1978).

2. J. A. Maniscalco, J. A. Blink, J. Hovingh, W. R. Meier, M. J. Monsler, and P. E. Walker, Topical Meeting on Inertial Confinement Fusion, Technical Digest, San Diego (1978) p. WC3-1.

3. J. M. Hoffman, E. L. Patterson, and R. A. Gerber, "Energy Extraction from a Large Volume HF Amplifier", submitted to J. Appl. Phys.

4. E. L. Patterson, G. N. Hays, F. K. Truby, and R. A. Gerber, "Laser Beam Characteristics of Phoenix: The Sandia HF Oscillator-Amplifier System", submitted to J. Appl. Phys.

5. M. A. Duguay, G. A. Fisk, J. M. Hoffman, J. B. Moreno, R. E. Palmer, M. E. Riley, and R. P. Sandoval, "Feasibility Study Relating to the Use of High Gain Lasers, Particularly HF, in Controlled Fusion Applications", Sandia Laboratories Report SAND76-0094, March 1976.

6. R. A. Gerber and E. L. Patterson, J. Appl. Phys. 47, 3524 (1976).

7. J. B. Moreno, Paper No. AIAA 76-36, presented at AIAA 13th Aerospace Science Meeting, Pasadena, CA, 1975 (Available for $2.50 from AIAA, Order Department, 1290 Avenue of the Americas, NY 10019); also, J. B. Moreno, private communcation.

8. S. D. Rockwood, G. H. Canavan, and W. A. Proctor, J. Quantum Electron., QE-9, 154 (1973).

9. A. J. Alcock, K. Kato, and M. C. Richardson, Opt. Commun., 6, 342 (1972).

10. G. C. Tisone, Sandia Laboratories, private communication.

11. R. A. Gerber, Sandia Laboratories, private communication.

12. F. K. Truby, Appl. Phys. Lett. 29, 247 (1976).

13. R. Limpaecher and J. Woodroffe, "Flameout in Repetitively-Pulsed Chemical Lasers", Paper No. AIAA 77-61, presented at AIAA 15th Aerospace Science Meeting, Los Angeles, CA, 1977 (Available for $2.50 from AIAA, Order Department, 1290 Avenue of the Americas, NY 10019).

14. J. Shwartz, R. J. Golik, C. L. Merkle, D. R. Ausherman, and E. Fishman, "Fluid Mechanics of Fusion Lasers", TRW Report 31775-6002-RU-00, April 1978.

15. J. C. Cummings and F. K. Truby, Sandia Laboratories, private communication.

16. Handbook of Chemistry, ed. N. A. Lange, McGraw-Hill Book Company, New York, N. Y. (1956) p. 1431.

17. JANAF Thermochemical Tables, Second Edition, Dow Chemical Company, NSRDS-NBS 37 (1970).

18. M. J. Sienko and R. A. Plane, Chemistry: Principles and Properties, McGraw-Hill Book Company, New York, N. Y. (1966) p. 538.

19. T. H. Martin, IEEE Trans. on Nucl. Sci., NS16, No. 3, 59 (1969); B. Bernstein and I. Smith, IEEE Trans. on Nucl. Sci., NS20, No. 3, 294 (1973); and T. H. Martin, IEEE Trans. on Nucl. Sci., NS20, No. 3, 289 (1973).

20. K. R. Prestwich, IEEE Trans. on Nucl. Sci., NS22, No. 3, 975 (1975); and T. H. Martin, J. P. VanDevender, D. L. Johnson, D. H. McDaniel and M. Aker, Proc. of the International Topical Conference on Electron Beam Research and Technology, Vol. I, (Albuquerque, New Mexico), SAND76-5122, (1975) p. 450.

21. K. R. Prestwich, Sandia Laboratories, private communication.

22. J. B. Gerardo, J. J. Ramirez, R. A. Gerber, E. L. Patterson, and K. R. Prestwich, Proc. of the International Conference on Electron Beam Research and Technology, Vol. II (Albuquerque, New Mexico), SAND76-5122, (1975) p. 169.

23. I. Smith, V. B. Carboni, G. B. Frazier, E. P. Zeehandelaar, Energy Storage, Compression, and Switching, ed. W. H. Bostick, V. Nardi and O. S. F. Zucker (Plenum Press, N. Y., 1976), p. 25.

24. K. R. Prestwich, Energy Storage, Compression, and Switching, ed. W. H. Bostick, V. Nardi and O. S. F. Zucker, (Plenum Press, N. Y., 1976), p. 415; and D. L. Johnson, Energy Storage, Compression and Switching, ed. W. H. Bostwick, V. Nardi, and O. S. F. Zucker (Plenum Press, N. Y., 1976), p. 515.

25. M. W. Thompson, Defects and Radiation Damage in Metals, Cambridge University Press, Cambridge, Great Britain, (1969) p. 123.

26. Y. Adda, "Report on the CEA Program of Investigations of Radiation-Induced Cavities in Metals: Presentation of Some Results", in Radiation-Induced Voids in Metals, ed. by J. W. Corbett and L. C. Ianniello, U.S. Atomic Energy Commission Office of Information Services (CONF-710601 from National Technical Information Service) (1972) p. 31.

27. H. H. Woodson, H. G. Rylander, and W. F. Weldon, Proc. IEEE International Pulsed Power Conference (Lubbock, Texas), IEEE Pub. No. 76CH 1147-8 Region 5, (1976) p. IIB-1.

28. R. A. Haas, M. J. Monsler, R. D. Franklin, and J. J. Ewing, Topical Meeting on Inertial Confinement Fusion, Technical Digest, San Diego, CA (1978) p. WC15-1; and J. H. Nuckolls, Topical Meeting on Inertial Confinement Fusion, Technical Digest, San Diego, CA (1978) p. TuA5-1.

IV.1. Appendix - Multiple Beam Extraction From an HF Amplifier

The HF laser, unfortunately, has a natural-pulse width that is much longer than is currently thought desirable for laser fusion. In order to generate a short pulse with high efficiency one is forced to extract the energy in a series of short pulses and combine these on target in such a way as to form a pulse of the desired shape (see Section IV.1.C.). This requires that one be able to handle each beam independently. Since there is no method of electrically or mechanically switching such large, high-energy beams, one must pass each beam through the amplifier at a slightly different angle and allow them to travel far enough that they physically separate. This allows one to handle the beams independently, but has the disadvantage in that the entire available active volume is no longer extracted by each beam. In this appendix we will calculate the volume fraction extracted for our particular design.

Our HF laser design requires that we extract 3 beams from each of 18 final amplifiers. Each laser cavity has a square optical aperture, 102 cm on a side, and a length of 34 cm. We chose to extract all three beams in the same plane because it results in simpler beam transport designs. With this configuration one beam will pass straight through the amplifier and can extract the entire available volume. The remaining two beams will pass through at angles such that one will emerge just above the central beam and one just below as shown in Fig. IV.1-23. Note that passing these two beams at an angle will reduce the beam size in only one dimension; the other dimension will remain the full size and one can extract from the full width of the amplifier.

MULTIPLE BEAM EXTRACTION OF THE HF FINAL AMPLIFIER

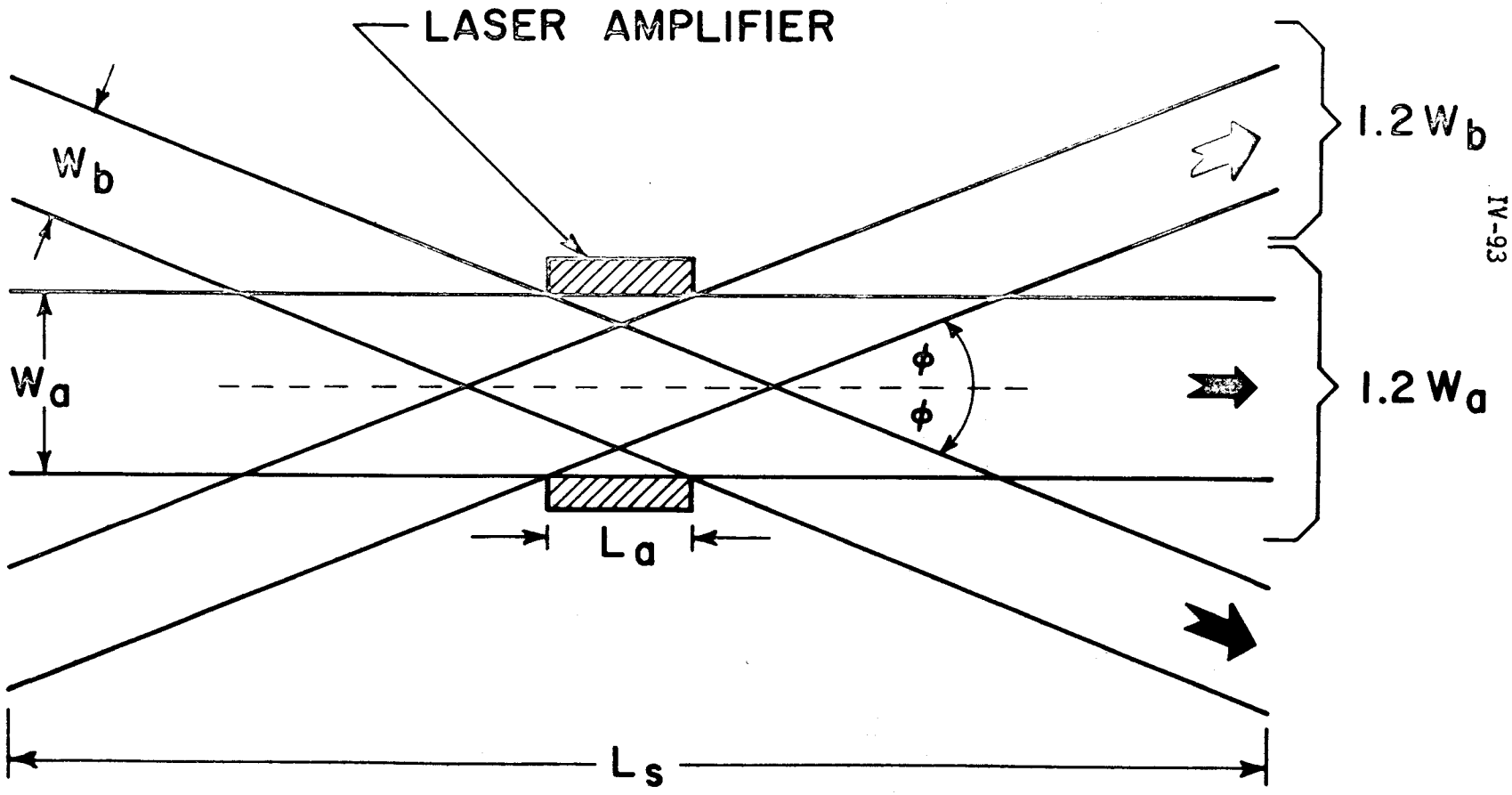

Fig. IV.1-23

Using geometrical arguments analogous to those used in SOLASE,[1] the width of a beam passing through an amplifier at an angle, ϕ, can be approximated as

$$W_b \approx \frac{L_s}{1.2}\ \phi - W_a$$

where W_b is the width of the beam, W_a is the width of the amplifier, and L_s is the distance required between the input and output optics. These parameters are illustrated in Fig. IV.1-23. It was also assumed in deriving this equation that the beams must separate far enough to allow room for optical support structure which was assumed to be 20% larger than the beam itself.

The angle, ϕ, in turn, can be approximated by the formula,

$$\phi \approx \frac{2W_a}{L_a + \frac{L_s}{1.2}}$$

where L_a is the length of the amplifier. Substituting for ϕ in the first equation yields,

$$W_b \approx \frac{L_s}{1.2}\left(\frac{2W_a}{L_a + \frac{L_s}{1.2}}\right) - W_a\ .$$

Evaluating this expression for the specific parameters of our design (W_a = 102 cm, $L_a \approx 40$ cm, and L_s = 24 m) one obtains for W_b a value of 98 cm. Thus, the total area extracted by the beams that pass at an angle is 98 x 102 = 9996 cm^2 which is very close to the desired 10^4 cm^2. Since the volume extracted is directly proportional to the area, these two beams will extract 96% of the volume available. The third beam which passes straight through extracts 100% of the available volume.

Comparing this system to that of SOLASE, one sees that a considerably higher volume fraction is extracted in HF (96% compared to 59% for CO_2) while at the same time the distance required between input and output optics is much less (24 m compared to 100 m for CO_2). This greatly improved performance with HF is the result of the much higher optical gain in the HF laser which results in very short amplifiers and because a more optimum cavity configuration is permissible with HF (square as opposed to annular).

A final factor to consider in the HF design is whether or not sufficient volume of the amplifier is covered in each pass to suppress amplified spontaneous emission (ASE). Covering 96% of the volume will probably be adequate but if it is not one could either increase the volume covered by decreasing the angle at which the beams pass through the amplifier or by running a bias beam through the amplifier at all times. The former method is probably preferable because it has the advantage of increasing the efficiency while suppressing the ASE.

IV.2 Optics and Beam Transport

IV.2.A. Beam Transport System for the HF Laser

IV.2.A-1. Introduction

The beam transport system has not been addressed in as much detail as the HF laser itself. This is due partly to the fact that the hybrid reactor study is not intended to result in a complete, fully integrated design, and also because such critical areas as the electron beam design were not optimized. Instead, we have designed a schematic beam transport system to glean some general indications of the size and complexity of the entire laser system. An optimized layout is not expected to differ dramatically from that presented here.

We have chosen to study in detail two problem areas of particular interest in the design of any laser fusion reactor beam transport system; the design of a beam port reduction scheme to reduce neutron leakage from the primary containment region, and the calculation of mirror damage thresholds for the rather singular laser pulse shapes envisioned for isentropic pellet implosion. Finally, we have collected a list of wavelength dependent effects pertinent to the increase in wavelength to 4.0 μm over the nominal 1.0 μm SOLASE value. The present section is devoted to describing the general features of the beam layout.

IV.2.A-2. Optical Requirements of the HF Laser

The HF laser consists of a master oscillator, preamplifiers, and the final power amplifiers. These have been discussed in detail in Sec. IV.1 and only those aspects relevant to the optics are discussed briefly below.

There are two preamplifier chains; one producing a single, long pulse and one from which three short pulses are extracted. The single pulse must be split in two in order to drive 2 of the 20 final amplifiers. Each of the 3 short pulses must be further divided into 18 equal pulses in order to drive the remaining 18 amplifiers. Thus, there are two final amplifiers from which a single beam is extracted and 18 from which 3 beams are extracted, for a total of 56 beams. In order to effectively extract 3 beams from a single amplifier, it is necessary to pass the beams through the amplifiers at slightly different angles and allow sufficient distance for them to physically separate. In our particular system the distance between the input and output optics is 24 meters. Each of these beams must be transported to the target with the appropriate time delays so that when they are combined on the target, the result is a pulse of the desired shape.

There are two principal extrapolations in the optics design. One is the assumption that large quartz optics can be manufactured with sufficiently low absorption of the HF wavelengths. While conventional quartz has an absorption band at these wavelengths, this absorption is introduced in the manufacturing process and is not inherent to the quartz itself. Theoretically, absorption can be eliminated by changing the fabrication process, but this requires experimental verification. The other major extrapolation is the assumed availability of large 50/50 beamsplitters for the HF wavelengths. Although this problem is complicated by the multi-wavelength nature of the HF laser, the development of such a beamsplitter appears feasible. It should

be noted, however, that these beamsplitters were incorporated merely to reduce the complexity of the design. Their development is therefore not essential.

There are two optical components that must handle the high energy beam: the quartz windows and bare metal mirrors. It is assumed that diamond-turned mirrors will be available to take advantage of their high reflectivity, high damage thresholds and lower cost. The aperture size (102 x 102 cm) is dictated by the damage threshold of the quartz window and is assumed to be a fairly conservative 10 J/cm^2 for our 12 nsec pulse. However, after leaving the final amplifier the beam will be reduced to 70 x 70 cm to take advantage of the higher damage threshold of the bare metal mirrors.

IV.2.A-3. Beam Layout

As in SOLASE, it was decided to irradiate the target from only two sides. Again, this decision was based on simplicity of design and not on fundamental laser-pellet physics since ultimate illumination requirements are not known at this time.

Similar to the SOLASE design, the amplifiers will all be housed in a single building to one side of the reactor cavity. After some consideration, it appears that one of the more practical arrangements for the final amplifiers is to orient the electron beams vertically and place all the amplifiers in a single line with the optical axes pointing toward the reactor building. In this particular configuration each amplifier module is a 3 x 3 meter rectangular box about 27 meters tall.

There appears to be no fundamental reason why this configuration could not be supported, but alternative horizontal arrangements can also be envisioned. The shape of the Marx generators can also be varied to some extent, providing the total volume is kept constant. In placing the amplifiers side-by-side in our design there is a 2 meter space between cavities which should provide ample room for the gas handling equipment.

In addition to the amplifiers themselves, about 24 m must be allowed for multi-passing. Thus, the building required for our final amplifiers is about 65 m wide, 30 m deep and 30 m high. In addition, it will probably be desirable to place the front end of the laser in a room on top of the power amplifiers, making the building another 5 to 10 m tall. Because the laser building is so large, it is essential for economic reasons that it not be a primary containment structure. However, because the electron beams will generate copious high energy X-rays (up to 2 MeV), substantial shielding around the lasers must be provided.

Another requirement of the laser system is a chemical reprocessing plant to allow recycling of the laser mixture. Because of the large chemical potential energy in the form of F_2 and H_2 that will be stored in the building, the ideal location for this plant is in a separate building to the side of the laser building opposite the reactor. This location will better isolate the chemical plant and the reactor in the event of an accident. While no estimate has been made of the size of this structure, it will probably be fairly large due to the large volume of gas that must be continuously reprocessed.

Having laid out the laser system, we will now consider the actual transport of the beam to the target. Each beam must first pass from the laser building to the reactor building. Since we desire that only the reactor building (and not the laser building) constitute a primary containment structure, the laser beam ports must penetrate primary containment. In order to minimize the impact of this, we have suggested focusing the beam to a "point" as it passes through the reactor wall. This would minimize neutron and tritium leakage and facilitate installation of a safety valve to close the port in the event of an accident. The optical requirements of this scheme are discussed in detail in Section IV.2.B.

After penetration of the reactor wall the beams must be directed to the final focusing mirrors. Care must be taken to adjust the path lengths such that all beams arrive at the target simultaneously. Some path length adjustments can be made in the front end with proper timing of the firing of the amplifiers.

As stated above, the target will be illuminated from only two sides. This requires placing 28 mirrors on opposite sides of the reactor cavity. The mirrors will be arrayed in two vertical adjacent columns of 14 mirrors each. These mirrors are located 22 meters from the target. The final turning angle is 90°.

One illumination requirement we are imposing is that the irradiation be symmetric in the sense the pellet should be irradiated equally from the two opposing sides at all times. The simplest way to accomplish this

is to have opposing mirrors face each other and deliver equal amounts of energy in time. However, as discussed in the SOLASE design, this could prove disastrous to the optics in the event that the laser pulse misses a target and is transported back through the opposing amplifier chain. Due to the compression of this beam and its further amplification by residual gain in the amplifiers the beam intensity would eventually exceed the optical damage threshold of the optical components causing intolerable damage to the system. Thus, unless a good optical protection scheme can guarantee the safety of the optics, this is not a viable last mirror configuration. However, the HF laser is particularly interesting, inasmuch as it has a naturally occurring mechanism that will at least partially protect the optics. The post-lasing HF amplifier does not possess residual gain, but is instead strongly absorbing. Thus, a returning pulse will not be amplified, but attenuated. In fact, there is a period in which the medium is totally absorbing. If the path lengths could be adjusted such that a returning pulse arrives at the amplifier during this time, adequate protection would be assured. Unfortunately, the time for total absorption is so short as to require impractically short path lengths. However, even at much longer times the medium is still sufficiently absorbing to greatly reduce the problem of returning light. This is a distinct advantage the HF laser has over its competitors.

IV.2.A-4. Beam Transport Efficiency

The efficiency of the beam transport system is important because it determines the fraction of the laser energy generated that can actually be focused onto the target. This is a function of the beam quality, mirror reflectivity, the number of mirrors, alignment errors, miscellaneous

absorption, and wavefront dislocations. For our parameters, assuming a state-of-the-art, 2 times diffraction limited beam (this can probably be improved), over 95% of the energy can be focused onto a 1 mm spot. The reflectivity of diamond-turned, bare-metal mirrors will be at least 99%. Combining these two facts and assuming 10 mirrors subsequent to final amplification, we find that 86% of the energy generated can be focused onto the target. If we then assume that not more than 6% is lost due to absorption, alignment and wavefront distortion errors, then the final beam transport efficiency is about 80%. Obviously, one would like to improve this value. This can be done by improving the beam quality, increasing the mirror reflectivity and decreasing the number of mirrors and windows required to deliver the beam to the target.

IV.2.B. Beam Port Reduction Scheme

IV.2.B-1. Introduction

An inherent difficulty in designing a laser fusion reactor is the excessive neutron leakage through the large optical apertures in the reactor cavity. For example, in the SOLASE design[1] over 10^4 cm^2 of aperture area is required to keep the 1 MJ, 1 nsec laser pulses from damaging the mirrors. Neutronics calculations reveal very high radiation levels (~ 10^6 Rem/hr) even after two reflections back through the optical train.[2] Ample amounts of shielding have failed to substantially reduce these levels. One approach to this problem entails locating the final mirrors a large distance (50-100 m) from the target.[3] However, this scheme poses difficult alignment problems.[4] In another design study,[5] annular beams are reflected via toric optics, a central reflector effectively plugging the aperture.

In this section we propose a beam port reduction scheme employing a pair of parabolic reflectors to condense and recollimate an initially collimated beam. A pair of off-axis paraboloids reduces the wall penetration to a small circular hole, as sketched in Fig. IV.2-1 while a pair of parabolic cylinders gives a line focus and a slot penetration, as depicted in Fig. IV.2-2. Either of these configurations would dramatically reduce the neutron leakage out of the primary containment volume. The point focus arrangement arose in fusion design meetings at Wisconsin[2] and also independently at Livermore.[3] The line focus scheme was recently proposed by M. Monsler as a means of avoiding gas breakdown. The present study is much more quantitative and differs in several important respects from the design described in Ref. 3.

Most laser fusion reactor designs involve a low pressure (0.1 - 1.0 torr) gas either in the form of lithium vapor[6] or a buffer gas such as neon or xenon.[7] As is well-known, gas breakdown will occur in the presence of high intensity laser radiation.[8] To this end we have calculated the irradiance in the focal

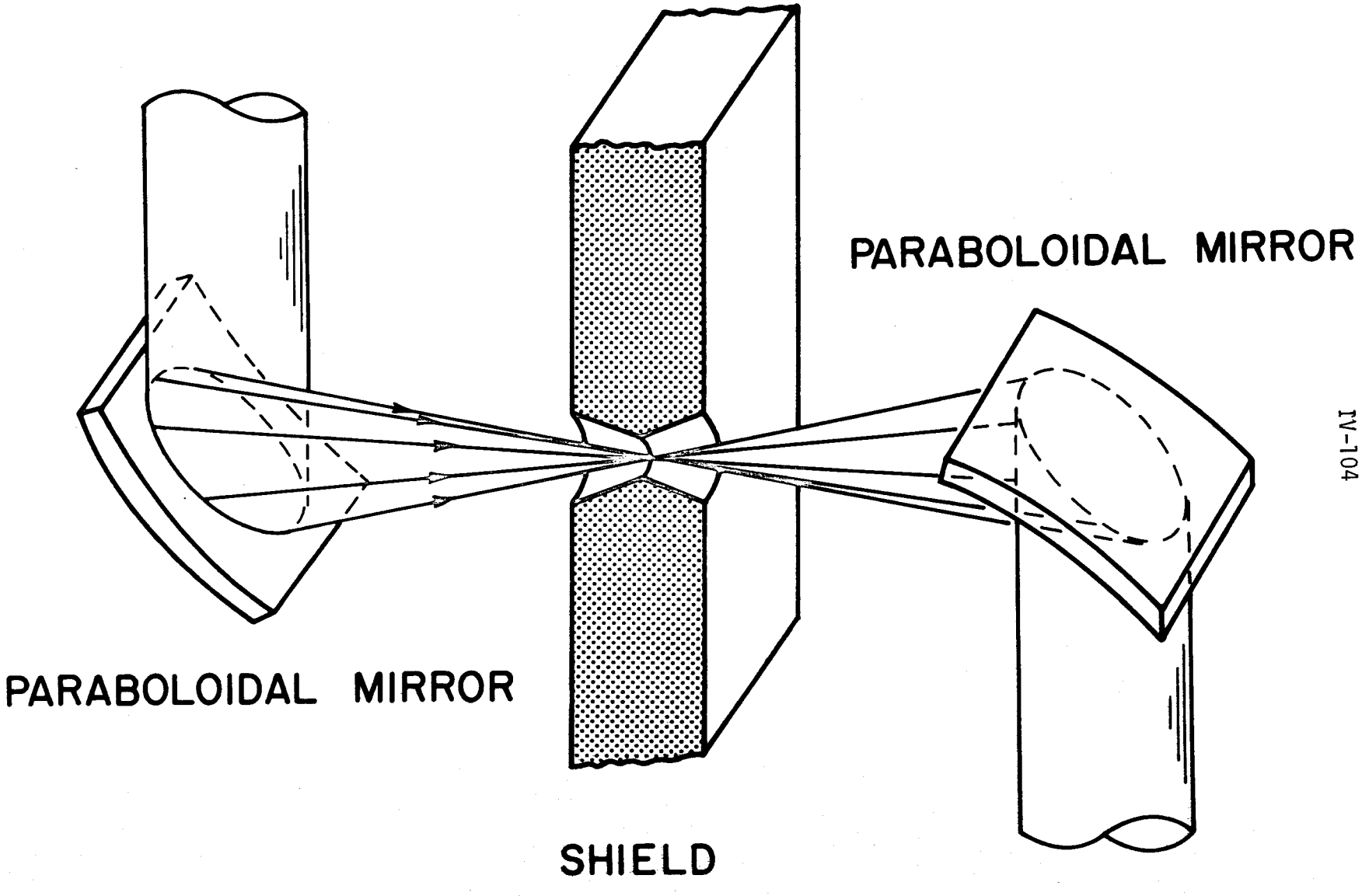

Fig. IV.2-1 Beam reduction using off-axis paraboloids.

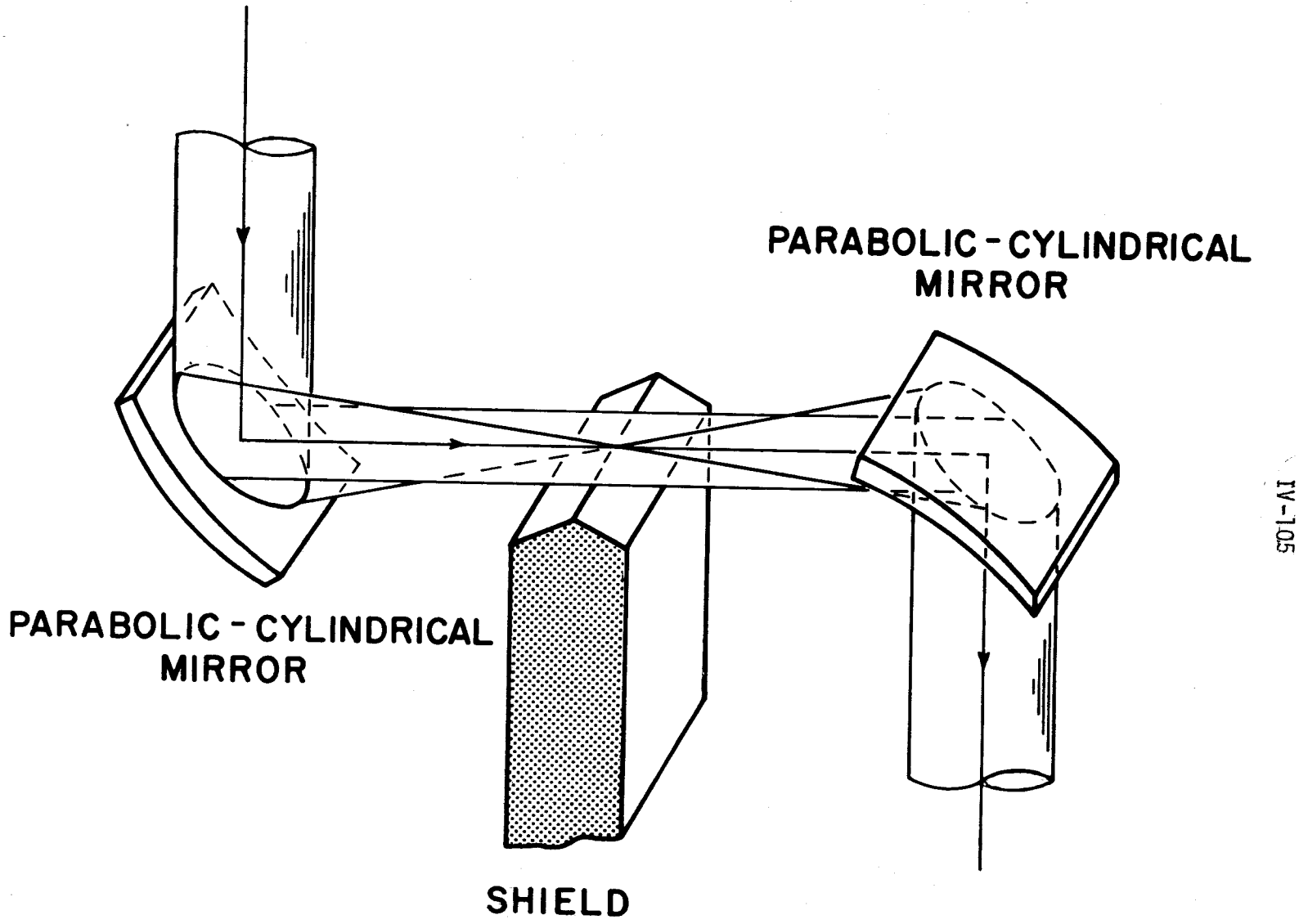

Fig. IV.2-2 Beam reduction using parabolic cylindrical mirrors.
Only the lower half of the wall is shown for clarity.

plane of a circular and a cylindrical focusing element using Fraunhofer diffraction theory. The resulting formulas are applied to a square aperture typical of an HF laser and reflecting our emerging fusion-fission hybrid design, and also to the more familiar case of a circular beam. Although the very high irradiance at a point focus is substantially reduced by going to a line focus, the peak irradiance is still large enough to cause gas breakdown at pressures on the order of one torr of neon or xenon.

Thus, using cylindrical mirrors doesn't really alleviate the breakdown problem and it is necessary to pump down the focal region to a low enough pressure that negligible refraction[9] and stimulated Raman scattering[10] occur. To accomplish this, it is desirable to enclose the mirrors in a vacuum chamber and install quartz windows (in the case of HF) to admit the beams. Following the example of the spatial filters installed in the SHIVA laser chains,[11] we estimate that a pressure of 10^{-5} torr would more than suffice.

Since evacuation is required in either case, one may ask whether a line focus is preferable to a point focus. It may turn out to be more difficult to align two mirrors at a common focal line than at a "point". One clear advantage is cost; cylindrical mirrors are cheaper to make than paraboloids. On the other hand, if it is desired to run the device as a spatial filter, a point focus would be appropriate. We elect to leave this option open, as it doesn't affect the basic features of our design.

We also consider briefly the possibility of a "fuzzy focus" system, in which aberrations are deliberately introduced into a first reflector, producing a lower focal irradiance. The second collector would hopefully compensate for these aberrations, producing a uniform collimated beam.

IV.2.B-2. Irradiance in the Focal Plane of a Paraboloid Mirror

This problem is formally the same as the well-known problem of calculating the irradiance in the focal plane of an ideal converging lens. Figure IV.2-3 depicts collimated light incident on an aperture and focused onto the image plane at distance f along the optical axis 0-0'. The diffracted wave for a rectangular aperture of dimensions 2a x 2b is given by the Fraunhofer integral[12]

$$U(x,y) = C \int_{-b}^{b} \int_{-a}^{a} e^{ik(x\xi+y\eta)/f} \, d\xi \, d\eta \, , \qquad (1)$$

where (x,y) is the image point, (ξ,η) is a source point within the aperture and $k = 2\pi/\lambda$. The irradiance is then

$$I = U^2 \, . \qquad (2)$$

Using Parseval's theorem or conservation of energy to determine the constant C, we obtain the familiar result,

$$U = \frac{\sqrt{PA}}{\lambda f} \frac{\sin(kxa/f)}{kxa/f} \cdot \frac{\sin(kyb/f)}{kyb/f} \qquad (3)$$

from which

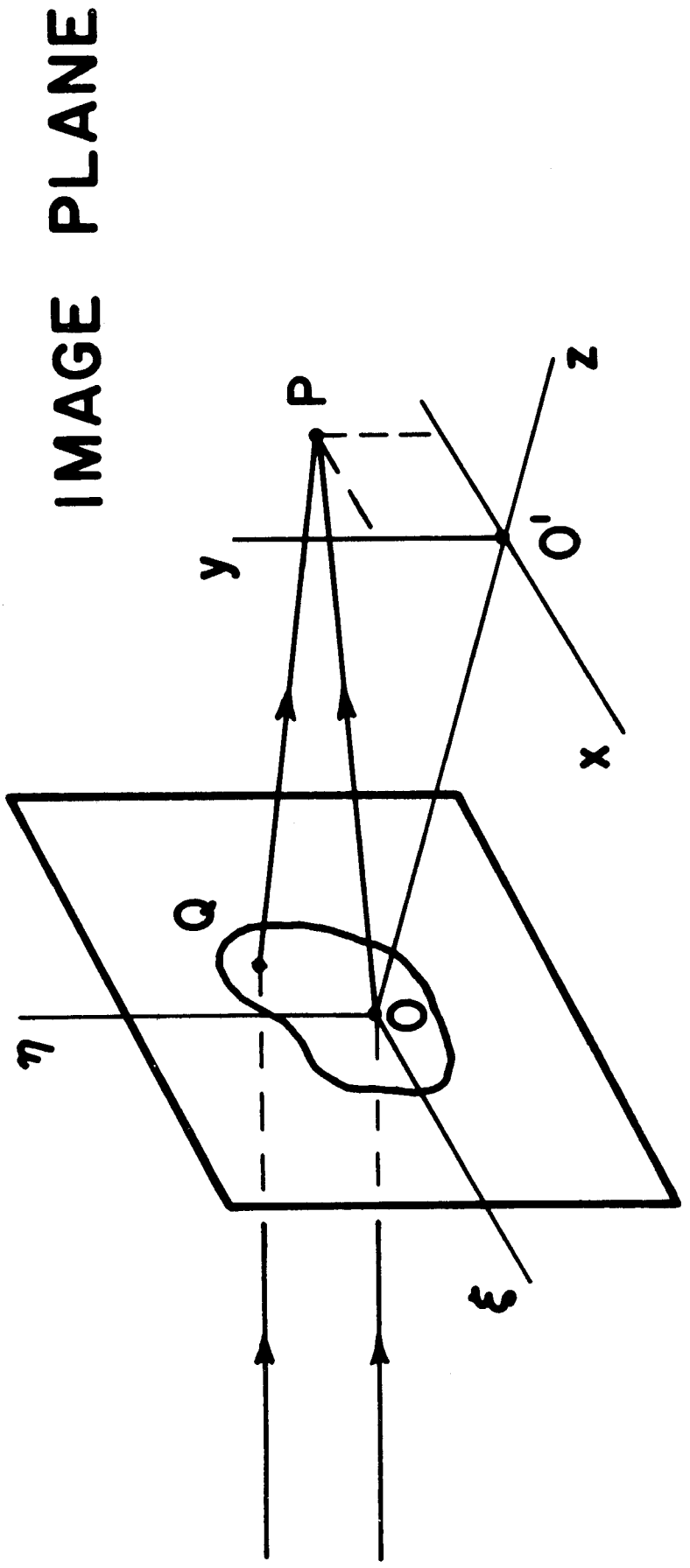

Fig. IV.2-3 Fraunhofer diffraction geometry in the focal plane of a converging lens or mirror (not shown)

$$I_{max} = \frac{PA}{\lambda^2 f^2} \quad . \tag{4}$$

Here $P = \iint U^2 \, dx \, dy$ is the total beam power and $A = 4ab$ is the aperture area.

For our HF conceptual design,[13] $\lambda = 3$ μm, $P_{max} = 300$ TW, and $a = b = 70$ cm. Taking $f = 2$m then gives

$$I_{max} = 4 \times 10^{20} \text{ W/cm}^2 \, ,$$

a very large irradiance indeed, far above the gas breakdown threshold of $\sim 10^{12}$ W/cm^2 for ~ 1 torr of neon or xenon.

IV.2.B-3. Irradiance in the Focal Plane of a Parabolic Cylinder Mirror

This problem, formally identical to the cylindrical lens case, does not seem to be treated in the standard literature, so we shall derive it from basic principles.

IV.2.B-3-a. Rectangular Aperture

As convergence occurs only in one direction, say the y-direction, the Fraunhofer integral becomes

$$U(y) = C \int_{-b}^{b} e^{iky\eta/f} \, d\eta \, , \tag{5}$$

where we have assumed uniform irradiance on the aperture. This is a Fourier integral, to which Parseval's theorem applies:

$$C^2 \int_{-b}^{b} d\eta = \frac{1}{\lambda f} \int_{-\infty}^{\infty} |U(y)|^2 \, dy = \frac{P}{\lambda f} \quad . \tag{6}$$

Thus,

$$C^2 = \frac{P}{2b\lambda f} \quad . \tag{7}$$

Carrying out the integral in Eq. (5), we obtain

$$U(y) = \sqrt{\frac{bP}{a\lambda f}} \quad \frac{\sin(kby/f)}{kby/f} \quad . \tag{8}$$

The peak irradiance is therefore

$$I_{max} = \frac{b}{a} \frac{P}{\lambda f} \quad , \tag{9}$$

independent of area. In terms of the incident irradiance I_o this takes the dimensionless form

$$I_{max} = \frac{b}{a} \left(\frac{A}{\lambda f}\right) I_o \quad . \tag{10}$$

Putting in numerical values we find

$$I_{max} = 5 \times 10^{15} \text{ W/cm}^2 \quad .$$

This is still large enough to induce gas breakdown in 1 torr of neon or xenon.

IV.2.B-3-b. Circular Aperture

Figure IV.2-4 illustrates the formation of the line focus, from a circular aperture of radius a. Since we are focusing in the y-direction only, we need only consider rays originating in a particular y-z plane and identify $x = \xi$. Rays from other ξ-values contribute only a little near-field Fresnel

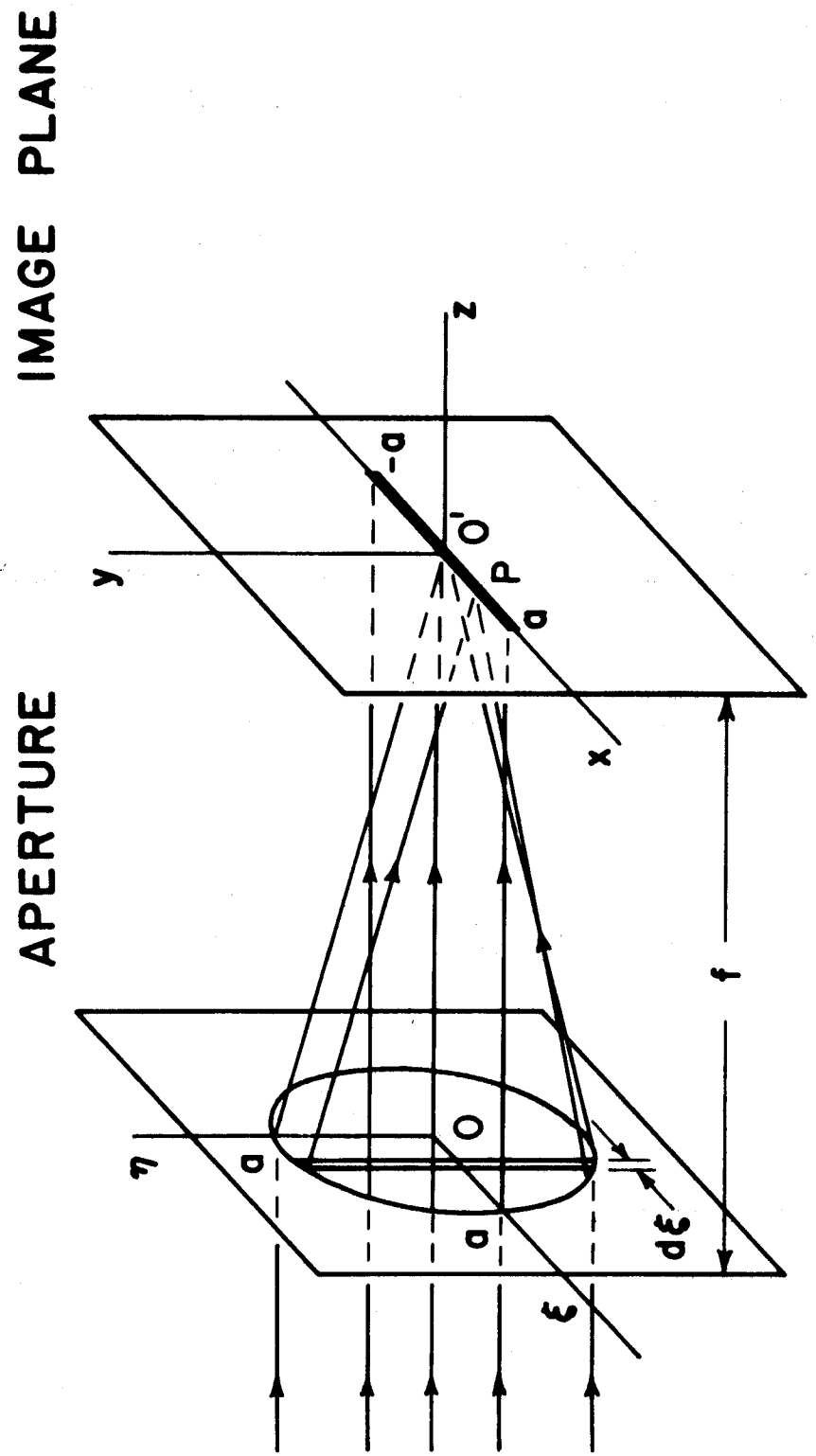

Fig. IV.2-4 Formation of line focus from a circular aperture and a cylindrical focusing element

diffraction, which we neglect. From Fig. IV.2-4, the relevant Fraunhofer integral is

$$U(x,y) = C \int_{-\sqrt{a^2-x^2}}^{\sqrt{a^2-x^2}} e^{ik\eta y/f}\, d\eta \qquad (11)$$

or

$$U(x,y) = \frac{2Cf}{ky} \sin\left(\frac{ky}{f}\sqrt{a^2-x^2}\right) . \qquad (12)$$

The Parseval relation is not applicable in this case so we must use conservation of energy directly to determine C:

$$P = \iint U^2\, dx\, dy = \left(\frac{2Cf}{k}\right)^2 \int_{-a}^{a} F(x)\, dx , \qquad (13)$$

where

$$F(x) = \int_{-\infty}^{\infty} \frac{1}{y^2} \sin^2\left(\frac{ky}{f}\sqrt{a^2-x^2}\right) dy \qquad (14)$$

or

$$F(x) = \frac{\pi k}{f}\sqrt{a^2-x^2} . \qquad (15)$$

Carrying out the x-integration then gives

$$P = \lambda f A C^2 . \qquad (16)$$

Using this result in Eq. (12) we obtain

$$U(x,y) = \sqrt{\frac{4P}{\pi\lambda f}}\ \frac{\sin\left(\frac{ky}{f}\sqrt{a^2-x^2}\right)}{kya/f}\ , \tag{17}$$

from which

$$I_{max} = \frac{4}{\pi}\left(\frac{A}{\lambda f}\right) I_o\ . \tag{18}$$

Figure IV.2-5 illustrates the irradiance $I = U^2$ in the x-y plane. Note that the central peak broadens as $x \to a$, the first null being given by

$$y^* = \frac{\lambda f}{2a\sqrt{1-x^2/a^2}}\ . \tag{19}$$

Applying Eq. (18) to the Livermore conceptual design[3] which calls for P_{max} = 500 TW, λ = 1.06 μm and f = 2m (say), we find $I_{max} = 3.2 \times 10^{16}$ W/cm^2.

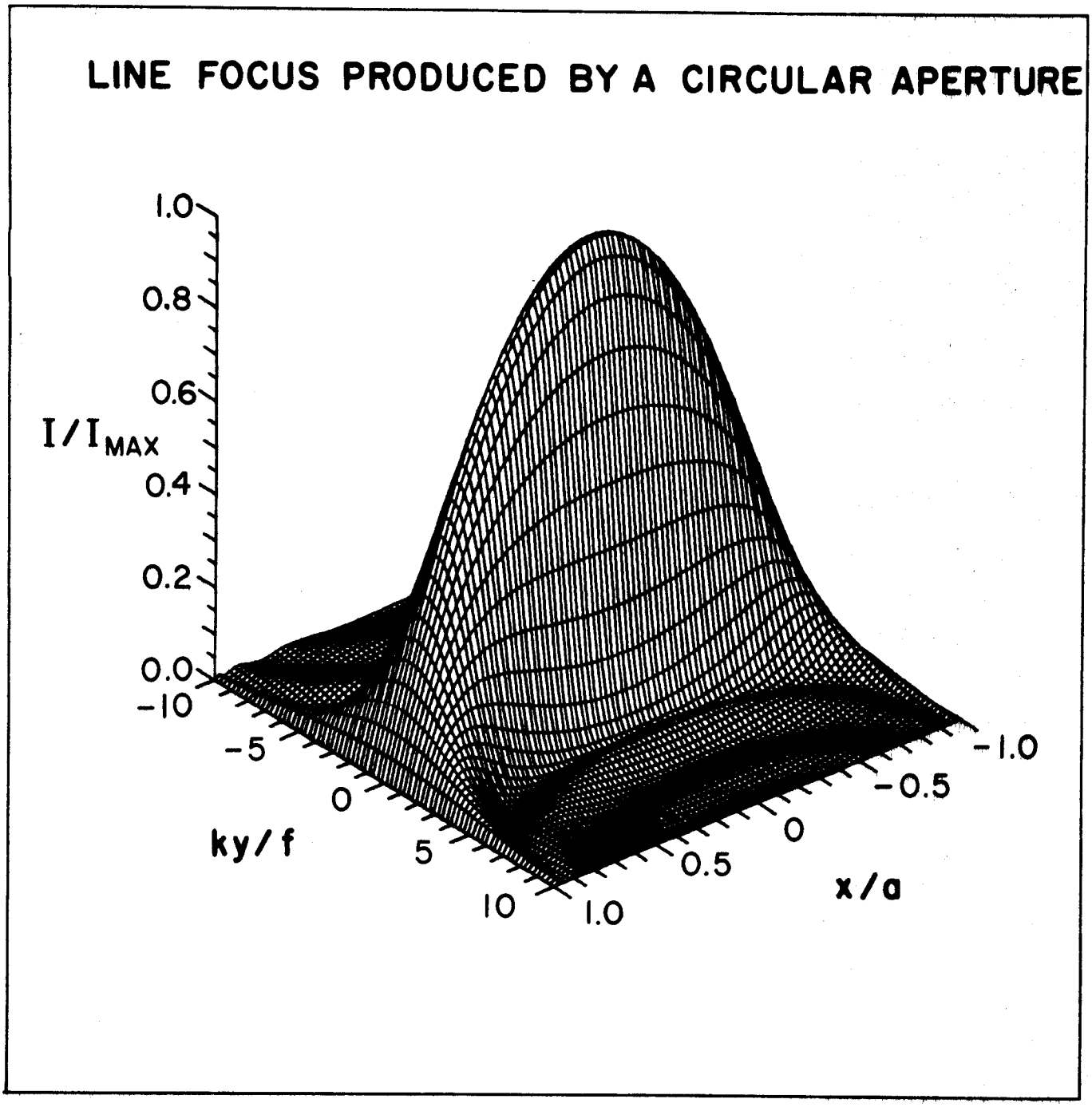

Fig. IV.2-5 Fraunhofer diffraction pattern produced by a circular aperture and a cylindrical focusing element

References for Section IV.2.B.

1. R.W. Conn et al., U. Wisconsin Nuclear Engineering Dept. Report UWFDM-220 (December, 1978).
2. M.M.H. Ragheb, A.C. Klein and C.W. Maynard, U. Wisconsin Nuclear Engineering Dept. Report UWFDM-239 (April, 1978).
3. M.J. Monsler and J.A. Maniscalco, Lawrence Livermore Laboratory Report UCRL-79990 (November, 1977).
4. J.E. Howard, to be published in Applied Optics.
5. L.A. Booth, Los Alamos Scientific Laboratory Report LA-4858-MS, Vol. 1 (February, 1972).
6. J.A. Maniscalco, W.R. Meier and M.J. Monsler, Lawrence Livermore Laboratory Report UCRL-79652 (July, 1977).
7. J.E. Howard et al., First Wall Protection Scheme for the SOLASE Conceptual Laser Fusion Reactor, presented at the Optical Soc. of America Topical Meeting on Inertial Confinement Fusion, Feb. 7-9, 1978, San Diego, California.
8. C. Grey Morgan, Rep. Prog. Phys. 38, 621 (1975).
9. D.B. Henderson, Nucl. Eng. and Design 30, 111 (1974).
10. J.J. Thompson, to be published in Phys. Fluids.
11. Lawrence Livermore Laboratory Laser Program Annual Report (1974), UCRL-50021-74, p. 169.
12. M. Born and E. Wolf, Principles of Optics, Pergamon Press (New York, 1964), p. 392.
13. G.W. Cooper, private communication.

IV.2.C. Schematic Design

Figure IV.2-6 is an overhead view of the proposed device. A 70 cm square beam is assumed incident from the laser some meters distant. After striking flat F_1 it is turned through 45^o, passing through a 2.5 cm thick quartz window. The window must be thick enough to ensure tritium containment but thin enough to hold down nonlinear optical effects. The beam is then simultaneously turned and focused by parabolic mirror P_1 of 3.5 m focal length, passing through the 2 m thick shielded primary containment wall. The wall would be of structural concrete with additional shielding placed behind flat F_2. The port is tapered to a diameter of approximately 1 cm. A fast acting valve could be installed in the port throat to ensure tritium containment in case of window failure. Next the beam is turned and recollimated by parabolic mirror P_2, exiting from the vacuum chamber through window W_2. Finally, the beam is turned by flat F_2 and directed to the reactor chamber some 20 m distant.

The entire region outlined in black and enclosing mirrors P_1 and P_2 is evacuated to 10^{-5} torr to avoid breakdown at the (point or line) focus. The region outside the chamber is at a pressure of about one torr. The beams would be enclosed in evacuated beam tubes (not shown) to maintain clean optical surfaces.

It should be noted that 45^o turning mirrors have been used rather than 90^o mirrors. This choice is based on our studies of the imaging properties of parabolic mirrors, which show that for the same tilt error

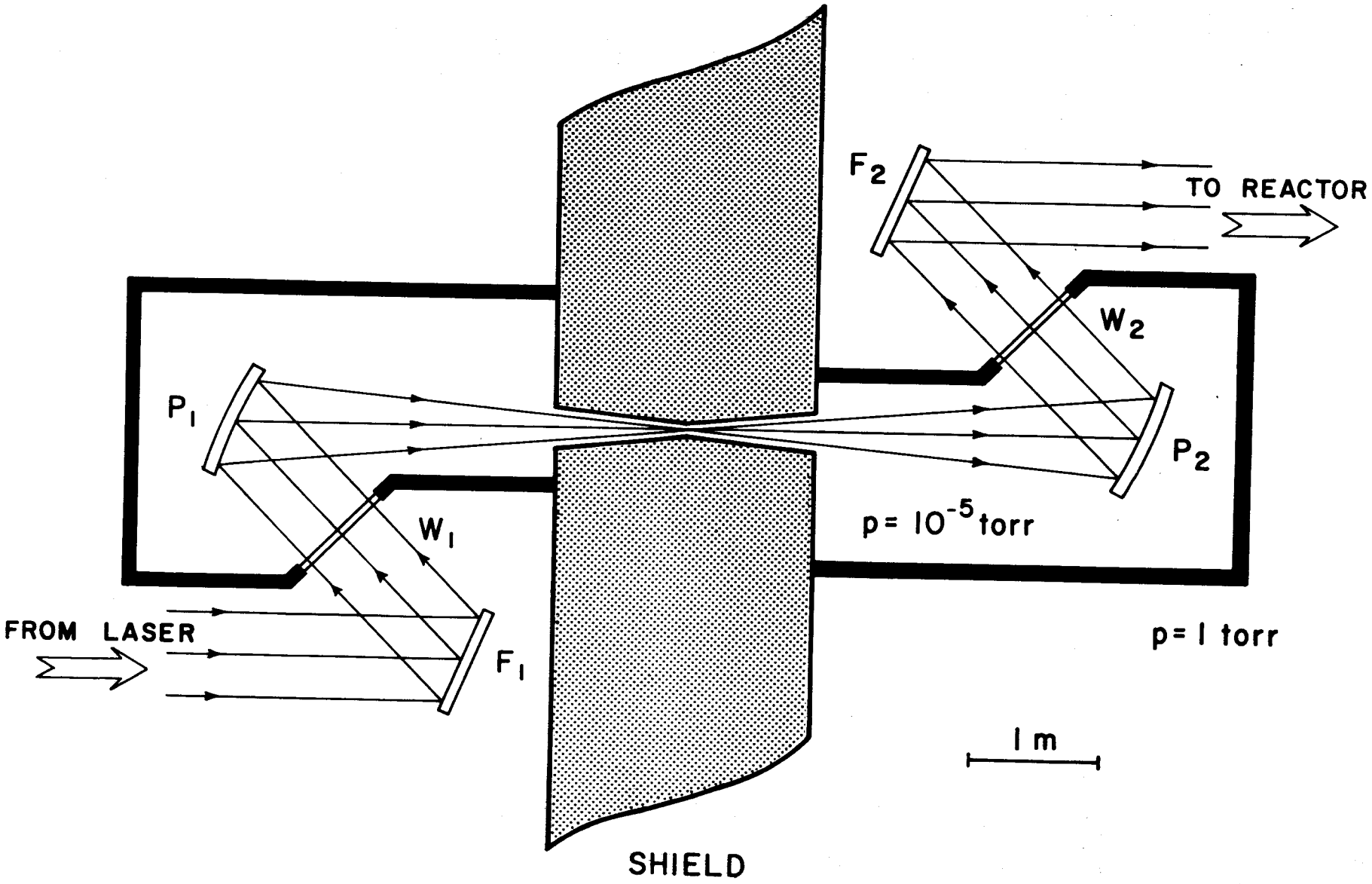

Fig. IV.2-6 Schematic design of proposed beam port reduction scheme, using effective f/5 off-axis paraboloids or parabolic cylinders. The minimum wall penetration width can be as small as 1 cm or less.

much larger irradiance distortions occur at larger deflection angles. Naturally space must be provided for rigid mirror mounts and automatic alignment systems. Also note that quartz window W_2 is not directly exposed to the neutron flux from the reactor chamber located to the right. This is an important feature of the design, since quartz is vulnerable to loss of transparency by neutron damage.

It would be very desirable to place beam reduction units closer to the target chamber in order to limit the high neutron flux in the immediate vicinity of the first wall and blanket. It seems fairly certain that an evacuated system such as the one described above could not be so installed due to the very short expected window lifetimes under intense neutron bombardment.

Assuming a gas breakdown threshold of 10^{12} W/cm^2, it is straightforward to show that a 10 cm focal radius would allow transmission of up to 300 TW peak power without evacuation. A spot of this size could in principle be produced by employing nonparabolic surfaces to deliberately induce aberrations in the focal region. Another possibility would be to tilt the parabolic mirrors a prescribed amount, which would also spread out the focal region. In both cases caustic formation would have to be investigated.

In summary, we have presented a schematic design for a beam reduction device, similar to a conventional spatial filter except for the use of reflective optics. Maintaining mirror alignment is expected to be difficult but not unattainable. The vacuum requirements are modest. Probably the Achilles' heel of this design is the optical response of the quartz windows to neutrons and X-rays. We are currently engaged in a study of these effects which will hopefully lead to a quantitative estimate of window lifetimes.

IV.2.D. Mirror Damage Thresholds for Laser Fusion Temporal Pulse Shapes

IV.2.D-1. Introduction

The maximum allowable energy density (J/cm^2) incident on bare metal mirrors is usually thought to be limited by surface melting under intense laser radiation. The damage threshold has been calculated analytically for (temporally) square pulses[1] using classical one-dimensional thermodynamics.[2] Numerical computations have also been performed[3] for an asymmetric model pulse typical of saturated operation of a high-power CO_2 laser.

In this section we calculate damage thresholds for two pulse shapes relevant to laser fusion: the truncated Gaussian, and the semi-empirical "ideal" pulse designed to produce isentropic compression of spherical targets.[4] A Gaussian pulse is characteristic of Nd : glass lasers operated below saturation, whereas the steeply rising ideal pulse would have to be produced by a device such as a pulse-stacker. The result for Gaussian pulses is reduced to a simple integral equation, while the ideal pulse threshold is given in completely closed form.

Although the emphasis here is on illumination of metallic surfaces, the results apply to any surface for which the depth of the heated zone is small compared to the beam radius, and the pulse width is long enough that a local temperature may be defined. It may be shown that radiation losses are almost always negligible in cases of practical interest.[1] We shall also ignore the small variation in thermal parameters with temperature.

IV.2.D-2. Square Pulse

Assuming zero penetration depth, the surface temperature rise for arbitrary flux I(t) W/cm^2 incident on a semi-infinite medium is[1]

$$\Delta T = \frac{(1-R)}{K} \left(\frac{k}{\pi}\right)^{1/2} F(t) \ , \tag{1}$$

where K is the thermal conductivity, $k = K/\rho c_p$ is the thermal diffusivity, R is the reflectivity and

$$F(t) \equiv \int_0^t I\ (t - t') \frac{dt'}{(t')^{1/2}} \ . \tag{2}$$

We are interested here in the maximum surface temperature rise:

$$\Delta T_{max} = AF_{max} \ , \tag{3}$$

where

$$A \equiv \frac{(1-R)}{K} \left(\frac{k}{\pi}\right)^{1/2} \ . \tag{4}$$

For a square pulse of magnitude I_o and width τ the solution of Eq. (1) is well known:

$$\Delta T = 2A\ I_o\ t^{1/2}, t \leq \tau \ . \tag{5}$$

The damage threshold is customarily expressed in terms of the energy density,

$$\Phi = \int_0^t I(t')dt' = I_o\, t \ . \tag{6}$$

Combining Eqs. (5) and (6) we arrive at the critical energy density for surface melting,

$$\Phi^* = \frac{(T_m - T_o)}{2A}\, \tau^{1/2} \ , \tag{7}$$

where T_o and T_m are the initial and melting temperatures.

IV.2.D-3. Gaussian Pulse

Consider a Gaussian pulse of maximum intensity I_o and total width 2τ, with origin at the leading edge, as indicated in Fig. IV.2-7:

$$I(t) = I_o \exp\,[-a^2(t - \tau)^2] \ . \tag{8}$$

Then

$$F(t) = I_o \int_0^t \exp\,[-a^2\,(t - t' - \tau)^2]\,(t')^{-1/2}\, dt' \tag{9}$$

or

$$F(t) = I_o\,(\tau/Y)^{1/2} \int_0^y \frac{\exp[-(Y-u)^2]du}{(y-u)^{1/2}} \ , \tag{10}$$

where $y = at$, $Y = a\tau$ and $u = a(t-t')$. Integrating by parts, we obtain

$$F(t) = 2\, I_o\, \tau^{1/2}\, \frac{G(y,Y)}{Y^{1/2}} \ , \tag{11}$$

with

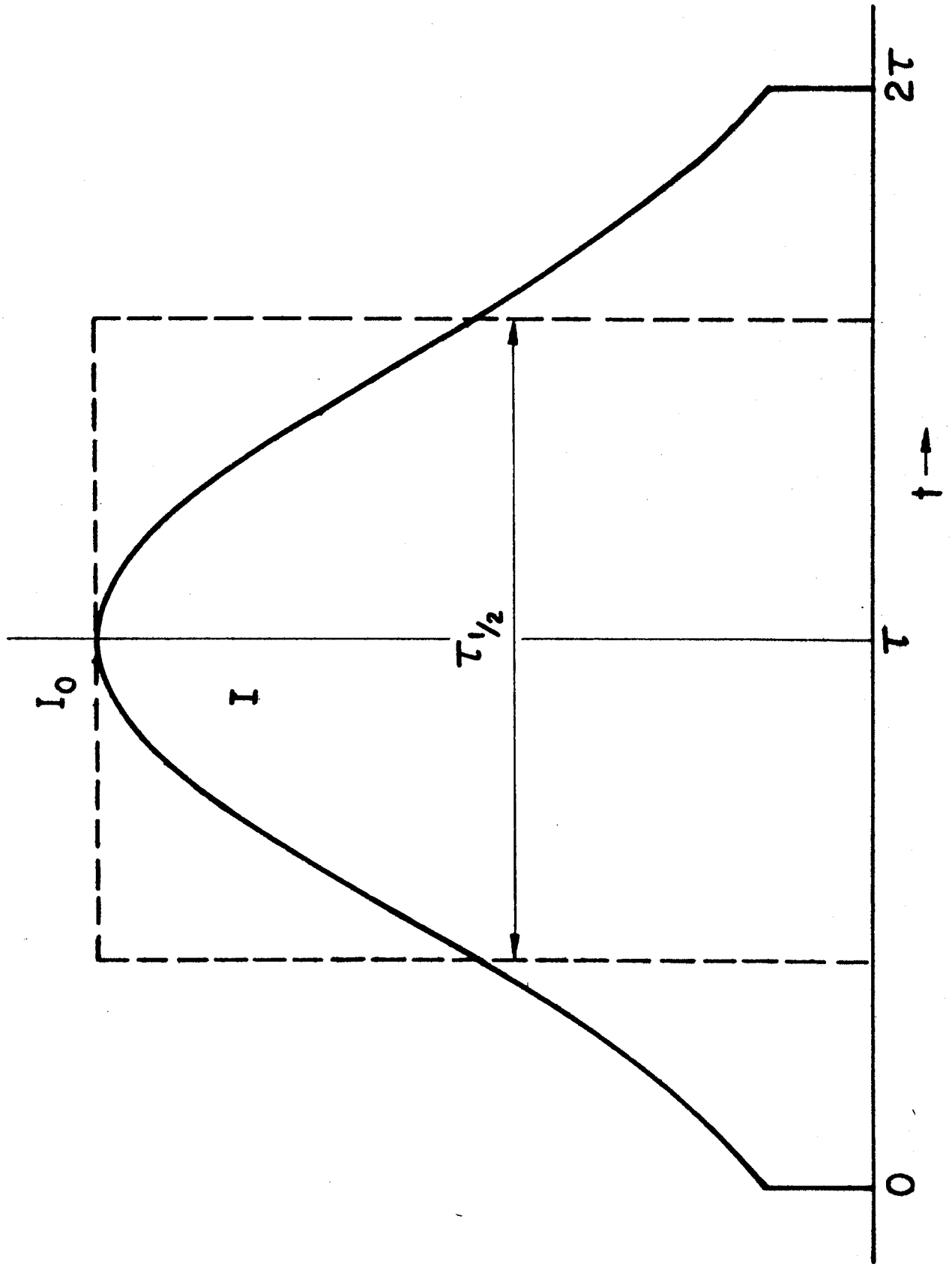

Figure IV.2-7 A Gaussian pulse of full width 2τ truncated after two e-foldings ($\gamma = \sqrt{2}$) superimposed on a square pulse of width equal to the FWHM, $\tau_{1/2}$

$$G(y,Y) = y^{1/2} e^{-Y^2} + 2 \int_0^y (Y-u)\,(y-u)^{1/2} \exp\,[-(Y-u)^2]du \ . \qquad (12)$$

Figure IV.2-8 depicts the function $GY^{-1/2}$ for $Y = 1, \sqrt{2}, \sqrt{3}$ and 2, Y^2 corresponding to the number of e-foldings at the pulse edge. The decrease in T_{max} with increasing Y is primarily due to the decrease in area (energy). Figure IV.2-9 depicts the same function for Y = 1, 2, 4 and 8, illustrating the rather slow decay in temperature for large Y.

The scaled time at which the maximum temperature occurs is given by solving $\partial G/\partial y = 0$ for y. This leads to the equation

$$\int_{-Y}^{\tilde{y}} \frac{v e^{-v^2} dv}{(\tilde{y}-v)^{1/2}} = \frac{e^{-Y^2}}{2(\tilde{y}+Y)^{1/2}} \ , \qquad (13)$$

to be solved for $\tilde{y} \equiv y - Y$. As $Y \to \infty$, this reduces to

$$\int_{-\infty}^{\tilde{y}} \frac{v e^{-v^2} dv}{(\tilde{y}-v)^{1/2}} = 0 \ . \qquad (14)$$

We have not found analytic solutions to Eqs. (13) or (14). Numerically obtained values of $\tilde{y}$ and G_{max} are shown in Fig. IV.2-10 as functions of Y. Convergence is seen to be quite rapid, the limiting values being

$$\lim_{Y\to\infty} \tilde{y} = 0.5409$$

$$\lim_{Y\to\infty} G_{max} = 1.0760 \ . \qquad (15)$$

It is of interest to compare the damage threshold for a truncated Gaussian pulse with that for a square pulse of equal peak power and total width equal to the FWHM (Fig. IV.2-7). The total energy is then equal to

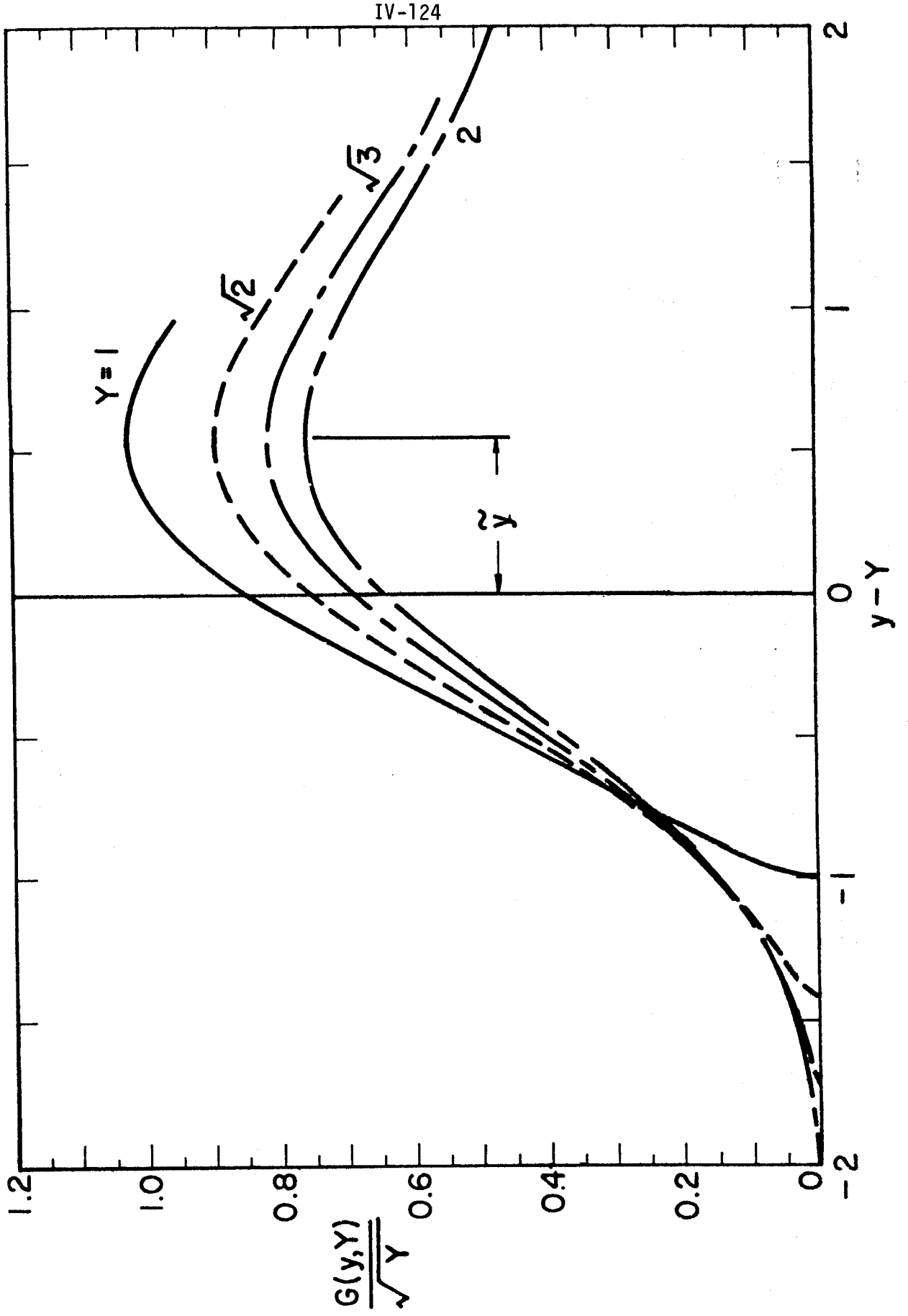

Figure IV.2-8 Scaled temperature-time histories for moderate Y-values. The maxima occur at $\tilde{y} = 0.5409$ for $Y > 2$.

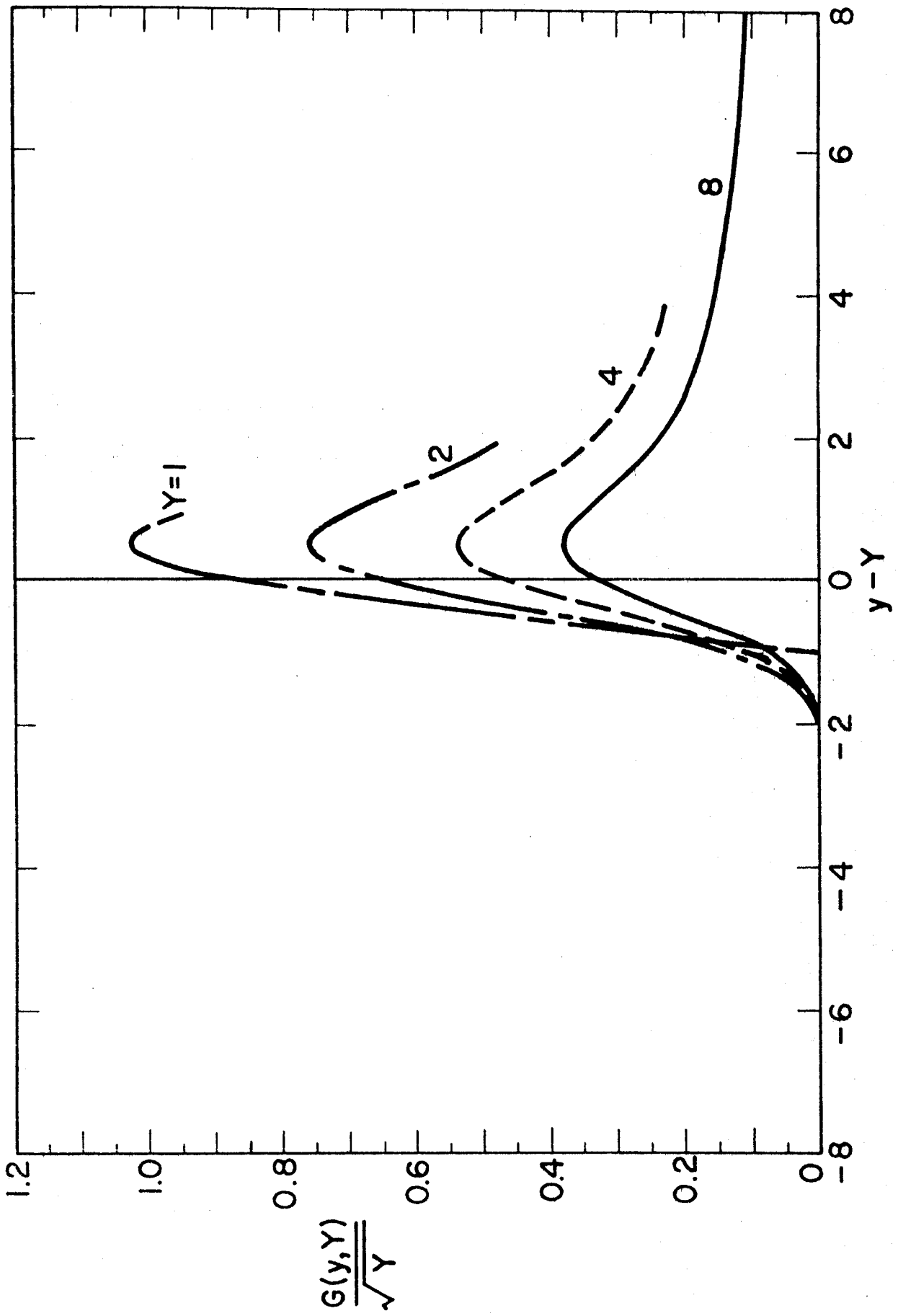

Figure IV.2-9 Scaled temperature-time histories for larger Y-values.

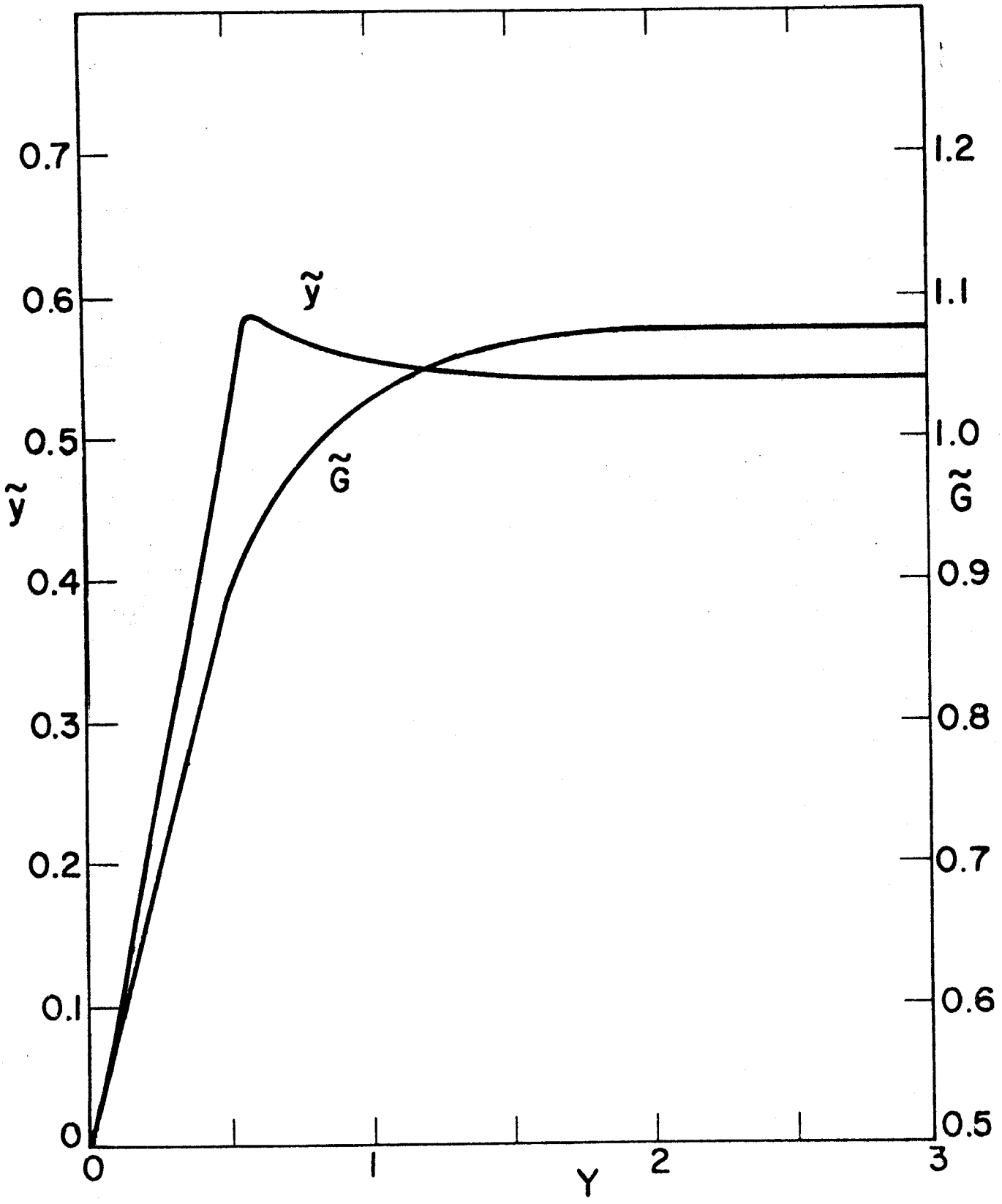

Figure IV.2-10 Location and magnitude of the maximum of G(y,Y)

within 2% for a two e-folding Gaussian ($\gamma = \sqrt{2}$). In general,

$$\Phi = 2\, I_o \int_o^\tau \exp\,(-a^2t^2)dt = \frac{\pi^{1/2} I_o \tau}{\gamma}\, \mathrm{erf}(\gamma) \ . \tag{16}$$

Combining Eqs. (3), (11) and (16) gives

$$\Phi = \left(\frac{\Delta T_m \tau^{1/2}}{2A}\right) \frac{\pi^{1/2}\mathrm{erf}(\gamma)}{\gamma^{1/2} G_{max}} \ . \tag{17}$$

Substituting for the FWHM,

$$\tau_{1/2} = \frac{(\ell n 16)^{1/2}}{\gamma}\, \tau \tag{18}$$

yields

$$\Phi^* = \frac{\pi^{1/2}\mathrm{erf}(\gamma)}{G_{max}(\ell n 16)^{1/4}}\, \Phi^*_{sp} \ , \tag{19}$$

where Φ^*_{sp} is the square pulse threshold, Eq. (7), with $\tau = \tau_{1/2}$. Taking $\gamma = \sqrt{2}$ in Eq. (19), we find

$$\Phi^* = 1.22\, \Phi^*_{sp} \ . \tag{20}$$

This 20% energy dividend is primarily due to the fact that the surface temperature reaches its maximum somewhat before the end of the pulse; any energy transmitted after this time cannot contribute to surface damage. Damage threshold experiments using Gaussian pulses should, therefore, be compared with a theoretical value about 20% higher than the square pulse value.

IV.2.D-4. "Ideal" Isentropic Pulse

A great deal of numerical simulation has been done using the steeply rising pulse form[4]

$$I(t) = I_0(1 - t/t_1)^{-2},\ 0 \leq t \leq \tau < t_1 \tag{21}$$

to obtain isentropic compression of spherical laser fusion targets. It should be noted that this semi-empirical pulse shape differs from Kidder's theoretical form,[5] in which the quantity t/t_1 is squared. As Fig. IV.2-11 illustrates, I_0 now denotes the initial irradiance, the peak value being

$$I_{max} = I_0\ (1 - \eta)^{-2}\ , \tag{22}$$

where $\eta = \tau/t_1$. The energy density and peak intensity are related by

$$\Phi = I_{max}\ \tau\ (1 - \eta)\ . \tag{23}$$

Thus,

$$\eta = 1 - \frac{\Phi}{I_{max}\ \tau}\ . \tag{24}$$

The integral in Eq. (2) may be carried out, with the result

$$F(t) = \frac{I_0 t_1^{1/2}}{(1-y)^{3/2}}\ [\sin^{-1} y^{1/2} + y^{1/2}\ (1 - y)^{1/2}], \tag{25}$$

where $y = t/t_1$. Thus, the temperature rise is monotonically increasing, reaching the maximum

$$F_{max} = I_{max}\ \tau^{1/2}\ [\varepsilon + (\frac{\varepsilon}{1-\varepsilon})^{1/2}\ \cos^{-1}\ \varepsilon^{1/2}]\ , \tag{26}$$

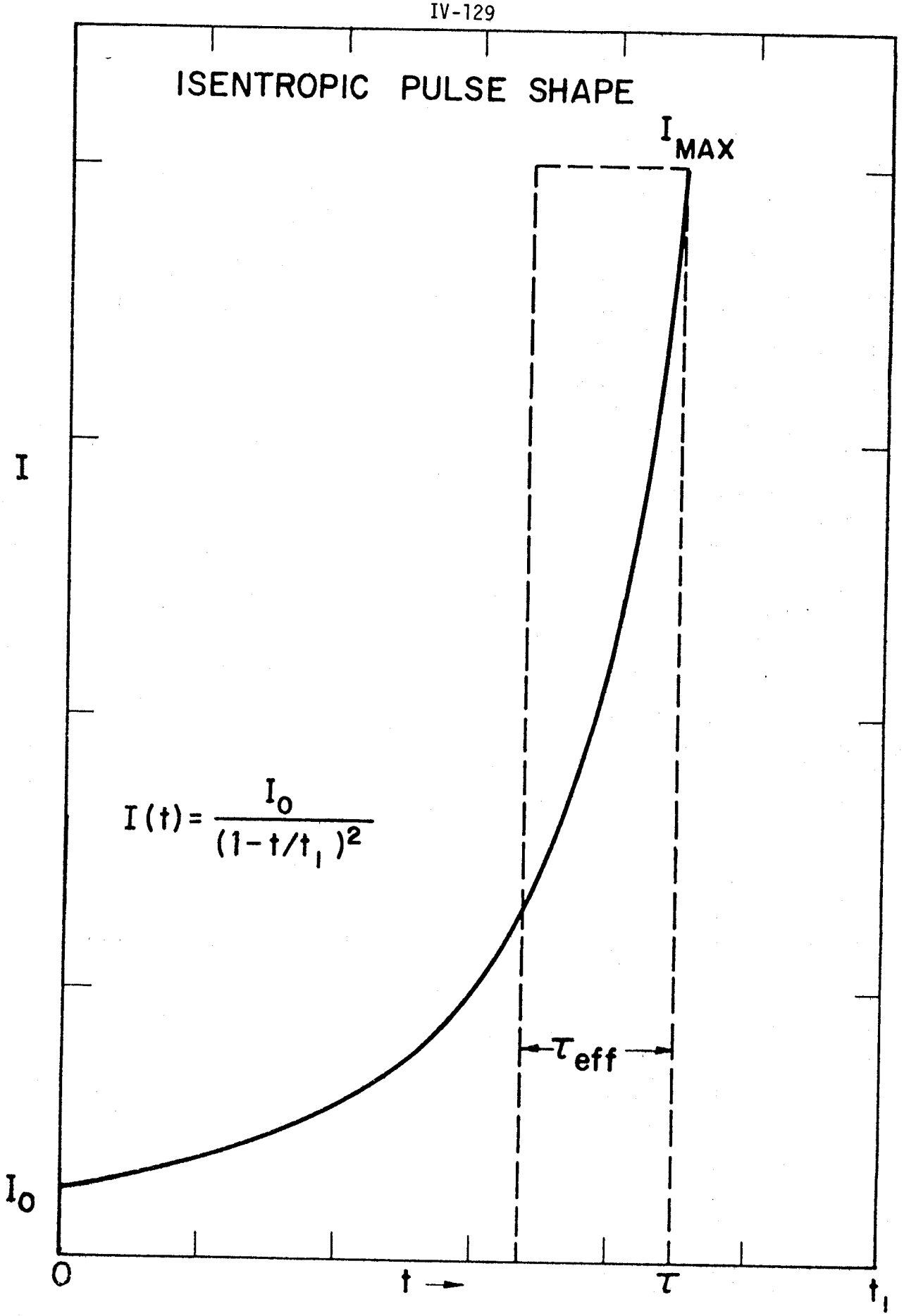

Figure IV.2-11 Ideal isentropic compression pulse. An atypical value of $\varepsilon = 0.25$ has been chosen for clarity.

where

$$\varepsilon = 1 - \eta = \frac{\Phi}{I_{max}\,\tau} << 1 \ , \tag{27}$$

at the end of the pulse. Typical reactor conditions are a total energy $E = 10^6$ J, peak power $P_{max} = 10^{15}$ W and $\tau = 40$ nsec[6], giving $\varepsilon = 0.025$. (Note that $\Phi/I_{max} = E/P_{max}$, independent of the shape of the spatial profile and the aperture area.) Taylor expanding Eq. (26) in powers of ε we find

$$F_{max} \simeq \frac{\pi}{2} I_{max} (\varepsilon\tau)^{1/2} \ . \tag{28}$$

Combining Eqs. (3), (23) and (28), we obtain the damage threshold

$$\Phi^* = \frac{2\Delta T_m}{\pi A} (\varepsilon\tau)^{1/2} \ . \tag{29}$$

This result may be compared with the square pulse threshold by defining an effective pulse width such that $I_{max}\,\tau_{eff} = \Phi$. Then $\tau_{eff} = \varepsilon\tau$ and Eq. (29) may be written

$$\Phi^* = \frac{4}{\pi} \Phi_{sp} \ . \tag{30}$$

Measured in this way, about 27% more energy may be safely handled using the ideal pulse. Due to the complicated pulse shape the physical reason for this increase is not obvious. One can only say that the slowly rising initial portion of the pulse dominates the rapidly rising final portion.

In conclusion, we have found rather modest enhancements of damage thresholds over the square pulse value for two pulse shapes commonly encountered in laser fusion.

References for Section IV.2.D.

1. J.F. Ready, Effects of High-Power Laser Radiation (Academic Press, New York, 1971), p. 67.

2. H.S. Carslaw and J.C. Jaeger, Conduction of Heat in Solids, 2nd Ed. (Oxford Univ. Press, New York, 1959), p. 75.

3. J.F. Ready, J. Appl. Phys. 36, 462 (1965).

4. J. Nuckolls, L. Wood, A. Thiessen and G. Zimmerman, Nature 239, 139 (1972).

5. R.E. Kidder, Nucl. Fusion 14, 797 (1974).

6. R.W. Conn, et al., University of Wisconsin Nuclear Engineering Report UWFDM-220.

V.1 Engineering Design Considerations for a Laser Driven, Direct Enrichment Hybrid Reactor

V.1.A. General Description

A schematic diagram of the SOLASE-H cavity is shown in Fig. V.1-1. The cavity is an upright circular cylinder 6 m in radius and 12 m high. The end caps are spherical segments, 6 m in radius and 1 m high so that the overall height of the cavity along the central axis is 14 m (Fig. V.1-1). Zircaloy-4 is used as structural material throughout the blanket in order to be compatible with the cladding of the PWR fuel rods to be directly enriched in SOLASE-H.

As can be seen from Fig. V.1-1, the SOLASE-H blanket is divided into two regions, viz., the cylindrical region where the fissile fuel is bred and the spherical end caps where most of the tritium is bred. Each region will be discussed separately.

The first wall in the cylindrical blanket region consists of 0.2 cm thick hemispherical scallops, 21 cm wide, running the full length of the cylinder. Each scallop subtends 2^{o} of circumference and makes up one side of a 47.5 cm thick cell of the cylindrical blanket. Each scallop is welded along with the adjacent one to a single strut, 0.3 cm thick which, in turn, is welded to the main back plate as shown in Fig. V.1-2. Each cell is, therefore, bounded by the hemispherical scallop, the two side struts and a back plate. The cell is divided into three regions. The first region contains lead-filled rods which constitute the first zone listed in Table V.1-1 with an effective thickness of 11 cm. The lead zone is followed by a single row of lithium-filled rods with an

THE SOLASE-H LASER FUSION HYBRID

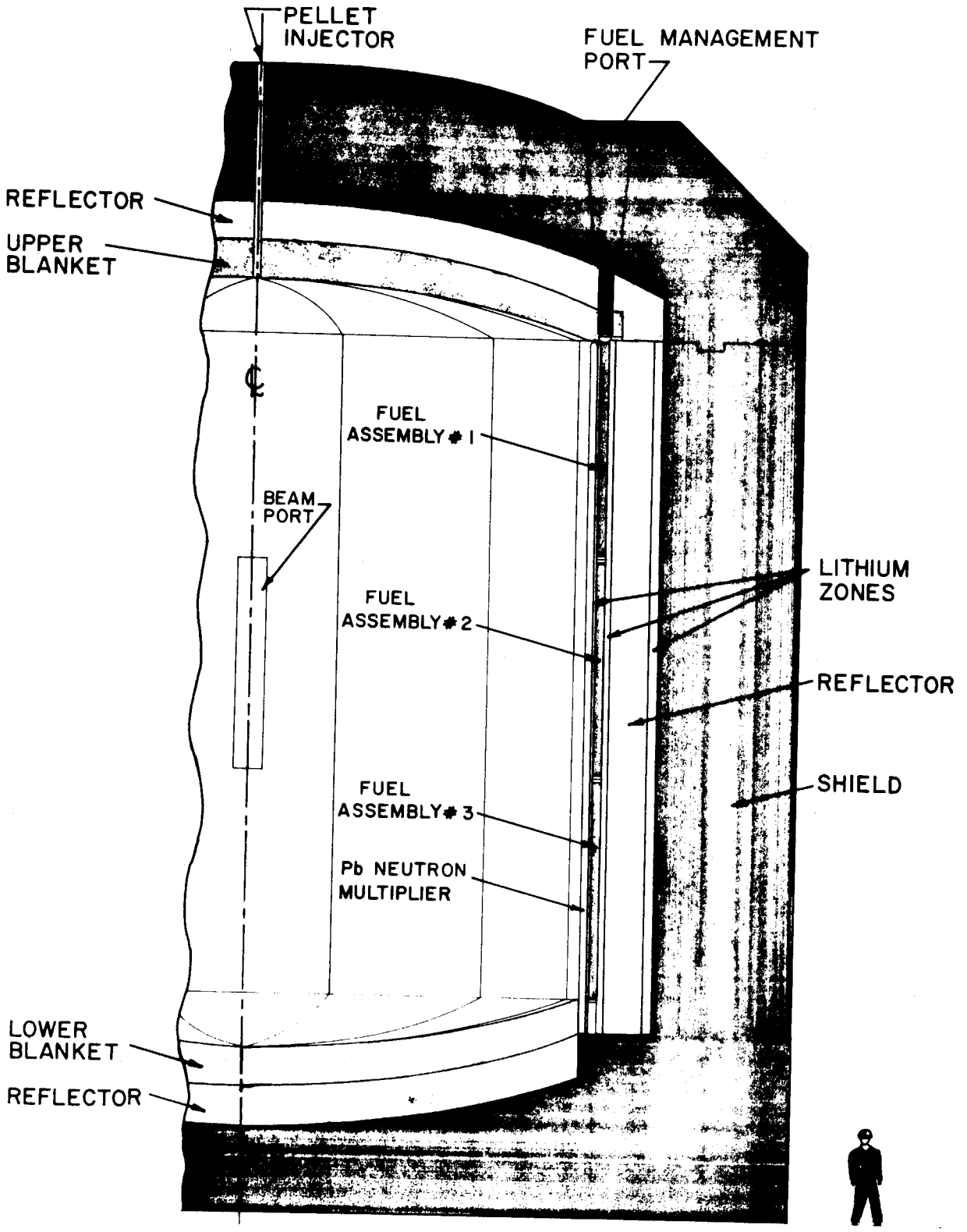

Fig. V.1-1

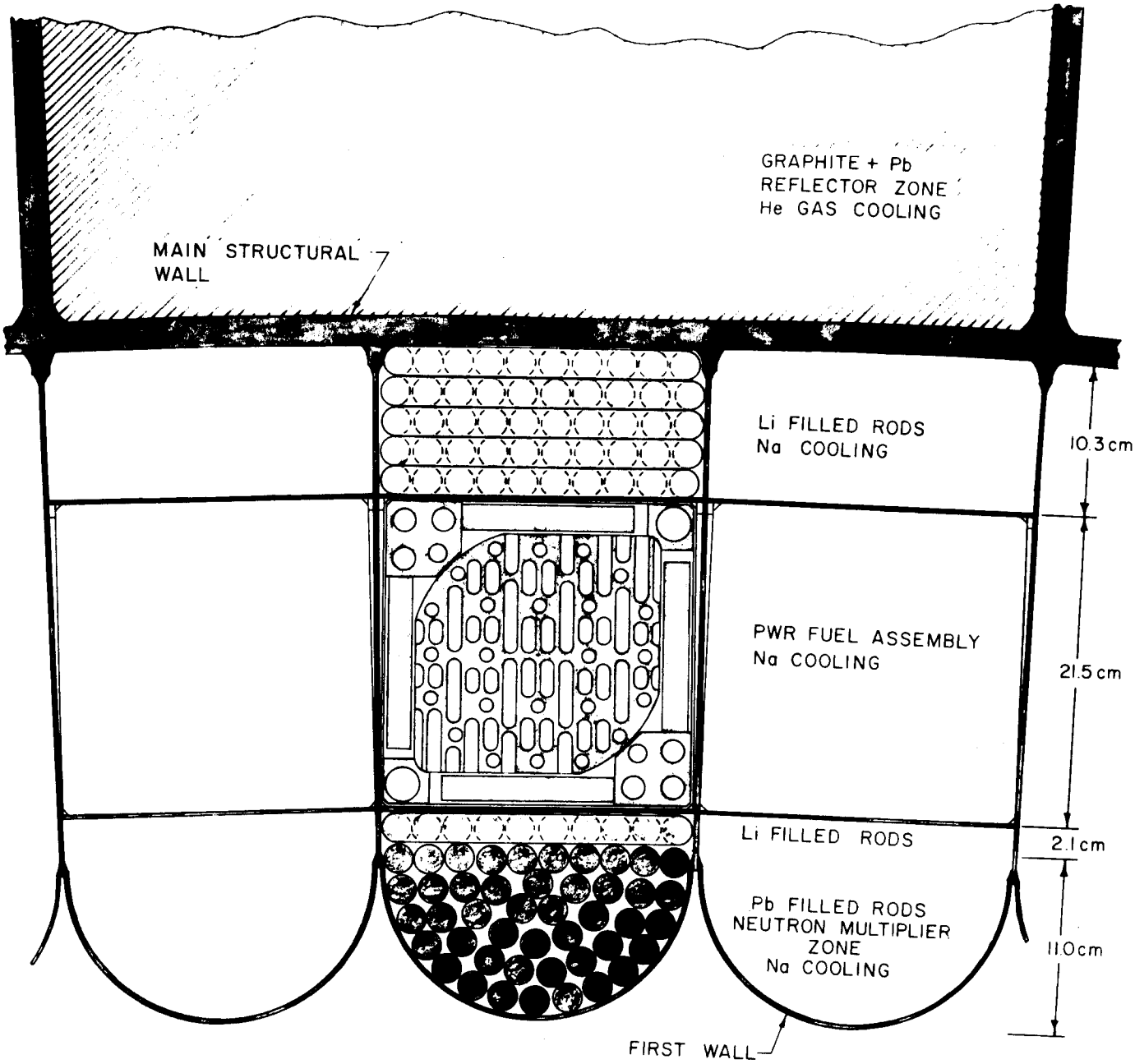

CROSS SECTION OF SOLASE-H BLANKET

Fig. V.1-2

Table V.1-1

Effective Composition of the Different Blanket Zones

Component	Zone	Effective Thickness (cm)	Composition (% Vol.)	
First Wall		0.2	Zr-4	100
	I	11.0	Pb	74
			Zr-4	9
			Na	17
	II	2.1	Li	70
			Zr-4	7
			Na	23
Divider		0.2	Zr-4	100
	III	21.5	Fuel Assembly	
Divider		0.2	Zr-4	100
	IV	10.25	Li	74
			Zr-4	9
			Na	17
First Back Plate		2	Zr-4	100
	V	70	Pb	28
			C	57
			Zr-4	5
			He	10
	VI	13	Li	74
			Zr-4	9
			He	17
Second Back Plate		2	Zr-4	100

effective thickness of 2.1 cm. The second region (zone III in Table V.1-1) is separated from the rest of the cell with tangential dividers 0.2 cm thick which are welded to the radial struts. This region, which is 21.5 x 21.5 cm, contains the fissile fuel assemblies and will henceforth be referred to as the fuel assembly compartment. Three PWR-type fuel rod assemblies stacked on top of each other are placed in each compartment. The last region (zone IV) in the cell contains lithium-filled rods and has an effective thickness of 10.25 cm. Placement of the various lead and lithium zones has been optimized neutronically as described in section II. Liquid sodium flowing vertically in the spaces between the rods in the different zones is used to cool the blanket. The flow in each region is controlled to produce an even temperature rise in the sodium coolant.

The zones behind the first back plate contain reflecting and absorbing materials as shown in Fig. V.1-3. Zone V has lead-filled rods in a graphite matrix and is 70 cm thick while zone VI has lithium filled rods and is 13 cm thick. Both of these zones are cooled with gaseous helium. The first back plate is 2 cm thick and is the barrier between the sodium and the helium cooled regions of the cylindrical blanket. The second back plate is the last boundary of the cylindrical blanket and besides being the barrier for the helium coolant it is also the structural member used to attach the blanket modules to the shield. Table V.1-1 lists the various regions in the blanket, their effective thickness and their composition by volume.

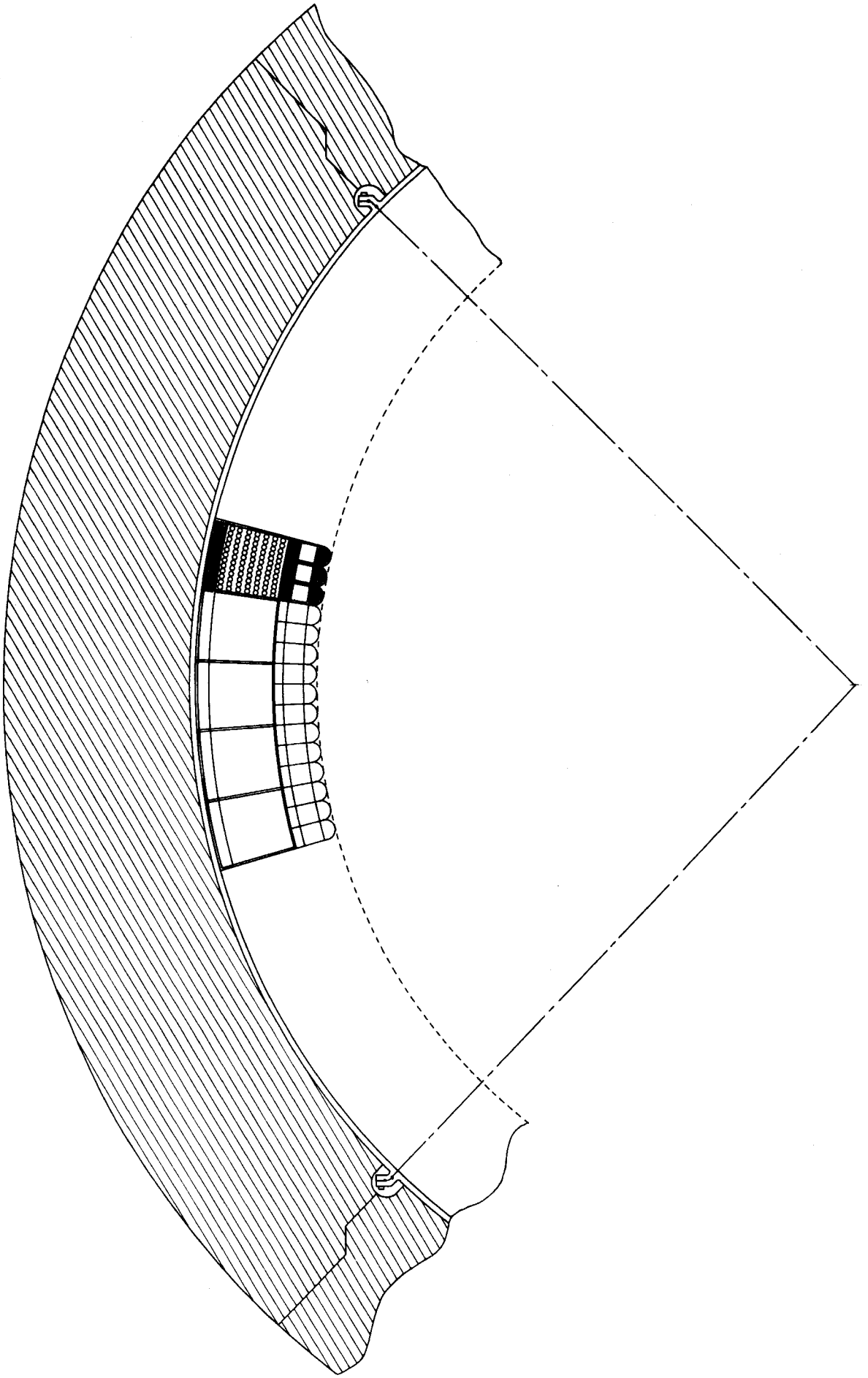

Fig. V.1-3

The cylindrical blanket is divided into 12 modules, 3 modules per shield quadrant. Each module has 15 cells as shown in Fig. V.1-3. Two diametrically opposite modules are equipped with beam ports for two-sided illumination of the pellet. The laser beams are stacked vertically to pass through a rectangular aperture in the blanket module (section IV). The beam apertures at the first wall are 60 cm wide and 4 m high, so that they occupy the space for three cylindrical blanket cells as shown in Fig. V.1-1. The lower sections of these cells are inaccessible from the top and cannot be used for fuel placement; they contain lead and lithium rods instead of fuel assemblies. A single fuel assembly will be placed in the upper compartment of each of these cells. This reduces the total number of fuel assemblies that can be accommodated within the SOLASE-H blanket from 540 to 528.

The top and bottom end caps of the SOLASE-H cavity are primarily devoted to tritium breeding and energy extraction. The lithium contained in these regions is circulated through a steam generator with a small stream diverted for tritium extraction. The top and bottom end caps are similar but not identical. The top blanket is 6.6 m in radius while the bottom is only 6.0 m. In addition, the top blanket has provision for pellet injection in its center and also has a rectangular port which is lined up radially with the fuel assembly compartment in the cylindrical blanket as can be seen in Fig. V.1-1. This port is 25 cm wide and 70 cm in the circumferential direction, spanning three cylindrical-blanket cells. It provides access to the fuel assembly zone for fuel management. Rotating the whole top shield and blanket 360^{o} about the central axis makes it possible to reach all the fuel assemblies within the reactor. This aspect of the design will be discussed in more detail in the fuel

management section.

Figure V.1-4 shows a segment of the upper blanket in which the arrows indicate the direction of lithium flow. The upper blanket is 60 cm deep and is divided into quadrants which are completely independent of each other. The blanket is followed by a helium-cooled reflector zone 75 cm thick. Each blanket quadrant has one supply tube connecting it to a circumferential header. Lithium from the supply header is routed into a labyrinth of rectangular passages bounded by the first wall and another sheet behind it. The entering lithium flows in passages of essentially constant area leading toward the center of the blanket, emerges into the interior of the blanket and then flows radially outward at a much lower velocity toward the return headers on the outer periphery. This design provides excellent heat transfer at the first wall where it is needed most, while maintaining a low pressure drop throughout the blanket. As a result, there is no need to scallop the first wall in the upper and lower blanket sections. The first wall is smooth and is connected to the back sheet with 0.3 cm thick spacers at 2^{o} intervals which define the rectangular passages for lithium flow. The distance between the first wall and the back sheet is tapered to provide a constant flow area and thus maintain an essentially uniform velocity at the first wall. Additional spacers also 0.3 cm thick at 4^{o} intervals connect the back sheet to the back plate of the blanket. The blanket and the reflector quadrants are attached to the upper shield structure which provides the support for them. The upper shield is a monolithic structure with massive radial ribs transferring the load to the cylindrical shield. The spaces between

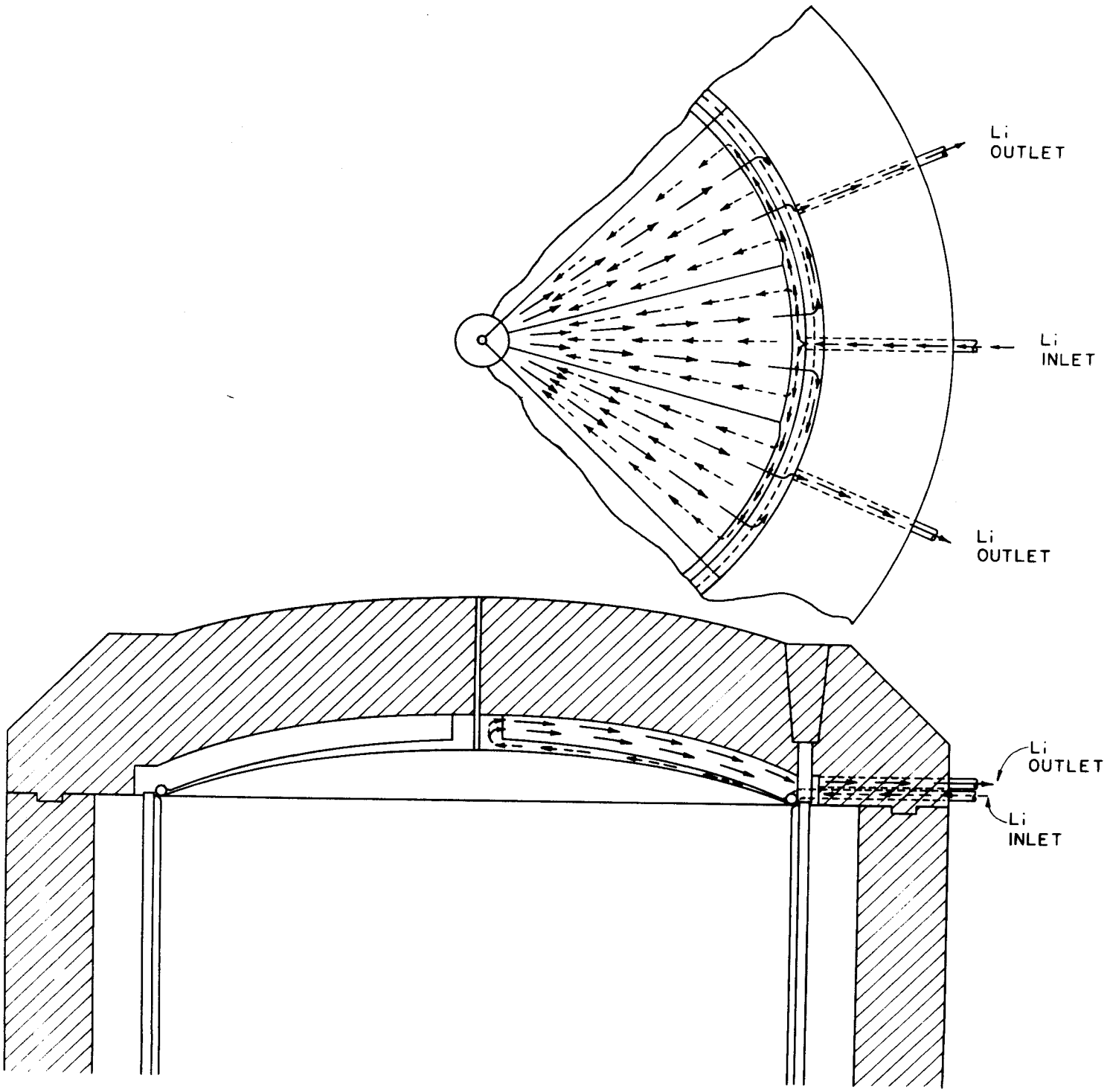

Fig. V.1-4

the radial ribs will have removable interlocking shield segments. Access to the interior of the reactor cavity is provided by removing the entire upper shield structure. In order to do this, the shield segments will have to be removed first to make the structure compatible with the available overhead crane capacity in the reactor building.

The shield under the lower blanket is divided into quadrants which are integral with the cylindrical shield quadrants. The lower blanket segments are attached to the bottom shield the same as at the top. Once the upper shield and blanket have been removed, the cavity can be taken apart in quadrants for maintenance or blanket replacement. This is done by sliding opposite shield quadrants radially outward, and will be discussed in the assembly and maintenance section.

The shield is 2 m thick everywhere except on the bottom where it is 1 m thick measured from the end of the reflector zone to the floor. It is composed of 90% concrete, 10% aluminum structure and has a 10 cm thick lead liner surrounding it on the outside except on the bottom. The total weight is about 8560 tonnes of which 6340 tonnes is concrete, 1520 tonnes is lead and 700 tonnes is high strength aluminum.

Similar to the SOLASE[1] reactor, the vacuum seals between quadrants will be made on the inner side of the shield as shown in Fig. V.1-3. The seal itself is a soft aluminum wire. Holes through the shield provide access to the captive seal bolts. These holes are normally plugged with shield dowels. The seal between the upper shield and the cylindrical shield can be an inflatable elastomer gasket, since the seal has to be made and broken every time the top shield is rotated. This seal is readily accessible from the outside and can be replaced frequently.

V.1.B. Structural Considerations of the Blanket and Shield

Stress analysis of the first wall has been treated in a separate section of this report. In this section we will be concerned with the mechanical support of the various components of the blanket and shield.

Although the structural components of the first wall and blanket are strong enough to support the weight of the lead and lithium filled rods, it was decided not to use them for that purpose. The ideal way to support these heavy components would be to attach them at the top and let them hang freely. However, that would be impossible in this case. The fuel assembly zone must be kept open at the top for fuel management purposes and structure cannot traverse it. The only other option is to support them on the bottom. For this reason the bottom blanket was made only 6 m in radius so that the cylindrical blanket can fit around it. The bottom closure on the cylindrical blanket is a flat plate 1 cm thick which is supported directly on the shield. A perforated stand-off plate also 1 cm thick is attached to the closure separated 8 cm away from it. This perforated stand-off plate is the surface on which the various elements of the blanket are supported. The space between the stand-off plate and the closure is the coolant plenum and the perforations in the plate regulate the amount of coolant entering the various zones in the blanket. The reflector zones also have a closure and a stand-off plate for supporting the elements in them. In this case, the space between them is the plenum for the helium gas used to cool the reflector components. The loads from the reflector zone are also transferred to the shield through the closure plate.

The lead rods in zone I are 12 m long and each weigh on the order of 43 kg. By themselves the rods would be very difficult to handle. However, if the rods are bundled into the correct configuration before they are filled with lead then the assembly will have the structural integrity to be handled as a unit. It will, therefore, be assumed that the lead rods in zone I will be first bundled, then filled, welded shut and then placed into the cell. Once in place, they will not be handled again until radiation damage necessitates their replacement. A complete unit of lead rods in each cell weighs 2 tonnes and can be easily handled with an overhead crane.

While the lead-filled rods are permanently sealed, the lithium-filled rods are not. Tritium bred in the lithium rods will have to be removed by slowly circulating the lithium through a tritium extraction system. Manifolding for all the lithium rods will be done from below. Incoming lithium is routed up through one-half of the rods in each cell, makes a U bend at the top and descends in the other half of the rods. It is, therefore, necessary that there be an even number of lithium rods in each cell. Each module will have a single supply and return line feeding 15 cells. The velocity in the rods will be determined from tritium inventory considerations but will be very low and thus the pressure drop will be negligible. Since the rods are externally cooled, the internal velocity is not critical from heat transfer considerations. During blanket changeout, the lithium in the rods can be drained out to simplify the handling process. The lead and lithium-filled rods in the reflector zones will be treated in much the same way. Table V.1-2 gives the specification of the different rods in the blanket.

Table V.1-2

Specifications of the Different Tubes in SOLASE-H

Zone	I	II	IV	V	VI
Filler	Pb	Li	Li	Pb	Li
No. of Tubes in Reactor	8100	1800	9000	7680	14280
No. of Tubes in Cell	45	10	50	N/A	N/A
No. of Tubes in Module	675	150	750	640	1190
Diameter of Tubes (cm)	2.1	2.1	2.15	4.0	2.1
Wall Thickness of Tube (cm)	0.05	0.05	0.05	0.15	0.05
Tube Length (cm)	1200	1200	1200	1200	1200
Surface Area of Tube (cm^2)	7917	7917	8105	15084	7917
Mass of Filler/Tube (kg)	42.7	1.72	1.802	146.3	1.72
Mass of Structure/Tube (kg)	2.50	2.50	2.57	14.2	2.50

As mentioned earlier, three fuel assemblies are stacked vertically in each cell. Because of the delicate nature of the fuel assemblies and the close tolerances that must be maintained within them, it was decided not to allow them to bear on each other but instead to have them supported individually. In this design the fuel assemblies will be supported on the walls of the compartment provided for them within the blanket cells. The bottom assembly will rest on the stand-off plate in the cell which also supports the walls of the compartment. As the first fuel assembly is inserted into its compartment it activates mechanical latches on the compartment walls which are the stops for the second fuel assembly. Similarly, the second assembly activates latches which are the stops for the third assembly. In this way, the second and third assemblies are supported on the walls and neither of the three is in contact with the others. Removing a fuel assembly resets the latches so that they would not interfere with the removal of subsequent assemblies. The compressive stress in the walls of the compartment due to the weight of the two assemblies is only 1.85×10^7 N/m^2 (< 3000 psi). Table V.1-3 gives the material specifications in the blanket.

V.1.C. Fuel Management

Periodic rearranging of the fuel assemblies will be needed to insure a uniform enrichment of the fissile fuel in them. In order to allow periodic fuel management, the top shield and blanket were designed with a port which is lined up radially with the fuel assembly compartment subtending three cells in the cylindrical blanket. During operation this port is covered with a special shield plug.

Table V.1-3

Material Specifications in the SOLASE-H Blanket

A-Cylinder Blanket (all masses in tonnes)		
Zircaloy-4 Blanket Structure	248	
Fuel Assemblies	270	
Zircaloy-4 in Rods	193	
Lead	1469	
Graphite	407	
Lithium	44	
Sodium	34	
Total Mass of Cylindrical Blanket	2665	2665
B-Top and Bottom Blanket		
Zircaloy-4 Blanket Structure	85	
Graphite	332	
Lithium	77	
Total Mass of Top & Bottom Blanket	494	494
Total Mass of SOLASE-H Blanket		3159 tonnes

In preparation for fuel management, the shield plug is removed and a special carriage is installed covering the port and extending high enough above the reactor to accommodate the extraction of a 4 m high fuel assembly. This carriage will have a storage compartment on the side adequate for three fuel assemblies and will have the capability of providing an inert atmosphere above the cell zone. This will obviate the need for draining the sodium out of the blanket during fuel assembly rotation. Integral with the carriage will be remotely operated tools for machining welds, making welds, handling the upper cell closures and, of course, extracting and inserting the fuel assemblies.

The sequence of operations needed to rotate the fuel assemblies in a module is described below:

1) The top shield is rotated until it reaches the module in question and locates on fiducial marks on the blanket.
2) A mechanism is actuated which effects a seal between the module and the carriage. The space in the carriage is evacuated and backfilled with an inert gas.
3) A machining tool (grinding, milling or plasma) is rotated into place on a track. The tool automatically rides the track and machines off the seal between the top flange and the closure. Chips are vacuum cleaned simultaneously.
4) A manipulator lifts the top closure and sets it in a designated area. This operation exposes three fuel assemblies to access from the carriage.
5) A crane in the carriage manipulates the fuel assemblies between the different compartments using the storage areas as temporary holding places.

6) The manipulator replaces the closure on the module.

7) A welding head (MIG, TIG) which is part of the machining tool complex is located and adjusted. The welding head rides the track making the seal weld.

8) The carriage space is evacuated and a set procedure followed to leak check the weld.

9) The carriage is backfilled with an inert gas. The seal is deactivated and the top shield rotates to the next three cells.

At the time when new fuel assemblies are inserted into the hybrid, or enriched assemblies are taken out for installation into a PWR, an additional transport container will be attached to the carriage. As the transport container is filled, it will be taken to a special area where the assemblies will be cleaned and inspected prior to shipment to the PWR site.

V.1.D. Assembly and Maintenance

Radiation damage to the first wall and blanket components will ultimately necessitate their replacement. The cavity in SOLASE-H is designed to be taken apart in order to provide access for routine and unexpected repair and maintenance.

In preparation for dismantling the cavity, obvious functions such as the draining of the coolants, the lithium from the breeding rods and disconnecting coolant and other lines has to be performed. Next, the pellet injector is removed from the upper shield and preparation is made to remove the upper blanket and shield assembly.

To alleviate the problem of lifting the entire upper assembly weighing on the order of 1300 tonnes, the upper shield was designed as a massive structure of aluminum radial ribs which supports removable interlocking segments of shielding material. Eight shield segments, each weighing

143 tonnes will be supported between the radial ribs. They will include the lead, concrete and the graphite zones. Once these shield segments are removed, the remaining structure composed of the Zr-4 blanket and the aluminum in the shield weighs on the order of 150 tonnes. This structure can now be lifted in its entirety and removed to a designated area for blanket replacement.

The next step is to separate the cylindrical shield quadrants. The bolted connections on the inner side of the shield have to be undone with tools penetrating the shield through access holes provided for that purpose. These holes are normally plugged with shielding material. Undoing this bolted connection also breaks the seal between quadrants.

The two quadrants which contain the laser beam ports will be designated as stationary. They will not normally be moved during blanket replacement. The remaining two quadrants will be moved radially out from the reactor. Each quadrant has three blanket modules which, when drained of sodium and lithium and with the fuel assemblies removed, weigh ~ 190 tonnes. The weight of a quadrant of cylindrical and lower blanket and shield is 2545 tonnes. Similar to SOLASE,[1] we envisage using gas bearings for moving the quadrants and the total excursion would be ~ 10 m. This would allow ample space for maneuvering the equipment needed for working on the blanket modules.

It will be assumed that a 250 tonne overhead crane will be available in the reactor building. Modules, still containing all the materials

except the fuel assemblies, the lithium and the sodium coolant, each weighing ~ 190 tonnes can now be unfastened from the shield and removed to the appropriate area. Salvageable materials will be removed for recycling, and the remainder will be compacted for storage as radwaste.

New blanket modules with fresh materials will then be brought in and attached to the shield quadrants, after which reassembly of the reactor cavity can commence. The quadrants are brought together and fastened with new bolts. The upper shield structure with new blanket segments is replaced on the cavity and the shield segments are reassembled on it. Finally, the pellet injector is returned to its location on the top shield and coolant and other lines are reconnected. The cavity is now ready for charging with the fuel assemblies and will follow the same prescribed procedure for fuel management.

Maintenance of a hybrid blanket of this nature is not an easy chore and like any other reactor system will require numerous specially designed remotely operated tools. Although the system has been simplified as much as possible under the circumstances, it still remains a rather formidable task.

Reference for Section V.1

(1) R.W. Conn, et al., "SOLASE, A Laser Fusion Reactor Study", UWFDM-220, University of Wisconsin, Nuclear Engr. Dept. (Dec. 1977).

V.2. The Fuel Cycle and Tritium Processing

V.2.A. Introduction

In this section we describe the tritium pathways for SOLASE-H. The areas investigated include: (1) reactor fueling, (2) tritium breeding and blanket design, (3) tritium extraction from the breeding material and reactor exhaust, and (4) tritium control in the sodium coolant.

The major fusion parameters characterizing SOLASE-H are given in Section III.1. The pellet yield is 310 MJ at a gain of 194, a repetition rate of 4 sec^{-1}, and a total energy per fusion event of 17.6 MeV, so that the total thermal fusion power for the reactor is 1241 MWt. The daily D-T fuel requirements for SOLASE-H are given in Table V.2-1. These values are based on a pellet core fractional burnup of 30% (Section III.1). The repetition rate is increased by 10% (4.4 sec^{-1}) to allow for misfirings so that the effective fractional burnup is 27%. A plant factor of 70% is assumed and a five-day emergency fuel supply is maintained to allow for continued plant operation in case of tritium system failure.

V.2.B. Pellet Composition

Design of laser fusion pellets is in its infancy and a wide range of pellet materials and output characteristics is possible. In general though, the pellets will be cryogenic and have in addition to the D-T fuel, a container material, a low-Z polymer ablator, and a high-Z material acting as a hot electron shield and fuel tamper. Since pellet manufacturing

Table V.2-1

Daily D-T Fuel Requirements for SOLASE-H

	D	T
Daily Consumption (moles/day)	64	64
Daily Consumption (kg/day)	0.13	0.19
Recycled Amount (kg/day)	0.34	0.51
Fabricated Amount (kg/day)	0.47	0.70

and delivery problems have been discussed elsewhere,[1] we shall deal with the effect of the pellet composition on the reactor exhaust. In order to examine this area, a pellet with deuterated polyvinyl alcohol (PVA) as the fuel container material is considered in detail. Although less data exist on plastic than glass shells, experiments have been conducted on plastic shells which demonstrate shorter D-T fill times than for glass shells. Shorter fill times in turn lead to a reduced plant tritium inventory. In addition, fuel containers composed of deuterated polyvinyl alcohol result in a less complicated reactor exhaust cleanup system compared to glass containers as glass results in the production of a large quantity of non-volatile species.

Xenon is the choice as the high-Z material since it is relatively inert and remains gaseous to -107.1°C so that it can be easily pumped out of the reactor chamber. A frozen layer of xenon on the inside surface of the plastic container protects the shell from the beta radiation produced by tritium decay during pellet storage. If a material of higher Z than xenon is required for better pellet performance, mercury may be used since it is easy to keep gaseous and pump; in addition, a well-developed mercury technology is in existence. Obviously, the least desirable choice would be a refractory high-Z material. Although the quantity per pellet for refractory material may be low, the 4×10^5 pellets fired into the reactor chamber per day will result in a large quantity of material either accumulating in the chamber or requiring a separation process to avoid damage to the pumps.

A polymer such as deuterated polyethylene is used as the low-Z ablator. Also, xenon is frozen on the outside surface of the pellet in order to ensure cryogenic conditions in the pellet during its flight to the cavity center. All the xenon evaporates prior to laser-pellet interaction. Therefore, starting from the inside, the pellet layers are as follows:

(1) 3.1 mg DT

(2) Xenon

(3) 3 mg deuterated polyvinyl alcohol

(4) Xenon

(5) 6 mg deuterated polyethylene

(6) Xenon

V.2.C. Xenon Cleanup Schemes

The reactor cavity is filled with xenon gas at 1 torr (300 K), sufficient to protect the front wall from the charged particles and X-rays produced (Section III.2). The pumping rate is 5×10^5 ℓ/sec at 1 torr and 300 K. Table V.2-2 gives the amount of deuterium, tritium, oxygen, carbon, neon, helium and xenon that are present in the exhaust. Possible compounds in the reactor exhaust include water, carbon oxides, hydrocarbons and any compounds such as metal oxides, carbides and hydrides formed by chemical sputtering of the zircaloy first wall. Examination of Table V.2-2 reveals that the reactor exhaust is predominantly xenon (99.9%), so that the separation scheme has to be designed to separate small quantities of gaseous species from a large volume of xenon.

Table V.2-2

Composition of Pellet Debris and Chamber Exhaust

Element	Pellet Debris (mg/pellet)	Chamber Exhaust (moles/day)
D	2.90	552
T	1.35	172
O	1.00	24
C	6.00	190
Xe	?	2.3×10^6*
He	---	64

*Xenon is present in the chamber to protect the wall from the micro-explosion.

Figure V.2-1 depicts the xenon recycle system. The exhaust from the reactor is scrubbed free of high temperature condensables and particulates, such as carbon and any metals, carbides and metal oxides and hydrides, formed by sputtering. The gas is then sent to a catalytic oxidizer where the hydrogen isotopes, hydrocarbons and carbon monoxide are oxidized to water and carbon dioxide.[2,3] At this point the exhaust from the plastic pellet contains 0.016 mole percent of water and 0.001 mole percent carbon dioxide, if the simplifying assumption is made that the hydrogen exits the reactor unoxidized and the oxygen exits as carbon monoxide. This is equivalent to 7 kg/day of water. Molecular sieves at 25°C absorb 32 kg of water per cubic meter of sieves with the effluent gas having a water partial pressure of 5×10^{-3} torr (125 ppm). Thus, two beds of $\sim 0.3\ m^3$ each remove about 97% of the water. More efficient scrubbing can be achieved by refrigerating the beds. The beds can be operated in tandem on a twenty-four hour basis so that one bed is being regenerated while the gas stream is switched to the other. The beds are regenerated by heating the molecular sieves to 350°C. The total tritium inventory on these beds is ~ 0.51 kg. After removal of the water, the xenon is passed through a "soda lime" bed to remove carbon dioxide.[2,3] Approximately 24 moles of carbon dioxide are removed per day. This requires about 3.5 kg of soda lime/day which ends up as waste.

At this stage the xenon contains only helium. A portion of the xenon is fed to the pellet fabricating system while the remainder is returned

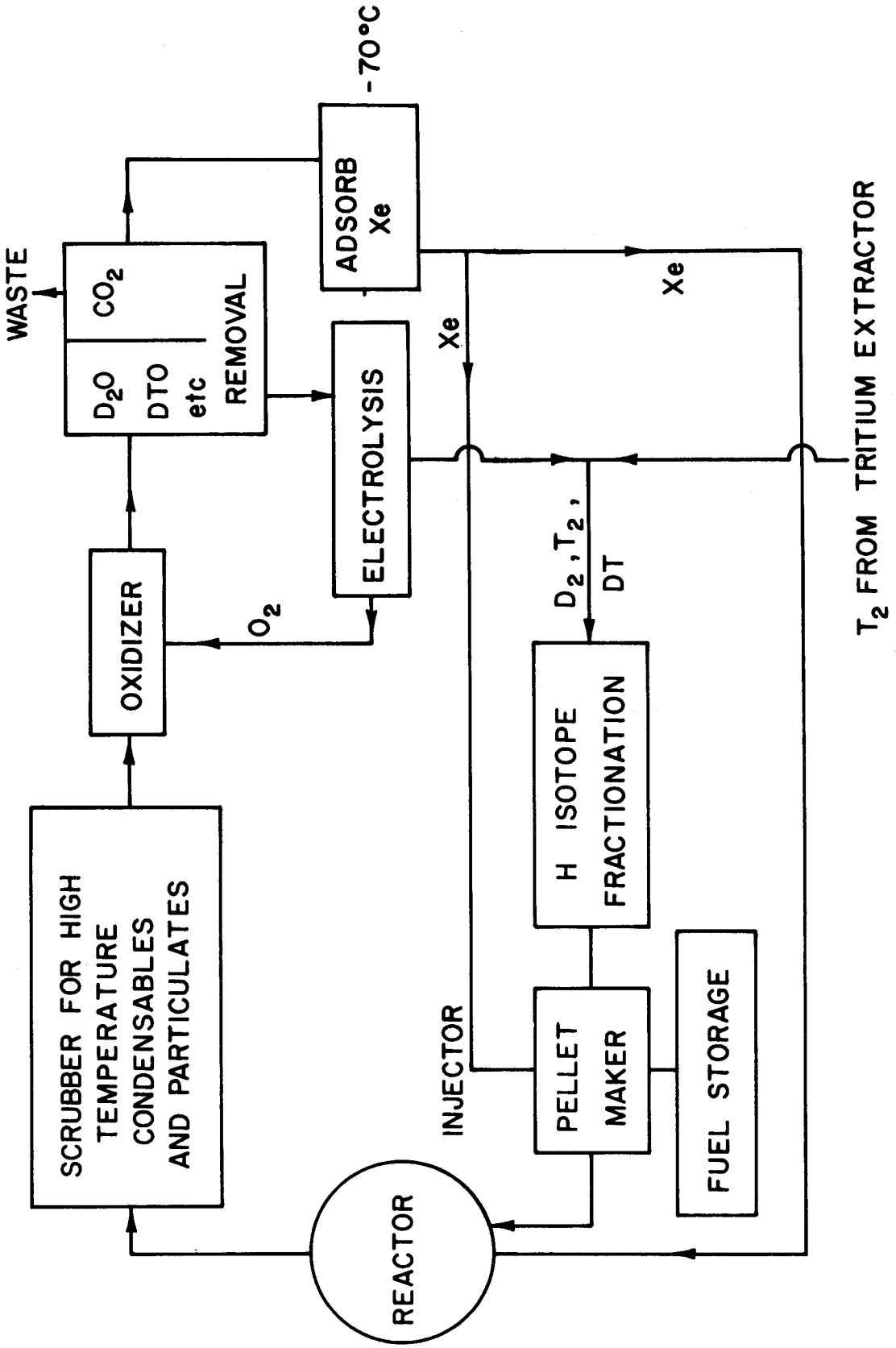

Fig. V.2-1

Scheme for Separation of Exhaust Gas Components

to the reactor chamber as sweep gas. If the helium concentration is at an unacceptable level for either of these purposes, it is necessary to purify the xenon. This can be accomplished by selective absorption of the xenon on activated carbon at -65 to -75°C.[3] To the extent that it is practical, closed loops are utilized in all systems involving the reactor exhaust. This is done to minimize the loss of tritium to the environment.

As an alternative to this xenon cleanup scheme it may be possible to first remove the D_2, DT and T_2 from the gaseous mixture by passing the gas over a bed of nickel plated yttrium at 540-760°C,[4] thus extracting 99.93% of the hydrogen isotopes. The nickel coating permits rapid diffusion of the hydrogen isotopes while preventing diffusion of oxygen or carbonaceous gas. Deuterium and tritium may be recovered from the yttrium by vacuum annealing. After the hydrogen isotopes are extracted from the xenon, the remaining gases are catalytically oxidized and treated as previously specified. In this scheme the elemental hydrogen isotopes would not be oxidized but rather sent directly to the isotope fractionating system for ultimate reinsertion into the reactor. Which route to adopt depends on whether the nickel coated yttrium idea is practical and on the quantities of elemental deuterium and tritium present in the reactor exhaust to be handled.

V.2.D. Hydrogen Isotope Recovery

The water recovered from the molecular sieves as a mixture of isotope compositions is sent to an electrolyzer where the elemental hydrogen species are produced. Electrolytic hydrogen generators capable of producing 300 ml/min (STP) of 99.9999% pure hydrogen are commercially available.(5) The electrical power requirement for such a unit is 220 watts. Since our total demand is 19 times larger (36 moles DTO, D_2O, T_2O/day), the equipment has to be scaled up accordingly and the power required should be about 4.2 kilowatts. The steady state tritium inventory in the electrolysis equipment is 0.02 kg.

The deuterium and tritium produced by the electrolyzer are sent to a hydrogen liquification and fractionation system along with the 0.20 kg/day of tritium bred in the blanket and recovered as T_2. The bred tritium is added at this point to dilute the deuterium and allow the fractionation process to handle more nearly equal moles of the two hydrogen isotopes. The combined liquid phase contains deuterium and tritium in a D:T atom ratio of 7:3. The fractionating columns will have to be designed to recover the deuterium and tritium as a one to one D-T mole ratio mixture. Fractionation columns described(6) for the UWTETR require a power expenditure of roughly 30 kW and are capable of producing 95+% pure streams of deuterium and tritium. They accommodate a hydrogen isotope mixture (78% tritium) that has a flow rate of 27 mmoles/sec and contains a steady-state tritium inventory of 0.19 kg. The corresponding parameters in the hybrid are a hydrogen isotope mixture of 30% tritium and a molecular flow rate of 4.6 mmoles/sec. Therefore, the tritium inventory in the SOLASE-H fractionating columns is 0.19 kg x (30%/78%) x $\left(\frac{4.6 \text{ mmoles/sec}}{27 \text{ mmoles/sec}}\right)$, or 0.012 kg. This is only a rough estimate

since many of the distillation system parameters can be expected to change due to the altered hydrogen isotope composition. Tritium losses to the environment as contaminated water are confined to less than 0.1 curie/day.

V.2.E. Fuel Supply Logistics

The fuel cycle requires storage to allow continued reactor operation in the event of a breakdown in the pellet fabricating or tritium extraction systems. The pellet inventory is dictated by the time required to fill a batch of shells with the D-T fuel mixture which depends on the permeability of the fuel container material. For plastics the fill time is no more than one day with the filling process occurring in a batch operation.[1] To ensure continuous operation of the reactor, at least one batch must be kept on hand to allow for an auxiliary pellet maker to be brought on line in the event the main pellet maker goes down. A 1-day pellet inventory corresponds to 0.71 kg of T. The pellet maker itself contains a one-batch inventory; in addition, the D-T atmosphere in the pellet maker contains about 0.25 kg of T. This value is based on a fill pressure of 150 atm (130^{o}C) with ~ 3 mm radius shells in a close-packed system (theoretical packing efficiency = 74%; undoubtedly the volume required for the pellet maker will be larger than the 0.06 m^3 based on the above assumptions). It is undesirable to fire the entire reserve storage of pellets while a batch is being filled since this entails firing the last storage pellet simultaneous to a new batch being ready. Therefore, the minimum tritium inventory in the pellet storage, manufacturing and delivery system is about 2.4 kg. In addition, if the tritium recovery system experiences a breakdown, there should be tritium on reserve, probably as uranium tritide, to avoid an interruption in the pellet fabrication

process. If it is assumed that the tritium recovery system can be repaired within 5 days, then 3.5 kg T is required for this purpose. Therefore, the total tritium inventory associated with storage, pellet manufacturing and delivery is about 5.9 kg. This constitutes a major fraction of the total tritium inventory in the plant (Table V.2-3).

Some pellets will probably fail during storage. To reduce the failure rate to a minimum cryogenic storage at liquid helium temperatures is necessary to reduce the hoop stress in the shells. The power required to maintain pellets with 1 kg of T at 5 K is approximately 0.24 MW.[1]

V.2.F. Tritium Breeding and Extraction

V.2.F-1. The Lithium Blanket

Liquid lithium is the breeding material in SOLASE-H. The cylindrical blanket will contain 3 zones of natural lithium in zircaloy pins, the first 2 are sodium-cooled at a temperature of 350°C while the outermost is helium-cooled at a temperature of ~ 200°C. The axial portions of the reactor (top and bottom caps) are filled with lithium at 350°C and it is here that ~ 65% of the tritium breeding occurs. The lithium and sodium inventories are given in Table V.2-4. Further blanket details can be found in Section V.1.

V.2.F-2. Extraction of Bred Tritium

The breeding process results in the loss of one lithium atom for each tritium atom bred.

Table V.2-3

Total Tritium Inventory
(Steady State Quantities)

Location	Quantity (kg)
Reactor, Scrubber, Oxidizer, CO_2 Absorber	< 0.01
H-isotope Fractionator	0.01
Electrolysis Equipment	0.02
Molecular Sieves	0.51
Lithium	0.22
Pellet Maker and Storage	5.9
Fuel Pins From Ternary Fissions	< 0.01
Retention in Zircaloy Structure*	1.22*
TOTAL	7.9

*See Section V.2.G

Table V.2-4

Liquid Metal Inventory in SOLASE-H

Item	Inventory (metric tons) Lithium	Sodium
Cylindrical Blanket		
(Na-cooled zones)	19	34
(He-cooled zone)	25	-
(Steam generator and piping)	-	68
Caps		
(T breeding region)	77	-
(IHX and steam generator)	77	34
Tritium Extractor and Piping	22	24
Total	220	160

Approximately 0.21 kg of tritium is bred each day in the SOLASE-H blanket. (Daily consumption = 0.19 kg T/day, and breeding ratio = 1.08.) The bred tritium is present in the lithium as LiT. Small scale experiments[7] have shown that LiT is preferentially extracted from liquid lithium by a molten salt of composition LiF-LiCl-LiBr(22-31-47 mol%) (melting point of 445°C). When this salt is contacted with an equal volume of liquid lithium containing tritium at 500°C, it is estimated[8] from experimental data[7] that the ratio of the tritium in the salt to the tritium in the lithium is ~ 2. The tritium extraction process operates at ~ 500°C in SOLASE-H, which is sufficient to maintain the salt in a molten state.

The tritium inventory in a lithium zone is allowed to grow to 1 wppm. This level is attained on the average in less than a day. Once a zone has reached a 1 ppm tritium inventory, a small stream of lithium is continuously circulated through the extraction system for tritium removal purposes. During steady-state operation of the extraction system, all the streams from the various zones are merged and brought to ~ 500°C by a regenerative heat exchanger before entering the extractor. Since the breeding rates and volumes of the separate zones are not equal, the flow rate of lithium to the extractor from each zone is adjusted so that a 1 ppm tritium concentration is maintained throughout the lithium zones.

The quantity of the blanket processed per second, X, is given by:[7]

$$X = \left(\frac{R_b}{I_{ss}} \cdot \frac{\varepsilon D_v \eta + 1}{\varepsilon D_v \eta}\right) I_{Li} \qquad (1)$$

where R_b (tritium breeding rate) = 2.4×10^{-6} kg/sec

ε (efficiency of tritium recovery from the salt) = 0.90

D_v (volumetric distribution coefficient of tritium between the lithium and the salt) = 2

η = efficiency factor which accounts for nonequilibrium tritium distribution during contacting and assumed to be unity

I_{ss} (steady-state tritium inventory) = 0.22 kg (for 1 ppm T inventory)

I_{Li} (lithium inventory in SOLASE-H) = 220 x 10^3 kg.

Therefore, 3.7 kg/sec (7.4 ℓ/sec) of lithium is processed to remove the 0.21 kg/day of tritium bred in the blanket. The lithium is fed into a high-capacity annular centrifugal contactor unit where it is contacted with an equal volume of the molten-salt eutectic. The lithium exits the contactor with a tritium concentration of only 0.37 ppm and is returned to the blanket. Further details on the pumping of the lithium are given in Section V.1.

The centrifugal extractor units are based on a single-stage network of units connected in parallel. Each unit is 25 cm in diameter and 45 cm high and processes ~ 23,000 liters of fluid (lithium plus salt) per hour.[7] Therefore, three of these units are needed in SOLASE-H. [(7.4 ℓ Li/sec + 7.4 ℓ salt/sec) x 3600 sec/hr ÷ 23,000 ℓ/hr .] The lithium residence time in these units is ~ 3 min.

The molten salt is then processed electrochemically to recover the tritium.[8] Experiments on molten LiF-LiCℓ-LiBr (22-31-47 mol%) show that the oxidation of lithium hydride readily occurs at an emf of ~ 0.9 volts, a voltage which is below that of the decomposition potential of the salt eutectic (> 2 volts). Electrolysis is carried out for 30 minutes resulting in 90% of the tritium being evolved as T_2 which is recovered from the melt by sweeping the porous stainless steel hydrogen electrode with a circulating stream of argon and subsequently trapping the tritium from the argon with a getter. A number of tanks having a total volume of roughly 13 m^3 are required for electrolysis purposes. The tritium is then desorbed from the getter and merged with the deuterium and tritium recycled from the exhaust gas (Section V.2.D).

A schematic diagram of the tritium extraction scheme is shown in Figure V.2-2.

V.2.G. Tritium Control System

The total tritium inventory in SOLASE-H is 7.9 kg (Table V.2-3). A complete analysis of the tritium containment and emergency recovery system is not attempted in this report. It is expected that in general tritium control is achieved by a three stage system.[1,6] Primary containment consists of the walls of the components which are in direct contact with tritium, secondary containment is provided by local enclosures, such as glove boxes, surrounding major tritium handling equipment, and tertiary containment is considered to be the exterior building walls. Tritium scrubbing equipment must have the capability of processing ~ 20% of the hybrid building volume per day to reduce the tritium present and limit losses out the stack to < 1 Ci/day.

The tritium escape route which will be analyzed in detail and which appears to be the most difficult to control is permeation to the sodium coolant and from there through the walls of the steam generator. Once tritium diffuses into the steam system, it is isotopically diluted to such an extent that separation is difficult with current techniques, and it must be considered lost to the environment. To understand the magnitude of the losses expected, the tritium permeation characteristics of zircaloy must be examined.

The only studies of hydrogen permeation through zirconium are those by Bernstein and Cubicciotti[9] and Albrecht and Goode.[10] Albrecht and Goode conducted their measurements on beta zirconium (9 to 33 atom % hydrogen) and Bernstein and Cubicciotti studied ductile zirconium at hydrogen pressures from 1 to 45 cm Hg and temperatures from 375 to 900°C. A wide variation

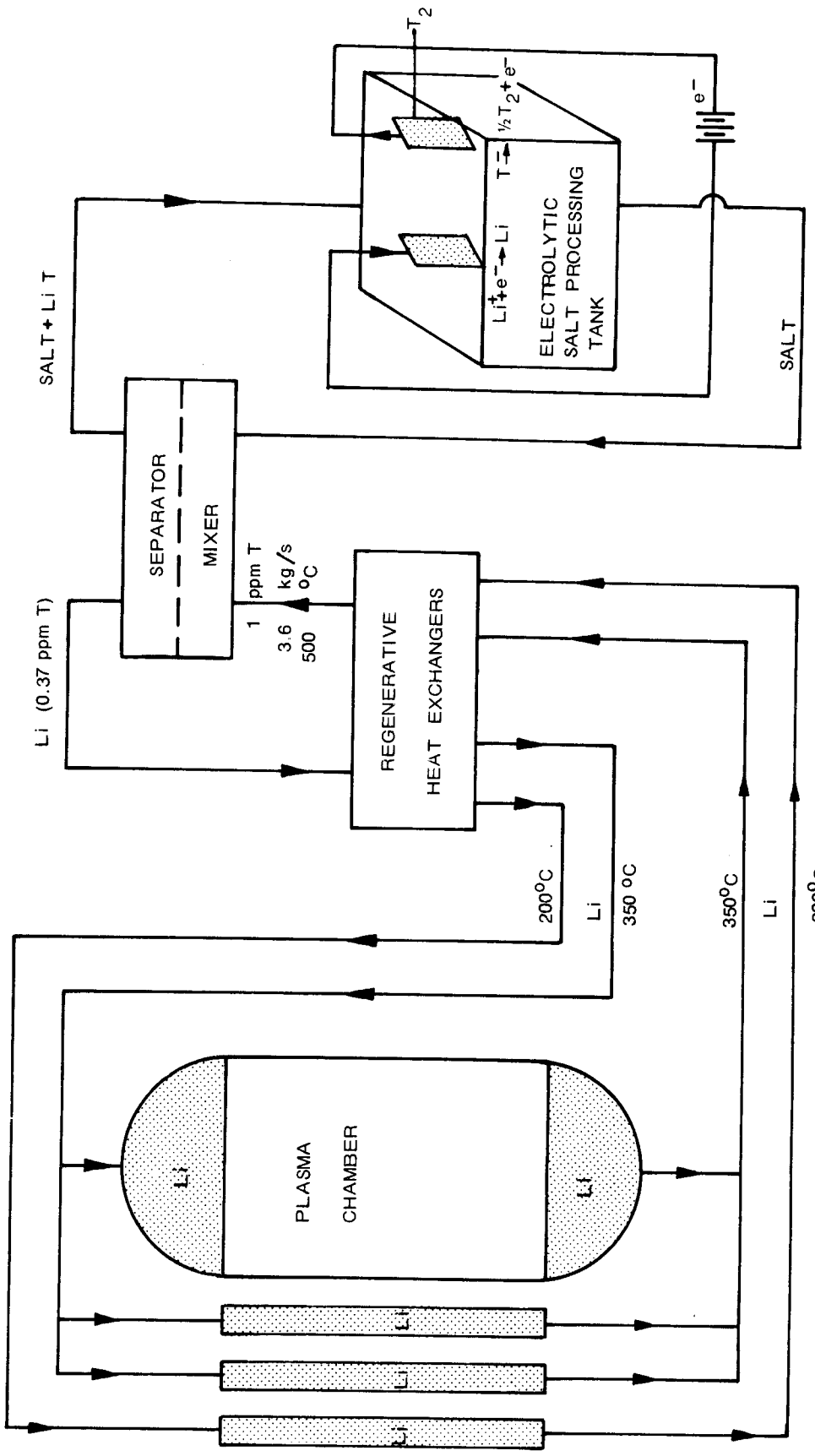

TRITIUM EXTRACTION SCHEME

Figure V.2-2

in permeabilities between different samples at comparable conditions of temperature and pressure makes it impossible to determine the temperature dependence of permeation or the effect of sample thickness on the rate of permeation. Non-reproducible oxide surface conditions probably account for the poor data. Austin et al.[11] found that the diffusion coefficient of tritium through a surface oxide layer of zircaloy is typically 8 orders of magnitude below the bulk diffusion coefficient. This shows that an oxide coating on zircaloy and undoubtedly zirconium serves as a barrier to tritium permeation. This has been verified under reactor conditions by the general observation that reactors with stainless steel clad cores have shown 50 times higher tritium activity in the coolant than those with zircaloy clad cores.[12,13] Tritium leakage to the sodium coolant may occur from the plasma through the first wall, from the lithium where tritium is bred through the tube side walls and from the fuel pins where tritium is produced by ternary fissions through the zircaloy cladding.

The first area analyzed is the tritium leakage from the plasma through the first wall. The molecular hydrogen isotope pressure in the reactor chamber is 4.0×10^{-4} torr at $500^{o}C$, the temperature of the first wall. The deuterium to tritium mole ratio in the pellet debris is 3.2 to 1. The first wall area in contact with sodium is 4.5×10^{6} cm^2. It is expected the zircaloy surface facing the reactor chamber where the pellet implodes will be in a clean, unoxidized state due to sputtering. The very poor data on unoxidized zirconium precludes a calculation of the permeation of tritium from the chamber to the sodium coolant and the permeation rate can, therefore, only be arbitrarily estimated as $\sim$ 0.1 g/day.

Tritium can also leak to the sodium from the lithium breeding zones. The first two lithium zones (350°C) in the cylindrical blanket are contained in zircaloy pins and are sodium-cooled. The lithium in the caps at 350°C is circulated to a sodium intermediate heat exchanger (Fig. V.1-1). The tritium pressure above lithium (1 wppm T or 2.3 appm T) calculated from the relation:[14]

$$\frac{(P_{T_2}\ (\text{torr}))^{1/2}}{N_T(\text{mole T/mole Li})} = \exp\left(9.226 - \frac{5085}{T(K)}\right) \qquad (2)$$

is found to be 4.5×10^{-11} torr in these lithium zones. The last lithium zone (~ 200°C) in the cylindrical blanket is helium-cooled. The low lithium temperature results in a tritium pressure of only 2.5×10^{-13} torr. The zircaloy surface facing the lithium will be unoxidized as lithium has been found[15] to reduce ZrO_2 to zirconium at 180-200°C. Because the tritium pressures in the reactor chamber are 7 to 9 orders of magnitude higher than those in the lithium, it is probable that tritium losses to the sodium from the lithium breeding zones are negligible compared to permeation from the reactor chamber.

Fast fissions in the UO_2 fuel pins account for ~ 500 to 3500 MWt of power in SOLASE-H. In general, tritium from fast fissions is produced at a rate 2.5[16] times higher than the rate of 0.0105[17] Ci/MWt•day for thermal fissions. This gives a hybrid tritium production rate of 13-91 Ci/day. It has been found that up to 1% of the tritium produced in zircaloy-clad cores is released to the coolant.[13] Thus taking 1% of 13-91 Ci/day gives a release to the sodium coolant of < 1 Ci/day (< 10^{-4} g/day). Therefore, little tritium enters sodium from the fuel pins and the tritium inventory in the sodium is due almost exclusively to losses from the plasma chamber.

The maximum partial pressure of tritium allowable in the sodium to limit tritium losses to the steam through the steam generator walls to ~ 1 Ci/day can be very roughly estimated if an oxide coating is present on the zircaloy. This is the case in the hybrid as an equilibrium oxide film is present on zirconium even at room temperature.[18] More importantly, liquid sodium contains oxygen[19] and zirconium has been found to getter oxygen from sodium.[20-23] The oxide coating on zirconium is adherent[24,25] and remains so even in a flowing sodium environment.[20,21]

Smith[26] has measured the hydrogen permeation of oxide films on zirconium and found the rate to be empirically defined by the equation

$$r = \left(\frac{1}{\delta}\right)\left(\frac{4.6\times10^{-3}P}{1+4.6\times10^{-3}P}\right)\left(4\times10^{-3}\exp\left(\frac{-43{,}000}{RT}\right)+k\exp\left(\frac{-9000}{RT}\right)\right) \quad (3)$$

where r is in moles $H_2/cm^2\cdot s$, δ is the oxide film thickness in cm, P is the pressure in torr, R is 1.987 cal/mole·K, T is the temperature in K and k can vary from 7×10^{-14} to 7×10^{-11} but has an average value of 4×10^{-12}. To employ the above equation it is necessary to know the thickness of the oxide coating. Although Austin et al.[11] have found tritium diffusion to be greatly inhibited in a 5×10^{-4} cm surface layer on zircaloy, a film thickness of only 2.5×10^{-5} cm is used here as this was the thickest film covered by Eqn. (3). The film thickness used in these calculations is less than that expected in SOLASE-H. So for a steam generator surface area of 2.8×10^{8} cm^2 and sodium temperature of 350°C (Table V.2-5) the permeation rate is 1 Ci/day (2.0×10^{-10} moles T_2/sec) if the T_2 pressure is 1.4×10^{-6} torr, or if the HT pressure is 2.8×10^{-6} torr (Eqn. (3)).

Table V.2-5

Steam Generator and Intermediate Heat Exchanger Parameters

		Steam Generator (1° Sodium Loop)	IHX (Li-to-Na)	Steam Generator (2° Sodium Loop)
Temp. (°C)	Steam	285° (1000 psi)	--	285°(1000 psi)
	Sodium	350°	350°	350°
	Lithium	-	350°	--
Area of tubes (m^2)		28,000	2,500	4,900
Wall material		Zircaloy	Zircaloy	Zircaloy

Solutions of hydrogen in liquid sodium obey Sievert's law. Sievert's constant is effectively temperature-independent in the 337 to 404°C range, and has a value of 4.6 ppm/torr$^{1/2}$.[27] Therefore, a hydrogen isotope pressure of 1.4×10^{-6} torr corresponds to only 5.4×10^{-3} ppm hydrogen or 1.6×10^{-2} ppm tritium in sodium at 350°C. If it is assumed that 0.1 g of tritium leaks into the primary sodium loop (1.0×10^{5} kg) per day (due almost solely to permeation from the reactor chamber), the 1.6×10^{-2} ppm level will be reached in only 16 days (or in 160 days for a 0.01 g/day leakage rate). Thus, it appears necessary to insert a tritium extraction unit in the sodium system.

To maintain sodium in a state of high purity the cold trap is used almost universally.[28] Cold trapping action depends upon the decreasing solubility of impurities with decreasing temperature. The cold trap is designed similar to those in EBR-II (volume = 1.1 m^3).[29-31] With a cold trap temperature of 115 to 117°C, the hydrogen concentration has been limited to between 0.06 and 0.08 ppm.[39] This system is not 100% efficient as the temperature dependence of hydrogen solubility in sodium, given by the expression [27]

$$\log n_H^S \text{ (ppm)} = 6.467 - \frac{3023}{T} \quad , \tag{4}$$

gives an expected hydrogen concentration of 0.047 ppm at 115°C. This type of efficiency, 1/2 - 3/4, has been observed for hydride cold-trapping in other large circulating sodium systems[32,33] though increasing

the sodium residence time in the cold trap gives higher efficiencies.[28,34] However, it is assumed that the hybrid has a cold trap operating at 115°C which maintains the hydrogen concentration $\leq$ 0.06 ppm with a sodium residence time in the cold trap of ~ 15 min. Tritium should be precipitated with the other hydrogen isotopes in the same ratio as they exist in solution.[34] Therefore, to maintain a tritium concentration of 0.016 ppm equivalent to 0.0054 ppm of hydrogen or a total of 0.81 moles of tritium in the sodium, there must be 11 times as many moles of hydrogen and deuterium as tritium, or for the 0.033 mole T/day (0.1 g T/day) entering the sodium there must be 0.36 mole of H and D/day entering the sodium. If 0.033 mole T/day permeate from the reactor chamber, three times as many mole of deuterium or 0.1 mole of D/day (0.2 g D/day) will also enter the sodium by permeation through the first wall so 0.26 mole of H must be added to the sodium per day. This is equivalent to 0.26 g/day which is on the order of the amount of hydrogen found entering the sodium in EBR-II/day[17,30] from sources such as steam corrosion of the steam generator components, neutron activation of reactor materials, proton emission during fast fission, impurities in the sodium cover gas, and various other sources. In Phenix[33] 6 g/day of hydrogen enter the sodium. Therefore, it appears that the quantity of hydrogen routinely entering the sodium will control the tritium concentration to acceptable levels. If less hydrogen than expected enters the sodium, the quantity necessary to control the tritium level could be injected into the sodium. Evidence that this cold trapping scheme is feasible for tritium control is shown by the results of EBR-II which show typical concentrations of

tritium in the EBR-II primary and secondary sodium systems of 2×10^{-6} to 1×10^{-5} ppm and 1×10^{-7} to 5×10^{-7} ppm, respectively.[35]

The secondary sodium loop is also purified by passage through a cold trap. Due to the low tritium pressures in the lithium in the caps (4.5×10^{-11} torr),little tritium is expected to permeate to the secondary sodium loop in any case.

Due to the large sorption capacity of zirconium for hydrogen isotopes, even at very low pressures, there is an inventory of tritium in the zircaloy structure and this inventory increases as a function of time until thermodynamic equilibrium is achieved. Calculations were made to determine the equilibrium quantity of tritium in the structure, despite the fact that the rate of approach to thermodynamic equilibrium for the conditions found in SOLASE-H is unknown. The simplifying assumption was made that the tritium inventory was due solely to the tritium pressure above the liquid lithium and the tritium pressure exerted by the plasma on the first wall, as surfaces in contact with the sodium are expected to be oxidized and represent tritium barriers. The solubility of tritium in zirconium can be extrapolated from data given in reference (36) and follows the equation:

$$\log \left(\frac{C\ (\text{wppm})}{\sqrt{P}\ (\text{torr}^{1/2})} \right) = 0.20 + \frac{3000}{T(K)} \quad . \qquad (5)$$

The parameters used in the tritium inventory calculations are given in Table V.2-6, along with the results of these calculations. Therefore, the structural tritium inventory is expected to be on the order of a kilogram. It should be emphasized that these calculations do not take into account any kinetic phenomenon.

Table V-2.6

Component	Temperature (^{o}C)	Zircaloy (tonne)	Tritium Pressure (torr)	Tritium (kg)
First Wall	500	9	$2.3x10^{-5}(T_2)$ $1.5x10^{-4}(DT)$	1.07
Zones II & IV	350	28	$4.5x10^{-11}$	0.02
Zone VI	200	36	$2.5x10^{-13}$	0.06
Top & Bottom Blanket Structure	350	85	$4.5x10^{-11}$	0.06
1 HX (Li-to-Na)	350	16	$4.5x10^{-11}$	0.01
Total Structural Tritium Inventory				1.22

References for Section V.2

1. R.W. Conn, et al., "SOLASE, A Laser Fusion Reactor Study", UWFDM-220, University of Wisconsin (Dec. 1977).

2. G.F. Hagenbach, "Gases From the Air", Argon, Helium and the Rare Gases, Vol. 11, G.A. Cook (ed.), Interscience Publishers, New York (1961), 413-436.

3. V.G. Fastovskii, A.E. Rovinskii and Yu. V. Petrovskii, Inert Gases, Israel Program for Scientific Translations, Jerusalem (1967), 101-112.

4. M.H. Cooper, "Filter for Removing Tritium From Inert Gases", U.S. Patent 3,848,067 (Nov. 12, 1974).

5. "Serfass Elhyden Mark V", Laboratory Data Control, Div. Milton Roy, Riviera Beach, Florida (1977).

6. B. Badger, et al., "TETR - A Tokamak Engineering Test Reactor", UWFDM-191, Chap.XII, University of Wisconsin (1977).

7. V.A. Maroni, R.D. Wolson, and G.E. Staahl, "Some Preliminary Considerations of a Molten Salt Extraction Process to Remove Tritium From Liquid Lithium Fusion Reactor Blankets", Nucl. Technol. 25 (1975), 83-91.

8. W.F. Calaway, "Electro-chemical Extraction of Hydrogen From Molten LiF-LiCl-LiBr and Its Application to Liquid-Lithium Fusion-Reactor Blanket Processing", Nucl. Technol. 39 (1978), 63-74.

9. R.B. Bernstein and D. Cubicciotti, "The Permeability of Zirconium to Hydrogen", J. Phys. and Colloid Chem. 55 (1951), 238-248.

10. W.M. Albrecht and W.D. Goode, Jr., "The Diffusion of Hydrogen in Beta Zirconium", BMI-1373, Battelle Memorial Institute (Aug. 25, 1959).

11. J.H. Austin, T.S. Elleman and K. Verghese, "Tritium Diffusion in Zircaloy-2 in the Temperature Range -78 to 204°C", J. Nucl. Mater. 51 (1974), 321-329.

12. P.M. Abraham, D. Chandra, J.M. Mintz, T.S. Elleman and K. Verghese, "Diffusion of Gases in Solids: Rare Gas Diffusion in Solids; Tritium Diffusion in Fission and Fusion Reactor Metals". Final report ORO-3508-10, North Carolina State University (1976).

13. H.L. Krieger, S. Gold and B. Kahn, "Tritium Released From Nuclear Power Stations", Tritium ed. by A.A. Moghissi and M.W. Carter, Messenger Graphics, Phoenix, Ariz. (1973), 557-564.

14. F.J. Smith, A.M. Batistoni, G.M. Begun, J.F. Land, "Solubility of Hydrogen Isotopes in Lithium", Report 1976, CONF-760631-1.

15. M.G. Barker, I.C. Alexander, and J. Bentham, "The Reactions of Liquid Lithium With the Dioxides of Titanium, Zirconium, Hafnium and Thorium," J. Less-Common Met. 42 (1975), 241-247.

16. J. Locante and D.D. Malinowski, "Tritium in Pressurized Water Reactors", Ref. (12), 45-57.

17. R. Kumar, "Tritium Transport in an LMFBR", ANL-8089, Argonne National Lab. (Aug. 1974).

18. E.A. Gulbransen and K.F. Andrew, "Mechanism of the Reaction of Hydrogen With Zirconium I. Role of Oxide Films, Pretreatments, and Occluded Gases", J. Electrochem. Soc. 101 (1954), 348-353.

19. J.W. Mausteller, F. Tepper and S.J. Rodgers, Alkali Metal Handling and Systems Operating Techniques, Gordon and Breach, New York (1967), 4-76.

20. A.W. Thorley and J.A. Bardsley, "Structural Changes in Materials Exposed to Liquid Sodium", J. Roy. Microsc. Soc. 88, Pt. 4 (1968), 431-447.

21. M. Davis and A. Draycott, UKAEA Report IGR-TN/C-857 (1958) as cited by M.G. Barker and D.J. Wood, "The Role of Dissolved Oxygen in the Corrosion of Titanium and Zirconium by Liquid Sodium", J. Chem. Soc. Dalton (1972), 2451-2454.

22. T.L. Mackay, "Oxidation of Zirconium and Zirconium Alloys in Liquid Sodium", J. Electrochem. Soc. 110 (1963), 960-964.

23. L.E. Chulos, "Operation Techniques Employed for the Liquid Sodium Source Term Control Loops", Proc. of the Intern. Conf. on Liq. Metal Technol. in Energy Production, M.H. Cooper (ed.), New York, Nov. 1976, CONF-760503-P1, Amer. Inst. of Mining, Metallurgical, and Petroleum Engineers, Inc., 116-119.

24. R.D. Misch, "Electrode Reactions of Zirconium Metal", The Metallurgy of Zirconium ed. by B. Lustman and F. Kerze, Jr., McGraw-Hill Book Co., Inc., New York (1955), 663-677.

25. U. Merten, J.C. Bokros, D.G. Guggisberg and A.P. Hatcher, "Thermal Migration of Hydrogen in Zirconium-Uranium-Hydrogen Alloys", J. Nucl. Mater., 10 (1963), 201-208.

26. T. Smith, "Kinetics and Mechanism of Hydrogen Permeation of Oxide Films on Zirconium", J. Nucl. Mater., 18 (1966), 323-336.

27. A.C. Whittingham, "An Equilibrium and Kinetic Study of the Sodium-Hydrogen Reaction and Its Relevance to Sodium-Water Leak Detection in LMFBR Systems", J. Nucl. Mater., 60 (1976), 119-131.

28. B.R. Grundy, "Experimental Characterization of Sodium Cold Traps and Modeling of Their Behavior", Ref. (25), P-2, 650-656.

29. J.T. Holmes and G.O. Haroldsen, "The Utilization of On-Line Monitors at EBR-II for Sodium Purity", Nucl. Technol. 21 (1974), 228-234.

30. J.T. Holmes, C.R.F. Smith and W.H. Olsen, "Sodium Technology at EBR-II", Ref. (25), 12-21.

31. J.T. Holmes, C.R.F. Smith, M.M. Osterhout, and W.H. Olsen, "Sodium Purification by Cold Trapping at the Experimental Breeder Reactor II", Nucl. Technol. 32 (1977), 304-314.

32. C.G. Allan, "Impurity Deposition in PFR Plugging Meters and Cold Traps", Ref. (25), 22-29.

33. A. Lacroix, "Some Aspects of Sodium Technology Issued From the Operating Experience of Rapsodie and Phenix", Ref. (25), 1-11.

34. C.C. McPheeters and D. Raue, "Control of Tritium in LMFBR Sodium by Cold Trapping", Ref. (25), 298-303.

35. C.R.F. Smith, W.J. Richardson and J.T. Holmes, "On-Line Sodium and Cover Gas Purity Monitors as Operating Tools at EBR-II", Ref. (25), P-2, 770-776.

36. M. Nagasaka and T. Yamashina, "Solubility of Hydrogen and Deuterium in Titanium and Zirconium Under Very Low Pressure", J. Less-Common Met. 45 (1976), 53-62.

V.3. Structural Considerations of the First Wall

The successful design of a laser fusion hybrid reactor first wall presents a difficult challenge to the structural engineer. A bare, unprotected wall is subjected to severe thermal and mechanical loads, among them:

First Wall Loads

- Reflected laser light from pellet
- Pulsed X-rays from TN pellet burn
- Ion bombardment from pellet debris
- Pulsed neutron irradiation
- Pressure shock wave from pellet blast
- Fluid pressure from sodium coolant
- Dead weight of structure
- Thermal cycling from scheduled shutdowns

The response of the first wall to these loadings can be described as either a material or structural response.

Material Response

- Temperature response
- Swelling
- Irradiation Creep
- Thermal Creep
- Embrittlement
- Transmutation
- Sputtering

- Blistering
- Spallation
- Evaporation
- Changes in fracture toughness
- Changes in fatigue life
- Changes in elastic and thermal properties
- Corrosion

Structural Response

- Thermal stresses
- Mechanical stresses
- Stress-wave propagation
- Deformation (strain)
- Ablation
- Fatigue crack growth
- Fracture
- Crack "leak-through"
- Creep rupture
- Buckling
- Induced radioactivity

When the pellet design is fixed, for example, at: yield = 310 MJ, repetition rate = 4 sec^{-1}, then the structural engineer has the task of choosing an appropriate set of design variables which satisfies the imposed performance criteria. These design variables include:

First Wall Design Variables

- Choice of material (metal, ceramic, other)
- Thickness
- Geometry (flat, cylindrical, etc.)
- Degree of constraint (free, fixed, ...)
- Operating temperature
- Distance from pellet blast
- Coolant pressure
- Protection methods

Performance Criteria

- Will it work?
- Will it last long enough?
- Will the cost be acceptable?
- Is it safe enough?
- Is the industrial capability and data base adequate?
- Is the resource availability adequate?

To complete the picture, the structural engineer should then evaluate the different methods of protecting the first wall, for example:

First Wall Protection Schemes[1]

	Laser Light	X-rays	Charged Particle Debris	Neutro
• Gas protection[2,3]	-	✓	✓	-
• Magnetic protection[4]	-	-	✓	-
• Wetted wall[5]	✓	✓	✓	-
• Flowing liquid metal curtain[6]	✓	✓	✓	✓

To include all of the phenomena listed above would clearly be beyond the scope of this report. In fact, there is no unified analysis of first wall structural design in the literature today. However, two excellent reviews of these problems have recently been published by Kulcinski[1] and Conn.[7] In addition, Daenner and Reader[8] have developed a computer code FWLTB (First Wall Long Term Behavior) which "combines nonstationary thermoelastic analysis of the wall with long term variation of the material performance characteristics". This computer code FWLTB appears to be a major contribution to the unified treatment of first wall design.

V.3.A. SOLASE-H First Wall Geometry

The first wall and blanket structure is shown in Fig. V.3-1. Global buckling of the structure due to its own dead weight is prevented by the cellular blanket design, i.e. circumferential shells intersected by radial rib dividers. The scalloped, cylindrical shell geometry of the first wall was chosen primarily to resist the sodium coolant pressure loading of 100 psi (see Figure V.3-2). With a 2 mm thick wall and a radius of curvature of R = 12.0 cm, the tensile hoop stress, uniform across the section, is given by:

$$\sigma_{hoop} = \frac{PR}{t} \qquad (1)$$

$$= \frac{(100)(120)}{(2)}$$

$$= 6000 \text{ psi} .$$

THE SOLASE-H LASER FUSION HYBRID

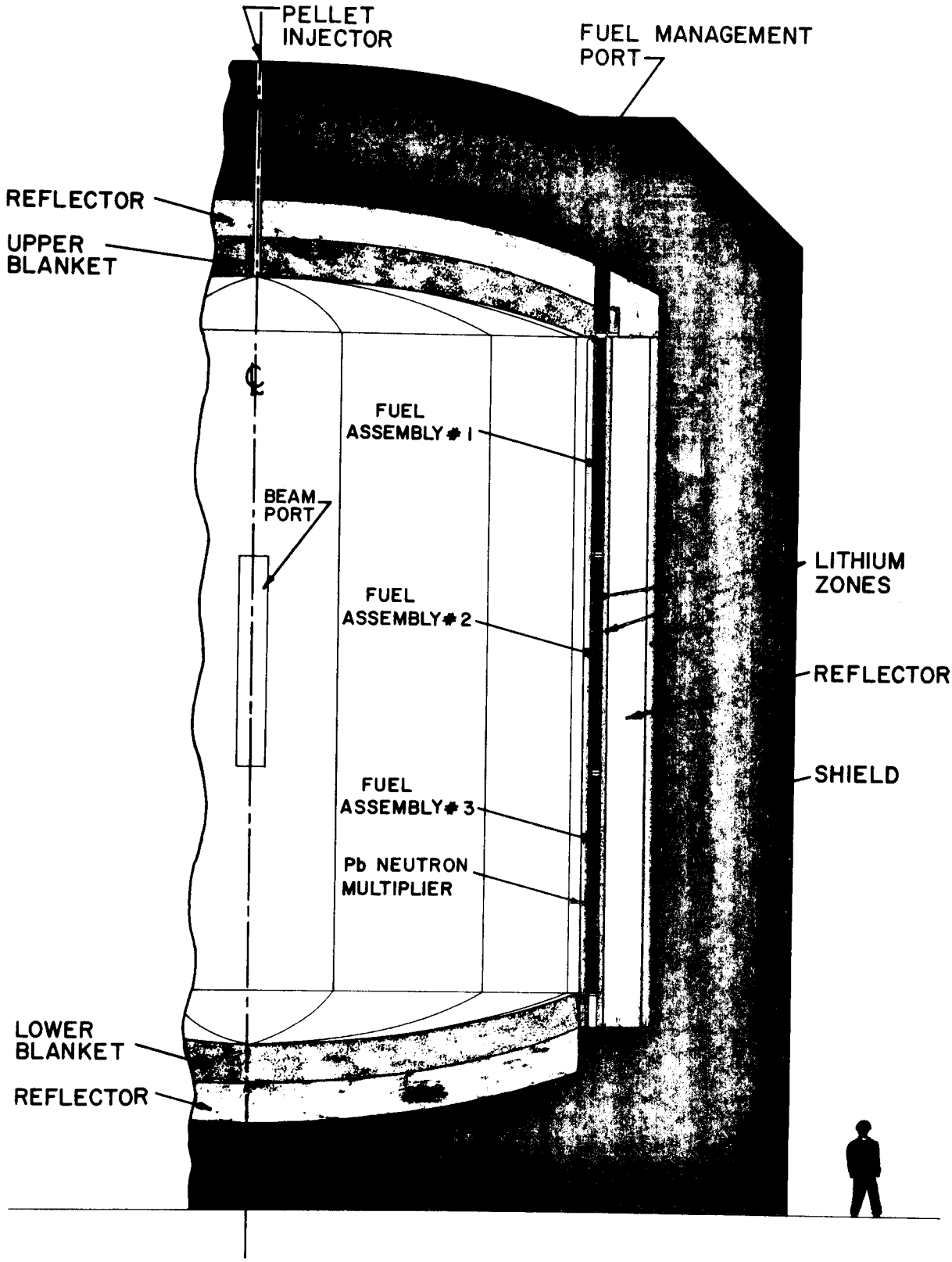

Fig. V.3-1

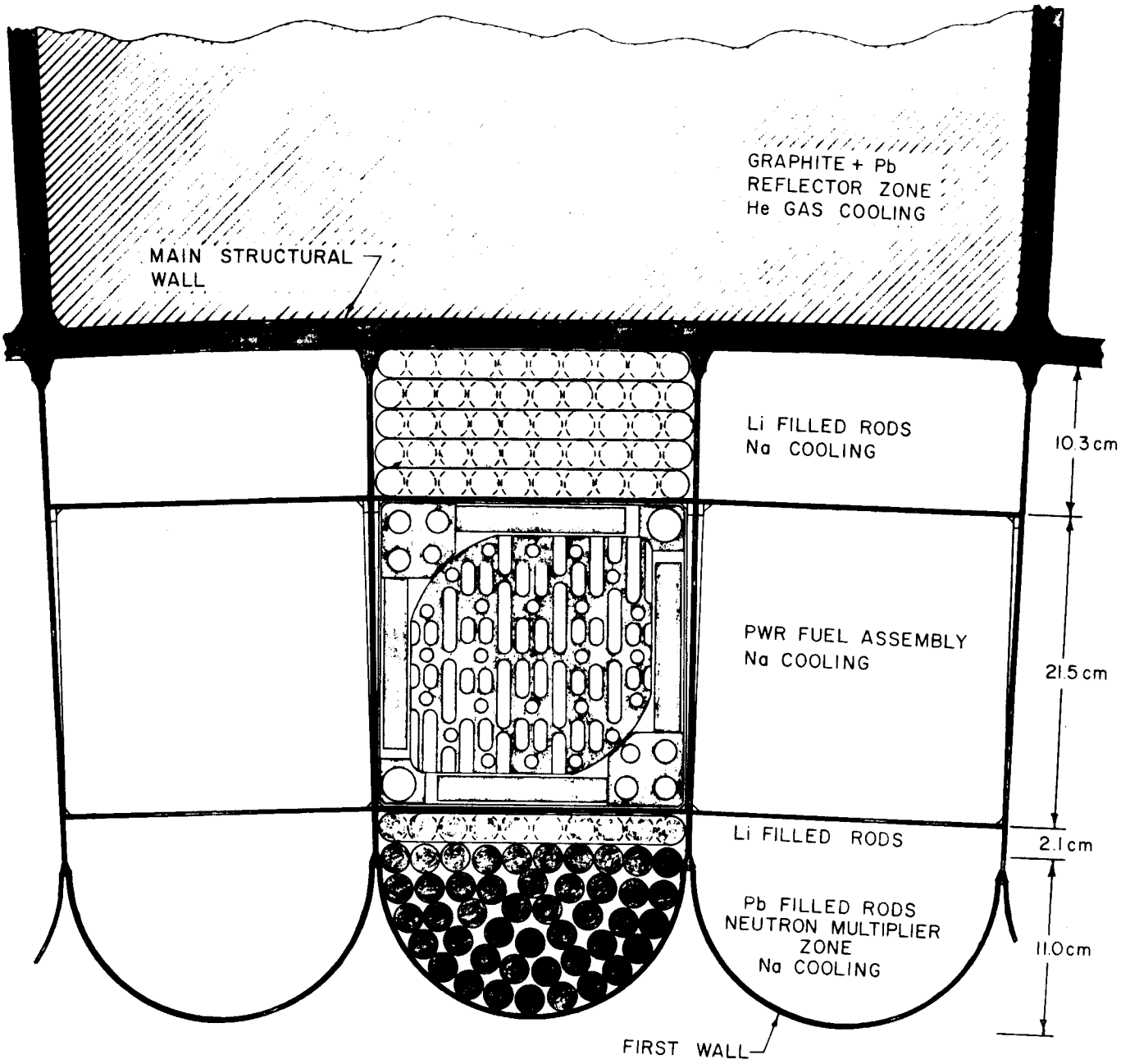

CROSS SECTION OF SOLASE-H BLANKET

Fig. V.3-2

As will be shown, this hoop stress of 6000 psi is small compared to the thermal stresses. The closest distance of the first wall to the pellet blast is 6 meters.

V.3.B SOLASE-H First Wall Protection Scheme

In order to protect the first wall, the laser cavity is filled with either 1/2 or 1 torr of xenon gas. Hunter[3] has shown that the surface temperature response from photons is substantially reduced by this. Likewise, the ΔT_s from ion deposition is reduced by a factor of ~ 2. Finally, Hunter states that displacement damage (dpa) is also significantly reduced. Without gas protection, the temperature rise of a bare, stainless steel first wall from a 100 MJ yield shot is sufficient to begin melting a first wall placed at a distance of 8 meters from the pellet blast.[7] Clearly, this would be unacceptable.

In a typical pellet blast, about 30% of the total yield appears as kinetic energy of photons and charged particles,[1] the rest (70%) going into neutron energy. Because the fast neutrons pass easily through the gas and first wall, their effect can be neglected. A second, more important assumption is that all of the remaining energy (30%) is deposited in the cavity gas. Here we assume that no ions or X-rays reach the first wall and that no laser light is reflected off the pellet. In this case, blistering and sputtering of the first wall would not be a problem.

The ionization of the cavity gas and subsequent reradiation has been described in another section of this report, as well as by Moses and Smatlak

in (9). As the gas reradiates, a transient surface heat flux is produced on the first wall, as shown in Fig. V.3-3. The peak heat flux is reached 0.2 msec after each pellet blast. A second but smaller peak is reached 1.1 msec after the blast, which is due to the arrival of the pressure shock wave at the wall. The pressure generated is only 257 torr (in the 1 torr Xe case) at the first wall and, therefore, generates negligible stresses (Fig. V.3-4).

V.3.C. Temperature Response

Given that the first wall is subjected to a transient surface heat flux as described by Fig. V.3-3 one can then calculate the temperature response for a given material. This is shown in Fig. V.3-5 for a zircaloy first wall with a constant back surface temperature of 300^{o}C. Clearly, the metal is responding adiabatically as the temperature profile peaks after only 1.5 msec. The steep gradient drops rapidly after this as the heat is conducted away to the sodium coolant on the back wall. The gradient is nearly linear for the remaining 200 msec of the total 250 msec pulse, with a difference of only 65^{o}C.

The most critical location of the first wall in terms of thermal stress is at the surface facing the incident heat flux. In Fig. V.3-6 we have plotted both the surface temperature T_s and the ΔT across the front and back surface as a function of time for a single pulse of transient heat flux (Fig. V.3-3). Here $\Delta T = T_s - 300^{o}C$. The temperature peaks after 1-6 msec and rapidly decreases to near its steady-state value after $\sim$ 50 msec. Figure V.3-7 indicates qualitatively the cyclic input and response.

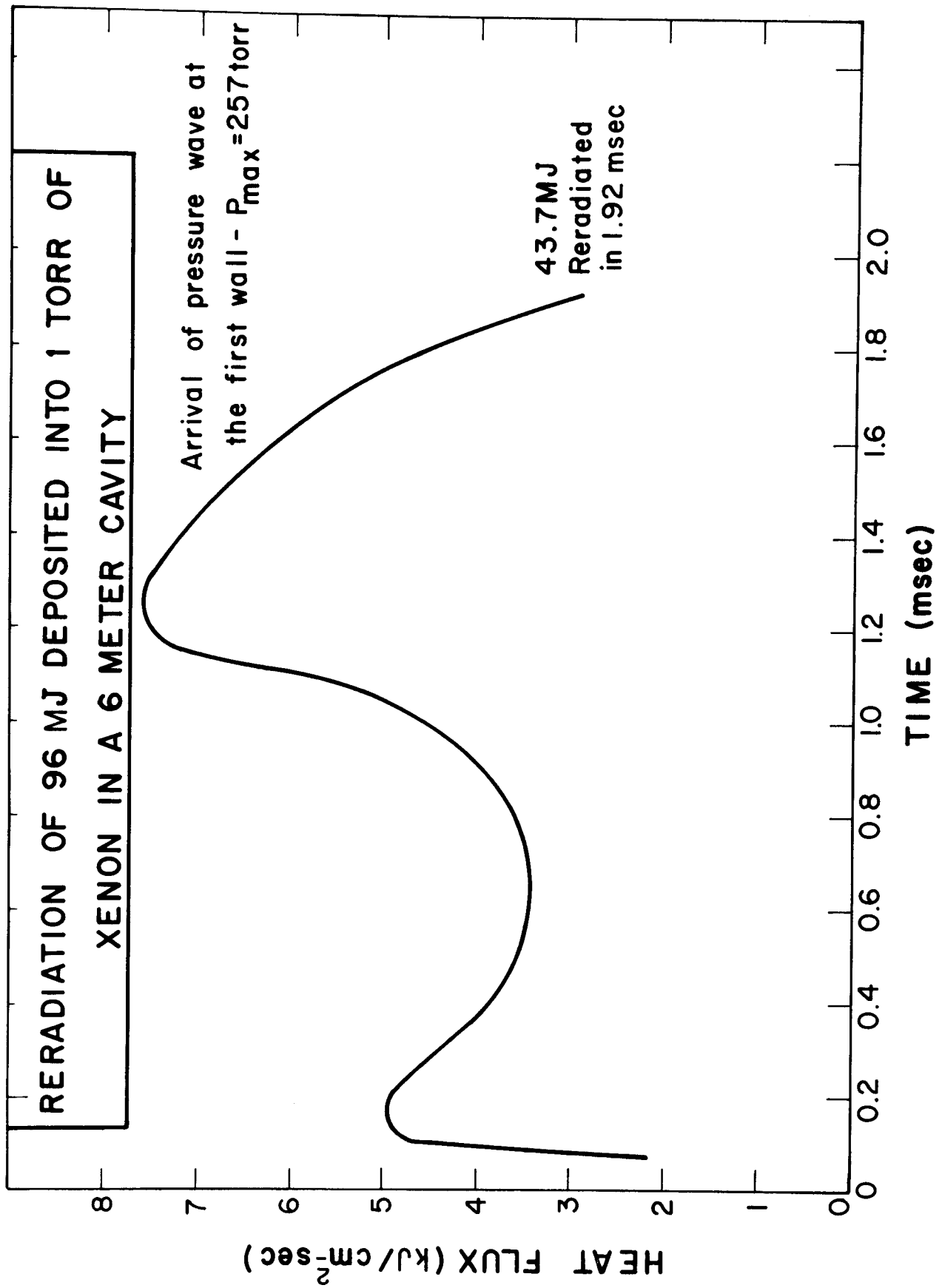
REARADIATION OF 96 MJ DEPOSITED INTO 1 TORR OF XENON IN A 6 METER CAVITY
Arrival of pressure wave at the first wall - P_{max}=257torr
43.7MJ Reradiated in 1.92 msec
HEAT FLUX (kJ/cm^2-sec)
TIME (msec)
0
1
2
3
4
5
6
7
8
0.2
0.4
0.6
0.8
1.0
1.2
1.4
1.6
1.8
2.0

Fig. V.3-3

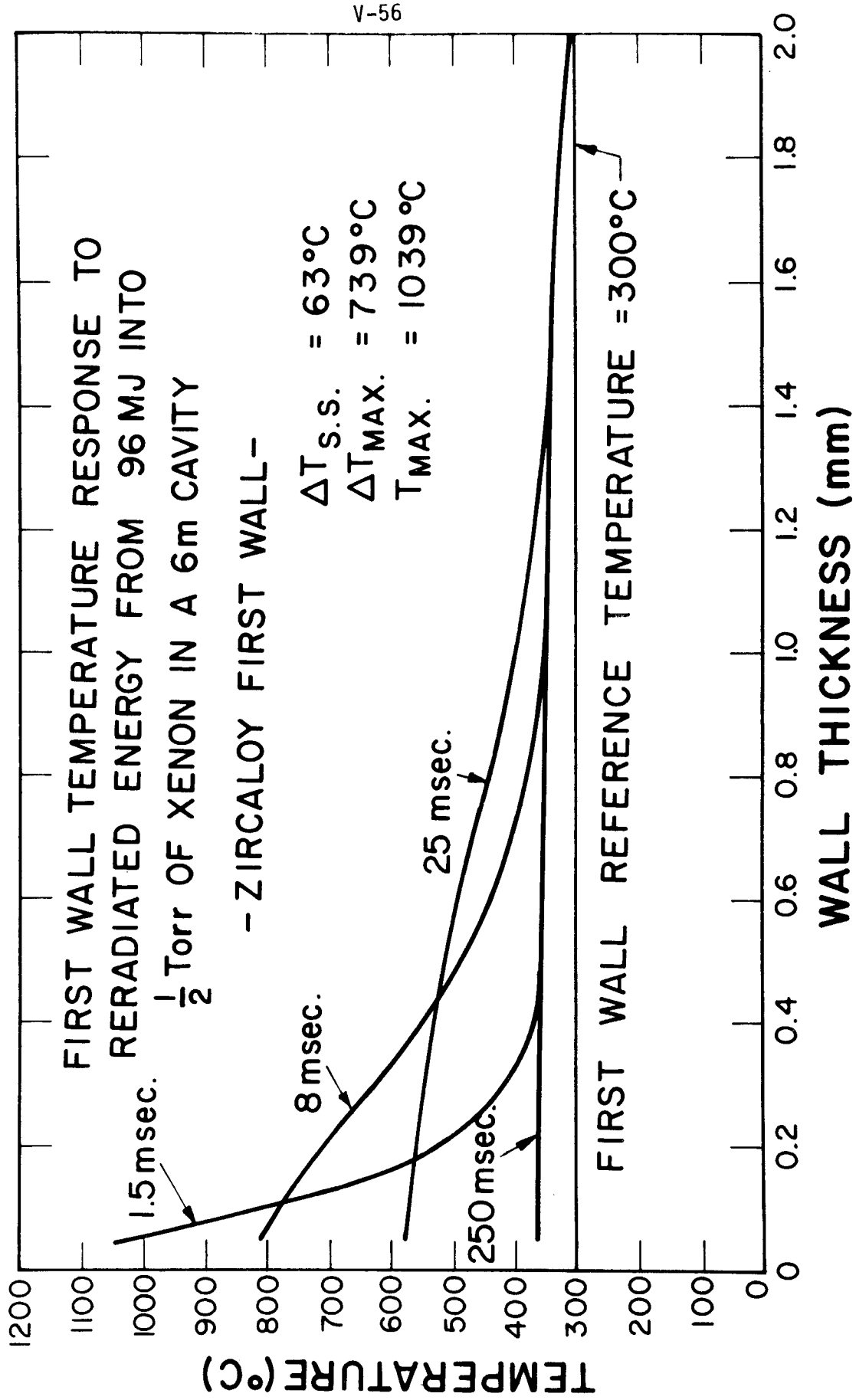
FIRST WALL TEMPERATURE RESPONSE TO
REIRRADIATED ENERGY FROM 96 MJ INTO
1/2 Torr OF XENON IN A 6m CAVITY
-ZIRCALOY FIRST WALL-
ΔT s.s. = 63°C
ΔT MAX. = 739°C
T MAX. = 1039°C
1.5 msec.
8 msec.
25 msec.
250 msec.
FIRST WALL REFERENCE TEMPERATURE =300°C
TEMPERATURE (°C)
WALL THICKNESS (mm)
0
100
200
300
400
500
600
700
800
900
1000
1100
1200
0.2
0.4
0.6
0.8
1.0
1.2
1.4
1.6
1.8
2.0

Fig. V.3-4

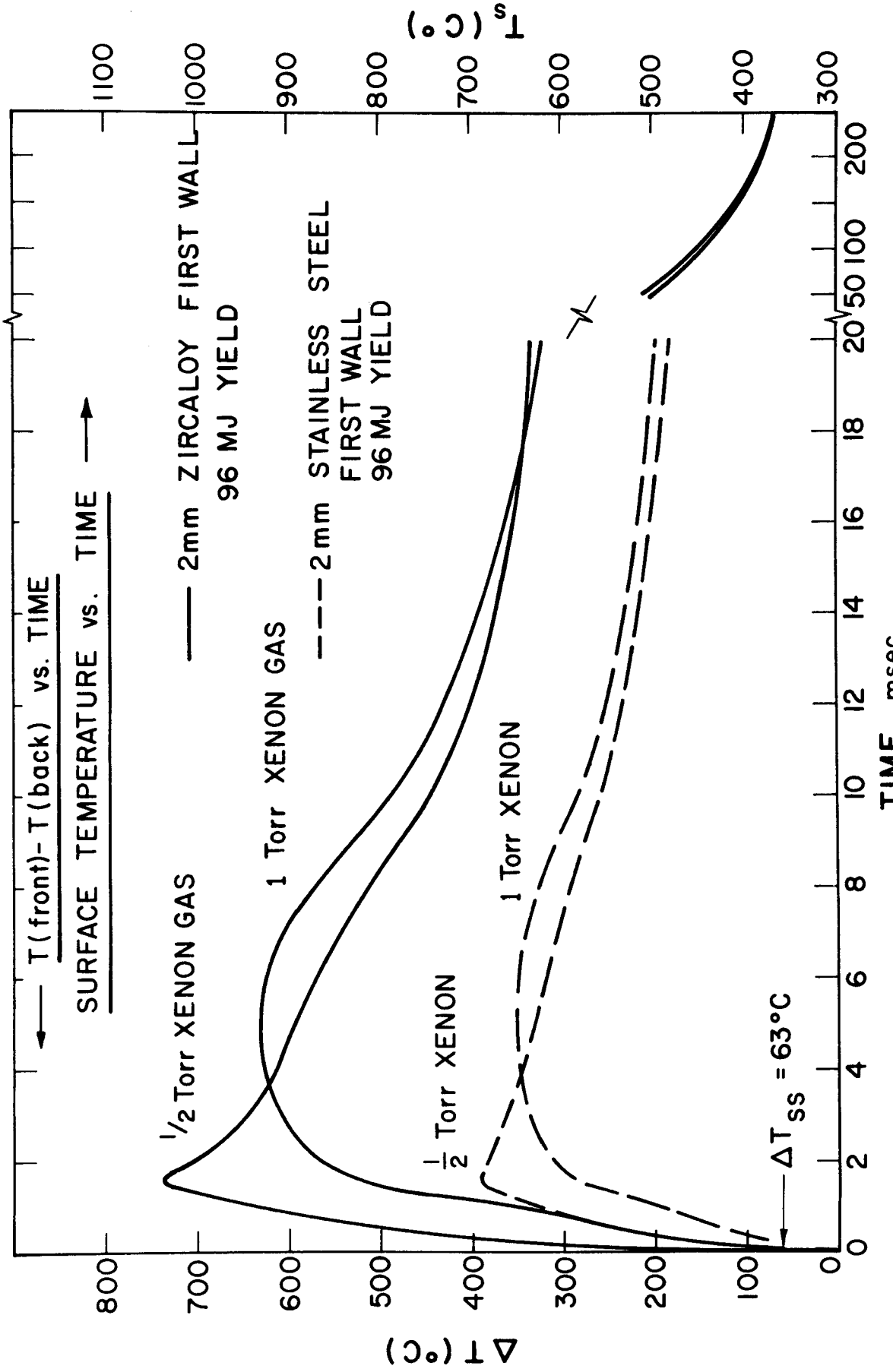
T(front)- T(back) vs. TIME
SURFACE TEMPERATURE vs. TIME
2mm ZIRCALOY FIRST WALL
96 MJ YIELD
2mm STAINLESS STEEL
FIRST WALL
96 MJ YIELD
1/2 Torr XENON GAS
1 Torr XENON GAS
1/2 Torr XENON
1 Torr XENON
ΔT ss = 63°C
ΔT (°C)
T s (C°)
TIME, msec

Figure V.3-5

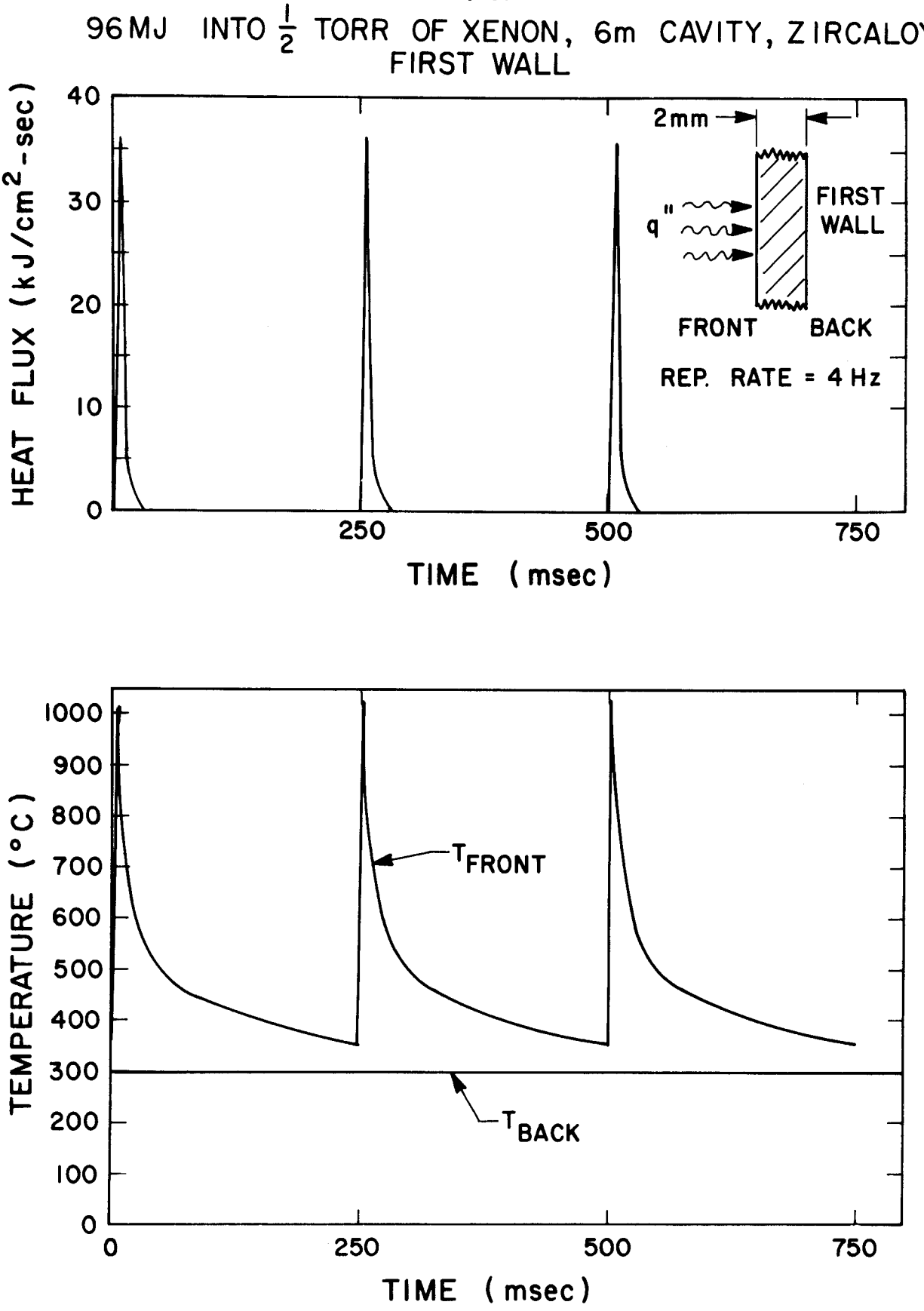

Fig. V.3-6 SURFACE HEAT FLUX AND TEMPERATURE RESPONSE OF ZIRCALOY FIRST WALL.

V.3.D. Structural Response

Now that the temperature response is known, the thermoelastic stresses in the structure can be calculated. An important question to be asked is whether or not stress waves will be generated by the rapid deposition of energy. Both Hunter[10] and Delessandro[11] have shown that no stress wave will be produced if:

a) $t_T >> t_M$

and

b) $t_q >> t_M$

where: t_T = thermal response time

t_M = mechanical response time

t_q = measure of rate of heat flux.

From Fig. V.3-5 we see that $t_T \simeq 2$ msec and from Fig. V.3-3 we find $t_q \simeq 0.2$ msec. We approximate $t_M = \delta/c$ where δ = characteristic length of temperature rise and c = speed of sound. From Fig. V.3-6 we find $\delta \cong 0.3$ mm and $c \cong 3000$ m/sec, so that

$$t_M = \frac{0.3}{3 \times 10^6} \cong 10^{-7} \text{ sec}$$

$$= 10^{-4} \text{ msec} .$$

Comparing:

a) $t_T = 2$ msec

b) $t_q = 0.2$ msec

c) $t_M = 10^{-4}$ msec .

We find indeed that $t_T >> t_M$ and $t_q >> t_M$, as required for no stress wave to be generated. Physically, this means that the material is responding much faster than the temperature changes and consequently the material is not responding inertially. Therefore, spallation from a tensile reflected

stress wave will not be a problem in gas protected first walls.

The thermal stresses were calculated by modelling the first wall as a long, axially-constrained, thin-walled cylinder with the radial temperature gradient as given in Figure V.3-4. In this case, the thermoelastic hoop stress $\sigma_\theta(r)$ is given by:[12]

$$\sigma_\theta(r) = \frac{\alpha E}{1-\nu} \frac{1}{r^2} \left[\frac{r^2+a^2}{b^2-a^2} \int_a^b Trdr + \int_a^r Trdr - Tr^2\right] .$$

where: $\sigma_\theta(r)$ = hoop stress

$T(r)$ = radial temperature distribution

a = inside radius of cylinder

b = outside radius of cylinder

α = thermal expansion coefficient

E = Young's Modulus

ν = Poisson's Ratio

The stresses calculated by this formula are shown in Figure V.3-7. In this model, we have assumed that the reference temperature is 300°C for zero stress in the first wall.

It can be seen here that the surface of the first wall which faces the pellet blast sustains a large compressive hoop stress due to the large temperature rise above 300°C. Alternatively, towards the back surface, a small tensile stress is developed so that equilibrium of the cross-section is maintained. The maximum stress occurs when the temperature rise ΔT_s at the surface peaks, at t = 1.5 msec after each pellet blast.

The net stresses in the first wall, then, are a superposition of the constant mechanical hoop stress from internal pressure and of the variable thermoelastic hoop stress described above. The effect of

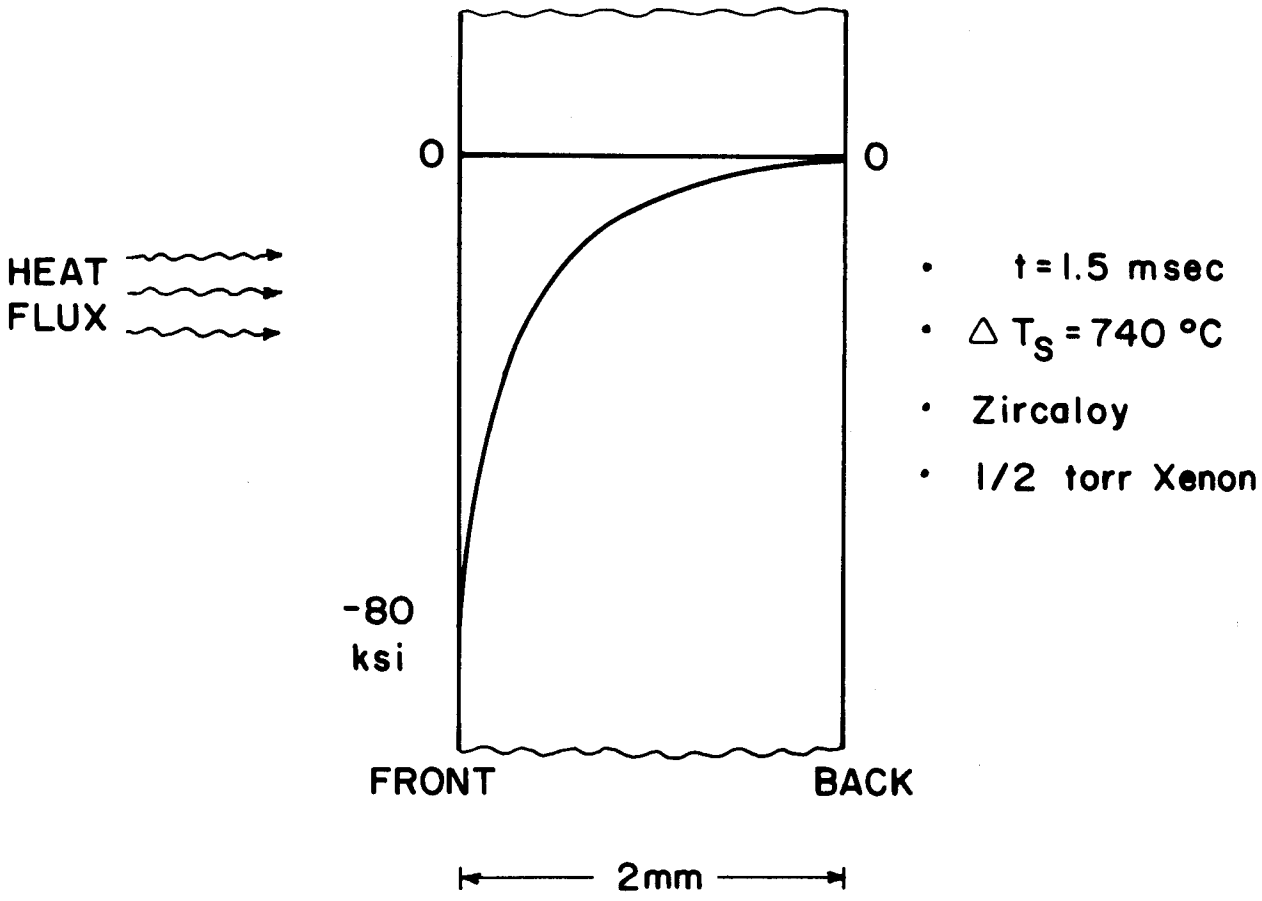

Fig. V.3-7 MAXIMUM THERMAL STRESS DISTRIBUTION IN FIRST WALL AT PEAK OF TEMPERATURE PULSE

adding a tensile 6000 psi mechanical hoop stress is to reduce the maximum compressive stress and to increase the maximum tensile stress. Schematically this is shown in Figure V.3-8. Using, then, the material properties as listed in Table V.3-1, we have listed the composite maximum hoop stresses for stainless steel and zircaloy first walls in Table V.3-2. A few important conclusions are clear from this table:

1. The large value of $\frac{E\alpha}{1-\nu}$ for stainless steel makes it clearly unacceptable because of large compressive thermal stresses which exceed the yield strength by factors of 5-6.
2. Zircaloy is marginally acceptable because the maximum net compressive stress exceedsthe yield strength by only 25 ksi in the 1 torr Xe case.
3. Increasing the xenon cavity gas pressure decreases the maximum stresses.

With the temperature "spikes" that are produced in the SOLASE-H zircaloy first wall, we would expect to develop cyclic plasticity in the regions where $\sigma_\theta \geq \sigma_y$. With the number of loading cycles equalling 3.8×10^9 cycles per 30-year lifetime, the first wall lifetime may be controlled by fatigue crack growth causing a "leak through" or fracture failure mode. Also, the phenomena of irradiation and thermal creep will cause stress redistribution in the first wall, thereby reducing the effective load-carrying cross-sectional area which increases the maximum tensile stresses as a function of time.

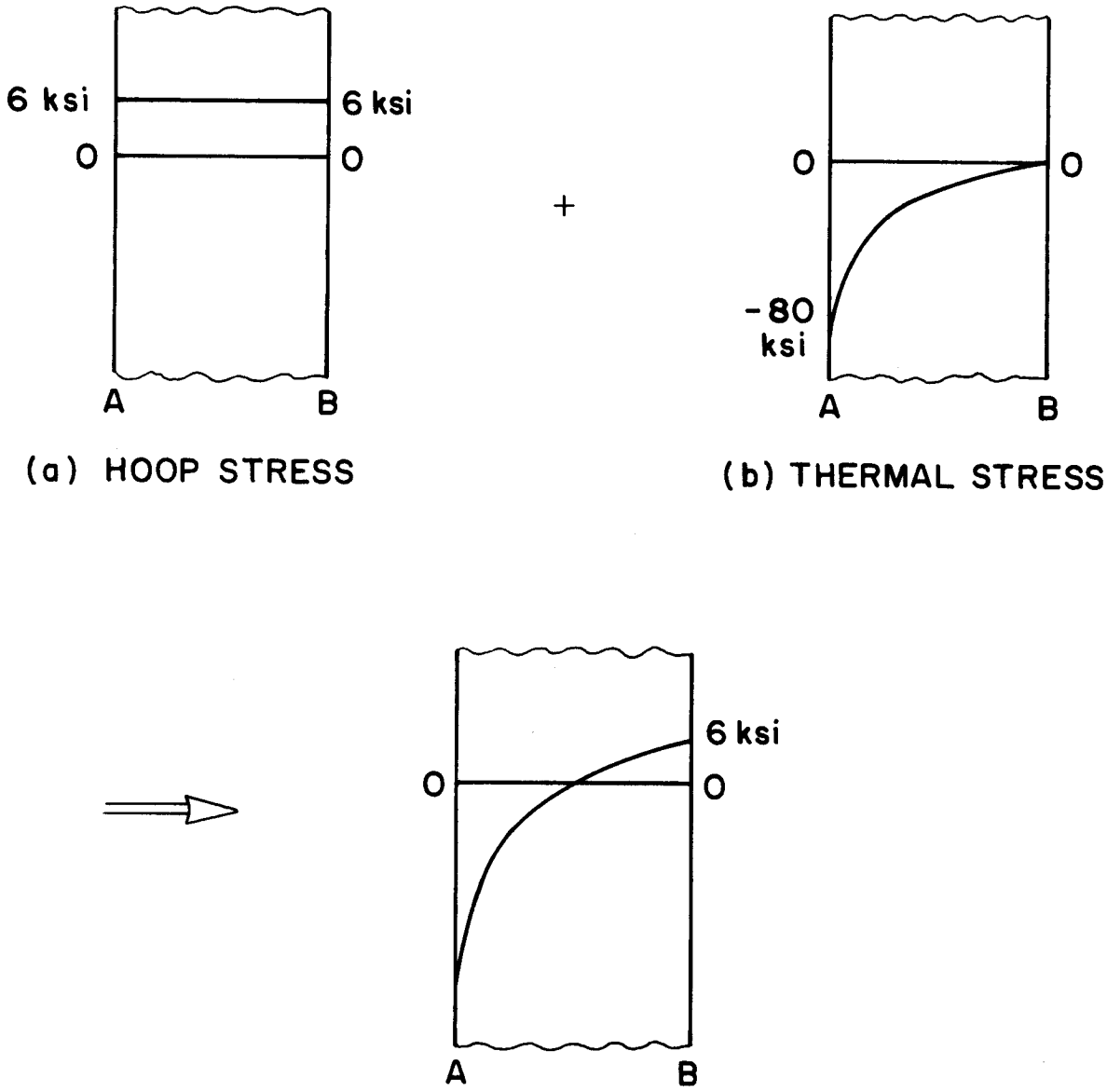

Fig. V.3-8 SUPERPOSITION OF MAXIMUM TRANSIENT THERMAL STRESS AND CONSTANT MECHANICAL (HOOP) STRESS IN FIRST WALL

Table V.3-1 Material Properties

Metal	E (psi)	α ($^{o}C^{-1}$)	k (W/cm^{o}C)	ν	σ_y(@400^{o}C) (psi)	$\frac{E\alpha}{1-\nu}$ (psi/^{o}C)
S.S.	28×10^6	18×10^{-6}	0.173	0.33	50,000	756
Zr-2	11×10^6	6.5×10^{-6}	0.125	0.33	30,000	107

Table V.3-2 Stress Summary

Metal	Xe Pressure	ΔT_{max} at surface	Maximum Net Compressive Stress	Maximum Net Tensile Stress	Yield Strength σ_y(@400°C)
S.S.	1/2 torr	390°C	-262 ksi	36 ksi	50 ksi
S.S.	1	350	-235	33	50
Zr-2	1/2	740	- 65	14	30
Zr-2	1	630	- 55	13	30

Stainless steel is a poor first choice because of its large modulus E and expansivity α. Other materials rate even better than zircaloy when compared on the basis of a figure of merit for thermal shock stresses (Table V.3-3). Delessandro has proposed[11]

$$f = \frac{\sigma_{ult} K(1-\nu)}{E\alpha\sqrt{\beta}} = \text{figure of merit}$$

where: E = Young's modulus

α = thermal expansion coeff.

β = thermal diffusivity = $\frac{K}{\rho c_p}$

σ_{ult} = ultimate strength

K = thermal conductivity

ν = Poisson's ratio

The larger value of "f" is preferred. Clearly, SiC and graphite appear to be better choices with respect to minimizing thermal stresses. Their use has been studied by Hopkins for inertial confinement reactors[14] and by Bourque for magnetic confinement reactors.[15] Graphite blocks attached to an S.S. or zircaloy first wall may be a better design.

Table V.3-3 Thermal Shock Stress Figure of Merit[11]

Material	Figure of Merit	Preference
SiC	18.7	1
Graphite	18.2	2
Zircaloy	14.2	3
Stainless Steel	0.6	4

V.3.E Summary and Discussion

The structural analysis of the SOLASE-H first wall has been described in this section. The basic model assumed that 100% of the energy of the photons and charged particles was deposited in the 1/2 Torr of xenon cavity gas. This gas then reradiates, providing a transient surface heat flux which, in turn, produces a large temperature pulse in the surface layer of the first wall. The rise time of the temperature "spike" is a relatively slow 1-2 msec, which permits the use of a quasi-steady-state stress analysis. A 2 mm thick zircaloy-2 first wall was chosen because of two important reasons. First, in comparison to stainless steel, zircaloy-2 has substantially reduced thermal stresses. A simple, thermoelastic stress calculation gave the maximum net compressive stress as -65 ksi and the maximum net tensile stress as 14 ksi for the 1/2 Torr Xe case. Fortunately, these maximum stresses only last a few milli-seconds. The quasi-steady-state stresses are -1 ksi and +7 ksi, respectively, for typically 90% of the time in one pulse.

The second reason zircaloy-2 was chosen was to minimize mass transfer of corrosion products in the hybrid blanket, which contains Zr-2 clad fuel rods.

The stresses from the pellet blast-induced pressure shock wave were found to be negligible.

Because all of the charged particles were assumed to be stopped in the cavity gas, there will be no sputtering, blistering or spallation of the first wall. Evaporation will be minimal because the peak surface

temperature is only ~ 1100°C. The effect of thermal creep may be significant in the way stresses will redistribute as a function of time (# pulses). Further work is proceeding in this area.

Effects that were not considered in this section include: irradiation creep, swelling, embrittlement, creep rupture, fatigue crack growth, fracture, cyclic material property changes and buckling. Clearly, much work is still needed to model these phenomena in a self-consistent and integrated manner.

V.3.F Conclusions

The design philosophy for the SOLASE-H blanket and cavity was to investigate the possibility of using an inert cavity gas to protect a bare metal first wall. Some important conclusions can be listed for the case of cavity radius = 6 meters, yield = 310 MJ, rep. rate = 4 sec^{-1}, gas pressure = 1/2 Torr xenon, 2 mm thick zircaloy-2 first wall:

1. Transient thermal stresses are large and compressive on the surface facing the pellet blast.
2. The response time of the cavity gas reradiation is slow enough so that no stress waves will be generated from energy deposition in the first wall.
3. The stresses from the pellet blast overpressure shock wave are negligible.
4. Increasing the cavity gas pressure from 1/2 Torr to 1 Torr will decrease the thermal stresses by ~ 15%.
5. Reducing the pellet yield will reduce the thermal stresses.
6. The first wall thickness has very little influence on the maximum thermal stresses because the pulse width of the transient surface

heat flux is $\cong$ 0.5 msec, producing a temperature rise that decays spacially by a factor of 8 over a distance of 0.3 mm. This contrasts with the design of a tokamak, where the first wall thickness is directly related to the steady-state heat flux.

7. The large temperature variations may activate thermal creep, causing relaxation of compressive stresses and growth of tensile stresses.
8. Non-metals such as SiC and graphite may give better performance due to their higher melting points and lower thermal stresses.

Therefore, to improve the lifetime of a bare metal first wall, the cavity gas pressure should be increased and the pellet yield decreased. Also, the wall thickness should be increased to reduce the hoop stress from the sodium coolant. Finally, other metals with lower values of E (Young's modulus) and α (thermal expansion coefficient) should be investigated.

In closing, the use of a xenon cavity gas protection scheme with a bare, zircaloy first wall appears to be a feasible design concept for a laser fusion hybrid reactor. Lifetime determination must await the development of more sophisticated models for irradiation effects on material and structural response.

References for Section V.3

1. G.L. Kulcinski, "The Newest Frontier in Radiation Damage Research-Laser Fusion Reactors", UWFDM-250, University of Wisconsin (May 1978).

2. R.W. Conn, et al., "SOLASE - A Conceptual Laser Fusion Reactor Design", UWFDM-220, University of Wisconsin (January 1978).

3. T.O. Hunter and G.L. Kulcinski, "Description of Response of Materials to Pulsed Thermonuclear Radiation (Part III)-Response Modification by Intermediate Gaseous Layers", UWFDM-232, University of Wisconsin (March 1977).

4. T. Frank, et al., Proc. 1st Topical Mtg. on Technology of Controlled Nuclear Fusion, G.R. Hopkins, Ed. (1974), 83.

5. L.A. Booth, et al., "Central Station Power Generation by Laser Driven Fusion", LA-4858, Vol. I (February 1972).

6. J.A. Maniscalco, W.R. Meier, and M.J. Monsler, Trans. Am. Nucl. Soc., 27 (1977), 34.

7. Robert W. Conn, "First Wall and Divertor Plate Material Selection in Fusion Reactors", UWFDM-237, University of Wisconsin (March 20, 1978).

8. W. Daenner and J. Raeder, "FWLTB - A Mathematical Model to Calculate the Lifetime of the Fusion Reactor First Wall", Proc. 3rd Topical Mtg. on Tech. of Controlled Nuclear Fusion (1978).

9. G. Moses and D. Smatlak, "Cavity Gas Response to Thermonuclear Micro-explosions in Inertial Confinement Reactors", University of Wisconsin (to be published).

10. T.O. Hunter, G.L. Kulcinski, "Description of the Response of Materials to Pulsed Thermonuclear Radiation - Part II", UWFDM-217, University of Wisconsin (September 1977).

11. J.A. Dalessandro, "First Wall Thermal Stress Analysis for Suddenly Applied Heat Fluxes", GA-A14931, Proc. 3rd ANS Topical Mtg. on the Tech. of Controlled Nuclear Fusion (1978).

12. Timoshenko and Goodier, Theory of Elasticity, 3rd ed., McGraw-Hill, Inc. (1970).

13. I.O. Bohachevsky, "Scaling of Reactor Cavity Wall Loads and Stresses"; LA-7014-MS, Los Alamos Scientific Laboratory (Nov. 1977).

14. G.R. Hopkins, et al., "An Assessment of Carbon and Silicon Carbide as First Wall Materials in Inertial Confinement Fusion Reactors", General Atomic Company, GA-A14979 (April 1978).

15. R.F. Bourque, "First Wall Conceptual Designs Using Low-Z Atomic Number Materials", Proceedings 2nd Topical Mtg. on Tech. of Controlled Nuclear Fusion (1976), 1526.

V.4. Thermal Hydraulic Considerations

A schematic diagram of the SOLASE-H cavity is shown in Fig. V.1-1. The cavity is an upright circular cylinder 6 m in radius and 12 m high with spherical end caps. The cylindrical portion of the cavity is surrounded by the fuel producing radial blanket while the end caps are used for tritium production. The fertile material is contained in standard (17 x 17) PWR fuel assemblies stacked in three layers around the cavity.

Directly behind the first wall of the radial blanket are pins of Pb clad in zircaloy followed by the breeding zone (Fig. V.1-2). The lead serves as a neutron multiplier to enhance the fissile production rate. The zone containing the LWR assemblies is surrounded in the front and rear with pins containing Li. These Li zones both breed tritium and filter thermal neutrons that might otherwise diffuse into the fuel assemblies and induce fission (Section II). Behind the LWR fuel zone and its Li filter is a Pb and carbon reflector. The reflector is followed by an outer Li zone to capture any leaking neutrons.

The radial blanket is cooled by sodium which enters at 300°C and leaves at 350°C except for the reflector and outermost tritium breeding zones which are helium cooled. One of the primary difficulties in designing the cooling and power systems for hybrid reactors with stationary blankets is the fact that the blanket multiplication increases significantly as the fissile content of the blanket builds up. For SOLASE-H the energy multiplication in the cylindrical blanket increases from an initial value of 1.57 under clean conditions (zero fissile content) to about 5.00 when all the assemblies reach a fissile content of 4%. The corresponding power swing for the entire

reactor (radial and axial blankets combined) would be from about 1600 to 3700 MWt. These values assume that 70% of the fusion power is carried away by the neutrons and that 70% of these neutrons are intercepted by the radial blanket; an energy multiplication of unity is assumed for the axial blankets. Larger power swings can take place in U/Pu systems with high fissile content. These power swings are obviously undesirable inasmuch as the cooling and power systems would have to be designed to accommodate the highest power output and will operate "full capacity" for only a small fraction of the time. The economic penalty associated with the overdesign problem along with these cyclical variations of power on grid design make it necessary to devise a fuel management scheme which would minimize these power swings without significant effect on plant availability. The thermal hydraulic parameters for the equilibrium cycle of SOLASE-H are discussed below.

V.4.A. Equilibrium Cycle for SOLASE-H

In order to reduce the power swings resulting from variations in the fissile content of the blanket, a fuel management scheme is devised so that 25% of the fuel inventory reaches the final enrichment (4%) and is removed at the scheduled shutdown time. This fuel is replaced by fresh fuel assemblies so that at the beginning of the equilibrium cycle there would be four batches of fuel in the blanket with average enrichment of 0, 1, 2, and 3%. Each of these batches is equal to 25% of the fuel inventory. At the end of the equilibrium cycle the average enrichments would be 1, 2, 3, and 4% respectively. Since the blanket multiplication varies nearly linearly with time, its values at the beginning and end of the equilibrium cycle will be 2.86 and 3.72 respectively. The corresponding power swing for the entire reactor is 2400-2900 MWt,

i.e. the thermal power output of the reactor will vary by approximately ±10% from its average value of 2650 MWt. The equilibrium cycle is reached after about 2 years of continuous operation from startup (0.75 • time to reach 4% enrichment). Power values at different times are listed in Table V.4-1.

V.4.B. Power Distribution in SOLASE-H Blanket

In addition to the temporal variations in the thermal power output of the reactor, the power density (W/cc) in the radial blanket varies radially and axially. The radial variation is caused by flux attenuation while the axial variation results from the isotropic point source at the center of the cylindrical cavity. Table V.4-2 lists values of the power generated within the different zones of the radial blanket for the clean condition (time=zero) and for the beginning and end of the equilibrium cycle; these values have been integrated over the entire length of the blanket (12 m). These values assume that except for the fuel region, the power generated within the different zones remains unchanged as the enrichment builds up in the fuel assemblies. Zones 1 thru 8 are sodium cooled with inlet and exit temperatures of 300 and 350°C respectively. The sodium flow rates and average velocities in the different zones are given in Table V.4-3. These values are somewhat lower than those encountered in LMFBRs; the highest value is only 6.5 m/sec and occurs in the fuel zone at the end of the equilibrium cycle.

The coolant velocity distribution within the fuel zone is given in Table V.4-4. These values are computed using the radial power distribution shown in Fig. V.4-1. The axial distribution is assumed to remain unchanged.

Table V.4-1

Power Variation for SOLASE-H

Initial Thermal Power (clean conditions)	1610 MWt
Initial Blanket Multiplication	1.57
Equilibrium Cycle Power	
- Initial	2390 MWt
- Final	2920 MWt
Equilibrium Cycle Multiplication	
- Initial	2.86
- Final	3.72
Average Thermal Power	2655 MWt
Percent Variation	±10%

Table V.4-2

Power Distribution Within the Radial Blanket

Zone #	Thickness (cm)	Power, (MWt) t=0	$t^*_{initial}$	t^*_{final}
1. First Wall	0.2	←	9.43	→
2. Neutron Multiplier	11.0	←	176.9	→
3. Lithium Filter (front)	2.1	←	41.2	→
4. Back Wall (front)	0.2	←	4.66	→
5. Fuel Zone	21.4	545.4	1329.0	1849.0
6. Back Wall (rear)	0.2	←	1.44	→
7. Lithium Filter (rear)	10.25	←	84.8	→
8. Support Wall	2.0	←	6.03	→
9. Reflector	70.0	←	79.5	→
10. Outer Lithium Zone	13.0	←	6.59	→

*Equilibrium Cycle Values

Table V.4-3

Sodium Flow Rates and Average Velocities in Radial Blanket Zones

Zone #	Na Flow Rate (kg/sec) t=0	$t_{initial}$*	t_{final}*	Na Av. Velocity t=0	$t_{initial}$*	t_{final}*(m/
2. Neutron Multiplier	←	2.72×10^3	→	←	4.34	—
3. Lithium Filter (front)	←	6.34×10^2	→	←	3.87	—
5. Fuel Zone	8.40×10^3	2.05×10^4	2.85×10^4	1.92	4.68	6.51
7. Lithium Filter (rear)	←	1.31×10^3	→	←	2.12	—

*Equilibrium Cycle Values

Table V.4-4

Coolant Velocity Distribution Within Fuel Zone

Zone	Thickness (cm)	Flow Area (cm^2)	Coolant Velocity (m/sec) t=0	$t_{initial}$*	t_{final}*
5.1 (front)	3.0	6.87×10^3	3.10	7.55	10.5
5.2	↓	6.87×10^3	2.56	6.24	8.68
5.3	↓	6.93×10^3	2.13	5.19	7.22
5.4	↓	6.99×10^3	1.79	4.36	6.07
5.5	↓	6.99×10^3	1.54	3.75	5.22
5.6	↓	7.04×10^3	1.34	3.27	4.54
5.7 (rear)	3.4	7.99×10^3	1.19	2.90	4.03

*Equilibrium Cycle Values

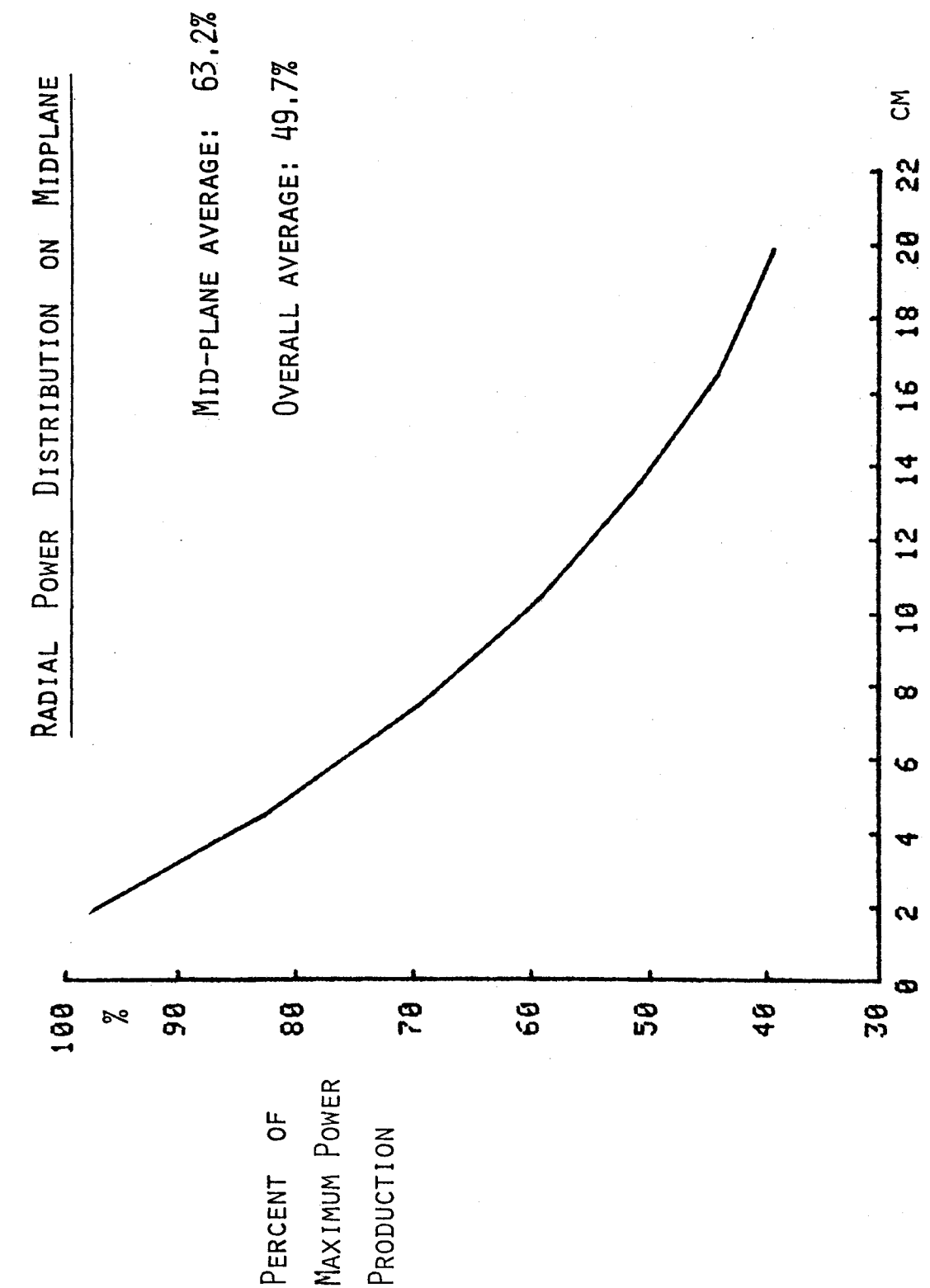
RADIAL POWER DISTRIBUTION ON MIDPLANE
MID-PLANE AVERAGE: 63.2%
OVERALL AVERAGE: 49.7%
PERCENT OF MAXIMUM POWER PRODUCTION
100
%
90
80
70
60
50
40
30
0
2
4
6
8
10
12
14
16
18
20
22
CM
RADIAL DISTANCE IN FUEL ASSEMBLY ZONE

Fig. V.4-1

The maximum value occurs in the front region of the fuel zone at the end of the equilibrium cycle and is equal to 10.5 m/sec. Orificing will be used to tailor the velocity distribution within the blanket while the temporal variations in power will be accommodated by varying the pump speed. The frictional pressure drop along the stacked fuel assemblies can be computed directly from the average velocity values given in Table V.4-4. These pressure drops are tabulated in Table V.4-5. The overall pressure drop within the radial blanket will be nearly equal to the frictional pressure in the front zone, hence, the maximum pressure drop is equal to ~240 psi. This means that the blanket inlet pressure will be approximately 250 psi. The hot sodium leaving the blanket at ~10 psi will be pumped through the intermediate heat exchanger before returning to the blanket. The pumping power corresponding to the maximum pressure drop in the blanket is equal to 48 MWe.

Table V.4-5

Frictional Pressure Drop Along Fuel Assemblies

Zone	Thickness (cm)	Pressure Drop (psi) t=0	$t_{initial}$*	t_{final}*
5.1 (front)	3.0	28.9	137.0	244.0
5.2		20.6	98.1	174.9
5.3		15.0	71.1	126.7
5.4		11.0	52.4	93.5
5.5		8.5	40.3	71.8
5.6		6.6	31.7	56.3
5.7 (rear)	3.4	5.4	25.7	45.7

*Equilibrium Cycle Values